Chiral complexes in catalysis and non-linear optics : study of non-linear effects in asymmetric catalysis and of sum-frequency generation

Yannick Geiger

UNIVERSITÉ DE STRASBOURG

ÉCOLE DOCTORALE DE PHYSIQUE ET CHIMIE-PHYSIQUE

Institut de Physique et Chimie des Matériaux de Strasbourg (IPCMS)

THÈSE présentée par :

Yannick GEIGER

soutenue le : **06 décembre 2019**

pour obtenir le grade de : **Docteur de l'université de Strasbourg**

Discipline/ Spécialité : Chimie

COMPLEXES CHIRAUX EN CATALYSE ET OPTIQUE NON-LINÉAIRE

Étude d'effets non-linéaires en catalyse asymétrique et de génération de somme de fréquences

THÈSE dirigée par :

M. BELLEMIN-LAPONNAZ Stéphane Directeur de recherche CNRS, IPCMS, Université de Strasbourg

---

RAPPORTEURS :

M. GADE Lutz Professeur, Anorgan.-Chem. Institut, Universität Heidelberg

Mme SCHULZ Emmanuelle Directrice de recherche CNRS, ICMMO, Université Paris Sud

---

AUTRE MEMBRE DU JURY :

Mme DESAGE-EL MURR Marine Professeure, Institut de Chimie, Université de Strasbourg

---

À Wolfgang & Silvia.

À ma beauté des dunes.

Remerciements

Ces travaux ont été réalisé à l'Institut de Physique et Chimie des Matériaux de Strasbourg (IPCMS), au sein de l'équipe du Département des Matériaux Organiques (DMO). Ils concluent presque 4 ans de travail au laboratoire.

J'aimerais tout d'abord exprimer ma plus profonde gratitude à Stéphane Bellemin-Laponnaz pour m'avoir guidé et accompagné pendant cette aventure. Je ne pourrais pas imaginer de meilleur encadrant que toi. Ça a été une grande aventure scientifique pour nous deux et je suis heureux de pouvoir encore continuer avec toi sur cette voie pendant un moment.

J'aimerais également exprimer ma profonde gratitude envers Thierry Achard, qui m'a également encadré tout au long de mon travail, surtout pendant mes débuts à la paillasse. Tu es un mentor inégalable, autant sur le point scientifique que sur tellement d'autres… !

Puis, je tiens à remercier l'équipe du DMO pour m'avoir aidé et soutenu, surtout la Team Bellemin. À commencer par Marco, qui pendant mes débuts en stage de Master 2 a su me motiver, à Mathilde, Damien, Maya et Julien. J'aimerais remercier aussi le personnel technique du DMO, à commencer par l'invincible Benoît Heinrich (le nombre de fois où tu m'as monté, réparé qqc ou aidé avec une bricole… !), Nicolas Beyer et les Émilies. Merci à Marion, Matthieu, Sophie, Anna, Janah, aux stagiaires avec qui j'ai travaillé et aux autres collègues. Merci aussi à Nicolas Del-Giudice pour son optimisme et sa capacité à être fasciné sans fin, à Senthil pour de nombreuses discussions intéressantes et un excellent curry, et merci à Melania pour les super moments qu'on a passé ensemble !

J'aimerais également remercier mes collaborateurs, à commencer par l'équipe SFG à l'IPCMS: Grégory Taupier pour m'avoir initié au projet, Alex Boeglin pour son temps et sa patience (expliquer la mécanique quantique à un chimiste moléculaire comme moi, c'est pas gagné!) et Honorat Dorkenoo ; Olivier Crégut et Pauline Gosset, sans qui je n'aurais jamais appris à utiliser la manip d'optique ; Bruno Vincent du service de RMN du Campus Esplanade qui a bien voulu enchainer mes demandes de DOSY; Emeric Wasielevski de la plateforme RMN de Cronenbourg pour son soutien permanent; Matthieu Chessé de l'ECPM qui m'a énormément aidé avec des problèmes de HPLC et de GC (et qui m'a mis le polarimètre à disposition); Matthias Pauly pour m'avoir laissé utiliser le spectro CD de l'ICS (et puis en plus pour avoir été un super collègue en enseignement) et Jean Muller pour me l'avoir réservé ; Ulrich, Guillaume, Guillaume #2, Felipe, Olalla, Martin Brinkmann et Aziz Dinia pour l'organisation du Congrès des Doctorants (c'était beaucoup de travail, mais qu'est-ce que c'était bien !) ; le personnel administratif de l'IPCMS qui a toujours été au taquet.

J'aimerais remercier aussi les organismes financiers : l'Université de Strasbourg pour une bourse de thèse, sans laquelle ce doctorat n'aurait pas eu lieu, et puis le Labex NIE pour nous permettre de continuer nos travaux pendant encore un petit bout de temps.

Cette aventure qu'a été la thèse n'est finalement que le dernier acte d'une pièce en plusieurs parties qu'est la vie étudiante. Cette pièce a commencé il y a huit ans quand je suis arrivé à Strasbourg. De nombreuses personnes m'ont accompagné, marqué et inspiré. J'aimerais remercier les enseignants que j'ai eu, surtout Aline Maisse-François qui m'a connu au tout début, bien avant qu'on devienne collègues de labo et de faculté ; Patrick Pale et Jean-Marc Weibel pour m'avoir ouvert les yeux sur la chimie organique ; Frédéric-Georges Fontaine de l'Université Laval à Québec pour m'avoir montré le monde fabuleux des métaux.

Et puis les amis… vous êtes trop nombreux pour que je vous cite tous ici mais au cours de ces 8 ans de vie étudiante on a passé tellement de bons moments ensemble, vous m'avez doré ma vie à Strasbourg et vous m'avez permis de grandir et d'aller au-delà de ce que j'ai pu être avant. Lucas, Mayou, Guigui, Laura, Thibault, Élodie, Coco, Morgane, Nathan, Julie, Benji, Erika, Steuh, Alexandra, Ian, Émeu, Fred, Gilles, Keupon, Jonath et puis encore tant d'autres… Merci à vous tous !

Fritz, Til, Marcel, unsere gemeinsame Zeit fing vor dem Studieren an und wird auch noch lange danach währen. Auch das hätte ich mir früher nicht erträumt. Danke für alles, danke für den Halt den ihr mir gegeben habt über diese Jahre und ich freu mich auf den nächsten der mit dem PhD dran ist! Und auf die nächste Runde Hungry Hungry Felhound in meiner Bude, und auf ein nächstes Mal Hong Kong, und und und… Patrick, Anna, Christina, Philippe, Xixi euch möcht ich auch nicht missen, danke euch allen!

Un grand merci à l'ASCS Athlétisme pour m'avoir procuré un environnement non seulement pour faire du sport, mais aussi des rencontres ! On n'oubliera pas le cadeau bonux et les compétitions sportives, qui m'ont été d'un grand soutien moral lors de mon stage de Master 2.

Pour finir, *special thanks* à Alcanes. Je ne peux pas m'imaginer ce que c'est d'être étudiant sans cette communauté, sans vous… !

Et finalement, *very special thanks* à Thomas Holstein. Frère Viking, nos domaines ne pourraient être plus loin l'un de l'autre, mais ta passion pour le tien m'a inspiré chaque fois qu'on s'est vu, que ce soit à Québec ou dans le sud, et toujours aux moments où j'en avais besoin. On a partagé une aventure et on en partagera encore d'autres, j'en suis certain. *Fuego !!!*

“Theory without practice is fantasy, but practice without theory is blind.”

Vincent Ostrom

Summary

General Introduction

At university, most chemistry students will probably get in contact with chirality during their initial courses about atoms and molecules, or during their first organic chemistry course. Chirality is presented there as the result from four different substituents on a tetrahedral carbon atom or of blocked movements around a rotational axis. The example of thalidomide (sold in West Germany under the name *Contergan*), whose *R*-enantiomer is a sedative and whose *S*-enantiomer is teratogen, is often cited to illustrate the importance of chirality in organic molecules and the control of chirality in organic synthesis. However, the concept and the implications of chirality go far beyond symmetry planes and stereogenic centres.

Chirality is defined, in a very general sense, as a system or object which exists in two different, enantiomeric states which can be interconverted by space inversion but not by time reversal.[1] This definition accounts for chiral motions as well as for 3D structures. For chemists, it is the latter which matters most, as it confers objects a high *spatial specificity*. Only chiral molecules have a structure which affords three different spatial axes to define them. This is exemplified by Figure 1: the bear and its mirror image are identical, except that their z-axis is inverted. Therefore, an *oriented* z-axis is necessary to spatially describe the bear, in addition to oriented x- and y-axes. For an achiral object, $z_1 = z_2$ since it is superimposable with its mirror plane. In this case, the z-axis' orientation is unimportant and its spatial configuration *less specific*.

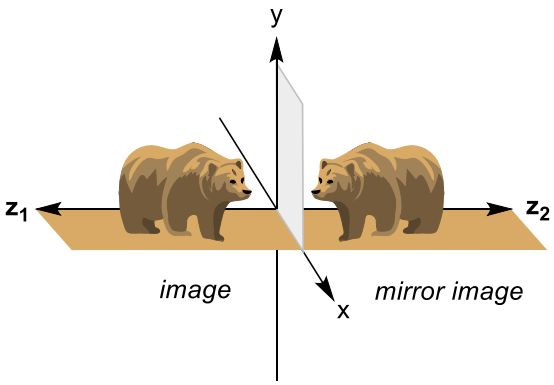

Figure 1: Illustration of the spatial specificity of chiral objects. Since the bear is chiral, its spatial configuration affords an oriented z-axis which is inverted in its mirror image.

The point where chirality comes into play for chemistry is that, the more molecules are well-defined in space, the more diverse are the interactions between them. Spatial specificity can lead to more specific interactions, which is important for chemical selectivity and information transfer. This is the reason why nature has chosen to encode biological information in chiral molecules and why proteins are particularly efficient (asymmetric) catalysts.

However, the spatial specificity of chiral molecules has not only an impact on molecular interactions, but also on light-matter interactions and physical properties. An example is the well-known difference of absorption of left- and right-handed polarised light in circular dichroism (CD), but it allows also to distinguish between "spin up" and "spin down" in electron transfer processes (chirality-induced spin selectivity, CISS)[2] and leads to the emergence of new phenomena in single molecule magnets (magneto-chiral effect).[3]

This PhD thesis will attempt to account for the vast implications of chirality on science by addressing two different domains: non-linear effects (NLEs) in asymmetric catalysis and sum-frequency generation (SFG) in non-linear optics. The first is based on specific (diastereoisomeric) interactions between chiral catalysts, which gives rise to new phenomena like chiral amplification. We will first study a catalytic system showing a new type of NLE (i.e. *Hyperpositive* NLE, Chapter I) and then have a look at the effect of metallopolymers as catalysts on NLEs (Chapter II). Finally, we will use chiral metallopolymers to study chiral SFG, which is one of the few non-linear optical phenomena allowed in certain conditions (e. g. isotropic media), due to the spatial specificity of the chiral substrate, and which might be useful as a tool in chiral microscopy. We will give an introduction, present and discuss the results we have obtained and conclude on each of the three subjects.

Chapter I: Hyperpositive Non-Linear Effects

I.1 Introduction to Non-Linear Effects in asymmetric catalysis

I.1.1 Early studies: diastereomeric interactions

Today, the synthetic chemist has various ways to obtain enantioenriched chiral products: racemic synthesis followed by separation of the enantiomers, "chiral pool" synthesis starting from natural, enantiopure molecules, enantioselective synthesis using chiral auxiliaries, biocatalysis or enantioselective catalysis. The latter is the most elegant method: the chiral catalyst transfers its chiral information to the prochiral substrate and allows an enantioselective reaction with the reactant, followed by release of the enantioenriched product. The catalyst can then engage in a new catalytic turnover (Figure 2). It requires a catalytic amount of chiral auxiliary, in contrast to the stoichiometric enantioselective synthesis, and may avoid the multiple (de-)protection and functionalisation steps often needed when starting from a chiral pool.

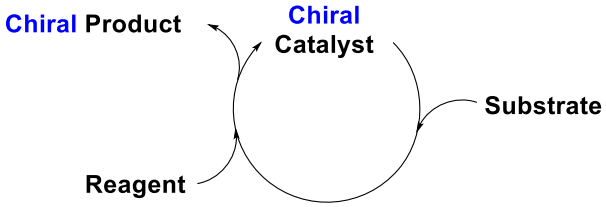

Figure 1: General scheme for enantioselective catalysis

In order to obtain the product with an optimal enantiomeric excess (ee), it seems logical to use an enantiopure catalyst. Equation (1) gives the linear relation between the product's enantiomeric excess (ee_P), the ligand's enantiomeric excess (ee_L, as we will consider only metallic catalysts with a chiral, organic ligand) and the maximal product enantiomeric excess which can be achieved for a given catalytic system (ee_{max}).

$$ee_P = ee_{max} \cdot ee_L \qquad (1)$$

Indeed, ee_P is maximised if $ee_L = 1$. If ee_L is diminished, ee_P decreases in a proportional, *linear* way.

It is only in the middle of the 1980's that the group of Henri Kagan became interested in verifying equation 1, suspecting that the relationship between ee_P and ee_L might be more complex in some cases.[4] At that time it was known that the relationship between a product's ee and some of its physical properties, such as fusion/boiling points, NMR spectra or the specific optical rotation, is not linear for certain compounds.[5] An impressive example is the optical rotary power of (*S*)-2-ethyl-2-methyl-succinic acid whose optical rotation sign changes from + to – upon dilution in chloroform (Figure 3).

This was suspected to be due to diastereomeric interactions: aggregates of the chiral molecule may have different physical properties than the discrete compound. In non-enantiopure mixtures, the association of enantiomers of the same (homochiral) or opposite sign (heterochiral) even gives rise to *different* aggregates which may have distinct physical properties and free energies of formation. Already in 1976, Wynberg and Feringa had followed up on the question whether a compound's ee influences not only its physical properties but also its chemical reactivity.[6] Indeed, they had found in a coupling reaction between chiral phenols that a racemic starting material had given different homocoupled products than an enantiopure starting material.

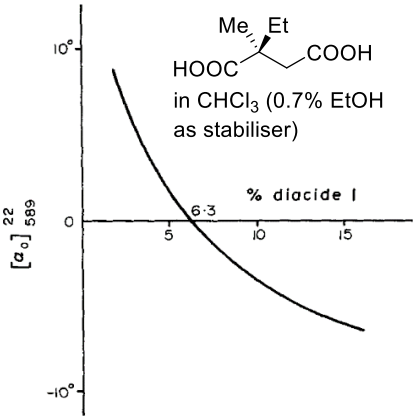

Figure 2: Concentration-dependent specific optical rotation of (S)-2-ethyl-2-methyl-succinic acid.[5]

This prompted Kagan to investigate whether *catalytic* reactions might be influenced by the catalyst's ee.[4] It turned out that the asymmetric oxygenation of a sulphide and a Robinson annulation, using non-enantiopure catalysts, yielded a lower product ee than expected from equation (1). On the other hand, the Sharpless epoxidation of geraniol gave rise to a product ee *higher* than expected. These phenomena were called "Non-Linear Effects" (NLE) since their principal characteristic is the deviation from the *linear* equation (1). Thus, a deviation leading to higher ee_P is called a positive non-linear effect ((+)-NLE, often coined as "asymmetric amplification") and to lower ee_P negative non-linear effect ((-)-NLE, "asymmetric depletion"), see Figure 4. Following this pioneering work, lots and lots of examples of NLEs have been reported.[7,8] This introduction will focus on NLEs in metal-catalysed synthetic reactions; NLEs in kinetic resolution[9–12] and stoichiometric asymmetric synthesis[13–17] have also been studied but will not be discussed here. It should be noted that Langenbeck and Triem[18,19] theorised already in 1936 (!) the possibility of asymmetric amplification in catalysis, after having observed an inherent increase of optical activity in the addition of scalemic (-)-menthol to oxalyl chloride – 50 years before Kagan's first paper on the subject.

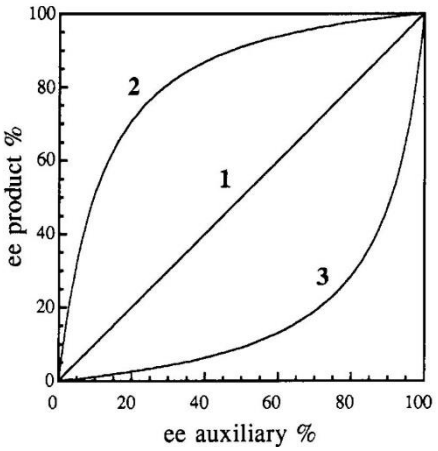

Figure 3: Examples of NLE in asymmetric catalysis. Curve 1 shows a linear ee_L vs ee_P correlation, 2 shows a (+)-NLE and 3 a (-)-NLE.[20]

I.1.2 Kagan's mechanistic models: ML_2 and reservoir effect

How do those NLEs arise? Kagan and co-workers reported an extensive theoretical study[20] in 1994 which is, up to now, a major reference in the field. They rationalised the existence of NLEs by the catalyst not being a discrete metal complex but forming aggregates, such as dimers. For a scalemic mixture of the catalyst, the dimers can be homo- or heterochiral and may then differ in their physical properties like thermodynamic stability, catalytic kinetics or solubility.

The *ML₂ model* (Figure 5) consists in the chiral ligand (R or S) and the metal M being in fast exchange with complexes bearing one metal and two ligands (the same model holds for two metals and two ligands) which are the actual catalytic species – monomeric MR or MS complexes are not considered as catalysts. From the three possible ML_2 species, two are *homochiral* and opposite enantiomer to each other (MRR and MSS) and therefore catalyse the formation of products with opposite configuration (with an ee of ee_{max} or $-ee_{max}$, respectively) and with the same kinetic constant ($k_{SS}=k_{RR}$).

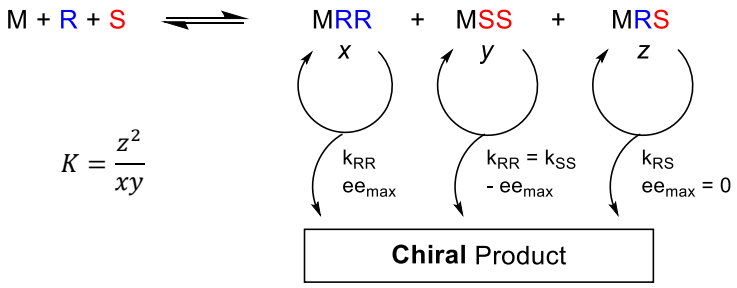

Figure 5: General scheme for enantioselective catalysis following the ML_2 model. x, y and z represent the concentrations of MRR, MSS and MRS, respectively.

The *heterochiral* complex MRS is a racemic *meso* compound, diastereoisomeric to MRR and MSS, and thus it yields a racemic product (ee_{max} = 0) with a kinetic constant k_{RS}. The relative stabilities of hetero- to homochiral dimers are represented through the equilibrium constant *K*. For *K* = 4 there is a statistical distribution of homo- and heterochiral dimers; for higher *K* values the balance is tipped towards the formation of the heterochiral dimer, lower *K* values favour homochiral dimers. From these relationships they derived equation (2), which corresponds to equation (1) with an additional correction factor:

$$ee_P = ee_{max} \cdot ee_L \frac{1+\beta}{1+g\beta} \tag{2}$$

With β being the ratio of hetero- to homochiral dimers and *g* being their relative activities:

$$g = \frac{k_{RS}}{k_{RR}} \tag{3}$$

$$\beta = \frac{z}{x+y} \tag{4}$$

With x, y and z as the concentrations of MRR, MSS and MRS, respectively. β can be further expressed as a function of *K* and ee_L:

$$\beta = \frac{-Kee_L{}^2 + \sqrt{-4Kee_L{}^2 + K(4 + Kee_L{}^2)}}{4 + Kee_L{}^2} \quad (5)$$

Kagan used the more general expression "ee auxiliary" (ee_{aux}) for the catalyst's ee since this model can also be applied to enantioselective synthesis. As our work treats only of catalytic reactions with one (or several) chiral, organic ligand(s) bound to a metal, we will stick to the term ee_L to describe the catalyst's ee.

From a qualitative point of view, a (+)-NLE arises when *homochiral dimers catalyse faster than their heterochiral counterparts*, therefore $g < 1$. This leads indeed to a correction factor > 1 in equation (2) and thus to a higher ee_P. The smaller the g value, the stronger the (+)-NLE. With $g > 1$, the reaction is dominated by the racemic catalysis of the heterochiral dimer and ee_P depletes, leading to a (-)-NLE. Both (-)- and (+)-NLEs can arise as long as heterochiral dimers are formed ($\beta > 0$). If this is not the case, then $\beta = 0$ and equation (2) turns back to equation (1). The higher β, and therefore the higher K, the stronger the NLE (negative or positive). (-)-NLEs take profit of a higher proportion of racemic catalysts, which depletes ee_P even more; in (+)-NLEs a bigger heterochiral pool changes the MRR/MSS ratio to the advantage of the major enantiomer, leading to a stronger asymmetric amplification. The ML_2 model can concord nicely with experimental results when choosing the appropriate K and g values. Nevertheless, this should be handled with care since guessed parameters don't necessarily represent the truth, nor does a spindle-shaped curve (as NLEs often are) necessarily follow the ML_2 model.

Kagan extended the ML_2 model to cases with higher aggregates (i.e., ML_3 and ML_4), which do not differ in their fundamentals but can result in more complex NLEs such as bell- or S-shaped curves; the mathematical expressions also become more complicated. A particular case of the ML_3 model leading to hyperpositive NLEs will be discussed in chapter I.2.1.3. Kagan developed also a different (and simpler) model which is called the *reservoir effect*. It considers a part of the catalyst being inactive, "trapped" in a reservoir. If the reservoir's ee (ee_{res}) is different from the active species' ee ($ee_{eff\ cat}$), then an NLE occurs. Such a reservoir could consist e. g. of polymeric or insoluble heterochiral aggregates, leaving only homochiral aggregates in solution and leading to an amplification of ee_P (Figure 6). The reservoir model is described by equation (6). Combination with equation (1) ($ee_L = ee_{eff\ L}$) gives an expression for ee_P, given by equation (7):

$$ee_{eff\ L} = \frac{ee_L - \alpha ee_{res}}{1 - \alpha} \quad (6)$$

$$ee_P = ee_{max} \frac{ee_L - \alpha ee_{res}}{1 - \alpha} \quad (7)$$

With $ee_{eff\ L}$ being the ee of the *active* catalyst, ee_{res} being the ee of the *resting* catalyst in the reservoir, ee_L being the overall catalyst ee and α the *fraction of total catalyst* which can be taken up into the inactive reservoir.

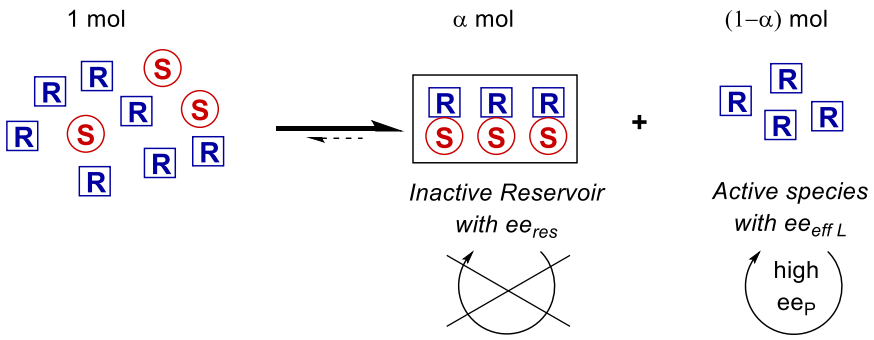

Figure 6: Schematic example of a reservoir effect with heterochiral dimers as inactive reservoir (ee_{res} = 0).

Equation (7) doesn't model a whole NLE curve as equation (2) does, it rather gives a rough estimation of the downward slope at low ee_L in (+)-NLEs or at high ee_L in (-)-NLEs. It is supplemented by a horizontal line with $ee_P = ee_{max}$ in (+)-NLEs or $ee_P = 0$ in (-)-NLEs; the rough fit is due to α and ee_{res} not necessarily being constant. Overall, it is much easier to handle than the ML_2 model: if ee_{res} is known, then α is obtained by solving equation (7) for α and using a couple of ee_P vs ee_L values lying on the downward slope of the studied NLE. Overall, the reservoir model is most interesting for extreme cases with ee_{res} = 0 or 100% and high (> 0.9) α values, which result in NLE curves featuring almost two straight lines joint by a sharp bend.

I.1.3 The Noyori Model

In 1986 the group of Ryoji Noyori investigated the enantioselective addition of dialkylzincs to aromatic aldehydes catalysed by diaminoisoborneol (DAIB), a camphor-based chiral aminoalcohol.[21] The ligand doesn't only achieve impressive yields and enantioselectivities (up to 98% ee), but exhibits also a very strong (+)-NLE. With benzaldehyde and $ZnEt_2$, they obtained a 95% ee product with an only 15% ee ligand (Figure 7).[22] This was the starting point for an extensive study[21–32] in which they investigated the reaction mechanism and proposed a model to explain the strong (+)-NLE. Similar (+)-NLEs were achieved later on with the morpholine-variant MIB[33] and a thiolated norphedrine derivative[34] for the same catalytic reaction.

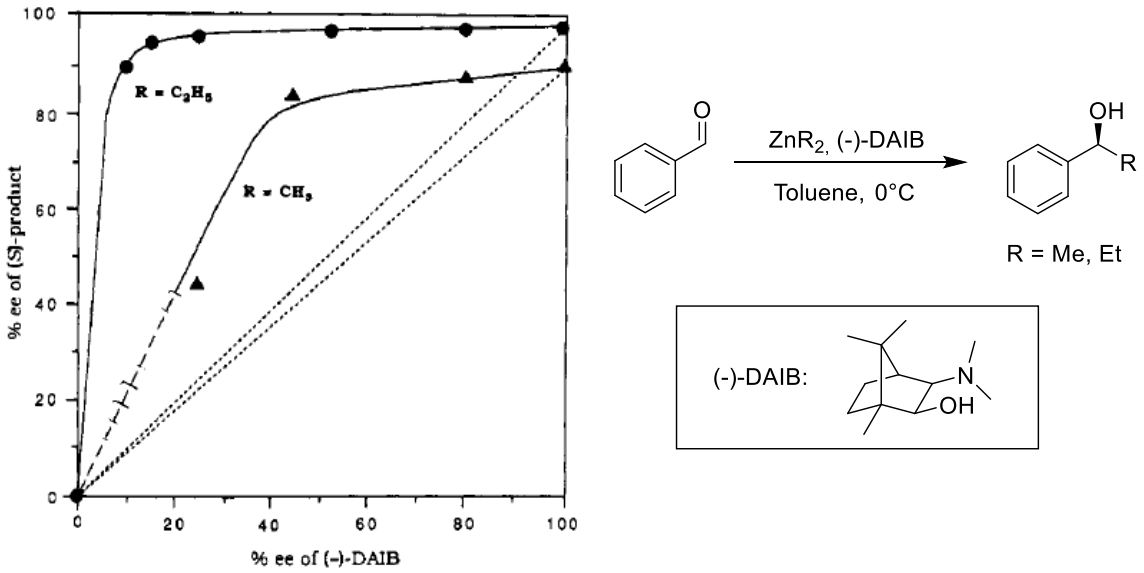

Figure 7: (+)-NLE observed for the (-)-DAIB-catalysed enantioselective addition of dialkylzinc to benzaldehyde.[22]

The proposed reaction mechanism is shown in Figure 8. In a first step, (-)-DAIB reacts with one equivalent of dialkylzinc to form a 5-membered zinc chelate, which is the actual catalytic species. In the second step, the aldehyde coordinates to the zinc atom and another molecule of dialkylzinc binds to the complex' oxygen atom. An alkyl transfer from ZnR_2 to the aldehyde generates a chiral zinc alcoholate (which is also the rate-limiting step), which upon decoordination releases the complex for a further catalytic turnover. The chiral zinc alkoxide product forms stable cubic tetramers, which usually do not interfere in the catalytic cycle (product inhibition is possible under certain reaction conditions),[29] until acidic work-up generates the chiral alcohol. The (-)-DAIB-zinc chelate acts here as a *bifunctional* catalyst: the electronically unsaturated sp^2-hybridized Zn atom is a Lewis acidic and the electron-rich oxygen a Lewis basic site. They both activate and bring into spatial proximity the aldehyde and ZnR_2. In addition, the chiral environment of (-)-DAIB's camphor scaffold privileges the orientation of the aldehyde's *Si*-face towards the ZnR_2 moiety (for (+)-DAIB it is the *Re*-face), thus causing enantioselection in the addition reaction. Dialkylzinc and benzaldehyde react only very slowly without ligand since the *sp*-hybridised unligated ZnR_2 is apolar.

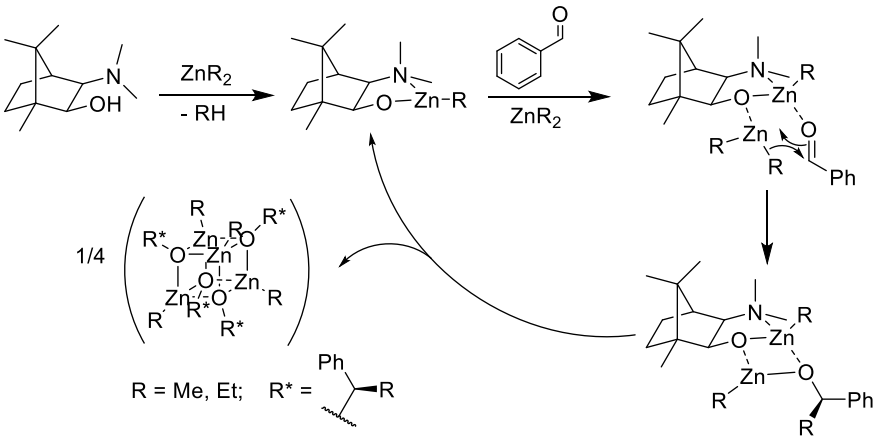

Figure 8: Mechanism of the (-)-DAIB-catalysed addition of dialkylzinc to benzaldehyde.

The complex' bifunctionality has also another consequence: it can associate with another complex to form stable, coordinatively saturated dimers (Figure 9). Those dimers are catalytically inactive and act as resting species. The heterochiral dimer (RS) is much more stable than the homochiral ones (RR and SS), therefore the latter dissociates more easily to form the active monomer.[25] Since the minor enantiomer is completely incorporated into the heterochiral aggregates, the homochiral ones consist of only one enantiomer and high ee_P values are achieved, even with a scalemic catalyst. This is somewhat related to Kagan's reservoir effect with the heterochiral dimers as an inactive reservoir (Figure 6). Kagan also applied a modified ML_2 model on the DAIB system considering an irreversible dissociation of ML_2 to ML species.[20] However, the zinc chemistry is known for fast and reversible coordination processes: neither the reservoir effect nor the modified ML_2 model depict accurately this behaviour. To overcome these shortcomings, Noyori developed a complex mathematical model based on the various equilibria shown in Figure 9, expressed by equations (8)-(10):

$$ee_P = ee_{max}\sqrt{\alpha^2 - 4\beta}/\alpha \tag{8}$$

$$ee_{cat} = \frac{(2\alpha/K_{homo}) + 1 + K_{assoc}[Rea][Sub]\sqrt{\alpha^2 - 4\beta}}{[C_{tot}]} \tag{9}$$

$$\beta = \frac{-K_{hetero}(2\alpha^2 + \alpha K_{homo} - ([C_{tot}] - K_{assoc}[Rea][Sub]\alpha)K_{homo})}{2(K_{homo} - 2K_{hetero})} \tag{10}$$

With α = [R] + [S] and β = [R][S] (β ≥ 0). Since equations (8) and (9) cannot be combined to form an equation of type $ee_P = f(ee_L)$, values for α have to be chosen arbitrarily to give paired values of ee_P and ee_L.

The approach of the Noyori model differs a lot from the ML_2 model and is much more complex, which is well illustrated by equations (8)-(10). The active species is monomeric, not dimeric; the actual catalytic species is the zinc chelate bound to one molecule of substrate and reactant, not the zinc chelate alone. This makes the NLE a function not only of the dimer's dissociation constants (K_{homo}, K_{hetero}) and the catalyst's enantioselectivity (ee_{max}) but also of the substrate, reactant and total catalyst concentrations ([Sub], [Rea], [C_{tot}]) and of the association constant of the catalyst-substrate-reactant complex (K_{assoc}). Concretely, it means that substrate and reactant are not innocent: their concentrations influence the monomer-dimer equilibrium. The higher they are, the more free *R* and *S*-catalysts are consumed, the more the dimers (homo- as well as heterochiral ones) dissociate. Another difference to the ML_2 model is the lack of kinetic constants: the NLE results from "enantiomorphic" catalytic cycles, where the only catalytic species are enantiomers of each other. These differ in their respective amounts, which the model aims to quantify, but not in their kinetic behaviours. This is in sharp contrast to the ML_2 model where the relative reactivities of homo- and heterochiral aggregates, expressed through the term *g*, are mainly responsible for the sign and the amplitude of the NLE; the catalytic cycles there are "diastereomorphic".

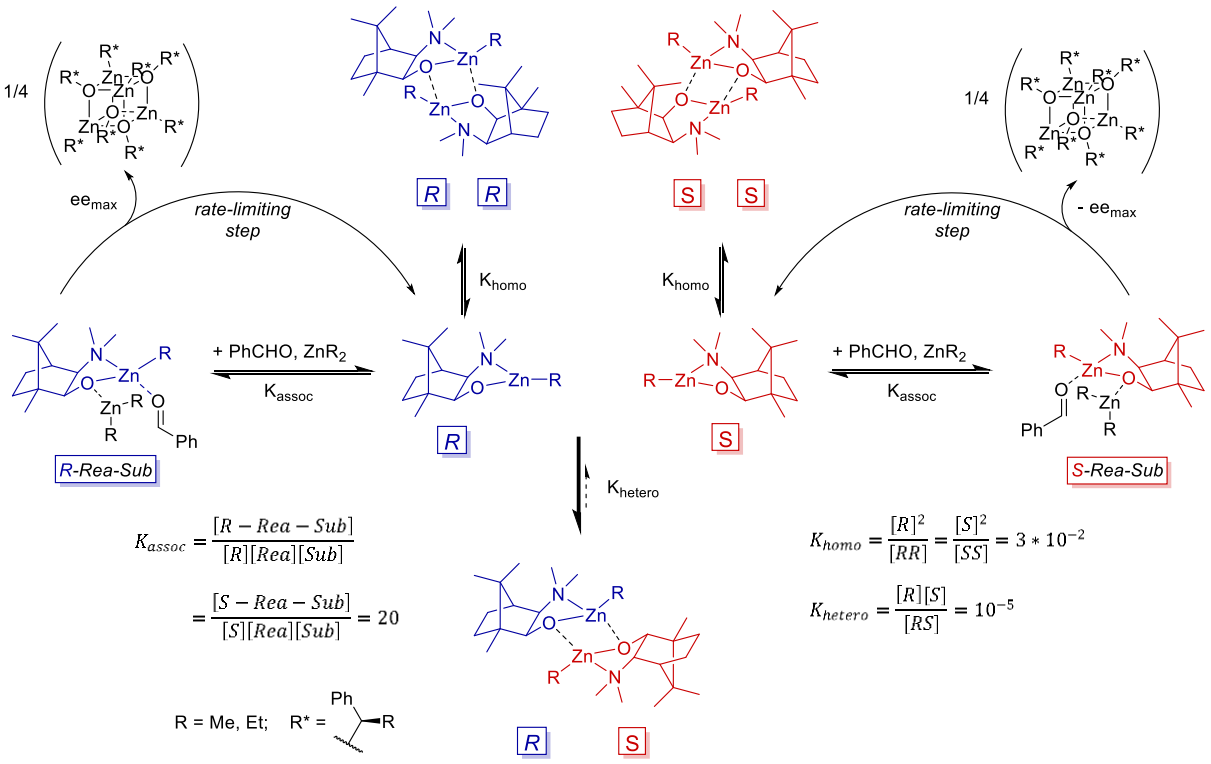

Figure 9: Mechanistic pathway for the (-)-DAIB-catalysed addition of dialkylzinc to benzaldehyde. The values given for K_{assoc}, K_{Homo} and K_{Hetero} are those for the (-)-DAIB-ZnMe complex at 40°C.[29]

The question of the substrate's influence on the NLE can also be extended to its electronic properties. Chen, Costa and Walsh observed consistently strong (+)-NLEs with electron-rich aldehydes using the DAIB-derivative MIB.[35] This was unexpected as electron-rich substrates should bind more strongly to the complex, thus driving the dimer's dissociation and depleting the (+)-NLE. This behaviour was later addressed by Buono, Walsh and Blackmond[36] who proposed an extension of the Noyori model: in the case of a *slow* dissociation of heterochiral dimers compared to the catalysis timescale, called "strong binding limit", even electron-rich substrates will only be catalysed by the homochiral pool.

I.1.4 The Soai autocatalytic system

Another catalytic system which has to be considered when dealing with NLEs and asymmetric amplification is the so-called "Soai reaction", which was first described by Kenso Soai and co-workers in 1995.[37] It has attracted the attention of many researchers and there are still articles regularly being published on this subject, more than 20 years later. It deals also with dialkylzinc chemistry but differs from the Noyori model as the reaction is *autocatalytic*: the reaction product, a pyrimidyl zinc alkoxide, catalyses its own production from the respective aldehyde and $Zn(iPr)_2$ – with a strong (+)-

NLE (Figure 10). The system relies on a chiral, not necessarily enantiopure, initiator to produce the first zinc alkoxide molecules, which will have a higher ee than the initiator. Then, they catalyse the production of further alkoxide molecules with again an increase in ee, and so forth. This continuously changing system is denoted as an "unstable equilibrium" or "far-from-equilibrium process".[38] In their first publication Soai and co-workers used 20 mol% of the pyrimidyl alkanol with 5% ee in toluene as initiator to obtain an overall product (which includes the initiator) of 39% ee. Successive runs with an enantioenriched initiator from the previous run lead to 76% and finally to 85% ee of the pyrimidyl alkanol product in the 3rd run.

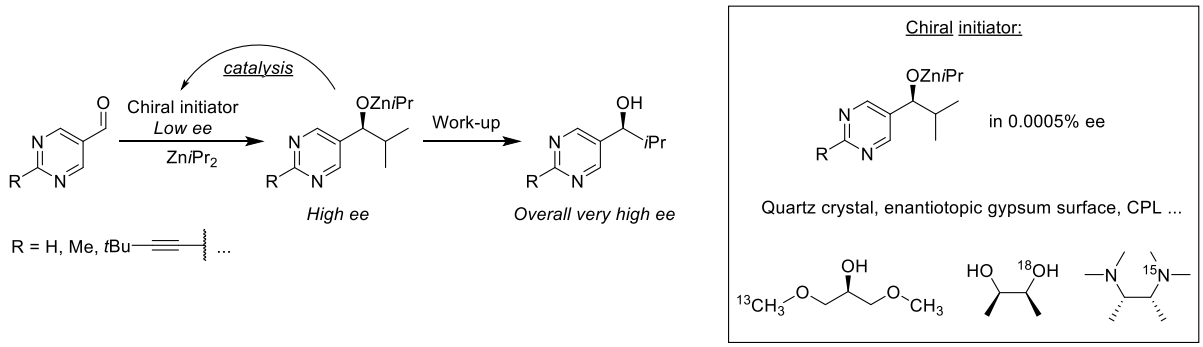

Figure 10: Autocatalytic enantioselective addition of $ZniPr_2$ to pyrimidyl-5-carboxaldehyde derivatives.

Although the absolute values of ee and the asymmetric amplification are not spectacular – Noyori's DAIB shows a much stronger chiral amplification with $ZnEt_2$, cf. Figure 7 – Soai recognised the system's potential and studied various derivatives of the pyrimidyl aldehyde. A breakthrough was the introduction of a *tert*-butyl-alkynyl group in position 2 of the pyrimidine moiety, which gave enantiopure products (>99.5% ee) when used as precursor (alkanol) and as substrate (aldehyde) in cumene as solvent.[39] A ridiculously low ee of ca. 0.00005 % for the pyrimidyl alkanol initiator was then sufficient to obtain >99.5% ee products over 3 consecutive steps (99% ee after two steps) in less than 24h per step.[40] Soai's group made then an extensive survey of chiral initiators over nearly two decades.[41] The incredible sensitivity of the *tert*-butyl alkynyl-substituted pyrimidyl aldehyde makes seemingly any kind of chirality sufficient to trigger the enantioselective autocatalysis and to end up with near to enantiopure products. Some examples are circularly polarised light,[42,43] enantiomorphic quartz crystals[44] and other inorganic and organic crystals, cryptochiral hydrocarbons (i. e. which are chiral but optically inactive)[45] or chiral isotopomers – compounds with a chiral centre whose substituents differ, in part, only by their isotopic composition ($^{12}C/^{13}C$, $^{16}O/^{18}O$, $^{14}N/^{15}N$, cf. Figure 10).[46]

The pyrimidyl aldehyde is even able to perform absolute asymmetric autocatalysis *without* initiator (Figure 11).[47] The slow direct addition of $Zn(iPr)_2$ to the aldehyde produces some first chiral zinc alkoxide molecules with an aleatory absolute configuration; the small initial statistical imbalance of *R* and *S* isomers is sufficient to trigger chiral amplification and to yield enantioenriched compounds. Over 37 experiments, Soai's group obtained an approximately equivalent number of *R*- and *S*-enantioenriched samples.

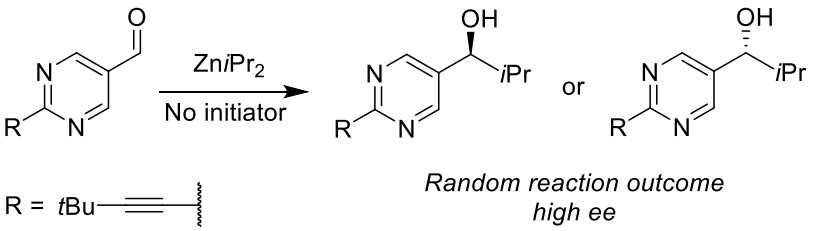

Figure 11: Absolute asymmetric autocatalysis with statistical reaction outcome.

Although the term "non-linear effect" almost never appears in the literature about the Soai reaction – he did only one NLE probe in his 1995 publication (Figure 12) – it is at the heart of its fascinating chiral amplification: autocatalysis alone doesn't induce any chiral enrichment. Frank[48] already published in 1953 a theoretical study about autocatalysis and asymmetric amplification in which he pointed out the necessity for a "specific mutual antagonism", which is nothing but the formation of inactive heterochiral aggregates outlined later by Kagan. Without this antagonism, the initiator's ee is preserved instead of amplified. The advantage of autocatalysis is that it *accelerates* the catalytic reaction, which would otherwise take phenomenal amounts of time and even be slower than the achiral background reaction. The kinetic aspects of NLEs have been pointed out by Donna Blackmond: the lower ee$_L$ in a (+)-NLE, the more the catalyst is taken in inactive heterochiral aggregates, the slower the catalytic reaction.[49,50] The mechanisms behind the Soai reaction are still a subject of debate but kinetic,[51,52] computational,[53–55] and X-ray diffraction studies[56] point towards catalysis by a dimeric or tetrameric homochiral aggregate, while its racemic counterpart is inert due to a fundamentally different spatial orientation. Aggregates including the substrate, through formation of hemiacetals, are also under investigation.[57]

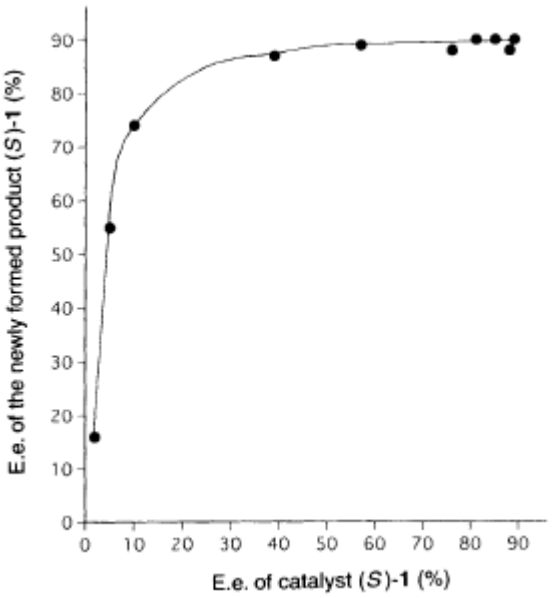

Figure 4: Measured NLE of the autocatalytic system with R = H (see Figure 10).[37]

I.1.5 Application and implication of non-linear effects

Apart fascinating the scientific community, NLEs have also found practical applications in chemistry, mostly in the investigation of reaction mechanisms. For example, Evans *et al.* developed a ML$_2$-type nickel catalyst bearing two diaminocyclohexane (DACH)-based ligands for the enantioselective addition of malonates to nitrostyrene.[58,59] They found a *linear* relationship between ee$_P$ and ee$_L$, suggesting that not the ML$_2$-complex catalyses the reaction but a monomeric species with only one ligand (Figure 13a). A (+)-NLE evidenced the aggregation of a Cu(II)/DiPPAM-catalyst in the

enantioselective 1,4- and 1,6-addition of $ZnEt_2$ to cyclic enones (Figure 13b) where other analytical methods such as mass spectrometry, NMR and X-ray diffraction had failed.[60] Pollice and Schnürch applied the principles of NLEs to analyse catalysis using different (co-)catalysts or substrates, going beyond enantioselective reactions.[61] Another potential utility of (+)-NLEs is their use in asymmetric synthesis. If the catalyst or chiral reagent doesn't need to be enantiopure to perform high enantioselectivity, then the costs of its synthesis may be greatly reduced. An example is α-pinene, whose cheap 85% ee-version has been used in the reduction of an aromatic ketone in 95% ee_P by the Merck laboratories in the USA.[13]

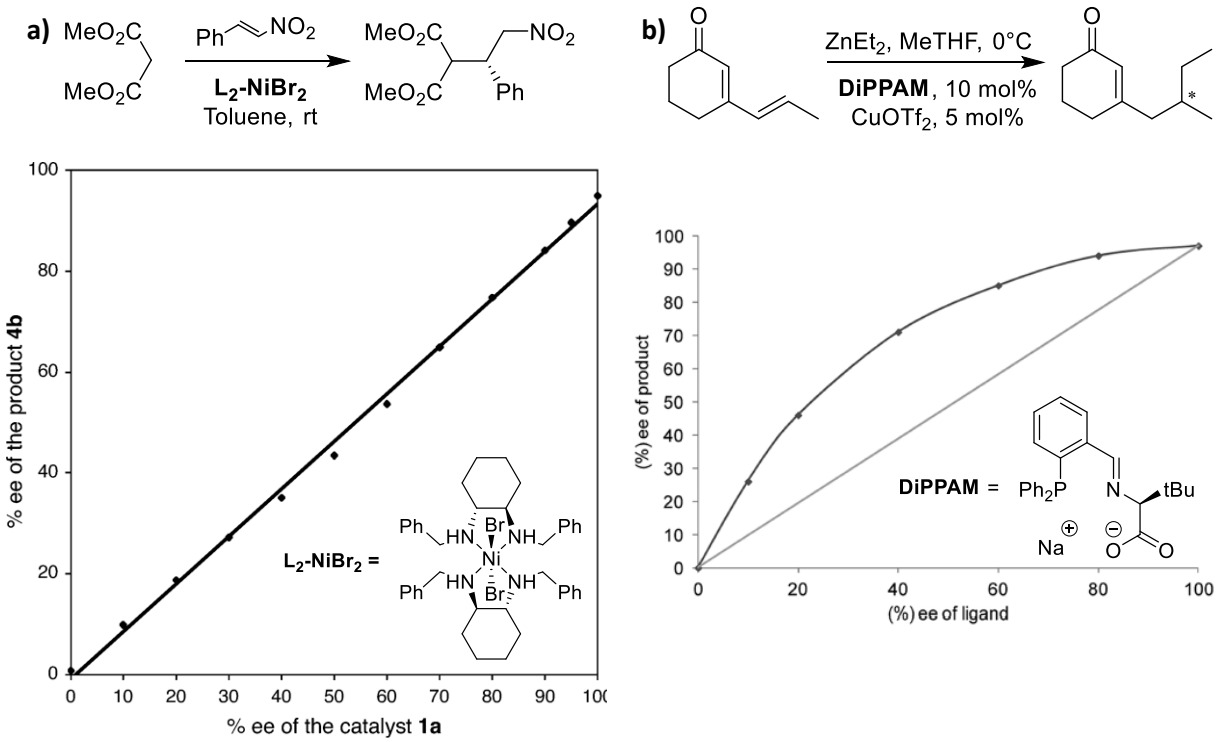

Figure 13: Examples for NLE probes which have been used as tools in mechanistic studies: a) linear effect of the nickel-catalysed addition of diethyl malonate to nitrostyrene,[59] b) (+)-NLE of the Cu(II)/DiPPAM-catalysed 1,6-conjugate addition of $ZnEt_2$ to an enone.[60]

Though the presence of NLEs attests the formation of catalyst aggregates, it doesn't tell if the catalysis is performed by dimers (Kagan ML_2 model) or rather by monomers (Noyori model). Both mechanisms give, for simple cases involving dimers, the same spindle-shaped graphs. Noble-Terán *et al.* developed a system based on reaction kinetics to discriminate between dimer and monomer catalysis depending on the presence and the nature of the NLE, the reaction speed depending on ee_L, the variation of ee_P as a function of $[C_{tot}]$, the catalyst and the substrate kinetic order.[62] From this they constructed a working decision table (Figure 14) which relates the results from a couple of simple experiments to one of the cases predicted by the authors, involving catalysis by dimers or monomers. Prior to this, the dependence of the nature of the NLE and of the reaction rate had been investigated by Blackmond.[49,50] She developed kinetic models derived from the ML_2 model which serve as an additional verification for the validity of the ML_2 model on a studied NLE.

ee_{prod} vs. ee_0	$t_{1/2}$ vs. ee_0	Catalyst kinetic order	ee_{prod} vs. r_0	Substrate kinetic order	Catalyst
ampli	↓	>1	↑	1	dim
ampli	↓	=1	→	0	dim
ampli	→	>1	↓	1	dim
atten	↑	=1	→	0	dim
ampli	↓	<1	↑	1	mono
neutr	→	=1	↑	0	mono
atten	→	<1	→	1	mono
neutr	→	=1	→	0	mono

Figure 14: Working decision table for an easy discrimination between monomeric and dimeric catalysis.[62] It relates the presence of a NLE (asymmetric amplification, attenuation, no NLE), evolution of the reaction half-time ($t_{1/2}$) when decreasing ee_L, the catalyst kinetic order, evolution of ee_P with the catalytic charge (r_0) and the substrate kinetic order.

It is also important to note that NLEs may occur *without* catalyst aggregation, in a very particular case. Kalek and Fu[63] investigated kinetic resolutions where the catalyst first converts the racemic starting material into an achiral intermediate and then into an enantioenriched final product, without the starting material being subject to racemisation (Figure 15a). These reactions exhibit an intrinsic (-)-NLE which arises purely from the reaction kinetics and not from aggregation phenomena. The NLE's amplitude depends strongly on the conversion (in the initial stage of the reaction, almost no NLE is observed) and on the selectivity factor *s*, which is the kinetic ratio between the catalyst's association with one or the other starting material enantiomer (Figure 15b).

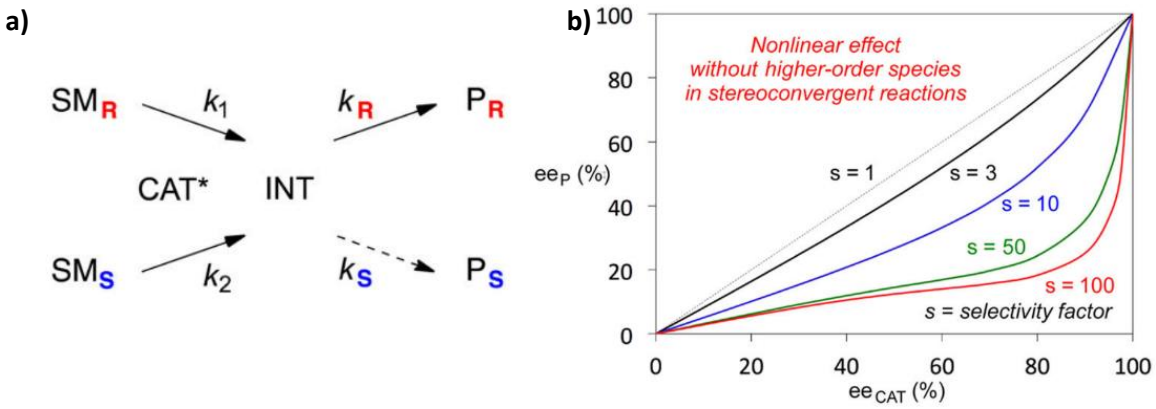

Figure 15: a) General scheme for stereoconvergent kinetic resolutions, b) intrinsic (-)-NLE of stereoconvergent kinetic resolutions.[63]

I.1.6 Biological homochirality

Although non-linear effects are of great utility in synthesis and mechanistic investigations, their most fascinating contribution lies in a much more fundamental subject: the origin of biological homochirality. It is well-known that building blocks of life such as sugars and amino acids are chiral.

Of the two possible enantiomers for each molecule, only one (with few exceptions) is used in Nature: D-sugars in polysaccharides and nucleotides, L-amino acids in proteins (Figure 16). This is the reason why the enantiomers of chiral molecules bear different properties when subjected to living organisms: (-)-carvone smells like mint while the (+)-enantiomer has a smell of caraway; (+)-thalidomide cures morning sickness while (-)-thalidomide causes birth defects. More than an curious outcome of evolution, the homochirality of biochemical systems is believed to be necessary for biomolecules to form higher-order aggregates[64] and oligomers[65,66] with a well-defined three-dimensional structure[67] without they cannot perform their biochemical functions. If amino acids had not all the same spatial configuration, well-defined secondary structures like α-helixes and β-sheets could not be formed. The homochirality of sugars makes DNA strands always twisted in the same way, allowing the formation of stable double-strands. In a general sense, the *spatial specificity* of homochiral molecules allows a more efficient encoding of information[67] and is moreover responsible for the extremely efficient electron transfer in proteins.[2] Therefore, homochirality is at the origin of life itself.

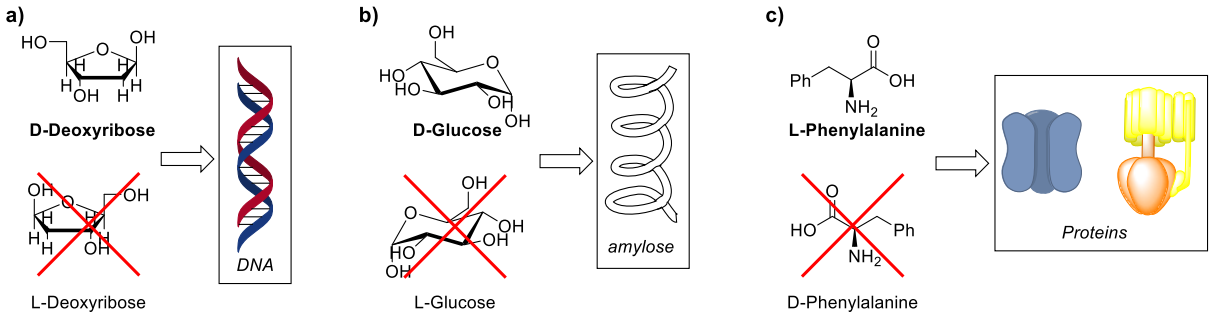

Figure 16: Scheme depicting the homochirality of biomolecules. a) DNA consists only of D-deoxyribose, b) polysaccharides, such as amylose, only of D-glucose, c) proteins only of L-amino acids.

Although our world is mostly governed by symmetrical laws, there must have been a symmetry-breaking event that tipped the balance towards one of the two enantiomers of a given substance pool – let it be sugars or amino acids.[68] There are several theories how this could have happened (see below), however, in all cases the generated ee is very small and cannot account for the total disappearance of the minor enantiomer. This is where asymmetric amplification comes into play: a reaction including a strong (+)-NLE could have amplified this small ee and led to today's homochirality in the biosphere (Figure 17). This subject is often mentioned in the context of the Soai reaction due to its phenomenal amplification power, although the reaction itself cannot have happened in aqueous conditions.

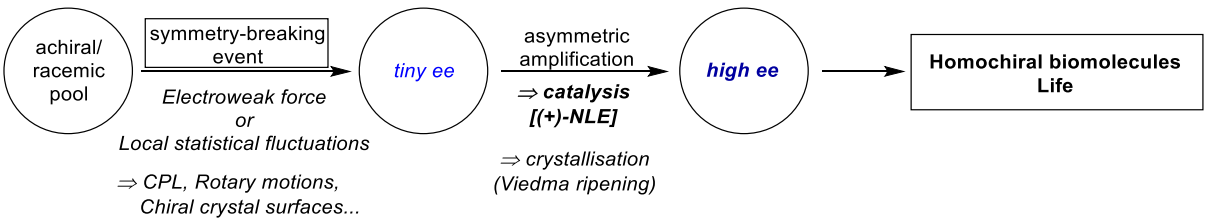

Figure 17: Scheme for the rise of biological homochirality through a symmetry-breaking event followed by asymmetric amplification.

The way how the origins of homochirality and of life are connected is a fascinating and broad subject, which has been discussed in various reviews,[38,68–71] which spans over a multitude of disciplines (catalysis, materials and surfaces chemistry, theoretical physics…) and which we can address here only briefly. The basics behind the symmetry breaking event have been under debate for decades: is today's homochirality predetermined by physical laws, since the electroweak interaction is inherently asymmetric and results e.g. in D-sugars and L-amino acids being slightly more stable than their enantiomers,[72–74] or is it the result of coincidence? The Soai reaction shows that, out of local statistical fluctuations, enantiomeric enrichment can be achieved without any source of asymmetry. Same goes for enantiomorphic $NaClO_3$ crystals or racemisable organic molecules crystallising as conglomerates, which lead randomly to a single enantiomorph/enantiomer when subject to attrition ("Viedma ripening", Figure 18).[69] A random local symmetry break on earth or in space, coupled with asymmetric amplification, might then have led to today's homochirality, but it could have as well resulted in the opposite sugar and amino acid enantiomers being the bricks of life ("frozen accident" scenario). Circularly polarised light[75] (which is emitted by certain stars, but which applies also to sunlight reaching earth at dawn and dusk),[76] selective adsorption on chiral crystalline surfaces like on quartz or sodium perchlorate[77] or earth's rotary motion[78,79] might also have served as a local source of asymmetry, followed by asymmetric amplification. A big question is also the role of (pre-)biotic systems in the asymmetric amplification process: did the first biomolecules arise from an already enantiopure pool, or did enantioenrichment happen *during* the emergence of biomolecules and -systems? Homochiral oligomers (peptides, small nucleotide strands) are not only more stable than heterochiral ones, they also catalyse the formation of complementary strands having only the same chirality, therefore the emergence of homochirality may be the result of a sort of natural selection[70] – in other words, homochirality arose when it was needed.

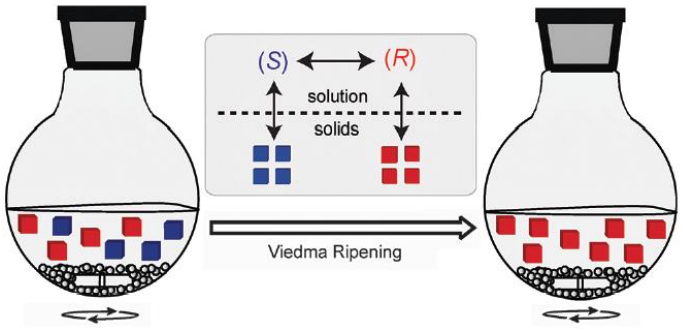

Figure 18: Schematic representation of Viedma ripening.[69] Continuous attrition makes larger crystals grow at the expense of smaller crystals, leading randomly only to R- or S-crystals through statistical imbalances. The product has to crystallise as a conglomerate of R- and S-crystals to perform this, not as a racemate or an achiral crystal. However, the molecule in itself can be achiral (e. g. $NaClO_3$) or a racemisable chiral compound (e. g. certain amino acid derivatives).

I.2 Results & Discussion

I.2.1 Ephedrine ligands: first investigations

I.2.1.1 Ephedrine-based ligands in enantioselective catalysis: literature survey

Ephedrine is an alkaloid (naturally occurring in plants of the *ephedra* type) which has been used a lot as medication against asthma, nasal congestion, narcolepsy, hypotension and other pathologies. Same goes for its diastereoisomer pseudoephedrine and their variants without N-methyl group, distinguished by the "nor" prefix in their names (Figure 19). Nowadays, these molecules are less used in medicine because of their various side effects, which include high blood pressure, stroke, heart attacks but also psychotropic effects. Ephedrine is easily converted into desoxyephedrine, better known as methamphetamine ("crystal meth"), an illegal drug. Thus, its commercialisation and that of the other ephedrine derivatives obey to strict regulation in most countries.

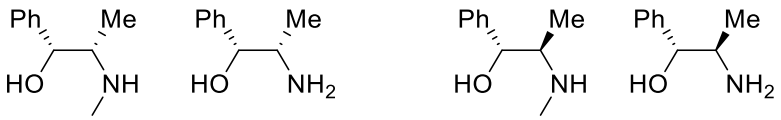

Figure 19: From left to right, (1R,2S)-(-)-Ephedrine, (1R,2S)-(-)-Norephedrine, their respective diastereoisomers (1R,2R)-(-)-pseudoephedrine and (1R,2R)-(-)-norpseudoephedrine.

Apart from their pharmaceutical applications, ephedrine-type molecules are also used as chiral scaffolds in organic synthesis[80] and coordination chemistry[81] and have been studied as a chiral auxiliary in asymmetric synthesis[82] and catalysis,[83] notably in the addition of dialkylzinc reagents to aromatic aldehydes (Figure 20). Their β-aminoalcohol scaffold promotes a similar catalytic action to Noyori's DAIB. Among the most active and selective ligands are di-*n*butyl- and cyclic -$(CH_2)_4$- substituted norephedrines, which catalyse the addition of $ZnEt_2$ to aromatic and also aliphatic aldehydes in up to 95% product ee.[84–86] Increasing or decreasing the length of the N-alkyl chains results in a loss of selectivity and, in some cases, of catalytic activity. Another important effect is the substitution of the aminoalcohol's oxygen atom by sulfur: ees consistently higher than 90%, again with *n*-butyl or cyclic alkyl substituents on nitrogen, have been achieved in the addition of $ZnEt_2$ to a large variety of aromatic or aliphatic aldehydes.[87,88] Even thioester derivatives give consistently high ees.[89]

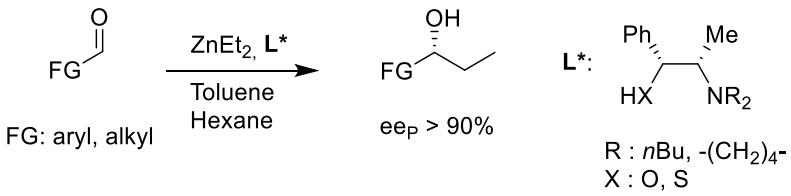

Figure 20: Some of the most selective ephedrine-type ligands in the asymmetric addition of $ZnEt_2$ to aldehydes.

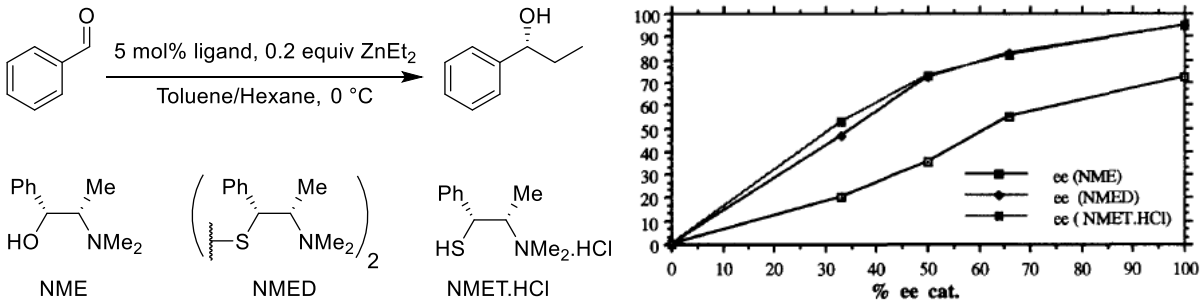

Figure 21: NLE curves of N-methyl ephedrine (NME) and its thiolated derivatives NMED and NMET.HCl in the enantioselective addition of $ZnEt_2$ to benzaldehyde.[90]

There have been only few mechanistic studies on ephedrine-mediated additions of dialkylzinc; most proposals simply follow Noyori's mechanism for DAIB. The thiol derivatives have received more attention due to their exceptionally high enantioselectivity and have also been checked for NLEs. Fitzpatrick and co-workers[90] found for *N*-methyl ephedrine (NME) an "essentially linear relationship" between ee_L and ee_P and a moderate (+)-NLE for some thiol derivatives (Figure 21). Cryoscopic weight measurements of NME and NMET.HCl gave molecular weight (MW) values beyond those of simple dimers, indicating that the zinc complexes form tri- or tetramers; extra $ZnEt_2$ breaks those aggregates down into monomers. They claimed that the sulfur derivatives tend to higher-order and more stable aggregates due to the higher polarizability of the sulfur atom and to the sulfur-bound zinc's higher Lewis acidity. However, this assumption should be treated with care since it relies only on information about the homochiral species.

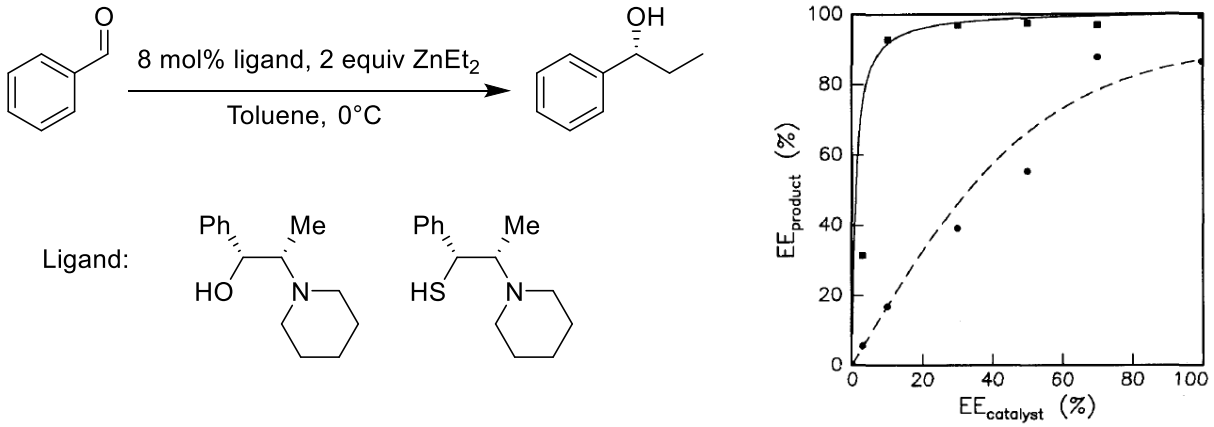

Figure 22: NLEs of N-piperidinonorephedrine ligand (dashed line) and its thiol derivative (full line).[34,91]

Another study was made by Kang.[34,91] (1*R*,2*S*)-*N*-piperidinonorephedrine showed a moderate (+)-NLE while its thiolated version gives a very strong asymmetric amplification similar to DAIB (Figure 22). They determined the ΔG_{Homo} and ΔG_{Hetero} values [which are related to K_{Homo} and K_{Hetero} through $\Delta G = -RTln(K)$] of the corresponding ethylzinc complexes, also through cryoscopic weight measurements. Although they found the heterochiral dimers to be more stable than their homochiral counterparts, the difference (1.12 kcal/mol) is not sufficiently high to explain the

thiolated ligand's strong (+)-NLE – it is even smaller than for the oxygen-containing ligand (1.60 kcal/mol). This also doesn't concord with the high $\Delta G_{Hetero}/\Delta G_{Homo}$ difference of DAIB (4.78 kcal/mol). The measured MW values didn't indicate the presence of aggregates higher than dimers, however they worked at lower concentration than Fitzpatrick. Investigation of the zinc complexes' coordination behaviour showed also that the zinc thiolates have a higher affinity for $ZnEt_2$ than the zinc alkoxides; the latter coordinate preferentially to benzaldehyde, indicating that not the zinc thiolates but the zinc alkoxides are the better Lewis acids. In summary, both studies show that substitution of oxygen by sulfur is not only beneficial for the enantioselectivity but also for the emergence of (+)-NLEs, but the reason for this is unclear. Kang proposed the homochiral zinc thiolate dimers to catalyse the reaction, with a higher rate than all other zinc thiolate and alkoxide species, without showing any evidence for this.

I.2.1.2 NLEs of alkylated and unsubstituted ephedrine

Following the weak knowledge of NLEs with ephedrine-type ligands, we decided to make our own investigation and to check a variety of ephedrine derivatives for the presence of NLEs in the asymmetric addition of $ZnEt_2$ to benzaldehyde. *N*-Methyl ephedrine (NME), *N*-*n*butyl ephedrine (NnBE) and *N*-benzyl ephedrine (NBE) were easily obtained from (1*R*,2*S*)-(-)-ephedrine via Eschweiler-Clarke methylation[92] and nucleophilic substitution on bromobutane[93] or benzyl bromide,[94] respectively (Figure 23).

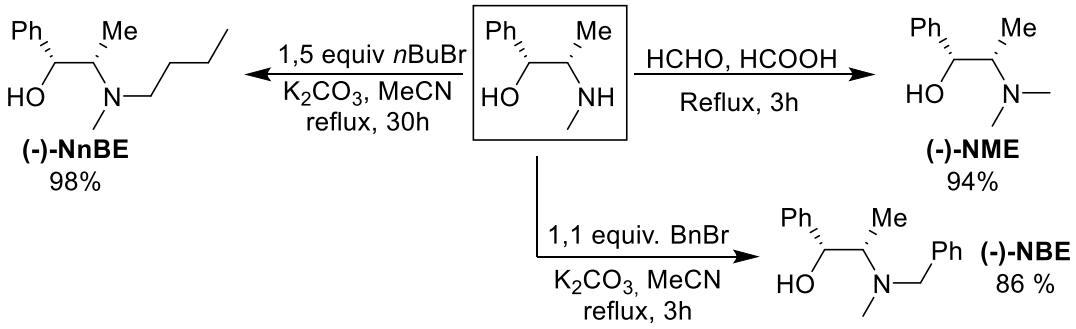

Figure 23: Reaction Scheme for the synthesis of NnBE, NME and NBE from ephedrine.

We then fixed our experimental conditions: 0.93 M benzaldehyde in toluene as the solvent, 20 mol% catalyst, 1.2 equiv. $ZnEt_2$. The standard in ephedrine-catalysed reactions is to use excess $ZnEt_2$ (2-4 equivalents) since it has been reported to enhance the product ee (ee_P),[95] but it also drives the dissociation of catalyst aggregates according to the Noyori model. Therefore, we chose to work with only 1.2 equivalents, from which 0.2 first react with the ligand to form the catalytically active complex. The reaction temperature was fixed at 0 °C to minimise the achiral background reaction[96] and the formation of the side-product benzyl alcohol.[23] The ligand ee was adjusted by mixing appropriate amounts of both enantiomers; each reaction was performed in triplicate, analysed via chiral stationary phase GC and the mean ee_P value used to build the NLE curves. The standard

deviation is mostly within ±0.5% ee and in most cases too small to be properly displayed with error bars.

The results for ephedrine, NME and NnBE are shown in Figure 24. The methyl- and *n*butyl-substituted ligands show a linear relationship between ee_P and ee_L, whereas unsubstituted ephedrine exhibits a weak (-)-NLE (blue dots). The absence of NLE for NME is consistent with the previous report by Fitzpatrick and co-workers.[90] The (-)-NLE with ephedrine may indicate a greater stability of homochiral dimers compared to their heterochiral counterparts, which can be due to additional H-bonding by the NH-group on ephedrine. The lack of an acidic hydrogen on the zinc alkoxides of NME and NnBE prevents them from making H-bonds. The maximum ee_P values are almost the same (NnBE: 66%, ephedrine: 67%, NME: 68% ee) for the three catalytic systems and are close to previous reports under similar conditions in the case of ephedrine (66% ee) and NME (64% ee, 5 mol% catalyst used).[97] Only NnBE has been reported to give a higher ee_P of 73% using 3 equiv. $ZnEt_2$ in a hexane-toluene mixture and 10 mol% ligand.[98]

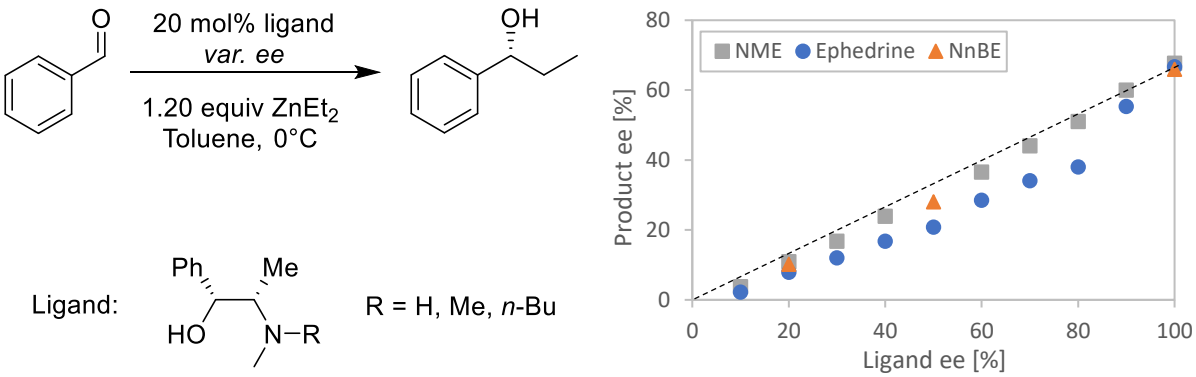

Figure 24: Observed NLEs using ephedrine, NME and NnBE as ligands in the enantioselective addition of $ZnEt_2$ to benzaldehyde.

I.2.1.3 NBE ligand: Hyperpositive NLE

We then moved on to *N*-benzyl ephedrine (NBE), which shows a dramatically altered picture (Figure 25). Variation of ee_L leads to a very strong (+)-NLE, ee_P stays high down to an ee_L of only 3%. There is, to the best of our knowledge, no precedent for a NLE with such a strong amplitude. Even more interesting is the shape of the curve: starting at 76% ee_P with the enantiopure ligand, ee_P *increases* to 81% when lowering ee_L to 10-20%. The scalemic, enantio*im*pure catalyst leads to a more enantioselective reaction than the enantiopure one! As for the previously tested ephedrine ligands, the standard ee_P deviation is negligible except for very low ee_L values (cf. error bars in Figure 25), therefore the ee_P increase (Δee_P) of 5% is significative.

We switched then from $ZnEt_2$ to $ZnMe_2$ as the dialkylzinc reagent, using the same reaction conditions as before (only the benzaldehyde conc. was decreased slightly to 0.83 M). The reaction resulted into a spectacular increase of Δee_P, the NLE curve resembles now an exponential function down to 5% ee_L (Figure 26). The enantiopure ligand yields a very poor ee_P of 16% but increases up to 53% at 5% ee_L!

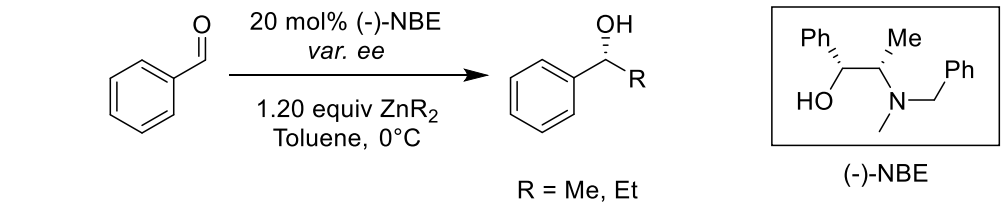

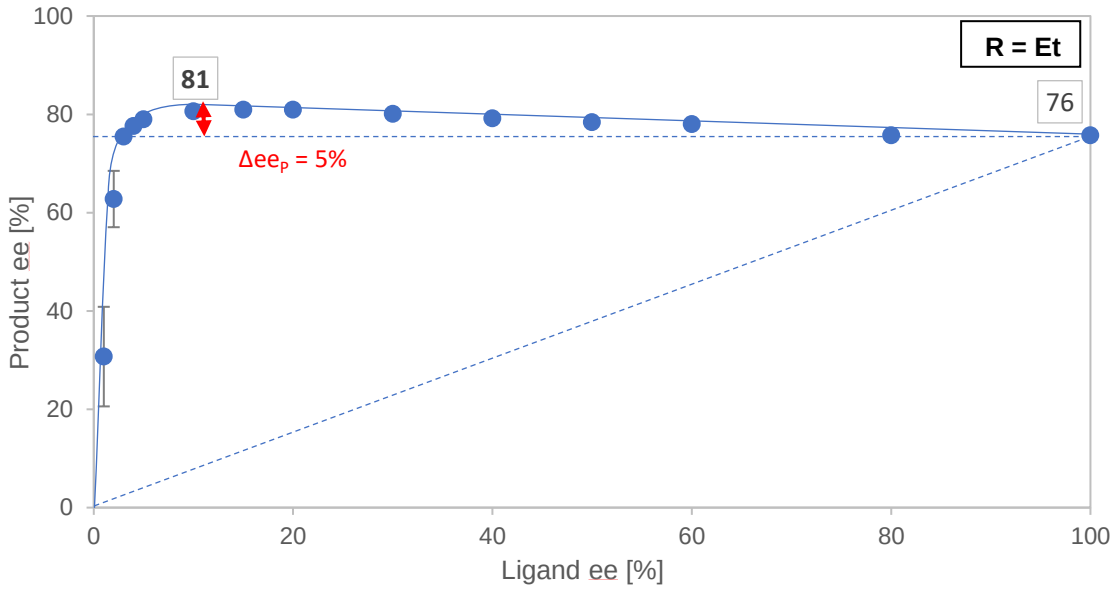

Figure 25: Observed hyperpositive NLE using (-)-NBE and $ZnEt_2$.

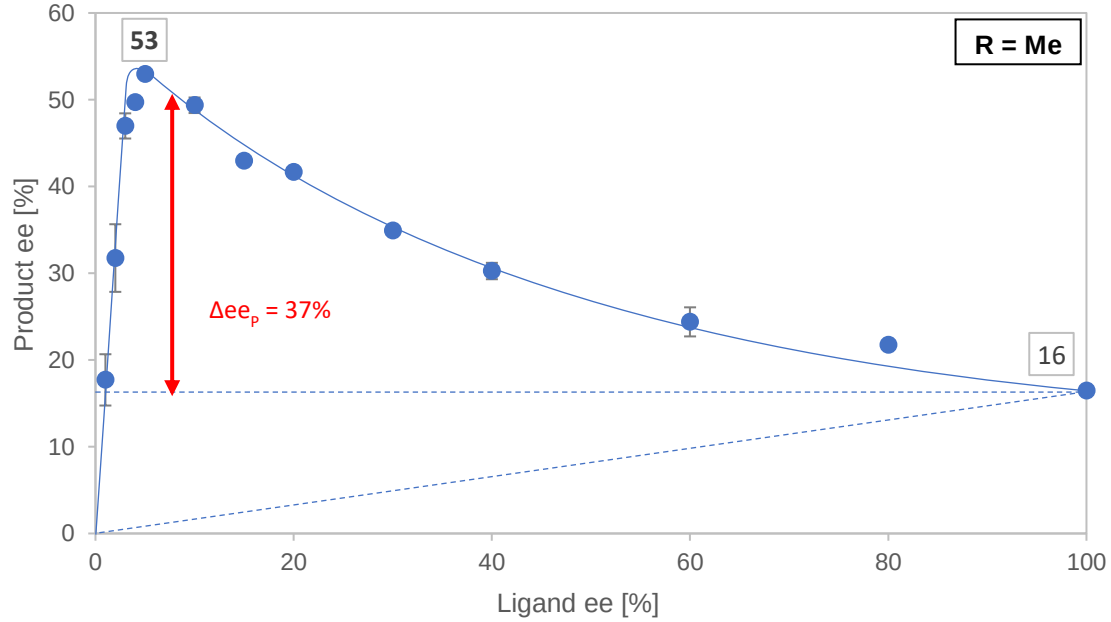

Figure 26: Observed hyperpositive NLE using (-)-NBE and $ZnMe_2$.

To the best of our knowledge, there is no experimental precedent for such a behaviour in asymmetric catalysis. However, there is a theoretical one: Henri Kagan discussed the possibility of an ee_P increase while lowering ee_L using the ML_3 model and named it a *hyperpositive non-linear effect*.[20] As mentioned in the introduction (I.1.2, p. 14), the ML_3 model is close to the ML_2 model but bears also some differences (Figure 27). As in the ML_2 model, monomers do not catalyse; the catalytic aggregates are trimers, which results in four different catalytic species: the homochiral trimers MRRR and MSSS and the heterochiral trimers MRRS and MSSR. In contrast to the ML_2 model the two heterochiral aggregates are not achiral *meso* compounds but are enantiomeric to each other and catalyse the reaction with the enantioselectivity ee_{max}(Hetero). In case where the heterochiral trimer is more selective (ee_{max}(Hetero) > ee_{max}(Homo)) and also faster (g > 1), ee_P necessarily increases when lowering ee_L as shown in Figure 28.

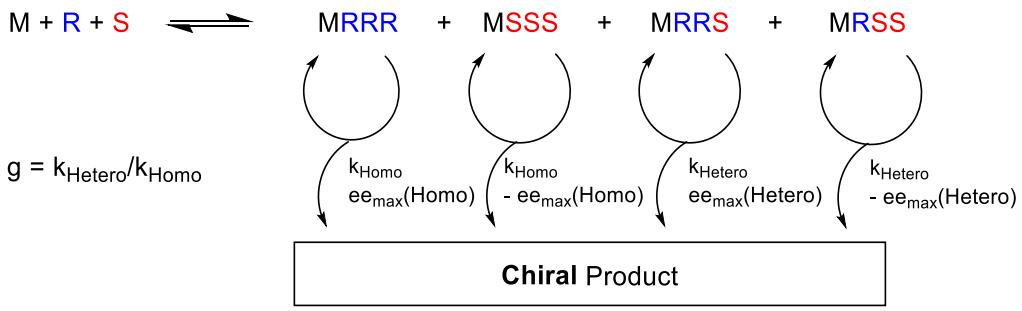

Figure 27: Scheme of Kagan's ML_3 model. The two homochiral trimers are enantiomeric to each other and catalyse with the same rate but opposite enantioselectivity; same goes for the two heterochiral trimers.

When comparing the graphics in Figure 25, Figure 26 and Figure 28 it becomes clear that the hyperpositive NLEs with NBE as chiral auxiliary do not follow the ML_3 model – the shape of the curves is totally different. Indeed, a system following the ML_3 model can be hyperpositive only in the upper half of the ee_L scale ("ee auxiliary" in Figure 28), whereas the maximum ee_P is attained with only 5% ee_L in Figure 26. Therefore, the mechanism behind NBE's hyperpositive NLE must be different.

The aim of the work presented in this chapter will be to identify and understand the causes of this hyperpositive NLE. In the following, we will make a mechanistic study and propose a model which explains NBE's behaviour in asymmetric catalysis.

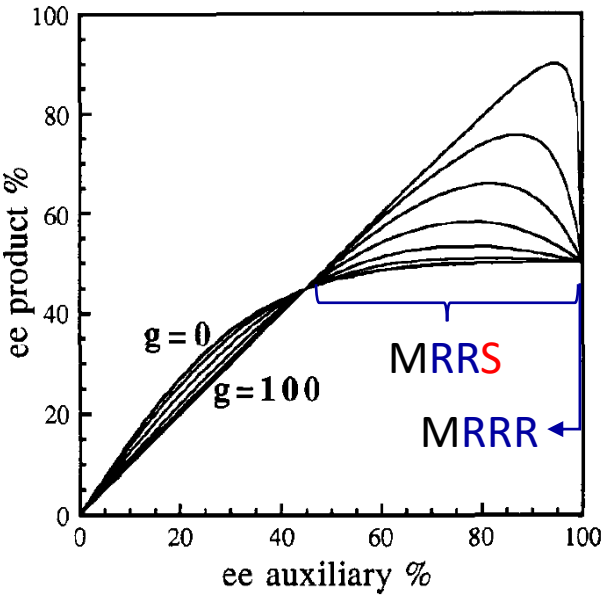

Figure 5: Graphical representation of computed hyperpositive NLE's using the ML_3 model, with ee_{max}(Homo) = 50%, ee_{max}(Hetero) = 100% and a statistical distribution of homo- and heterochiral complexes (minor enantiomer: S).[20]

I.2.2 Hyperpositive NLE: mechanistic study

I.2.2.1 Catalyst loading

An additional observation we made when performing the experiments from Figure 25 and Figure 26 is the formation of a precipitate upon addition of $ZnMe_2$ or $ZnEt_2$ to *scalemic* NBE ligand (Figure 29). Solutions with enantiopure NBE stay clear, at 80% ee_L a slight haze appears and at lower ee_L the precipitate is thick and well-visible; it persists over the whole course of the reaction. The reaction becomes also much slower at low ee_L: with $ZnEt_2$, the yellow colour indicating the presence of free benzaldehyde vanishes after a couple of hours at high ee_L but persists even after overnight stirring for ee_L < 20%. Reactions with $ZnMe_2$ and enantiopure ligand reach 70-80% conversion after 3 days, with 5% ee_L and lower 40-50% conversion is observed after 4 weeks. It seems obvious that the precipitate is an insoluble heterochiral aggregate of the zinc aminoalkoxide, which does not exist in enantiopure samples. Filtration of a 50% ee_L sample with $ZnMe_2$ (same conditions as for catalytic runs, without addition of benzaldehyde) and subsequent hydrolysis in HCl/acetone yielded indeed the NBE ligand in its racemic form, as seen in polarimetry measurements.

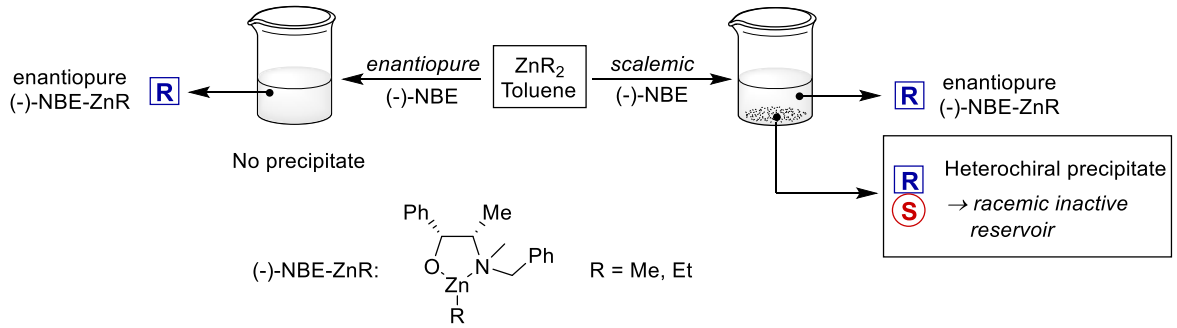

Figure 29: Presence or absence of a precipitate upon reaction of enantiopure or scalemic (-)-NBE with ZnR_2 in toluene. The precipitate with a scalemic ligand corresponds to a racemic, heterochiral aggregate while the supernatant contains only enantiopure NBE-ZnR.

This is a classic example for Kagan's reservoir effect where only the major enantiomer catalyses because of an insoluble heterochiral aggregate (see Figure 6, p. 17); some examples of (+)-NLEs induced by racemic precipitates[99–107] and nonracemic insoluble aggregates[108] are known. It is also consistent with the observed reaction times: the lower ee_L, the less active catalyst is in solution and the slower the reaction becomes. The precipitate could be a heterochiral dimer, a conglomerate of enantiopure *R*- and *S*-complexes or of heterochiral trimers: co-crystallising *RRS* and *RSS* trimers would also lead to an overall racemic precipitate. Zinc aminoalkoxides have been reported to form tri- and even tetramers.[90,109–111] For convenience, we will treat the precipitate as a heterochiral dimer in the following discussion.

The reservoir effect explains the emergence of a (+)-NLE but not of a hyperpositive one. We soon came up with the idea that the hyperpositive ee_P increase with decreasing ee_L might be correlated with the decrease of catalyst concentration: the lower ee_L, the lower the catalyst concentration, the higher ee_P. Aggregation is a parameter affected by concentration; we also have to assume that NBE-ZnMe probably forms a homochiral dimer (or higher aggregate) in addition to the insoluble heterochiral one, similar to DAIB. *If the homochiral aggregate is catalytically active,* in addition to the

monomer, and gives a different ee_P, then the overall ee_P should be strongly affected by the catalyst concentration. The reaction outcome would then be the result of *two different catalytic cycles*, one catalysed by the monomeric species, the other by the homochiral dimer. The latter being less enantioselective than the monomeric catalyst would explain the hyperpositive NLE: at high ee_L the overall catalyst concentration is high, therefore the equilibrium shifts to the dimer and the overall ee_P decreases (Figure 30).

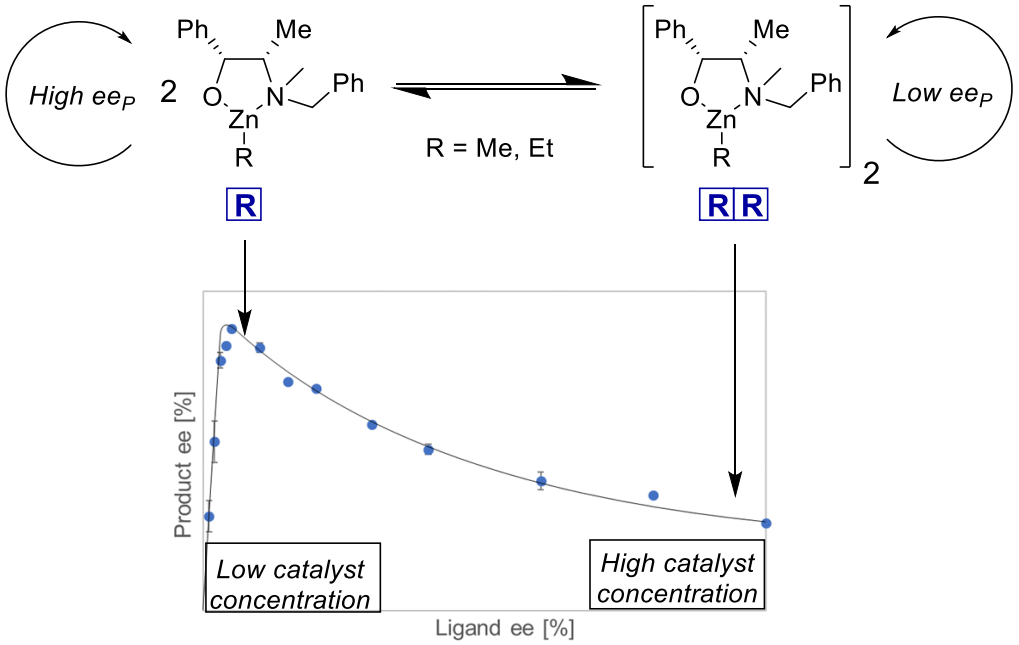

Figure 30: Scheme of the proposed hypothetical monomer/homochiral dimer equilibrium of the NBE zinc aminoalkoxide. Aggregation is favoured at high catalyst concentration. Both catalyse the addition of ZnR_2 to benzaldehyde with different enantioselectivities, leading to the observed hyperpositive NLE.

To check this hypothesis we performed the catalytic reaction with enantiopure (-)-NBE and varied the catalyst loading; the other reaction conditions were left unchanged. The results are shown in Figure 31. Indeed, we observe an ee_P increase as the catalyst loading is decreased from 20 to 2.5 mol%: the ee_P increases only slightly with $ZnEt_2$ (76 to 84% ee) and in a much more pronounced way with $ZnMe_2$ (16 to 49%). The increase is non-linear and fits best to a 2nd order polynomial trendline in both cases, which we have drawn in Figure 31 (orange dotted line). We have added the trendlines here just for illustration purposes, however we will have a use for them in the application of Kagan's reservoir effect in chapter I.2.3.1.

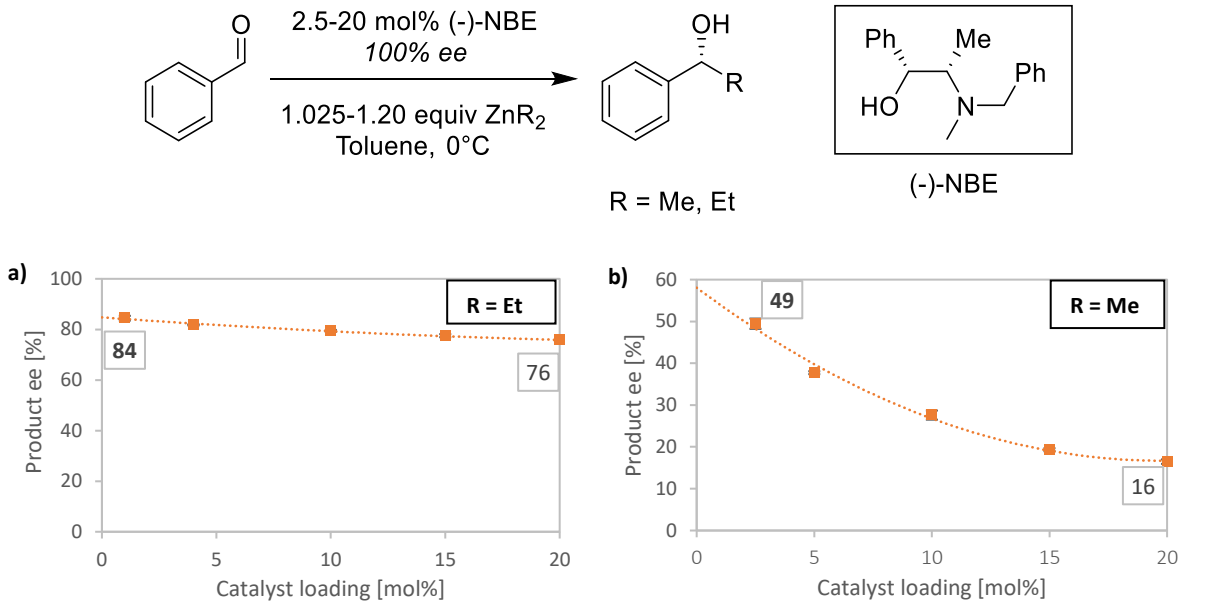

Figure 31: Catalyst loading screening of the (-)-NBE catalysed addition of a) $ZnEt_2$ or b) $ZnMe_2$ to benzaldehyde. The trendlines (2nd order polynomial) are intended for illustration purposes only.

As the curvatures of the two plots look quite similar to those of the hyperpositive NLE curves in Figure 25 and Figure 26, we decided made a superimposition the catalyst loading screening and the hyperpositive NLE. This is possible since we can convert the "catalyst loading" axis in Figure 31 to an "ee_L" axis if we consider that the heterochiral aggregate fully precipitates. For example, the ee_P of a reaction with 20 mol% and 50% ee_L (half of the catalyst has precipitated) must be equivalent to one with 10 mol% (half catalyst loading) of an enantiopure ligand. This way, the catalyst loading curve is changed into a simulated NLE curve. Figure 32 shows the superimposition of the hyperpositive NLE (blue dots) and the converted catalyst loading screening (orange squares). The match between both curves is excellent, as well with $ZnEt_2$ as with $ZnMe_2$. The catalyst loading screening models accurately the ee_P evolution between ee_L = 100% and the hyperpositive NLE's maximal ee_P. The latter is probably the point where the major catalyst enantiomer's concentration is sufficiently low for the minor's concentration to become significant, so ee_P decreases beyond that point when ee_L is further lowered.

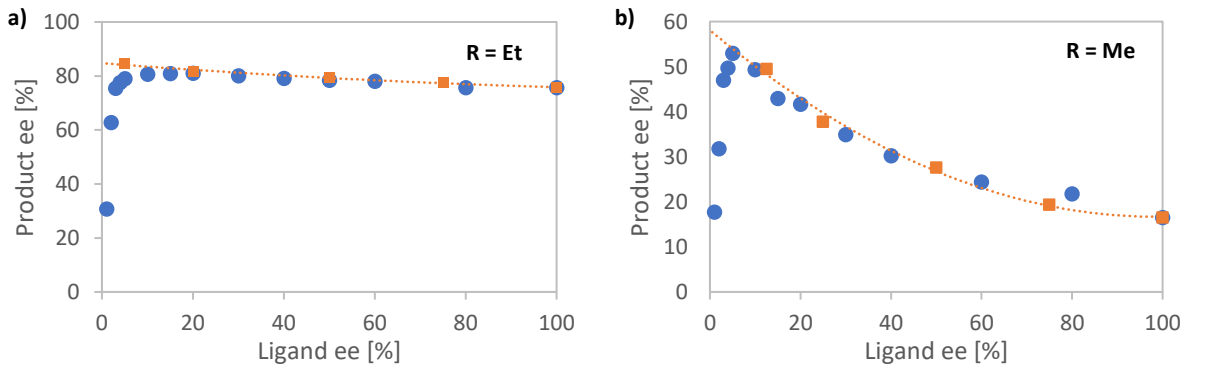

Figure 32: Superimposition of the hyperpositive NLE (blue), the catalyst loading screening (orange) with a) $ZnEt_2$ or b) $ZnMe_2$.

The excellent fit of both curves supports our theory of the ee_P increase being a function of the catalyst concentration, which is itself a function of ee_L due to heterochiral aggregate precipitation. In addition, we made a series of experiments where the overall benzaldehyde/ZnR_2-concentration is varied, while keeping the catalyst loading constant (Figure 33). As in the catalyst loading screening, ee_P increases at lower overall concentration. However, the overall concentration affects the concentration of all the components at the same time, therefore it is difficult to conclude on these results.

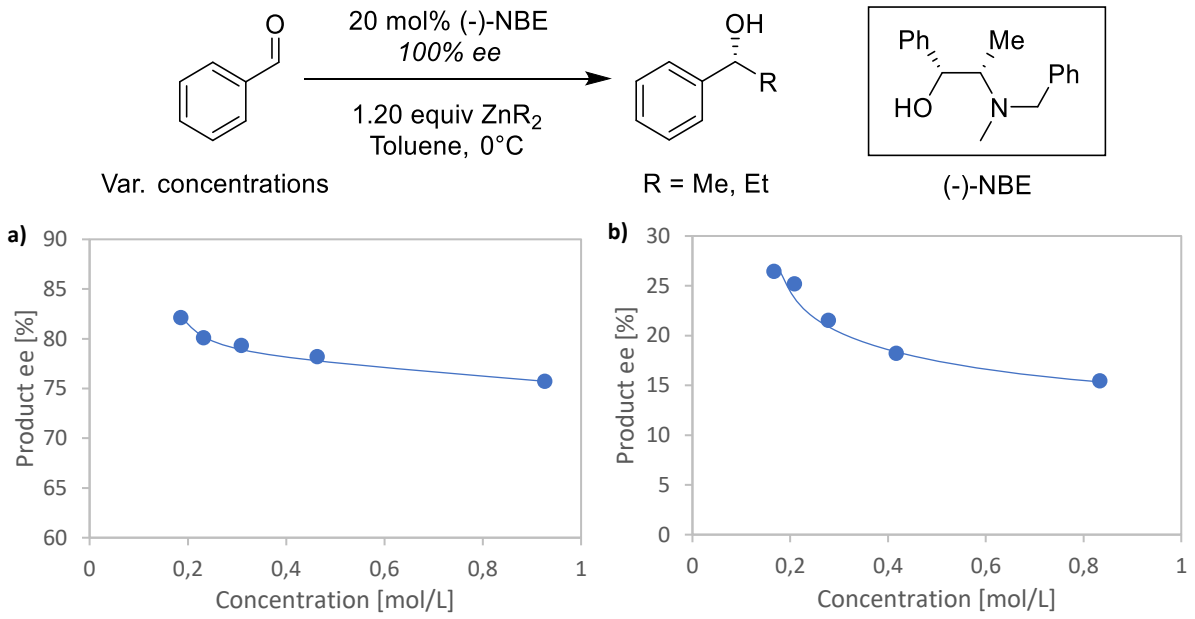

Figure 33: Enantioselective NBE-catalysed addition of a) $ZnEt_2$ and b) $ZnMe_2$ to benzaldehyde at different concentrations.

I.2.2.2 Reaction temperature

Aggregation is a phenomenon sensitive not only to concentration but also to temperature: the dissociation of dimers is entropically favoured and thus driven by an increase in temperature. An example for this is the Soai autocatalytic reaction which becomes slower with increasing temperature, due to a dissociation of the catalytic aggregate.[52] Therefore, we performed a temperature screening of the catalytic reaction with 20 mol% of an enantiopure and of a 20% ee ligand, under otherwise unchanged conditions (Figure 34).

The system using $ZnMe_2$ and enantiopure ligand (Figure 34b, blue dots) shows an impressive ee_P increase from 16% at 0°C to 44% at 60 °C; with the scalemic ligand (orange dots) a slightly less pronounced ee_P increase takes place. With $ZnEt_2$ and enantiopure ligand (Figure 34a, blue dots) ee_P stays constant around 76% ee; the scalemic ligand (orange dots) shows an ee_P decrease above 0°C, falling below the blue line at 60 °C – the NLE is not hyperpositive anymore at this point.

Usually, ee_P *decreases* with increasing temperature, since the difference between the kinetic barriers leading either to *R*- or *S*-product becomes smaller; this is the reason why asymmetric catalysis is

often performed at low temperature. The results shown here are clearly the consequence of a change of the active catalyst. It is also coherent with our hypothesis developed in I.2.2.1: at high temperature the homochiral dimers would break up to the monomeric and more enantioselective catalyst, therefore the overall ee_P would increase. The increase with 20% ee_L in Figure 34b is lower than with 100% ee_L probably because the homochiral dimers are already partly broken up; an increase of the heterochiral aggregate's solubility has also to be taken into consideration. With $ZnEt_2$ and 100% ee_L (Figure 34a), the ee_P-gain might be smaller and therefore just enough to compensate the usual ee_P decrease, leading to an almost constant ee_P at 76%; with the scalemic catalyst the ee_P decrease is not compensated anymore.

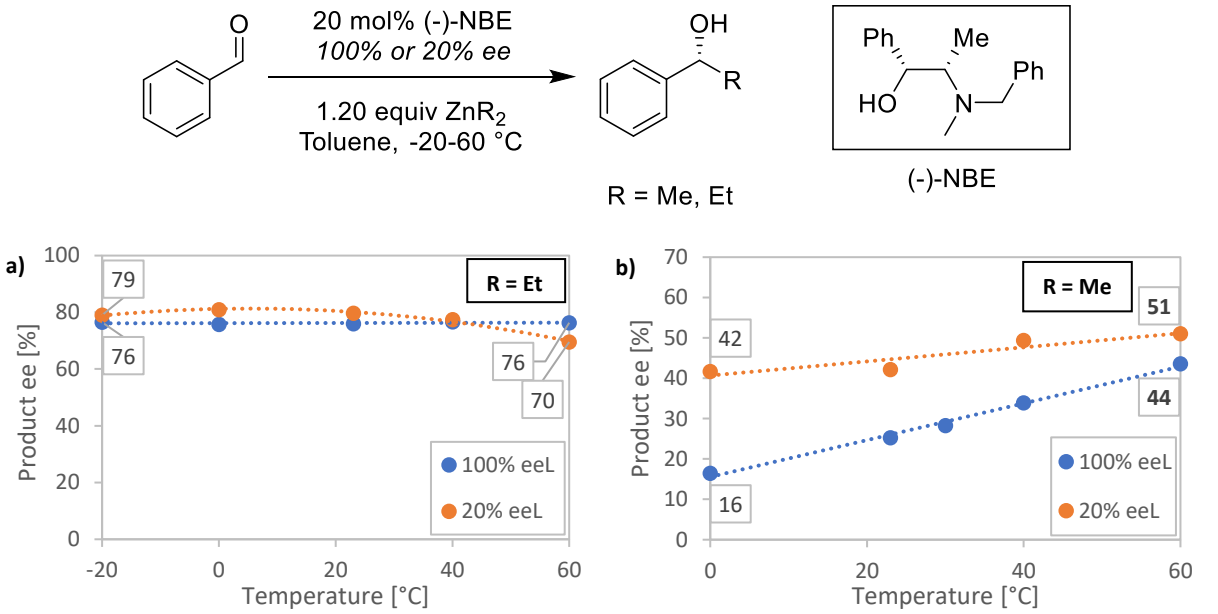

Figure 34: Temperature screening of the (-)-NBE (100% ee: blue dots, 20% ee: orange dots) catalysed addition of a) $ZnEt_2$ and b) $ZnMe_2$ to benzaldehyde. The trendlines (1st and 2nd order polynomial functions) are intended for illustration purposes only.

I.2.2.3 Mass spectrometry

Next, we sought to gather more information about the catalytic NBE-zinc complex and its homochiral aggregate, as we presume it also to be catalytically active. We didn't succeed in obtaining a crystal structure from enantiopure NBE-ZnMe so far (same goes for racemic NBE-ZnMe) but we could obtain some results from electrospray ionisation mass spectrometry (ESI-MS): two sets of peaks were identified to correspond to monomeric (Figure 35) and dimeric (Figure 36) NBE-ZnMe, both monoprotonated. The latter is a homochiral dimer since the sample was made from enantiopure (-)-NBE. The experimental spectra fit excellently to the simulated isotopic patterns. Since the sample is heated to 180 °C during the injection it is not self-evident to observe adducts originating from weak interactions like coordination bonds. This is a first proof for NBE-ZnMe forming a homochiral dimer, however it is not representative for the complexes' behaviour in solution. Therefore, we went on to analysis of NBE-ZnMe in solution by ^{1}H DOSY NMR.

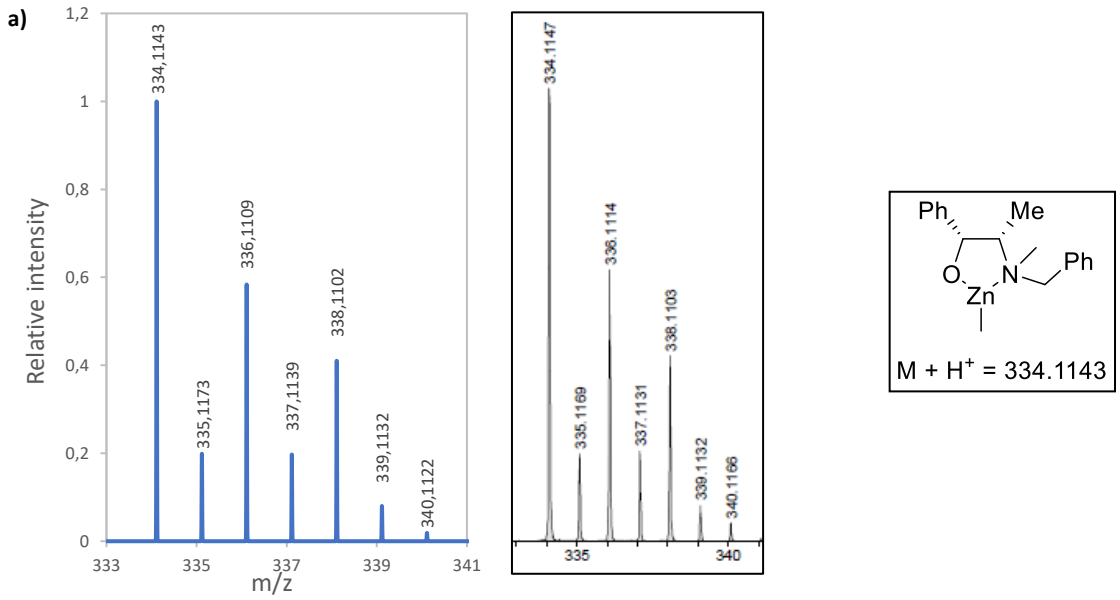

Figure 35: a) Simulated and b) experimental ESI-MS spectra of monomeric NBE-ZnMe. The simulation was obtained from Prot Pi online Mass Spec simulator, www.protpi.ch.

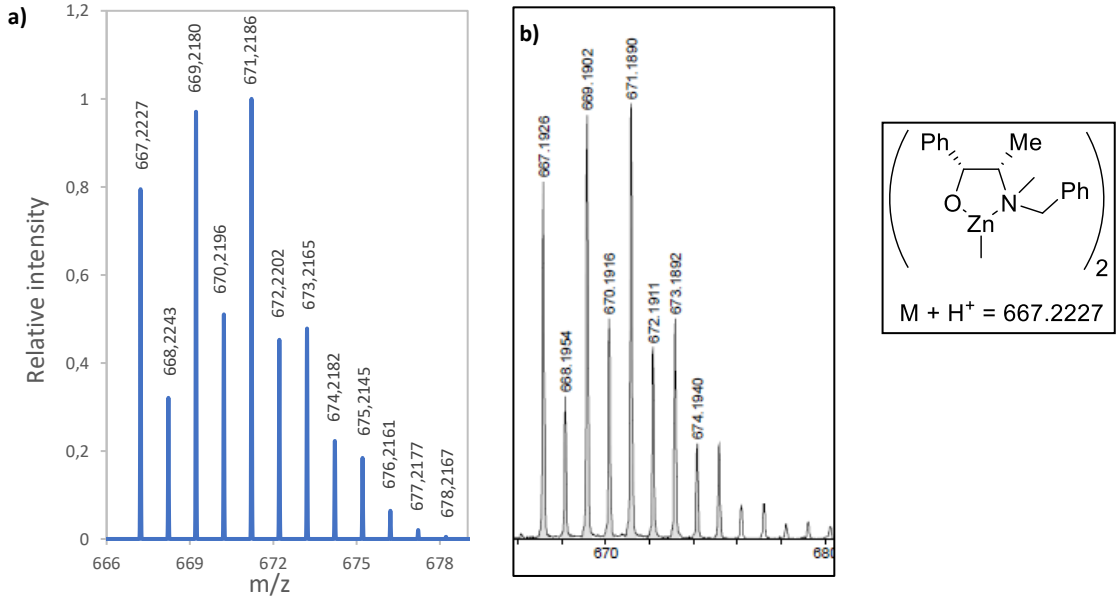

Figure 36: a) Simulated and b) experimental ESI-MS spectra of dimeric NBE-ZnMe. The simulation was obtained from Prot Pi online Mass Spec simulator, www.protpi.ch.

I.2.2.4 ^{1}H DOSY NMR

^{1}H DOSY NMR measures the diffusion coefficient (*D*) of the solubilised analyte which can be related to its volume or its molecular weight (MW). This allows us to work in conditions much closer to the catalytic reactions, namely in solution, at the same temperatures and in presence of reactant and/or substrate. We used Stalke's External Calibration Curves (ECC) to relate the measured diffusion

coefficient to MW values.[112–115] A detailed explanation of the methodology and why it is our method of choice can be found in the supporting information, p. 161.

(a) ^{1}H NMR of NBE-ZnMe

For the analysis of the NBE zinc aminoalkoxide issued from $ZnMe_2$ (NBE-ZnMe) we chose to work in the same conditions as in the catalytic runs for the temperature screening (0.83 M $ZnMe_2$ and 20 mol% NBE-ZnMe) in toluene-d_8, at temperatures from -20 to 60 °C. The ^{1}H NMR spectra (Figure 37) gave broad peaks at 25°C and higher (red spectrum), which can be easily attributed to the NBE-ZnMe complex. At lower temperature the peaks sharpen and new peaks appear, at -20°C the spectrum becomes extremely complex (blue spectrum). However, nearly all the peaks are correlated to a single *D* value: the exchange between the different species is too fast for the DOSY NMR timescale, therefore only mean *D* values were obtained. ^{1}H ROESY NMR confirmed the presence of several, interconverting species. The ^{1}H NMR spectrum's complexity at -20 °C is not surprising: the monomeric complex exists as a pair of diastereoisomers since the *N* atom becomes chiral upon coordination to zinc; the complexes may be coordinated to the excess $ZnMe_2$ or not; and finally, NBE-ZnMe and its expected dimer probably have a different set of signals.

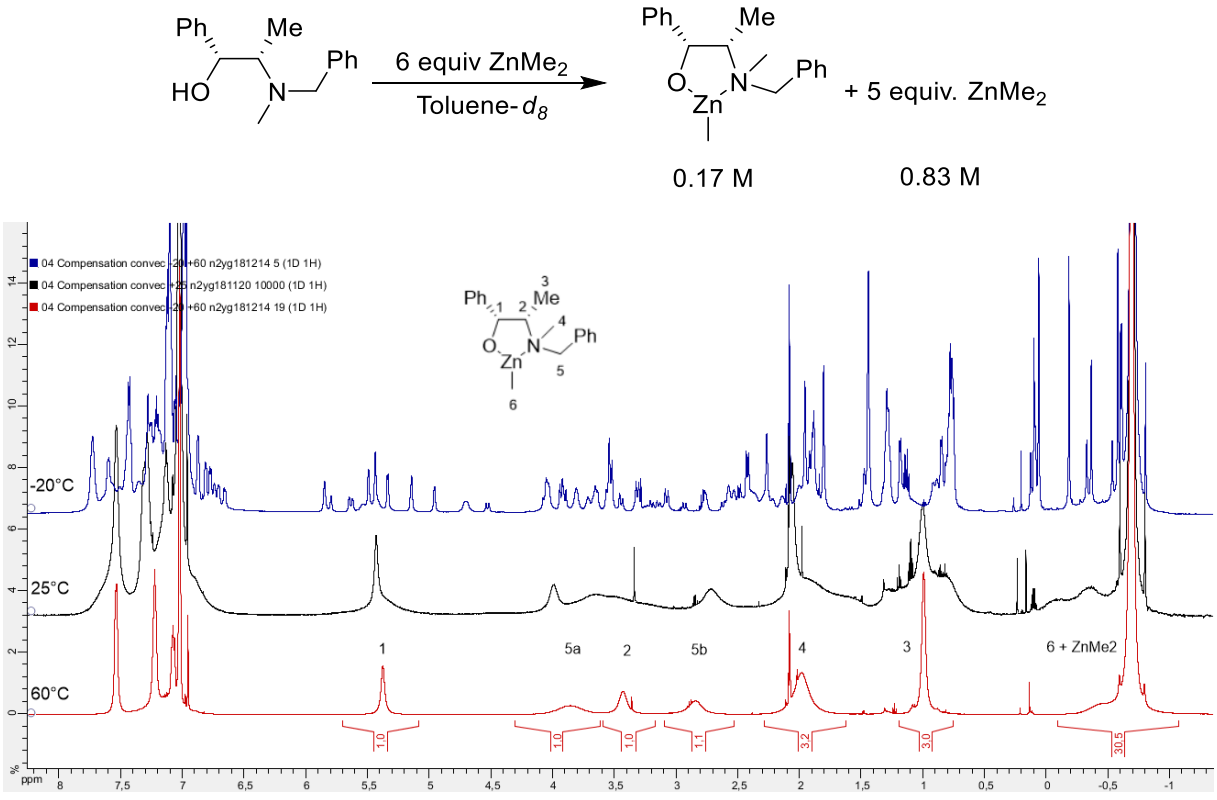

Figure 37: ^{1}H NMR spectra of (-)-NBE-ZnMe in presence of 5 equiv. $ZnMe_2$ at -20, 25 and 60°C.

In addition, we analysed also a sample in which one equivalent of benzaldehyde was added to be closer to the conditions of the catalytic reactions. We could analyse it only at low temperature (-20 to

10 °C) to slow down the catalytic reaction. The formation of the chiral zinc alkoxide leads to changing peak intensities and chemical shifts and therefore complicates the DOSY measurements.

(b) ^{1}H DOSY NMR and MW determination

For the DOSY experiments, we used the residual signal of toluene-d_8 as a reference to calculate $D_{x,norm}$; mean MW values were obtained from the Dissipated Spheres and Ellipsoids (DSE) ECC, as NBE-ZnMe's shape neither is a compact sphere nor an expanded disk. Stalke's ECC methodology is valid only if the analyte falls into a certain range of Molecular Weight Density (MW_D, which is the analyte's MW divided by its volume, calculated from its sum of Van-der-Waals radii). Table 1 shows the calculated MW_D values of NBE-ZnMe and of its adducts with $ZnMe_2$ and/or benzaldehyde. All are within the limits in which the ECC is valable ($4.3 \cdot 10^{-29}$ - $5.2 \cdot 10^{29}$ $gmol^{-1}m^{-3}$), except NBE-ZnMe + $ZnMe_2$ which is a borderline case due its high Zn/C ratio. The MW of possible $ZnMe_2$ and/or benzaldehyde adducts of monomeric, dimeric and trimeric NBE-ZnMe complexes are compiled in Table 2.

Complex	MW_D [$gmol^{-1}m^{-3}$]
NBE-ZnMe only	$4.96 \cdot 10^{29}$
+ $ZnMe_2$	$5.22 \cdot 10^{29}$
+ Benzaldehyde	$4.92 \cdot 10^{29}$
+ $ZnMe_2$ + Benzaldehyde	$5.15 \cdot 10^{29}$

Table 1: Calculated MW_D for NBE-ZnMe and its adducts with $ZnMe_2$ and/or benzaldehyde. All are within the upper MW_D limit of $5.20 \cdot 10^{29}$ $gmol^{-1}m^{-3}$, with exception of NBE-ZnMe + $ZnMe_2$.

The results from the DOSY experiments are summarised in Figure 38. At any temperature, the measured mean MW without benzaldehyde (orange dots) are clearly above the value of monomeric NBE-ZnMe; at 60°C, the measured value of 474 g/mol is close to the MW of the NBE-ZnMe-$ZnMe_2$ complex but still above. In presence of benzaldehyde (grey dots) the overall MW is lower but still well above the values for NBE-ZnMe and also of the $ZnMe_2$-benzaldehyde adduct (536 g/mol). In both cases, the mean MW decreases with increasing temperature, confirming the presence of homochiral aggregates which dissociate upon increase of the temperature.

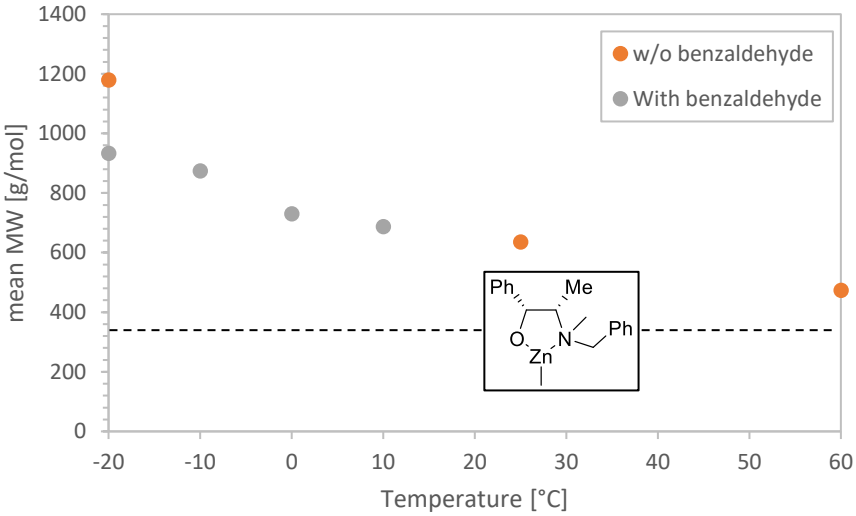

Figure 38: ^{1}H DOSY NMR analysis of (-)-NBE-ZnMe (0.1 M) in presence of $ZnMe_2$ (0.83 M, orange dots) and of additional benzaldehyde (0.83 M, grey dots). Depicted are also the calculated MW of the monomeric NBE-ZnMe (black dashed line).

The absolute MW values of Figure 38 are all between the values for a monomeric and the heaviest possible dimeric NBE-ZnMe complex (bound to $ZnMe_2$ or $ZnMe_2$+benzaldehyde, respectively), except those at -20°C which are even higher (Table 2). This is interesting as it implies higher-order aggregates such as trimers, which have been excluded in the Noyori model for DAIB. On the other hand, this is consistent with the work of Fitzpatrick et al. where they claim to have found aggregates up to tetramers with the ZnEt complex of N-methyl ephedrine.[90]

Complex	MW monomer [g/mol]	MW dimer [g/mol]	MW trimer [g/mol]
NBE-ZnMe only	335	670	1004
+ $ZnMe_2$	430	765	1100
+ Benzaldehyde	441	776	1110
+ $ZnMe_2$ + Benzaldehyde	536	871	1206

Table 2: MW of $ZnMe_2$ and/or benzaldehyde adducts of monomeric, dimeric or trimeric NBE-ZnMe complexes.

(c) NBE-ZnMe-mimics: synthesis and ^{1}H DOSY NMR-analysis

To check the validity of Stalke's methodology we synthesised molecules **1** and **2** (Figure 39). They are designed to mimic NBE-ZnMe's shape (same five-membered ring, same substituents and spatial configuration on the carbon backbone) but without being able to aggregate via coordination bonds like zinc aminoalkoxides do. The compounds were analysed in ^{1}H DOSY NMR in the same conditions as NBE-ZnMe (0.17 M, toluene-d_8, various temperatures). The DSE-ECC gave the best results and confirmed our choice for its use with NBE-ZnMe.

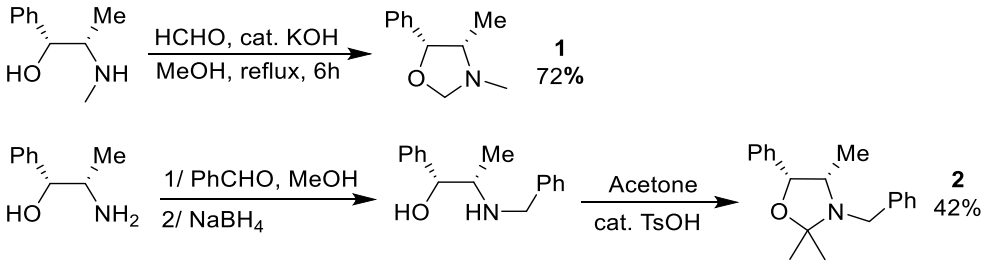

*Figure 39: Reaction scheme for the synthesis of the DOSY reference products **1** and **2**.*

Figure 40 shows the deviation of the measured MW from the calculated MW (MW_{dev}). The results fit excellently at rt and higher (MW_{dev} < 4%) but at lower temperatures the molecules' MW is overestimated, by 8% for **1** and by 18% for **2** at -20°C. Given the fact that **2** bears one aromatic ring more than **1**, the deviation most probably results from π-interactions with the solvent (solvation sphere) or between analyte molecules (intramolecular aggregation). NBE-ZnMe and its aggregates also bear two aromatic rings per ephedrine unit, plus one if benzaldehyde is coordinated. Even though the data in Figure 38 is sufficient to conclude qualitatively that NBE-ZnMe indeed does form homochiral aggregates and that those dissociate at higher temperatures, the absolute measured MW values may not necessarily reflect the real monomer-dimer distribution; especially the conclusion on trimers at low temperature is questionable and should be verified by further experimental work.

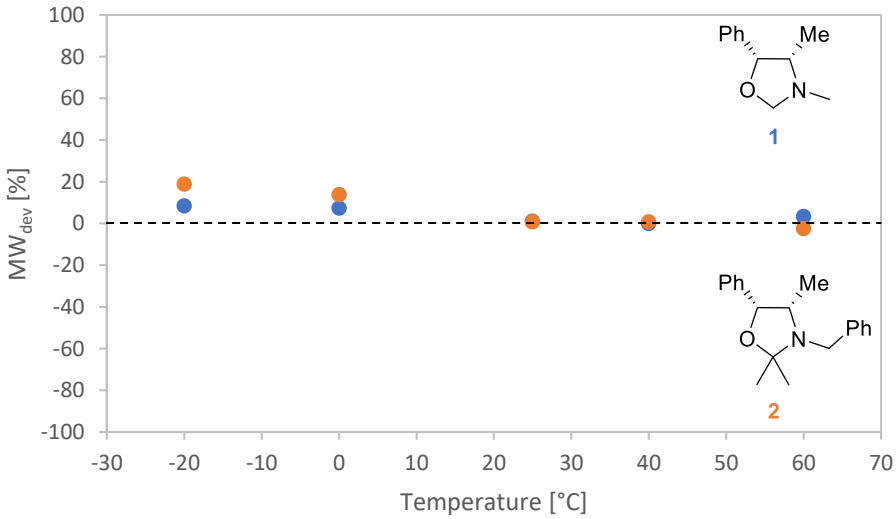

*Figure 40: Deviation of the measured MW (toluene-d_8, 0.17 M) from the calculated MW of **1** (blue dots) and **2** (orange dots). MW_{dev} is calculated MW(measured)/MW(calculated), positive values mean that MW is overestimated (differs from Stalke's definition of MW_{dev}).*

We also tried to synthesise boron complexes of NBE but without success; other complexes, based on zinc and bidentate and tetradentate ligands gave overestimated MW values in DOSY NMR, probably due to aggregation. We will not discuss these results here, but they can be found in the Supporting Information (V.2.1, p. 166).

I.2.2.5 Kinetics

To gain further insight into the NBE-catalysed addition of dialkylzincs to benzaldehyde, we decided to investigate the reaction's kinetic behaviour. Conversion *vs* time- and ee_P *vs* time-plots can give valuable information about a reaction's underlying mechanics. The present study will first focus on the determination of the catalyst's partial order *c* and then examine the evolution of ee_P over time.

(a) Partial catalyst order and aggregation

In general, the rate of catalysed reactions can be described by equation (11):

$$\frac{d[Prod]}{dt} = \frac{-d[Sub]}{dt} = k_{obs}[Cat]^c[Sub]^x[Rea]^y \qquad (11)$$

With [Prod] being the product concentration, [Sub] the substrate concentration, [Rea] the reactant concentration, [Cat] the catalyst concentration, k_{obs} the observed kinetic constant, *x* the partial substrate order, *y* the partial reactant order and *c* the partial catalyst order.

Equation (11) is true for simple catalytic reactions but can change for more complex ones. If e. g. the reaction product inhibits the reaction, then an additional "$[Prod]^P$" term appears on the right side of equation (11), with the partial product order P < 0. [Prod], [Sub] and [Rea] change over the course of the reaction; the other variables usually are constants but this may also not be true for all catalytic systems. Especially the partial orders are interesting: they reflect the number of molecules involved in the rate-determining step, e. g. a reaction where two catalyst molecules intervene simultaneously will have *c* = 2. However, the *measured* catalyst order can differ much if the catalyst is involved in other processes for which equation (11) does not account for. Those can be aggregation, deactivation by an impurity and others; there are even general methods to analyse changing catalyst or reactant orders ("elasticity coefficient").[116]

An example for a changing partial order in catalyst *c* is shown in Figure 41: Bures et al. investigated the effect of [Cat] on *c* in a Pd-catalysed cross-coupling reaction.[117] At low [Cat] *c* is close to 1, which reflects the mechanism of the Heck reaction where only *one* Pd moiety is involved. However, at higher [Cat] *c* drops to 0.55. This is due to the palladium complex aggregating to a catalytically inactive dimer: the higher [Cat], the higher the fraction of inactive catalyst. Since the *effective* [Cat] is lower than the *initial* [Cat], which is used in equation (11), *c* decreases to compensate for this discrepancy.

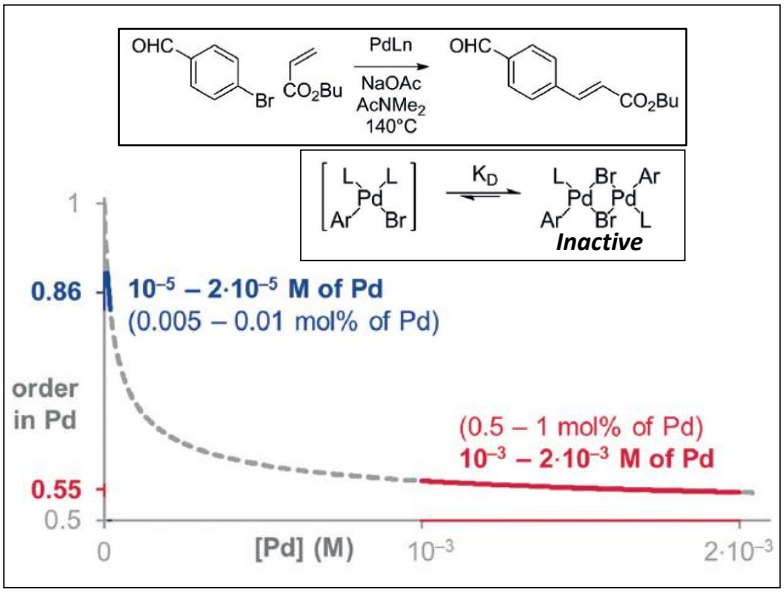

Figure 41: Example for a [Cat]-dependent change in catalyst order due to aggregation of the Pd-catalyst to an inactive dimer, in a Pd-catalysed Heck coupling.[117]

Since our system with NBE does also deal with catalyst aggregation, we decided to investigate its catalyst order *c* by varying [Cat]. The kinetics of DAIB have been shown to follow equation (11) (except at high [Sub] and [Rea], where $x = y = 0$ because the catalyst is saturated in Rea and Sub; the reaction rate then depends only on the concentration of the catalytic Cat-Sub-Rea adduct) and should be applicable to NBE.

(b) Theoretical model

Prior to the experimental determination of kinetic profiles, we developed a simple theoretical model to describe the kinetics of a reaction which is catalysed by both a monomeric and a dimeric catalyst. We will consider the case of homochiral (-)-NBE where two different species catalyse: the monomeric complex NBE-ZnMe and its dimeric aggregate. The concentration of both is given by [R] and [RR], respectively. We can consider two extreme cases where only [R] or only [RR] catalyse:

$$\frac{-d[Sub]}{dt} = k_1[R]^{c_1}[Sub]^{x_1}[Rea]^{y_1} \tag{12}$$

$$\frac{-d[Sub]}{dt} = k_2[RR]^{c_2}[Sub]^{x_2}[Rea]^{y_2} \tag{13}$$

With x_1, y_1, c_1 and k_1 being the partial orders and the kinetic constant of the monomer-catalysed reaction and x_2, y_2, c_2, and k_2 those of the dimer-catalysed one. From a practical point of view, equation (12) could be valid only at very low catalyst concentration and/or high temperature (only

monomers present) and equation (13) in the opposite conditions – very high catalyst concentration and/or low temperature. The conditions in which we worked so far are intermediate, [R] and [RR] are simultaneously present and catalyse both. The reaction's kinetics are then described by a combination of equations (12) and (13):

$$\frac{-d[Sub]}{dt} = k_1[R]^{c_1}[Sub]^{x_1}[Rea]^{y_1} + k_2[RR]^{c_2}[Sub]^{x_2}[Rea]^{y_2} \tag{14}$$

For the next step we will make an assumption: the inherent mechanism of both monomer- and dimer-catalysed reactions is similar and therefore also the nature of their rate-limiting step (similar to DAIB, see Figure 9). In this case, $x_1 = x_2 = x$, $y_1 = y_2 = y$ and $c_1 = c_2 = c$. k_1 and k_2 can but don't need to be equal, therefore we will treat them separately. Equation (14) then becomes equation (15):

$$\frac{-d[Sub]}{dt} = (k_1[R]^c + k_2[RR]^c)[Sub]^x[Rea]^y \tag{15}$$

Since we cannot measure [R] and [RR] directly, we have to express them as a function of the total catalyst concentration [Cat_{tot}]. Equation (16) defines *a*, the monomer's *fraction* of the total catalytic species [Cat_{tot}] in a given reaction. It is dependent from a dimerisation constant, K_{Homo}, which we won't further develop at this stage (it will be further discussed in chapter I.2.3.2(b), p. 60); we will also assume *a* to be constant over time, which means that the [R]/[RR] distribution doesn't change over the course of the reaction. [Cat_{tot}] is equal to the quantity of ligand weighed and engaged at the beginning of the reaction and is thus a known reaction parameter. It is related to [R] and [RR] via equation (17), assuming that no higher aggregates than dimers exist in solution.

$$a = \frac{[R]}{[Cat_{tot}]} \tag{16}$$

$$[Cat_{tot}] = [R] + 2[RR] \tag{17}$$

Using equations (16) and (17) we can now eliminate [R] and [RR] from equation (15), giving equation (18):

$$\begin{aligned} \frac{-d[Sub]}{dt} &= \left(k_1(a[Cat_{tot}])^c + k_2\left(\frac{(1-a)}{2}[Cat_{tot}]\right)^c\right)[Sub]^x[Rea]^y \\ \Leftrightarrow \frac{-d[Sub]}{dt} &= \underbrace{\left(k_1 a^c + k_2\left(\frac{(1-a)}{2}\right)^c\right)}_{= k_{obs}}[Cat_{tot}]^c[Sub]^x[Rea]^y \end{aligned} \tag{18}$$

Equation (18) now has the same form as equation (11), with a more complex expression for k_{obs}. k_1, k_2 and c are constants while a depends on $[Cat_{tot}]$. If $a = 1$ only monomers are present and equation (18) simplifies to equation (12). Same for $a = 0$ where equation (18) simplifies to equation (13) because only dimers catalyse. For $0 < a < 1$, k_{obs} in equation (18) becomes an intermediate value between k_1 and $k_2/2$ which depends on $[Cat_{tot}]$. Therefore, *a change of $[Cat_{tot}]$ induces a change in k_{obs}* as long as $0 < a < 1$. An exception to this rule is given if $c = 1$ and $k_1 = k_2/2$, meaning [RR] catalyses twice as fast as [R]. In this case the lowering of catalytic molecules due to aggregation is counterbalanced by the aggregates' higher catalytic activity: k_{obs} stays constant whatever the value of a since $k_{obs} = k_1 = k_2/2$.

(c) Catalyst order of the NBE-catalysed reaction

To study NBE's catalyst order we performed several kinetic runs in which the reaction progress was monitored via infrared spectroscopy (IR). Benzaldehyde has an intense C=O stretch around 1700 cm^{-1} which is perfectly suited for IR monitoring. The kinetic runs were performed with $ZnMe_2$ in the same conditions as for the catalyst loading screening in Chapter I.2.2.1, with exception of the temperature which was elevated to 30°C to speed up the reaction.

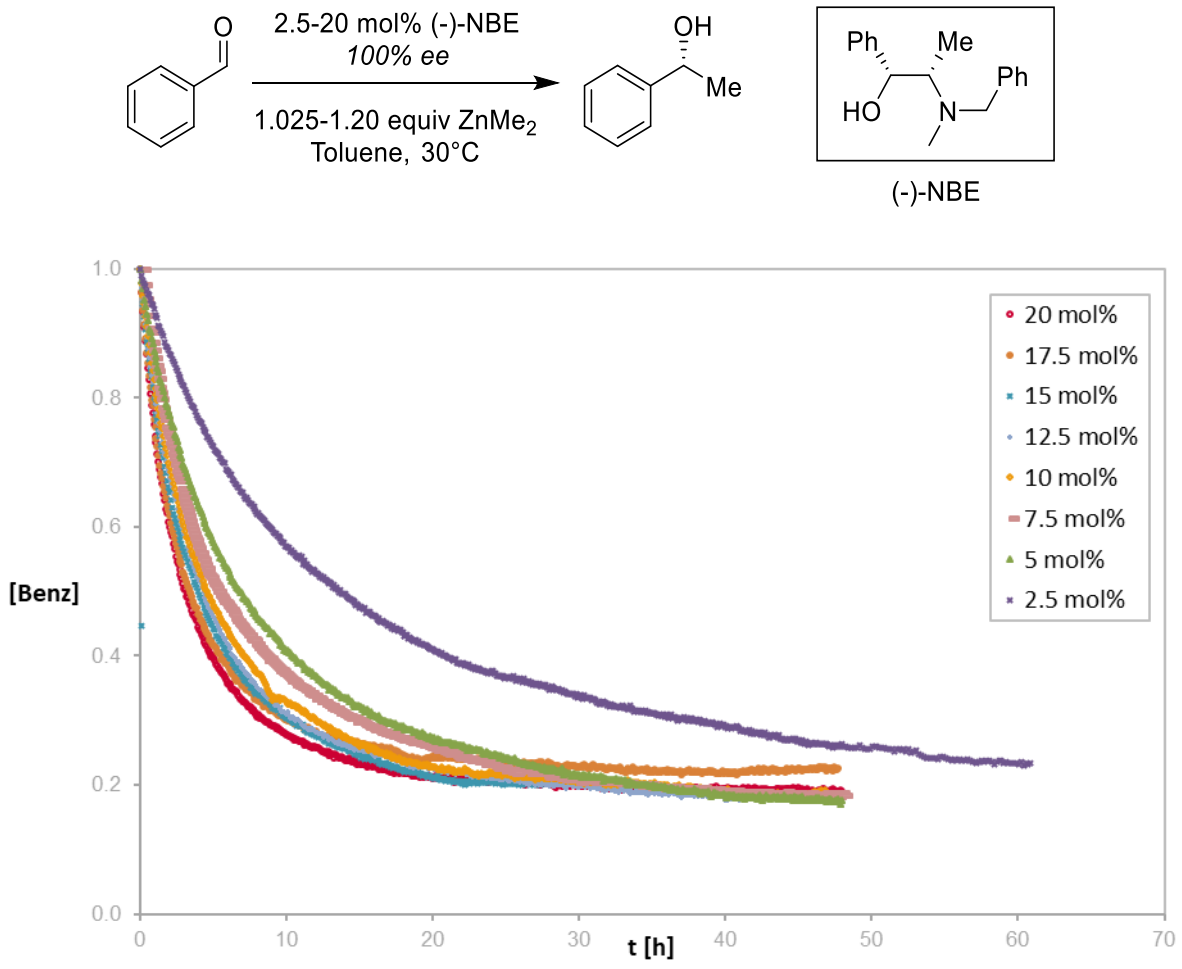

Figure 42: Kinetic profiles of the (-)-NBE-catalysed addition of $ZnMe_2$ to benzaldehyde with varying catalyst concentrations. The values of the benzaldehyde concentration were normalized to the initial concentration of 0.83 mol/L.

Figure 42 shows the results from kinetic runs with varying catalyst loadings from 2.5 to 20 mol%, in 2.5 mol%-steps. On a first glance it strikes that the reaction is significantly sped up when going from 2.5 to 5 mol%, however from 5 to 7.5 or 10 mol% the difference is much lower; at high catalyst loading the curves are almost identical. The reactions also don't reach full conversion but reach a plateau around 80% conversion, which is consistent with what we observed in former experiments; this may be the result from product inhibition.

To extract *c* from the kinetic rate profiles in Figure 42, we analysed the data using Visual Time-normalised Analysis (VTNA). It consists in a mathematical transformation of the time-axis which becomes "normalised" to the catalyst concentration. It results in the rate profiles being identical, i. e. overlaying, if they differ in their reaction parameters only in the catalyst concentration and if the right *c* has been chosen. Thus, *c* can be determined by a simple visual check. An example for VTNA is shown in Figure 43; a more detailed explanation of VTNA can be found in the supporting information, p. 163.

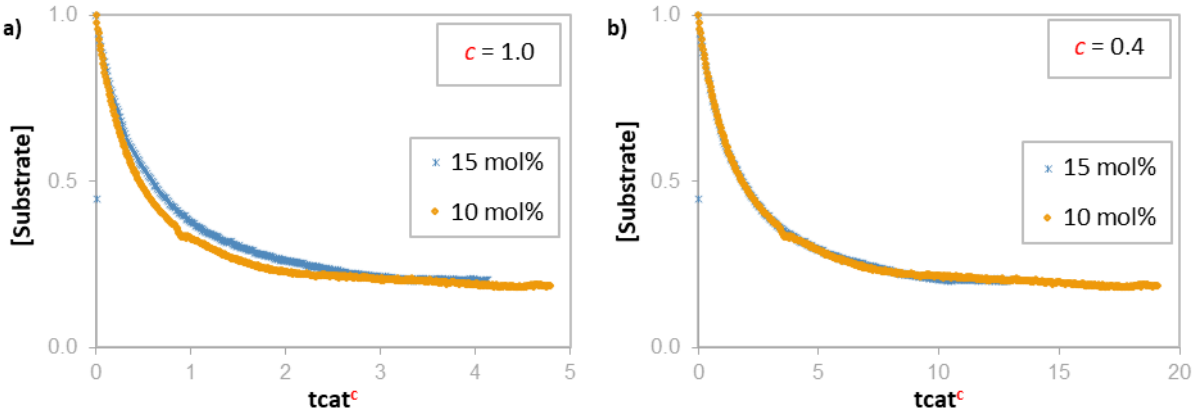

Figure 43: Example of c adjusting using VTNA with a) c = 1.0 and b) c = 0.4. The two curves in each graph were obtained from different catalyst concentrations (blue curve: 0.15 M; orange curve: 0.10 M). The best overlay is obtained for c = 0.4 which is therefore the partial order in catalyst.

Application of VTNA to the data from Figure 42 resulted in time-normalised rate profiles for which we could not find any *c* value which makes all of the curves overlay at the same time. This is indicative of a non-constant catalyst order. Therefore, we made a segmented analysis in which we overlaid only two neighbouring curves at a time to determine a *c* value valid for both curves: this allows us to monitor *c* over a range of catalyst loadings. The lower the difference in [Cat], the less the curves are visually affected by a change in *c*. Thus, we had to increase the difference in catalyst loading Δ[Cat] between two compared curves at higher catalyst loadings: curves with a Δ[Cat] of 2.5-5 mol% were compared from 2.5 to 10 mol%, between 10 and 20 mol% we had to increase Δ[Cat] to 5-7.5 mol%. Figure 44 shows the *c* vs catalyst loading plot, with Δ[Cat] represented by a horizontal bar for each determined *c* value.

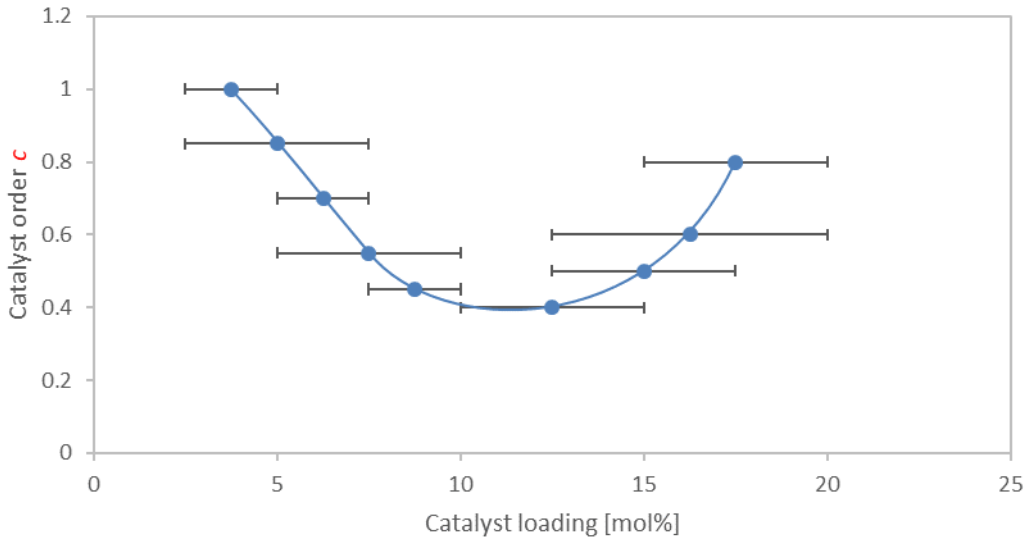

Figure 44: Catalyst order c vs catalyst loading, with c being defined by equation (11). The error bars on each dot indicate which two kinetic curves have been used to determine c, which can be considered as a mean value over the respective Δ[Cat].

Figure 44 gives a very interesting picture of *c*'s evolution: it starts at *c* = 1 at low catalyst loading, decreases to 0.4 between 10 and 15 mol% but then increases back to 0.8 between 15 and 20 mol%. There is indeed a change of catalyst order when varying [Cat] but it is quite different from what is described in Figure 41, where *c* converges to a lower value when increasing [Cat]. To the best of our knowledge, there is no precedent for such a behaviour where *c* decreases and increases again in a U-shaped curve. However, it can be interpreted in a way which fits into our theory on a joint catalysis by monomers and dimers, and which concords with the theoretical kinetic model from chapter I.2.2.5(b).

We observe *c* = 1 at low catalyst loading, which is the expected value for the monomeric NBE-ZnMe (like its DAIB-based equivalent). If the dimeric catalyst works with a similar mechanism, we then expect its order also to be of one. Therefore, *c* should be equal to 1 in the far right and far left parts of the catalyst loading scale, where either only monomers or dimers are present, respectively (Figure 45). Figure 44 comes close to this with *c* = 1.0 on the left and *c* = 0.8 on the right.

Moreover, we know from equation (18) that k_{obs} changes over varying [Cat] when both monomer and dimer exist in solution and catalyse. However, VTNA assumes k_{obs} to be constant, according to equation (11). *This leads the measured c to change over different [Cat] to compensate for the variation in* k_{obs}. This can be exemplified on Figure 43: it might be not because the wrong catalyst order is chosen that the curves do not overlay at *c* = 1, but because of their respective k_{obs} are different. Therefore, the exemplified value of 0.4 in Figure 43b would be a purely mathematical construction to make equation (11) fit into equation (18). This applies to all the overlays used to construct Figure 44.

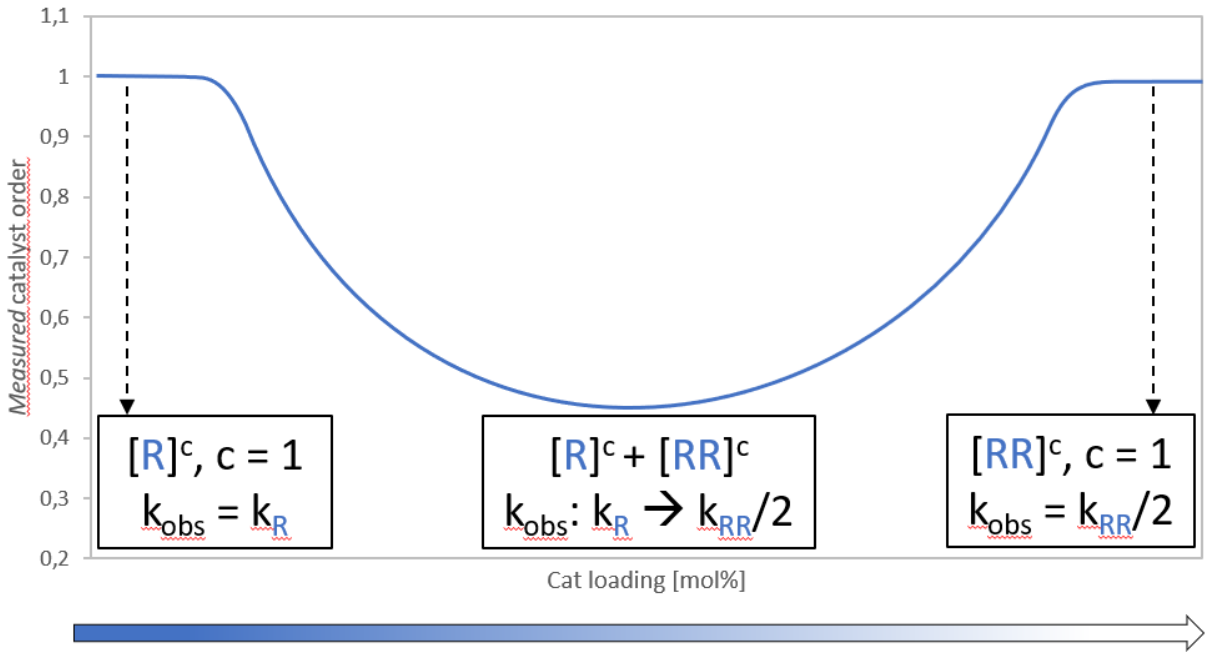

Figure 45: Schematic hypothetical representation of the measured order c as a function of the catalyst composition, with c being defined by equation (11). At very low and very high catalyst loading only one catalyst is present, either monomeric R or dimeric RR; both have an intrinsic catalyst order of 1, which corresponds also to the measured catalyst order. For intermediate reaction conditions, where both catalysts exist at the same time, the gradually changing k_{obs} value leads to a non-linear rate increase upon increasing catalyst loading, therefore $c \neq 1$.

However, this interpretation has to be taken with care as the theoretical model is built on certain assumptions and approximations which may turn out to be oversimplified or incorrect (this will be discussed in the next section). What seems to be quite certain is that the behaviour of *c* in Figure 44 shows that the *nature* of the catalytic species changes over variation of [Cat], not just its active fraction as in the example with Palladium in Figure 41. This supports our theory of homochiral aggregates also catalysing the reaction and being responsible for the hyperpositive NLE.

(d) ee_P *vs* time

For now, we have considered only the reaction's conversion over time, without making the difference between *R* and *S* products. Noyori found ee_P to be non-constant over time in the DAIB-catalysed enantioselective addition of $ZnMe_2$ to benzaldehyde at 20% ee_L.[29] It increases from 82% (5% conversion) to 89% (84% conversion). This could be rationalised from the decreasing benzaldehyde and $ZnMe_2$-concentrations over time: less binding to substrate/reactant results also in less catalyst dimer dissociation; less dissociation of heterochiral DAIB-ZnMe dimer leads necessarily to higher ee_P.

Under certain conditions he observed also product inhibition of the catalyst, as the product's desorption from the catalyst is, in fact, not irreversible but an equilibrium process (Figure 46). The zinc alkoxide product forms tetramers, which may be of homo- or heterochiral composition, the latter being less stable than the homochiral one. Therefore, if the reaction gives a low ee_P at the beginning (e. g. with low DAIB-concentration and low ee_L), the product is more likely to stay bound to

the catalyst instead of forming tetramers, which drives further the dissociation of DAIB-ZnMe dimers and thus diminishes the (+)-NLE. Blackmond and co-workers did a kinetic study of the DAIB-variant Morpholinoisoborneol (MIB) in which they evidenced product inhibition.[118] A new model taking into account product desorption from the catalyst allowed an accurate prediction of the kinetic data.

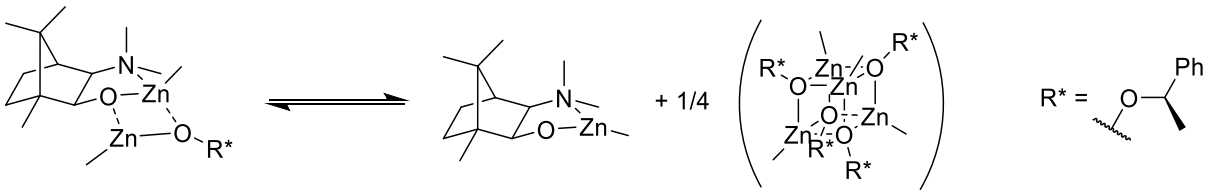

Figure 46: Scheme for the equilibrium between the DAIB-ZnMe/zinc alkoxide adduct and uncomplexed DAIB-ZnMe + free zinc alkoxide, as a tetrameric aggregate. The Noyori model (see Figure 8 and Figure 9, p. 18) assumes that this is not an equilibrium but that the zinc alkoxide dissociates irreversibly from DAIB-ZnMe.

In the light of Noyori's work, we decided to investigate the evolution of ee_P over time in the NBE-catalysed reaction. We performed another series of kinetic runs using similar conditions as for the runs in Figure 42, except for the temperature which was lowered to 0°C. Instead of in situ-monitoring by IR spectroscopy, aliquots were taken at the indicated reaction time and quenched rapidly, followed by GC analysis. In situ-monitoring of ee_P is possible but affords special instrumentation which records IR and vibrational circular dichroism (VCD) spectra simultaneously.[119]

Figure 47 shows the results from the kinetic runs (the results for 10, 12.5 and 17.5 mol% have been omitted for clarity; the full graph can be found in the experimental part, IV.1.2.5, p. 144). Indeed, in all runs ee_P is not constant over time but it increases as the reaction proceeds. The lower the catalyst loading, the higher the ee_P at which the reaction starts; the shape of the different curves seems to be quite similar. The reaction at 20 mol%, from which we know it gives 16 % ee_P at the end of the reaction, starts with only 4% ee_P after 10 minutes (1% conversion). The reaction with 2.5 mol% already is at 34% ee_P after 20 min (0.4% conversion) but increases to 44% after 2h reaction time (2.2% conversion) and ends up at 49% ee_P (see Figure 31b, p. 35).

The ee_P increase over time in Noyori's system with scalemic DAIB was rationalised to come from an intrinsic increase of the (+)-NLE. Here, we use enantiopure (-)-NBE so the origin of the ee_P increase must be different. Several scenarios could explain this behaviour:

- *A participation of the reaction product in catalysis.* An NBE-ZnMe/product-adduct could be imagined, catalysing the reaction in a more enantioselective way than NBE-ZnMe alone. However, Figure 47 shows that the catalyst-loading dependent ee_P increase already takes place at the very beginning of the reaction, where a participation of the product is negligible. The zinc alkoxide alone is known to catalyse the reaction but yields racemic products and is very slow at 0°C.[29]
- *The reaction product influences the equilibrium between monomeric and dimeric NBE-ZnMe.* After the enantioselective alkyl-transfer to benzaldehyde, the product must decoordinate from the catalyst (monomer and dimer) to allow a new catalytic cycle. If the product decoordinates only slowly from the catalysts the amount of free, uncomplexed NBE-ZnMe diminishes the more the reaction goes on. This acts like a drop in catalyst concentration and should drive the dimer's dissociation. The higher monomer/dimer ratio results then in an ee_P increase.

- Also, the decoordination doesn't need to happen at the same rate or to the same extend on both monomeric and dimeric catalyst. A *higher affinity of the dimer for the product* would selectively trap the dimers and increase the uncomplexed monomer/dimer ratio, at least at the beginning of the reaction. However, a too high affinity for the dimeric catalyst might also drive the monomer-dimer equilibrium to the formation of dimers.
- If the reaction product has an influence on the monomer-dimer equilibrium, then *the absence of starting material,* which is consumed over the course of the reaction, could also have an impact, as it is in the case of the Noyori system. However, its influence is probably lower than that of the reaction product since the zinc alkoxide probably is a stronger coordinant than benzaldehyde and $ZnMe_2$ are.

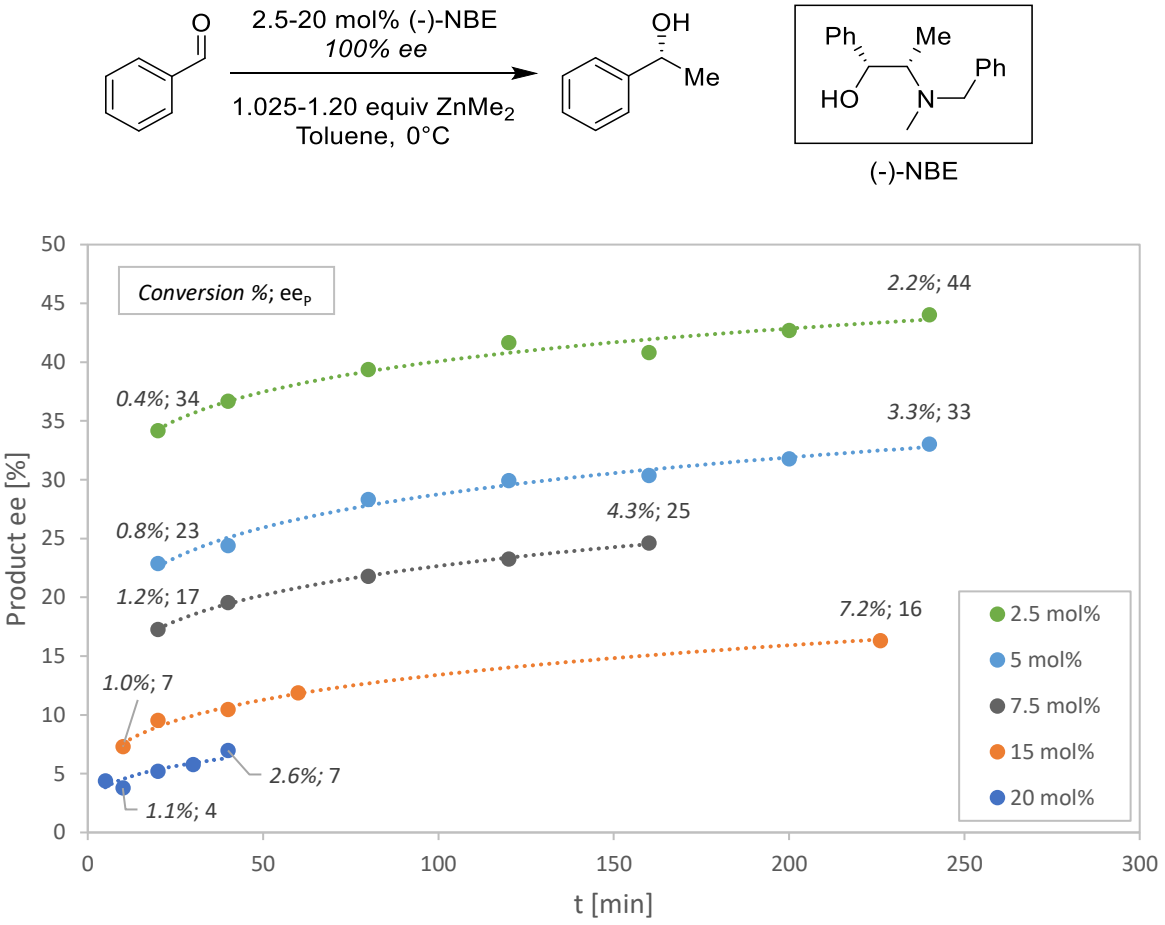

Figure 47: Time-dependent ee_P evolution of the (-)-NBE-catalysed addition of $ZnMe_2$ to benzaldehyde at various catalyst loadings. The italic percentages indicate the approx. benzaldehyde conversion. The trendlines are for illustration purposes only.

So far, a dissociation of the dimers induced by product inhibition – due to a higher dimer's affinity for the product or not – is the most probable scenario. These results show also that the kinetic model presented in I.2.2.5(b) (where we assume the monomer/dimer ratio to be constant over time) is too simple to describe the NBE-catalysed reaction accurately, although it might be sufficient to discuss the catalyst order for now.

The possibility for a high affinity of the dimer for the product can also be illustrated by an observation made by Noyori: he mixed 3 mM (*S*)-DAIB-ZnMe with the (*S*)-zinc alkoxide (both enantiopure) in a 1:5 ratio in toluene-d_8.[29] ^{1}H NMR analysis gave rise to a spectrum which he interpreted as originating from an aggregate with a 6-membered Zn_3O_3 cycle, containing two DAIB-ZnMe and one product zinc alkoxide (Figure 48) – in other words, a homochiral dimeric complex bound to one product molecule.

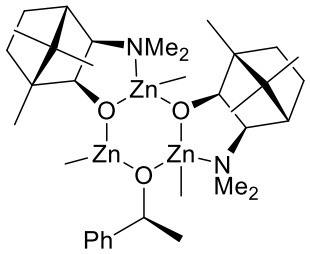

Figure 6: Presumed (DAIB-ZnMe)$_2$-zinc alkoxide adduct.

I.2.2.6 Extended Noyori Model

The data gathered in this present chapter I.2.2 from the catalyst loading screenings, temperature screenings, DOSY analysis and kinetic studies allow us to make an extension of the Noyori model for the DAIB-catalysed addition of dialkylzincs to benzaldehyde. Noyori's model (cf. Figure 9, p. 20) is based on two different enantiomorphic cycles, where (-)-DAIB-ZnR as well as (+)-DAIB-ZnR catalyse in the same way but are not present in the same quantities; the enantiomer ratio of the catalysts depends on the catalyst concentration, but also on the substrate and reactant concentrations (which change over time); product inhibition is considered to be negligible as long one works in a certain range of concentration and catalyst/substrate ratio.

Figure 49 shows our proposed model. It includes the same enantiomorphic, monomer-catalysed cycles but adds also the respective dimer-catalysed cycles. Therefore it combines as well elements from the from Noyori and as from the Kagan model. We kept the Noyori nomenclature for K_{assoc}, k and ee_{max}, which are denoted with 1 and 2 for the monomer and dimer-catalysed reactions, respectively. K_{Homo} and K_{Hetero} are defined as the respective *association* constants (in the Noyori model those are dissociation constants) to form the respective dimeric species. We added also the term K_{dissoc}, which quantifies the product's dissociation from the catalyst, and K_S to account for the heterochiral dimer's solubility.

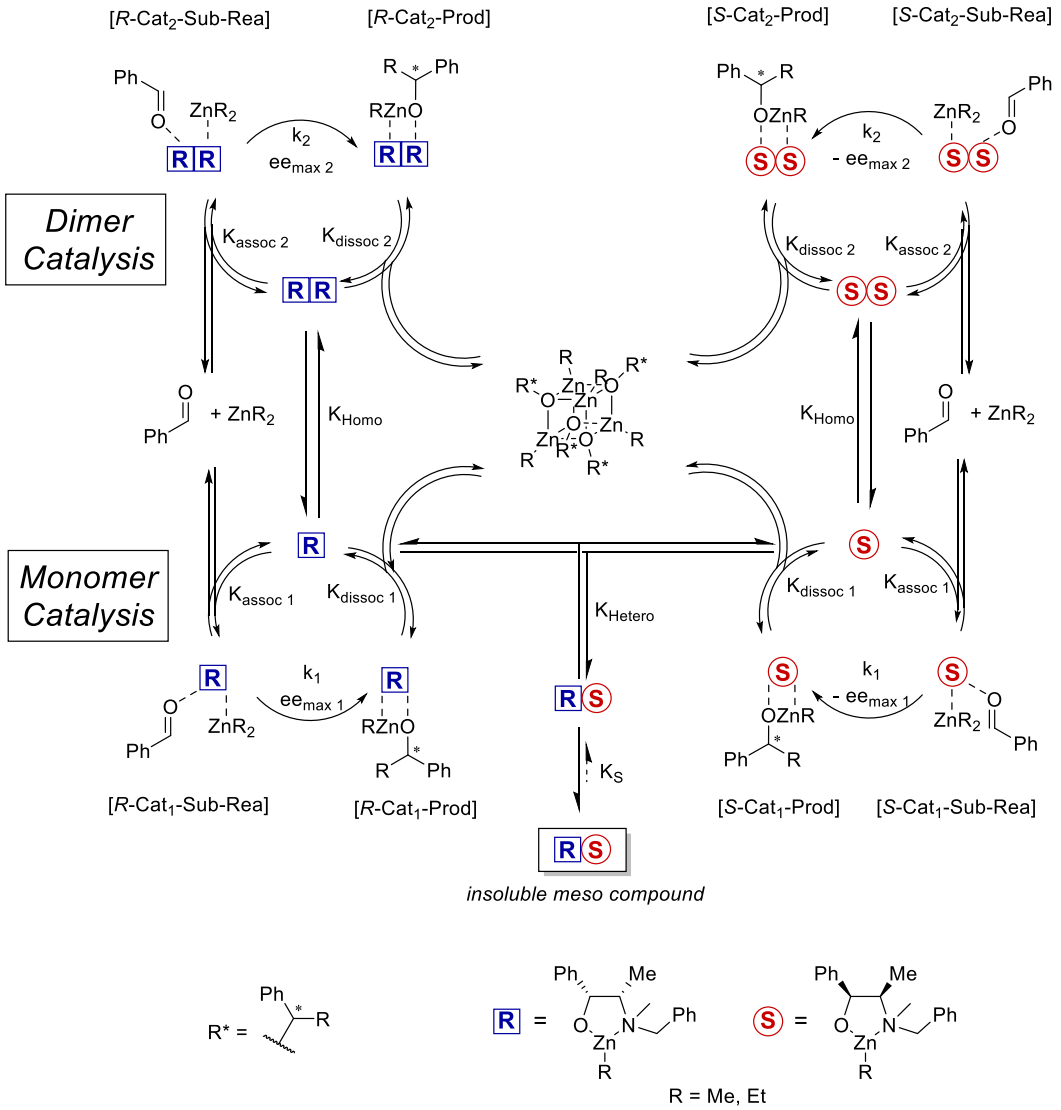

Figure 49: Proposed extension of the Noyori model for the enantioselective addition of dialkylzincs to benzaldehyde.

Each catalytic cycle starts with the coordination of benzaldehyde and ZnR_2, ruled by the association constant K_{assoc}, to give the catalytic complex Cat-Rea-Sub. In an irreversible step Rea and Sub react to form the Cat-Prod complex, defined by the kinetic constant *k* and ee_{max} for the *R*-catalyst, $-ee_{max}$ for the *S*-catalyst. Cat-Prod dissociates back to Cat and Prod, the latter gets incorporated into tetrameric aggregates. We introduce here the thermodynamic constant K_{dissoc} which quantifies the catalyst's affinity for the product. However, the dissociation probably is much more complex than shown here: it should be differentiated between the product's desorption from the catalyst and the subsequent aggregation into tetramers, which are two different steps. The first may be different if the catalyst and the product are of the same or opposite chirality; the latter depends heavily on the product ee, as it is known that the tetramer is more stable when made of enantiopure zinc alkoxides.[120] Thus, product inhibition depends not only on conversion, but also on ee_P at a given time *t*. For simplicity we assume that the heterochiral dimer doesn't catalyse as we don't have any indication for or against its participation in the catalytic reaction.

I.2.3 Further studies on the NBE-catalysed reaction

The present section gathers studies we have performed on the NBE-catalysed reaction which do not aim at investigating the reaction mechanism, but to obtain more information about the ligand and the catalytic reaction. We will have a closer look at the role of the benzyl group in NBE, at the influence of different substrates on the hyperpositive NLE and the catalytic reaction in general, and we will also determine quantitatively some of the reaction parameters.

I.2.3.1 Reservoir effect & K_S/K_{Hetero}

(a) Application of Kagan's reservoir effect model

Since the precipitation of a heterochiral aggregate is a classic example for Kagan's reservoir effect model (see chapter I.1.2, p. 16), we decided to apply it to both of our hyperpositive NLE curves. As the reservoir effect model is not intended to be used on a hyperpositive NLE, we made some modifications before we applied it to our data.

The parameter ee_{max} is defined as the maximum ee the enantiopure ligand can yield, which is usually the ee_P obtained from enantiopure catalyst. However, in our case the enantiopure ligand doesn't give highest ee_P – it increases further at lower ee_L. Therefore, we used the data from the catalyst loading screening which we had converted to a simulated NLE curve (chapter I.2.2.1, p. 33). The converted catalyst loading screening simulates the ee_P obtained from enantiopure NBE as a function of ee_L. Therefore, we define ee_{max} to be equal to the trendline (2nd order polynomial function) fitted to the catalyst loading screening, which we had shown in I.2.2.1 just for illustration purposes. The catalyst loadings, their trendlines, the trendline functions and the hyperpositive NLEs are shown in Figure 50.

Now, we can determine the parameter α from equation (7), which stands for the fraction of catalyst trapped in the inactive reservoir. For ee_P and ee_L we used the datasets at ee_L = 1 and 2% (also 3 % with $ZnMe_2$; black circled datasets in Figure 50) from the hyperpositive NLE curves and calculated ee_{max} independently for each ee_L. The reservoir is a racemic *meso*-aggregate, therefore ee_{res} = 0. The two (or three, respectively) α-values were averaged and used to draw equation (7) as a function of ee_L (Figure 50, black dashed line).

We obtained nearly identical α-values for the $ZnEt_2$- (97.3% ± 0.03) and the $ZnMe_2$-system (96.6% ± 0.15). The NLEs' steep slope at ee_L < 4% fits well to the graphical expression of equation (7), so that we can say that the hyperpositive NLEs are now fully and accurately modelled by the catalyst loading screening and the reservoir effect.

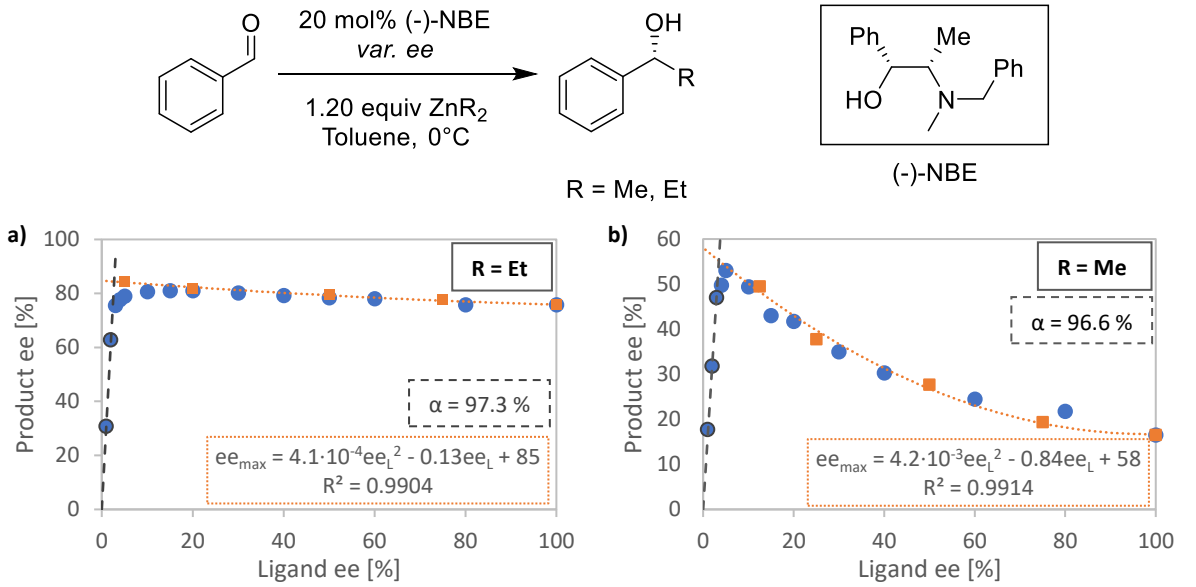

Figure 50: Observed hyperpositive NLE curves (blue dots), catalyst loading screening (orange squares) and the reservoir effect (equation (7), dashed black line) obtained from the respective α-value with a) $ZnEt_2$ and b) $ZnMe_2$. α was calculated from datasets at low ee_L (black circled blue dots). The trendline for the catalyst loading screening (orange dotted line; the respective function is shown in the orange rectangles) determines ee_{max} for given ee_L-values.

(b) Calculation of K_S/K_{Hetero} from α

In the reservoir effect model, α represents the fraction of catalyst which is trapped inside a reservoir, in our case a precipitate. The formation of the *meso*-aggregate is governed by a solubility constant, K_S (see the extended Noyori model, p. 53). It seems logical that K_S and α must be linked somehow, therefore we made a theoretical study to determine K_S from α.

First, we have to consider the following equilibria, which are defined by the equilibrium constants in equations (19) and (20):

$$[R] + [S] \underset{}{\overset{K_{Hetero}}{\rightleftharpoons}} [RS] \overset{K_s}{\rightleftharpoons} [RS]_p$$

$$K_{hetero} = \frac{[RS]}{[R][S]} \tag{19}$$

$$K_s = \frac{[RS]}{[RS]_p} = [RS] \tag{20}$$

With [R] and [S] being the concentrations of the respective monomeric catalyst enantiomers, [RS] the concentration of soluble heterochiral dimer and $[RS]_p$ the precipitated heterochiral dimer. Since the latter's activity is 1, $K_S = [RS]$.

To simplify the system, we will integrate K_{hetero} into K_S to obtain an apparent solubility constant, K_S', which is related directly to [R] and [S] through equation (21). This goes along with the assumption made in chapter I.2.2.6 that both [RS] and $[RS]_p$ do not catalyse the reaction.

$$K_S' = \frac{K_S}{K_{hetero}} = [R][S] \tag{21}$$

Now, we have to relate K_S' to the known values α, $[Cat]_{tot}$ and ee_L. For this, we will neglect the contribution of [RR] and [SS] to the catalytic process, the only catalytic species considered are [R] and [S]. We will also neglect the influence of the substrate and the catalysis product on the equilibria involving [R] and [S].

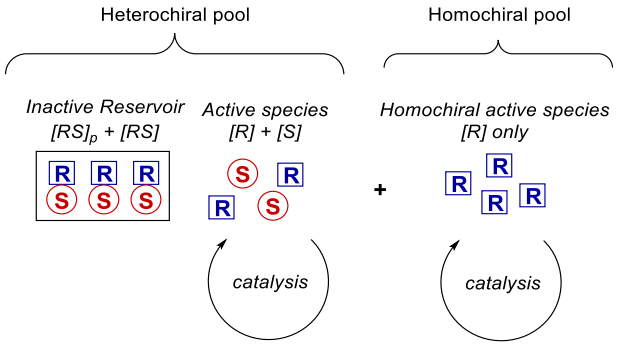

Figure 51: Scheme of the catalytic system considered as consisting of a heterochiral pool, which includes the inactive heterochiral dimers (precipitated as well as solubilised dimers) and an equal amount of active R- an d S-monomers, and of a homochiral pool consisting of the excess of major R enantiomer.

Let's consider the total catalyst $[Cat_{tot}]$ consisting of an enantiopure *R* pool and a racemic heterochiral pool. The heterochiral pool consists of the inactive reservoir and from an equal quantity of free, catalytically active *R*- and *S*-monomers in equal parts (Figure 51). The concentrations of *R*- and *S*-catalysts in the pools and in the reservoir are defined by equations (22) and (23):

$$[R]_{Homo\ pool} = ee_L[Cat_{tot}] \tag{22}$$

$$[R]_{Hetero\ pool} = [S]_{Hetero\ pool} = \frac{(1 - ee_L)[Cat_{tot}]}{2} \tag{23}$$

In addition, we can describe, as a function of α, the catalytically *inactive part* (i. e. reservoir) of the heterochiral pool. It consists of *R* and *S*-monomers in equal parts and is therefore expressed by equation (24):

$$[R]_{res} = [S]_{res} = \frac{\alpha[Cat_{tot}]}{2} \tag{24}$$

The total amount of *active* [R] has to be equal to the homochiral pool plus the amount of *R*-catalyst incorporated in the *soluble part* of the heterochiral pool [equation (25)]. On the other hand, the active *S* catalyst is issued only from the heterochiral pool's soluble part [equation (26)].

$$\begin{aligned} [R]_{active} &= [R]_{Homo\ pool} + [R]_{Hetero\ pool} - [R]_{res} \\ \Rightarrow [R]_{active} &= ee_L[Cat_{tot}] + \frac{(1-ee_L)[Cat_{tot}]}{2} - \frac{\alpha[Cat_{tot}]}{2} \\ &= \left(ee_L + \frac{1-ee_L-\alpha}{2}\right)[Cat_{tot}] = \frac{1+ee_L-\alpha}{2}[Cat_{tot}] \end{aligned} \tag{25}$$

$$\begin{aligned} [S]_{active} &= [S]_{Hetero\ pool} - [S]_{res} \\ \Rightarrow [S]_{active} &= \frac{(1-ee_L)[Cat_{tot}]}{2} - \frac{\alpha[Cat_{tot}]}{2} = \frac{1-ee_L-\alpha}{2}[Cat_{tot}] \end{aligned} \tag{26}$$

Now, equations (25) and (26) can be incorporated into equation (21):

$$\Rightarrow K_S' = \left(\frac{1+ee_L-\alpha}{2}\right)\left(\frac{1-ee_L-\alpha}{2}\right)[Cat_{tot}]^2$$

$$\Leftrightarrow K_S' = (1 - ee_L - \alpha + ee_L - ee_L^2 - ee_L\alpha - \alpha + ee_L\alpha + \alpha^2)\frac{[Cat_{tot}]^2}{4}$$

$$\Leftrightarrow K_S' = (1 - 2\alpha - ee_L^2 + \alpha^2)\frac{[Cat_{tot}]^2}{4}$$

$$\Leftrightarrow K_S' = [(1-\alpha)^2 - ee_L^2]\frac{[Cat_{tot}]^2}{4} \tag{27}$$

Since $[Cat_{tot}]$ is a fix reaction parameter and α has been determined in chapter I.2.2.1, we can calculate K_S' from equation (27). For ee_L, we chose the same values used to determine α and calculated mean K_S' and subsequently the solubility s' of [RS] (more detailed data can be found in the Supporting Information, V.2.2, p. 170). The results are shown in Table 3.

ZnR_2	α	K_S'	s' [mol/L]
R = Et	0.966	$4.11 \cdot 10^{-6}$	$2.03 \cdot 10^{-3}$
R = Me	0.973	$4.78 \cdot 10^{-6}$	$2.19 \cdot 10^{-3}$

Table 3: Calculated K_S' and s' values of dimeric heterochiral NBE-ZnR for R = Et and R = Me.

The calculated K_S' and solubility values are close and indeed quite low, however we cannot conclude on them without a counter-check by an experimental determination of K_S and K_{Hetero}, especially because of the approximations made at the beginning of the calculations. In a related system, Kagan calculated the eutectic composition (minimum ee_L a solution can have without forming a racemic precipitate) of an insoluble *meso* catalyst from the fusion temperatures and fusion enthalpies of the enantiopure and racemic catalyst.[107] This might be also applicable to our system.

I.2.3.2 Eyring plots

(a) Determination of $ee_{max\ 1}$

We know that the homochiral catalyst dimer can be dissociated by decreasing the total catalyst concentration or increasing the reaction temperature (chapter I.2.2.1 and I.2.2.2). A combination of low [Cat_{tot}] and high temperature might enable us to reach conditions in which only the monomer catalyses. That would give us the opportunity to determine certain constants associated to the monomer mentioned in I.2.2.6: its enantioselectivity ($ee_{max\ 1}$), its kinetic constant (k_1), its association constant with the benzaldehyde and the dialkylzinc reagent ($K_{assoc\ 1}$) and the dissociation constant from the reaction product ($K_{dissoc\ 1}$). We will focus here on $ee_{max\ 1}$ as it can be directly obtained from ee_P using Eyring plots.

The enantioselectivity of a reaction is defined as the difference ($\Delta\Delta G^{\neq}$) between the free energies of the two transition states ($\Delta G^{\neq}_R$ and $\Delta G^{\neq}_S$) of the rate-determining step leading either to *R* or *S*-product (P_R and P_S). The kinetic constants of those rate-determining steps are related through $\Delta\Delta G^{\neq}$ to the corresponding enthalpy and entropy terms:

$$\ln\left(\frac{k_R}{k_S}\right) = \frac{-\Delta\Delta G^{\neq}}{RT} = \frac{-\Delta\Delta H^{\neq}}{RT} + \frac{\Delta\Delta S^{\neq}}{R} \qquad (28)$$

With k_R and k_S as the kinetic constants of the rate-determining steps leading to P_R and P_S, respectively, $\Delta\Delta H^{\neq}$ as the difference in transition enthalpy, $\Delta\Delta S^{\neq}$ as the difference in transition entropy, *R* as the ideal gas constant and *T* as the reaction temperature.

The interesting point about equation (28) is that it can be represented as a linear function, if one plots $\ln(k_R/k_S)$ [which is equal to $\ln(P_R/P_S)$ for a single-catalyst reaction; the enantiomeric ratio P_R/P_S can be calculated directly from ee_P] vs. T^{-1}. $-\Delta\Delta H^{\neq}/R$ then corresponds to the line's slope and $\Delta\Delta S^{\neq}/R$ to the y-intercept. Those so-called "Eyring plots" can give valuable information about the reaction, especially if they contain curvatures – that is usually an indication for a change of the reaction mechanism.[121] The $\Delta\Delta S^{\neq}$-term also explains why a catalyst's enantioselectivity is not a constant, but a temperature-dependent variable, which leads to lower ee_Ps with increasing temperatures. The higher $\Delta\Delta S^{\neq}$, the more ee_P is sensitive to the reaction temperature. An Eyring plot of the NBE-catalysed reaction in conditions where either *only the monomer* or *only the dimer* catalyse would give us access to their respective $\Delta\Delta H^{\neq}$ and $\Delta\Delta S^{\neq}$; we would then also be able to predict their enantioselectivities $ee_{max\ 1}$ and $ee_{max\ 2}$ for any reaction temperature.

This prompted us to extend the temperature screening from chapter I.2.2.1 (Figure 34, p. 37) to a broader range of temperatures. Figure 52a shows the extended temperature screening using $ZnEt_2$, with 2.5 and 20 mol% NBE. From -20 to 40 °C ee_P either decreases slightly (2.5 mol%, orange dots) or forms a wave-like curve (20 mol%, blue dots). At 60 °C and higher, ee_P starts to decrease strongly in both cases. With $ZnMe_2$ (Figure 52b) ee_P increases with temperature in a linear way, only the 2.5 mol%-plot shows a curvature above 60 °C.

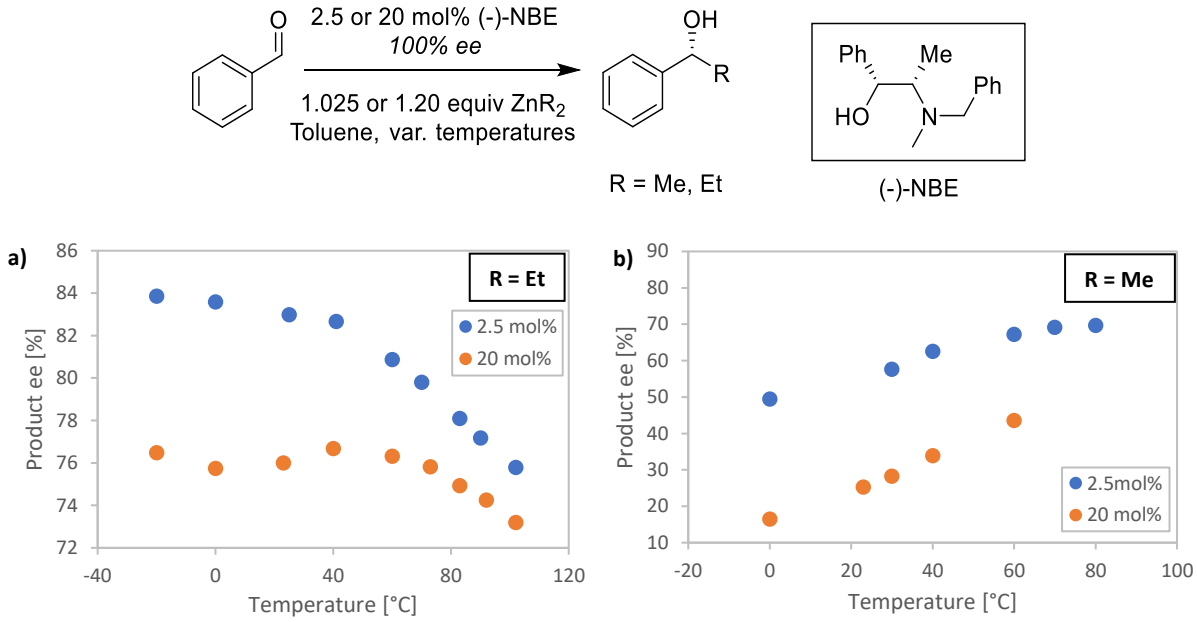

Figure 52: Extended temperature screenings at 2.5 and 20 mol% (-)-NBE with a) $ZnEt_2$ and b) $ZnMe_2$.

The linear downslope with $ZnEt_2$ at high temperature is interesting as it might indicate that only the monomeric catalyst is active; at lower temperatures, the temperature-driven ee_P decrease is probably compensated by dimer dissociation, so the slope is less inclined. Conversion of the datasets in Figure 52a from [ee_P, T] to [$\ln(k_R/k_S)$, $10^{-3}/T$] allowed us to build the Eyring plot shown in Figure 53. Indeed, the 5 high-temperature datasets at 2.5 mol% NBE give an excellent linear fit (R^2 = 0.9988), which indicates most likely that only one species catalyses – the monomeric NBE-ZnEt catalyst. Therefore, the line is equal to the monomer's $-\Delta\Delta G^{\neq}/RT$, from which we could obtain $\Delta\Delta H^{\neq}_1$ and $\Delta\Delta S^{\neq}_1$ (shown on the right, Figure 52b). This allows us now to predict the monomer's enantioselectivity $ee_{max\ 1}$ for any temperature by converting the [$\ln(k_R/k_S)$, $10^{-3}/T$]-dataset back to [ee_P, T]. At our standard catalysis temperature of 0 °C (corresponding to 3.6 1000/T, red dot in Figure 52a) we obtain an ee_P of 88%: this is the ee_P monomeric NBE-ZnEt would yield if it would be the only catalyst to be active at this temperature.

However, it should be noted that the four far-left datasets at 20 mol% also fit to a linear function, with an only slightly lower R^2 (0.9955, not shown). This is probably due to the 20 mol%-plot converging over a very broad T^{-1}-scale to the $-\Delta\Delta G^{\neq}_1/RT$-line, thus being almost linear although there is some dimeric NBE left in these conditions. Therefore, the $-\Delta\Delta G^{\neq}_1/RT$-line should be confirmed by temperature screenings at even lower catalyst loading than 2.5 mol%.

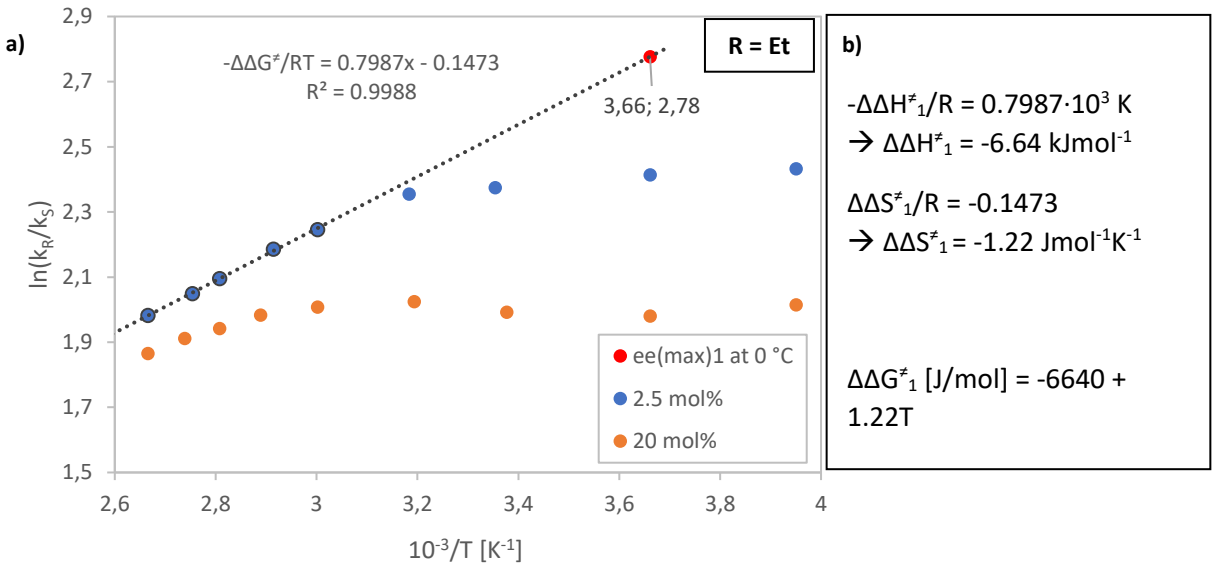

Figure 53: a) Eyring plot for the (-)-NBE-catalysed addition of $ZnEt_2$ to benzaldehyde with 2.5 (blue dots) and 20 mol% ligand (orange dots). The dotted line was obtained from a fit to 5 points between 2.6 and 3.2 $10^{-3}/T$ (black circled blue dots) and represents the monomer's $-\Delta\Delta G^{\neq}/RT$. The red dot corresponds to represents NBE's enantioselectivity ($\rightarrow ee_{max\ 1}$ = 88%) if it was the only one to catalyse at 0°C. b) Calculation of monomeric NBE's thermodynamic data ($\Delta\Delta H^{\neq}_1$, $\Delta\Delta S^{\neq}_1$ and $\Delta\Delta G^{\neq}_1$) from the linear $-\Delta\Delta G^{\neq}_1/RT$-plot.

(b) Construction of an Eyring Plot Model

The dimeric catalyst's enantioselectivity $ee_{max\ 2}$ might also be determined by the Eyring plot but affords additional datasets at lower temperature and/or higher catalyst loading, in order to reach the linear domain which corresponds to $-\Delta\Delta G^{\neq}_2/RT$. The wave-like shape for the 20 mol%-data at low temperature (Figure 52a and Figure 53) raises also questions about how the plot might look like. Since we don't have more experimental data at hand, we opted for a modelling of the Eyring plot.

The Eyring plot is defined by $\ln(k_R/k_S)$, as discussed in the previous section. To account for the contribution of both monomer and dimer to the reaction, we defined the observed kinetic constants k_R and k_S as linear combinations of k_{R1} and k_{R2} or k_{S1} and k_{S2}, respectively, as shown in equations (29) and (30):

$$k_R = ak_{R1} + \left(\frac{1-a}{2}\right)k_{R2} \tag{29}$$

$$k_S = ak_{S1} + \left(\frac{1-a}{2}\right)k_{S2} \tag{30}$$

With k_{R1} and k_{S1} as the kinetic constants of monomeric catalyst, k_{R2} and k_{S2} for the dimeric catalyst. *a* is the fraction of monomeric catalyst [R] of the total amount of catalyst [Cat_{tot}], as defined by equation (16) in the model of NBE's kinetics in chapter I.2.2.5(b), p. 45. *a* is considered to be constant over time. Integration of equations (29) and (30) into (28) gives equation (31):

$$\frac{-\Delta\Delta G^{\neq}}{RT} = \ln\left(\frac{k_R}{k_S}\right) = \ln\left(\frac{ak_{R1} + \left(\frac{1-a}{2}\right)k_{R2}}{ak_{S1} + \left(\frac{1-a}{2}\right)k_{S2}}\right) \tag{31}$$

The term for $-\Delta\Delta G^{\neq}/RT$ now has become more complex and cannot be expressed as a linear function, unless a = 0 (only dimeric NBE catalyses) or a = 1 (only monomeric NBE catalyses). Those are the extreme cases were the Eyring plot is linear. Since we want to see what happens in between, we developed all terms in equation (31) which are a function of the temperature. First, we express the kinetic constants as the exponential containing their respective $\Delta H^{\neq}$ and $\Delta S^{\neq}$:

$$\ln\left(\frac{k_R}{k_S}\right) = \ln\left(\frac{ae^{\frac{-(\Delta H^{\neq}_{R1} + T\Delta S^{\neq}_{R1})}{RT}} + \left(\frac{1-a}{2}\right)e^{\frac{-(\Delta H^{\neq}_{R2} + T\Delta S^{\neq}_{R2})}{RT}}}{ae^{\frac{-(\Delta H^{\neq}_{S1} + T\Delta S^{\neq}_{S1})}{RT}} + \left(\frac{1-a}{2}\right)e^{\frac{-(\Delta H^{\neq}_{S2} + T\Delta S^{\neq}_{S2})}{RT}}}\right) \tag{32}$$

With R as the ideal gas constant (8.314 $Jmol^{-1}K^{-1}$). Next, we developed a. The fraction of monomeric or dimeric catalyst must necessarily be a function of the total catalyst concentration $[Cat_{tot}]$ and the dimerisation constant K_{Homo}. Integration of equation (33) into (34) leads to a quadratic equation which can be solved for [R], giving equation (35):

$$K_{Homo} = \frac{[RR]}{[R]^2}$$

$$\Leftrightarrow K_{Homo}[R]^2 = [RR] \tag{33}$$

$$[Cat_{tot}] = [R] + 2[RR] \tag{34}$$

$$\Longrightarrow [Cat_{tot}] = [R] + 2K_{Homo}[R]^2$$

$$\Leftrightarrow 2K_{Homo}[R]^2 + [R] - [Cat_{tot}] = 0$$

$$\Leftrightarrow [R]_{\pm} = \frac{-1 \pm \sqrt{1 + 8K_{Homo}[Cat_{tot}]}}{4K_{Homo}} \tag{35}$$

The only solution giving positive values is $[R]_+$, which gives equation (36) when integrated into the expression for a (cf. equation (16), p. 45):

$$\Longrightarrow a = \frac{-1 + \sqrt{1 + 8K_{Homo}[Cat_{tot}]}}{4K_{Homo}[Cat_{tot}]} \tag{36}$$

$[Cat_{tot}]$ is a fixed reaction parameter, while K_{Homo} can be further developed as a function of the temperature:

$$K_{Homo} = e^{\frac{-(\Delta H_{Homo} + T\Delta S_{Homo})}{RT}} \quad (37)$$

Equation (32) can now be expressed, through equations (36) and (37), as a function of $[Cat_{tot}]$, ΔH_{Homo}, ΔS_{Homo} and the $\Delta H^{\neq}$ and $\Delta S^{\neq}$ terms of each kinetic constant.

$$\Delta\Delta H_2^{\neq} = \Delta H_{R2}^{\neq} - \Delta H_{S2}^{\neq}$$

$$\Delta\Delta S_2^{\neq} = \Delta S_{R2}^{\neq} - \Delta S_{R2}^{\neq}$$

Now, we must choose the parameters. For $[Cat_{tot}]$ we chose the same concentration as used for our catalytic reactions with 20 mol% NBE; the ideal gas constant R is known; $\Delta H^{\neq}_{Homo}$ and $\Delta S^{\neq}_{Homo}$ were calculated from $K_{Homo}(T)$ at 25 and 60 °C, which was obtained from the mean MW values determined by DOSY NMR in chapter I.2.2.4(b). It should be noted that this was done only to have an idea of the order of magnitude of $K_{Homo}(T)$; the data from I.2.2.4(b) is not sufficient and not adapted (the excess $ZnMe_2$ influences the complex' aggregation state) to perform an accurate determination of $K_{Homo}(T)$. As we already know $\Delta\Delta H^{\neq}_1$ and $\Delta\Delta S^{\neq}_1$ (6.64 $kJmol^{-1}$ and 1.22 $Jmol^{-1}K^{-1}$, respectively) from the experimental Eyring plots, we chose $\Delta H^{\neq}_{R1}$ and $\Delta H^{\neq}_{S1}$ as well as $\Delta S^{\neq}_{R1}$ and $\Delta S^{\neq}_{S1}$ in order to fulfil equations (38) and (39):

$$\Delta\Delta H_i^{\neq} = \Delta H_{Ri}^{\neq} - \Delta H_{Si}^{\neq} \quad (38)$$

$$\Delta\Delta S_i^{\neq} = \Delta S_{Ri}^{\neq} - \Delta S_{Si}^{\neq} \quad (39)$$

All other parameters were chosen arbitrarily. Our basic set of parameters is shown in Table 4; we will use this set to model Eyring plots and vary some of these parameters to study their influence on the plot. We do not intend to make a full theoretical study of the model, but rather to illustrate how our experimental Eyring plots should behave.

$\Delta H^{\neq}_{R1}$ [$kJmol^{-1}$]	-16.6	$\Delta S^{\neq}_{R1}$ [$Jmol^{-1}K^{-1}$]	-100
$\Delta H^{\neq}_{S1}$	-10	$\Delta S^{\neq}_{S1}$	-98.8
$\Delta H^{\neq}_{R2}$	-16.6	$\Delta S^{\neq}_{R2}$	-100
$\Delta H^{\neq}_{S2}$	-16	$\Delta S^{\neq}_{S2}$	-105
$\Delta H^{\neq}_{Homo}$	-35	$\Delta S^{\neq}_{Homo}$	-80
$[Cat_{tot}]$ [mol/L]		0.166	
R [$Jmol^{-1}K^{-1}$]		8.314	

Table 4: Basic set of parameters used to model the Eyring plots

Figure 54a shows the Eyring plot model with different values for ΔH_{Homo}. There are two linear domains, which correspond to catalysis by the monomer (left, $a \sim 1$) and by the dimer only (right, $a \sim 0$). The domain in between, which we will call "intermediate region", is the one where both complexes catalyse and which bears, in this parameter configuration, a wave-like shape similar to what we see in the experimental Eyring plot (Figure 53).

The temperature range of this region depends on ΔH_{Homo}: the more negative it is ($a_1 \rightarrow a_2 \rightarrow a_3$), the more the wave is shifted to smaller 1000/T-values. Since the two lines converge around $1 \cdot 10^{-3}$/T, the wave also becomes smaller. This is consistent with equation (37): the more negative $\Delta H^{\neq}_{Homo}$, the higher K_{Homo}, the more the equilibrium is shifted to the dimeric catalyst. Therefore, it is necessary to increase the temperature to fully dissociate the dimer, therefore the left linear domain is reached only at lower 1000/T-values.

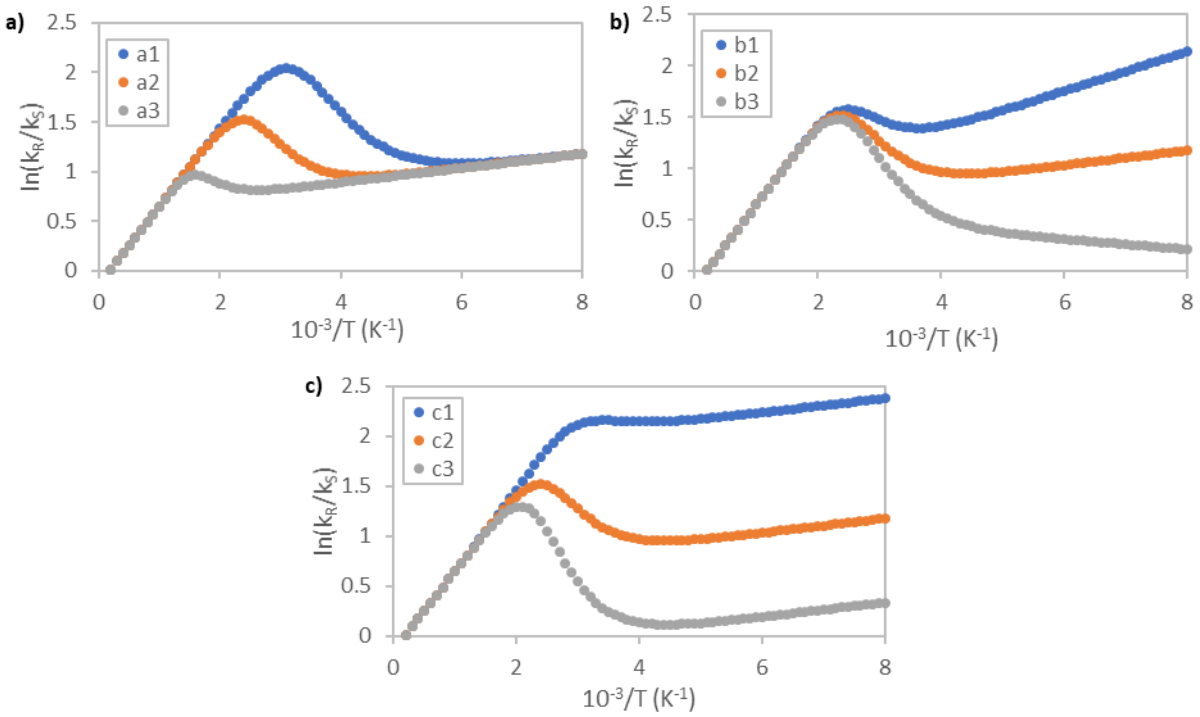

Figure 54: Modelled Eyring plots. a) ΔH_{Homo} equal to a_1) -25, b_1) -35, c_1) -60 kJmol^{-1}; b) $\Delta\Delta H^{\neq}_2$ equal to b_1) –1.6 (-17.6), b_2) -0.6 (-16.6), b_3) +0.4 (-15.6) kJmol^{-1}, the values in brackets are the $\Delta H^{\neq}_{R2}$-values used to make $\Delta\Delta H^{\neq}_2$ vary; c) $\Delta\Delta S^{\neq}_2$ equal to c_1) 15 (-115), c_2) 5 (-105), c_3) -2 (-98) Jmol^{-1}, the values in brackets are the $\Delta S^{\neq}_{S2}$-values used to make $\Delta\Delta S^{\neq}_2$ vary.

Next, we varied the parameters associated with the dimeric catalyst only, in the linear domain on the right side. The line's slope depends on $\Delta\Delta H^{\neq}_2$ according to equation (28), therefore we varied $\Delta H^{\neq}_{R2}$ and left $\Delta H^{\neq}_{S2}$ constant to obtain graphs with different $\Delta\Delta H^{\neq}_2$ values. The results are shown in Figure 54b. As long as $\Delta\Delta H^{\neq}_2$ is negative (b_1 and b_2) the right line has a positive slope; a positive $\Delta\Delta H^{\neq}_2$ (b_3, grey dots) gives a negative slope. In the latter case the intermediate domain has no wave-like shape anymore, it resembles a peak. Therefore, we may deduct that in the NBE-catalysed system, $\Delta\Delta H^{\neq}_2$ must have a negative value. Since the dimeric catalyst is *less* enantioselective than the monomeric one, the slope for dimeric catalyst's line must be less steep than for the monomeric's, therefore $\Delta\Delta H^{\neq}_1$ has to be more negative than $\Delta\Delta H^{\neq}_2$. From that, we can conclude $-6.64 < \Delta\Delta H^{\neq}_2 < 0$ kJmol^{-1}.

Finally, we will vary the dimer's $\Delta\Delta S^{\neq}_2$, which defines the y-intercept of the right line. We have varied $\Delta S^{\neq}_{S2}$ to obtain graphs with different $\Delta\Delta S^{\neq}_2$ shown in Figure 54c. The position of the right line has an

influence on the shape of the intermediate domain: the lower it is, the more both linear domains diverge in the intermediate region, the more the wave-like shape is pronounced.

In principle, such model can be fitted to experimental data to determine unknown parameters. However, our model is probably not accurate enough to do this. We know from I.2.2.5(d) (p. 49) that ee_P changes during the reaction, therefore the monomeric/dimeric catalyst-ratio changes over time. This means that the variable *a* cannot be constant over time and must be described by a much more complex expression than equation (36). However, our simplified model should be sufficient to get an idea of what the Eyring plot of our NBE-catalysed reaction should look like.

I.2.3.3 Influence of the ligand structure

(a) NBE-derivatives

In order to get more information about effect of ligand structure on the hyperpositive NLE, we studied some derivatives of NBE. The absence of NLEs with ephedrine, NnBE and NME in chapter I.2.1.2 indicates that the benzyl substituent on NBE has a major influence on the catalytic system. It is very likely that it is responsible for the insolubility of the heterochiral NBE-ZnMe/Et aggregate, e. g. via extensive π-π stacking which stabilises the crystalline state. The question is also whether it has an influence on the catalytic activity of the homochiral aggregate. Therefore, we made variants of NBE with *para*-substituents on the benzylic ring, one electron-donating (X = Me) and one electron-attracting (X = Br). Additionally, we made also a 2-naphtyl variant (*N*-2-naphtyl ephedrine, N2NE). The extended aromaticity might enhance π-π stacking in the crystalline state and further decrease the heterochiral aggregate's solubility in toluene.

The results are shown in Figure 55, Figure 56 and Figure 57. All ligands show a hyperpositive NLE quite similar to the one of NBE (see Figure 25, p. 31), all form a white precipitate at the beginning of the reaction if they are scalemic. In general, the substituents don't seem to affect a lot the catalytic system. Br-NBE shows a slightly lower enantioselectivity (75% ee_P at 100% ee_L, 79% at 20% ee_L) than NBE (76 and 81% ee_P, respectively). Me-NBE is also slightly less enantioselective than NBE (80% ee_P at 10%-20% ee_L). On the other hand, N2NE is slightly more enantioselective (77% ee_P at 100% ee_L, 83% at 20% ee_L) but then shows an ee_P drop at 10% ee_L, where it isn't hyperpositive anymore; same goes for Br-NBE. The 2-naphtyl-group probably improves the ligand's $ee_{max\ 1/2}$ or destabilises the homochiral aggregate, so that more of the more selective monomer catalyses, but decreases the heterochiral aggregate's solubility rather than increasing it.

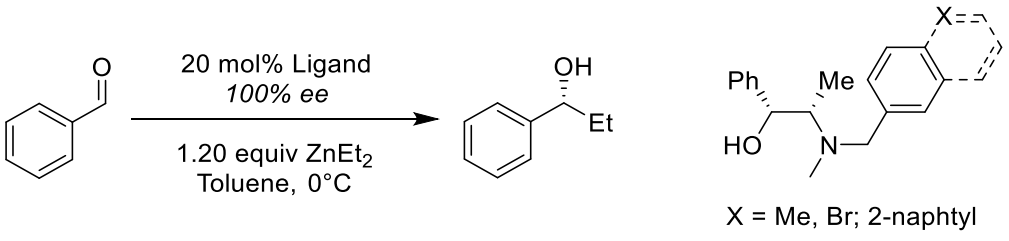

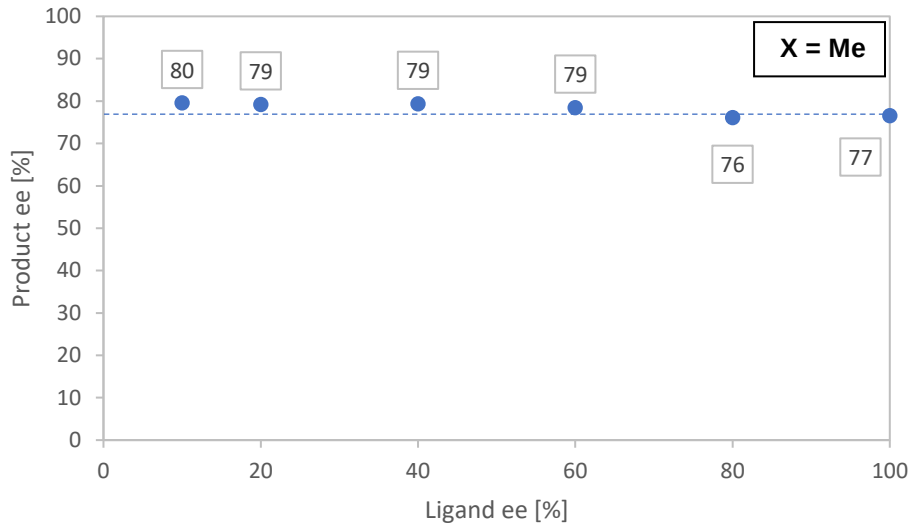

Figure 55: Hyperpositive NLE of the Me-NBE catalysed addition of $ZnEt_2$ to benzaldehyde.

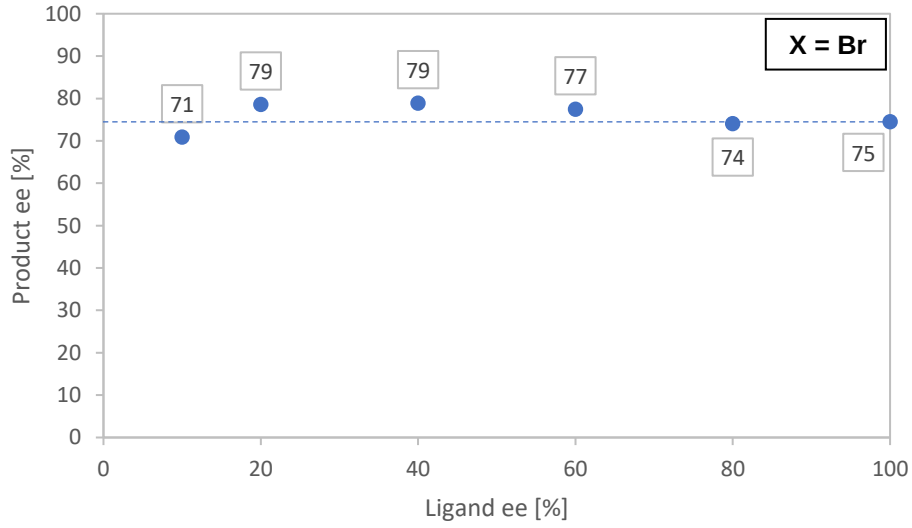

Figure 56: Hyperpositive NLE of the Br-NBE catalysed addition of $ZnEt_2$ to benzaldehyde.

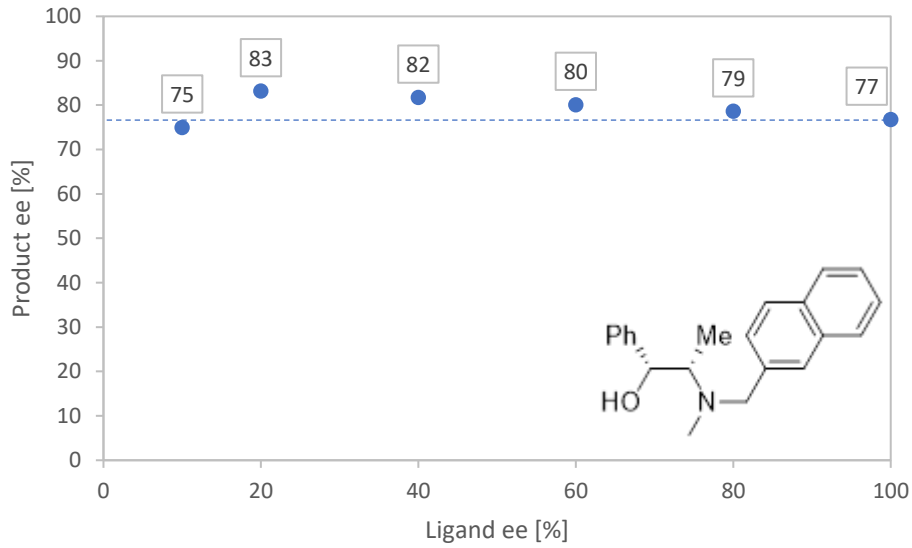

Figure 57: Hyperpositive NLE of the (-)-N-2-naphtyl Ephedrine [(-)-N2NE] catalysed addition of $ZnEt_2$ to benzaldehyde.

(b) NME: Catalyst loading screening

Finally, we went back to one of the first ligands we have investigated in this work: NME. Contrary to NBE and the derivatives shown in the previous section, NME doesn't show a NLE (see Figure 24, p. 30), probably due to the absence of a heterochiral precipitate. However, that doesn't rule out the possibility of catalysis by homochiral aggregates, so we checked for this by performing a catalyst loading screening on the NME-catalysed addition of $ZnEt_2$, similar to the study on NBE in chapter I.2.2.1. Figure 58 shows a strong ee_P increase upon reduction of the catalyst loading, from 68% ee_P at 20 mol% to 80% ee_P at 2.5 mol%. The ee_P increase is even slightly stronger than with (-)-NBE (76% to 84% ee_P at 1 mol%).

This is interesting as it shows that the benzyl substituent is responsible for the precipitation of the heterochiral aggregate, but not for the catalytic activity of the homochiral dimer. Theoretically, NME could also generate a hyperpositive NLE if the heterochiral aggregate would precipitate.

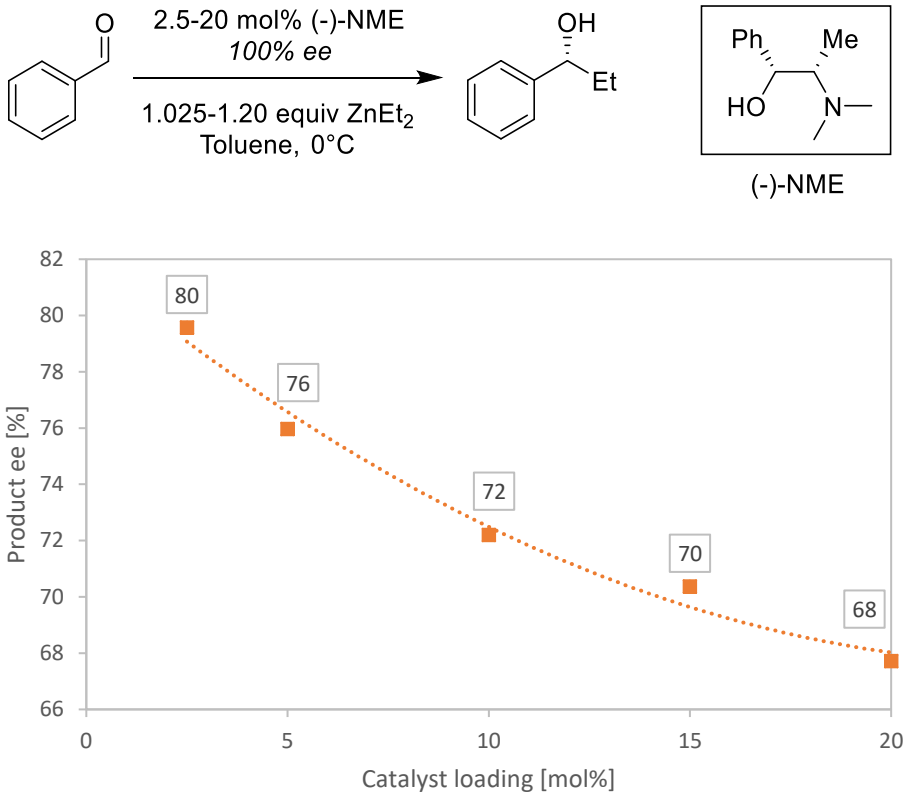

Figure 58: Catalyst loading screening in the (-)-NME-catalysed addition of $ZnEt_2$ to benzaldehyde.

I.2.3.4 Effects of para-substituents on the substrate

So far, we have studied the catalysis by NBE mostly by varying the reaction conditions (temperature, concentration); apart from the dialkylzinc ($ZnMe_2$ or $ZnEt_2$) the compounds have been mostly the same in every experiment: benzaldehyde, NBE and toluene. We will now make a survey of substituted benzaldehydes in the NBE-catalysed addition of dialkylzincs and see if electron-donating/-attracting or bulky substituents have an impact on the catalysis, notably on the hyperpositive NLE. We will then make Hammett plots to see if the substituents' effects can be quantified.

(a) Screening of *para*-substituted benzaldehydes

We started to screen for different substrates with $ZnEt_2$ as the dialkylzinc. The conditions are the same as for the hyperpositive NLE in Chapter I.2.1.2, datasets were obtained from enantiopure and from 20% ee ligand to probe for NLEs. We chose to work with *para*-substituted benzaldehydes to minimise any possible steric influence of the substituent on the aldehyde. The electron-donating or -attracting effect of the substrate can be quantified by Hammett's σ_p-scale (see section V.1.3, p. 165

for further details); Table 5 lists the *para*-substituents of the different benzaldehydes in increasing order of their respective σ_p value.

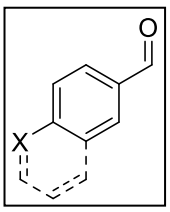

X	OiPr	OMe	OPh	tBu	Me	H	2-napht
σ_p	-0.45	-0.27	-0.32	-0.20	-0.17	0	0.04
X	F	Cl	Br	OCF_3	CF_3	CN	SF_5
σ_p	0.06	0.23	0.23	0.35	0.54	0.66	0.68

*Table 5: List of para-substituents **X** and their σ_p used in this chapter. 2-napht refers to 2-naphtaldehyde.*

Figure 59 shows the results of the substrate screening with $ZnEt_2$. With enantiopure ligand (blue line), ee_P remains constant between 75 and 78% for most substituents; only CN (73%), OMe (48%) and OiPr (69%) are out of this trend. The values for 20% ee_L (orange line) show a much bigger variation: it is only for σ_ps around 0 (H, F, 2-naphtaldehyde) and with OiPr that they are clearly above the ee_P of enantiopure NBE (Δee_P > 3%), thus rendering the NLE hyperpositive. For the other substituents both ee_Ps are close or equal, only OCF_3 and the strongly electron-withdrawing CN- and SF_5-substituents have significantly lower ee_Ps with 20% ee_L than with enantiopure ligand, leading to a positive but not *hyper*positive NLE at 20% ee_L.

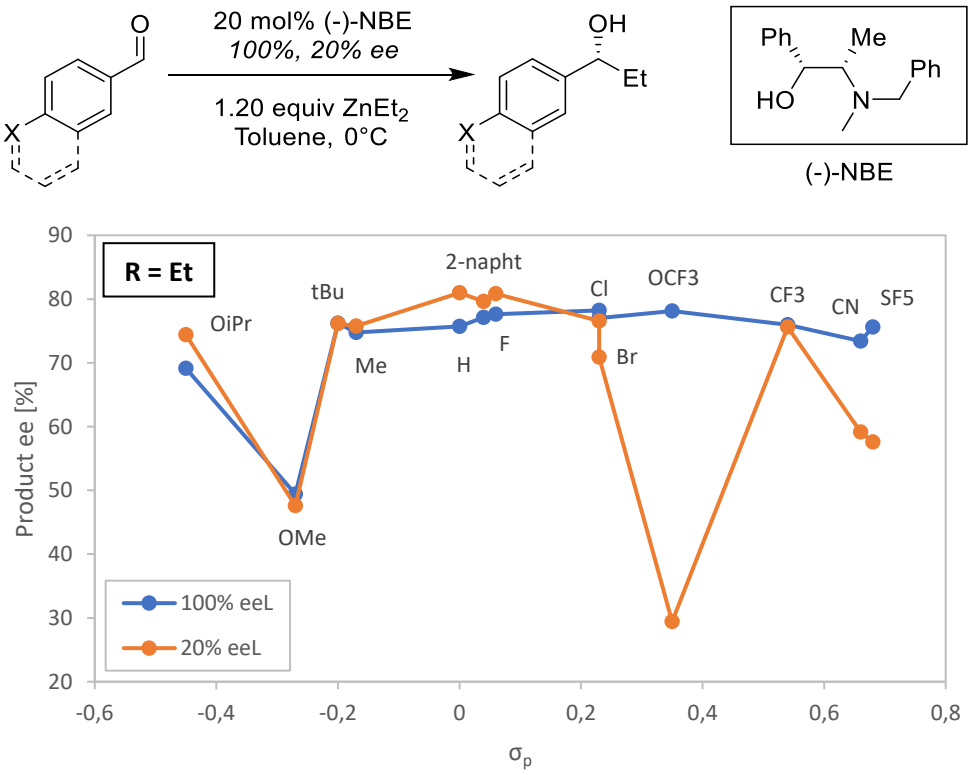

Figure 59: Screening of para-substituted benzaldehydes in the (-)-NBE-catalysed addition of $ZnEt_2$. Each substrate was used in a reaction with enantiopure (blue dots) and 20% ee ligand (orange dots).

There are no clear trends to read from Figure 59, apart that the best substituents to obtain a hyperpositive NLE are those around $\sigma_p = 0$ if we consider OiPr to be an exception. The ee_P-drop with scalemic ligand and OCF_3, CN and SF_5 indicates an increased activity of the minor NBE-enantiomer. This may come from a changed affinity of the substrate or the chiral zinc alkoxide product with the catalyst which drives the solubilisation of the heterochiral precipitate (although a precipitate was persistent in all reactions with 20% ee_L).

Next, we screened *para*-substituted benzaldehyde using $ZnMe_2$. We applied the same set of substrates as before, with exception of 2-naphtaldehyde, and added 4-Iodobenzaldehyde to the screening. The picture given by Figure 60 is somewhat clearer than the previous one: all substrates give hyperpositive NLEs [ee_P(20% ee_L) > ee_P(100% ee_L)], except OCF_3 and SF_5 which show again a strong ee_P-drop with scalemic ligand. Apart those two substituents, all those with $\sigma_p > 0.1$ show constant ee_Ps around 44% with scalemic ligand. On the other hand, as σ_p becomes lower than 0.1, ee_P decreases continuously. The ee_Ps with enantiopure NBE globally follow the trend of the scalemic ligand. OCF_3 and SF_5 are, again, exceptions: their ee_Ps at 100% ee_L are higher than the overall trend, which contributes to their NLE not being hyperpositive anymore.

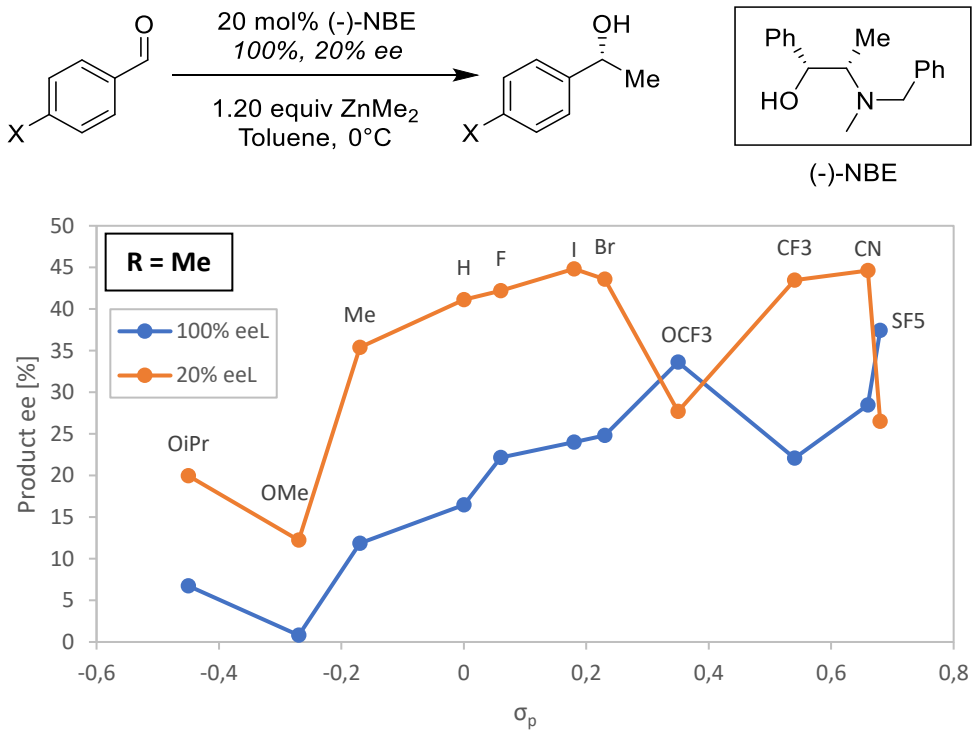

Figure 60: Screening of para-substituted benzaldehydes in the (-)-NBE-catalysed addition of $ZnMe_2$. Each substrate was used in a reaction with enantiopure (blue dots) and 20% ee ligand (orange dots).

We also had a look at the conversion of the reactions in Figure 60 which we won't discuss here, but which can be found in the supporting information (V.2.3, p. 171).

(b) Catalyst loading screening of *p*CF_3- and *p*CN-benzaldehyde

In addition, we also made catalyst loading screenings on *p*CF_3- and *p*CN-benzaldehyde to compare them with unsubstituted benzaldehyde. The catalyst loading screenings were performed as previously discussed in chapter I.2.2.1. The results are shown in Figure 61. ee_P increases for CF_3 and CN when lowering the catalyst loading, but the effect is less strong than with unsubstituted benzaldehyde. From the present data it is difficult to conclude why, it can be because of a lower $ee_{max\ 1}/ee_{max\ 2}$-difference or a less catalyst loading-sensitive monomer/dimer-ratio. It should also be noted that the overall ee_Ps are lower with CN than with CF_3 or H.

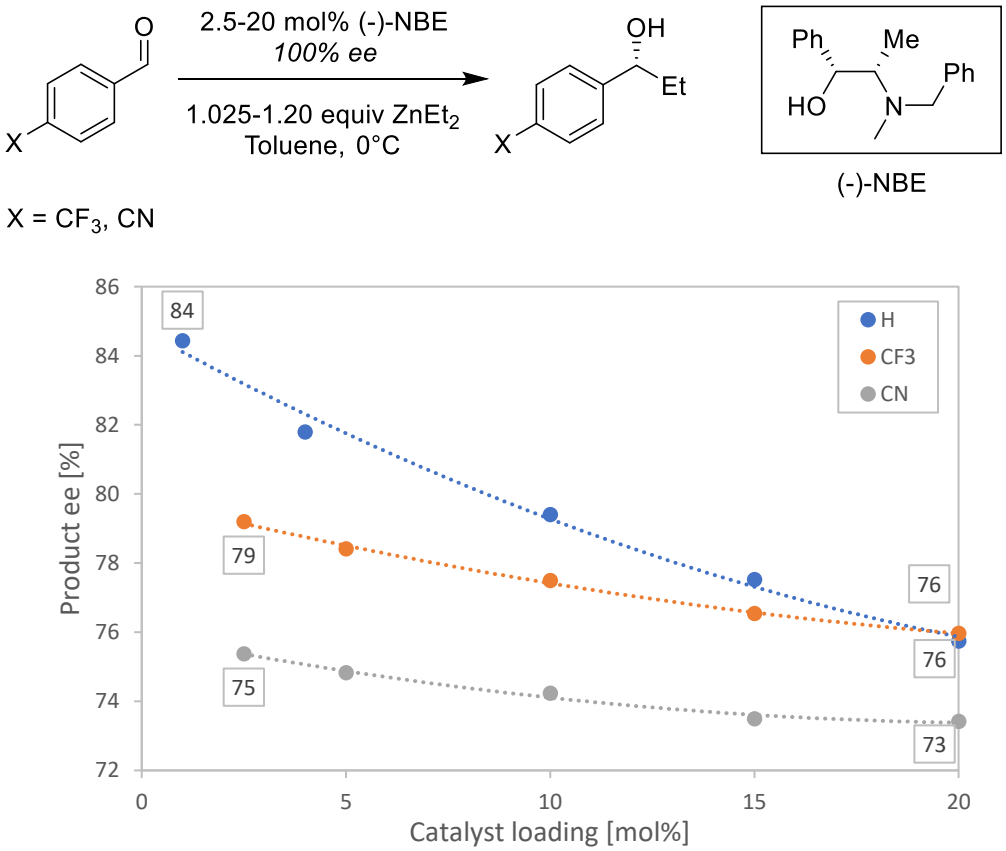

Figure 61: Catalyst loading screening of pCF_3 (orange dots) and pCN-benzaldehyde (grey dots) in the NBE-catalysed addition of $ZnEt_2$. The results for unsubstituted benzaldehyde (blue dots) are shown for comparison. The trendlines (2nd order linear fits) are intended for illustration purposes only.

We also made a full NLE curve with *p*CF_3-benzaldehyde, $ZnEt_2$ and NBE and compared it with the catalyst loading screening, as we have done before with unsubstituted benzaldehyde in chapter I.2.2.1. Figure 62 shows the superimposition of NLE (blue dots) and catalyst loading screening (orange squares). The NLE with *p*CF_3-benzaldehyde is not hyperpositive as ee_P stays constant at 76% from 100 to 20% ee_L, it starts to drop only at lower ee_Ls. This concords with the catalyst loading screening: if the ee_P increase at lower catalyst concentration is less pronounced than with unsubstituted benzaldehyde, then the NLE curve should also be less hyperpositive (lower Δee_P), which is the case here.

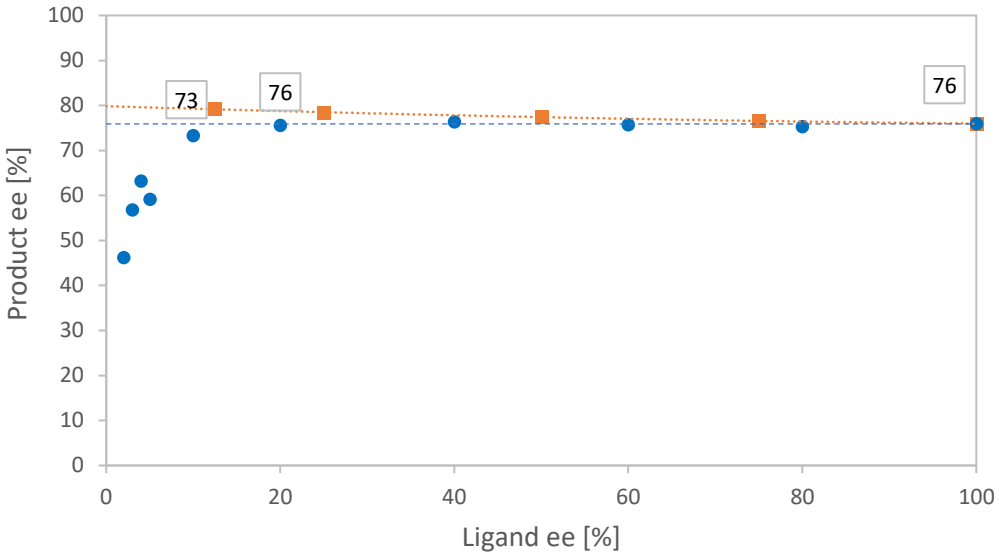

Figure 62: NLE-curve for the (-)-NBE-catalysed addition of $ZnEt_2$ to pCF_3-benzaldehyde (blue dots). Catalyst loading screening of enantiopure (-)-NBE (2.5 to 20 mol%, orange squares) adapted to the ee_L-scale as in chapter I.2.2.1. The orange trendline (2nd order polynomial function) is intended for illustration purposes only.

I.2.3.5 Hammett plots

(a) Comparison of NBE with DAIB

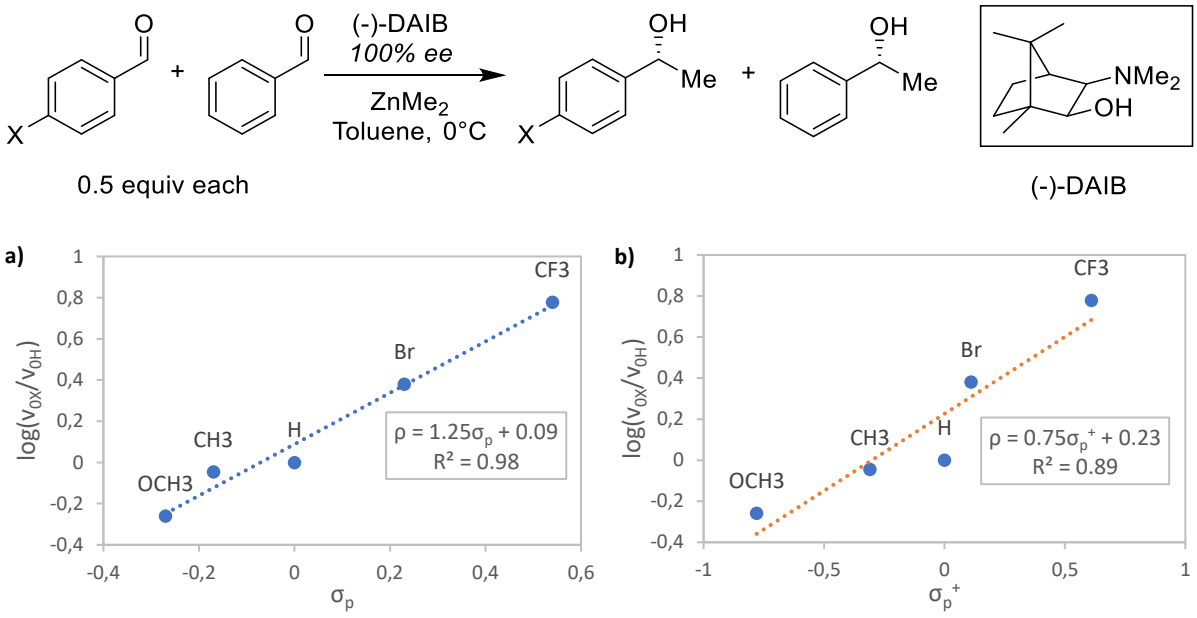

Figure 63: Noyori's Hammet plots for the enantiopure DAIB-catalysed addition of $ZnMe_2$ to para-substituted benzaldehydes using the a) σ_p-scale or the b) σ_p^+-scale. The graphs have been made from the reported tabular data.[30]

Noyori made Hammett plots (see section V.1.3, p. 165 for more details about Hammett plots) for DAIB-catalysed addition of $ZnMe_2$ to *para*-substituted benzaldehydes, with the intention to rule out the possibility of the heterochiral dimer catalysing the reaction.[30] For this, he made competitive reactions in which 0.5 equivalents of both substituted and unsubstituted benzaldehyde were reacted with $ZnMe_2$, in presence of a catalytic amount of (-)-DAIB. He determined the initial rates (v_{0X} and v_{0H}, respectively) of both substrates and plotted $\log(v_{0X}/v_{0H})$ vs σ_p of the respective substituted benzaldehyde. This resulted in a Hammett plot with $\rho = 1.25$ with an excellent fit (Figure 63a). In addition, we show here also a Hammett plot of the same data using the σ_p^+-scale (Figure 63b).

In order to get more information about the NBE-catalysed reaction, we made Hammett plots for the NBE-catalysed addition of $ZnMe_2$ using a strategy similar to Noyori's. We left our reaction conditions unchanged, except for the substrates which are both 0.5 equiv. instead of 1. The tabular data with the different conversion and ee_P-values of the competitive runs can be found in the experimental section (IV.1.2.3, p. 142). Figure 64 shows the plot $\log(v_{0X}/v_{0H})$ vs σ_p for NBE using the same set of substrates as Noyori did (Cl was replaced by Br, both have the same σ_p of 0.23). The resulting Hammett plot looks quite similar to DAIB's plot in Figure 63a: the fit is good ($R^2 = 0.96$) and only Me deviates significantly from the plot. However, ρ is with a value of 1.89 much higher than for DAIB (1.2).

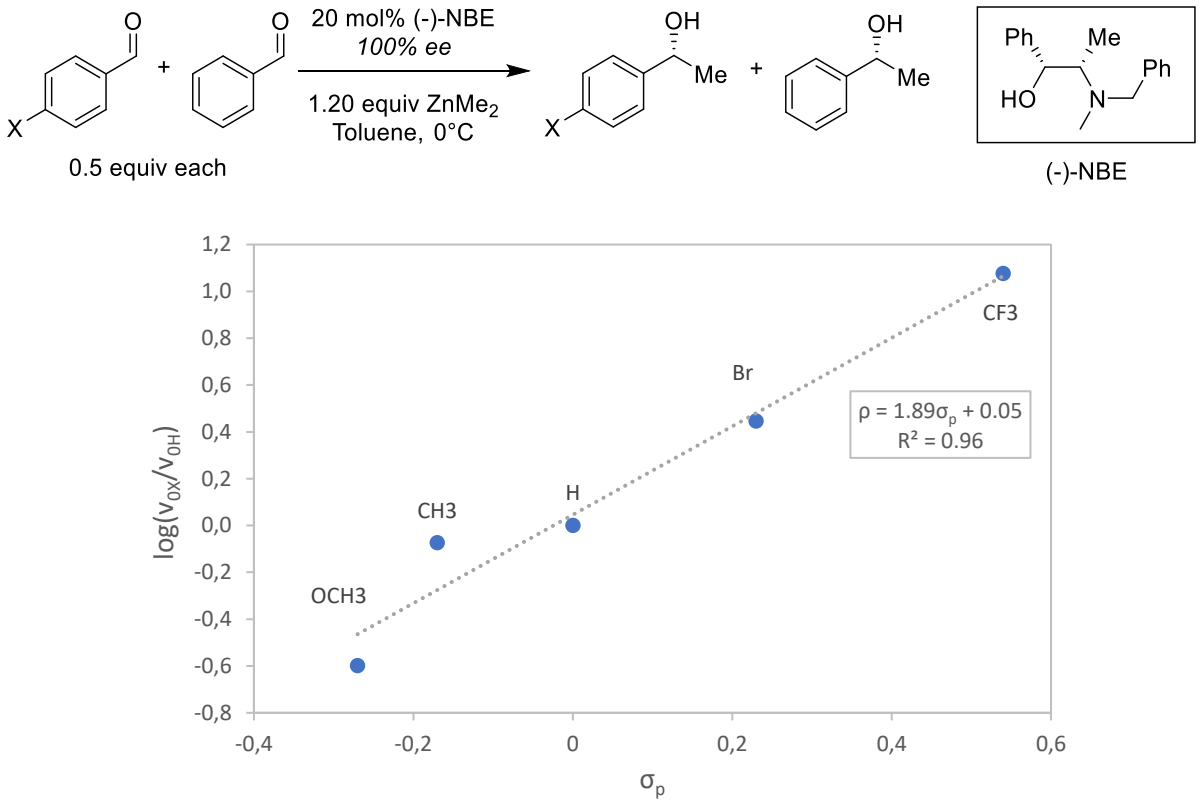

Figure 64: σ_p-Hammett plot of the NBE-catalysed addition of $ZnMe_2$ to substituted benzaldehydes.

A higher ρ-value means that the NBE-catalysed reaction is more susceptible to substituent effects than DAIB, and that the transition state of the rate-determining step builds up more negative charge. A big difference between monomeric NBE-ZnMe's and DAIB-ZnMe's catalytic transition states would be rather surprising since their reactive centres are similar. However, it may be different for *dimeric*

NBE-ZnMe as we don't know its structure; the differing ρ might then be an indication for the monomer not being the only catalyst. The substituted benzaldehydes might have different relative affinities for monomeric/dimeric NBE-ZnMe ($K_{assoc\ 1}/K_{assoc\ 2}$, see chapter I.2.2.6) and react with different relative rates (k_1/k_2); the relative product inhibition of the substituted chiral zinc alkoxide ($K_{dissoc\ 1}/K_{dissoc\ 2}$) might also differ from the unsubstituted one.

(b) Extension of the substrate scope: σ_p and σ_p^+

We then extended the competitive catalytic runs to other substrates, from strongly e⁻-donating (OiPr) to strongly e⁻-attracting substituents (CN). The resulting Hammett plot (Figure 65) shows a still linear but quite scattered relationship, especially at low σ_p, with a moderate R^2 of 0.83. The ρ-value of 1.24 is now close to Noyori's ρ for DAIB.

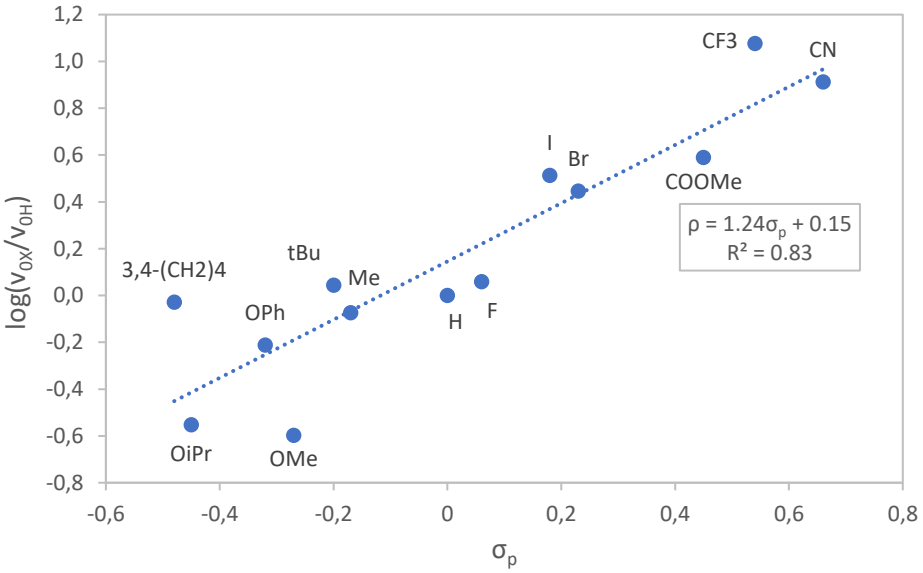

Figure 65: Extended σ_p-Hammett plot of the NBE-catalysed addition of $ZnMe_2$ to substituted benzaldehydes.

Since scattering can originate from using the wrong σ-scale, we decided to check for other LFER-scales.[121] σ_p^+ gave a better linear correlation (R^2 = 0.94) and visibly less scattering, especially the strongly e⁻-donating substituents now fit better to the linear trendline. The ρ-value is of 1.02; both ρ and R^2 are higher than for the Hammet plot of DAIB using the same σ_p^+-scale (0.75 and 0.89, respectively, cf. Figure 63b). DAIB fits better to σ_p than to σ_p^+ and therefore shows a behaviour contrary to NBE.

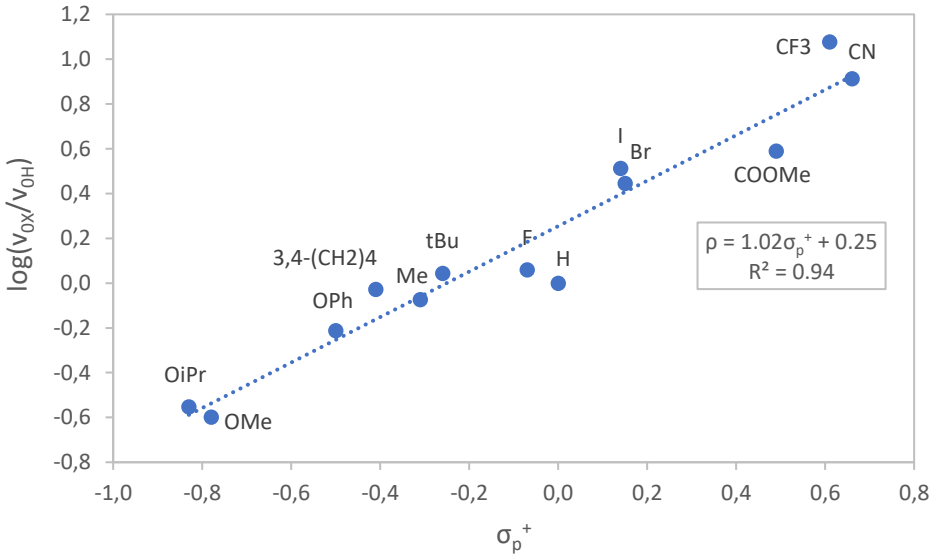

Figure 66: σ_p^+-Hammett plot of the NBE-catalysed addition of $ZnMe_2$ to substituted benzaldehydes.

Hammett plots can also be constructed for stereo- or regioselective reactions, using the ratio of the two stereo- or regioisomers' kinetic constants for either H and X. In enantioselective reactions, $\log(k_X/k_H)$ becomes $\log(er_X/er_H)$ with the enantiomeric ratio $er = k_R/k_S$. The plots vs σ_p (Figure 67) and σ_p^+ (Figure 68) result in linear fits bearing low ρ values of 0.10 and 0.08, respectively. This is consistent with enantioselectivity usually being much more governed by steric than by electronic effects. As for the $\log(v_{0X}/v_{0H})$-plots, the σ_p^+-scale gives a better overall correlation than σ_p, even though the R^2 remains moderate (0.83).

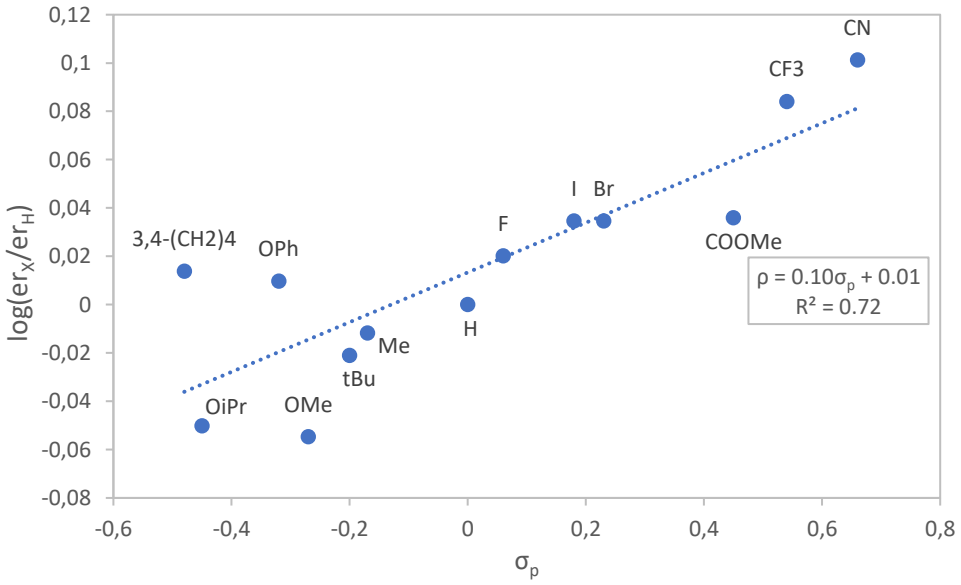

Figure 67: σ_p-Hammett plot of the enantioselectivity of the NBE-catalysed addition of $ZnMe_2$ to substituted benzaldehydes.

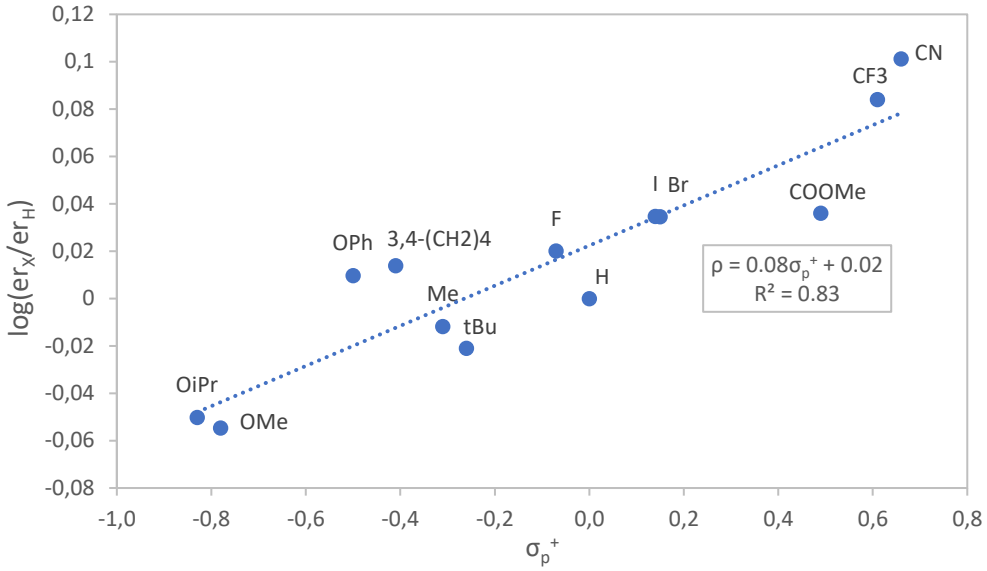

Figure 68: σ_p^+-Hammett plot of the enantioselectivity of NBE-catalysed addition of $ZnMe_2$ to substituted benzaldehydes.

The better fit to the σ_p^+-scale for both $\log(v_{0X}/v_{0H})$ and $\log(er_X/er_H)$ indicates that the catalysis may be sensitive to "through-conjugation". This is the delocalisation of electrons from the aromatic cycle and the *para*-substituent, if it is a mesomeric donor, into the aldehyde (cf. supporting information V.1.3, p. 165). This makes the aldehyde more electron-rich and a better coordinant, therefore these results may be indicative of the NBE catalyst being more electron-poor and a stronger Lewis acid than the DAIB catalyst. As mentioned before, monomeric NBE-ZnMe is not likely to be a fundamentally different catalyst than DAIB-ZnMe, this holds also for their Lewis acidity. However, dimeric NBE-ZnMe may be different from DAIB-ZnMe and be more Lewis acidic. Therefore, the better fit to the σ_p^+-scale may be an indication for the joint catalysis by monomeric and dimeric NBE-ZnMe. A way to check this would be to repeat the competitive catalytic runs with a lower catalyst loading; the decreasing dimer/monomer ratio should then result in a Hammett plot which is closer to DAIB's and which fits less good to the σ_p^+-scale.

(c) Size-optimised Hammett plots

However, the conclusion from the previous section should be treated with care. There can be other elements influencing the catalytic reaction, e. g. coordination of the substituents to other species. The alkoxy-substituents, CN and especially COOMe may coordinate to $ZnMe_2$ or the catalyst and influence the various equilibria, their own catalytic reaction or induce side-reactions. The deviation of the electron-rich substituents in Figure 64 may also be due to their steric instead of their electronic properties. The alkoxy- (except OMe), 3,4-$(CH_2)_4$- and tBu-groups are much bigger than the halogens, CF_3 or CN. Therefore, we made a size-optimised Hammett plot using the σ_p-scale (Figure 69) which excludes the mentioned bulky substituents (orange crosses), as well as COOMe. ρ takes an intermediate value of 1.64, still higher than for DAIB in Figure 63a but lower than for NBE in the equivalent plot with all substituents included (cf. Figure 64); the accuracy of the fit is with R^2 = 0.92 also intermediate. A similarly adapted Hammett plot for the reactions' enantioselectivities (Figure 70) gives an even better fit with R^2 = 0.97 and ρ = 0.15.

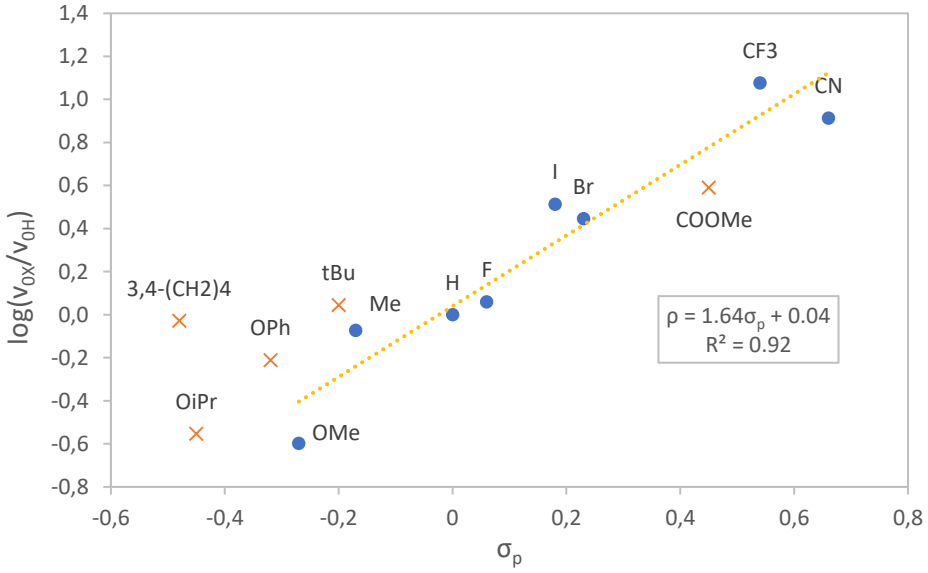

Figure 69: σ_p-Hammett plots of the NBE-catalysed addition of $ZnMe_2$ to substituted benzaldehydes. Bulky substituents (orange crosses) have been excluded from the linear fit to build the plot.

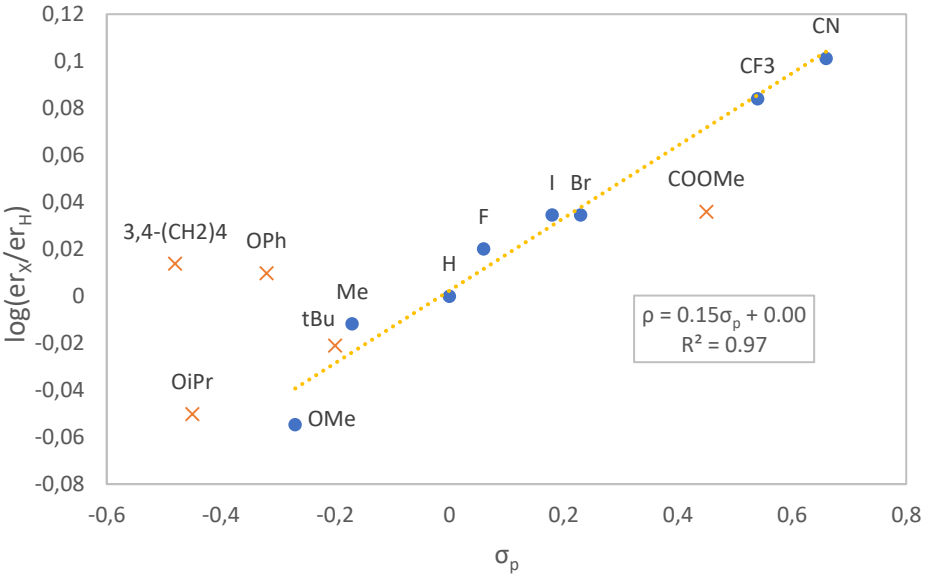

Figure 70: size-optimised σ_p-Hammett plot of the enantioselectivity of the NBE-catalysed addition of $ZnMe_2$ to substituted benzaldehydes. Bulky substituents (orange crosses) have been excluded from the linear fit to build the plot.

At this point, it is difficult to say whether the standard σ_p-/σ_p^+-plots or the size-optimised plots are more representative for the NBE-catalysed system. It would be useful to extend DAIB's Hammett plot to the substituents we have used in this study and see if the bulky substituents do also deviate.

I.2.3.6 Effects of ortho-substituents on the substrate

In addition, we tested also two substrates which are sterically crowded around the aldehyde, with one or two methyl substituents in the *ortho* position in addition to the *para* position. The results are shown in Table 6. The *o*,*p*-disubstituted benzaldehyde doesn't behave differently than its *p*-monosubstituted counterpart in Figure 59: the ee_P difference between enantiopure and scalemic ligand is very small but still hyperpositive. However, the trisubstituted benzaldehyde yields an ee_P at 100% ee_L which is significantly higher than with the other substrates; it is the only one to be over 80% ee_P. The ee_P with scalemic ligand is with 79% on the level of the mono- and dimethyl substituted benzaldehydes.

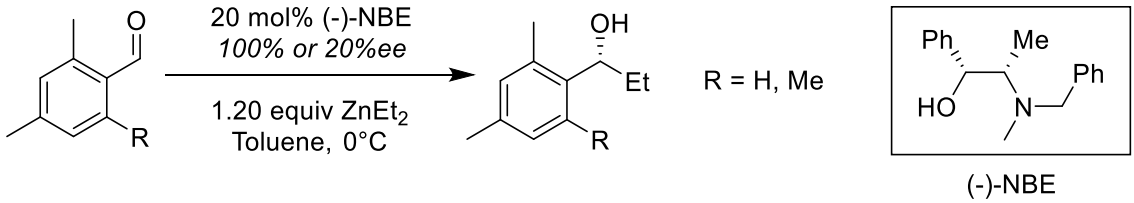

ee_L [%]	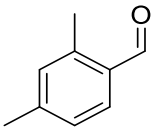	ee_P [%]	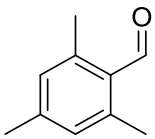
100	76%		85%
20	78%		79%

Table 6: ee_Ps at 20 and 100% ee_L with ortho,para-dimethyl- and ortho,para,ortho'-trimethylbenzaldehyde.

The high ee_P at 100% ee_L of the trisubstituted aldehyde can have different origins, but since ee_P at 20% ee_L is not different from the other aldehydes, one possibility stands out: the trisubstituted benzaldehyde might have a lower affinity for or a slower reaction with the dimeric NBE catalyst than the other substrates. Thus, it may be catalysed mainly by the monomeric catalyst which yields higher ee_Ps. This is interesting as it would preclude that the dimeric catalyst is more sensitive to steric effects than the monomeric one. Another possibility would be that $ee_{max\ 1}$ and/or $ee_{max\ 2}$ are higher than with the other substrates, but then the trisubstituted's ee_P with scalemic ligand should also be higher – which is not the case.

The behaviour of the trimethyl-substituted benzaldehyde prompted us to make a catalyst loading screening with $ZnEt_2$ as in chapter I.2.2.1 (Figure 31a, p. 35). The results are shown in Figure 71. ee_P increases from 20 to 10 mol% but then *decreases* at lower catalyst loading. A decrease can be explained by the achiral background reaction becoming nonnegligible, since a lower catalyst loading implicates a slower catalytic conversion. Globally, we observed that the reaction with the trisubstituted benzaldehyde is slower than with unsubstituted one. The background reactions are negligible at 0°C using benzaldehyde[96] but there is, to the best of our knowledge, no data for the trisubstituted one.

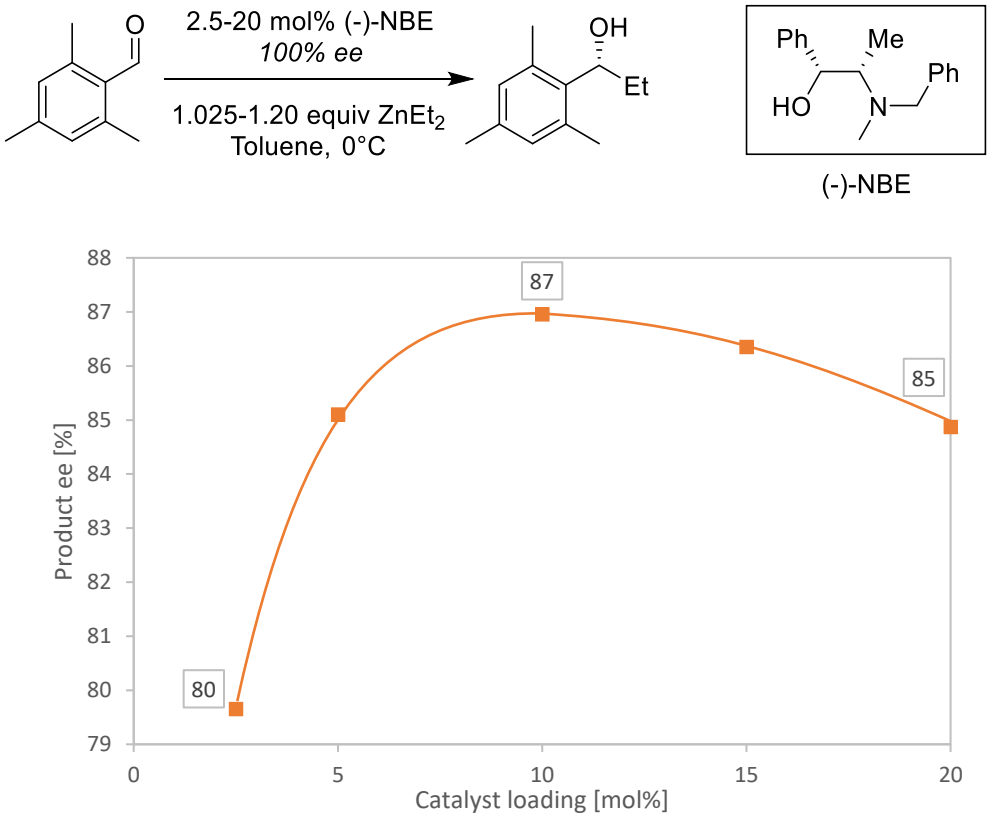

Figure 71: Catalyst loading screenings of para-CN- and CF_3-, ortho,para-ortho'-trimethyl substituted and unsubstituted benzaldehyde in the (-)-NBE-catalysed addition of $ZnEt_2$.

We made a full NLE curve of the reaction with the trisubstituted benzaldehyde and performed a superimposition of the concentration screening (Figure 72, orange squares) with the NLE curve (blue dots). The NLE follows the concentration screening, the maximal ee_P being attained at ca. 50% ee_L and decreasing at lower ee_L. This is probably also at the origin of the downslope at low ligand ee (ee_L < 30%) being larger and much more gradual than the sharp slope of the unsubstituted benzaldehyde's NLE (which is only at 10% ee_L and lower) in Figure 25, p. 31.

These results concord with the hypothesis we have expressed earlier: the high ee_P of 85% (enantiopure ligand) which increases only slightly to 87% ee_P (60-40% ee_P) might come from the trisubstituted benzaldehyde having a low affinity for the dimeric catalyst. Thus, it would be mainly catalysed by the monomer even at 100% ee_L (= high catalyst concentration) and cannot be subject to a strong ee_P increase at lower ee_L or lower catalyst loading. This should be verified by determination of the monomer's enantioselectivity $ee_{max\ 1}$ from an Eyring plots using the trisubstituted benzaldehyde as substrate. Indeed, the $ee_{max\ 1}$ of the monomer-only catalysed addition on unsubstituted benzaldehyde (88%), calculated from an Eyring plot, is close to the trisubstituted's maximum ee_P of 87% with 10 mol% (see Figure 53, p. 60).

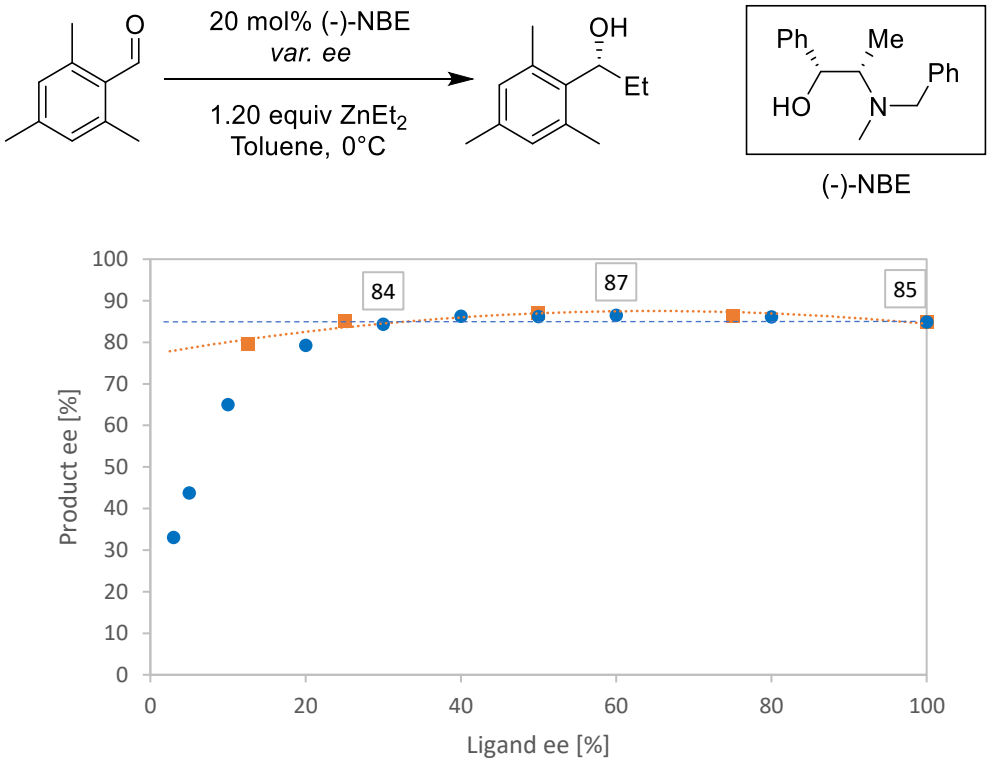

Figure 72: NLE-curve for the (-)-NBE-catalysed addition of $ZnEt_2$ to ortho,para,ortho'-trimethylbenzaldehyde (blue dots). The catalyst loading screening of enantiopure (-)-NBE (2.5 to 20 mol%, orange squares) has been adapted to the ee_L-scale as in chapter I.2.2.1. The trendline (orange dotted line, 2nd order polynomial) is for illustration purposes only.

I.3 Conclusion on Hyperpositive NLEs & Outlook

In summary, we have evidenced within the enantioselective NBE-catalysed addition of dialkylzincs to benzaldehyde an unprecedented catalytic system, in which both a monomeric and a dimeric complex catalyse simultaneously, giving products with different ee_Ps. This has been evidenced by catalyst loading screenings, temperature screenings, ^{1}H DOSY NMR experiments and kinetic investigations. Moreover, along with a precipitation of a *meso*-aggregate of the catalyst, this system is at the origin of a hyperpositive non-linear effect, which has never been observed before but which has been theorised by Henri Kagan 30 years ago – albeit with a different catalytic model than in our case. We have proposed an extension of the Noyori model to explain this catalytic system and have been able to determine the monomer's enantioselectivity in the reaction with $ZnEt_2$ and benzaldehyde, $ee_{max\ 1}$. We have also proposed a way to calculate the system's K_S' from Kagan's reservoir model, studied the role of the benzylic substituent in the NBE ligand and investigated the effects of *ortho*- and *para*-and substituents on the substrate. The latter's effect on the catalytic reaction has been quantified by constructing Hammett plots.

Further work will aim at completing some of the studies here. It would also be interesting to apply an NBE-derivative whose alcohol has been replaced by a thiol – such aminothiols have proven to give high ee_Ps and strong (+)-NLEs[34,90,91] – and to study its effects on the hyperpositive NLE.

The ultimate goal would be to make a full modelling of the monomer/dimer catalytic system and of the hyperpositive NLE, similar to what Noyori did with DAIB. However, the complexity of the reaction and the number of different parameters which have to be accounted for will probably make this a very difficult task.

The hyperpositive NLE in itself is a fascinating curiosity, as it shows that something totally counter-intuitive – the obtention of higher ee_Ps with scalemic ligand than with the enantiopure ligand – is possible. It probably won't have an impact on subjects usually associated to NLEs in asymmetric catalysis, like the discussion about the origin of biological homochirality. The way how the (+)-NLE arises – precipitation of a heterochiral aggregate – is not new (although its extent is exceptional). However, the joint catalysis by a monomeric and a dimeric complex deserves further discussions. It is in striking contrast to the Noyori model where catalysis by aggregates is excluded, a factor which has been rarely questioned in the literature of dialkylzinc chemistry.

In this context, the main question is whether our catalytic system is an exception in the aminoalcohol-catalysed addition of dialkylzincs to aromatic aldehydes or not. In this study, we have shown that the NME ligand probably also catalyses through both a monomeric and a dimeric complex. A look into literature reveals that some catalysts show a similar behaviour to NBE and NME: Chaloner noticed, when using N-isopropyl ephedrine as catalyst, an ee_P increase when diluting the reaction and increasing the equivalents of $ZnEt_2$ (the latter should drive the dissociation of dimers, as does the dilution).[95,97] They also observed a 40% ee_P-drop when decreasing the temperature from 20 to -20°C with unsubstituted ephedrine as catalyst. An even more dramatic temperature effect has been reported by Zhang and Chan using a chiral *ortho*-(2-pyridyl)-phenol.[122] Those observations concord with our model in which both monomeric and dimeric complexes catalyse, the latter yielding a lower ee_P than the first; diluted conditions and high temperatures favour the monomer over the dimer. Chaloner even stated: "*If we assume that other alkylation reactions, occurring through different intermediates, are less optically efficient, this would account for the dependence of the optical yield on the Et_2Zn:ArCHO ratio*",[97] and Zhang and Chang wrote : *"The possible temperature-dependent competing reactions between the monomeric and dimeric zinc species as the active catalyst might account for the inversion temperature"* .[122]

Another point which might be of importance is the astonishing absence of $ZnMe_2$ in the literature of aminoalcohol-catalysed dialkylzinc additions; only Noyori makes in his studies of DAIB an extensive use of it. When looking at our results with $ZnMe_2$ and NBE as the catalyst, the low ee_Ps (16-54%) and the long reaction times are indeed disappointing if one seeks to develop a high-performing and efficient catalytic reaction. Might similar results with other aminoalcohols have led the scientific community to put $ZnMe_2$ aside? Noyori obtained up to 95% ee_P with $ZnMe_2$ and DAIB, this proves that $ZnMe_2$ is not a bad reactant in itself, and we know that in our case the low ee_Ps come from the dimeric catalyst's contribution to the reaction. Therefore, low ee_Ps with $ZnMe_2$ and other aminoalcohols might be a hint that the joint monomer/dimer catalysis is a much more common case than one might think.

Finally, it should be noted that even Noyori didn't totally rule out the possibility of catalysis by dimeric DAIB-complexes. He could exclude it when working in a certain range of concentrations and of DAIB:benzaldehyde:$ZnMe_2$-ratios, but also stated explicitly: *"The dimer mechanism […] should be seriously considered under some special conditions, e.g. at very high concentrations of the catalyst and reactants"*.[30]

Chapter II: Non-linear effects with metallopolymers

The dialkylzinc chemistry we have been dealing with so far, as well as most of the reported systems bearing NLEs, encompasses discrete complexes consisting of a ligand with a single coordination site (usually a bidentate one) and a metal. Those complexes may then form aggregates which are responsible for the emergence of NLEs. However, very little is known about NLEs with ligands bearing *two* coordination sites (i. e. ditopic ligand) or even more. Those ligands can, if bound to the appropriate amount of metal ions, form higher aggregates known as *metallosupramolecular polymers* (abbreviated here as *metallopolymers*) or *coordination polymers*. This chapter will treat of chiral metallopolymers applied to asymmetric catalysis and how their structure induces NLEs or influences existing ones.

II.1 Introduction to metallopolymers

II.1.1 Covalent and non-covalent polymers

Classic polymers are chain- or network-like macromolecules consisting of repeating subunits (monomers) which are linked via covalent bonds. Most synthetic polymers in our everyday-life such as polyethylene (PE) or polystyrene (PS) are issued from radical chain reactions on ethylene-derived monomers (Figure 73a); cationic and anionic polymerisation do also exist, e. g. activation and ring-opening of epoxides with a Lewis or Bronsted acid. Polycondensations, performed by the addition of a diamine or a dialcohol to a di-carboxylic acid derivative, lead to polyamides (e. g. Kevlar, Nylon) and polyesters (e. g. polyethylene terephthalate, PET, Figure 73b). Those linear, one-dimensional polymers can have different lengths and shapes according to the way how they fold and interact with other polymeric chains. This gives them properties like thermoplasticity; branched polymers can have additional properties like elasticity and superabsorbtion (gels).

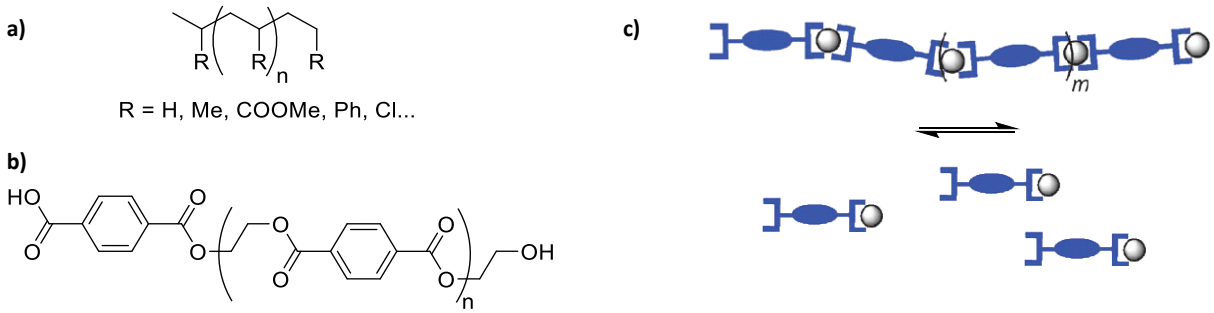

Figure 73: Examples for a) ethylene-derived polymers, b) a polymer issued from polycondensation, polyethylene terephthalate (PET) and c) a metallopolymer consisting of a ditopic ligand (blue) and a metal (grey). The metallopolymer can be in equilibrium with smaller subunits, e. g. discrete ligand-metal complexes.

Metallopolymers differ from classical polymers as they are built not only of organic material and covalent bonds. They are formally copolymers consisting two different monomers: a ditopic, organic ligand and a metal capable of binding to two different ligands[123] – in other words, a bifunctional Lewis base and a bifunctional Lewis acid (Figure 73c). Trifunctional ligands and metals do also exist,

but since we will work only on chain-like metallopolymers we won't discuss them further. The incorporation of metals into polymers may add features such as redox activity, magnetism and photophysical properties, which lead to application in optoelectronics,[124] light-emitting and -responsive devices,[125] electronic conduction,[126] energy production and conservation,[127] information storage[128] and more. The metal *as part of the polymeric chain* adds also another property: dynamics. The non-covalent nature of the metal-ligand bond opens the possibility of reversible association: in contrast to covalently bonded polymers (except, e. g. polymers issued from reversible polycondensation), metallopolymers may break as easily as they are formed as shown in Figure 73c, especially if they are constituted of 1st-row d-block metals with a high ligand exchange rate (such as Ni, Cu and Zn) bound to L-type ligands. X-type ligands, which necessarily act as counterions, are bound too tightly to the metal to allow reversible bonding; certain L-type ligand/metal-bonds may also be irreversible because of an exceptional affinity, e. g. Fe or Ru with terpyridine ligands. Most ligands in dynamic metallopolymers will have nitrogen-based L-ligands but oxygen, sulphur and phosphorus are also possible. The reversible bonding confers the material a certain adaptability which is exploited for example in self-healing materials.[129]

II.1.2 Dynamic metallopolymers in asymmetric catalysis

The bonding reversibility allows to combine the properties of discrete metal complexes with those of polymeric chains, such as activity in homogeneous catalysis from the first and insolubility in certain solvents from the latter. Polymers tend (but do not need) to be less soluble than related small molecules because the interaction of the chain with the solvent is in competition with the interaction with itself; the system's gain in entropy may also be small or even unfavourable if a solvation sphere consisting of a multitude of small molecules is needed to solubilise a single, big molecule. Our group has been taking advantage of this to apply chiral metallopolymers in recyclable enantioselective catalysis, coined as *dynamic self-supported catalysis*.[130] A general scheme is shown in Figure 74. The catalyst, consisting of a chiral ditopic ligand and a metal ion, is a metallopolymer in its resting state. Upon dissolution in a coordinating solvent it dissociates into discrete complexes with free coordination sites on the metal, which are able to perform catalysis. The addition of a non-coordinating solvent at the end of the reaction regenerates metallopolymer and drives its precipitation; filtration allows the recovery of the complex for a further catalytic reaction.

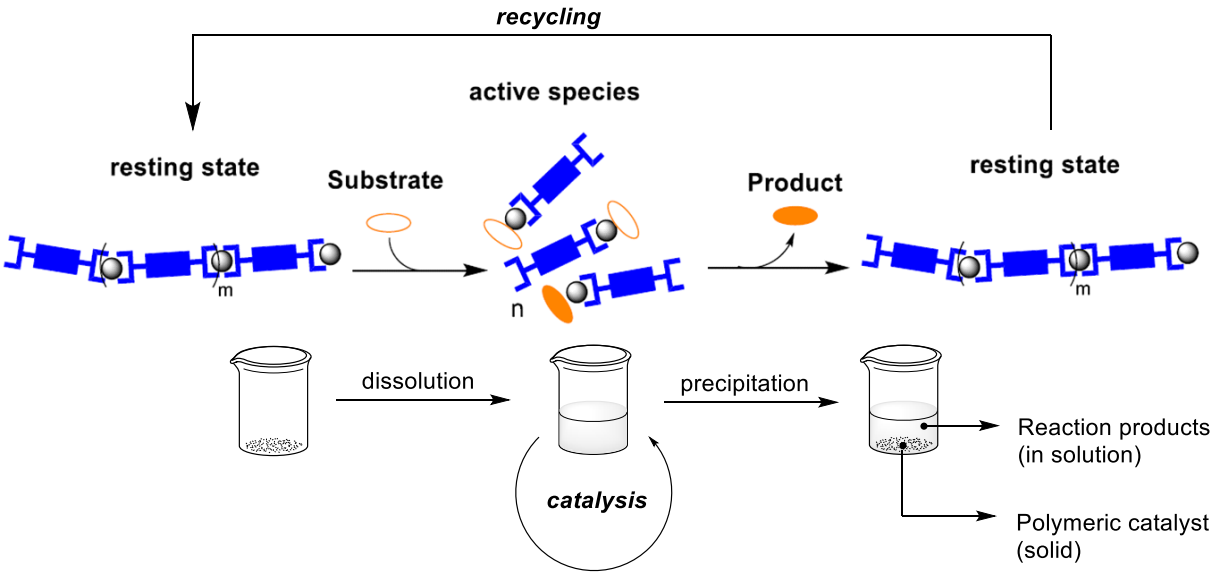

Figure 74: General scheme for dynamic self-supported catalysis with metallopolymers.

This method to recycle catalysts is particularly elegant since the catalysis is performed in a homogeneous way while the recovery is heterogeneous. The literature is full of examples of homogeneous catalysts attached on solid supports such a covalent polymers or silica, non-dynamic metallopolymers do also exist ("self-supported catalysis"). However, those adducts don't dissolve at all so the catalysis has to take place on the surface of the material, in a heterogeneous way. This often leads to a loss of product ee in enantioselective catalysis. Dynamic self-supported catalysis circumvents this problem by making the catalyst homogeneous only when needed, but it has also some drawbacks. The reaction (by-)product shouldn't prevent the metallopolymer's regeneration and should also not co-precipitate; the reaction further should not change the nature of the ligand or the metal. Reactions involving changes in the metal's oxidation state may be problematic as the oxidation state has to be controlled in order to properly regenerate the metallopolymer. Thus, the metal mostly plays only the role of a Lewis acid in dynamic self-supported catalysis.

Our group mostly has worked with di-, tri- and tetratopic bisoxazoline ligands and Cu(II) salts, such as ditopic ligand **3** and $CuOTf_2$ (Figure 75a), to perform Michael additions of β-ketoesters to azodicarboxylates,[131] chiral resolutions of *rac*- or and desymmetrisations of *meso*-1,2-diols (also Arai and Sakagami)[132] and Henry reactions.[133] The group of Garcìa used azabisoxalines and Cu(I)/(II) salts in the allylic oxidation of cyclic alkenes,[134] Henry reactions[135,136] and in cyclopropanation reactions.[137–139] The procedure of the latter example is particularly elegant as the metallopolymer is not soluble in dichloromethane but solubilises as soon as the diazo starting material is added – not the solvent but the reactant is responsible for the dissociation of the metallopolymer. Once the reactant is consumed the metallopolymer regenerates and precipitates, without the need for adding a non-solvent. Non-copper examples for dynamic self-supported catalysis are a modified Ru/NHC-complex for the (achiral) ring-closing metathesis of dienes[140,141] and the enantioselective Michael addition of malonates and β-ketoesters to nitrostyrenes, catalysed by a diaminocyclohexane (DACH) based ditopic ligand **4** and $NiBr_2$ (Figure 75b).[142]

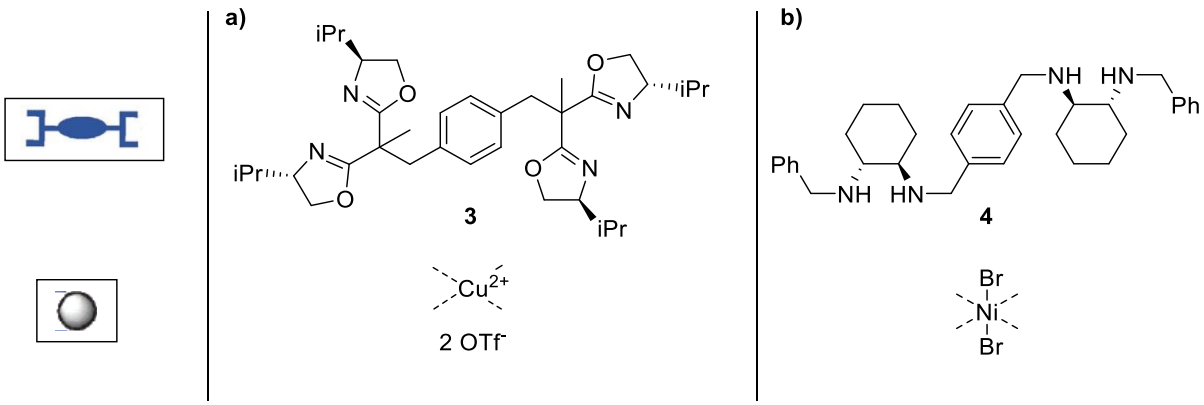

*Figure 75: Structures of metallopolymer-forming a) **3** and $CuOTf_2$, b) **4** and $NiBr_2$.*

II.1.3 Metallopolymers and NLEs

Since NLEs are an excellent tool to study catalyst aggregation in asymmetric catalysis, our group checked for their presence in two reactions: the **3-Cu(OTf)$_2$**-catalysed α-hydrazination of β-ketoesters (Figure 76a) and the **4-NiBr$_2$**-catalysed addition of malonates to nitrostyrene (Figure 76b). Both exhibit (-)-NLEs with a bell-shaped curve, which is an indication for higher-order aggregates (ML_3 and upwards according to the Kagan model).[20] The negative sign of the NLE is also expected since the ligands are pseudo-C_2-symmetrical in both cases: this favours a homochiral configuration around the metal when in a *square planar* environment, like on Cu(II) in these complexes;[143] the nickel atom in **4-NiBr$_2$** is octahedral but with the Br anions on the apical sites, the ligands therefore coordinate in a square-planar fashion. On the other hand, a tetrahedral coordination as on Zn(II) and Cu(I) favours a heterochiral arrangement.[144–146] This is accordance with a Ph-substituted bisoxazoline/Cu(I)-complex being reported to have a (+)-NLE,[147] other NLEs with Zn(II) and Cu(II) result from the insolubility of a *meso* complex which complements or prevails over favoured coordination modes.[100,103] One report depicts a *square planar* heterochiral Ph-substituted bisoxazoline/Cu(II) complex as the origin for a (+)-NLE but without providing any proof for, nor any discussion about the metal's coordination mode.[148]

However, the origin of the NLE with **4-NiBr$_2$** is less clear: Evans and co-workers' homoleptic complex **5$_2$-NiBr$_2$** (cf. Figure 77), from which **4-NiBr$_2$** is inspired, shows a linear relationship between ee_L and ee_P.[58,59] Either both homochiral and heterochiral **5$_2$-NiBr$_2$** are equally stable, which is unlikely, or the lability of the 2nd ligand is sufficiently high in both cases to be completely displaced by the substrate, so that there is no remaining **5$_2$-NiBr$_2$** which could act as a resting species. Mechanistic investigations point to the latter option. This makes the emergence of **4-NiBr$_2$**'s (-)-NLE even more interesting: the ditopic ligand **4** shouldn't be a significantly better or poorer coordinant compared to **5**.

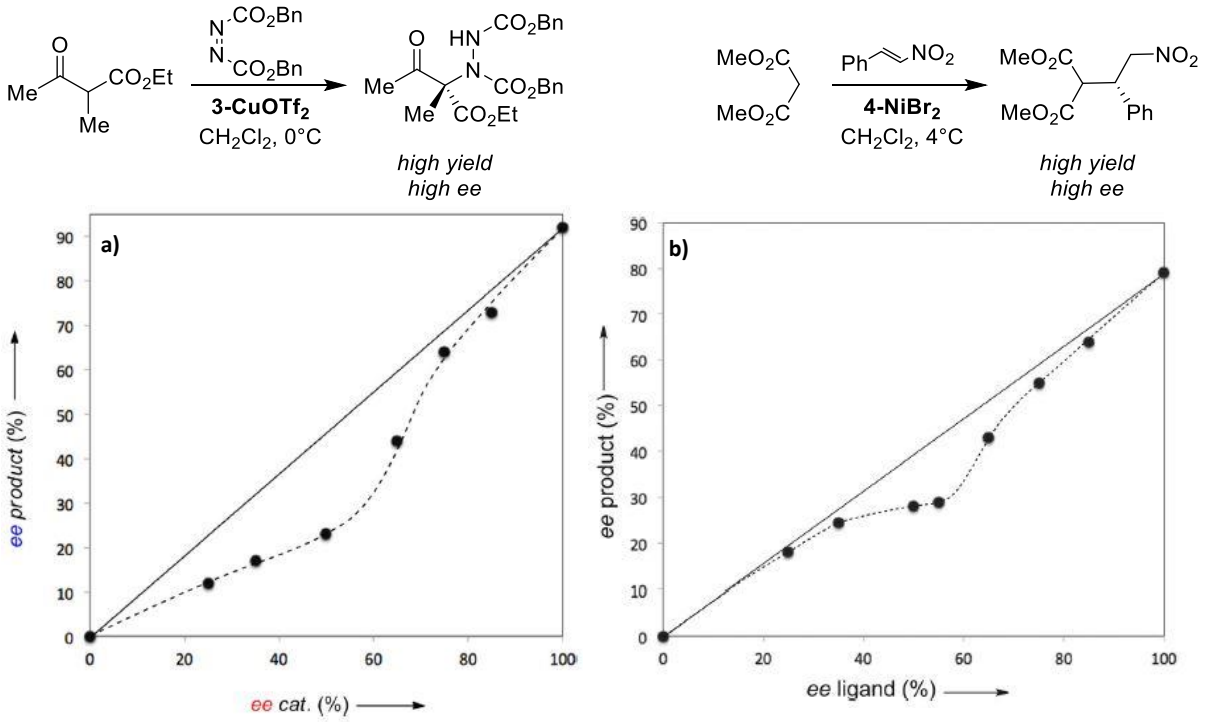

*Figure 76: (-)-NLEs of enantioselective Michael additions catalysed by a) **3-Cu(OTf)$_2$** and b) **4-NiBr$_2$**.*

At the moment we can only speculate on the origin of this NLE. A possible explanation could be the emergence of a reservoir effect through coil-like structures. We know that the coordination polymer can be broken at any time and at any monomer through dissociation of a Ni-N-bond, leaving a vacant coordination site on the metal to which the substrate can bind; an associative mechanism for substrate binding is not possible on the coordinatively saturated, octahedral Ni(II) atom. However, if such a break point is somewhere in the middle of the polymeric chain and thus possibly *wrapped inside a coil* where the substrate cannot diffuse into, the break is much more likely to close through re-coordination. Therefore, the potential catalytic sites are on the *surface* of the coil while the inside is kinetically blocked. This is true for both homochiral and heterochiral polymers; however, if the homochiral configuration around Ni(II) is more stable, then we can expect homochiral polymers to form longer chains since they are less prone to spontaneous rupture. The longer the polymer, the higher the chance to form coils in which a part of the chain is buried and acts as a homochiral reservoir.

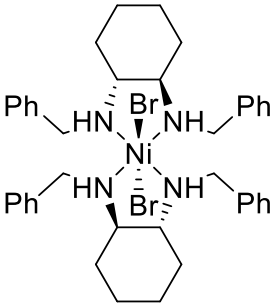

*Figure 7: Structure of complex **5$_2$-NiBr$_2$**.*

We have also to consider that chiral polymers might not just form random coils but well-defined 2nd-order structures, like helixes in proteins and DNA for example. Those structures are more stable when consisting of homochiral components, which is believed to be a reason why homochirality is a necessity for biomolecules.[66] Stable and well-defined secondary structures might favour inter-strand interactions and thus induce a reservoir effect, similarly to what we have described above. It should be noted that in contrast to **5$_2$-NiBr$_2$** and also **3-Cu(OTf)$_2$**, **4-NiBr$_2$** is only partially soluble in DCM or toluene during the reaction. The interactions between polymeric strands, favoured by 2nd-order structures, may decrease the solubility of the homochiral polymers and contribute to the formation of a homochiral reservoir.

These reflections show how a polymeric structure may add properties to the catalyst which don't exist in discrete complexes. This has led us to think about the possibilities it offers: if the polymeric structure can induce NLEs which don't exist in the discrete version of the complex, what happens if we make a polymer based on a discrete complex which is already known for generating NLEs (Figure 78)? Might the additional reservoir effect from 2nd-order structures or precipitation further amplify a complex' *inherent* NLE by making a ditopic version the ligand?

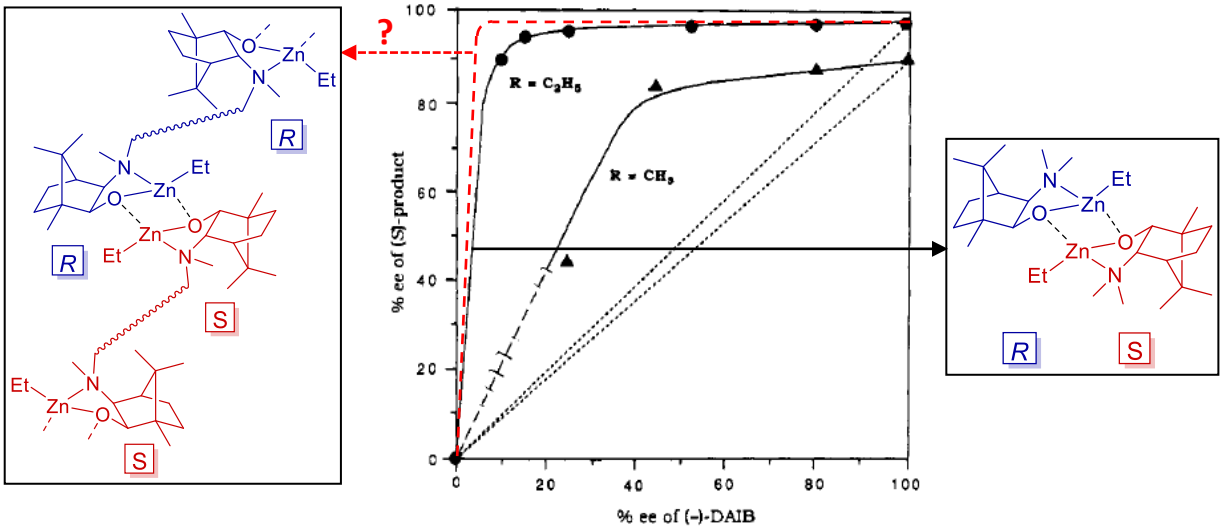

Figure 8: Scheme for the stipulated (+)-NLE[22] amplification by using a ditopic version of DAIB capable of forming heterochiral metallopolymers.

The aim of this chapter will be to find an answer to those questions by designing new metallopolymers which we will probe for NLEs. DAIB is not only one of the most enantioselective ligands for the addition of dialkylzincs to benzaldehydes, it bears also one of the most powerful (+)-NLEs known to date (cf. Chapter I.1.3, p. 17).[22] Therefore, we will synthesise a ditopic version of DAIB capable of forming a metallopolymer and study its behaviour in NLEs. In addition, we will also investigate ephedrine as a building block for ditopic ligands and compare its NLEs with the results presented in Chapter I.

II.2 Results & Discussion

II.2.1 Ditopic DAIB

II.2.1.1 Ligand design and synthesis

The synthesis of (-)-DAIB is a well-documented 5 step-synthesis starting from cheap (+)-camphor, as shown in Figure 79.[149,150] *t*BuOK-mediated nucleophilic addition of (+)-camphor to *iso*-amylnitrite gives oxime **6** in a single step and has proven to be superior to the 2-step procedure involving oxidation of (+)-camphor with toxic SeO_2, followed by condensation of hydroxylamine.[151] In the next step, reduction with $LiAlH_4$ affords aminoalcohol **7** which is then methylated twice by conversion into carbamate **8** and addition of iodomethane, a second reduction with $LiAlH_4$ affords the final DAIB ligand.

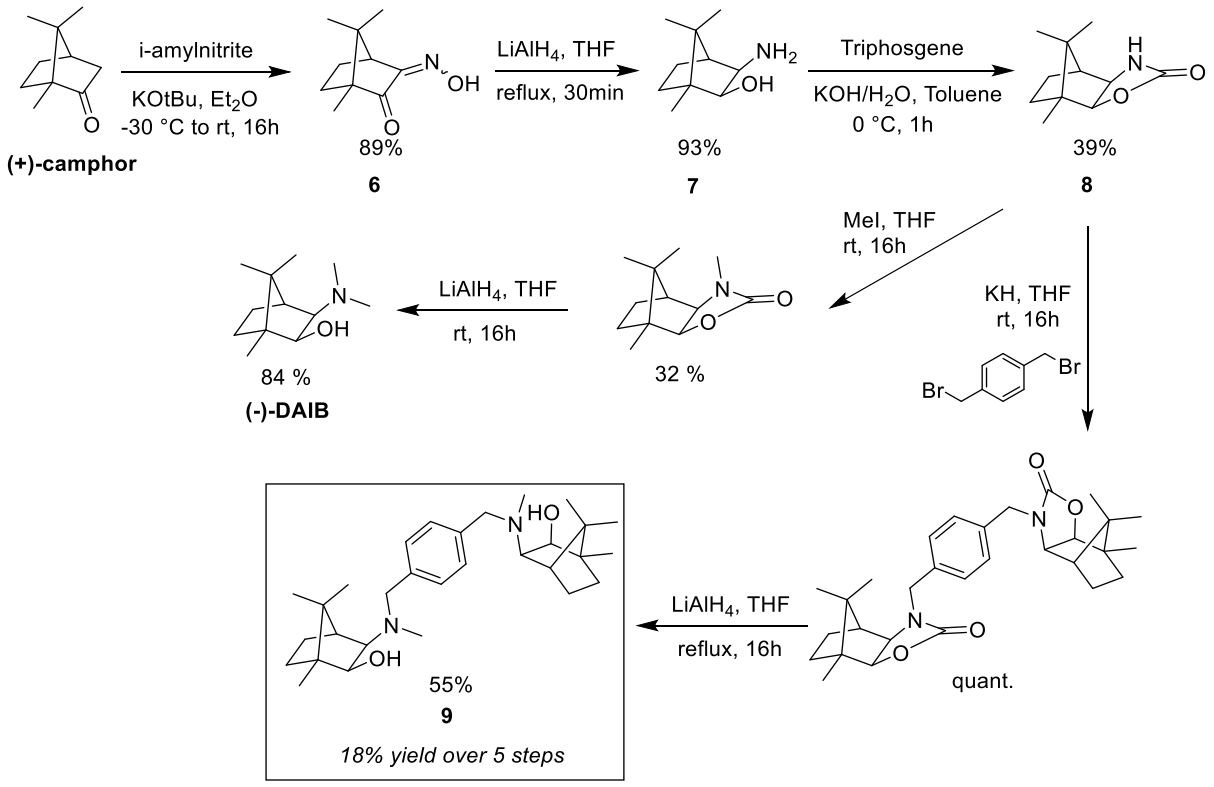

*Figure 79: Synthetic pathway for (-)-DAIB and its ditopic version **9**.*

To make DAIB a ditopic ligand, we introduced an aromatic motif on the nitrogen atom which links to ligand moieties, similar as in ligand **4**. Therefore, we reacted carbamate **8** with *p*-α,α'-dibromoxylene instead of MeI and reduced it to the final ditopic ligand **9**, which was recovered in 55% yield after recrystallisation from MeOH. The purity of the starting carbamate **8** proved to be crucial for the success of the synthesis: aminoalcohol **7** contains small amounts of unwanted *endo*-diastereoisomers which persist in **8** and which may react with the dibromide. Once attached to the linker and a moiety of **8**, the impurity is difficult to remove. A recrystallisation of **8** in AcOEt/Hexane is reported in the literature but proved to be difficult, we didn't obtain more than 39% yield.[152] Thus, ditopic ligand **9**

is obtained in 18% overall yield from (+)-camphor in 5 steps. An alternative to the synthetic path depicted in Figure 79 would have been a double reductive amination of **7** on terephtaldehyde, as in the synthesis of **4**, followed by methylation; a parent reaction with benzaldehyde is described.[153] However, the reaction gave a complex mixture due to hemiaminal ether formation and incomplete conversion, therefore we didn't pursue this synthetic pathway.

II.2.1.2 NLE with ditopic DAIB

Next, we evaluated **9** in the enantioselective addition of $ZnEt_2$ to benzaldehyde. The procedure differs from the one used in Chapter I with NBE: the overall concentration is ca. two times lower, most datasets were obtained with 8 mol% catalyst loading (16 mol% catalytic sites) but a few, notably at low catalyst ee, were also made with 4 and 16 mol% catalyst loading. The reactions were performed in a toluene/hexane 1:0.9 mixture, some additional runs also in toluene only. Each reaction was run only once; ee_Ps were determined via HPLC on a Chiralcel OD-H column. The results are shown in Figure 80, along with the NLE of DAIB reported by Noyori (orange dashed line).[22]

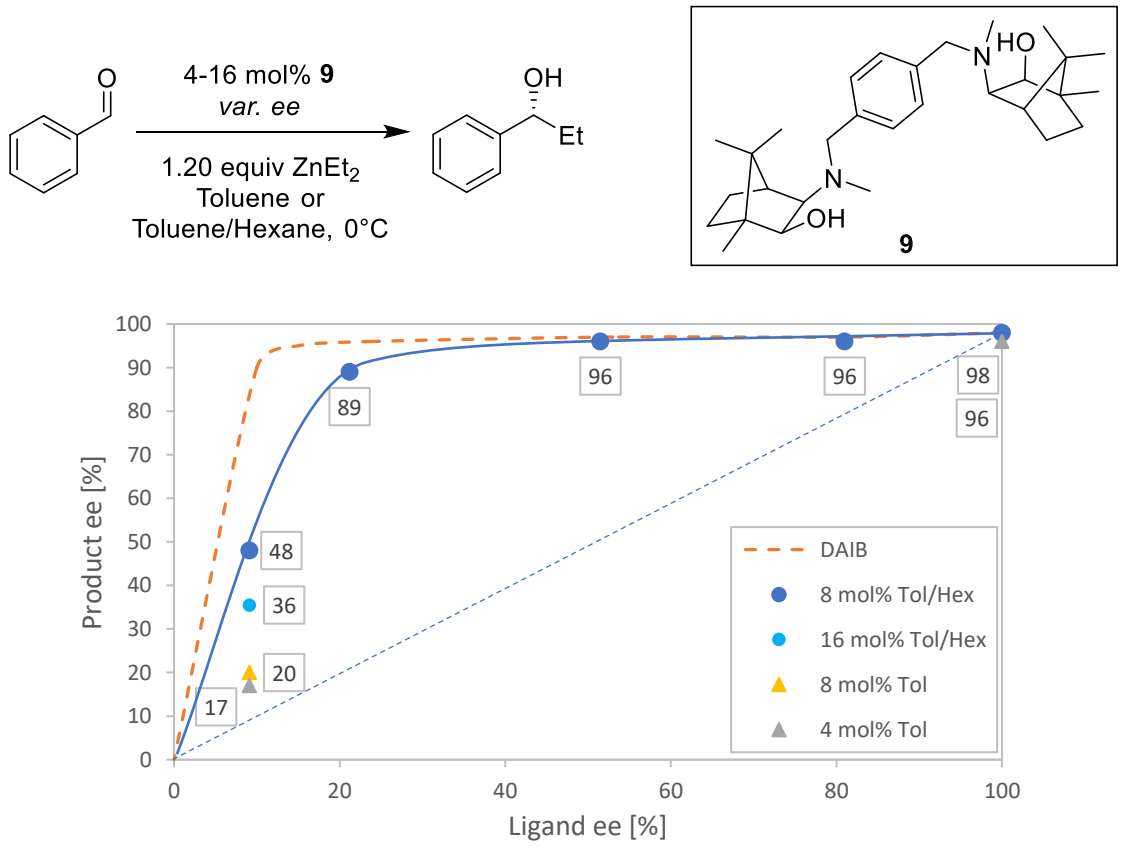

*Figure 80: NLE curve of the addition of $ZnEt_2$ to benzaldehyde catalysed by 8 (blue dots) and 16 mol% (turquoise dot) **9** in a toluene/hexane mixture. Some experiments were also run in toluene only with 8 (yellow triangle) and 4 mol% (grey triangle) **9**. The orange dashed line represents Noyori's NLE from (-)-DAIB (same benzaldehyde concentration, 8 mol% ligand).[22]*

The enantiopure ligand in 8 mol% catalyst loading in toluene-hexane affords excellent 98% ee_P products which is close to the 98% of DAIB; a benzylated derivative of DAIB has been reported to yield 95% ee_P at 20°C.[96] However, the enantioselectivity starts to drop already at 20% ee_L (89% ee_P). A higher catalyst loading (16 mol%) doesn't give a higher but a lower ee_P with scalemic ligand. Switching to toluene as the only solvent (orange and grey triangles) lowered ee_P even more. No precipitate was formed during the reaction.

Globally, the chiral amplification with **9** is weaker than with DAIB. A 2nd-order chirality like described in the introduction, which favours homochiral polymers, may work against the ligand's inherent (+)-NLE. The more probable scenario is that the functionalisation on the N-atom perturbs the dimerisation constants, so that the K_{Homo}/K_{Hetero}-difference becomes smaller. This is not surprising: to be so much more stable than the homochiral dimer, the heterochiral one must be a finely tuned and optimised system which is already altered by small modifications. The ee_P decrease through higher catalyst loading is difficult to interpret: Noyori observed only an ee_P *increase* with 20% ee_L DAIB, until ee_P reached saturation at ca. 8 mol% catalyst loading. A higher catalyst loading favours aggregation: in case of DAIB it benefits the heterochiral dimer while the homochiral stays sufficiently labile not to interfere in the NLE. In our case the heterochiral aggregation is maybe already at its maximum, a further increase of catalyst loading would lead only to more homochiral aggregation, which would work against the (+)-NLE – as a result, the amplification decreases. The catalyst loading increase may also have an impact on factors like the polymer chain length, whose impact on the NLE is difficult to predict. Concerning the ee_P decrease using pure toluene as solvent: Noyori found enantiopure DAIB to catalyse as good in toluene as in mixtures with hexane and Et_2O but he didn't check the solvent's effect on the NLE.[21] It is possible that with **9** the solvent influences the K_{Hetero}/K_{Homo} ratio in a way that the heterochiral aggregate is disfavoured when switching to pure toluene. It is well-known that the solvent can have a strong impact on 2nd-order structures.[154,155]

II.2.1.3 Outlook: alternative ligand design

The data presented in the last section are mere preliminary results but they are sufficient to conclude that we have to rethink the ligand design: it is highly doubtful that even an extensive optimisation of the reaction conditions might amplify the (+)-NLE to the level of DAIB or above. Moreover, we cannot be sure whether this is due to the ligand's polymeric structure or to the attachment of the linker to the nitrogen atom. To properly investigate the polymeric structure's effect on the NLE we have to rule out any influence of the linker on the coordination site. Therefore, the ditopic ligand must be redesigned with the linker being attached at some distance of the aminoalcohol.

A look into the literature reveals that there are indeed options to functionalise the back part of the bornane skeleton at carbons 5, 6 and 9, but they involve 2-4 synthetic steps starting from camphor (Figure 81). The first step is in common and consists of a bromination at the *endo*-3 position. A rearrangement (involving a chirality inversion) gives **10**;[156] bromination at position 9 followed by debromination at position 3 gives **11**;[157] a series of other transformations can also lead to **12**. **10** can be further converted into alkene **13**, which opens new options for functionalisation at C-5 and C-6 (hydroborations, Heck reactions).[156] A much more simple strategy is to iodinate cheap and available (+)-10-camphorsulfonic acid to give **14**, however C-10 is closer to the future aminoalcohol – it is

questionable whether a linker at this position will be without influence on the final ligand's active site.[158,159]

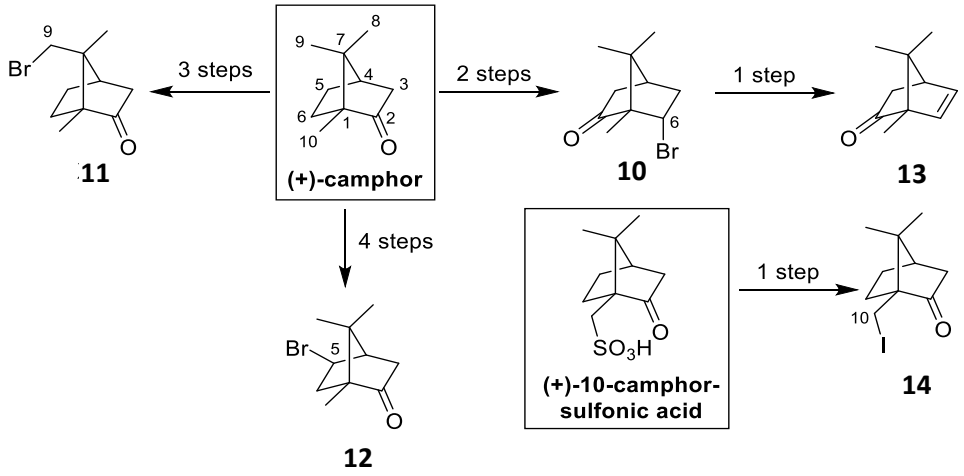

Figure 81: Reaction scheme for the bromination of (+)-camphor at positions 5, 6 and 9, and for the iodination of (+)-10-camphorsulfonic acid. (-)-6-endo-bromocamphor can be further converted into (-)-5,6-dehydrocamphor.

Once the camphor moiety has been halogenated we can proceed with the synthesis of the ditopic ligand, we propose the three different pathways shown in Figure 82. **11** can be dimerised via e. g. Pd- or Ni-catalysed cross-couplings (path A), however this has to be done *before* we form the aminoalcohol using the methodology shown in Figure 79, otherwise the bromine might be removed during the steps involving $LiAlH_4$. Given the purity problems we had for the synthesis of aminoalcohol **7**, a double functionalisation on a ditopic camphor moiety might be even more problematic. Therefore, it might be better to substitute the halogen either by an alcohol which can be activated later, after having formed the methylated carbamate, by triflation or back-conversion into a halogen (path B). Cross-coupling followed by reduction of the ditopic carbamate would then yield the final ditopic DAIB. The alcohol may also be activated after reduction of the carbamate, but this affords a selective method leaving the aminoalcohol unmodified. The alcohol may also need an additional protection/deprotection step as it might interfer in other steps (carbamate formation, oxime addition).

In addition, we propose an alternative pathway (path C) where first an allyl group is attached to **11**. This group is chemically inert to all transformations which will follow; the resulting aminoalcohol may then be dimerised via olefin metathesis with a Grubbs/Hoveyda-type catalyst. This is probably the shortest and less complicated pathway, but it also is the most limited concerning the choice of the linker. In path B we can choose to use longer or shorter linkers, aromatics, alkyl chains etc, which would be interesting since the nature of the linker (rigid, flexible, oriented…) is likely to have a great impact on the metallopolymer's properties. The three pathways are shown with **11** as starting material but applies as well to **14**. The steps involving cross-couplings using **10** and **12** might be difficult because of the presence of β-hydrides, therefore the cross-coupling-method would have to be chosen carefully.

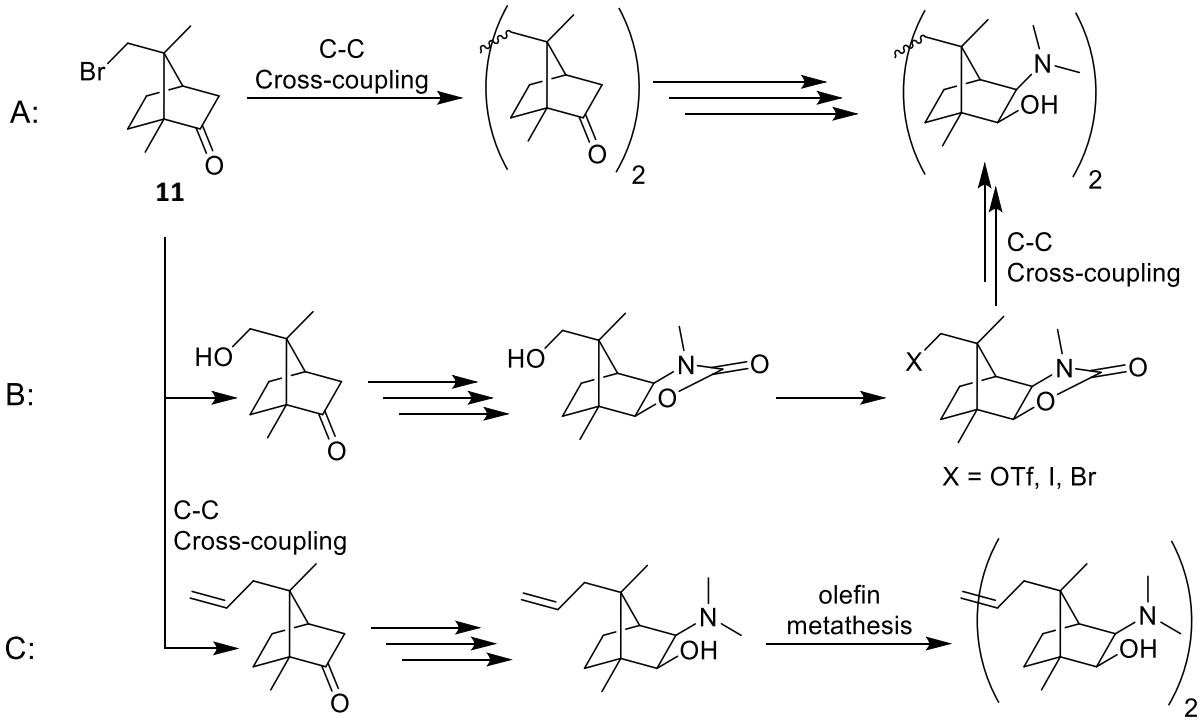

*Figure 82: Proposed synthetic pathways for a C-9-bridged ditopic DAIB ligand starting from **11**; similar pathways can be envisioned using **10**, **12** and **14**.*

II.2.2 Ditopic Ephedrine

*II.2.2.1 Ditopic Ephedrines **15** & **16**: synthesis*

Since the work on ditopic DAIB necessitates a lot of synthetic effort, we turned to ephedrine as a building block for ditopic ligands as it is cheap and readily available. The bridging group will also have to be attached to the nitrogen but this will be less of an issue in this project, as our goal here is not to obtain products with maximal ee_P but to study the metallopolymer's behaviour in NLEs, to see if and how a polymeric catalyst influences catalysis and NLEs. For this purpose, we have synthesised two different ditopic ligands which differ in the nature of their linker: **15** has a flexible alkyl chain while **16** has a rigid, aromatic linker. The flexibility of the ditopic ligand has a big impact on the polymer's structure: a rigid one is more likely to form well-defined 2nd-order structures while a flexible ligand should form more aleatory, coil-like structures.

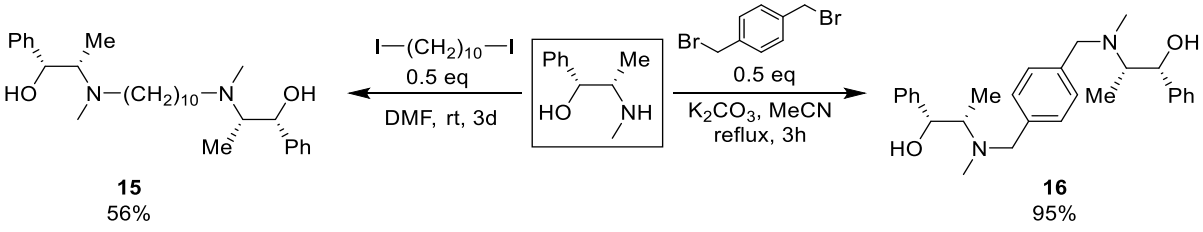

*Figure 83: Synthesis of ditopic ligands **15** and **16**.*

15 and **16** have been obtained from a double nucleophilic substitution of ephedrine on 1,10-diiododecane or *p*-α,α'-dibromoxylene, respectively (Figure 83). While the second is easily obtained with excellent yields, the first one needs purification via column chromatography to eliminate side-products, probably originating from elimination reactions on the alkyl iodide, resulting in a moderate yield of 56%. Both were applied in the enantioselective addition of $ZnEt_2$ to benzaldehyde. The protocol follows the procedure for NBE in Chapter I, with the difference that we work with 10 mol% ligand since it represents 20 mol% in terms of active catalytic sites.

*II.2.2.2 Ditopic ligand **15**: catalysis & NLE*

Figure 84 shows the ee_L vs ee_P plot of the **15**-catalysed addition of $ZnEt_2$ to benzaldehyde. The enantiopure ligand achieves a moderate ee_P of 65%, which is very close to the alkyl-substituted monotopic ephedrine ligands NnBE and NME (cf. Chapter I.2.1.2, p. 29). What they also have in common is the absence of an NLE; the dots at 20 and 30% ee_L are likely to be mere outliers.

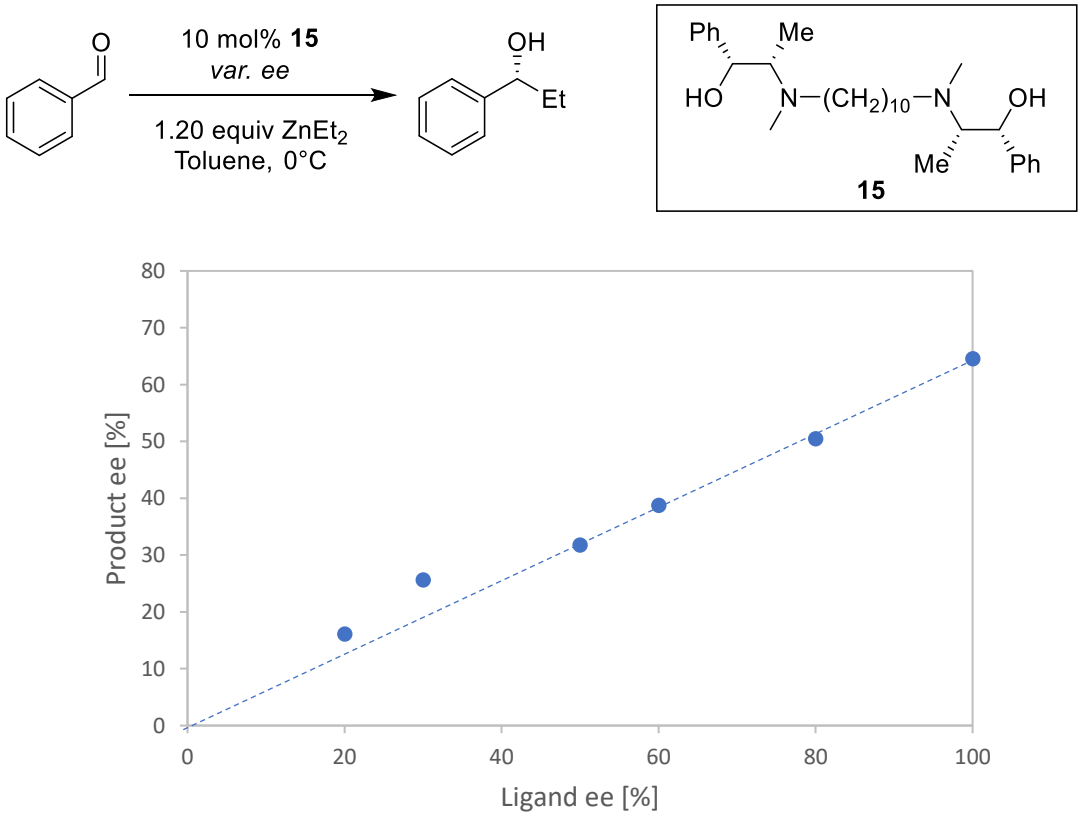

*Figure 84: Linear effect of the **15**-catalysed addition of $ZnEt_2$ to benzaldehyde.*

It seems the ligand behaves like the other alkyl-substituted ephedrines; however, we should consider the C_{10}-chain being long enough to let the complex **15-(ZnEt)$_2$** coordinate to itself, forming a

macrocycle. Although this is a homochiral interaction between both ends of the ditopic ligand, it is not an aggregation as it involves only one molecule. Therefore, it is concentration-independent and cannot generate NLEs. This phenomenon might be ruled out by using a ligand with a shorter linker which renders self-coordination impossible. Soai has worked with C_2- and C_3-linkers but without probing for NLEs.[160] Anyway, catalysis in conditions comparable to ours (except that he mostly deprotonates the ligands with butyllithium prior to $ZnEt_2$ addition) yielded extremely low ee_P with the C_2-ligand (14%): the linker is probably so short that the neighbouring coordination site disturbs the catalytic reaction, and therefore also its aggregation. Slightly longer linkers such as C_4- or C_5-chains are probably better suited for our studies.

*II.2.2.3 Ditopic ligand **16**: catalysis & NLE*

(a) Temperature-dependent NLE

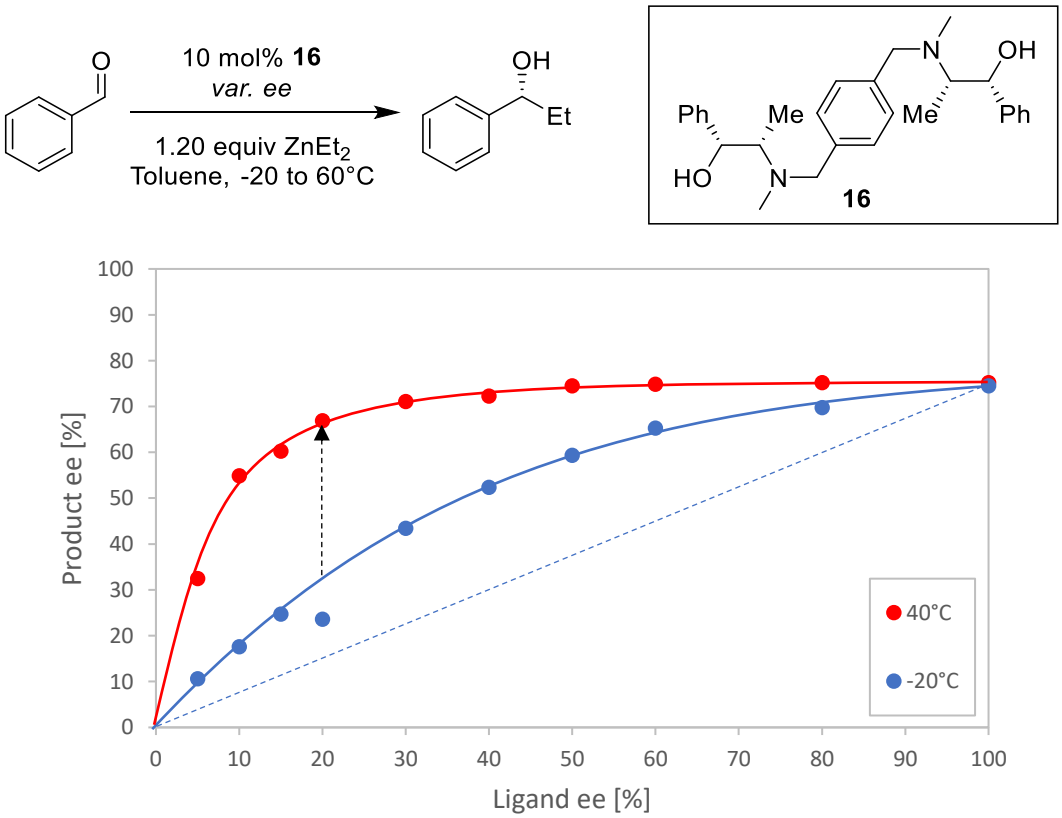

*Figure 85: Temperature-dependent NLE of **16** in the addition of $ZnEt_2$ to benzaldehyde. The values for 60°C are essentially the same as for 40°C and thus not visible.*

Next, we evaluated **16** in enantioselective catalysis, which gives a dramatically altered picture. As shown in Figure 85, **16** generates a significant (+)-NLE. It is rather moderate at -20 °C but increasing the temperature enhances also the asymmetric amplification, resulting in a strong (+)-NLE at 40 °C. Increasing the temperature to 60°C doesn't further enhance the (+)-NLE. The temperature profile in Figure 86 gives an overview of this evolution: while the 100% ee_L-reaction stays almost perfectly

constant at 75% ee_P (similar value to NBE in Chapter I and higher than with **15**) from -20 to 60°C, ee_P at 20% ee_L increases with temperature until it reaches a plateau of 67% ee_P at 40°C.

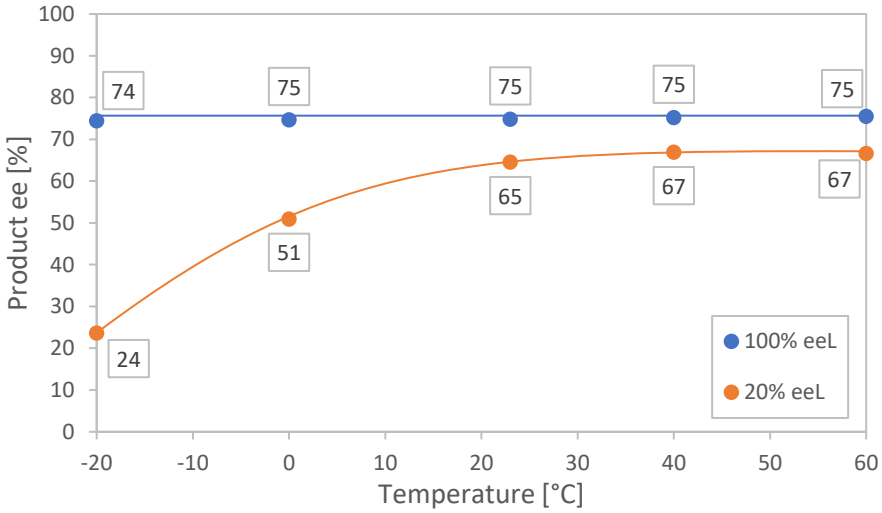

*Figure 86: Temperature profile of the **16**-catalysed addition of $ZnEt_2$ to benzaldehyde in Figure 85 with 100% ee_L (blue dots) and 20% ee_L (orange dots).*

This kind of behaviour is, to the best of our knowledge, unpreceded and counter-intuitive: high temperatures should break aggregates and *diminish* the amplitude of NLEs, not enhance them. There are no temperature studies on classical NLEs in the literature, but the temperature screening on NBE in Chapter I.2.2.2 shows how the asymmetric amplification diminishes with increasing temperatures.

Interestingly, our observations with **15** and **16** parallel those with the monotopic ligands in Chapter I.2.1, where the ligand with an aromatic substituent also stands out with a distinct behaviour. However, there is a point where catalysis with **16** differs from NBE: no precipitate persists during the reaction. Only the *enantiopure* ligand forms a glassy, gel-like solid upon addition of $ZnEt_2$, which disappears quickly after addition of benzaldehyde; the scalemic ones give clear solutions right from the start. Therefore, the chiral amplification with **16** is not precipitation-induced like with NBE and must have a different origin.

(b) Catalyst loading screening

This curious behaviour prompted us to make further investigations on **16**. To see if there are more parallels to NBE we performed a screening of the catalyst loading as in Chapter I.2.2.1, the results are shown in Figure 87. The enantiopure ligand (blue dots) shows a behaviour similar to NBE: ee_P increases as the catalyst loading is decreased, indicating catalysis by a less enantioselective homochiral aggregate (here, probably a polymer rather than a dimer). On the contrary, ee_P goes up when the catalyst loading is *increased* using scalemic catalyst (20% ee_L). The increase is significant between 1.25 and 5 mol%, at higher catalyst loading ee_P reaches a plateau at 51% ee_P.

The ee_P increase at high catalyst loading using scalemic ligand is a normal behaviour in NLEs of dialkylzinc chemistry: the higher the catalyst concentration, the more aggregates are formed which could act as an inactive reservoir; reaching a plateau means that all the minor enantiomer is trapped in inactive heterochiral aggregates. Noyori observed this behaviour with DAIB.[22] However, with **16** the ee_P increase should be in competition with an ee_P *decrease* due to a higher proportion of homochiral aggregate catalysis, as in the experiment with enantiopure ligand.

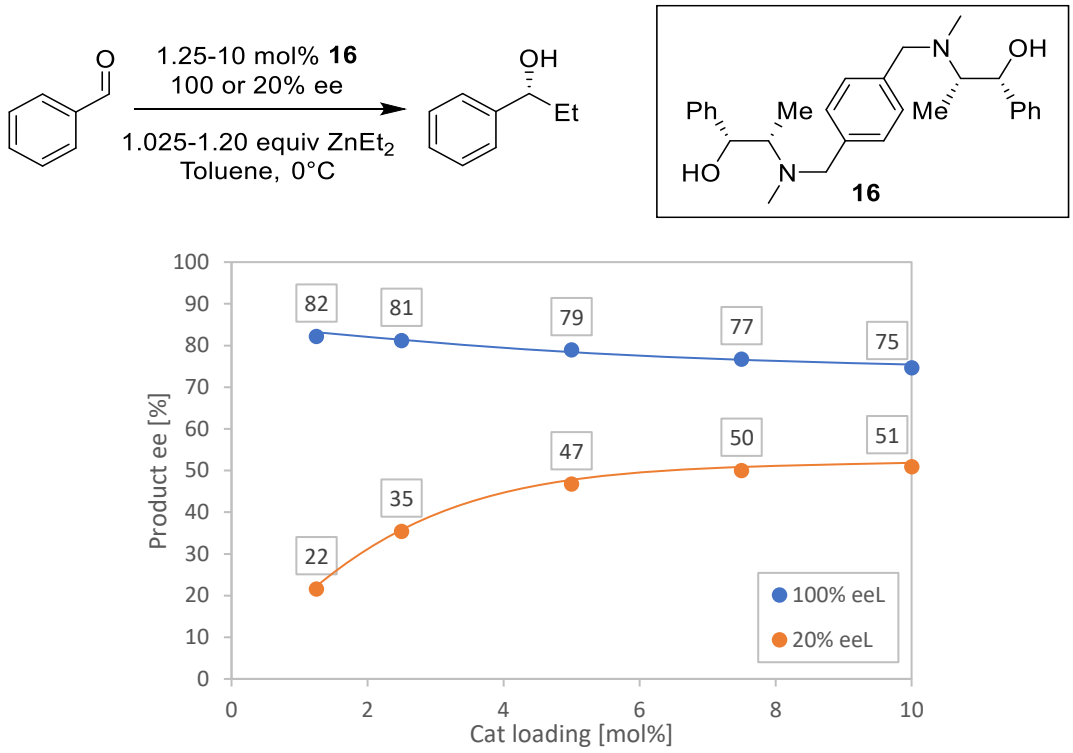

*Figure 87: Catalyst loading screening in the **16**-catalysed addition of $ZnEt_2$ to benzaldehyde with enantiopure (blue dots) or 20% ee ligand.*

It should be noted that we performed a similar catalyst loading screening using $ZnMe_2$ as the dialkylzinc reagent. However, the results are again very different and not comparable with the presented work so far, therefore we won't discuss them here; they can be found in the supporting information (V.2.4, p.171).

(c) Temperature-driven equilibrium shifts?

How can we interpret this peculiar behaviour? It is tempting to say that both **15** and **16** have inherited from the properties of their monotopic counterparts. Alkyl-substituted ligands NnBE and NME have no NLE (cf. chapter I.2.1.2, p. 29), as does **15**; Benzyl-substituted NBE gives a positive or even hyperpositive NLE, as does **16**. While this relation is coherent for **15** (which has to be confirmed by experiments with shorter alkyl spacers, as discussed in II.2.2.2) the case of **16** is less clear. **12** and NBE catalyse both via monomeric and homochiral aggregated ligand-ZnR-complexes, as shown by the

catalyst loading screenings, but contrary to NBE the heterochiral aggregate issued from **16** is not insoluble. Therefore, its (+)-NLE with $ZnEt_2$ is issued from a *soluble but less catalytically active* heterochiral aggregate compared to monomer and the homochiral aggregate.

The point in which **16** clearly differs from NBE, and which is also the most peculiar one, is the amplification of the (+)-NLE at high temperatures with $ZnEt_2$. This can be explained in two ways:

- the relative activity of heterochiral to homochiral/monomeric catalyst diminishes with increasing temperature. This would correspond to a decreasing *g* value in Kagan's ML_2 model;
- the distribution of hetero- and homochiral aggregates changes over temperature (Figure 88). A higher proportion of heterochiral aggregate at higher temperature would lead to an increasing β-value, which leads also to a stronger (+)-NLE as long as $g < 1$ according to the ML_2 model.

Without more data at hand, it is difficult to say which of the two (or if both) phenomena are taking place. However, the first hypothesis is viable only if there is a big difference in the $\Delta G^{\#}$ of the kinetic constants of both hetero- and homochiral/monomeric catalysts. Both kinetic constants increase with temperature, therefore the latter has to increase much more than the first at high temperatures.

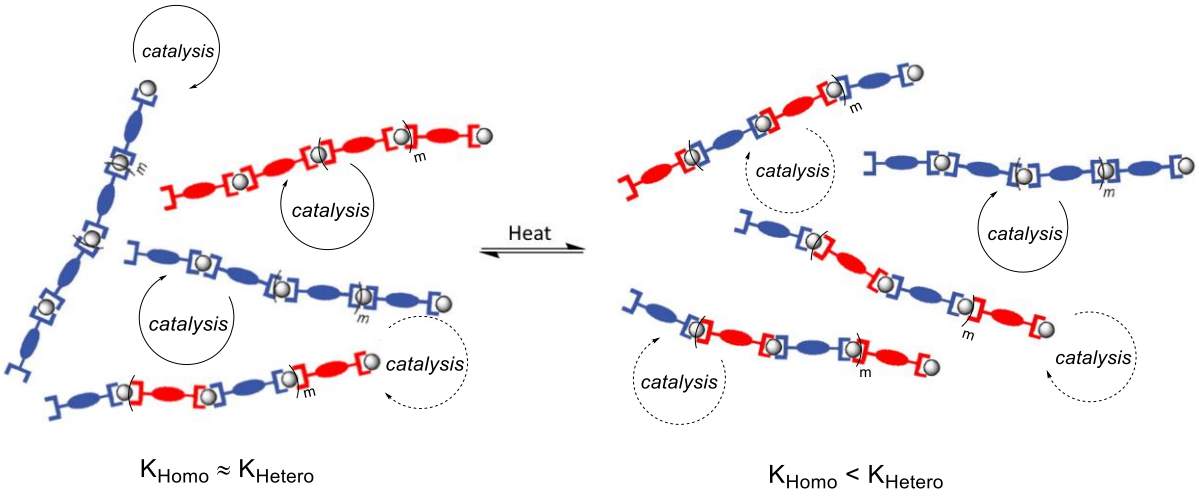

Figure 88: Scheme for the temperature-dependent formation of heterochiral metallopolymers out of homochiral R and S-metallopolymers. The heterochiral polymers must be less active than the homochiral polymers in order to allow the emergence of a (+)-NLE.

A temperature-driven recombination of the aggregates, from homochiral- to more heterochiral polymers as in Figure 88, is interesting as it might be related to properties due to polymeric structures. If we consider the aggregates to consist of linear chains, then the heterochiral polymer may, for example, have a greater degree of freedom because of a less well defined 2nd-order structure, which would be entropically favoured.

Another scenario is the formation of heterochiral macrocycles (Figure 89). Technically, an assembly of ditopic ligands and metals can also form a closed chain; it depends much on the constituents' structure and flexibility. A different relative stability of hetero-/homochiral macrocycles, compared to the corresponding linear polymers, might account for the temperature-dependent NLE. However, it is difficult to say which one would be entropically favoured: a single, polymeric chain may lead to several macrocycles and thus to an increased number of molecules in solution, however a linear chain should also have a greater degree of freedom than a closed cycle.

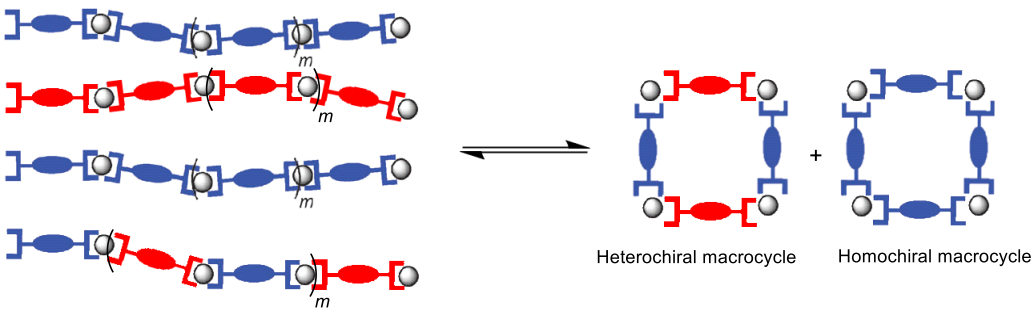

Figure 89: Schematic equilibrium between homo- and heterochiral polymers and the corresponding macrocycles. The macrocycles have been chosen to consist of four ligands/metal ions for illustration purposes, smaller or larger macrocycles are also conceivable.

An interesting precedent for such macrocycle formation is trianglimine **17** (Figure 90): it is formed quantitatively from enantiopure DACH and terephtaldehyde instead of the corresponding polymer.[161] Computational studies have led to the conclusion that **17** is not a thermodynamic but a kinetic product, resulting from conformational constraint of the reactive intermediates.[161,162] The use of racemic DACH yields a mixture of homo- and heterochiral isomers in a 1:1:3:3 ratio [(RRR):(SSS):(RRS):(RSS)], the heterochiral isomers being preferred.[163]

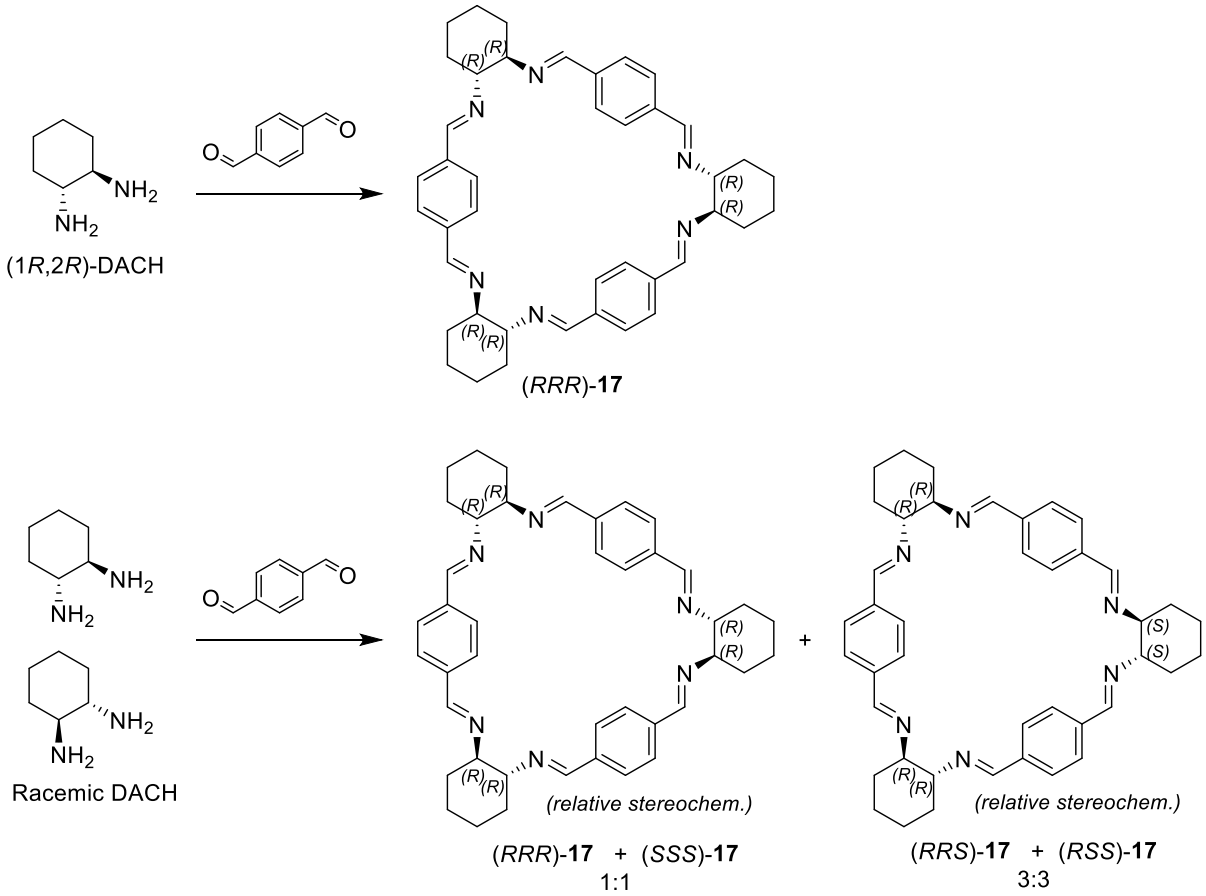

*Figure 90: Synthesis of trianglimines **17** from enantiopure and racemic DACH. The latter gives a mixture of diastero- and enantiomers in a 1:1:3:3 ratio [(RRR):(SSS):(RRS):(SSR)].*

II.3 Conclusion on NLEs with chiral metallopolymers

In summary, we have synthesised three new ditopic ligands: DAIB-derived ligand **9** and ephedrine-based ligands **15** and **16**. All ligands have been applied in the enantioselective addition of $ZnEt_2$ to benzaldehyde and probed for NLEs. **9** gave a less pronounced (+)-NLE than its monotopic counterpart; a redesign of the ligand in order to improve the NLE has been discussed. Ligands **15** and **16** have shown peculiar behaviours in NLEs: while the first has no NLE at all, the latter shows a strong (+)-NLE which increases with temperature; a catalyst loading screening showed that there are different catalytically active species even with enantiopure ligand, similar to NBE. The results with ligands **16** are promising as they might be an indication for the catalyst's polymeric structure having a significant impact on the NLE. However, more work is necessary to understand this behaviour, especially to find out which supramolecular structures complex **16-$(ZnMe)_2$** adopts in solution and if those structures, or their distribution, change with temperature.

Chapter III: Sum-frequency generation with chiral metallopolymers

This chapter will also deal with chiral metallopolymers, but in a different context than in chapter II: they are used as materials and not as catalysts, in the application of a physical phenomenon called sum-frequency generation (SFG).

This project was done in collaboration with Grégory Taupier, Alex Boeglin and Kokou Dodzi (Honorat) Dorkenoo from the *Département d'Optique ultra-rapide et Nanophotonique* (DON) at IPCMS. The SFG microscopy setup was designed and built by the aforementioned group and the SFG spectra recorded by Grégory Taupier (except Figure 114, which was made by the author); DFT calculations were performed by Alex Boeglin.

III.1 Introduction: sum-frequency generation

III.1.1 Principles of chiral SFG in isotropic media

Sum-frequency-generation (SFG) consists in the irradiation of a chiral material, usually in form of a thin film (solid or high-concentration solution), with two linear polarised laser beams (k_1 and k_2, Figure 91). The laser beams interact with the material to generate a new radiation k_s whose frequency ω_s is the *sum* of the two incident frequencies ω_1 and ω_2. Outside of mathematical equations, the wavelength (λ; $\omega^{-1} = \lambda$) will be used to describe the beams instead of the frequencies. Our setup uses incident beams with wavelengths λ_1 = 900 nm and λ_2 = 450 nm, therefore the generated signal has λ_s = 300 nm.

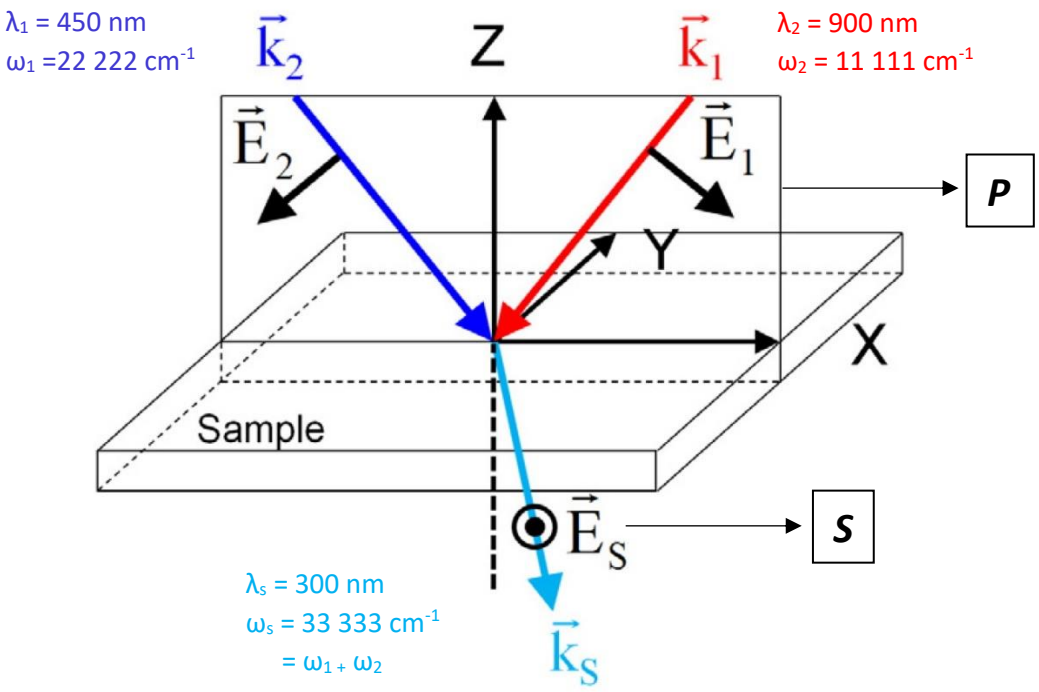

Figure 91: Scheme for chiral optical sum-frequency generation in isotropic media.[164] The incident beams k_1 and k_2 are polarised in the same plane P, to which the SFG signal k_s is polarised orthogonally (S).

Chiral SFG was first described theoretically by Giordmaine in 1965,[165] but it is only in 2000 that Shen's group reported first experimental evidence using a concentrated solution of chiral limonene and IR-radiation.[166] A couple of years later, they published two studies using 1,1'-bi-2-naphtol (BINOL) where they expanded the application of SFG into the visible electromagnetic spectrum.[167,168] They used it also to perform 3D-imaging and to distinguish between layers of enantiopure and racemic BINOL, the latter being SFG-inactive.[169] Taupier and co-workers then applied SFG to solid samples by incorporating BINOL into a silica sol-gel.[164,170]

Since the signal is generated only if the material is chiral, chiral SFG microscopy holds the promise of becoming an efficient tool to probe for molecular and supramolecular chirality, as quadratic optics allow much higher spatial resolution than linear optics. It responds to changes in concentration of media but may also reveal structural irregularities in solid samples. In addition, Taupier has been able to use SFG as an encryption tool: the BINOL-doped silica sol-gel becomes irreversibly damaged over prolonged irradiation. This is not detectable with a standard optical microscope but only with the SFG setup, as the deactivated zones do not generate any SFG signal (Figure 92).

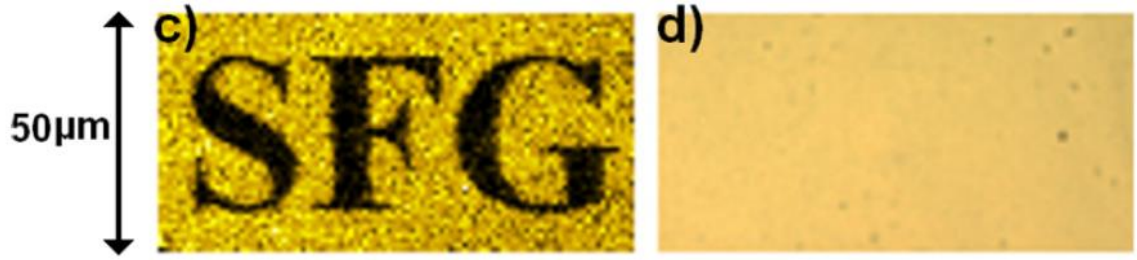

Figure 92: Example of encryption using a SFG on a (2R,2'R)-BINOL-doped sol-gel film.[170] The letters "SFG" in c) have been etched into the sample by prolonged irradiation with the SFG setup, leading to an irreversible damage of the BINOL. These appear black because the SFG signal cannot be generated any more, while the surroundings (yellow) are still SFG-active. d) shows the same sample seen through an optical microscope, which cannot distinguish between etched and unetched material.

III.1.2 Fundamentals of chiral SFG

Chiral SFG is possible in any material which fulfils the following requirements:

- the material is isotropic, i. e. has no specific spatial orientation and extends uniformly in all directions,
- it absorbs at the same λ as the generated k_s radiation (300 nm in our setup),
- it is not centrosymmetric, which is given if the material is chiral and enantiopure.

The requirements for SFG result from how the incident beams interact with the material. In this section, we will briefly discuss the physical fundamentals of SFG and non-linear optics in general, in order to understand the origin of these requirements.

III.1.2.1 Linear and non-linear optics

The interaction of a radiation's electric field *E* with a material leads to a polarisation of the latter, denoted as *P*, which is in turn a source of a new electromagnetic field. Usually, it is assumed that the polarisation increases in a *linear* way with *E* following equation (40) :

$$\vec{P} = \epsilon_0 \chi \vec{\boldsymbol{E}} \tag{40}$$

With ε_0 being the vacuum permittivity and χ the electrical susceptibility. Equation (40) is an approximation valid for radiations at weak intensities; for high intensity radiation, e. g. resulting from a laser beam, additional higher-order terms must be considered, as described by the general equation (41):

$$\vec{P}^{(n)} = \epsilon_0 \sum_n \chi^{(n)} \vec{\boldsymbol{E}}^{(\boldsymbol{n})} = \epsilon_0 \left[\chi^{(1)} \vec{\boldsymbol{E}}^{(\boldsymbol{1})} + \chi^{(2)} \vec{\boldsymbol{E}}^{(\boldsymbol{2})} + \chi^{(3)} \vec{\boldsymbol{E}}^{(\boldsymbol{3})} \ldots \right] \tag{41}$$

In contrast to (40), equation (41) is not a linear equation any more. Therefore, light-matter interactions following equation (41) are denoted as *non-linear optics*; in analogy to chapters I and II, we can speak also of a "non-linear effect" generated by the lasers' intensity. The interaction of the non-linear *P* with the electric field is at the origin of new optical phenomena, for instance SFG but also second- (SHG) and third-harmonic generation (THG), multi-photon-absorption and many others (Figure 93).

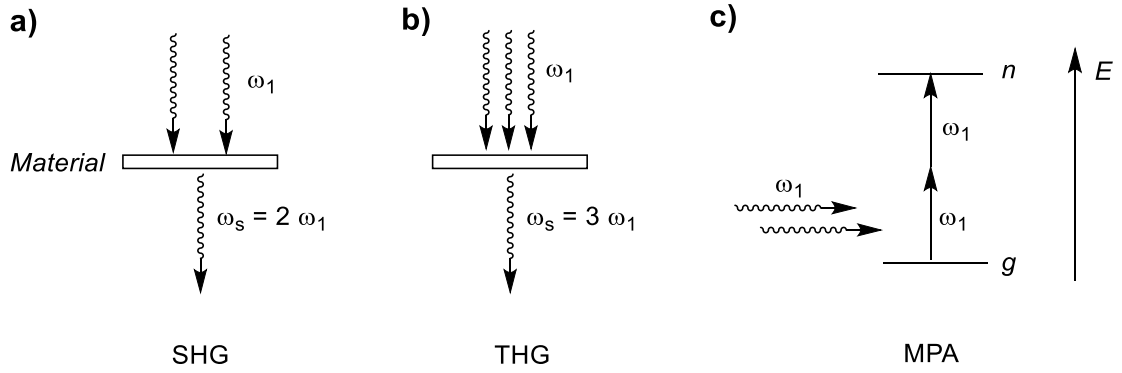

Figure 93: Some examples for non-linear optic phenomena. a) Second-harmonic generation (SHG) or frequency doubling, b) third-harmonic generation (THG) or frequency tripling, c) multi-photon absorption (MPA), here exemplified by absorption of two photons of the same frequency bringing the material from its ground state g to an excited state n.

III.1.2.2 Polarisation and susceptibility in isotropic media

In chiral SFG, the generated radiation k_S results from a 2nd-order polarisation of the material, which is described by equation (42) in case of an isotropic material (we will discuss the non-isotropic case later in this section). It depends on the cross-product of the two incident electric fields ($E(\omega_1)$ and $E(\omega_2)$) and on χ_{chiral}. This cross-product leads to the polarisation of k_S being orthogonal to the plane defined by k_1 and k_2, which we will later refer to as "SPP mode".

$$\vec{P}_{SFG}^{(2)} = \epsilon_0 \chi_{chiral}^{(2)} \left[\vec{E}(\omega_1) \times \vec{E}(\omega_2)\right] \tag{42}$$

χ_{chiral} is the *non-linear susceptibility* in chiral isotropic media. It accounts for the material's ability to generate the polarisation P_{SFG} and thus to give rise to an SFG signal. According to equation (43), it depends on two factors: the density of molecules N and the orientationally averaged hyperpolarizability β. The higher these factors, the higher the probability to perform SFG: this is the reason why SFG has been mostly observed in the solid state or in highly concentrated solutions since diluted solutions lead to a low N.

$$\chi_{chiral}^{(2)} = N\langle\beta\rangle \tag{43}$$

β is the most interesting factor as it accounts for two of the three prerequisites: chirality and absorption at the generated frequency ω_s. It is expressed by equation (44):

$$\langle\beta\rangle = \frac{1}{6\hbar\epsilon_0} \sum_{mn} \frac{(\boldsymbol{\omega_1 - \omega_2})\left(\vec{\boldsymbol{\mu}}_{\boldsymbol{ng}} \cdot \left(\vec{\boldsymbol{\mu}}_{\boldsymbol{gm}} \times \vec{\boldsymbol{\mu}}_{\boldsymbol{nm}}\right)\right)}{\left(\boldsymbol{\omega_s - \omega_{ng} + i\gamma_{ng}}\right)(\omega_1 - \omega_{mg})(\omega_2 - \omega_{mg})} \tag{44}$$

In equation (44) the material is considered in three different states: the ground state g, a first electronically excited state n and a second excited state m. This gives rise to three possible energetic transitions, as shown in Figure 94a. Each of these transitions is associated to a different *transition dipole moment* μ.

The three transition dipole moments are found in the **blue part** of equation (44) as a triple product. The vectors must not be coplanar but oriented along all three spatial dimensions (Figure 94b), otherwise the blue term turns zero and no polarisation is possible any more. This is possible only if the molecule itself has a well-defined spatial orientation along all three axes x, y and z, *which requires the molecule to be chiral*. Non-chiral molecules have a symmetry plane, therefore it is impossible to define an oriented z-axis for them (Figure 95). This leads their three μ to be in the same plane, the blue term would then turn 0. In the case of a chiral but *racemic* compound the blue term is ≠0 for each molecule, however it is of opposite sign for the two enantiomers. Therefore, the sum of the interactions is 0 and no SFG can take place.

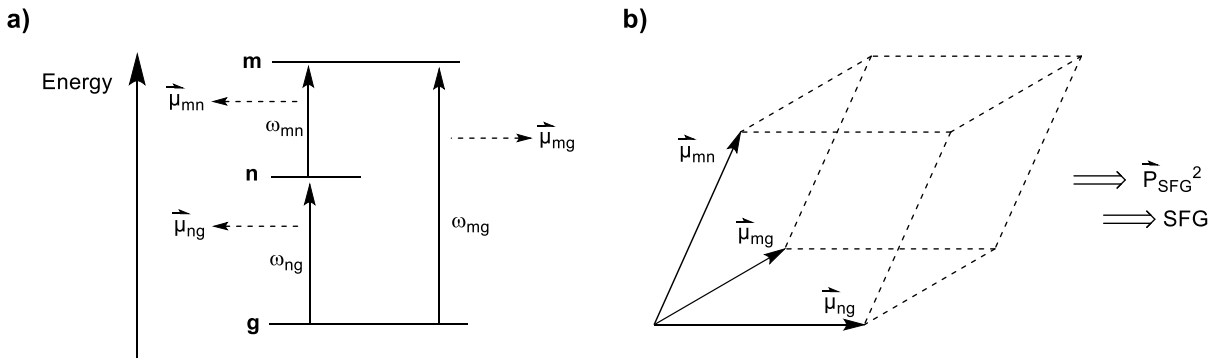

Figure 94: a) Diagram of the material's electronic energy states g (ground state), n (1st excited state) and m (2nd excited state). The three possible transitions are each associated to a frequency (ω) and a transition dipole moment (μ). b) shows the required configuration of the three μ's to generate an SFG signal: they have to extend in all three spatial dimensions, i. e. form a volume.

The **red part** of equation (44) is a resonance factor: the closer it gets to 0, the higher β becomes, which is achieved with $\omega_s \approx \omega_{ng}$; ω_{ng} is the frequency associated to the transition from the ground- to the 1st excited state. This why this phenomenon is also referred to as "SFG near electronic resonance": if the material absorbs at a frequency ω_{ng} close or equal to the frequency of the emitted radiation ω_s, β gets maximised and SFG is likely to be observed. iγ_{ng} is an empirical correction factor which accounts for several attenuating effects, e. g. a variability in ω_{ng}, and is the reason why in practice the red term never gets equal to 0.

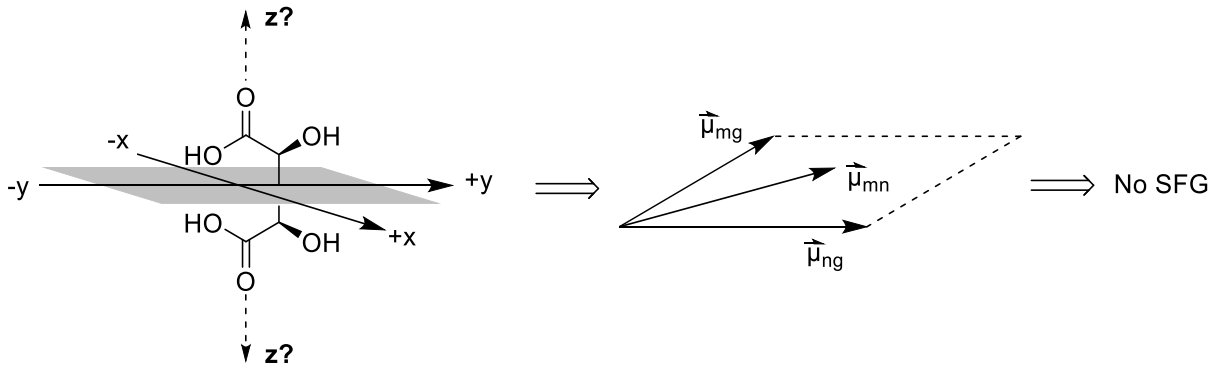

Figure 95: Scheme illustrating the spatial non-specificity of achiral molecules (with meso-tartaric acid as an example). Due to the symmetry plane (here the xy-plane) the molecule's 3rd spatial axis cannot be clearly defined, as both sides of the plane are identical. This leads the three transition dipole moments to be coplanar, which forbids SFG.

Technically, resonance of ω_{mg} with ω_1 or ω_2 is also possible according to equation (44). However, the material would then directly absorb the laser beams (1-photon absorption), which would destroy the material given the lasers' intensity. Resonance at ω_s also has another advantage: due to our experimental setup λ_s is necessarily at 300 nm, which is a wavelength easily attained in UV-vis-absorption by substituting an aromatic ring with some donor and/or acceptor groups; 450 and 900 nm would afford a much more extensive e^--delocalisation and/or metal-to-ligand transitions. We can also check a given molecule's λ_{ng} to be close to 300 nm using UV-vis-spectroscopy, whereas λ_{mg} is difficult to verify – as well with experimental as with computational tools.

III.1.2.3 The advantage of isotropic media

As mentioned before, equation (42), and therefore also equations (43) and (44), are valid only for an isotropic material. Isotropicity is not a necessary requirement as SFG arises also from anisotropic materials but it simplifies the system considerably. In an anisotropic medium, with a crystalline structure for example, the interaction of k_1 and k_2 with the material and its response k_s would not be independent from space anymore; it is not the same if the beams are e. g. parallel or perpendicular to one of the crystal's coordinates. Therefore, in an anisotropic material ω_s, ω_1 and ω_2 would have to be expressed as vectors, which would lead to a multitude of different expressions for χ_{chiral}.

Moreover, an anisotropic material can give rise to SFG of *non-chiral* origin. The obtained signal thus would not be a reliable indicator for supramolecular chirality anymore, as it is difficult to distinguish between chiral and non-chiral SFG. Therefore, the isotropic medium does not only simplify the mathematical expressions but also the system's output. The only 300 nm-radiation emitted by an isotropic sample is SFG, and only if the material is chiral; SHG (Figure 93a) is forbidden in isotropic media because it would preclude that both incident lasers have the same frequency ($\omega_1 = \omega_2$) which would turn the **green part** of equation (44) to 0. The only problematic side-effect is frequency tripling (THG, Figure 93b) of the 900 nm-beam, leading also to a 300 nm signal. It arises in isotropic as well as anisotropic media, regardless of the material's chirality. However, our experimental setup allows us to cut the THG signal's contribution off, as we will explain in the following section.

III.1.3 SFG microscopy setup

Figure 96 shows the setup used for SFG experiments. A Ti:Sa-laser generates a 900 nm-beam which is split in two by a separator (S). One of the beams is converted to 450 nm in a BBO crystal (β-barium borate) and its intensity regulated with a filter; the other beam stays at 900 nm but is sent through a delay line to keep it in phase with the 450 nm-beam. Both then are polarised and sent through a 1st objective, which focuses them to the same spot on the sample: this is where SFG takes place and where the 300 nm-signal is generated. A 2nd objective turns the beams collinear again; the residual 450 and 900 nm-beams are filtered off and the 300 nm-signal is detected in a spectrograph.

As mentioned before, equation (42) precludes that the two incident polarised beams form a plane (P) which is perpendicular to the polarisation of the signal (S). This means that the polariser, placed at the right angle, can let the S-signal pass through and block orthogonally polarised signals; we refer then to the "SPP" mode (Figure 97a). Rotation of the polariser by 90° allows to selectively measure radiation which is not perpendicular, but *parallel* to the plane P ("PPP" mode, Figure 97b).

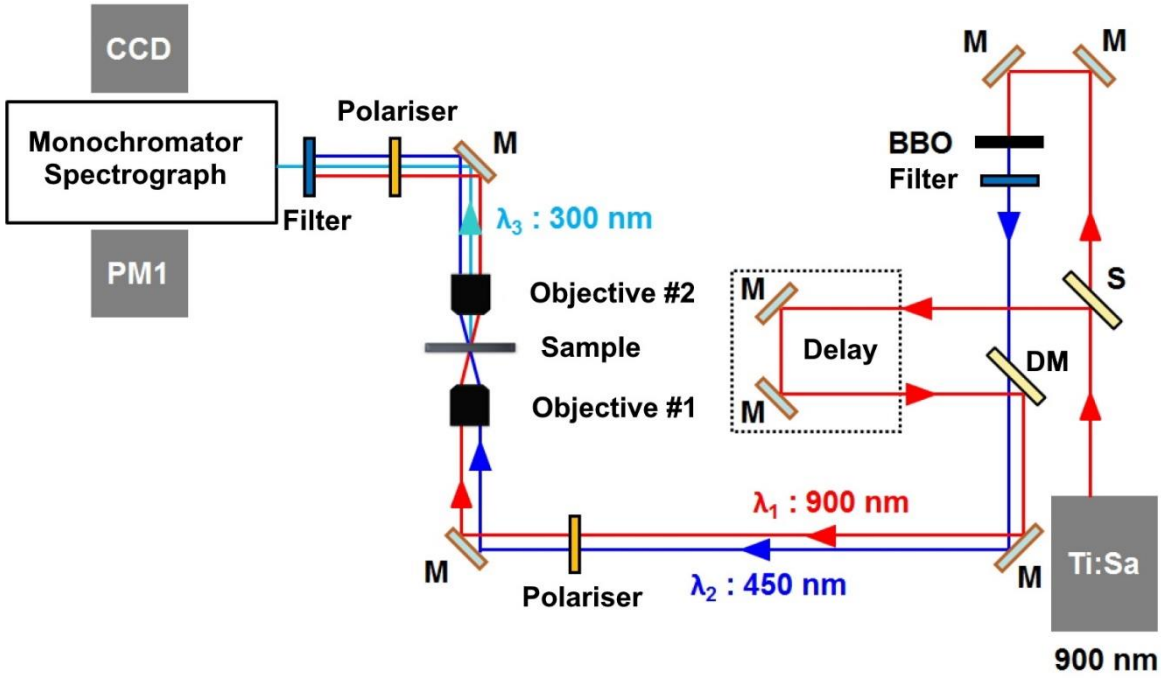

Figure 96: Scheme of the setup for the generation and detection of SFG.[171] M: mirror, S: separator, DM: dichroic mirror, BBO: β-barium borate.

Differentiating between SPP and PPP is useful to make sure that the recorded signal actually is of chiral origin. Achiral SFG, originating from possible anisotropic regions in the sample, may be polarised in several directions, not only along the S plane. A signal in PPP mode therefore indicates that the sample is not anisotropic and SPP signal possibly not or not entirely of chiral origin.

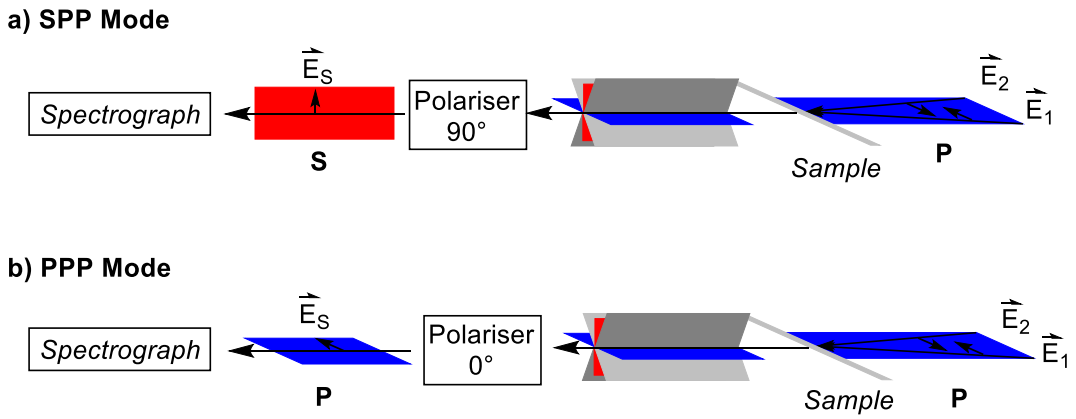

Figure 97: Scheme depicting the a) SPP and b) PPP acquisition modes.

In addition to achiral SFG there are also signals arising from single-beam-non-linear optics, like SHG and THG. SHG signals can arise only from anisotropic regions, interfaces or from impurities and are easy to differentiate from our chiral SFG signal, since λ_1 and λ_2 give SHG signals at 600 and 450 nm, respectively. However, THG from λ_1 is at 300 nm and is allowed in isotropic as well as anisotropic material. Therefore, it is necessarily acquired along with the SFG signal. THG can be reduced by

lowering the 900 nm-beam's intensity $I_{\lambda 1}$ ($I_{THG} \sim I_{\lambda 1}^3$) but at the expense of the SHG signal's intensity, see equation (42). Increasing the 450 nm beam-intensity to compensate is problematic as it may result in sample destruction due to two-photon absorption – the resulting 225 nm match the intense UV-bands of most aromatic molecules.

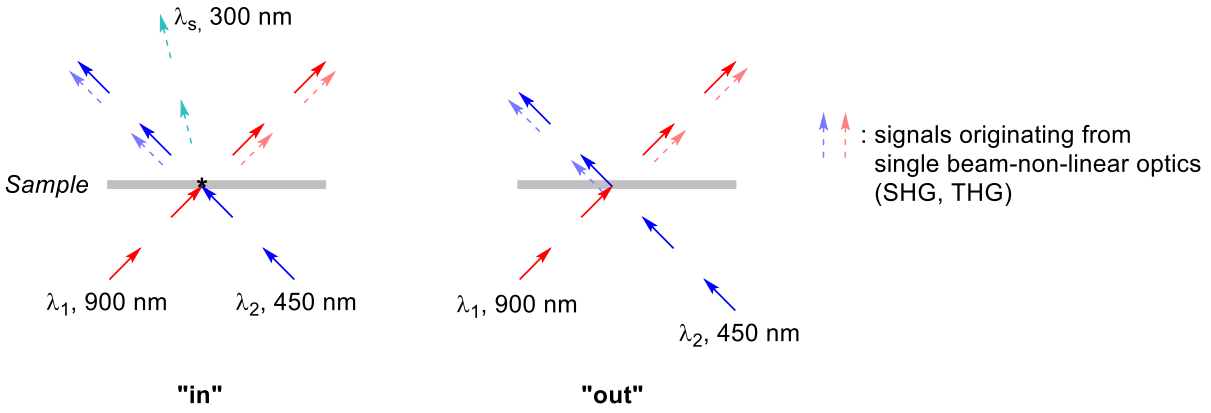

Figure 98: Scheme for the "in" and "out" modes in SFG microscopy experiments. In both modes single-beam phenomena like SHG and THG (dashed blue and red arrows) are generated, but only the "in" mode generates also sum-frequency (dashed green arrows). The "out" mode precludes SFG because λ_1 and λ_2 do not pass the sample at the same time.

To supress the THG's contribution from the measured signal, we record SPP and PPP spectra in an additional mode, "SSP out" and "PPP out" (Figure 98). The "out" modes (for *out of coincidence*) differ from the previous ones by putting a delay on one of the beams, so that both laser pulses do not pass the sample at the same time and SFG is not possible. This allows us to selectively acquire single-beam signals like THG which we then subtract from the "in"-mode spectra. This outcut has been realised on all SFG spectra shown in this work.

III.1.4 Metallopolymers in SFG

Our group started to work on this subject as it came out that one of our ditopic ligands has the properties needed to perform SFG microscopy. Ditopic bisoxazoline ligand **18** (Figure 99) is an unsaturated version of ligand **3** discussed in chapter II.1.2, the bisoxazolines being attached to the aromatic linker through a C-C double bond, and has been used before in a chirality- and coordination-mode-dependent copolymerization with metal ions.[144,145] The advantage of using a metallopolymer in SFG is that it has a lower tendency to crystallise, therefore it is isotropic and renders workarounds such as high-concentration solutions or incorporation into sol-gels unnecessary. The bisoxazolines are chiral and the doubly conjugated aromatic core acts not only as a linker but also as a chromophore absorbing close to 300 nm, so all requirements for SFG are fulfilled.

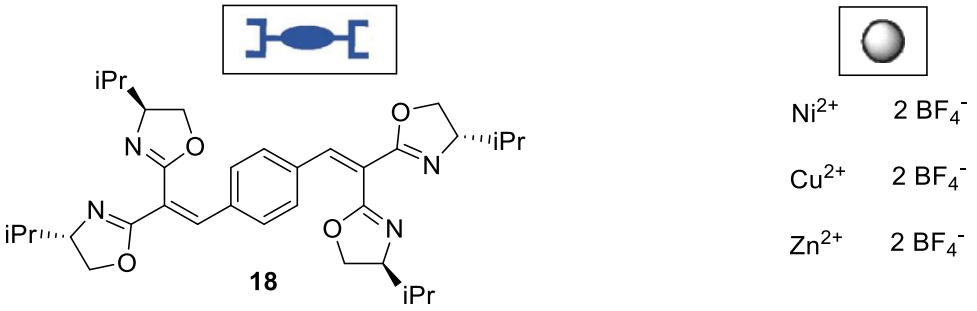

*Figure 99: Scheme for ligand **18** and the metals salts used to form chiral metallopolymers.*

Indeed, our group has been able to obtain an SFG signal from **18-Ni(BF$_4$)$_2$** by sandwiching a 0.05 M solution of **18** and Ni(BF$_4$)$_2$ in MeOH between two glass plates.[172] Slow evaporation of the solution yielded a film from which the SFG signal was obtained (Figure 100a). Cu(II) and Zn(II) gave also an SFG signal.[171] The absence of a PPP signal ensures that the SPP signal is of chiral origin. However, the ligand alone is SFG-inactive (Figure 100b); discrete Ni(II) and Cu(II)-dinuclear complexes with a 2:1 metal-to-ligand ratio gave an only a weak SFG signal (Figure 100c). Therefore, the SFG experiment acts as a probe for the complexes' polymeric organisation. Only the dinuclear complex from Zn(II) stands out with an SFG signal comparable to the metallopolymers.

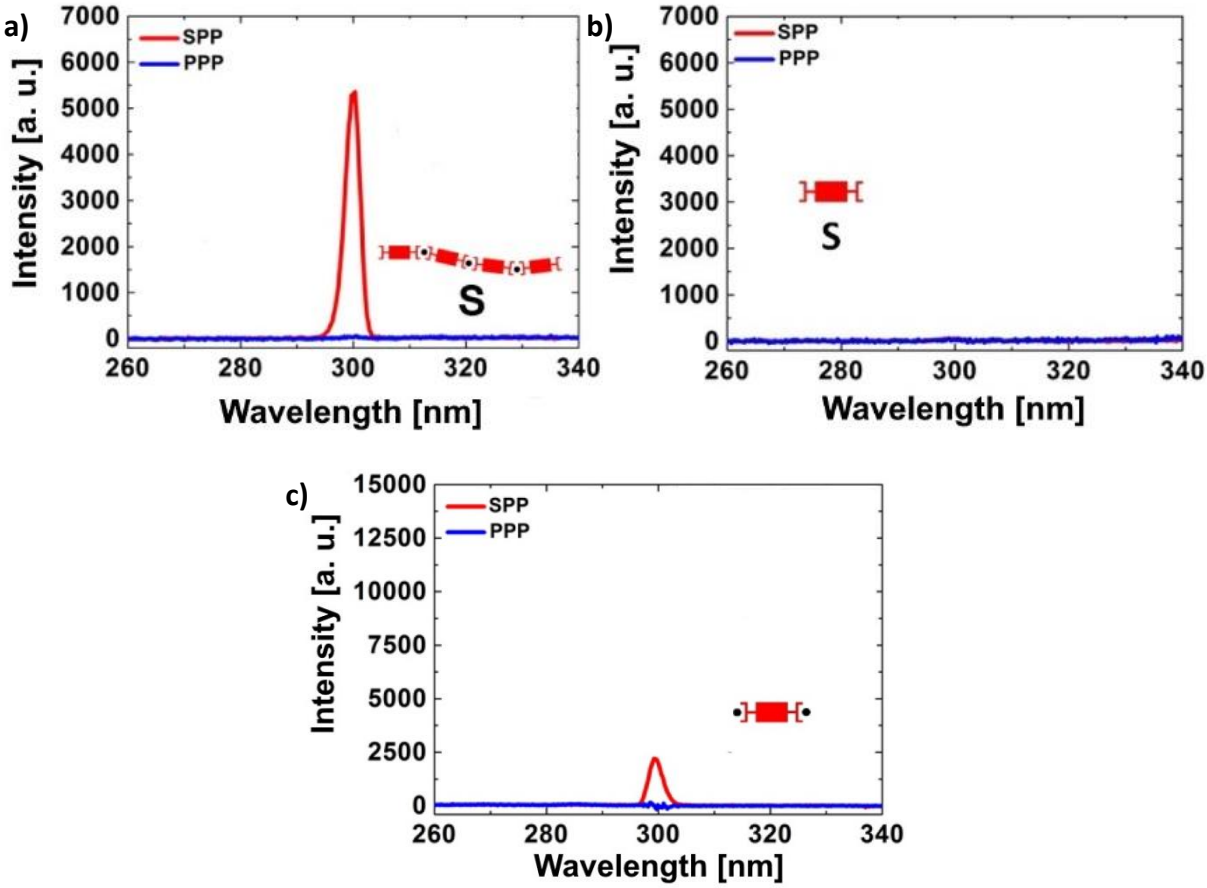

*Figure 100: SFG spectra of a) **18-Ni(BF$_4$)$_2$** (**18-Cu(BF$_4$)$_2$** and **18-Zn(BF$_4$)$_2$** gave similar spectra), b) **18** without metal and c) dinuclear complex **18-[Ni(BF$_4$)$_2$]$_2$**, 180s acquisition time.[171]*

The authors then checked for an SFG signal using a racemic ligand. Racemic limonene and BINOL have proven to be SFG-inactive.[164,166–168] Metallopolymers constituted of racemic **18** form either homochiral metallopolymers of both enantiomers with Cu(II) or an alternated heterochiral copolymer with Zn(II).[144] Both yielded weak SFG signals (Figure 101). This may indicate SFG-active homochiral zones due to an inhomogeneous distribution of the enantiomers; a similar residual signal in racemic BINOL has been attributed to resonantly enhanced parametric light scattering.[169]

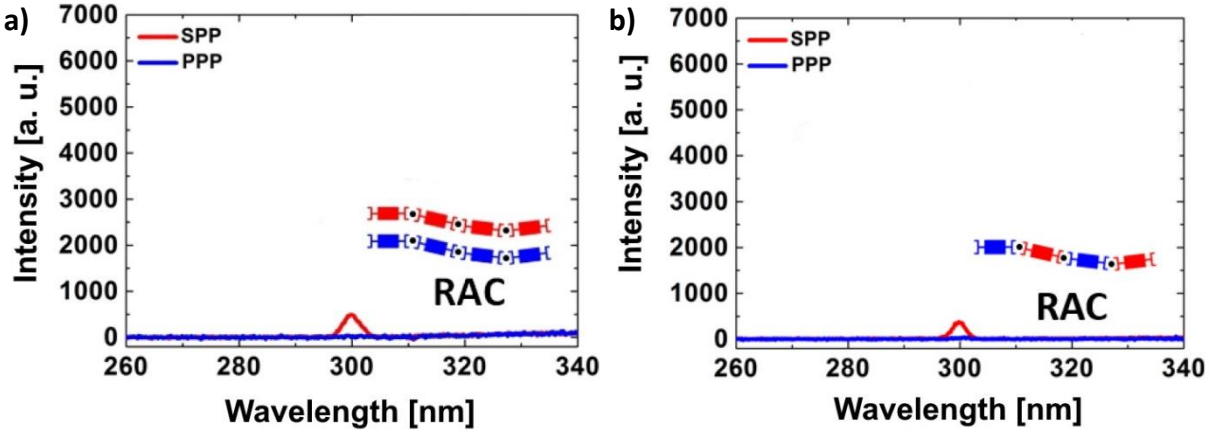

*Figure 101: SFG spectra of a) racemic **18-Cu(BF$_4$)$_2$** and b) racemic **18-Zn(BF$_4$)$_2$**.*

The absence of an SFG signal with uncomplexed **18** is interesting as it gives rise to questions about the origin of the signal: the molecule just being chiral and absorbing at 300 nm is obviously not sufficient for SFG to take place. DFT calculations on free and complexed **18** have shown that the metal forces the two adjacent oxazolines to be in the same plane, leading to a distortion of the bis-conjugated aromatic linker.[146] One of the possible conformations is a chiral helix-like twist which induces activity in circular dichroism (CD) spectroscopy; the uncomplexed ligand shows only negligible activity in CD. Therefore, the structure change-induced CD may be linked to the generation of sum-frequency. The lower conjugation of the double bonds with the aromatic core may also be the reason for the blue-shift of the linker's band in UV-vis spectroscopy upon addition of the metal.

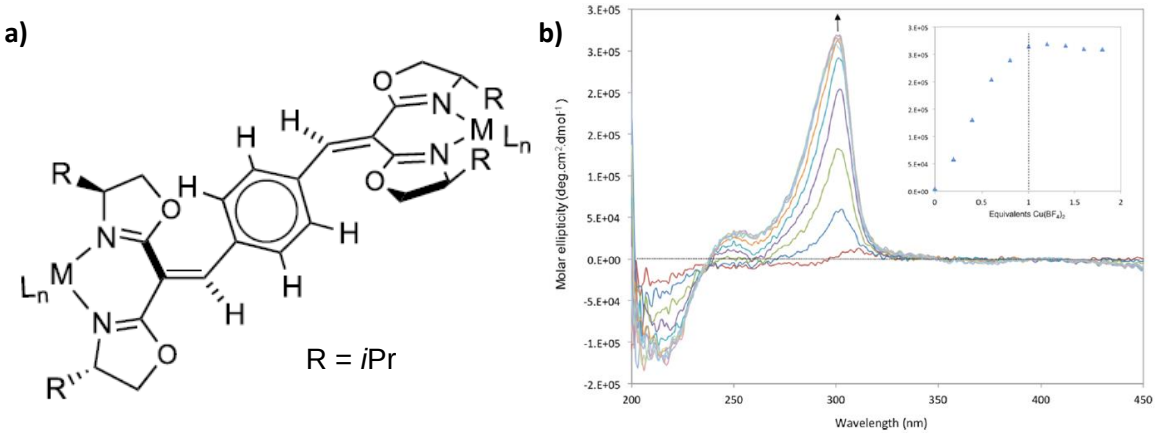

*Figure 102: a) DFT-calculated „boat"-configuration of a dinuclear complex from **18** in which the ligand's chromophore is twisted in a chiral way, b) titration of **18** with $Cu(BF_4)_2$ monitored by CD, $2.5 \cdot 10^{-5}$ M in MeOH. While **18** bears only negligible CD features, the progressive addition of $Cu(BF_4)_2$ gives rise to an intense CD band. The inset shows the increase in CD intensity at 302 nm.*[146]

The aim of the work in this chapter will be to gather more information about chiral metallopolymer-induced SFG. For this purpose, we will design new ditopic ligands able to form metallopolymers and to apply them in SFG. Most of the ligands will be based on a structure similar to **18**, namely with a bis-conjugated aromatic core, to obtain the required optical properties.

III.2 Results & Discussion

III.2.1 Ditopic iminoalcohol and iminoamine ligands

III.2.1.1 Ligand design & synthesis

The main component to have in mind when designing a ditopic ligand for application in SFG is, apart the chiral structure, the UV-vis-absorption: the molecule has to contain a chromophore absorbing at 300 nm. In **18**, it is the bis-alkene-conjugated aromatic linker (Figure 103, red part of the left molecule). We wondered if a bis-*imine*-conjugated linker might have similar optical properties. The ligand could then be obtained from simple condensation of readily available chiral aminoalcohols and diamines on terephtaldehyde.

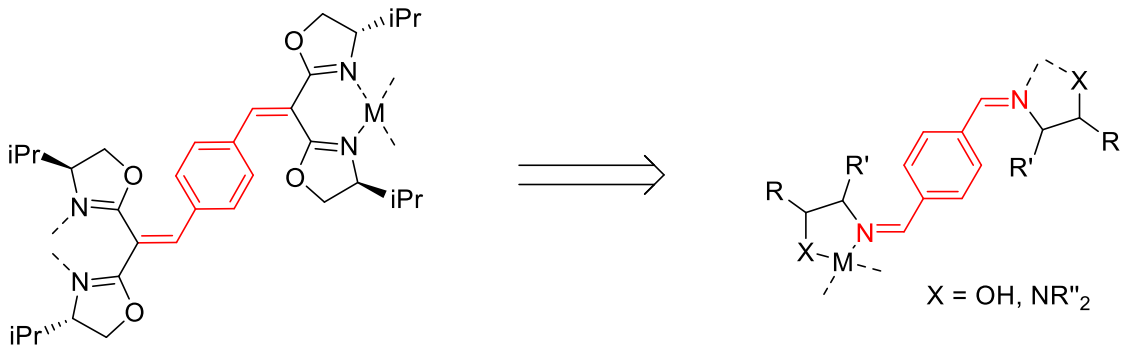

*Figure 103: Scheme for the design of a novel ditopic ligands with a bis-imine-conjugated aromatic linker, inspired from ligand **18**.*

(a) Aminoalcohol-based diimine ligands

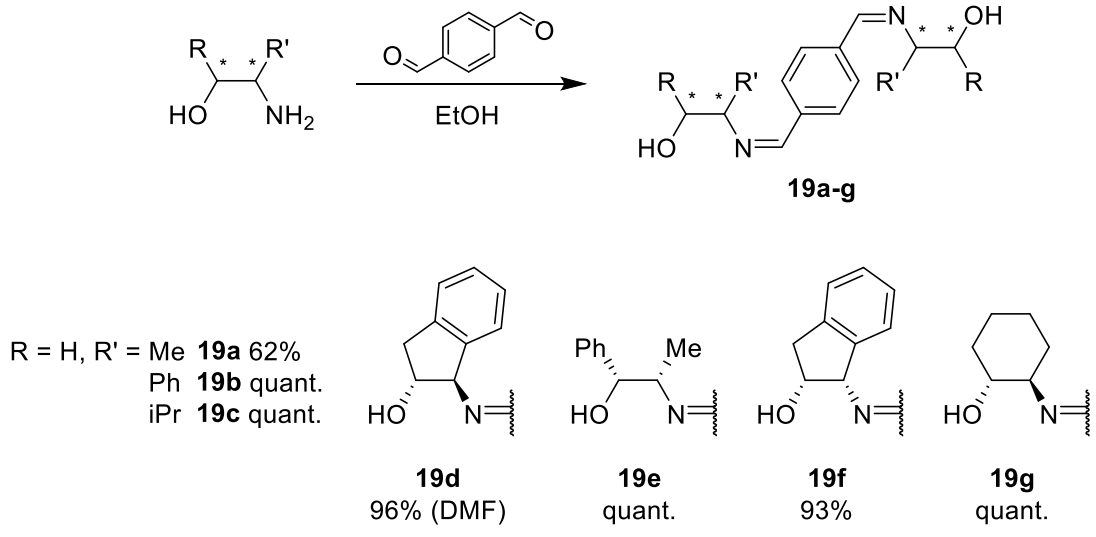

*Figure 104: Reaction scheme for the synthesis of bis-iminoalcohols **19a-g**.*

A series of diimines **19a-19g** was synthesised from chiral aminoalcohols available in our lab and from terephtaldehyde in EtOH (Figure 104); only *trans*-2-aminoindanol **19d** was reacted in DMF due to solubility issues. The final ditopic iminoalcohols were isolated mostly by evaporation giving quantitative yields; in some cases the product precipitates and was filtered, resulting in more variable yields.

Most of the ligands are in equilibrium with a closed form in which the alcohol has been added to the imine ("hemiaminal ether", Figure 105). This is possible on both coordination sites and gives rise to new stereocentres, resulting sometimes in complicated ^{1}H NMR spectra. For example, **19f** exists almost only as hemiaminal ether in $CDCl_3$, whereas only the open form of **19a**, **19d** and **19g** is visible in ^{1}H NMR. The hemiaminal ether-part of **19e** decreases from 40 to 10% when switching from $CDCl_3$ to MeOH-d_4. The closed form seems to be favoured by bulky substituents on the aminoalcohol-backbone; the effect is even stronger if both substituents form a closed cycle, as long as the stereochemistry allows it – the *trans*-configuration of alcohol and imine in **19d** and **19g** probably prevents hemiaminal ether formation.

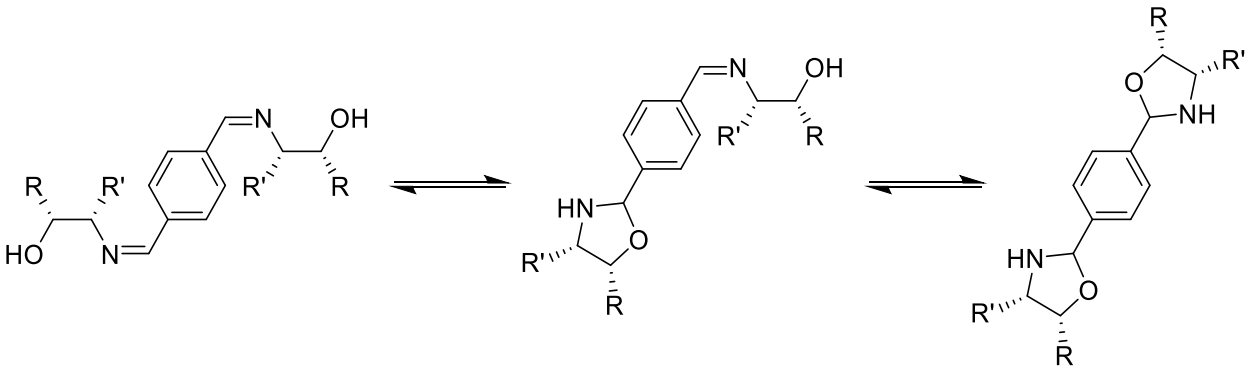

Figure 105: Scheme for the equilibrium of ditopic iminoalcohol ligands with a simple and a double hemiaminal ether.

(b) DACH-based diimine ligand

We made also a ligand derived from diaminocyclohexane (DACH). This originally started with ditopic ligand **4**, which has been used before by our group in self-supported asymmetric catalysis (cf. Chapter II.1.2, p. 83).[142] We attempted to oxidise the benzylic positions to obtain tetraimine ligand **20** using a method reported by Nicolaou (Figure 106).[173,174] However, the reaction of **4** with IBX in DMSO yielded a complex mixture of products with broad NMR peaks, some imine hydrolysis was also observed. Since the product cannot be purified by silica gel chromatography (all imines in this chapter hydrolyse on SiO_2), we changed the synthetic strategy and attempted to condense two DACH units on terephtaldehyde. However, this resulted into the macrocycle **17** already discussed in Chapter II.2.2.3(c), p. 98.[161] **21** was formed quantitatively only when using a great excess of DACH (10 equiv), the purification being again difficult because of the hydrolysable imines.

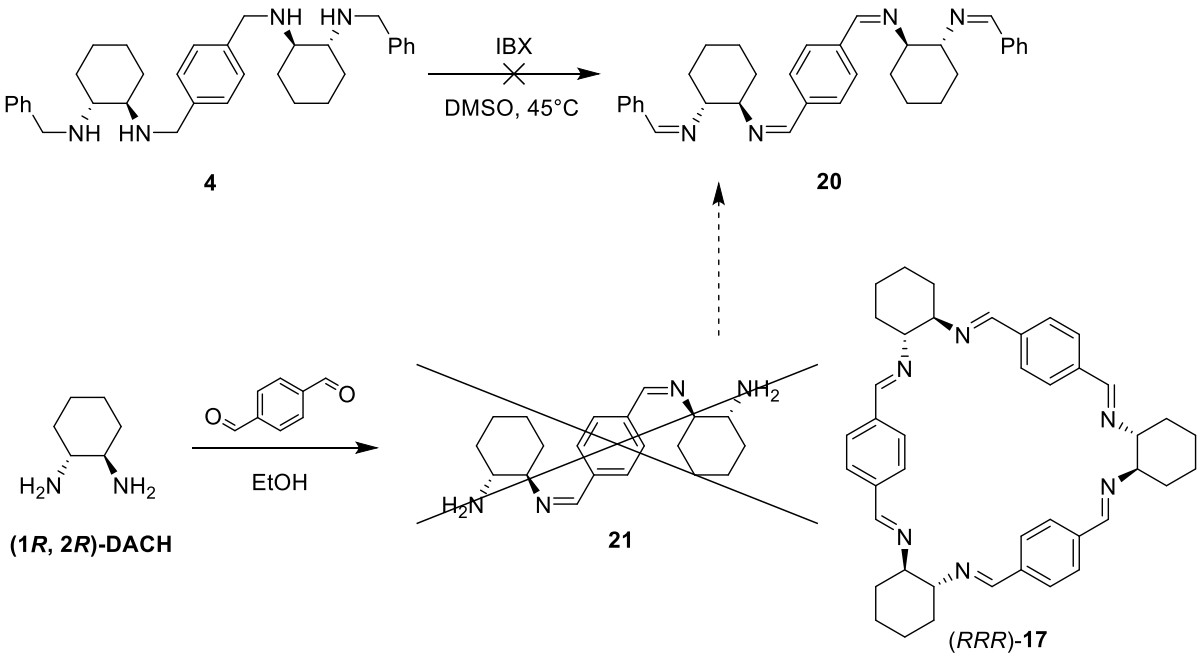

*Figure 106: Reaction schemes for the attempted synthesis of tetraimine ligand **20**.*

In order to circumvent trianglimine formation, we monofunctionalised DACH in three steps to obtain the dissymmetric amine **22,** following a literature procedure (Figure 107).[175] **22** has only one primary amine and cannot form trianglimine **17**, therefore condensation on terephtaldehyde gave ditopic iminoamine **23** in a similar fashion as the ditopic iminoalcohols. The whole synthesis is straightforward, high-yielding and doesn't require any further purification.

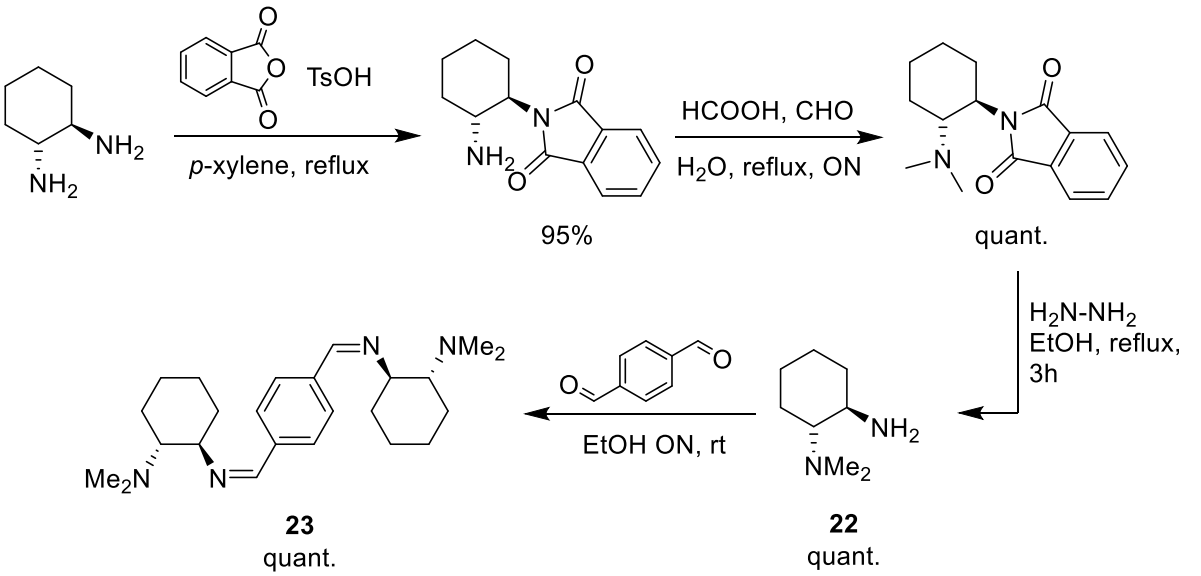

*Figure 107: Reaction scheme for the synthesis of **23** from (1R,2R)-DACH. The synthesis of intermediate **22** has been reported before.[175]*

III.2.1.2 Complex synthesis & properties

(a) Complex synthesis

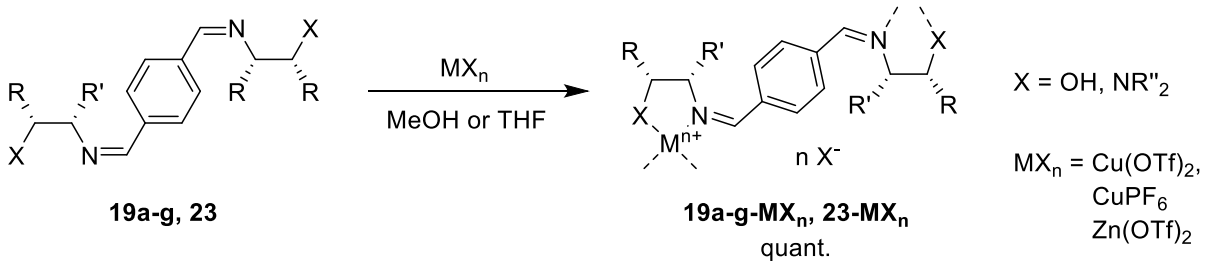

*Figure 108: Reaction scheme for the synthesis of the Cu(I)-, Cu(II)- and Zn(II)-complexes of ligands **19a-g** and **23**.*

We then went on with the synthesis of metallopolymers (Figure 108). We chose Cu(II)-, Cu(I)- and Zn(II)-salts with weakly coordinating triflate or PF_6^- anions to drive the coordination of two ligands on one metal; $Ni(OTf)_2$ proved to be only sparingly soluble in common solvens. The complexes turned out to be all extremely sensitive to water, which precluded the use of hydrated BF_4-salts. The $Cu(OTf)_2$-complexes of ligands **19a-c** are so sensitive that the solid compounds liquefy at air within a few seconds, even quick handling of the material didn't allow us to obtain a clean IR spectrum. Complexes from ligands **19f-g** and **23** are stable enough to be handled at air for a short time, therefore our studies will focus on them. The Cu(I)-complexes are less sensitive to hydrolysis but oxidise rapidly at air, which is not surprising since there are no soft ligand atoms such as P or S to stabilise the +I oxidation state. Ligand **19d** and its complexes proved to be problematic as they are insoluble in most solvent suited for complexation. The reaction works in DMF but remaining traces of the solvent, which we didn't achieve to eliminate, hindered the complexes' characterisation. Therefore, **19d** and its complexes were not studied further.

(b) IR spectroscopy

Next, we characterised the complexes. IR spectroscopy proved to be a valuable tool as it gives us information about the materials in the solid state. Moreover, it can tell us if the complexes are metallopolymers or discrete molecules, like 1:1 metal/ligand complexes which do not polymerise because of e. g. steric hindrance.

The ligands' and complexes' most characteristic IR feature is the C=N-stretching. It usually doesn't overlay with other bands and is in the range of 1633-1644 cm^{-1} for the free ligands. Coordination on a metal leads either to a shift of the band to lower wavenumbers (+II salts: 8-11 cm^{-1}, $CuPF_6$: 13-38 cm^{-1}) or to the appearance of additional bands at higher wavenumbers. The number of imine bands for each ligand/metal combination is shown in Table 7.

Ligand	$CuPF_6$	$Cu(OTf)_2$	$Zn(OTf)_2$
19a	-	[a]	-
19b	-	[a]	-
19c	-	[a]	-
19d	[b]	[b]	[b]
19e	1	2	2[a]
19f	1	1	2[a]
19g	1	2	2
23	1	1	1

*Table 7: Number of imine stretching bands in the IR spectra of the respective metal complexes of ligands **19a-g** and **23**. a) compound is too water-sensitive to be properly analysed; b) the DMF solvent couldn't be completely evaporated and masks the imine bands in the IR spectrum.*

The presence of a single imine band in the complex precludes that all imine groups are equivalent, therefore the material is necessarily a metallopolymer. Two different imine bands are indicative of a discrete 1:1 metal/ligand complex in which one imine is coordinated to the metal and the other isn't; another possibility is a mixture of 2:1 complexes and of free ligand. We will consider only the complexes with a single imine band as metallopolymers, although we cannot exclude the possibility of non-equivalent imines inside of a metallopolymer.

Globally, the iminoalcohols form metallopolymers only with $CuPF_6$, with exception of **19d-CuOTf$_2$**. Iminoamine **23** is the only ligand to give a single imine band with all metal salts tested and is therefore the best ligand to form metallopolymers. This may be due to the stronger donor properties of the amine: the alcohol in ligands **19e-g** may be a too weak coordinant to displace the triflate ions, which occupy coordination sites and hinder the addition of a 2nd ligand to the metal. Cu(I) is not as electron-poor as the +II-metals and doesn't require strong donor ligands to displace the PF_6^- anion (which might also be a weaker coordinant than OTf^-), therefore it facilitates the metallopolymer formation.

(c) UV-vis spectroscopy

Next, we verified the absorbance of the ligands and complexes by analysing them in UV-vis spectroscopy. Figure 109 shows the spectra of ligands **19e-g** and **23** and their respective complexes. The cyclohexane-derived ligands **19g** and **23** (black lines) have an intense absorption band at 277 nm and extending beyond 300 nm. Complexation on $Cu(OTf)_2$ (blue lines) and $Zn(OTf)_2$ (red line) shifts the band to 255 nm but doesn't affect much its intensity; a similar red-shift is observed with ditopic bisoxazoline **18**.[144,146] This is due to the C-C double bonds not being fully conjugated any more with the central aromatic, thus increasing the energy required for the electronic transition. It is

reasonable to think that a similar phenomenon takes place with our bis-imine ligands. The band of **19e-Cu(OTf)$_2$** shifts less to the red than the other +II complexes (267 nm) and is less intense, however the spectrum was made in MeOH instead of THF – care should be taken when comparing this to the other complex spectra. It is also the only ligand whose chiral backbone is not fused with a cycle.

The $CuPF_6$-complexes (orange lines) show a very distinct behaviour: the band shifts less to the blue (to 276 and 267 nm), loses approximately half of its intensity and becomes much broader. **23-CuPF$_6$** even has a very large shoulder spanning from 350 to 600 nm: it could be the result of some additional phenomena, like metal-to-ligand charge transfer (MLCT) or exciton coupling between two nearby chromophores.

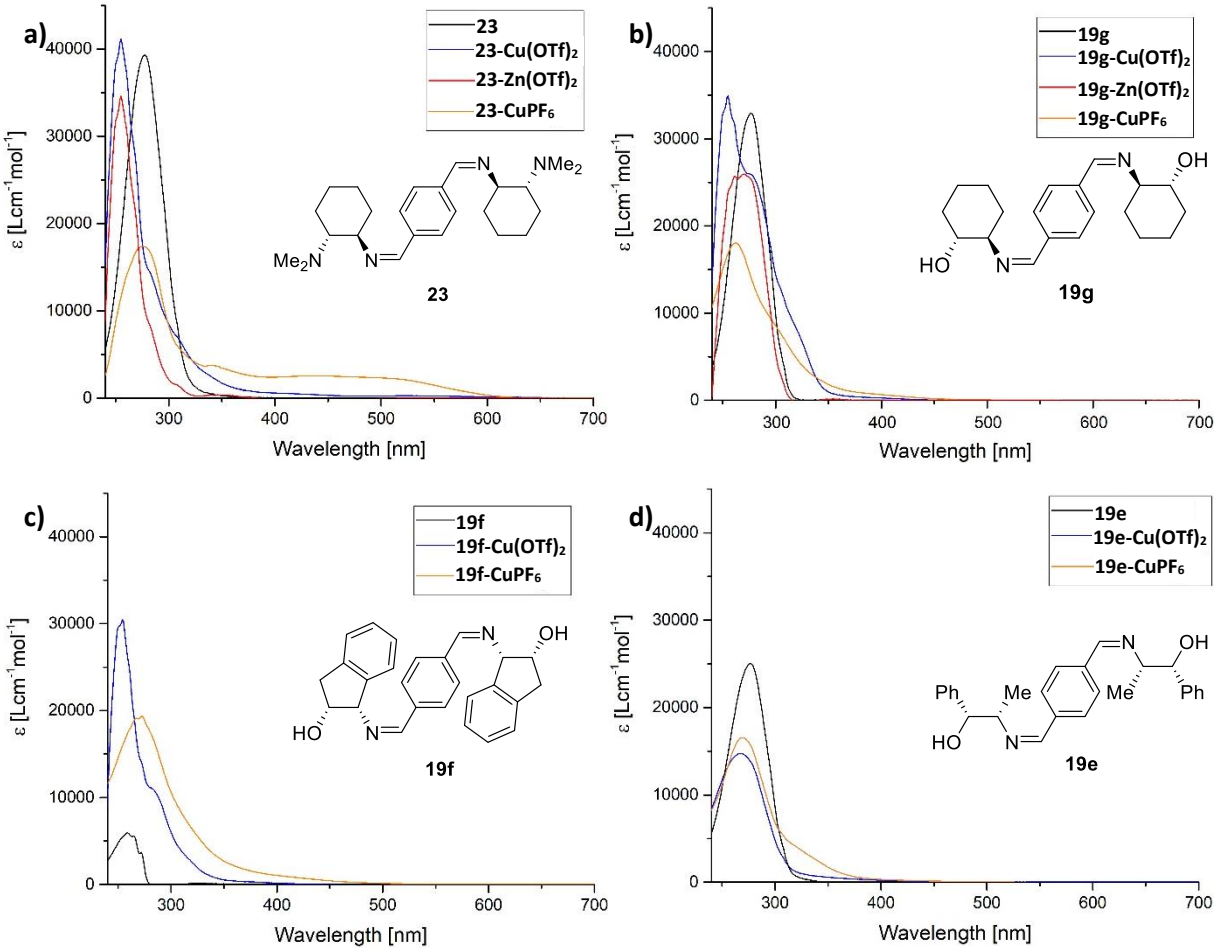

*Figure 109: UV-vis spectra of ligands a) **23**, b) **19g**, c) **19f**, d) **19e** (black) and their respective Cu(OTf)$_2$- (blue), Zn(OTf)$_2$- (red) and $CuPF_6$-complexes (orange). All spectra were made in THF, 3-6·10^{-5} M, except **19f** and **23-CuPF$_6$** (DCM), **23**, **19e** and **19e-Cu(OTf)$_2$** (MeOH).*

Indanol-derived ligand **19f** (Figure 109c) differs from the other ligands as it has an only weak absorption band, which is consistent with the ligand being mostly in its hemiaminal ether form and thus breaking the conjugation of the aromatic with the imines. The coordination on metals drives the opening of the hemiaminal ethers, thus **19f-CuOTf$_2$** and **19f-CuPF$_6$** show the same features as their counterparts with ligands **19g** and **23**.

It should be noted that the bands of **19g-Cu(OTf)$_2$** and **19g-Zn(OTf)$_2$** have a shoulder at 277 nm, which corresponds to the free ligand's absorption band: it may indicate the presence of free ligand.

This is consistent with the different imines bands in IR (from which one is similar to the free ligand's band) indicating the presence of different species; it could also be due to a low association constant, driving the complex' dissociation at the low concentration used to make the spectra.

Globally, the complexes all absorb at 300 nm with molar extinction coefficients mostly around 8000 $Lcm^{-1}mol^{-1}$, which makes them à priori suitable for SFG. Though, we should be careful with this conclusion as not the solution, but the solid-state properties of the complexes are of importance for the SFG experiments. The UV-spectra may be different in the solid state; Taupier observed an additional band at 350 nm on a solid sample of **18-Ni(BF_4)$_2$**.[171] We also do not know if the complexes are present as metallopolymers, -oligomers or as mononuclear complexes in solution, at the concentration used in Figure 109. A UV-vis-monitored titration of the ligand with a metal salt solution can tell if a metallopolymer is formed (cf. chapter III.2.2.3(c), p. 128), however this is difficult to perform with air-sensitive compounds without specialised equipment.

(d) Circular Dichroism

The free ligands have a negative band around 277 nm with an intensity of $-2\cdot10^{-4}$ to $-8\cdot10^{-4}$ °cm^2dmol^{-1} which is of the same order of magnitude than bisoxazoline ligand **18**; indanol-derived ligand **19f** shows, as in UV, a very weak signal. However, the CD signal does not increase but *de*crease upon addition of a metal salt, which is in striking contrast to **18**. Cu(II)-complexes of **19e**, **19g** and **23** give only very weak CD signals; same goes for **23-Zn(OTf)$_2$**. **19g-Zn(OTf)$_2$** and **19f-Cu(OTf)$_2$** are the only +II-complexes with a relatively high molar ellipticity of $-4\cdot10^{-4}$ to $-6\cdot10^{-4}$ °cm^2dmol^{-1}.

By analogy with the UV-vis-spectra, the Cu(I)-complexes behave differently than their Cu(II)/Zn(II)-counterparts. The intensity stays at -2 to $-5\cdot10^{-4}$ °cm^2dmol^{-1}, there is even a sign inversion with **19f-CuPF$_6$**. Moreover, the spectra are more complex: an additional, small band appears at 340-350 nm with **19e-**, **19f-** and **19g-CuPF$_6$** which is of inversed polarity. **23-CuPF$_6$** shows a sinusoidal curve between 350 and 600 nm: such spectra can arise from exciton coupling between two nearby chiral chromophores. The wave-like shape is also present in its Cu(II)-counterpart, albeit with a weaker amplitude. Here again, we must treat the data with care as the CD in solution might be different from the CD in solid state. Taupier observed a slight blue-shift of the 300 nm-band of **18-Ni(BF_4)$_2$** in the solid state, the dinuclear complex **18-[Ni(BF_4)$_2$]$_2$**, however, gives rise to a new band of opposite sign. We also cannot tell if the low CD intensity comes from the complexes being weakly CD-active or from a mutual cancelation of positive and negative signals at the same wavelength. This will be further discussed in chapter III.2.2.3(d), p. 131.

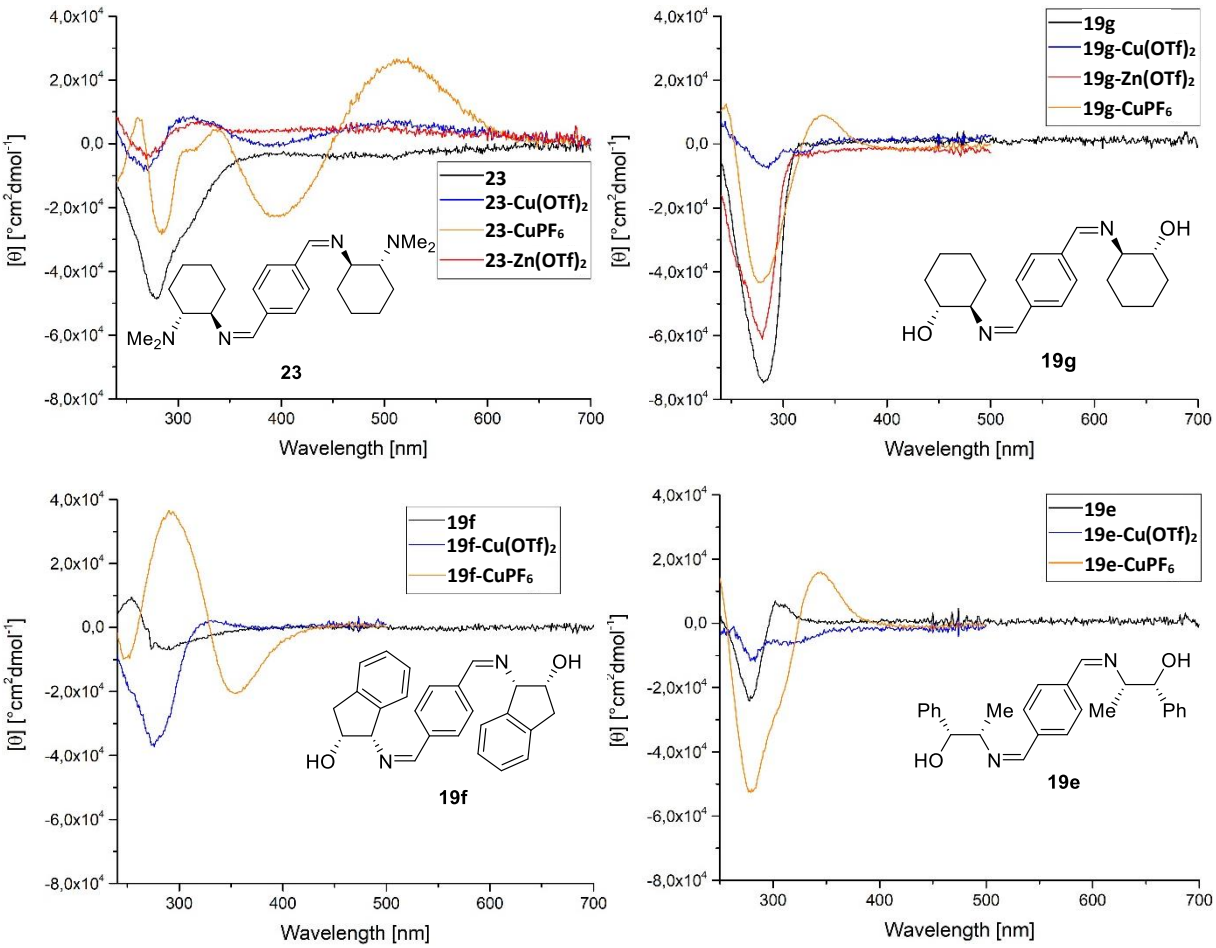

*Figure 110: CD spectra of ligands a) **23**, b) **19g**, c) **19f**, d) **19e** (black) and their respective $Cu(OTf)_2$- (blue), $Zn(OTf)_2$- (red) and $CuPF_6$-complexes (orange). All spectra were made in THF, $3\text{-}6\cdot10^{-5}$ M, except **19f** and **23-CuPF$_6$** (DCM), **23**, **19e** and **19e-Cu(OTf)$_2$** (MeOH).*

III.2.1.3 Application in SFG spectroscopy

After having studied the ligands and complexes by classical spectroscopic means, we went on to apply them in SFG microscopy. Due to limitations in our technical and human resources we could test only a few compounds, derived from ligands **23** and **19f**.

(a) Ditopic iminoamine 23

First, we examined the complexes of ligand **23** as it is the most promising candidate, forming metallopolymers in the solid state with all three tested metal salts. The films for the SFG experiments were obtained by drop-casting a THF solution of the respective complex on a quartz plate

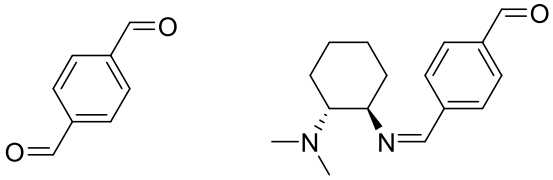

*Figure 9: Decomposition products from hydrolysis of the metal complexes of ligand **23**.*

and letting the solvent evaporate at air. The films were then irradiated for a given time in the "in" and "out" modes and each mode recorded in the PPP and SPP modes. Figure 112 shows the SFG spectra of **23-CuPF$_6$** and **23-Cu(OTf)$_2$**, the SPP and PPP signals resulting from subtraction of the respective "out" from the "in" acquisitions, as explained in chapter III.1.3, p. 105. The results shown in Figure 112 are mere preliminary results, as the complexes were made from a batch of **23** containing significant amounts of terephtaldehyde (20 mol%) and a monocondensed terephtaldehyde-diamine adduct (40 mol%, see Figure 111).

23-CuPF$_6$ exhibits an SPP signal with an intensity of ca. 3000 after 180 s irradiation, which is comparable to that of the bisoxazoline complexes (see Figure 100, p. 108). However, **23-Cu(OTf)$_2$** gives an SPP signal of 5500 in only a 10th of the time, namely 18 s: the signal is much more intense than with the bisoxazoline polymers. On the other hand, **23-Zn(OTf)$_2$** exhibits no SPP signal and thus no activity in SFG.

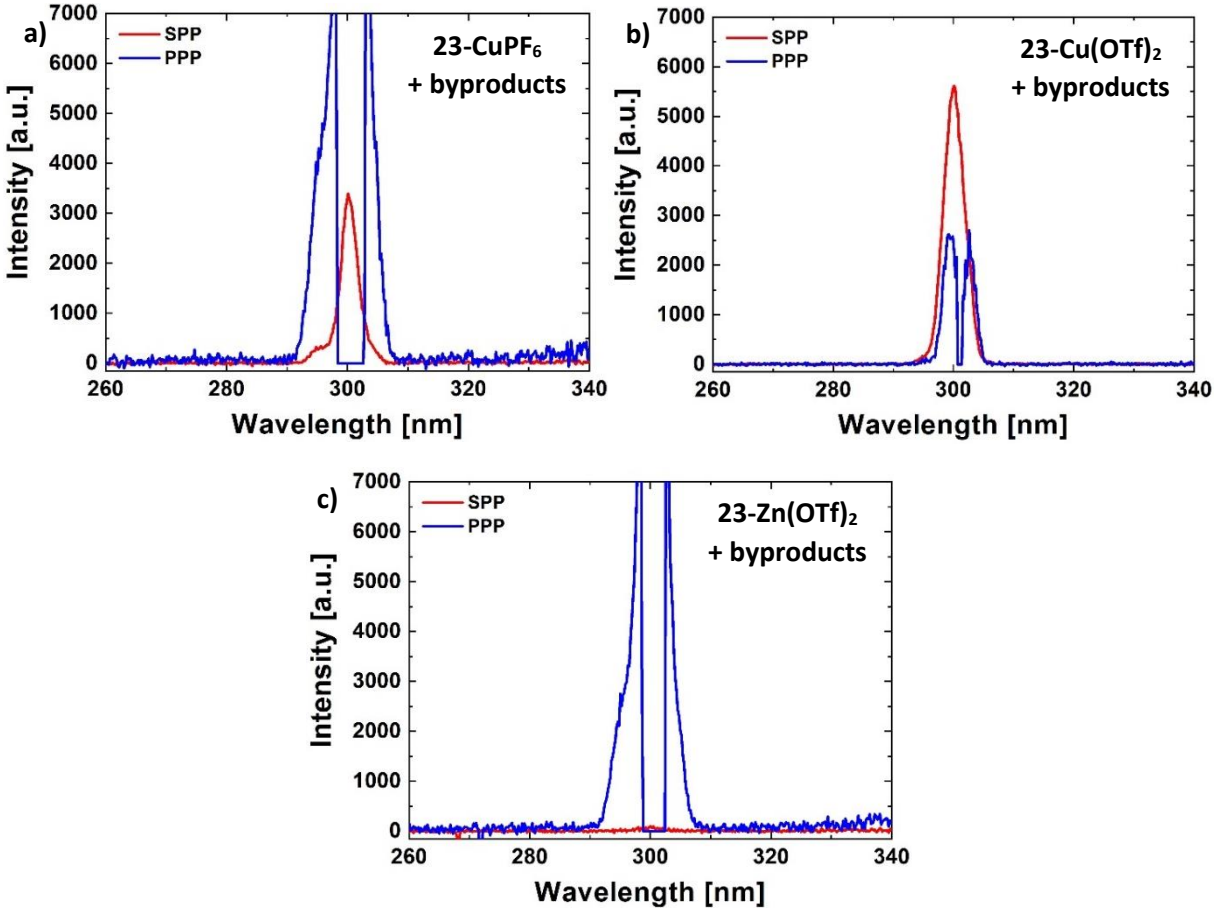

*Figure 112: SFG spectrum of complex a) **23-CuPF$_6$** (180 s acquisition time), b) **23-Cu(OTf)$_2$** (18 s) and c) **23-Zn(OTf)$_2$** (180 s), containing byproducts shown in Figure 111, in SPP (red) and PPP-mode (blue).*

All three spectra exhibit also an extremely strong PPP signal; its broken shape comes from "PPP in" and "PPP out" acquisitions both saturating the detector, the subtraction thus resulting in a value of 0. An SFG spectrum of uncomplexed **23** (Figure 113) shows the same strong PPP signal, but no SPP.

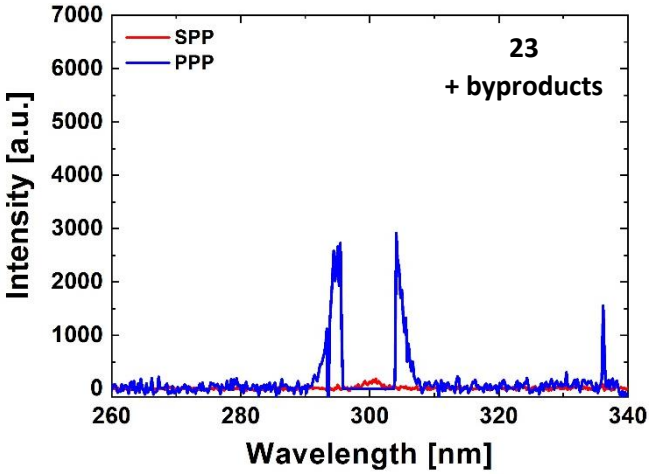

*Figure 113: SFG spectrum of ligand **23**, containing byproducts shown in Figure 111, in SPP (red) and PPP-mode (blue), 180 s acquisition time.*

Despite the bad purity of ligand **23** used for these SFG experiments, the results are rather promising: an SPP signal, which is not existent in the ligand alone, appears in the copper complexes; in case of Cu(II) the signal even is of exceptional intensity. The strong PPP signal seems to originate from the ligand itself, probably from the mentioned byproducts. Figure 114 shows the SFG spectrum of **23-CuOTf$_2$** originating from a pure batch of **23**: the strong PPP signal has given place to a weaker one, of approximately same intensity as the SPP signal whose intensity (ca. 4500) hasn't changed much. This indicates that the saturating PPP signals in Figure 112 and Figure 113 come from the byproducts. As **23-CuOTf$_2$** is sensitive to moisture and the SFG experiment has been made at air, the remaining PPP in Figure 114 may origin from a small amount of hydrolysis byproducts (which are the same as in the bad **23** batch: terephtaldehyde and possibly a monohydrolysed ligand) formed during the sample preparation and the SFG experiment. The quick colour-change from violet to brown of the **23-CuOTf$_2$**-solution after drop-casting may be indicative of that.

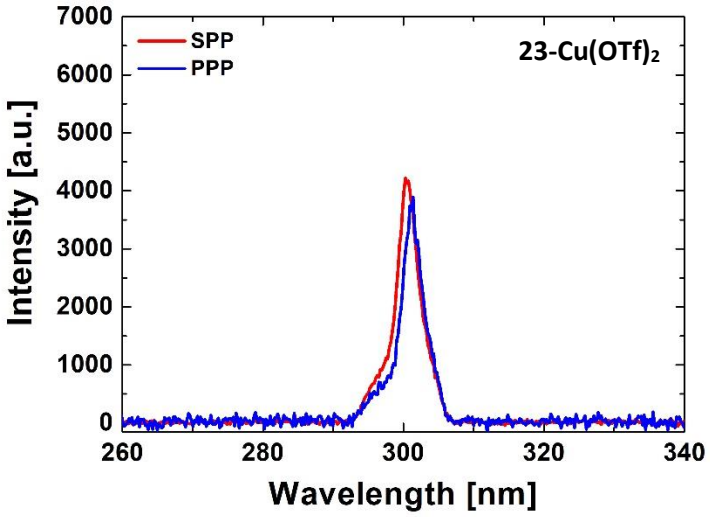

*Figure 114: SFG spectrum of complex **23-Cu(OTf)$_2$**, from a pure batch of **23**, in SPP (red) and PPP-mode (blue), 18s acquisition time.*

Though, the nature of the PPP signal is not totally clear. The byproducts may cause crystalline regions in the sample which allow achiral SFG (see chapter III.1.2.3, p. 105), however it would mean that the crystals are oriented in a precise fashion which generates achiral SFG only in the P plane. Another possibility is THG (see chapter III.1.3, p. 105), whose contribution is meant to be cut off by subtraction of the "PPP out" acquisition. Fluctuations in the THG intensity may cause a non-zero PPP signal after subtraction. It is also questionable if the stabilisers present in the THF solvent (BHT, a phenol which absorbs at 300 nm) may have an influence. Finally, we cannot exclude the metallopolymer itself also to contribute to the PPP signal via achiral SFG.

(b) Ditopic Iminoalcohol 19f

We achieved also to obtain an SFG spectrum from **19f-CuPF$_6$** (Figure 115). Similar to **23**-Cu(OTf)$_2$, the SPP signal with an intensity of ca. 3000 was acquired in only 18 seconds and attests the complex' high SFG activity. A curiosity here is the intense and *negative* PPP signal. This may be again an artefact caused by a fluctuating THG; having in mind the hydrolysis problematic discussed before with ligand **23** and the O_2-sensitivity of **19f-CuPF$_6$**, it might be also due to ligand decomposition *during* the SFG experiment. The "in" modes are usually acquired before the "out" modes, so if hydrolysis takes place in between, the sample is enriched in hydrolysis products when making the "out" acquisition. A stronger "PPP out" than "PPP in" spectrum results then in a negative signal.

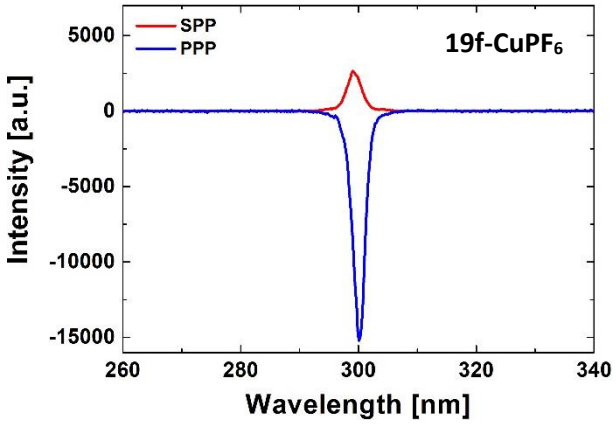

*Figure 115: SFG spectrum of complex **19f-CuPF$_6$** in SPP (red) and PPP-mode (blue), 18s acquisition time.*

In conclusion, we can say that the iminoalcohol and -amine complexes are very promising for applications in SFG, however their water-sensitivity complicates considerably the interpretation of the spectra. Therefore, they are unsuited for SFG microscopy. Nevertheless, those preliminary results encouraged us to continue to work with the bis-imine scaffold; in the following, we will focus on the development of water-stable alternatives to the ditopic iminoalcohol and -amine ligands.

III.2.2 Ditopic iminoaniline ligands

In the following, we will present design, synthesis and metal complexation of a new imino*aniline* ligand. Although we didn't have the occasion to apply it in SFG microscopy, we could make a more extensive study on the ligand's and its complexes' structure as it presents some peculiar spectroscopic characteristics.

III.2.2.1 Ligand design

It is known that imines become less water-sensitive with an increasing number of aromatic substituents: doubly aliphatic imines afford water-trapping techniques (addition of molecular sieves, Dean-Stark apparatus) during their synthesis to obtain them in high yields. Simple aromatic imines such as in our iminoalcohol/-amine ligands don't need special precautions during the synthesis; doubly aromatic imines are even more stable. Therefore, we decided to replace the aliphatic backbone of the ligand's chelating part by an aromatic ring (Figure 116). Since the aromatic is not chiral we introduced a chiral substituent on the X atom, which may be achieved by the addition of chiral amines or alcohols on the aromatic ring. In analogy the iminoalcohols and -amines, we will call this type of ligand a ditopic iminoaniline.

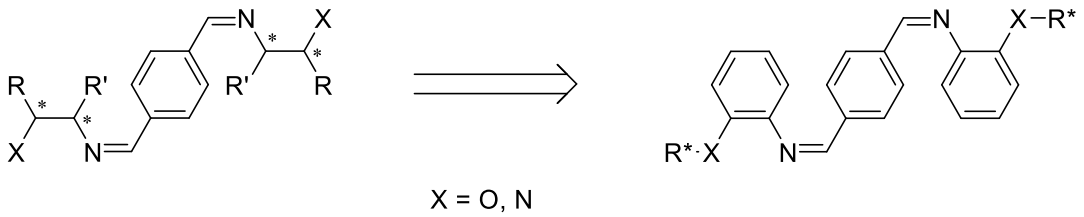

Figure 116: Scheme for design of new and possibly more stable ditopic iminoaniline ligand.

III.2.2.2 Ligand & complex synthesis

We chose to start with a chiral amine, as nitrogen-based ligands are the better coordinants (the superior coordination capacities of **23** over the iminoalcohols confirms this). (*R*)-1-Phenylethylamine is a cheap and readily available amine which was added to 2-fluoronitrobenzene via nucleophilic substitution, following a method described by Žurek.[176] We could confirm refluxing 1-butanol and DABCO as a base to be more performant than toluene/K_2CO_3.[177] A slight modification of the procedure allowed us to obtain pure **24** in quantitative yield without any purification by chromatography. We then reduced the nitro group with metallic zinc as it is cheaper and more convenient to handle as Pd/C-catalysed hydrogenation with H_2 gas or toxic hydrazine. The reduction goes smoothly and yields dianiline **25** after 3 h under inert atmosphere, however the light green solution darkens within moments as it is exposed to air. Žurek and co-workers noticed their own dianilines to be very O_2-sensitive. Some impurities are visible in ^{1}H NMR even after quick work-up; column chromatography on SiO_2 didn't yield a purer product. We decided to go on and to condense **25** on terephtaldehyde. Ditopic iminoaniline **26** precipitates in MeOH, however filtration didn't allow

us to get fully rid of the impurities from the previous step. Therefore, we obtained **26** in an only moderate but sufficient purity for preliminary investigations.

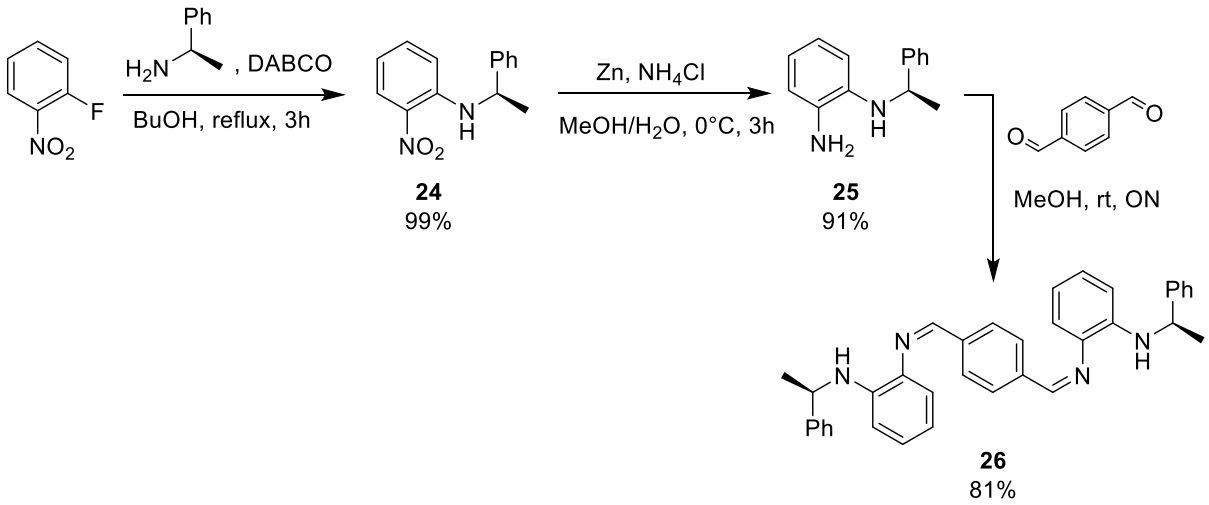

*Figure 117: Scheme for the three-step synthesis of ditopic iminoaniline ligand **26**.*

For future work, we consider ameliorating the synthetic procedure by forming **26** and condensing it on terephtaldehyde in a one-pot procedure, so that **25** doesn't need to be handled at air. However, we either must make sure that the zinc reductant does reduce the imine or aldehyde group or filter excess Zn dust prior to terephtaldehyde addition under argon using Schlenk techniques. Korich and Hughes have reported a procedure in which nitroarenes are reduced and added to benzaldehyde in a one-pot reaction using metallic iron and HCl.[178]

In the next step, we made the corresponding metal complexes using the same metal salts as with the iminoalcohol/-amine ligands. We were delighted to observe no hydrolysis when performing the reaction in wet THF, the ligand indeed is resistant to hydrolysis. This allowed us to make also a Ni(II)-complex from hydrated $Ni(BF_4)_2$. However, the $CuPF_6$-complex remains as O_2-sensitive as the previous ones. All complexes have single, broad imine bands which are slightly shifted to higher wavenumbers, indicating that all are metallopolymers in the solid state.

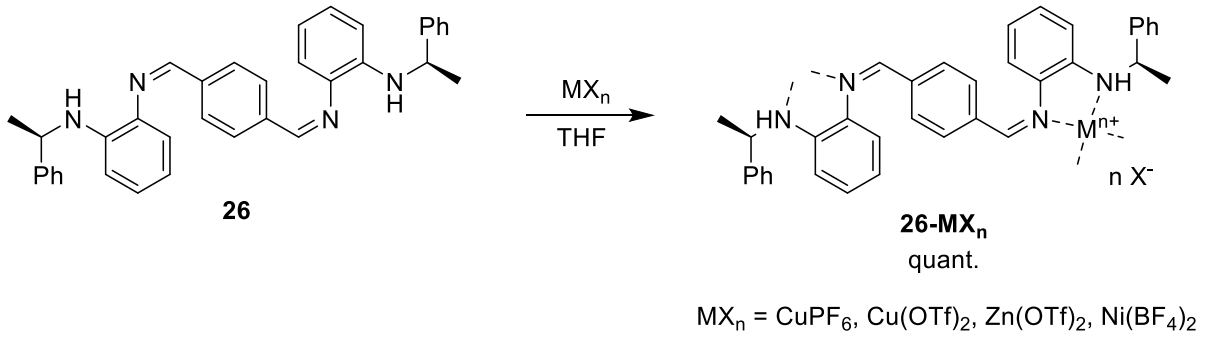

*Figure 118: Synthesis of Cu(I)-, Cu(II), Zn(II)- and Ni(II)-complexes of ditopic iminoaniline ligand **26**.*

III.2.2.3 Spectroscopic and structural studies

Once we had obtained the iminoaniline complexes, we went on to spectroscopic studies by UV-vis and CD. As shown in the following, the ligand bears some peculiar properties in UV-vis which made us perform a broader study than before, including DFT calculations and a study of the metallopolymer formation in solution.

(a) UV-vis spectroscopy

As the previous diimine ligands and complexes, we analysed the iminoaniline ligand **26** and its complexes by UV-vis spectroscopy. The ligand has a UV-band at 306 nm which shifts to ca. 286 nm upon complexation (Figure 119, a). The band is less intense with the complexes than with the free ligand, except for **26-Cu(OTf)$_2$** which shows even a slight intensity increase. At 300 nm, the complexes have rather high molar extinction coefficients in the range of 16 000 to 24 000 Lcm^{-1}mol^{-1}.

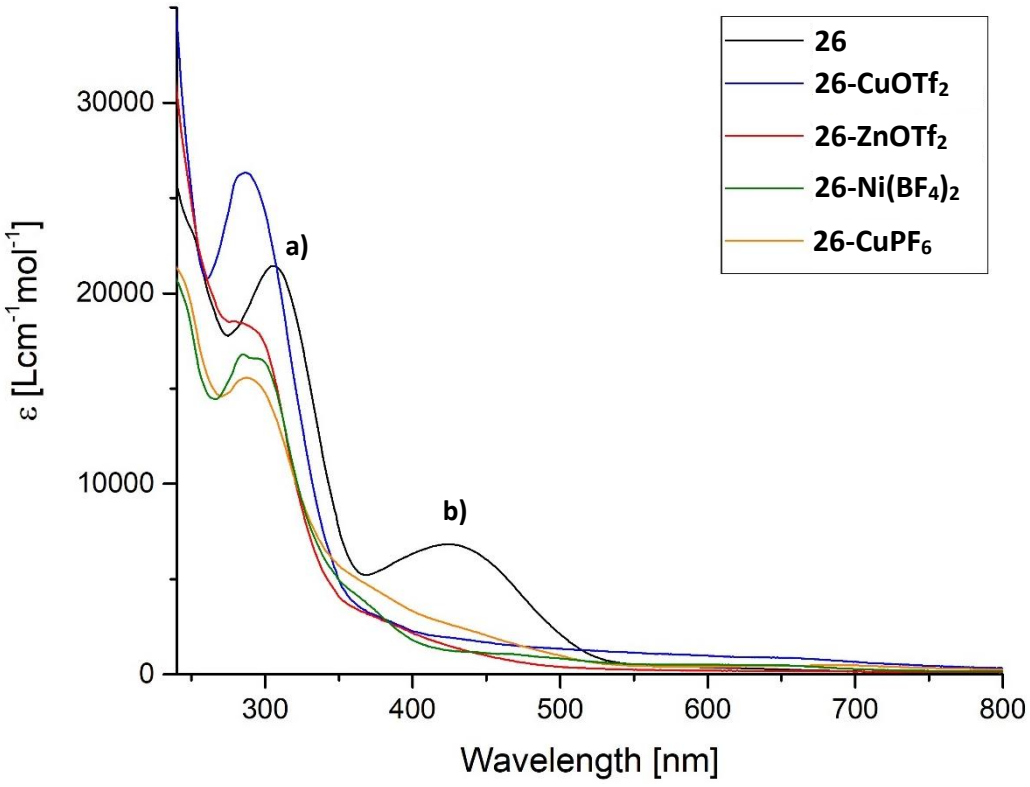

*Figure 119: UV-vis-spectra of **26** and **26-Cu(OTf)$_2$/-Zn(OTf)$_2$/-Ni(BF$_4$)$_2$** in THF, 3.3·10^{-5}-5.7·10^{-5} M.*

Surprisingly, the free ligand shows an additional intense and broad band in the visible region, centred around 446 nm, which doesn't exist in the metal complexes (Figure 119, b). It probably arises from an extended conjugation including both the linker and the chelating aromatic groups, thus lowering the π-π* energy difference and shifting the absorption into the visible region. For comparison, we

synthesised molecule **27**, which is an analogue of **26** lacking the chiral amines. Its UV-vis-spectrum is shown in Figure 120.

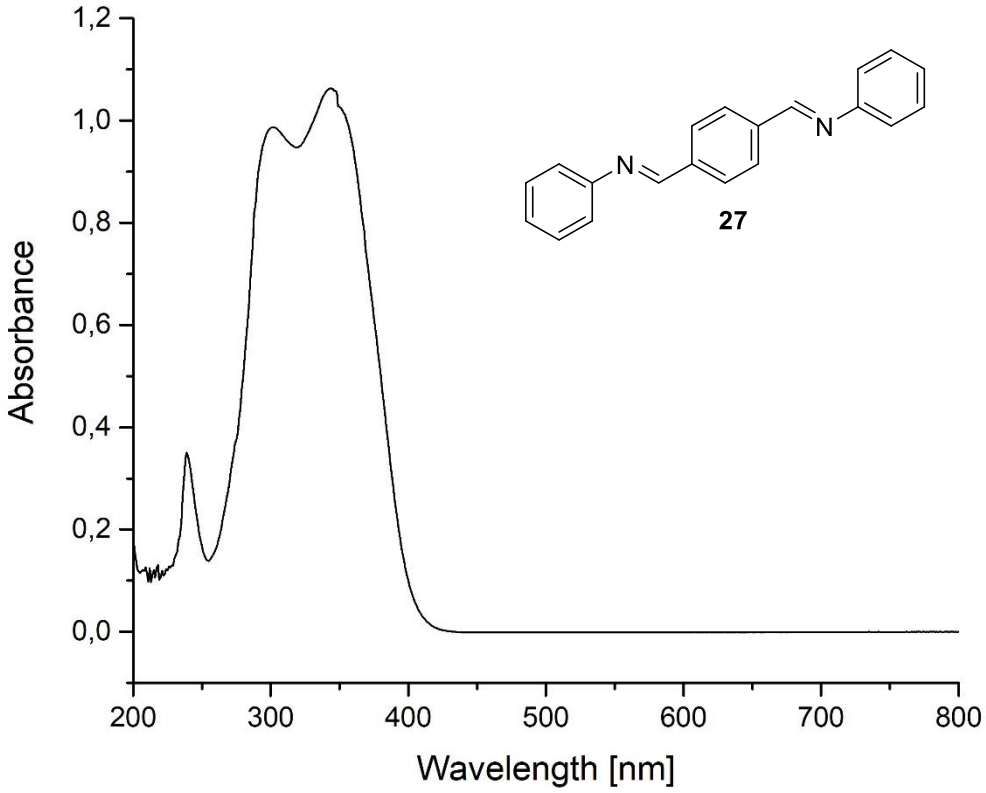

*Figure 120: UV-vis spectrum of **27** in THF, 4.23·10^{-5} M in THF.*

27 has a band centred close to 300 nm similar to all our diimine ligands, but like ditopic iminoaniline **26** it has also an additional band with a maximum at 344 nm. This shows that there is indeed additional conjugation of the pending phenyl groups with the diimine linker, giving rise to a new absorption band. In **26** the chiral amines provide additional conjugation, thus shifting the band to higher wavelengths. The breakdown of the 446 nm-band upon addition of a metal salt shows not only that the metal occupies the amine's lone e$^-$-pair, thus preventing conjugation with the aromatic system, but that the peripheric aromatics might also be not conjugated anymore with the diimine linker (Figure 121).

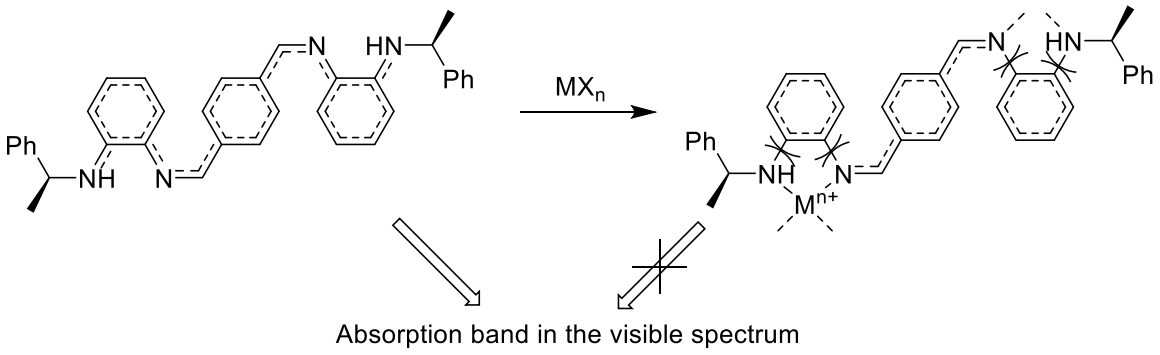

*Figure 121: Scheme for the conjugation break in **26** upon coordination on a metal.*

(b) Negative solvatochromism

Ligand **26**'s unusual band at 446 nm prompted us to make further studies, as it might reveal more information about the ligand's structure and how it changes upon addition of the metal. It turned out that the band shifts to the blue upon addition of more polar solvents like acetone ("negative solvatochromism", Figure 122).

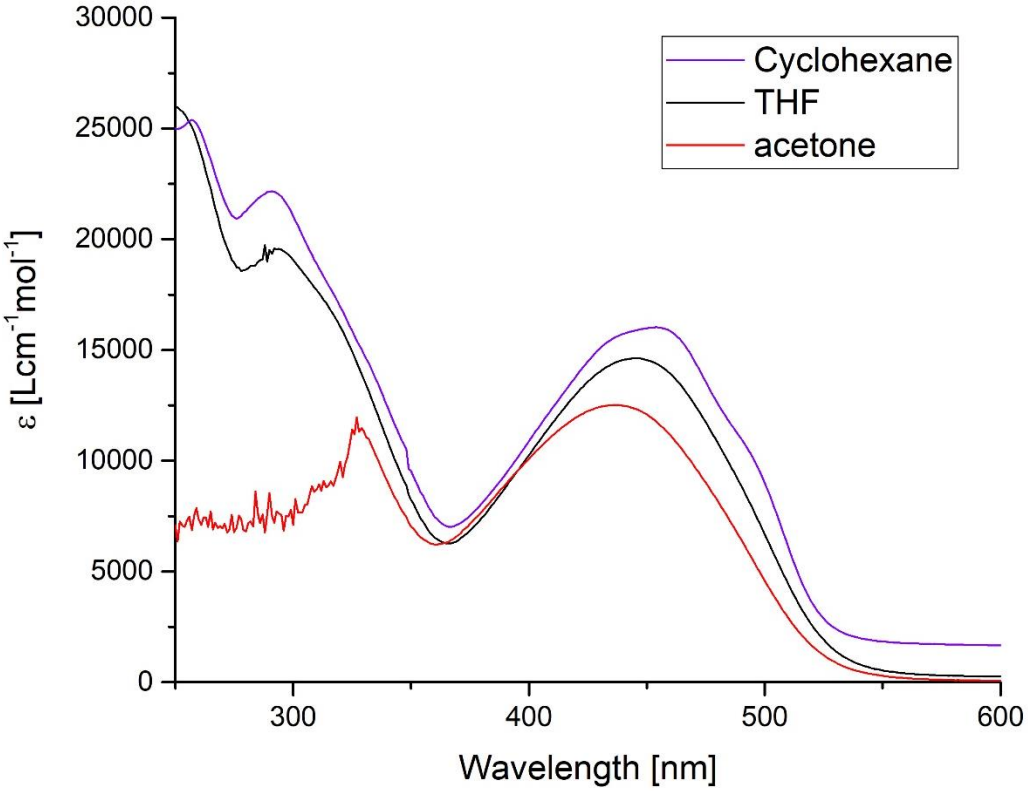

*Figure 122: Extract of the solvent screening for the Kamlet-Taft analysis of the visible band of ligand **26**.*

Such solvent-dependent shift can be quantified using the Kamlet-Taft-parameters.[179,180] Kamlet and Taft established empirical scales which account for a solvent's polarity (π*), its H-bond-donor (α) and its H-bond-acceptor capacity (β).[181,182] Equation (45) gives the studied band's $\bar{\nu}_{max}$ (maximal frequency, expressed in wavenumbers) as a function of the maximal frequency in the reference solvent cyclohexane ($\bar{\nu}_0$) and the parameters *s*, *a* and *b* which account for the influence of the individual solvent parameters π*, α and β on the band:

$$\bar{\nu}_{max} = \bar{\nu}_0 + s\pi^* + a\alpha + b\beta \qquad (45)$$

The analyte's $\bar{\nu}_0$, *s*, *a* and *b* can be determined by measuring $\bar{\nu}$ in a variety of solvents whose π*, α and β-parameters are known, followed by a linear regression. We performed such a Kamlet-Taft-analysis by measuring the $\bar{\nu}_{max}$ of **26**'s band in the visible region in 13 different solvents; the tabular

data and details to the calculations are found in the experimental part (IV.2.2.2, p. 160). Linear regression gave values for $\bar{\nu}_0$, *s*, *a* and *b* (in cm^{-1}) with an excellent fit, summarised in equation (46):

$$\bar{\nu}_{max}(cm^{-1}) = 22\,026 + 783\pi^* + 431\alpha + 395\beta \quad | \quad R^2 > 0.99 \qquad (46)$$

s, *a* and *b* have moderate positive values, which accounts for a slight blue-shift upon solvent polarity increase: the higher π*, α and β, the higher the overall $\bar{\nu}_{max}$, the lower the wavelength λ_{max}. The highest λ_{max} is with cyclohexane (454 nm), the lowest with MeOH (428 nm). The band of **26** in the visible region responds to solvent polarity but also to H-bond-donors and -acceptors, in a somewhat lower measure.

The negative solvatochromism of ligand **26** indicates that its ground state is more polar than the excited state.[179,180] The higher the solvent polarity (and/or, in our case, its H-bond donor/acceptor capability) the more ground state is low in energy, the higher the gap to the first exited state. DFT calculations of **26** in several conformations confirmed this when considering the molecule being a quadrupole, with both negative poles centred on the peripheral parts of the ligand and both positive poles being in the linker (Figure 123). This is consistent with the ligand structure containing electron-donating amines on the outer parts and electron-withdrawing imines in the central part. The transition into the excited state is accompanied by a partial charge transfer from the peripheral parts into the centre of the molecule, making it locally less polar and, therefore, less sensitive to the solvent's polarity; this leads to the observed negative solvatochromism in UV-vis spectroscopy. The molecule's *dipolar* moment changes only slightly upon excitation and is not sufficient to explain the observed blue-shift of the visible band.

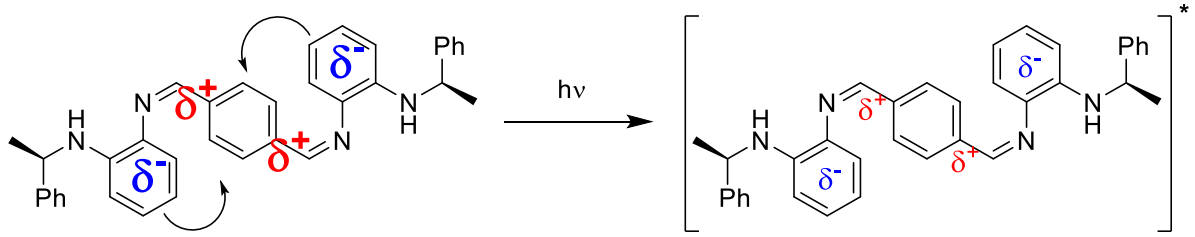

*Figure 123: Scheme for the partial charge transfer from the outer parts into the centre of ligand **26** upon excitation with visible light. The positive (δ^+) and negative (δ^-) partial charges are lower in the excited state, making it less sensitive to the solvent's polarity than the ground state.*

(c) UV-vis titration

Since **26** and its complexes have distinct UV-features and are stable towards moisture, we performed a UV-vis titration. It is one of the few methods allowing us to study the metallopolymer formation in solution, as long as the free ligand and the complex have distinct UV-vis features.[183,184] It consists in monitoring by UV-vis spectroscopy the continuous addition of a metal salt-solution to a solution of the ligand. The spectra's evolution shows with how many metal equivalents the ligand reacts and thus if it forms a metallopolymer or rather a mononuclear species, followed by a dinuclear one (Figure 124). Intermediate species, like 1:2 metal-ligand-complexes, may also be revealed.

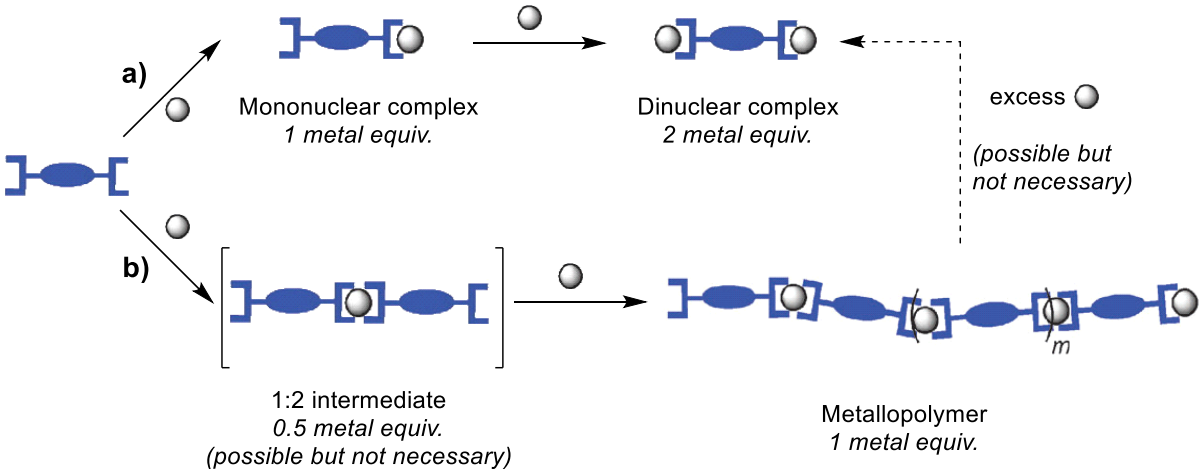

Figure 124: scheme for the possible outcomes of the addition of metal to a ditopic ligand. a) the ligand forms first a mononuclear, then a dinuclear complex, b) the metal forms a metallopolymer, with a 1:2 metal/ligand-complex as a possible intermediate. The metallopolymer may also be broken up to form a dinuclear complex, but usually it takes an excess of metal salt to achieve this. The evolution from one complex to the other can be visualised by a titration of the ligand with a metal, monitored by UV-vis spectroscopy.

The results of the titration of **26** with $Cu(OTf)_2$ in THF are shown in Figure 125: the 446 nm-band indeed decreases upon addition of metal solution, after addition of 1.2 equiv. the band has vanished (Figure 125a). The slight increase with more $Cu(OTf)_2$ is probably due to the d->d transition of uncomplexed $Cu(OTf)_2$. The plot of the absorption at 375 nm (where free copper doesn't absorb) vs metal equivalents (Figure 125b) shows an induction period until 0.2 equiv., then the absorption falls until it reaches a plateau at 1.2 equiv.; addition of more metal doesn't change the curve anymore. The UV-band at 292 nm (Figure 125c) increases and shifts progressively to 298 nm until 1.2 equiv. $Cu(OTf)_2$, the addition of more $Cu(OTf)_2$ further increases the band slightly because of the UV-band of uncomplexed $Cu(OTf)_2$. The simultaneous decrease of the visible and increase of the UV-band takes place around an isobestic point at 329 nm.

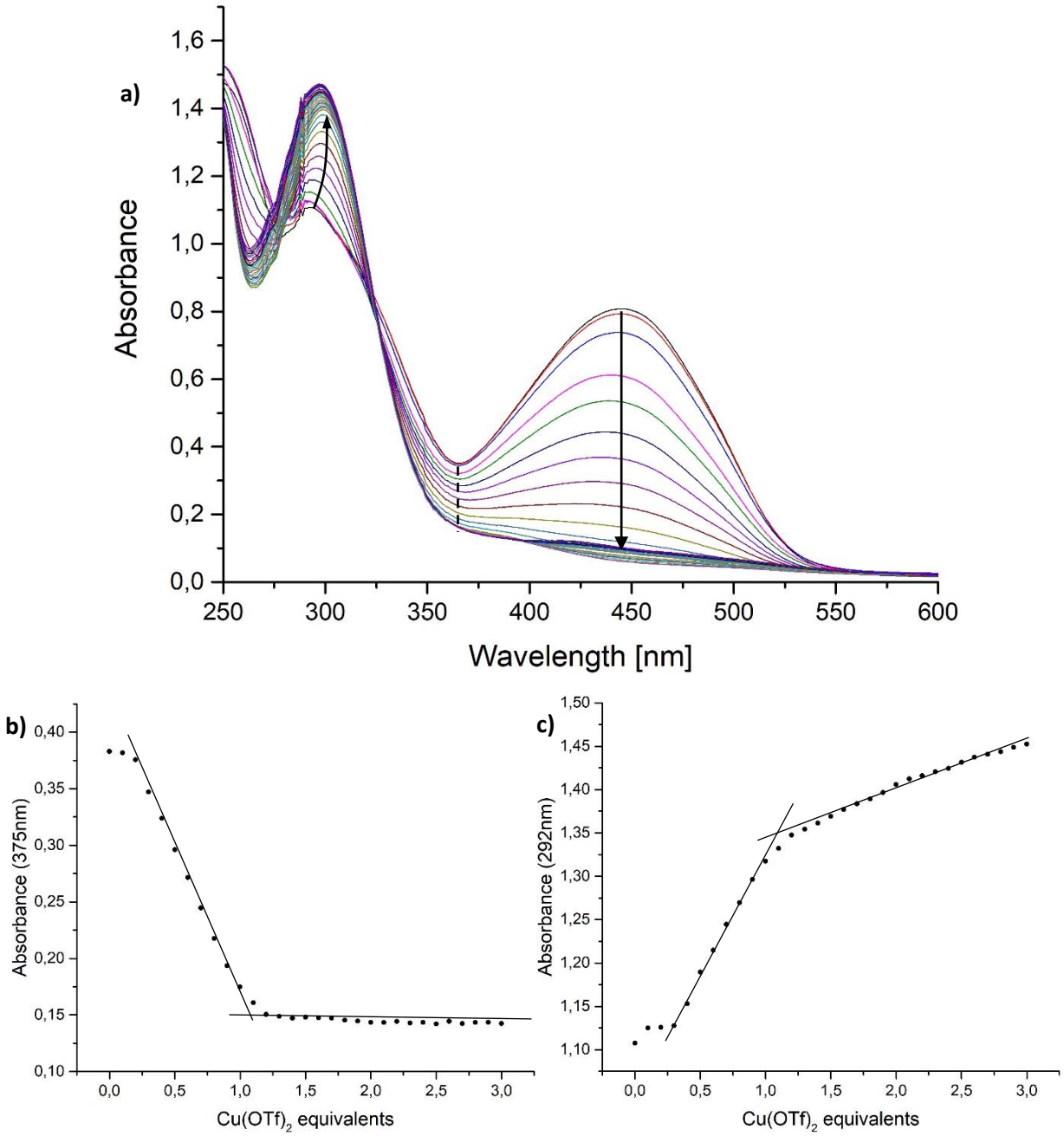

*Figure 125: a) UV-vis titration of ligand **26** ($5{,}74 \cdot 10^{-5}$ M in THF) with $CuOTf_2$-aliquots (0.1 equiv. each); evolution of the absorbance at b) 375 nm and c) 292 nm over the course of the titration. The spectra differ slightly from those in Figure 119 in the UV-region as the titration was done in BHT-stabilised THF.*

The plateau at 1.2 equiv. and the evolution of the 292 nm-band prove that the ligand and the metal indeed form a metallopolymer and not a discrete 1:1 complex, otherwise we should see significant changes in the spectra at >1.2 equiv. (Figure 126). The impulsion at the beginning of the titration and the reaching of the plateau at 1.2 instead of 1.0 equiv. indicate that, at this concentration, the complex is in equilibrium with free **26** and $Cu(OTf)_2$, so that a slight excess of metal is needed to drive the metallopolymer formation. From 0.2 to 1.2 equiv. the spectra evolve gradually, as seen by the presence of the isobestic point at 329 nm, and do not reveal any intermediate species.[184]

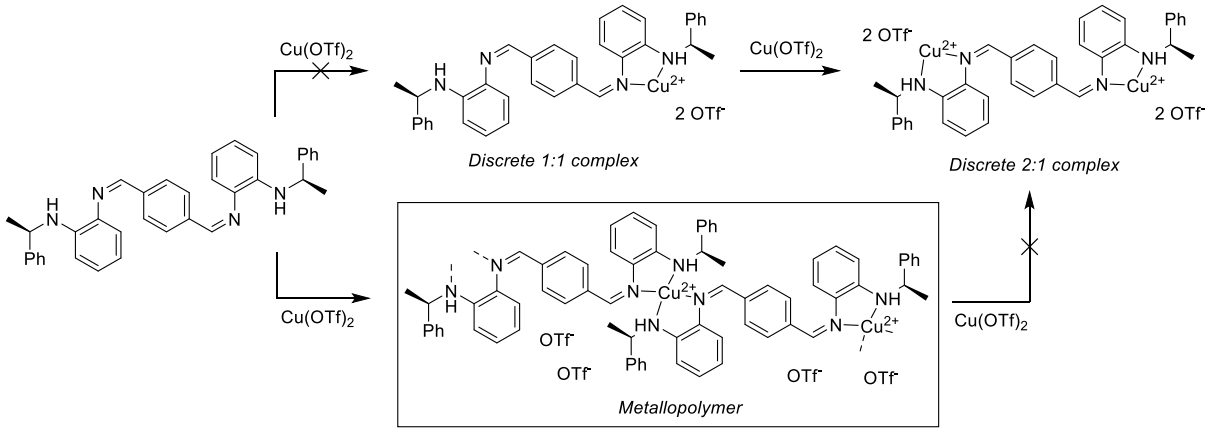

*Figure 126: Pathway for the $Cu(OTf)_2$-complexation of **26**. The ligand does not form a mononuclear complex but a metallopolymer, as seen by the absence of changes in the UV-vis spectra after addition of 1.2 equiv. of metal.*

Titration of the **26** with $Ni(BF_4)_2$ (Figure 127) and $Zn(OTf)_2$ (Figure 128) resulted only in minor changes of the UV-vis-spectrum, apparently the complex is not formed at this concentration. This is surprising since we obtained the UV-vis-spectra of **26-Zn(OTf)$_2$** and **26-Ni(BF$_4$)$_2$** (see Figure 119), by dissolution of the isolated complexes, at the same concentration. There is probably a kinetic issue, either preventing the complex from formation during the titration or from dissociation when dissolving the isolated complex.

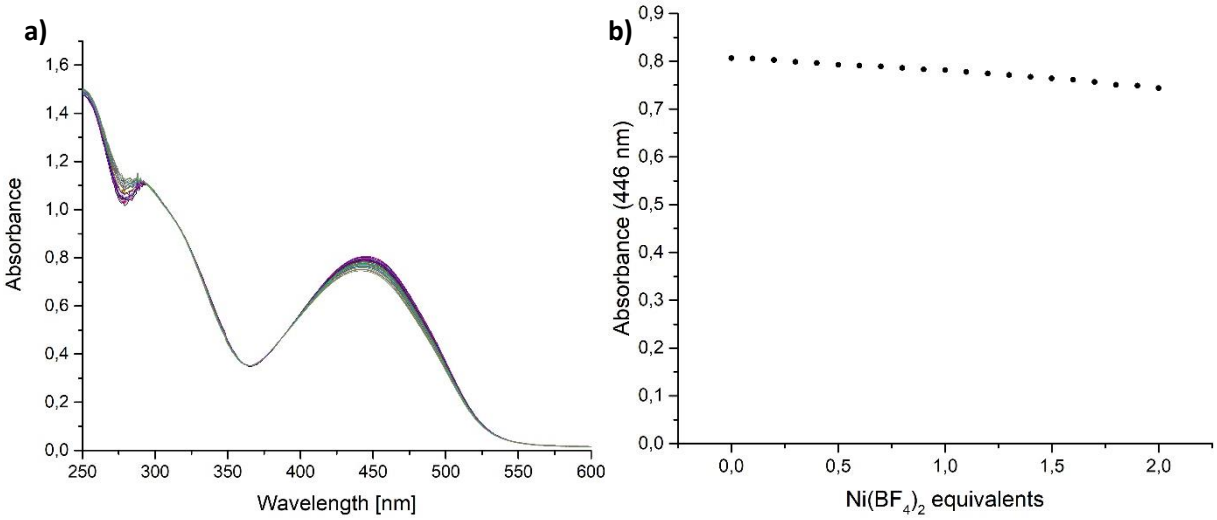

*Figure 127: a) UV-vis titration of ligand **26** ($5{,}74 \cdot 10^{-5}$ M in THF) with $Ni(BF_4)_2$-aliquots (0.1 equiv. each), b) evolution of the absorbance at 446 nm over the course of the titration.*

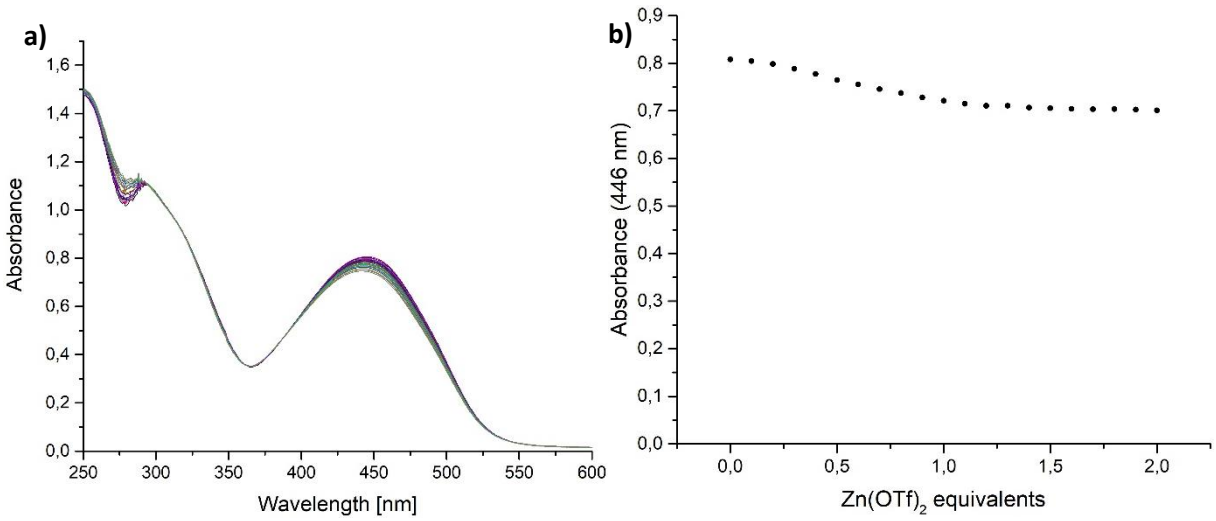

*Figure 128: a) UV-vis titration of ligand **26** ($5{,}74 \cdot 10^{-5}$ M in THF) with $ZnOTf_2$-aliquots (0.1 equiv. each), b) evolution of the absorbance at 446 nm over the course of the titration.*

(d) Circular Dichroism

Next, we measured circular dichroism for **26** and its metal complexes; the spectra are shown in Figure 129. Similar to the iminoalcohols and -amine, the ligand exhibits a weak negative CD-band at 300 nm; there is also a broad band around 440 nm. Complexation with metals makes the 440 nm-band disappear, as in UV, and the 300 nm-band's intensity decreases.

We know from the UV-vis studies in chapter III.2.2.3(a) that the aniline and bis-imine moieties in the complexed ligand are not conjugated anymore. Therefore, the complexed ligand probably is not planar, but the absence of strong CD features indicates that the complexes' conformation either is not chiral, or it doesn't have a significant preference for a chiral conformer over its mirror image in solution. We know that first-row d-block metals usually are quite flexible in their coordination mode. Therefore, it might be reasonable to presume that in solution the metals bind to two ligands in various distorted modes. Those different structures may give rise to both positive or negative CD signals, the CD spectrum in Figure 129 would then represent the sum of the contributions of those different conformations.

This hypothesis is supported by an interesting tendency: while Cu(II) and Ni(II) give weaker but still negative bands, Cu(I) and Zn(II) switch to a positive sign. The latter are known to favour a tetrahedral coordination sphere while Cu(II) and Ni(II) tend to make planar structures. This might be an indication of the influence of the coordination sphere on the complexes' structure: the tetrahedral mode might cause a structure change in the chromophore leading to the opposite helicity, while a planar coordination mode rather preserves the initial chromophore structure. If the metals indeed have a certain degree of freedom in their coordination mode, it would not be surprising to have various different conformations causing CD signals of opposite signs in one sample. This may apply also to the complexes from the ditopic iminoamine- and alcohols.

Therefore, it might be interesting to study the effect of less flexible 2nd or 3rd-row d-block metals on the CD spectrum. Moreover, since the conformational flexibility is favoured by the high degree of freedom in solution, it might also be interesting to perform CD in the solid state.

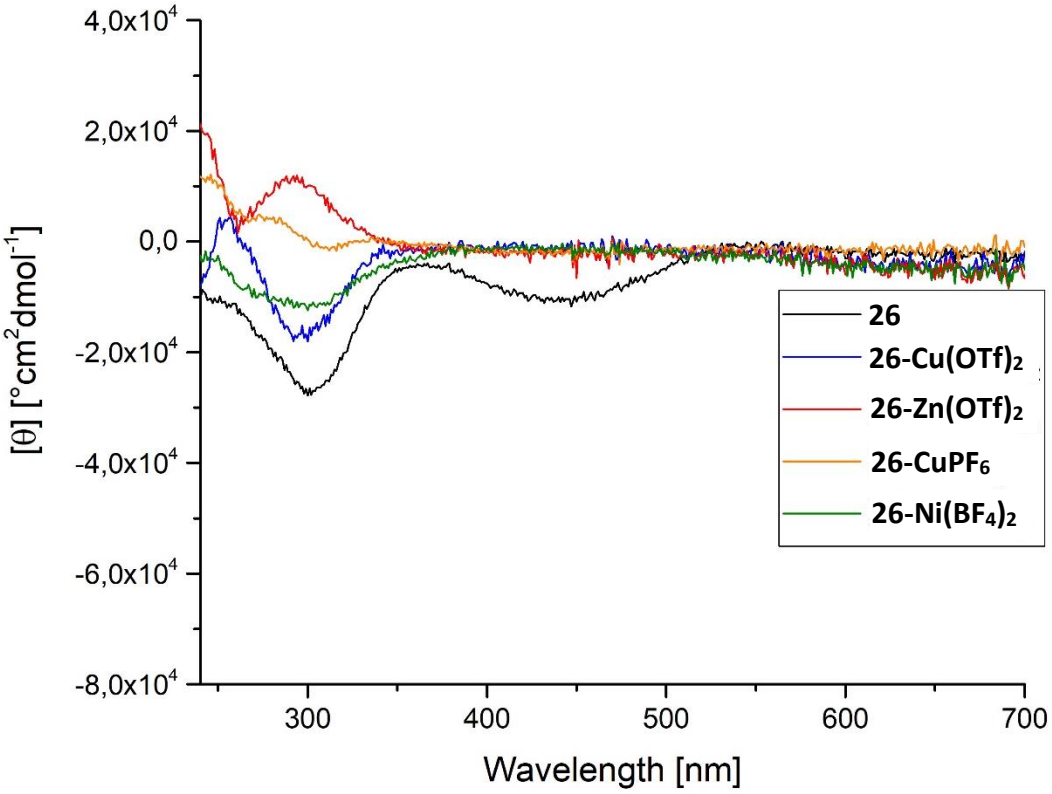

*Figure 129: CD spectra of **26** and its $CuPF_6$-, $Ni(BF_4)_2$-, $Cu(OTf)_2$- and $Zn(OTf)_2$-complexes in THF, 2.7-4·10^{-5} M.*

Finally, we also have to consider another factor possibly influencing the CD signal. The metal ion must be a chiral centre in these homoleptic complexes, except if it is in a perfect square planar coordination mode. As the metal is coordinated to the chromophore, it is not only proximate but also electronically connected to it. This can have an influence on the chromophore's CD activity, independently of any coordination-induced change of the chromophore's structure.[185]

III.3 Conclusion on chiral metallopolymers in SFG

In summary, we have developed a new type of ditopic, bis-imine ligands based on chiral aminoalcohols and diamines. The ligands and their complexes with Cu(I), Cu(II) and in parts also Zn(II) and Ni(II) have been characterised by IR, UV-vis and CD spectroscopy. While the aminoalcohol-based ligands form metallopolymers only with Cu(I) in the solid state, except complex **19f-Cu(OTf)$_2$**, the DACH- and dianiline-based ones form metallopolymers also with the +II-metals. In addition, we have shown through a UV-vis titration that **26-CuOTf$_2$** also forms a metallopolymer in solution. All compounds have an intense absorption band close to 300 nm in UV-vis spectroscopy but bear only moderate features in CD. The complexes mostly have less intense CD-bands than the corresponding ligands alone, indicating that, if the coordination of the metal induces a chiral conformation of the ligand's chromophore, it doesn't favour one conformer over its mirror image when in solution. Ligand **26** bears also some peculiar features in UV-vis which have given us information about the extent of the e^--delocalisation in the free and in the complexed ligand.

Furthermore, we have been able to perform chiral SFG experiments on complexes of ligands **19f** and **23**. Despite the persistence of a PPP-signal, probably due to complex decomposition on moisture, the bis-imine scaffold proves to be a promising structure for the study of SFG on chiral metallopolymers. In future work we will apply the water-stable complexes derived from ligand **26** in SFG microscopy, in order to circumvent the hydrolysis problems encountered with the ditopic iminoalcohols and -amines. We will also extend the spectroscopic studies (UV-vis, CD) to solid films of the bis-imines to see if there are difference to the liquid phase. This is especially interesting concerning the features in CD, as the activity of complexes from bisoxazoline **18** in SFG has been correlated to their intense activity in CD so far. From this, we hope to gain more insights into the origin of the SFG signal in chiral metallopolymers.

IV : Experimental Part

All reactions were performed at air using technical grade solvents unless specified otherwise. Dry solvents for reactions were purchased from Acros or Aldrich and used without further purification. O_2-free solvents were degassed using standard techniques. Substrates for catalysis (benzaldehyde and derivatives) and (*R*)-(+)-1-Phenylethylamine were distilled prior to use and stored at 4°C under inert atmosphere. All other reagents were used without further purification. Amino alcohols used in catalysis and metal complexes from ditopic iminoalcohols/-amine were stored in a N_2-filled glovebox.

NMR spectra were recorded on a Bruker Avance III HD 500 MHz (equipped with a CPPBBO "Prodigy" cryo-probe) and a Bruker Avance I 300 MHz spectrometer, with the residual signal of the NMR solvent as reference.[186] ^{1}H DOSY NMR spectra were recorded on a Bruker Avance III 600 MHz spectrometer. Electrospray ionization mass spectra (ESI-MS) were recorded on a Bruker microTOF Q. Fourier-transformed Infrared spectra (FTIR) were recorded on a PerkinElmer Spectrum Two equipped with a UATR Two module. UV-vis-spectra were recorded on an Agilent Technologies Cary 100 UV-vis spectrometer. Circular dichroism spectra were recorded at 16 °C on a Jasco J-1700. THF was distilled prior to use in UV-vis/CD spectroscopy and stored under argon; water-sensitive compounds were analysed in dry THF obtained by distillation over Na/Benzophenone. Other dry solvents (MeOH, DCM) were purchased from Acros or Aldrich and used without further purification.

Details concerning GC analysis and IR-monitored kinetic runs are specified in the respective sections.

IV.1 Procedures for Chapters I & II

IV.1.1 Synthesis

IV.1.1.1 Ephedrine-derived ligands

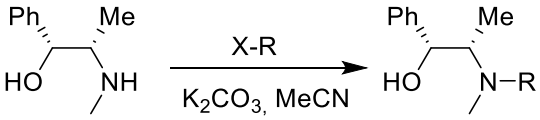

(1*R*,2*S*)-*N*-benzylephedrine **(-)-NBE**

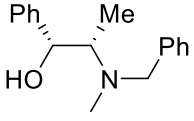

(-)-NBE was prepared by a modified literature protocol.[94] (-)-Ephedrine (5 g, 30.3 mmol, 1 equiv) and BnBr (3.95 mL, 33.3 mmol, 1.1 equiv) were dissolved in MeCN (50 mL), then K_2CO_3 (12.6 g, 90.8 mmol, 3 equiv) was added and the mixture stirred at reflux for 3h. After letting the mixture cool down to rt, water (50 mL) was added, the phases separated and the aqueous phase washed with AcOEt (2x40 mL). The combined organic phases were dried over Na_2SO_4 and evaporated. The residue was taken in DCM, placed on a plug of SiO_2 gel (ca. 300 mL, 4.5 cm height), washed with 300 mL DCM and then eluted with 800 mL DCM/MeOH 97.5/2.5. Evaporation yielded a white amorphous solid. 6.622 g, 86% yield. Spectral properties are identical with literature data.[94]

(1*R*,2*S*)-*N*-methylephedrine **(-)-NME**

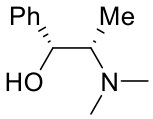

(-)-NME was prepared from (-)-ephedrine, formaldehyde and formic acid in an Eschweiler-Clarke reduction following a reported procedure.[92] Spectral properties are identical with literature data.

(1*R*,2*S*)-*N*-*n*-butylephedrine **(-)-N*n*BE**

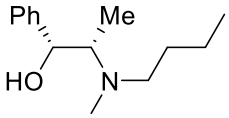

(-)-N*n*BE was prepared from (-)-ephedrine (3.0 g, 18.2 mmol, 1 equiv), *n*butyl bromide (2.9 mL, 27.2 mmol, 1.5 equiv), K_2CO_3 (7.53 g, 54.5 mmol, 3 equiv) in MeCN (30 mL) following the procedure for **(-)-NBE** (30h reflux).[93] The product was purified by direct elution with DCM/MeOH 95/5 on 40 mL SiO_2 gel. Evaporation yielded a colourless oil. 3.95 g, 98% yield. Spectral properties are identical with literature data.[98]

(1*R*,2*S*)-*N*-(2-naphtyl)ephedrine **(-)-N2NE**

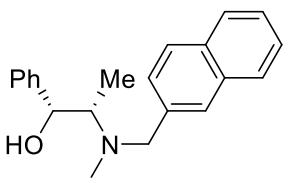

(-)-N2NE was prepared from (-)-ephedrine (2.24 g, 13.6 mmol, 1 equiv), 2-(bromomethyl)naphthalene (3 g, 13.6 mmol, 1 equiv), K_2CO_3 (5.63 g, 40.7 mmol, 3 equiv) in MeCN (30 mL) following the procedure for **(-)-NBE**. Purification over 40 mL SiO_2 gel, direct elution of the product with DCM/MeOH 95/5. Evaporation yielded a white amorphous solid. 4.03 g, 97% yield. Spectral properties are identical with literature data.[187]

(1*R*,2*S*)-*N*-(4-methylbenzyl)ephedrine **(-)-Me-NBE**

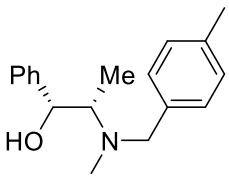

(-)-Me-NBE was prepared from (-)-ephedrine (3 g, 18.2 mmol, 1 equiv), 4-methylbenzyl bromide (3.36 g, 18.2 mmol, 1 equiv), K_2CO_3 (7.53 g, 54.5 mmol, 3 equiv) in MeCN (30 mL) following the procedure for **(-)-NBE**. After aqueous work-up, the product was recrystallised from AcOEt/Hexane at 0°C. White crystalline solid, 4.77 g, 98% yield.

^{1}H NMR (500 MHz, $CDCl_3$): δ = 7.36-7.30 (*o*- and *mCH*$_{arom}$, m, 4H), 7.26-7.22 (*p*CH$_{arom}$, m, 1H), 7.15 (C*H*$_{arom}$-C-CH$_2$, d, *J* = 8.2 Hz, 2H), 7.12 (C*H*$_{arom}$-C-CH$_3$, *J* = 8.4 Hz, 2H), 4.89 (O-C*H*, d, *J* = 4.7 Hz, 1H), 3.61 (N-C*H*$_2$, d, *J* = 13.3 Hz, 1H), 3.56 (N-C*H*$_2$, d, *J* = 13.3 Hz, 1H), 2.93 (N-C*H*, qd, *J* = 6.8, 4.7 Hz, 1H), 2.35 (C*H*$_3$-C$_{arom}$, 3H), 2.19 (N-C*H*$_3$, s, 3H), 0.98 (N-CH-C*H*$_3$, d, *J* = 6.8 Hz, 3H) ppm.

^{13}C NMR (125 MHz, $CDCl_3$): δ = 142.6 (O-CH-*C*$_{arom}$), 136.70 (*C*$_{arom}$-CH$_3$) 136.45 (*C*$_{arom}$-CH$_2$), 129.1 (*C*H$_{arom}$-C$_{arom}$-CH$_3$), 128.8 (*C*H$_{arom}$-C$_{arom}$-CH$_2$), 128.1 (*mC*H$_{arom}$), 127.1 (*pC*H$_{arom}$), 126.4 (*o*CH$_{arom}$) 73.6 (O-*C*H), 63.4 (N-*C*H), 59.0 (N-*C*H$_2$), 38.8 (N-*C*H$_3$), 21.2 (*C*H$_3$-C$_{arom}$), 10.1 (N-CH-*C*H$_3$) ppm.

FTIR (ATR): $\bar{\nu}_{max}$ = 3200, 3088, 3046, 3020, 2969, 2935, 2905, 2855, 2794, 1601, 1585, 1448, 1417, 1379, 1358, 1338, 1317, 1295, 1250, 1208, 1173, 1154, 1140, 1119, 1107, 1063, 1028, 1019, 989, 970, 950, 933, 915, 854, 815, 781, 764, 738, 700, 674, 644, 559, 506, 487, 440, 414 cm^{-1}.

MS (ESI+): *m/z* = 270.1881 ([*M* + H$^+$], 100%).

$[\alpha]_D^{20}$(EtOH, *c* = 1.00 g/100 mL) = +11.0 cm³g^{-1}dm^{-1}.

(1*R*,2*S*)-*N*-(4-methylbenzyl)ephedrine **(-)-Br-NBE**

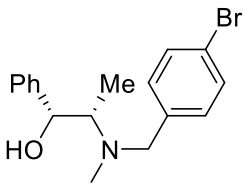

(-)-Br-NBE was prepared from (-)-ephedrine (3 g, 18.2 mmol, 1 equiv), 4-bromobenzyl bromide (4.54 g, 18.2 mmol, 1 equiv), K_2CO_3 (7.53 g, 54.5 mmol, 3 equiv) in MeCN (30 mL) following the procedure for **(-)-NBE**. After aqueous work-up, the product was recrystallised from DCM/Hexane at 0 °C. White crystalline solid, 4.418 g, 73%. Spectral properties are identical with literature data.[188]

(1*R*,1'*R*,2*S*,2'*S*)-2,2'-(decane-1,10-diylbis(methylazanediyl))bis(1-phenylpropan-1-ol) **15**:

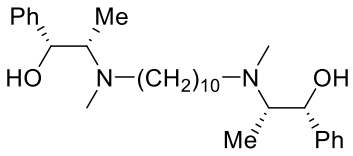

(-) Ephedrine (2.05 g, 10.2 mmol, 2 equiv), 1,10-diiododecane (2.00 g, 5.10 mmol, 1 equiv) and K_2CO_3 (2.81 g, 20.3 mmol, 4 equiv) were taken in anhydrous DMF (25 mL) and stirred at rt for 48h under argon. The mixture was concentrated under reduced pressure, then water (50 mL) was added. The mixture was extracted with DCM (3x50 mL), the combined org. phases were dried over Na_2SO_4 and evaporated. The crude product was purified by column chromatography (NEt_3-treated SiO_2, cyclohexane/AcOEt 60:40) to yield a colourless oil. 1.34g, 56% yield.

^{1}H NMR (500 MHz, $CDCl_3$): δ = 7.32 (*o*- and *m*C*H*$_{arom}$, d, *J* = 4.4 Hz, 8H), 7.23 (*p*C*H*$_{arom}$, m, *J* = 4.4 Hz, 2H), 4.85 (O-C*H*, d, *J* = 4.1 Hz, 2H), 2.82 (N-C*H*, qd, *J* = 6.8, 4.1 Hz, 2H), 2.50 (C*H*$_2$-N, dt, *J* = 13.2, 7.1 Hz, 2H), 2.42 (C*H*$_2$-N, dt, *J* = 13.2, 7.1 Hz, 2H), 2.27 (C*H*$_3$-N, s, 6H), 1.27 ((C*H*$_2$)$_6$-CH$_2$-CH$_2$-N, s, 12H), 1.48 (C*H*$_2$-CH$_2$-N, tt, *J* = 7.1, 7.1 Hz, 4H), 0.86 (C*H*$_3$-CH, d, *J* = 6.8 Hz, 6H) ppm.

^{13}C NMR (125 MHz, $CDCl_3$): δ = 142.5 (*C*$_{arom}$), 128.0 (*m*CH$_{arom}$), 126.9 (*p*CH$_{arom}$), 126.2 (*o*CH$_{arom}$), 72.9 (O-*C*H), 63.6 (N-*C*H), 55.1 (*C*H$_2$-N), 39.1 (N-CH$_3$), 29.7 (*C*H$_2$), 27.6 (*C*H$_2$), 27.4 (*C*H$_2$), 10.3 (CH-*C*H$_3$) ppm.

FTIR (ATR): $\bar{\nu}_{max}$ = 3404, 3085, 3061, 3025, 2924, 2851, 2794, 1603, 1493, 1450, 1370, 1330, 1257, 1195, 1121, 1041, 1026, 996, 962, 914, 885, 834, 793, 742, 699, 677, 639, 553 cm^{-1}.

MS (ESI+): *m/z* = 469.3804 ([*M* + H$^+$], 100%).

$[\alpha]_D^{20}$(EtOH, *c* = 0.952 g/100 mL) = -3.68 cm³g^{-1}dm^{-1}.

(1*R*,1'*R*,2*S*,2'*S*)-2,2'-((1,4-phenylenebis(methylene))bis(methylazanediyl))bis(1-phenylpropan-1-ol) **16:**

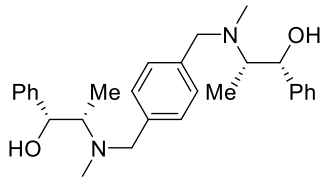

16 was prepared from (-)-ephedrine (4.10 g, 24.8 mmol, 2 equiv), α,α'-Dibromo-*p*-xylene (3.27 g, 12.4 mmol, 1 equiv) and K_2CO_3 (13.7 g, 99.2 mmol, 8 equiv) in MeCN (50 mL) following the procedure for **(-)-NBE**. The resulting oily product was filtered over a plug of SiO_2 and eluted with AcOEt, then evaporated under reduced pressure to yield a colourless liquid which solidifies over time to a white solid. 5.09 g, 95% yield.

^{1}H NMR (500 MHz, $CDCl_3$): δ = 7.33 (*o*- and *m*C*H*$_{arom,}$ d, *J* = 4.4 Hz, 8H), 7.29-7.23 (*p*C*H*$_{arom}$, m, 2H), 7.17 (C*H*$_{arom}$-C-CH$_2$, s, 4H), 4.88 (O-C*H*, d, *J* = 4.7 Hz, 2H), 3.61 (N-C*H*$_2$, d, *J* = 20.8 Hz, 2H), 3.59 (N-C*H*$_2$, d, *J* =

20.8 Hz, 2H), 2.93 (N-C*H*, qd, *J* = 6.9, 4.7 Hz, 2H), 3.43 (O*H*, br s, 2H), 2.19 (N-CH_3, s, 6H) 0.99 (CH-CH_3, d, *J* = 6.9 Hz, 6H) ppm.

^{13}C NMR (125 MHz, $CDCl_3$): δ = 142.6 (*C*-CH-O), 138.3 (*C*-CH_2-N), 128.8 (*C*H_{arom}-C-CH_2), 128.1 (*m*CH_{arom}), 127.1 (*p*CH_{arom}), 126.3 (*o*CH_{arom}), 73.8 (O-*C*H), 63.5 (N-*C*H), 59.1 (N-*C*H_2), 38.8 (N-*C*H_3), 10.1 (CH-*C*H_3) ppm.

FTIR (ATR): $\bar{\nu}_{max}$ = 3086, 3054, 2979, 2939, 2875, 1602, 1512, 1492, 1449, 1425, 1385, 1369, 1344, 1249, 1215, 1163, 1119, 1065, 1032, 1007, 988, 964, 939, 861, 842, 822, 796, 747, 736, 701, 672, 653, 640, 600, 540, 476, 441, 412 cm^{-1}.

MS (ESI+): *m/z* = 433.2850 ([*M* + H$^+$], 100%).

$[\alpha]_D^{20}$(EtOH, *c* = 1.09 g/100 mL) = +18.3 cm^{3}g^{-1}dm^{-1}.

*IV.1.1.2 Camphor-derived ligand **9***

(1*R*,2*S*,6*R*,7*S*)-1,10,10-Trimethyl-4-oxo-5-aza-3-oxatricyclo[5.2.1.0]decane **8**:

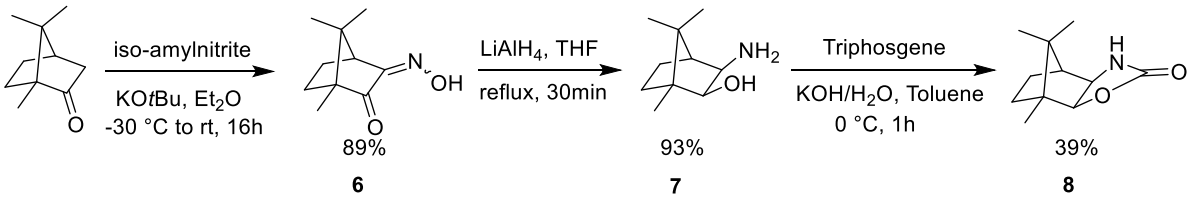

8 was synthesised in 3 steps from (+)-camphor following a reported procedure.[149,150] It was additionally purified by recrystallisation from AcOEt/Hexane. Spectral properties are identical with literature data.

(3a*R*,4*S*,7*S*,7a*S*)-7,8,8-trimethyl-3-(4-(((3a*R*,4*S*,7*R*,7a*S*)-7,8,8-trimethyl-2-oxohexahydro-4,7-methanobenzo[d]oxazol-3(2H)-yl)methyl)benzyl)hexahydro-4,7-methanobenzo[d]oxazol-2(3H)-one **8a:**

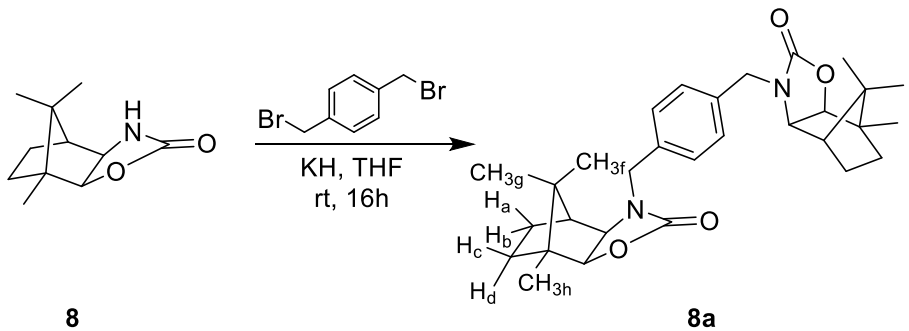

8 **8a**

Potassium hydride 35% w/w in oil (892 mg, 7.78 mmol, 4 equiv) was placed in an oven-dried two-necked 100 mL flask under argon and washed twice with pentane, then anhydrous THF (40 mL) was added, followed by **8** (760 mg, 3.89 mmol, 2 equiv). The mixture stirred at rt for 10 min during which H_2 bubbling occurred, then α,α'-dibromo-p-xylene (514 mg, 1.95 mmol, 1 equiv) was added. The mixture stirred overnight to give a white suspension, which was diluted with DCM (40 mL) and

quenched carefully with H_2O (40 mL). Brine (20 mL) was added after H_2 evolution had ceased, the phases were separated and the aqueous phase extracted with DCM (2x40 mL). The combined organic phases were dried over anhydrous Na_2SO_4 and evaporated to give a white crystalline solid. 1.15 g, quantitative yield.

^{1}H NMR (500 MHz, $CDCl_3$): δ = 7.28 (CH_{arom}, s, 4H), 4.67 (N-CH_2, d, J = 15.0 Hz, 2H), 4.22 (O-CH, d, J = 8.1 Hz, 2H), 4.12 (N-CH_2, d, J = 15.0 Hz, 2H), 3.49 (N-CH, d, J = 8.1 Hz, 2H), 1.85 (N-CH-CH, d, J = 4.6 Hz, 2H), 1.69 (H_a, tt, J = 12.3, 4.4 Hz, 2H), 1.51 (H_c, ddd, J = 12.9, 12.2, 3.9 Hz, 2H), 1.03 (CH_{3h}, s, 6H), 0.98 (CH_{3f} + H_d, m, 8H), 0.86 (CH_{3g} + H_b, m, 8 H) ppm.

^{13}C NMR (125 MHz, $CDCl_3$): δ = 158.7 (C=O), 135.8 (C_{arom}), 128.9 (CH_{arom}), 85.3 (CH-O), 63.6 (CH-N), 48.5 (C-$CH_{3g/f}$), 46.8 (CH_2-N), 46.5 (C-CH_{3h}), 45.6 (CH-CH-N), 31.9 ($CH_{2\ c/d}$), 24.9 ($CH_{2\ a/b}$), 23.3 ($CH_{3g\ or\ f}$), 19.4 ($CH_{3g\ or\ f}$), 10.8 (CH_{3h}) ppm.

FTIR (ATR): $\bar{\nu}_{max}$ = 3007, 2963, 2930, 2880, 1729, 1515, 1485, 1444, 1416, 1327, 1288, 1236, 1114, 1089, 1040, 962, 931, 850, 757, 692, 653, 609, 550 cm^{-1}.

MS (ESI+): m/z = 493.160 ([M + H$^+$], 100%).

$[\alpha]_D^{20}$(DCM, c = 0.13 g/100 mL) = -85.4 cm^{3}g^{-1}dm^{-1}.

(1S,2S,3R,4S)-3-((4-((((1S,2R,3S,4R)-3-hydroxy-4,7,7-trimethylbicyclo[2.2.1]heptan-2-yl)(methyl)amino)methyl)benzyl)(methyl)amino)-1,7,7-trimethylbicyclo[2.2.1]heptan-2-ol **9**:

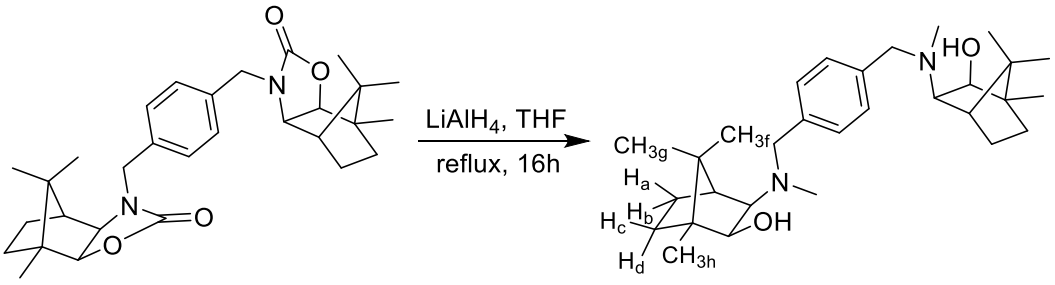

8 **9**

9 (1.10 g, 2.23 mmol, 1 equiv) was added in one portion to a solution of $LiAlH_4$ (847 mg, 22.3 mmol, 10 equiv) in anh. THF (30 mL), then the mixture was refluxed overnight. The mixture was let to cool to rt and then carefully quenched with AcOEt (5 mL). Saturated aqueous Na_2SO_4 (5 mL) was added and the mixture let to stir until a fine white, easy-to-stir precipitate had formed. The mixture was filtered over celite and filter cake washed with AcOEt (3x15 mL). The filtrate was dried over Na_2SO_4 and evaporated under reduced pressure. The product was recrystallised at -20 °C from boiling MeOH to give a white solid. 575 mg, 55% yield.

^{1}H NMR (500 MHz, $CDCl_3$): δ = 7.23 (CH_{arom}, s, 4H), 4.50 (OH, br s, 2H), 4.20-2.96 (N-CH_2, br, 4H) 3.54 (CH-O, d, J = 6.9 Hz, 2H), 2.53 (CH-N, d, J = 7.1 Hz, 2H), 2.13 (N-CH_3, br s, 6 H), 2.10 (CH-CH-N, d, J = 3.9 Hz, 2H), 1.84-1.68 (H_a, m, 2H), 1.53-1.38 (H_c, m, 2H), 1.13 (CH_{3f}, br s, 6H), 1.08-0.97 (H_b + H_d, m, 4H), 1.00 (CH_{3h}, s, 6H), 0.79 (CH_{3g}, s, 6H) ppm.

^{13}C NMR (125 MHz, $CDCl_3$): δ = 137.6 (C_{arom}), 129.2 (CH_{arom}), 79.2 (CH-O), 73.6 (CH-N), 49.4 (C-CH_{3h}), 47.0 (N-CH$_3$), 46.8 (C-$CH_{3g/f}$), 32.4 ($CH_{2\ c/d}$), 28.2 ($CH_{2\ a/b}$), 22.2 (CH_{3g}), 21.1 (CH_{3f}), 11.7 (CH_{3h}) ppm. The N-CH$_2$ signal is not visible at rt.

FTIR (ATR): $\bar{\nu}_{max}$ = 3456, 2948, 2926, 2870, 2815, 2788, 1513, 1460, 1388, 1368, 1348, 1261, 1091, 1039, 1019, 930, 901, 814, 785, 587, 555, 513, 487, 433 cm^{-1}.

MS (ESI+): *m/z* = 469.3791 ([*M* + H^+], 100%).

$[\alpha]_D^{20}$(DCM, *c* = 1.28 g/100 mL) = -5.80 $cm^3g^{-1}dm^{-1}$.

IV.1.1.3 NBE-mimics for ^{1}H DOSY NMR

(4*S*,5*R*)-3,4-dimethyl-5-phenyloxazolidine **1**:

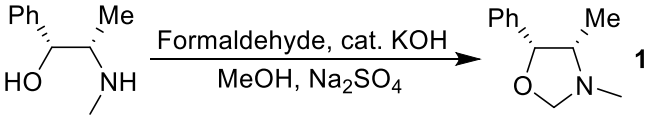

1 was prepared from (-)-ephedrine and formaldehyde following a literature procedure.[189] Spectral properties are identical with literature data.

(4*S*,5*R*)-3-benzyl-2,2,4-trimethyl-5-phenyloxazolidine **2**:

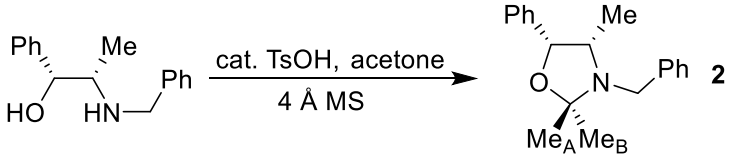

(1*R*,2*S*)-N-benzylnorephedrine[190] (413 mg, 1.71 mmol, 1 equiv) and TsOH·H_2O (9.77 mg, 51.3 µmol, 0.03 equiv) were dissolved in 10 mL dry acetone, then activated 4 Å MS were added. The mixture stirred under argon at reflux for 7 days (ca. 50% conversion in ^{1}H NMR), then the mixture was let to cool down to rt and evaporated. The product was taken in a small amount of DCM, placed on a plug of SiO_2 gel, and eluted with DCM. Evaporation yielded a slight yellow oil. 202 mg, 42% yield.

The ^{1}H and ^{13}C signals of Me_A and Me_B were attributed using NOESY NMR (cross-peaks between Me_B and the Ph and Me groups on the asymmetric carbon atoms; no cross-peaks with Me_A).

^{1}H NMR (500 MHz, $CDCl_3$): δ = 7.44-7.40 (N-CH_2-C-CH_{arom}, m, 2H), 7.40-7.35 (O-CH-C-CH_{arom}, m, 2H), 7.34-7.27 (CH_{arom}, m, 4H), 7.27-7.19 (CH_{arom}, m, 2H), 5.09 (C*H*-O, d, *J* = 7.3 Hz, 1H), 3.85 (N-CH_2-Ph, d, *J* = 14.7 Hz, 1H), 3.63 (N-CH_2-Ph, d, *J* = 14.6 Hz, 1H), 3.42 (C*H*-N, qd, *J* = 6.9, 6.3 Hz, 1H), 1.45 (Me_A, s, 3H), 1.37 (Me_B, s, 3H), 0.45 (CH_3-CH-N, d, *J* = 6.6 Hz, 3H) ppm.

^{13}C NMR (125 MHz, $CDCl_3$): δ = 141.2 (N-CH_2-*C*), 140.3 (O-CH-*C*), 128.23 (*C*H_{arom}), 128.18 (*C*H_{arom}), 127.9 (*C*H_{arom}), 127.6 (*C*H_{arom}), 127.4 (*C*H_{arom}), 126.8 (*C*H_{arom}), 95.1 (O-*C*-N), 80.7 (*C*H-O), 60.5 (*C*H-N), 51.7 (N-*C*H_2-Ph), 27.7 (Me_A), 21.3 (Me_B), 16.0 (*C*H_3-CH-N) ppm.

FTIR (ATR): $\bar{\nu}_{max}$ = 3086, 3063, 3027, 2975, 2929, 2883, 1604, 1586, 1494, 1454, 1373, 1315, 1294, 1259, 1218, 1186, 1143, 1094, 1079, 1061, 1042, 1027, 1006, 946, 909, 878, 858, 803, 750, 696, 667, 632, 586, 546, 523, 462 cm^{-1}.

MS (ESI+): *m/z* = 282.1866 ([*M* + H^+], 100%).

$[\alpha]_D^{20}$(EtOH, *c* = 1.05 g/100 mL) = -3.98 $cm^3g^{-1}dm^{-1}$.

IV.1.2 Catalysis

IV.1.2.1 General procedure – Aminoalcohol-catalysed addition of dialkylzincs to aromatic aldehydes

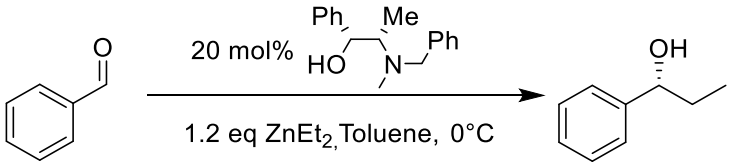

In an N_2-filled glovebox, (-)-NBE (23.7 mg, 20 mol%, 92.6 µmol) and a magnetic stirring bar were placed in an oven-dried vial, which was then closed with a septum-containing screwcap. The vial was put out of the glovebox and a 15% $ZnEt_2$ solution in toluene (0.5 mL, 1.2 equiv, 556 µmol) was added via syringe; gas evolution occurred. The mixture stirred for 10 min, then was cooled to 0 °C and the aromatic aldehyde (1 equiv, 463 µmol) was added via syringe. The yellow solution stirred overnight at 0 °C and turned colourless, then was quenched carefully with 3 M aqueous HCl in an ice-water bath under vigorous stirring. The isolated organic phase was diluted with toluene, dried over Na_2SO_4 and analysed by chiral stationary phase GC (cf. Table 14).

The ligand ee was adjusted by preparing appropriate mixtures of the (1*R*,2*S*)- and (1*S*,2*R*)-enantiomers. The reaction temperature was adapted and controlled standard with heating plates or a Huber TC45E cryostat equipped with a Pt 100 temperature probe. $ZnMe_2$ was used as a 1.2 M solution in toluene (0.5 mL, 1.2 equiv, 600 µmol), diluted to 1 M with dry toluene (0.1 mL), with adapted monotopic ligand (20 mol%, 100 µmol) and substrate quantities (1 equiv, 500 µmol). Reaction media with $ZnMe_2$ stayed colourless and were let to stir for 4 days (100% ligand ee), 7 days (80-5% ligand ee) or 30 days (4-1% ligand ee). Ditopic ligands were used in half the molar quantity (10 mol%, 46.3 µmol). Solid substrates were added to the ligand inside the glovebox. The vial was then closed, put outside the glovebox and the ZnR_2 solution was added via syringe at the appropriate temperature.

IV.1.2.2 Catalyst loading screening

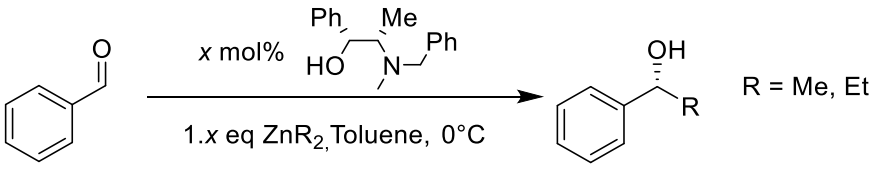

The general procedure was applied with adapted ligand and aldehyde quantities, as shown in tables Table 8 to Table 12. “x” refers the catalyst loading in mol%. ZnR_2 was kept at 0.5 mL unless the

amount of ligand fell below 5 mg, in which case the reaction was upscaled to 1, 1.5 or 8.0 mL. To keep the benzaldehyde concentration at 0.93 mol/L (with $ZnEt_2$) or 0.83 mol/L (with $ZnMe_2$), anhydrous toluene was added prior to aldehyde addition as indicated in the tables below.

Table 8: Product quantities for catalyst loading screening of NBE/Benzaldehyde.

X	**(-)-NBE**	**$ZnEt_2$, 15% in toluene (1,*x* equiv)**	**Benzaldehyde (1 equiv)**	**Toluene**
15	18.5 mg, 72.5 µmol	0.50 mL, 556 µmol	49 µL, 483 µmol	22 µL
10	12.9 mg, 50.5 µmol	0.50 mL, 556 µmol	52 µL, 505 µmol	43 µL
4	10.9 mg, 42.7 µmol	1.0 mL, 1.11 mmol	110 µL, 1.07 mmol	150 µL
1	11.2 mg, 44.0 µmol	8.0 mL, 8.89 mmol	0.90 mL, 8.80 mmol	1.5 mL

***x* [mol%]**	**(-)-NBE**	**$ZnMe_2$, 1 M in toluene (1,*x* equiv)**	**Benzaldehyde (1 equiv)**	**Toluene**
15	16.7 mg, 65.2 µmol	0.50 mL, 500 µmol	44 µL, 435 µmol	22 µL
10	11.6 mg, 45.5 µmol	0.50 mL, 500 µmol	46 µL, 455 µmol	46 µL
5	12.2 mg, 47.6 µmol	1.0 mL, 1.00 mmol	97 µL, 952 µmol	140 µL
2.5	6.2 mg, 24 µmol	1.0 mL, 1.00 mmol	99 µL, 976 µmol	175 µL

Table 9: Product quantities for catalyst loading screening of NBE/pCF3-Benzaldehyde.

***x* [mol%]**	**(-)-NBE**	**$ZnEt_2$, 15% in toluene (1,*x* equiv)**	***p*CF_3-Benzaldehyde (1 equiv)**	**Toluene**
15	18.5 mg, 72.5 µmol	0.50 mL, 556 µmol	66 µL, 483 µmol	22 µL
10	12.9 mg, 50.5 µmol	0.50 mL, 556 µmol	69 µL, 505 µmol	43 µL
5	13.5 mg, 52.3 µmol	1.0 mL, 1.11 mmol	145 µL, 1.06 mmol	145 µL
2.5	10.4 mg, 40.7 µmol	1.5 mL, 1.67 mmol	223 µL, 1.63 mmol	260 µL

Table 10: Product quantities for catalyst loading screening of NBE/o,o',p-TriMe-Benzaldehyde.

***x* [mol%]**	**(-)-NBE**	**$ZnEt_2$, 15% in toluene (1,*x* equiv)**	**o,o',p-TriMe-Benzaldehyde (1 equiv)**	**Toluene**
15	18.5 mg, 72.5 µmol	0.50 mL, 556 µmol	65 µL, 483 µmol	22 µL
10	12.9 mg, 50.5 µmol	0.50 mL, 556 µmol	68 µL, 505 µmol	43 µL

5	13.5 mg, 52.3 µmol	1.0 mL, 1.11 mmol	143 µL, 1.06 mmol	145 µL
2.5	10.4 mg, 40.7 µmol	1.5 mL, 1.67 mmol	219 µL, 1.63 mmol	260 µL

Table 11: Product quantities for catalyst loading screening of NBE/pCN-Benzaldehyde.

***x* [mol%]**	**(-)-NBE**	**$ZnEt_2$, 15% in toluene (1,*x* equiv)**	**pCN-Benzaldehyde (1 equiv)**	**Toluene**
15	18.5 mg, 72.5 µmol	0.50 mL, 556 µmol	63.4 mg, 483 µmol	22 µL
10	12.9 mg, 50.5 µmol	0.50 mL, 556 µmol	66.2 µL, 505 µmol	43 µL
5	13.5 mg, 52.3 µmol	1.0 mL, 1.11 mmol	139 mg, 1.06 mmol	145 µL
2.5	10.4 mg, 40.7 µmol	1.5 mL, 1.67 mmol	213 µL, 1.63 mmol	260 µL

*Table 12: Product quantities for catalyst loading screening of ditopic Ephedrine **16**/Benzaldehyde.*

***x* [mol%]**	**X**	**$ZnEt_2$, 15% in toluene (1,*x* equiv)**	**Benzaldehyde (1 equiv)**	**Toluene**
7.5	15.7 mg, 36.2 µmol	0.50 mL, 556 µmol	49 µL, 483 µmol	22 µL
5	10.9 mg, 25.3 µmol	0.50 mL, 556 µmol	66 µL, 505 µmol	43 µL
2.5	11.5 mg, 26.5 µmol	1.0 mL, 1.11 mmol	108 µL, 1.06 mmol	145 µL
1.25	8.8 mg, 20.3 µmol	1.5 mL, 1.67 mmol	165 µL, 1.63 mmol	260 µL

***x* [mol%]**	**X**	**$ZnMe_2$, 1.2 M in toluene (1,*x* equiv)**	**Benzaldehyde (1 equiv)**	**Toluene**
7.5	16.9 mg, 39.1 µmol	0.50 mL, 600 µmol	53 µL, 522 µmol	162 µL
5	11.8 mg, 27.3 µmol	0.50 mL, 600 µmol	55 µL, 545 µmol	154 µL
2.5	12.4 mg, 28.6 µmol	1.0 mL, 1.20 mmol	116 µL, 1.14 mmol	368 µL
1.25	9.5 mg, 22.0 µmol	1.5 mL, 1.80 mmol	178 µL, 1.76 mmol	611 µL

IV.1.2.3 Competitive reactions for Hammett Plots

The competitive reactions were performed following the general procedure, with a reversed addition order. The two aldehydes were first added to the ligand in half quantities each (0.5 equiv, 417 µmol), followed by dry toluene (0.1 mL). 1.2 M $ZnMe_2$ (0.5 mL, 1.2 equiv, 600 µmol) was then added at 0°C. A 75 µL-aliquot was taken and quenched quickly after 120 min (or 20 min for some exceptions, see Table 13), diluted with 225 µL toluene, dried over Na_2SO_4 and injected directly in GC. Conversion and ee_P were determined by GC from the integrated signals of the respective aldehyde and its *R*- and *S*-

products. The response of the aldehyde and the chiral alcohols to the FID detector were approximated to be equal since their number of carbon atoms differ only slightly, which allowed us to calculate the conversion following equation (47):

$$Conversion = 1 - \frac{Area(aldehyde)}{Area(aldehyde) + Area(R\ product) + Area(S\ product)} \quad (47)$$

The initial rates v_{0X} and v_{0H} were obtained from equation (48):

$$v_{0X/H} = \frac{Conversion \cdot 0.417\ mol/L}{Reaction\ time\ [min]} \quad (48)$$

The enantiomeric ratio (er) was obtained from ee_P using equation (49):

$$\frac{P_R}{P_S} = \frac{1 + ee_P}{1 - ee_P} \quad (49)$$

Table 13 shows the ee_P and conversion data of the competitive runs. Conversions of benzaldehyde were mostly around 6% for the 120 min-lasting reactions while the substituted benzaldehydes showed quite variable conversions from 2 (e^--donating) to 20% (e^--attracting). The ee_P(X) and ee_P(H) follow the same trend: the more X is attracting, the higher ee_P(X) and ee_P(H), with some exceptions (OPh, 3,4-$(CH_2)_4$, COOMe). OiPr and OMe have barely detectable ee_P(X)s under 1%.

Table 13: Conversion and ee data from the competitive catalytic runs after 120 min reaction time. The results are sorted by increasing σ_p. a): Some data for F and Cl was not e determined due to signal overlapping. b): After 20 min reaction time.

X	Conversion (H) [%]	Conversion (X) [%]	ee_P(H) [%]	ee_P(X) [%]	σ_p	σ_p^+
3,4-$(CH_2)_4$	6.2	1.6	6.8	0.5	**-0.48**	**-0.41**
OiPr	6.7	7.4	7.2	4.8	**-0.45**	**-0.83**
OPh	6.5	5.5	7.3	5.9	**-0.32**	**-0.50**
OMe	5.5	-	7.8	-	**-0.27**	**-0.78**
tBu	-	-	9.2	11	**-0.20**	**-0.26**
Me	6.0	20	9.7	14	**-0.17**	**-0.31**
H	6.6	19	11	15	**0**	**0**
F[a]	-	-	-	14	**0.06**	**-0.07**
I	1.3	16	9.0	18	**0.18**	**0.14**
Br	1.2	9.7	11	22	**0.23**	**0.15**
Cl[a]	6.2	1.7	6.5	0.7	**0.23**	**0.11**
COOMe	6.3	3.9	6.7	7.8	**0.45**	**0.49**
CF_3[b]	5.5	2.0	8.0	11	**0.54**	**0.61**
CN[b]	2.0	1.9	4.9	6.5	**0.66**	**0.66**

The data was used to calculate $\log(v_{0X}/v_{0H})$ and $\log(er_{0X}/er_{0H})$, which were then plotted in Microsoft Excel 2016 against σ and fitted to a linear trendline to obtain the Hammett plots.

IV.1.2.4 IR-monitored kinetic runs

The kinetic runs were performed following the procedure for catalyst loading screenings on a 2 mL scale in a Schlenk tube at 30 °C as single runs. The benzaldehyde's concentration was monitored by a ReactIR 15 equipped with a DS AgX Comp probe. The acquisition was started 30 sec after the addition of benzaldehyde to the NBE/$ZnMe_2$ solution, during which the IR probe was poured into the solution. Acquisition parameters: 2000 to 650 cm^{-1}, 4 cm^{-1} resolution; one acquisition every 5 min; 128 scans per acquisition. The experiments were let to run over 2 days; two additional days were added for low catalyst loading-experiments (2.5 and 5 mol%) with one acquisition every 10 min.

The kinetic profiles were obtained by integrating the 1739 to 1675 cm^{-1} region of the IR spectra (benzaldehyde ν(C=O) at 1706 cm^{-1}) from a single point baseline at 1739 cm^{-1}. The integral values were normalised to the integral of the first acquisition, which is considered being approximately equal to the benzaldehyde signal prior to the $ZnMe_2$ addition. The data was then pasted into the appropriated excel spreadsheet provided by Bures and Nielsen to obtain the normalised kinetic profiles.[191] The catalyst order *c* between two curves was determined by adjusting *c* to make the curves overlay over the first 50% conversion.

IV.1.2.5 GC-monitored kinetic runs

The kinetic runs were performed with NBE (2.5-20 mol%) following the general procedure on a 1.5 mL scale. Aliquots were taken and quenched rapidly at the indicated reaction times, diluted with toluene if necessary, dried over Na_2SO_4 and injected directly into GC. The conversion was determined using equation (47), as in the competitive reactions. The complete set of data can be found in Figure 130**.**

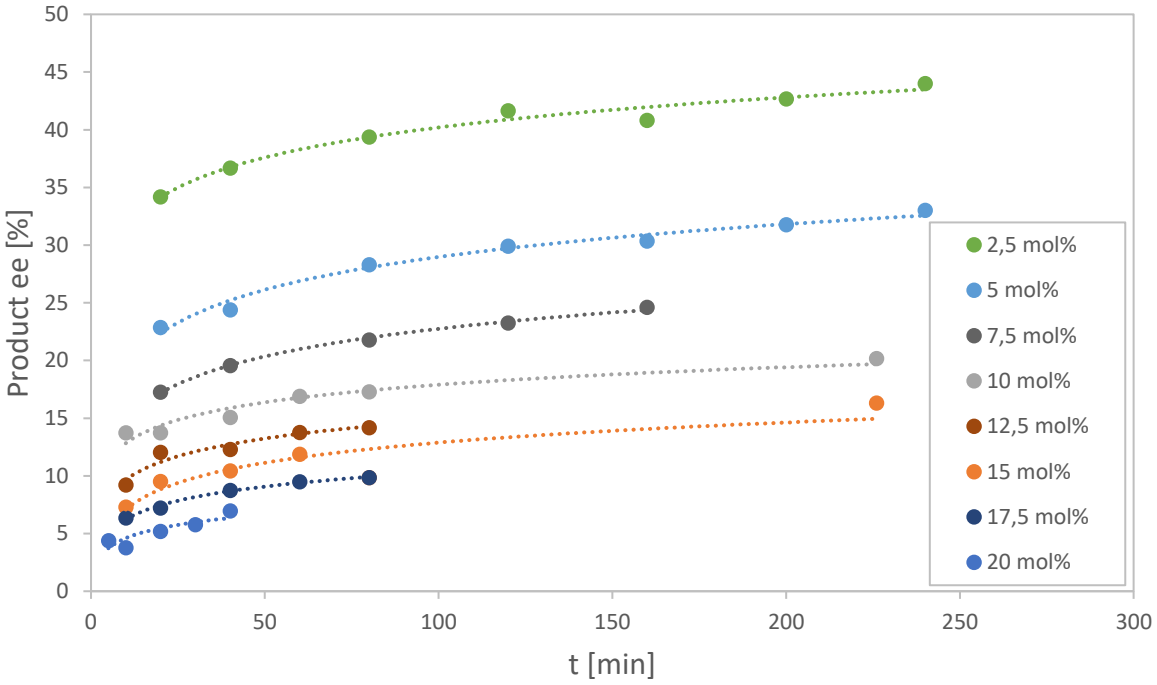

Figure 130: Complete time-dependent ee_P evolution of the (-)-NBE-catalysed addition of $ZnMe_2$ to benzaldehyde at various catalyst loadings.

IV.1.3 General conditions for GC analysis

The ee's of the catalytic runs' products were determined by analysis on a Varian 3900 GC with CP-8400 Autosampler, Chiraldex GT-A 25 m x 0,25 mm column, carrier gas: He, sample concentration: ~$1.3x10^{-2}$ M, sample volume: 1 µL, split: 1/20. The separation of the two considered enantiomers was verified by injecting racemic samples of the chiral alcohols, obtained by addition of 3 M EtMgBr or MeMgBr on the corresponding aldehyde in anh. THF under argon, followed by aqueous work-up with sat. aq. NH_4Cl and DCM.

For the competitive catalytic reactions (Hammett plots) the conditions for X = H were applied in first time. Once the respective aldehyde and chiral alcohols were eluted, the pressure was adapted and the oven was heated (20 °C/min) to the conditions listed for the respective substituted aldehyde.

Table 14: GC conditions and retention times of chiral alcohols.

Substrate	**Chiral alcohol (*R*)**	**Temperature [°C]**	**P(He) [psi]**	**t_{major}** (min)	**t_{minor}** (min)
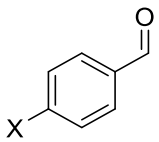	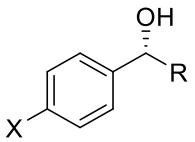				

X = H	R = Et	110	16	36.6	38.3
	R = Me	110	16	23.4	24.7
X = Br	R = Et	145	17	39.7	41.1
	R = Me	145	17	27.9	29.1
X = CF_3	R = Et	130	17	22.3	23.4
	R = Me	125	16	20.0	21.4
X = Me	R = Et	125	16	28.4	29.7
	R = Me	120	16	23.3	24.6
2,4-Dimethylbenzaldehyde	R = Et	140	17	24.0	25.3
2,4,6-Trimethylbenzaldehyde	R = Et	150	18	24.5	25.3
X = *t*Bu	R = Et	130	16	62.1	63.7
	R = Me	120	16	70.9	73.2
X = OMe	R = Et	135	16	44.3	45.6
	R = Me	135	16	30.3	31.2
2-Naphtaldehyde	R = Et	140	17	141	146
X = O*i*Pr	R = Et	140	17	47.2	48.8
	R = Me	140	17	33.2	34.0
X = O*t*Bu	R = Me	135	17	50.4	51.4
X = OPh	R = Me	160	18	94.1	95.9
X = I	R = Et	150	17	54.5	56.2
	R = Me	155	17	32.1	33.1
X = F	R = Et	120	16	28.2	30.3
	R = Me	120	16	19.2	20.3
X = CN	R = Et	160	18	42.5	44.5
	R = Me	155	18	37.3	39.7
X = Cl	R = Et	135	16	27.5	28.9
X = OCF_3	R = Et	130	16	20.9	22.0
	R = Me	130	16	15.5	16.3
X = SF_5	R = Et	140	17	41.2	42.9
	R = Me	140	17	29.0	30.3
X = NMe_2, NEt_2, O*n*Bu	R = Et, R = Me	No separation			

IV.2 Procedures for Chapter III

IV.2.1 Synthesis

IV.2.1.1 Ditopic iminoalcohols and -amine

General procedure - Synthesis of diimines from aminoalcohols and DACH-derived diamine **23**:

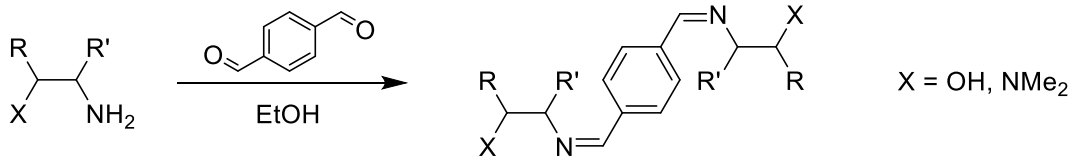

The aminoalcohol or diamine (2 equiv) and terephtalaldehyde (1 equiv) were dissolved in EtOH (10 mL) and left to stir for 3h at rt, then the solvent was evaporated. Z/E-isomerism of the imine groups was not determined. Some iminoalcohols are, when in solution, in equilibrium with the hemiaminal ether resulting from nucleophilic addition of the alcohol to the imine group and gave rise to complex NMR spectra.

(2*S*,2'*S*)-2,2'-((1,4-phenylenebis(methaneylylidene))bis(azaneylylidene))bis(propan-1-ol) **19a:**

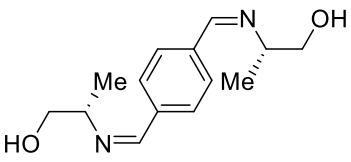

From L-Alaninol (1 g, 13.3 mmol, 2 equiv) and terephtaldehyde (893 mg, 6.66 mmol). After 3h stirring a white precipitate had formed which was filtered off and washed with EtOH. The filtrate was evaporated under reduced pressure, redissolved in EtOH (10 mL), stored at -20 °C overnight and the newly formed precipitate filtered and washed with cold EtOH. White solid, combined mass: 1.03 g, 62% yield. No hemiaminal ether formation.

^{1}H NMR (500 MHz, MeOH-d^4): δ = 8.41 (C*H*=N, s, 2H), 7.85 (CH_{arom}, s, 4H), 3.65 (CH_2-O, dd, *J* = 10.8, 4.5 Hz, 2H), 3.60 (CH_2-O, dd, *J* = 10.8, 8.1 Hz, 2H), 3.51 (C*H*-N, qdd, *J* = 6.4, 8.1, 4.5 Hz, 2H), 1.24 (CH-CH_3, d, *J* = 6.4 Hz, 6H) ppm.

^{13}C NMR (125 MHz, MeOH-d^4): δ = 163.0 (*C*H=N), 139.4 (C_{quat}), 129.7 (*C*H$_{arom}$), 69.4 (*C*H-N), 67.5 (*C*H$_2$-OH), 18.6 (CH-*C*H$_3$) ppm.

FTIR (ATR): $\bar{\nu}_{max}$ = 3187, 2977, 2963, 2930, 2899, 2871, 2832, 2771, 1635 ($\nu_{C=N}$), 1569, 1445, 1434, 1397, 1373, 1355, 1343, 1309, 1250, 1218, 1144, 1119, 1090, 1052, 988, 919, 895, 853, 820, 808, 713, 635, 554, 530, 496, 441 cm^{-1}.

MS (ESI+): *m/z* = 249.158 ([M + H$^+$], 100%).

$[\alpha]_D^{20}$(EtOH, *c* = 0.996 g/100mL) = +105 cm^{3}g^{-1}dm^{-1}.

UV-vis (MeOH, 3.16·10^{-5} M): ε_{max} = 28 800 (274 nm) Lmol^{-1}cm^{-1}.

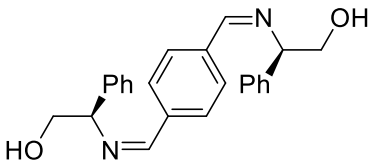

(2*R*,2'*R*)-2,2'-((1,4-phenylenebis(methaneylylidene))bis(azaneylylidene))bis(2-phenylethan-1-ol) **19b:**

From (*R*)-(−)-2-Phenylglycinol (1 g, 7.29 mmol, 2 equiv) and terephtaldehyde (489 mg, 3.64 mmol). Yellow solid, 1.36 g, quantitative yield. Complex NMR spectra due to hemiaminal ether formation.

^{1}H NMR (500 MHz, $CDCl_3$): δ = 8.40 (N=C*H*, m, 1.7H), 7.90-7.58 (N=CH-C-CH_{arom}, m, 4H), 7.48-7.27 (CH_{arom}, m, 10H), 5.80-5.50 (hemiaminal ether O-C*H*-NH, m, 0.3H), 4.60-4.30 (N-C*H*, m, 2H), 4.10-3.70 (O-CH_2, m, 4H), 2.19 (O*H*, br s, 2H) ppm.

^{13}C NMR (125 MHz, $CDCl_3$): δ = 162.2 (N=*C*H), 140.6 (N-CH-C_{quat}), 138.2 (N=CH-C_{quat}), 126.0-130.0 (all *C*H_{arom}), 93.1 (hemiaminal ether O-*C*H-N), 92.3 (hemiaminal ether O-*C*H-N), 77.6 (N-*C*H), 67.9 (O-*C*H_2), 63.1 (N-*C*H), 60.9 (N-*C*H) ppm.

FTIR (ATR): $\bar{\nu}_{max}$ = 3313, 3059, 3028, 2924, 2854, 1601, 1583, 1635 ($\nu_{C=N}$), 1567, 1491, 1451, 1416, 1381, 1338, 1298, 1216, 1053, 1026, 969, 900, 828, 801, 755, 698, 632, 578, 535, 508, 450 cm^{-1}.

MS (ESI+): *m/z* = 373.191 ([M + H$^+$], 100%).

$[\alpha]_D^{20}$(EtOH, *c* =1.08 g/100 mL) = +127 cm^{3}g^{-1}dm^{-1}.

UV-vis (MeOH, 3.34·10^{-5} M): ε_{max} = 30 600 (277 nm) Lmol^{-1}cm^{-1}.

(2*R*,2'*R*)-2,2'-((1,4-phenylenebis(methaneylylidene))bis(azaneylylidene))bis(3-methylbutan-1-ol) **19c:**

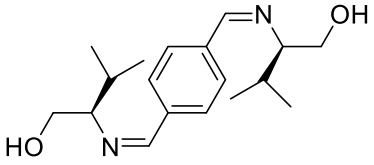

From D-Valinol (1 g, 8.70 mmol, 2 equiv) and terephtaldehyde (650 mg, 4.85 mmol). Yellow waxy solid, 1.48 g, quantitative yield. Complex NMR spectra due to hemiaminal ether formation.

^{1}H NMR (500 MHz, $CDCl_3$): δ = 8.36-8.24 (N=C*H*, m, 1.2H), 7.95-7.44 (CH_{arom}, m, 4H), 5.60-5.40 (hemiaminal ether O-C*H*-N, m, 0.8H), 4.03 (O-CH_2, m, 1H), 3.82 (O-CH_2, m, 2H), 3.48 (O-CH_2, m, 1H), 3.15 (N-C*H*, m, 0.5H), 2.99 (N-C*H*, m, 1.5H), 1.96 (CH_3-C*H*-CH_3, m, 1H), 1.65 (CH_3-C*H*-CH_3, m, 1H), 0.85-1.10 (CH_3-CH-CH_3, m, 12H) ppm.

^{13}C NMR (125 MHz, $CDCl_3$): 162.0-161.2 (N=*C*H), 142.3-136.3 (*C*), 128.9-128.3 (*C*H_{arom}), 126.6-126.3 (*C*H_{arom}), 93.3-91.8 (hemiaminal ether N-*C*H-O), 79.1-79.3 (N-*C*H), 69.7-70.2 (O-*C*H_2), 66.4 (N-*C*H), 64.71 (O-*C*H_2), 64.35 (N-*C*H), 30.1-32.1 (CH_3-*C*H-CH_3), 21.0-19.0 (*C*H_3-CH-*C*H_3) ppm.

FTIR (ATR): $\bar{\nu}_{max}$ = 3329, 2957, 2931, 2871, 1640 ($\nu_{C=N}$), 1568, 1456, 1417, 1385, 1365, 1343, 1295, 1215, 1169, 1143, 1076, 1056, 1017, 962, 898, 829, 799, 735, 631, 498, 416 cm^{-1}.

MS (ESI+): *m/z* = 305.219 ([M + H$^+$], 100%).

$[\alpha]_D^{20}$(EtOH, *c* = 0.924 g/100 mL) = -49.6 cm^{3}g^{-1}dm^{-1}.

UV-vis (MeOH, 2.55·10^{-5} M): ε_{max} = 26 400 (275 nm) Lmol^{-1}cm^{-1}.

(1*R*,1'*R*,2*R*,2'*R*)-1,1'-((1,4-phenylenebis(methaneylylidene))bis(azaneylylidene))bis(2,3-dihydro-1H-inden-2-ol) **19d:**

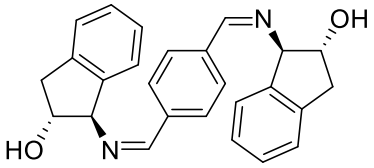

From (1*R*,2*R*)-(-)-trans-1-amino-2-indanol (900 mg, 2 equiv, 6.03 mmol) and terephtaldehyde (4.05 mg, 3.02 mmol) in DMF. A precipitate appears after a few minutes. The solid was filtered off under reduced pressure after overnight stirring at rt and washed with $CHCl_3$ (3 x 10 mL). White solid, 1.15 g, 96% yield. No hemiaminal ether formation.

^{1}H NMR (500 MHz, DMSO-d_6): δ = 8.60 (N=C*H*, s, 2H), 7.91 (N=CH-C-CH_{arom}, s, 4H), 7.26 (CH_{arom}-C-CH_2, d, *J* = 7.0 Hz, 2H), 7.23 (CH_{arom}-CH-C-CH_2, t, *J* = 7.5 Hz, 2H), 7.17 (CH_{arom}-CH-C-CH-N, t, *J* = 7.3 Hz, 2H), 6.99 (CH_{arom}-C-CH-N, d, *J* = 7.4 Hz, 2H), 5.38 (O*H*, d, *J* = 5.5 Hz, 2H), 4.64 (C*H*-N, d, *J* = 5.9 Hz, 2H), 4.43 (C*H*-O, dddd, *J* = 7.7, 7.1, 5.9, 5.5 Hz, 2H), 3.25 (O-CH-CH_2, dd, *J* = 15.5, 7.1 Hz, 2H), 2.83 (O-CH-CH_2, dd, *J* = 15.5, 7.7 Hz, 2H) ppm.

^{13}C NMR (125 MHz, DMSO-d_6): δ = 162.0 (*C*-CH-N), 140.4 (*C*-CH2), 138.5 (*C*-CH=N), 128.9 (*C*H$_{arom}$-C-CH=N), 128.1 (*C*H$_{arom}$-CH-C-CH_2), 127.0 (*C*H$_{arom}$-CH-C-CH-N), 125.2 (*C*H$_{arom}$-C-CH_2), 124.6 (*C*H$_{arom}$-C-CH-N), 81.8 (*C*-N), 78.9 (*C*-O), 39.8 (*C*H_2-C-O, overlaps with the residual signal of DMSO-d_6, visible in DEPT and HSQC NMR) ppm.

FTIR (ATR): $\bar{\nu}_{max}$ = 3200, 3073, 3048, 3032, 2954, 2907, 2883, 2832, 1633 ($\nu_{C=N}$), 1564, 1476, 1460, 1415, 1307, 1273, 1221, 1198, 1170, 1091, 1063, 1009, 988, 970, 902, 863, 839, 802, 742, 693, 642, 613, 581, 534, 511, 479, 465, 422 cm^{-1}.

MS (ESI+): *m/z* = 397.188 ([M + H$^+$], 100%).

$[\alpha]_D^{20}$: not sufficiently soluble in common solvents.

(1R,1'R,2S,2'S)-2,2'-(((1Z,1'Z)-1,4-phenylenebis(methaneylylidene))bis(azaneylylidene))bis(1-phenylpropan-1-ol) **19e:**

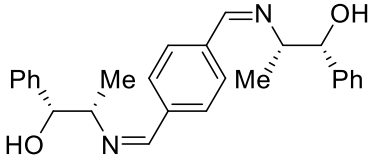

From (1*R*,2*S*)-(-)-Norephedrine (1 g, 6.61 mmol, 2 equiv) and terephtaldehyde (444 mg, 3.31 mmol). Yellow, amorphous solid, 1.32 g, quantitative yield. Some traces of hemiaminal ether in MeOH-d_4.

^{1}H NMR (500 MHz, MeOH-d_4) : δ = 8.04 (N=C*H*, s, 1H), 7.61 (N=CH-C-CH_{arom}, s, 2H), 7.31 (*o*CH_{arom}, dd, *J* = 8.4, 1.4 Hz, 2H), 7.25 (*m*CH_{arom}, dd, *J* = 8.4, 6.8 Hz, 2H), 7.17 (*p*CH_{arom}, tt, *J* = 7.2, 1.4 Hz, 1H), 4.67 (O-C*H*, d, *J* = 6.8 Hz, 1H), 3.59 (N-C*H*, p, *J* = 6.4 Hz, 1H), 1.36 (CH_3, d, *J* = 6.4 Hz, 3H) ppm.

^{13}C NMR (125 MHz, MeOH-d_4): δ = 162.7 (N=*C*H), 143.8 (O-CH-*C*), 139.3 (N=CH-*C*), 129.4 (N=CH-C-*C*H$_{arom}$), 128.9 (*mC*H$_{arom}$), 128.3 (*o*- and *pC*H$_{arom}$), 78.8 (O-*C*H), 73.5 (N-*C*H), 18.8 (CH-*C*H_3) ppm.

FTIR (ATR): $\bar{\nu}_{max}$ = 3354, 3085, 3061, 3028, 2971, 2929, 2868, 1639 ($\nu_{C=N}$), 1493, 1451, 1451, 1372, 1335, 1296, 1217, 1198, 1129, 1073, 1042, 1025, 997, 967, 830, 748, 699, 631, 518 cm^{-1}.

MS (ESI+): *m/z* = 402.2216 ([M + H$^+$], 100%).

$[\alpha]_D^{20}$(EtOH, *c* = 0.822 g/mL) = -285 $cm^3g^{-1}dm^{-1}$.

UV-vis (MeOH, $5{,}28 \cdot 10^{-5}$ M): ε_{max} = 25 000 (277 nm) $Lmol^{-1}cm^{-1}$.

CD (MeOH, $5.14 \cdot 10^{-5}$ M): $[\theta]_{max}$ = -24 100 (278 nm) $°cm^2dmol^{-1}$.

(1*S*,1'*S*,2*R*,2'*R*)-1,1'-((1,4-phenylenebis(methaneylylidene))bis(azaneylylidene))bis(2,3-dihydro-1H-inden-2-ol) **19f :**

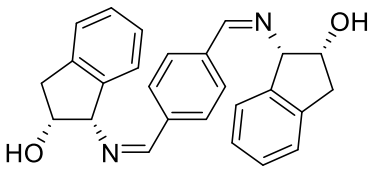

From (1*S*,2*R*)-*cis*-1-Amino-2-indanol (500 mg, 3.35 mmol 2 equiv) and terephtaldehyde (225 mg, 1.68 mmol, 1 equiv). A white precipitate appears at the beginning of the reaction. After 3h stirring at rt, the precipitate was filtered and washed with EtOH. The filtrate was stored at -20 °C overnight and the newly formed precipitate filtered and washed with cold EtOH. White solid, combined mass: 622 mg, 93% yield. Complex NMR spectra due to hemiaminal ether formation.

^{1}H NMR (500MHz, $CDCl_3$): δ = 8.64-8.50 (N=C*H*, m, 0.2H), 7.90-7.00 (all CH_{arom}, m, 14H), 5.60-5.10 (hemiaminal ether O-C*H*-N, m, 1.7H), 5.10-4.60 (N-C*H* and O-C*H*, m, 4H), 3.40-3.10 (O-CH-CH_2, m, 4H) ppm.

^{13}C NMR (125 MHz, $CDCl_3$): δ = 165.0-138.0 (*C*), 131.0-123.0 (all *C*H_{arom}), 94.0-68.0 (O-*C*H, N-*C*H, hemiaminal ether O-*C*H-N), 41.0-38.0 (O-CH-*C*H_2) ppm.

FTIR (ATR): $\bar{\nu}_{max}$ = 3286, 3058, 3023, 2931, 2848, 1642 ($\nu_{C=N}$), 1606, 1585, 1518, 1479, 1460, 1434, 1361, 1326, 1298, 1255, 1214, 1192, 1169, 1095, 1075, 1034, 1019, 967, 902, 874, 859, 847, 822, 755, 710, 696, 654, 629, 590, 554, 509, 528, 509, 465, 423 cm^{-1}.

MS (ESI+): *m/z* = 397.188 ([M + H^+], 100%).

$[\alpha]_D^{20}$(DCM, *c* = 1.09 g/100 mL) = -96,9 $cm^3g^{-1}dm^{-1}$.

UV-vis (DCM, $5.92 \cdot 10^{-5}$ M): ε_{max} = 5950 (259 nm) $Lmol^{-1}cm^{-1}$.

CD (DCM, $5.86 \cdot 10^{-5}$ M): $[\theta]_{max}$ = -7070 (291 nm) $°cm^2dmol^{-1}$.

(1*R*,1'*R*,2*R*,2'*R*)-2,2'-((1,4-phenylenebis(methaneylylidene))bis(azaneylylidene))bis(cyclohexan-1-ol) **19d**:

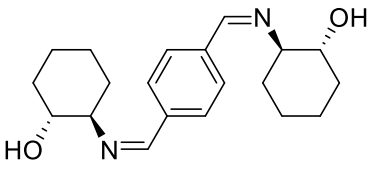

From (1*R*,2*R*)-2-Aminocyclohexanol (1 g, 8.68 mmol, 2 equiv) and terephtaldehyde (582 mg, 4.34 mmol). Light brown solid, 1.43g, quantitative yield. No hemiaminal ether formation.

^{1}H NMR (500 MHz, $CDCl_3$): δ = 8.32 (C*H*=N, s, 2H), 7.72 (CH_{arom}, s, 4H), 3.74 (C*H*-O,), 3.03 (C*H*-N,), 2.39 (O*H*, br s, 2H), 2.08 (C$H_{2\ eq}$-CH-O, 2H), 1.86-1.74 ($CH_{2\ eq}$-CH_2-CH-N + $CH_{2\ eq}$-CH-CH-O, m, 4H), 1.74-1.68 ($CH_{2\ eq}$-CH-N, m, 2H), 1.68-1.58 ($CH_{2\ ax}$-CH-N, m, 2H), 1.46-1.28 ($CH_{2\ ax}$-CH-N + $CH_{2\ ax}$-CH_2-CH-N + $CH_{2\ ax}$-CH-CH-O, m, 6H) ppm.

^{13}C NMR (125 MHz, $CDCl_3$): δ = 161.4 (*C*H=N), 138.1 (C_{arom}), 128.6 (CH_{arom}), 73.9 (*C*H-N), 73.9 (*C*H-O), 32.7, 32.6 (*C*H_2-CH-N + *C*H_2-CH-O), 24.7, 24.5 (*C*H_2-CH_2-CH-N + *C*H_2-CH_2-CH-O) ppm.

FTIR (ATR): $\bar{\nu}_{max}$ = 3368, 3029, 2922, 2877, 2850, 1643 ($\nu_{C=N}$), 1567, 1510, 1454, 1418, 1379, 1346, 1282, 1240, 1223, 1198, 1129, 1078, 1058, 1039, 972, 947, 932, 907, 855, 847, 829, 755, 567, 530, 494, 474, 450, 437, 415 cm^{-1}.

MS (ESI+): *m/z* = 329.2234 ([M + H^+], 100%).

$[\alpha]_D^{20}$(EtOH, *c* = 1.16 g/100 mL) = -101 $cm^3g^{-1}dm^{-1}$.

UV-vis (MeOH, $3.56\cdot10^{-5}$ M): ε_{max} = 32 900 (277 nm) $Lmol^{-1}cm^{-1}$.

CD (MeOH, $4.97\cdot10^{-5}$ M): $[\theta]_{max}$ = -74 700 (281 nm) $°cm^2dmol^{-1}$.

(1*R*,1'*R*,2*R*,2'*R*)-2,2'-((1,4-phenylenebis(methaneylylidene))bis(azaneylylidene))bis(N,N-dimethylcyclohexan-1-amine) **23**:

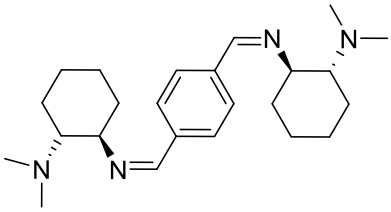

From **22** (1.03 g, 7.26 mmol, 2 equiv; prepared from (1*R*,2*R*)-DACH following a literature procedure)[175] and terephtaldehyde (487 mg, 3.63 mmol). Off-white solid, 1.39 g, quantitative yield.

^{1}H NMR (500 MHz, $CDCl_3$): δ = 8.27 (N=C*H*, s, 2H), 7.76 (CH_{arom}, s, 4H), 3.28 (C*H*-N=C, td, *J* = 9.5, 5.8 Hz, 2H), 2.73 (C*H*-NMe_2, ddd, *J* = 11.2, 9.5, 3.7 Hz, 2H), 2.28 (NMe_2, s, 12H), 1.90-1.83 ($CH_{2\ eq}$-CH-NMe_2, m, 2H), 1.83-1.78 ($CH_{2\ eq}$-CH_2-CH-NMe_2, m, 2H), 1.77-1.70 ($CH_{2\ eq}$-CH_2-CH-N=C, m, 2H), 1.69-1.61 (CH_2-CH-N=C, m, 4H), 1.38-1.24 ($CH_{2\ ax}$-CH_2-CH-NMe_2 + $CH_{2\ ax}$-CH_2-CH-N=C + $CH_{2\ ax}$-CH-NMe_2, m, 6H) ppm.

^{13}C NMR (125 MHz $CDCl_3$): δ = 159.1 (*C*=N), 138.4 (C_{arom}), 128.5 (CH_{arom}), 72.4 (*C*H-N=C), 66.7 (*C*H-NMe_2), 41.0 (NMe_2), 34.9 (*C*H_2-CH-N=C), 25.6 (*C*H_2-CH_2-CH-NMe2), 25.4 (*C*H2-CH-NMe_2), 24.8 (*C*H_2-CH_2-CH-N=C) ppm.

FTIR (ATR): $\bar{\nu}_{max}$ = 2963, 2926, 2855, 2824, 2779, 2765, 1644 ($\nu_{C=N}$), 1570, 1447, 1371, 1292, 1272, 1256, 1186, 1120, 1074, 1027, 944, 872, 841, 817, 754, 543, 507, 461 cm^{-1}.

MS (ESI+): *m/z* = 383.3184 ([M + H^+], 100%).

$[\alpha]_D^{20}$(EtOH, *c* = 1.04 g/100 mL) = -230 $cm^3g^{-1}dm^{-1}$.

UV-vis (MeOH, $3.05\cdot10^{-5}$ M): ε_{max} = 39 300 (277 nm) $Lmol^{-1}cm^{-1}$.

CD (MeOH, $5.22\cdot10^{-5}$ M): $[\theta]_{max}$ = -48 700 (279 nm) $°cm^2dmol^{-1}$.

*IV.2.1.2 Ditopic iminoaniline **26***

(*R*)-2-nitro-N-(1-phenylethyl)aniline **24:**

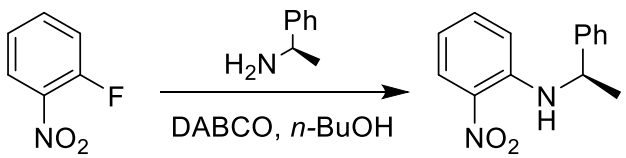

24 was prepared by adapting a published procedure.[176] DABCO (8.35 g, 3.5 equiv, 74.4 mmol) was dissolved in n-butanol (20 mL) under an argon atmosphere, then 1-Fluoro-2-nitrobenzene (2.24 mL, 1 equiv, 21.3 mmol) was added via syringe, followed by (R)-(+)-1-Phenylethylamine (3.25 mL, 1.2 equiv, 25.5 mmol). The solution refluxed under argon for 3 h and became deep red after a few minutes. The mixture was let to cool to rt, the solvent was evaporated and the residue taken in toluene (20 mL) and water (20 mL). 3 M HCl was added slowly until a pH of 1 was reached (approx. 35 mL), then the mixture was thoroughly shaken and extracted with toluene (3 x 30 mL). The combined organic phases were dried over Na_2SO_4 and evaporated to yield a bright red-orange oil. No further purification was necessary. Mass: 5.61 g, 99% yield.

^{1}H NMR (500 MHz, $CDCl_3$): δ = 8.42 (N*H*, br d, *J* = 3.8 Hz, 1H), 8.17 (CH_{arom}-C-NO_2, dd, *J* = 8.6, 1.5 Hz, 1H), 7.36-7.31 (*o*- and *p*CH_{arom}, m, 4H), 7.26 (*p*CH_{arom}, tt, *J* = 8.7, 1.0 Hz, 1H), 7.25 (CH_{arom}-CH-C-NH, ddd, *J* = 8.6, 7.1, 1.4 Hz, 1H), 6.63 (CH_{arom}-C-NH, dd, *J* = 8.6, 1.2 Hz, 1H), 6.60 (CH_{arom}-CH-C-NO_2, ddd, *J* = 8.6, 7.1, 1.2 Hz, 1H), 4.69 (C*H*-NH, m, *J* = 6.5 Hz, 1H), 1.65 (CH_3-CH-NH, d, *J* = 6.7 Hz, 1H) ppm.

^{13}C NMR (125 MHz, $CDCl_3$): δ = 144.6 (*C*-NH), 143.6 (*C*$_{quat}$-CH-CH_3), 136.0 (*C*H_{arom}-CH-C-NH), 132.2 (*C*$_{quat}$-NO_2), 129.0 (*mC*H_{arom}), 127.5 (*pC*H_{arom}), 126.8 (*C*H-C-NO_2), 125.6 (*oC*H_{arom}), 115.6 (*C*H_{arom}-CH-C-NO_2), 115.2 (*C*H_{arom}-C-NH), 53.2 (*C*H-NH), 25.1 (*C*H_3-CH-NH) ppm.

FTIR (ATR): $\bar{\nu}_{max}$ = 3377, 3084, 3061, 3028, 2970, 2927, 2870, 1615, 1572, 1501, 1451, 1441, 1417, 1375, 1349, 1307, 1264, 1233, 1202, 1153, 1071, 1038, 1028, 1000, 947, 911, 859, 842, 823, 777, 762, 739, 699, 678, 629, 617, 608, 539, 520 cm^{-1}.

UV-vis (THF, 3.86 x 10^{-5} M): ε_{max} = 4146 (271 nm), 6641 (420 nm) $Lmol^{-1}cm^{-1}$.

$[\alpha]_D^{20}$(EtOH, *c* = 1.13·10^{-2} g/100 mL) = -830 $cm^3g^{-1}dm^{-1}$.

CD (MeOH, 4.33·10^{-5} M): $[\theta]_{max}$ = -22 200 (281 nm) $°cm^2dmol^{-1}$.

(*R*)-*N*^{1}-(1-phenylethyl)benzene-1,2-diamine **25**:

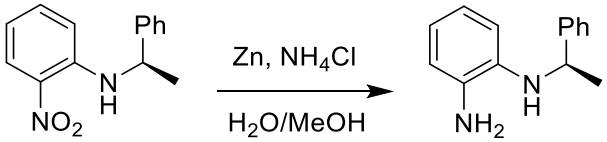

24 (3 g, 12.4 mmol) and NH_4Cl (13.3 g, 247 mmol, 20 equiv) were placed in a two-necked flask under argon, then freshly degassed MeOH (20 mL) and H_2O (5 mL) were added via syringe. The mixture was cooled to 0 °C, then Zn powder (4.86 g, 74.3 mmol, 6 equiv) was added. The mixture became quickly dark and turned to a light forest green solution after 3 h stirring at rt. The mixture was filtered through a celite pad under reduced pressure, during which the solution turned black, and the filter cake thoroughly washed with DCM (3 x 30 mL). The filtrate was dried over Na_2SO_4 and evaporated to yield a black viscous product which was used without further purification. 2.62 g, 99% yield.

^{1}H NMR (300 MHz, $CDCl_3$) : δ = 7.42-7.27 (*o*- and *p*CH_{arom}, m, 4H), 7.22 (*p*CH_{arom}, ddt, *J* = 8.2, 6.1, 1.4 Hz, 1H), 6.73 (CH_{arom}-C-NH_2, dd, *J* = 7.1, 1.9 Hz, 1H), 6.67 (CH_{arom}-CH-C-NH, td, *J* = 7.3, 1.9 Hz, 1H), 6.61

(C*H*$_{arom}$-CH-C-NH$_2$, td, *J* = 7.3, 1.6 Hz, 1H), 6.42 (C*H*$_{arom}$-C-NH, dd, *J* = 7.5, 1.7 Hz, 1H), 4.49 (NH-C*H*-CH$_3$, q, *J* = 6.6 Hz, 1H), 3.49 (N*H* and N*H*$_2$, br s, 3H), 1.55 (NH-CH-C*H*$_3$, d, *J* = 6.7 Hz, 3H) ppm.

2,2'-(((*1Z,1'Z*)-1,4-phenylenebis(methaneylylidene))bis(azaneylylidene))bis(*N*-((*R*)-1-phenylethyl)aniline) **26:**

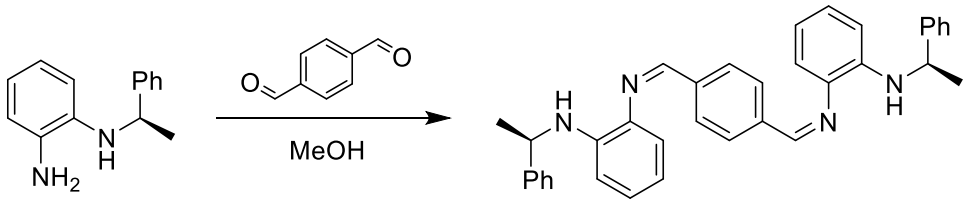

25 (1.53 g, 2.4 equiv, 7.21 mmol) and terephtaldehyde (403 mg, 3.00 mmol, 1 equiv) were dissolved in MeOH (20 mL) and stirred overnight at rt, during which an orange precipitate formed. The precipitate was filtered off, washed with MeOH (4 x 5 mL) and dried under vacuum. Orange powder, 1.27 g, 81% yield.

^{1}H NMR (500 MHz, CDCl$_3$): δ = 8.66 (C*H*=N, s, 2H), 8.07 (C*H*$_{arom\ linker}$, s, 4H), 7.42 (*m'*- and *m*C$_{Harom}$, m, 4H), 7.34 (*p*C*H*$_{arom}$, tt, *J* = 7.6, 1.6 Hz, 2H), 7.25 (*o*C*H*$_{arom}$, dt, *J* = 6.7, 1.2 Hz, 2H), 7.23 (*o'*C*H*$_{arom}$, dt, *J* = 6.7, 1.2 Hz, 2H), 7.11 (C*H*$_{arom}$-C-N=CH, dd, *J* = 7.9, 1.4 Hz, 2H), 7.01 (C*H*$_{arom}$-CH-C-NH, ddd, *J* = 8.2, 7.3, 1.4 Hz, 2H), 6.66 (C*H*$_{arom}$-CH-C-N=CH, td, *J* = 7.6, 1.2 Hz, 2H), 6.45 (C*H*$_{arom}$-C-NH, dd, *J* = 8.2, 0.9 Hz, 2H), 5.52 (N*H*, br s, 2H), 4.59 (NH-C*H*-CH$_3$, q, *J* = 6.7 Hz, 2H), 1.63 (NH-CH-C*H*$_3$, d, *J* = 6.7 Hz, 6H) ppm.

^{13}C NMR (125 MHz, CDCl$_3$): 155.9 (*C*H=N), 145.5 (*C*$_{arom}$-CH-CH$_3$), 143.2 (*C*$_{arom}$-NH), 138.9 (*C*$_{arom\ linker}$), 136.0, (*C*$_{arom}$-N=CH), 129.0 (*C*H$_{arom\ linker}$), 128.7 (*pC*H$_{arom}$), 128.4 (*C*H$_{arom}$-CH-C-NH), 126.9 (*oC*H$_{arom}$), 125.9 (*mC*H$_{arom}$), 116.6 (*C*H$_{arom}$-CH-C-N=CH), 116.4 (*C*H$_{arom}$-C-N=CH), 111.7 (*C*H$_{arom}$-C-NH), 53.5 (NH-*C*H-CH$_3$), 53.5 (NH-CH-*C*H$_3$) ppm.

FTIR (ATR): $\bar{\nu}_{max}$ = 3401, 3060, 3028, 2971, 2925, 2875, 1611 ($\nu_{C=N}$), 1590, 1504, 1452, 1427, 1374, 1326, 1280, 1250, 1202, 1179, 1161, 1141, 1071, 1019, 963, 922, 877, 832, 743, 737, 697, 611, 568, 527, 492, 460 cm^{-1}.

MS (ESI+): *m/z* = 519.2568 ([M – 2 H$_2$ + H$^+$], 100%); 521.2723 ([M – H$_2$ + H$^+$], 100%); 523.2866 ([M + H$^+$], 100%). The first two peaks result probably from *in situ*-oxidation of one or two benzylic amines, respectively.

UV-vis (THF, 3.58·10^{-5} M): ε_{max} = 21 419 (306 nm), 6256 (446 nm) Lmol^{-1}cm^{-1}.

CD (THF, 5.68·10^{-5} M): $[\theta]_{max}$ = -27 800 (300 nm), -10 900 (441 nm) °cm^{2}dmol^{-1}.

$[\alpha]_D^{20}$(EtOH, *c* = 9.96·10^{-3} g/100mL) = -1054 cm^{3}g^{-1}dm^{-1}.

*IV.2.1.3 UV-vis reference compound **27***

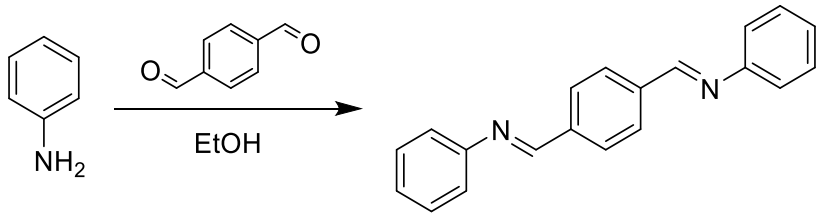

Terephtaldehyde (1 g, 7.46 mmol, 1 equiv) was suspended in EtOH (15 mL), then aniline (1.7 mL, 18.6 mmol, 2.5 equiv) was added. The suspension dissolved instantly, then a precipitate formed within a few minutes. After 1 h ^{1}H NMR indicated full conversion, the mixture was then filtered over reduced pressure and the filter cake washed three times with EtOH. The slightly yellow, thin plates were dried under vacuum. 1.87 g, 88% yield. Spectral properties are identical with reported data.[192]

IV.2.1.4 Complex synthesis

General procedure - Complex synthesis from diimines:

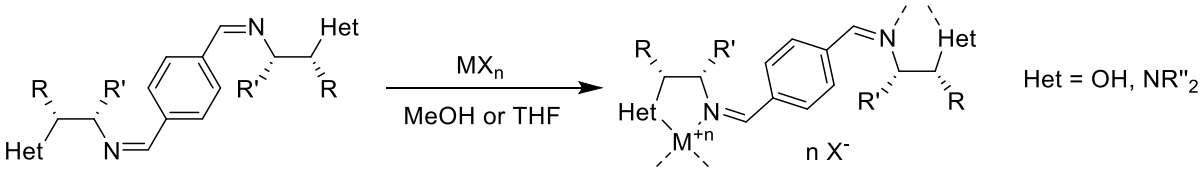

The diimine (1 equiv) and the corresponding metal salt (1 equiv) were dissolved in anh. MeOH or THF and stirred for 30 min athh rt under argon, then the solvent was evaporated. Reactions with $ZnOTf_2$ were let to stir in a 1:1 THF-MeCN mixture overnight. The resulting product was recovered in quantitative yield and stored in a N_2-filled glovebox. Complexes from aniline-derived ligand **X** were made at air, in technical grade THF and were stored at air. The complexes proved to be all too strongly coloured to obtain their $[\alpha]_D^{20}$.

19e-CuPF$_6$:

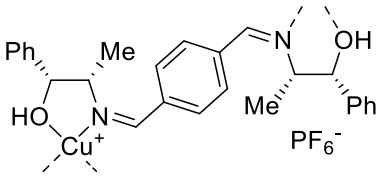

From **19e** (50 mg, 0.125 mmol) and $Cu(MeCN)_4PF_6$ (46.5 mg, 0.125 mmol) in MeOH, precipitates during the reaction. Bright yellow powder.

^{1}H NMR (500 MHz, MeOH-*d*$_4$): δ = 8.74 (C*H*=N, s, 2H), 7.73 (C*H*$_{arom}$, s, 4H), 7.66 (*o*C*H*$_{arom}$, d, *J* = 7.3 Hz, 4H), 7.48 (*m*C*H*$_{arom}$, t, *J* = 7.3 Hz, 4H), 7.36 (*p*C*H*$_{arom}$, t, J = 7.3 Hz, 2H), 5.22 (C*H*-O, s, 2H), 4.11 (C*H*-N, m, 2H), 1.28 (C*H*$_3$-CH-N, d, *J* = 6.4 Hz, 6H) ppm.

^{13}C NMR (125 MHz, MeOH-*d*$_4$): δ = 166.9 (*C*=N), 142.1 (*C*$_{arom}$), 139.5 (*C*$_{arom\ linker}$), 129.6 (*m*CH$_{arom}$), 128.9 + 128.8 (*m*CH$_{arom}$ + *C*H$_{arom}$), 127.5 (*o*CH$_{arom}$), 76.5 (*C*H-O), 73.5 (*C*H-N), 14.9 (*C*H$_3$-CH-N) ppm.

FTIR (ATR): $\bar{\nu}_{max}$ = 3546, 3243, 3030, 2959, 2941, 2874, 1626 ($\nu_{C=N}$), 1494, 1451, 1376, 1296, 1219, 1200, 1129, 1078, 1037, 992, 833, 752, 701, 640, 616, 557, 516 cm^{-1}.

UV-vis (THF, $6.40 \cdot 10^{-5}$ M): ε_{max} = 16 539 (269 nm) $Lmol^{-1}cm^{-1}$.

CD (THF, $6.40 \cdot 10^{-5}$ M): $[\theta]_{max}$ = -52 700 (279 nm), +15 500 (343 nm) $°cm^2dmol^{-1}$.

19e-Cu(OTf)$_2$:

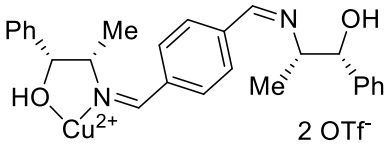

From **19e** (50 mg, 0.125 mmol) and $Cu(OTf)_2$ (45.2 mg, 0.125 mmol) in MeOH. Green powder.

FTIR (ATR): $\bar{\nu}_{max}$ = 3243, 3155, 3066, 1698, 1680 ($\nu_{C=N}$), 1634 ($\nu_{C=N}$), 1496, 1454, 1395, 1278, 1224, 1167, 1026, 982, 823, 751, 702, 635, 575, 516 cm^{-1}.

UV-vis (MeOH, $5.64 \cdot 10^{-5}$ M): ε_{max} = 14 700 (267 nm) $Lmol^{-1}cm^{-1}$.

CD (MeOH, $3.41 \cdot 10^{-5}$ M): $[\theta]_{max}$ = -11 800 (283 nm) $°cm^2dmol^{-1}$.

19f-CuPF$_6$:

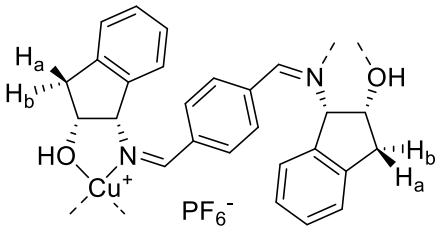

From **19f** (100 mg, 0.252 mmol) and $Cu(MeCN)_4PF_6$ (94.0 mg, 0.252 mmol) in THF. Red solid. ^{1}H NMR shows broad as well as sharp and well-defined peaks; only the latter are listed.

^{1}H NMR (500 MHz, CD_2Cl_2): δ = 8.63 (C*H*=N, s, 2H), 7.75 (C*H*$_{arom}$-C$_{arom}$-CH=N, s, 4H), 7.36 (C*H*$_{arom}$- CH$_{arom}$-C$_{arom}$-CH$_2$, t, *J* = 7.3 Hz, 2H), 7.33 (C*H*$_{arom}$-CH$_{arom}$-C$_{arom}$-CH-N, t, *J* = 7.3 Hz, 2H), 7.08 (C*H*$_{arom}$-C$_{arom}$-CH-N, d, *J* = 7.1Hz, 2H), 7.01 (C*H*$_{arom}$-C$_{arom}$-CH$_2$, d, *J* = 7.1Hz, 2H), 5.02 (C*H*-N=C, d, *J* = 5.6 Hz, 2H), 4.81 (C*H*-O, m, 2H), 3.20 (H$_a$, dd, *J* = 16.9, 5.9 Hz, 2H), (H$_b$, dd, *J* = 17.2, 4.0 Hz, 2H), 2.32 (O*H*, br s, 2H) ppm.

^{13}C NMR (125 MHz, CD_2Cl_2): δ = 168.9 (*C*H=N), 140.4 (*C*$_{arom}$-CH-O), 139.3 (*C*$_{arom}$-CH-N), 138.0 (*C*$_{arom}$-CH=N), 129.4 (*C*H$_{arom}$-CH$_{arom}$-C$_{arom}$-CH$_2$), 128.1 (*C*H$_{arom}$), 127.5 (*C*H$_{arom}$-CH$_{arom}$-C$_{arom}$-CH-N), 126.0 (*C*H$_{arom}$-C$_{arom}$-CH$_2$), 124.9 (*C*H$_{arom}$-C$_{arom}$-CH-N), 77.2 (*C*H-N=C), 73.8 (*C*H-O), 39.7 (*C*H$_2$-CH-O) ppm.

FTIR (ATR): $\bar{\nu}_{max}$ = 3561, 2944, 1615 ($\nu_{C=N}$), 1477, 1460, 1431, 1397, 1302, 1212, 1177, 1156, 1094, 1052, 1014, 992, 826, 746, 584, 556, 514, 470, 422 cm^{-1}.

UV-vis (THF, $6.28 \cdot 10^{-5}$ M): ε_{max} = 19 300 (273 nm) $Lmol^{-1}cm^{-1}$.

CD (THF, $6.28 \cdot 10^{-5}$ M): $[\theta]_{max}$ = +36 600 (290 nm), -20 600 (354 nm) $°cm^2dmol^{-1}$.

19f-Cu(OTf)$_2$:

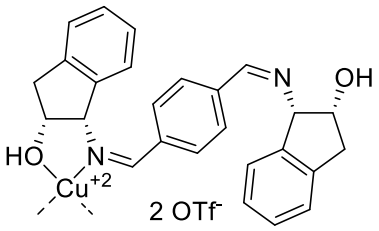

From **19f** (50 mg, 0.126 mmol) and Cu(OTf)$_2$ (45.6 mg, 0.126 mmol) in THF. Dark green solid.

FTIR (ATR): $\bar{\nu}_{max}$ = 2957, 1631 ($\nu_{C=N}$), 1478, 1461, 1428, 1281, 1222, 1162, 1093, 1048, 1024, 909, 881, 832, 753, 709, 634, 574, 515, 471, 453, 417 cm^{-1}.

UV-vis (THF, 4.35·10^{-5} M): ε_{max} = 30 450 (254 nm) Lmol^{-1}cm^{-1}.

CD (THF, 4.35·10^{-5} M): $[\theta]_{max}$ = -37 300 (276 nm) °cm^{2}dmol^{-1}.

19g-CuPF$_6$:

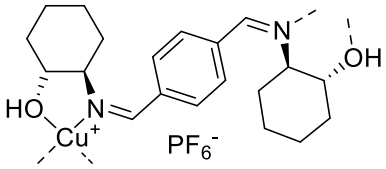

From **19g** (100 mg, 0.304 mmol) and Cu(MeCN)$_4$PF$_6$ (113 mg, 0.304 mmol) in THF. Yellow solid.

FTIR (ATR): $\bar{\nu}_{max}$ = 3557, 2935, 2862, 1621 ($\nu_{C=N}$), 1450, 1393, 1344, 1302, 1243, 1222, 1190, 1126, 1063, 1043, 1023, 828, 739, 556, 490 cm^{-1}.

UV-vis (THF, 7.45·10^{-5} M): ε_{max} = 18 100 (262 nm) Lmol^{-1}cm^{-1}.

CD (THF, 7.45·10^{-5} M): $[\theta]_{max}$ = -43 400 (278 nm), 9 130 (338 nm) °cm^{2}dmol^{-1}.

19g-Cu(OTf)$_2$:

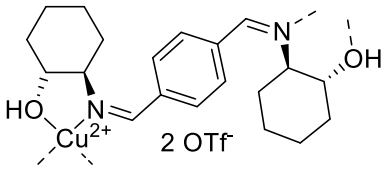

From **19g** (100 mg, 0.304 mmol) and Cu(OTf)$_2$ (110 mg, 0.304 mmol) in THF. Green solid.

FTIR (ATR): $\bar{\nu}_{max}$ = 2941, 2865, 1679 ($\nu_{C=N}$), 1642 ($\nu_{C=N}$), 1610, 1573, 1453, 1278, 1234, 1222, 1161, 1089, 1065, 1024, 923, 858, 819, 760, 634, 573, 515, 410 cm^{-1}.

UV-vis (THF, 4.35·10^{-5} M): ε_{max} = 34 900 (255 nm), 26 000 (276 nm) Lmol^{-1}cm^{-1}.

CD (THF, 4.35·10^{-5} M): $[\theta]_{max}$ = -7 260 (284 nm) °cm^{2}dmol^{-1}.

19g-Zn(OTf)$_2$:

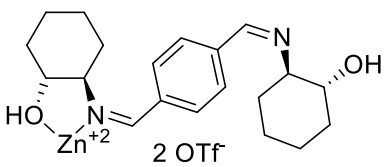

From **19g** (100 mg, 0.304 mmol) and Zn(OTf)$_2$ (111 mg, 0.304 mmol) in THF. Light yellow solid.

FTIR (ATR): $\bar{\nu}_{max}$ = 3321, 2940, 2864, 1678, 1644, 1609, 1574, 1453, 1422, 1392, 1276, 1236, 1223, 1164, 1025, 857, 821, 761, 635, 574, 516 cm^{-1}.

UV-vis (THF, $4.19 \cdot 10^{-5}$ M): ε_{max} = 25 900 (270 nm) $Lmol^{-1}cm^{-1}$.

CD (THF, $4.19 \cdot 10^{-5}$ M): $[\theta]_{max}$ = -61 200 (280 nm) $°cm^2dmol^{-1}$.

23-$CuPF_6$:

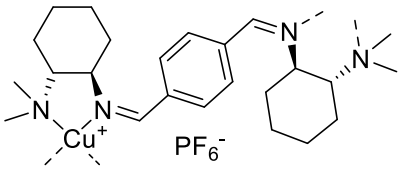

From **23** (100 mg, 0.261 mmol) and $Cu(MeCN)_4PF_6$ (97.4 mg, 0.142 mmol) in THF. Dark brownish-red solid.

^{1}H NMR (500 MHz, CD_2Cl_2): δ = 8.44 (N=C*H*, s, 2H), 7.66 (CH_{arom}, s, 4H), 3.67 (C*H*-N=C, m, 2H), 2.92 (C*H*-NMe_2, m, 2H), 2.55 (NMe_2, s, 12H), 2.07 (C$H_{2\ eq}$-CH-NMe_2, m, 2H), 1.98 (C$H_{2\ ax}$-CH_2-CH-N=C + C$H_{2\ eq}$-CH-N=C, m, 4H), 1.85 (C$H_{2\ eq}$-CH_2-CH-N=C, m, 2H), 1.54 (C$H_{2\ eq}$-CH_2-CH-NMe_2 + C$H_{2\ ax}$-CH-N=C, m, 4H), 1.46-1.37 (C$H_{2\ ax}$-CH-NMe_2, m, 2H), 1.36-1.24 (C$H_{2\ ax}$-CH_2-CH-NMe_2, m, 2H) ppm.

^{13}C NMR (125 MHz, CD_2Cl_2): δ = 160.4 (N=*C*H), 138.4 (*C*$_{arom}$), 128.4 (*C*H$_{arom}$, br), 70.7 (*C*H-NMe_2), 69.4 (*C*H-N=C), 42.0 (NMe_2), 36.6 (*C*H_2-CH-N=C), 25.4 (*C*H_2-CH_2-CH-N=C + *C*H_2-CH_2-CH-NMe_2), 21.0 (*C*H_2-CH-NMe_2) ppm.

FTIR (ATR): $\bar{\nu}_{max}$ = 2935, 2863, 1606, 1449, 1376, 1352, 1296, 1246, 1175, 1110, 1059, 1027, 1017, 978, 937, 872, 833, 739, 576, 556, 531, 511, 469, 441 cm^{-1}.

UV-vis (DCM, $5.07 \cdot 10^{-5}$ M): ε_{max} = 17 400 (276 nm) $Lmol^{-1}cm^{-1}$.

CD (DCM, $5.07 \cdot 10^{-5}$ M): $[\theta]_{max}$ = -28 500 (284 nm), -22 900 (399 nm), +26 600 (512 nm) $°cm^2dmol^{-1}$.

23-$Cu(OTf)_2$:

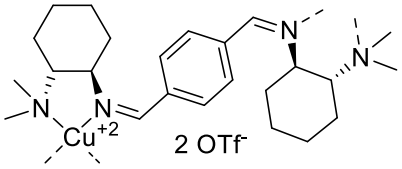

From **23** (100 mg, 0.261 mmol) and $Cu(OTf)_2$ (94.5 mg, 0.142 mmol) in THF. Brick-red powder.

FTIR (ATR): $\bar{\nu}_{max}$ = 3091, 2940, 2865, 1699, 1634 ($\nu_{C=N}$), 1608, 1567, 1465, 1451, 1274, 1242, 1222, 1153, 1112, 1062, 1026, 936, 872, 854, 820, 757, 634, 573, 516 cm^{-1}.

UV-vis (THF, $4.16 \cdot 10^{-5}$ M): ε_{max} = 41 100 (255 nm) $Lmol^{-1}cm^{-1}$.

CD (THF, $4.03 \cdot 10^{-5}$ M): $[\theta]_{max}$ = -8 330 (284 nm), 7 350 (324 nm) $°cm^2dmol^{-1}$.

23-$Zn(OTf)_2$:

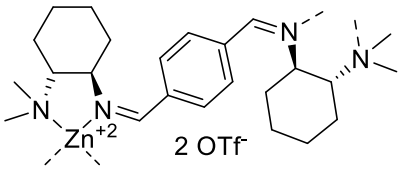

From **23** (100 mg, 0.261 mmol) and $Cu(OTf)_2$ (95.0 mg, 0.142 mmol) in THF. Light yellow solid.

FTIR (ATR): $\bar{\nu}_{max}$ = 3500, 2962, 2927, 2856, 2825, 2780, 2765, 1645 ($\nu_{C=N}$), 1570, 1448, 1416, 1371, 1332, 1291, 1271, 1245,

1224, 1187, 1163, 1120, 1107, 1074, 1028, 944, 914, 872, 841, 818, 637, 574, 543, 517, 461, 445, 417 cm^{-1}.

UV-vis (THF, $4.16 \cdot 10^{-5}$ M): ε_{max} = 34 600 (255 nm) $Lmol^{-1}cm^{-1}$.

CD (THF, $4.02 \cdot 10^{-5}$ M): $[\theta]_{max}$ = -4 180 (273 nm) $°cm^2dmol^{-1}$.

26-$CuPF_6$:

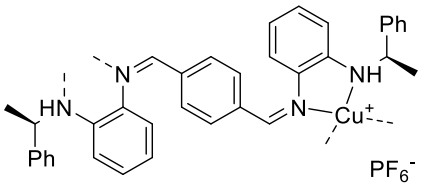

From **26** (100 mg, 0.191 mmol) and $Cu(MeCN)_4PF_6$ (71.3 mg, 0.191 mmol) in technical grade THF under air. Evaporation of the solvent yielded a purple solid. Broad and complex features in ^1H and ^{13}C NMR.

FTIR (ATR): $\bar{\nu}_{max}$ = 3390, 3059, 3028, 2971, 2867, 1613 ($\nu_{C=N}$), 1593, 1494, 1453, 1427, 1373, 1323, 1280, 1252, 1205, 1180, 1160, 1141, 1098, 1063, 1027, 1017, 911, 832, 740, 699, 556 cm^{-1}.

MS (ESI+): *m/z* = 581.180 ([(**26**-Cu^{2+})$_2$ – 4 H_2 + 2 e^-], 92%). Two ligands/two metals complex, all four benzylic amines oxidized.

UV-vis (THF, $5.61 \cdot 10^{-5}$ M): ε_{max} = 15 600 (287 nm) $Lmol^{-1}cm^{-1}$.

CD (THF, $5.61 \cdot 10^{-5}$ M): CD features are too weak to be quantified properly.

26-$Cu(OTf)_2$:

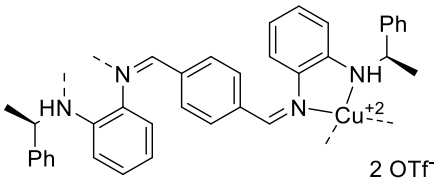

From **26** (100 mg, 0,191 mmol) and $CuOTf_2$ (69.2 mg, 0.191 mmol) in technical grade THF under air. Evaporation of the solvent yielded a purple solid.

FTIR (ATR): $\bar{\nu}_{max}$ = 3252, 3053, 2982, 2878, 1614 ($\nu_{C=N}$), 1498, 1455, 1429, 1281, 1235, 1222, 1157, 1099, 1052, 1025, 852, 751, 698, 635, 573, 515, 442 cm^{-1}.

MS (ESI+): *m/z* = 581.180 ([(**26**-Cu^{2+})$_2$ – 4 H_2 + 2 e^-], 92%). Two ligands/two metals complex, all four benzylic amines oxidized, both metals reduced to Cu(II). Peaks are identical with those of **26-$CuPF_6$**.

UV (THF, $3.32 \cdot 10^{-5}$ M): ε_{max} = 26 300 (286 nm) $Lmol^{-1}cm^{-1}$.

CD (THF, $3.32 \cdot 10^{-5}$ M): $[\theta]_{max}$ = -18 000 (292 nm) $°cm^2dmol^{-1}$.

26-$Zn(OTf)_2$:

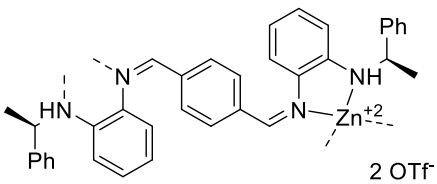

From **26** (100 mg, 0.191 mmol) and $ZnOTf_2$ (69.5 mg, 0.191 mmol) in technical grade THF under air. Evaporation of the

solvent yielded an orange solid. Broad and complex features in ^{1}H and ^{13}C NMR.

FTIR (ATR): $\bar{\nu}_{max}$ = 3362, 3032, 2979, 2878, 1619 ($\nu_{C=N}$), 1598, 1494, 1456, 1428, 1286, 1222, 1166, 1025, 915, 882, 849, 753, 699, 635, 574, 515 cm^{-1}.

MS (ESI+): not found.

UV (THF, $3.31 \cdot 10^{-5}$ M): ε_{max} = 18 400 (285 nm) $Lmol^{-1}cm^{-1}$.

CD (THF, $2.71 \cdot 10^{-5}$ M): $[\theta]_{max}$ = +11 800 (292 nm) $°cm^2dmol^{-1}$.

26-Ni(BF_4)$_2$:

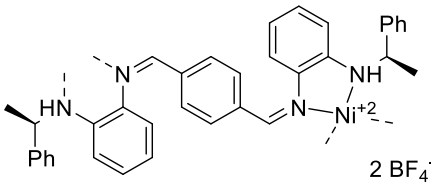

From **26** (100 mg, 0.191 mmol) and Ni(BF_4)$_2$(H_2O)$_6$ (69.5 mg, 0.191 mmol) in technical grade THF under air. Evaporation of the solvent yielded a brown solid.

FTIR (ATR): $\bar{\nu}_{max}$ = 3520, 3272, 3158, 3062, 2972, 2875, 1615 ($\nu_{C=N}$), 1598, 1492, 1455, 1376, 1282, 1159, 1047, 1028, 1017, 915, 885, 851, 753, 700, 650, 587, 520, 452, 439 cm^{-1}.

MS (ESI+): not found.

UV (THF, $3.91 \cdot 10^{-5}$ M): ε_{max} = 16 800 (285 nm) $Lmol^{-1}cm^{-1}$.

CD (THF, $3.91 \cdot 10^{-5}$ M): $[\theta]_{max}$ = -11 200 (298 nm) $°cm^2dmol^{-1}$.

IV.2.2 Spectral investigations

IV.2.2.1 UV-vis-titration experiments

A solution of **26** (2 ml, $5.74 \cdot 10^{-5}$ mol/L) in THF was placed in a quartz cuvette. A THF solution of a given metal salt (20 µl, 5.74 x 10^{-4} mol/L, 0.1 equiv) was added successively; a UV-vis spectrum of the mixture was taken after each addition. To compensate for the solution's ongoing dilution, the absorption values of all spectra were corrected following equation (50):

$$Abs(\lambda)_n^{corrected} = Abs(\lambda)_n \cdot \frac{V_n}{V_0} \qquad (50)$$

With $Abs(\lambda)_n$ being the absorbance at wavelength λ after *n* additions of metal salt, V_n the total volume after *n* additions of metal salt, and V_0 the initial volume (2 mL). The corrected absorption values now refer all to the initial ligand concentration of $5.74 \cdot 10^{-5}$ mol/L.

IV.2.2.2 Kamlet-Taft analysis

Solutions of ligand **26** in different solvents were analysed by UV-vis spectroscopy, the λ_{max} of the band in the visible region determined and converted into wavenumbers (Table 15). The solvents' Kamlet-Taft parameters were all taken from Kamlet's collection,[181] except the ones for *t*BuOMe.[193] *s*, *a* and *b* were calculated from the data in Table 15 using the "Multiple Linear Regression" tool in Origin 16 software.

*Table 15: Compilation of the λ_{may} and ν_{max} of ligand **26** in UV-vis-spectroscopy as a function of the solvent and of the π*, α and β parameters of the corresponding solvent.*

Solvent	λ_{max} [nm]	ν_{max} [cm^{-1}]	π*	α	β
THF	436	22935.77982	0.58	0	0.55
acetone	436	22935.77982	0.71	0.08	0.48
DMF	443	22573.36343	0.88	0	0.69
MeCN	435	22988.50575	0.75	0.19	0.31
Cyclo	454	22026.43172	0	0	0
tBuOMe	443	22573.36343	0.25	0	0.45
MeOH	428	23364.48598	0.60	0.93	0.62
iPrOH	442	22624.43439	0.48	0.84	0.76
EtOH	430	23255.81395	0.54	0.83	0.77
Et_2O	441	22675.73696	0.27	0	0.47
Dioxane	446	22421.52466	0.55	0	0.37
AcOEt	442	22624.43439	0.55	0	0.45

V : Supporting Information

V.1 Methodologies

This section gives explanations to some of the methodologies used in this work which may be not familiar to all readers. Those are Stalke's ECCs for DOSY NMR, VTNA for the determination of the kinetic order in catalyst and the Hammett plots using different σ-scales.

V.1.1 ^{1}H DOSY NMR: External Calibration Curves (ECCs)

The classical method to relate *D* to the analyte's volume is to use the Stokes-Einstein equation:[194]

$$D = \frac{k_B \cdot T}{6\pi \cdot \eta \cdot r} \tag{51}$$

With k_B being the Boltzmann constant, T the temperature, η the sample's viscosity and r the molecule's (hydrodynamic) radius. The molecule's volume can then be calculated from r.

The Stokes-Einstein equation is used a lot for the analysis of globular macromolecules like proteins. It assumes the analyte to be spherical but it can be modified to account for elliptic or flat molecular shapes. Nevertheless, it has a lot of disadvantages: it is adapted only to molecules much bigger than the solvent; the viscosity can be approximated to the solvent's viscosity at the chosen temperature only when working in dilute solutions; even though the Stokes-Einstein equation takes temperature into account, the analyte's diffusion behaviour can change over different temperatures, making D values representative only at room temperature; convection movements due to temperature gradients along the NMR tube can also falsify the measured *D* values. Those are inevitable especially at high temperature since the sample is heated with an airflow blowing from the bottom of the spectrometer, thus creating an inhomogeneous temperature distribution in and along the tube. However, convection can be reduced by using narrow NMR tubes (e. g. 3 instead of 5 mm diameter) and further compensated by the choice of an appropriate convection compensating pulse sequence.

To get representative diffusion values we will work in the same conditions as when performing catalysis, that is at high concentration (0.833 M with $ZnMe_2$) and at different temperatures to follow the evolution of the aggregates' sizes or distribution. This disqualifies the use of the Stokes-Einstein equation and made us move to another method: Dietmar Stalke's External Calibration Curves (ECC).[112,114,115] It consists in measuring not only the analyte's diffusion coefficient but also the one of a reference molecule, which doesn't need to be inside the same NMR tube (this is why the calibration curves are coined as "external"), to obtain a *normalised* diffusion coefficient :

$$D_{x,norm} = \frac{D_x}{D_{ref}} D_{ref,fix} \tag{52}$$

With $D_{x,norm}$ being the analyte's normalised diffusion coefficient, D_x the analyte's measured diffusion coefficient, D_{ref} the reference's measured diffusion coefficient and $D_{ref,fix}$ a constant specific to the reference molecule.

Dividing D_x through D_{ref} allows to cut off influences like temperature and viscosity since both molecules are subjected to the same conditions. However, it results also in a dimensionless factor which is meaningful only when comparing analytes to the same reference. Multiplying with $D_{ref,fix}$, which is a constant value and empirically determined through linearization of Equation (52) (in fact, it is nothing but the *reference's* $D_{x,norm}$), turns $D_{x,norm}$ back to a diffusion coefficient which is now "normalised", free of the beforementioned influences. The power of the ECC method lies in its general applicability: whatever the reference used, the same $D_{x,norm}$ will be obtained; even the residual NMR solvent signal can be used as a reference. Stalke and co-workers have determined $D_{ref,fix}$ for a variety of reference molecules and plotted the obtained $D_{x,norm}$ of a multitude of small molecules against their known molecular weight (MW) using the power law :

$$D_{x,norm} = K \cdot MW^{\alpha} \tag{53}$$

With $D_{x,norm}$ being the normalised diffusion coefficient, K being a system-dependant prefactor, MW the analyte's molecular weight and α a factor accounting for the analyte's compactness. Linearisation by taking the logarithm of both sides allows isolation of MW.

From the various analytes (pentane, $Si(SiMe_3)_4$, BINAP, anthracene…) they obtained shape-optimised calibration curves which divide the analytes into three classes: compact spheres (CS, compact globular molecules), expanded disks (ED, flat polyaromatic molecules) and dissipated spheres & ellipsoids (DSE, less compact spheric or ellipsoidal molecules). The calibration curves (when used for a molecule with the appropriate shape) relate $D_{x,norm}$ to MW with an astonishing precision: the standard deviation is of 4% and the maximum deviation of 9%. This is also true independently from concentration and temperature: the analysis of adamantane with the residual signal of toluene-d_8 gave accurate MW from -75 to 100°C; various analytes at 120 mM gave identical or similar MW values compared to the standard concentration of 15 mM. It should only be ensured that reference and analyte cannot make unwanted intermolecular interactions: the MW of some molecules with large π-systems have been overestimated at high concentration, probably due to π-interactions; the residual signal of THF-d_8 as a reference gave also overestimated MW values for $Si(SiMe_3)_4$ at temperatures below -50°C, presumably because of hydrogen bonding. Another factor is the *molecular weight density*: p-block and d-block elements from the 3rd period on have a higher mass than C, H, O, or N but their volume does not increase in the same extend – their molecular weight density (MW_D) is higher. If such elements contribute significantly to the analyte's MW they can lead to underestimated MW values from the present ECCs. For a whole molecule, MW_D is defined by its molecular weight divided by the sum of the atom's volumes (approximated from their Van-der-Waals radii):

$$MW_D = \frac{MW}{V_W} = MW \Big/ \sum_{i=1}^{n} \frac{3}{4} \pi r_{w,i}^3 \tag{54}$$

With MW_D being the molecular weight density, V_W the analyte's total Van-der-Waals volume and r_W the Van-der-Waals-radius of the atoms constituting the analyte.

Stalke and co-workers have defined their ECCs to work with molecules whose MW_D are between 4.3 and $5.2 \cdot 10^{-29}$ $gmol^{-1}m^{-3}$. Thus, the sheer presence of heavy heteroatoms is not necessarily a problem as long as the analyte's total MW is within those limits. The ECCs have been successfully applied, e. g. in the determination of solution structures of Rb- and Cs-containing molecules.[113,195] However, analytes with MW_D higher than $5.2 \cdot 10^{-29}$ $gmol^{-1}m^{-3}$ are underestimated in their MW using the present ECCs. This deviation can be corrected with an empirical correction factor (X_{cor}); special calibration curves for bromine and iodine containing molecules have also been developed. Those workarounds work fine for organic molecules containing heavy halides but can be tricky for simple d-block metal complexes: Ferrocene and $CpMn(CO)_3$ give reasonable MW values while $PdCl_2(PhCN)_2$ is heavily underestimated.[115]

V.1.2 Kinetics: Visual Time-Normalised Analysis (VTNA)

VTNA is a technique which uses whole kinetic curves to determine the partial orders of the considered reaction and can even determine k_{obs}. This is superior to the "v_0-method" which consists in determining the initial rate v_0 and then to plot $\log(v_0)$ against log[Cat]. The data from several runs with different [Cat] gives a linear correlation which slope is equal to *c*, however this can be misleading if v_0 is not representative for the whole catalytic reaction, e. g. because there is an induction period; it also affords considerable experimental effort and the correct determination of v_0 can be difficult. On the other side, VTNA takes into account the whole reaction curve and is quite easy to set up. The techniques behind VTNA have already been used for more than a century by biologists but have been formalised and introduced to the chemistry community only recently by Jordi Burés.[117,191,196]

The outcome of a kinetic runs consists of a plot [Sub] (or [P]) vs. time (t). It is mathematically described by the integrated form of equation (11):

$$-d[Sub] = k_{obs}[Cat]^c[Sub]^x\,[Rea]^y dt$$

$$\rightleftarrows \frac{-d[Sub]}{[Sub]^x\,[Rea]^y} = k_{obs}[Cat]^c dt$$

$$\rightleftarrows -\int_{[Sub]_0}^{[Sub]_t} \frac{d[Sub]}{[Sub]^x\,[Rea]^y} = k_{obs}[Cat]^c \int_0^t dt$$

$$\rightleftarrows F([Sub]_t, [Sub]_0, \nu_{Sub}, [Rea]_0, \nu_{Rea}) = k_{obs}[Cat]^c t$$

$$\rightleftarrows [\boldsymbol{Sub}]_{\boldsymbol{t}} = G(k_{obs}, [Cat], [Sub]_0, \nu_{Sub}, [Rea]_0, \nu_{Rea})\boldsymbol{t} \quad (55)$$

With $[Sub]_0$ and $[Rea]_0$ being the initial concentration and v_{Sub} and v_{Rea} the consumption rate of [Sub] and [Rea]. Equation (55) shows what we usually see on a kinetic curve: the substrate's concentration (y-axis) as a function of time (x-axis) and of a function *G* including k_{obs}, [Cat] (which is considered to stay constant over the course of the reaction), $[Sub]_0$, $[Rea]_0$ and v_{Sub} and v_{Rea}.

VTNA consists in taking out one of the factors, e. g. $[Cat]^c$, from *G* to integrate it with *t* into the x-axis – the time scale is "normalised" for $[Cat]^c$. This leads to equation (56) :

$$[\boldsymbol{Sub}]_{\boldsymbol{t}} = G(k_{obs}, [Sub]_0, v_{Sub}, [Rea]_0, v_{Rea})\boldsymbol{t}[\boldsymbol{Cat}]^{\boldsymbol{c}} \quad (56)$$

The x-axis is now a "t$[cat]^c$"-axis as shown in Figure 131. The effect of the normalisation is that it cuts out [Cat]'s kinetic effect from the plot: if [Cat] is varied over different experiments while all other variables remain unchanged, then *G* will be *identical* for all chosen [Cat]. Graphically, it means that the curves all have the same shape; if put into the same graph those curves will overlay – as long as the right catalyst order is chosen. This is where the elegant simplicity of VTNA reveals itself: it is sufficient to plot the kinetic profiles into an Excel spreadsheet, to normalise their time axis and to adjust *c* until the curves visually overlay – this means that the right *c* has been chosen. In Figure 131 the two curves with 10 and 15 mol% catalyst do not overlay for *c* = 1 but they do for *c* = 0.4, so 0.4 is the partial catalyst order.

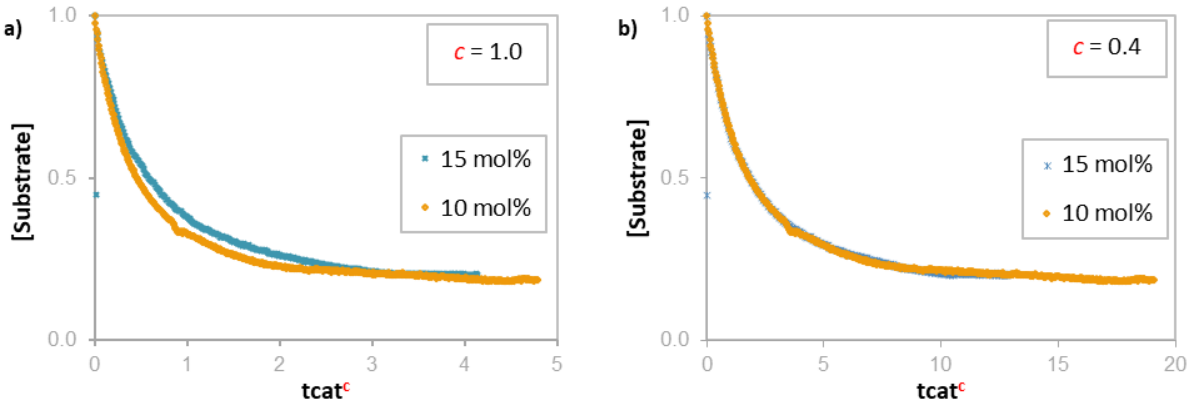

Figure 131: Example of c adjusting using VTNA with a) C = 1.0 and b) c = 0.4. The two curves in each graph were obtained from different catalyst concentrations (blue curve: 0.15 M; orange curve: 0.10 M). The best overlay is obtained for c = 0.4 which is therefore the partial order in catalyst.

The visual check is not an exact method but is sufficiently accurate to get reliable values; the human eye is also astonishingly good in identifying trends and outlying values.[117] The accuracy of the overlay may be additionally verified with mathematical tools such as linear regression. VTNA works even if there are only few points per curve or if there is a large error in the measured $[Sub]_t$ values. The time-scale normalisation is valid not only for [Cat] but also for the other reaction components [Sub] and [Rea], their partial orders *x* and *y* can also be determined this way. Moreover, the time scale can be normalised for [Cat], [Sub] and [Rea] simultaneously: this results in a single straight line whose slope is equal to k_{obs}.

V.1.3 Linear Free Energy Relationships (LFER): Hammett plots

Louis Plack Hammett developed in the early 20th century a methodology to compare different reactants in a reaction and to quantify the effect of their electron-donating or -withdrawing capabilities. For this, he developed the σ-scale which quantifies the electron-attracting (σ < 0) or -donating (σ > 0) effect of para- and meta-substituents on aromatic rings; it has been greatly extended since then.[197,198] Ortho-substituents have also significant steric influence on the reaction centre, therefore no σ-scale has been defined for them. The relationship between the substrate's reactivity (i.e. its reaction rate, expressed through the kinetic constant) and σ proved in many cases to be linear and became to be known as "Linear Free Energy Relationship" (LFER), following equation (57):[121]

$$\log\left(\frac{k_X}{k_H}\right) = \rho\sigma \tag{57}$$

With k_X being the kinetic constant of the reaction with substituted substrate, k_H the kinetic constant of the reference substrate (X = H), σ the substrate's respective σ-value and ρ the "sensitivity constant".

Plots with $\log(k_X/k_H)$ vs σ are called "Hammett plots" and usually are linear, with ρ as their slope (Figure 132). ρ is an indicator for a charge buildup in the transition state associated to the rate-limiting step. If it builds up positive charge, it will be stabilised (and the reaction therefore accelerated) by electron-donating substituents and ρ is negative. A positive ρ-value stands for a negative charge-buildup which is stabilised by electron-attracting groups. In certain cases, ρ is not constant over a given range of σ; the plot then has the shape of a broken line or even a V-shape if ρ changes its sign. Such *non-linear* Hammett plots indicate a change in the rate-limiting step and/or a change of mechanism.

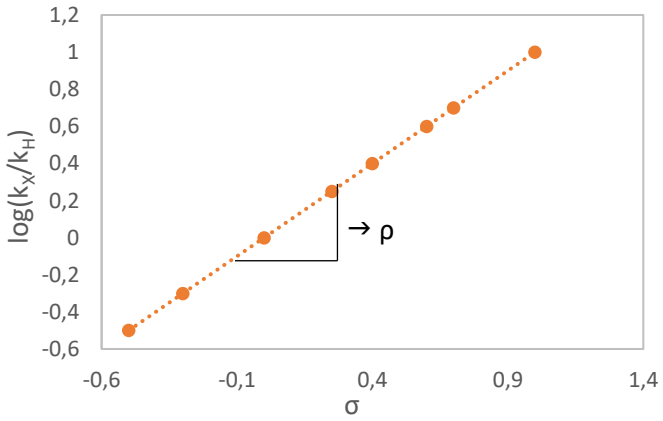

Figure 132: Example of a Hammett plot. The slope of the fitted line corresponds to ρ.

One should keep in mind that the σ-scale is obtained from the pKas of the corresponding substituted benzoic acids (Figure 133a): the lower the pKa, the more the carboxylate anion is stabilised – i. e. by electron-attracting substituents – the higher the σ-value. The substituent's influence can be split into field, polarizability, inductive (the three are often summed up as "Field effects") and resonance effects. The latter depends a lot on the substituent's position (*para*-substituents can delocalise positive or negative charge onto the carbon *ipso* to the carboxylate, whereas *meta*-substituents

don't) and its π-accepting (e. g. aldehydes, nitriles) or -donating properties (alcohols, amines). Specialised scales like σ_i/σ_r, the Swain-Lupton or Taft-Topsom-parameters separate field- from resonance effects. However, resonance is always defined as *being confined inside of the aromatic ring* as the benzoate cannot delocalise its negative charge into the ring, nor is the carboxylate a good π-acceptor. To account for molecules where there is significant "through-conjugation" into the reactive centre, special resonance scales have been developed (Figure 133b and c). The σ^+-scale, obtained from the dissociation of phenyldimethyl chloromethanes, allows to quantify the effect of positive charge delocalisation; the σ^--scale (from the deprotonation of phenols) does the same for the stabilisation of negative charges. As it is not always evident if through-conjugation is significant in a given reaction, or if there is a particular sensitivity to either field or resonance effects, it is best practice to plot the $\log(k_X/k_H)$ data against the different scales and to see which fits best.

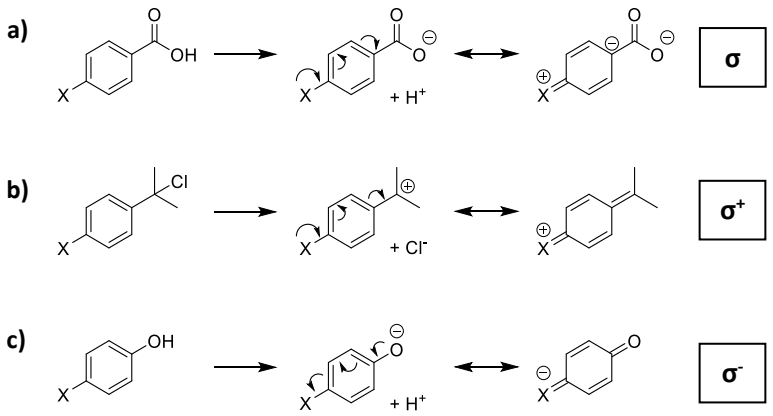

Figure 133: Reactions of para-substituted a) benzoic acids, b) phenyldimethyl chloromethanes and c) phenols that define the σ, σ⁺ and σ⁻-scales, respectively.

V.2 Additional Results & Discussion

The present section gathers results which are not conclusive enough to add to the discussion in chapters I-III, but which are still of interest and which we wish to keep in this manuscript.

V.2.1 Additional complexes as references for ^{1}H DOSY NMR

V.2.1.1 Boron Complexes

The idea was to make metallacycles which cannot aggregate through coordination bonds, and therefore to be even closer to the structure of monomeric NBE-ZnMe (Figure 134). There are reports for BX_2-aminoalkoxides similar to **28** in the literature.[190,199] Therefore, we attempted to react NBE boron halogenides; the reaction schemes are shown in Figure 134. Reaction of NBE with $BF_3{\cdot}OEt_2$ in

presence of NEt_3 or NaH didn't show any reproducible conversion; reaction with DABCO yielded a product with a messy ^{1}H NMR spectrum. Same goes for the reaction with DABCO and BCl_3 or BBr_3. The sole presence of two different stereoisomers due to the chiral tetracoordinate N atom cannot explain the complexity of the NMR spectra, there have to be more conformers and/or product degradation.

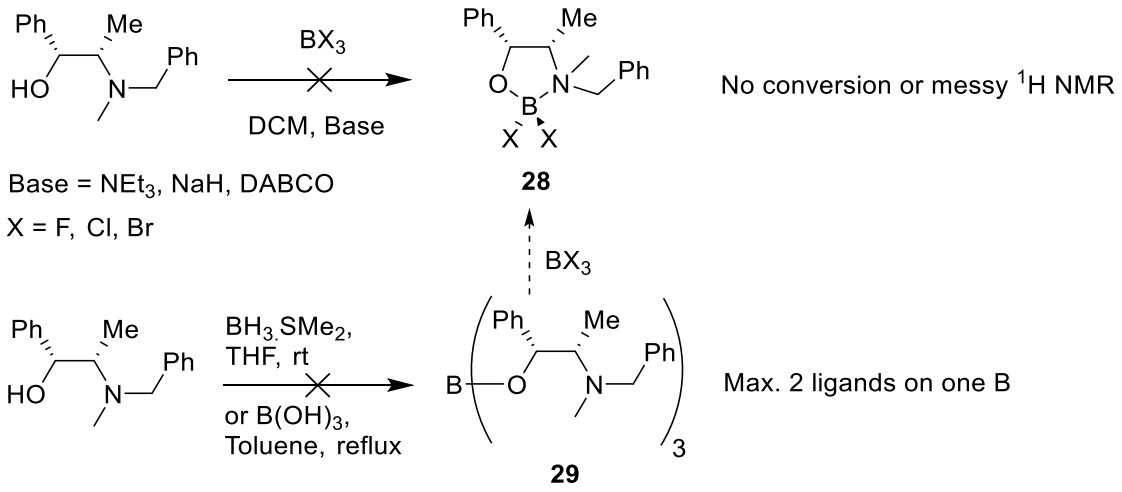

*Figure 134: Scheme for the unsuccessful synthesis of NBE-based boracycle **28** and its boric ester precursor **29**.*

We then changed the strategy and attempted first to synthesise the boric ester **29** and then to obtain **28** from a metathesis reaction; however, even after days at reflux in toluene with a Dean-Stark apparatus the condensation of NBE on boric acid didn't go past 2 equiv. of NBE for one boron. Reaction with $BH_3{\cdot}SMe_2$ in THF at room temperature didn't give better results. NBE probably generates too much steric hindrance to allow the condensation of a 3rd molecule on boron.

We turned then to another type of boracycle derived from catechol (Figure 135). The reaction of NME with catecholborane yielding **30-Me** is described and has been successfully reproduced by us.[200] However, the same reaction using NBE instead of NME to give **30-Bn** resulted again in complex ^{1}H NMR spectra. Substitution of catecholborane by pinacolborane gave clean ^{1}H NMR spectra for **31-Me** and **31-Bn**, but the products are most probably not suited for DOSY experiments. Both NMe-groups in **31-Me** appear as a single singlet, which indicates that the B-N-bond is labile at room temperature – the parent compound **30-Me** shows two different NMe-singlets which are reported to merge together only at 55°C and higher.[200] The ^{1}H NMR spectrum of **31-Bn** is even almost identical with that of the starting material NBE, only the CH-O-signal shifts significantly. This indicates that the boric ester has formed but that the boron is not coordinated to the nitrogen atom at all. The pinacol group seems to be too large to allow the coordination of boron to the nitrogen atom. Further evidence may be gained from ^{11}B NMR, where non-coordinated and N-coordinated boric esters bear signals with distinct chemical displacements (around 23 and 12 ppm, respectively).[200] Except **30-Me** and maybe **31-Me**, the present complexes are no suitable reference molecules to validate the DOSY methodology.

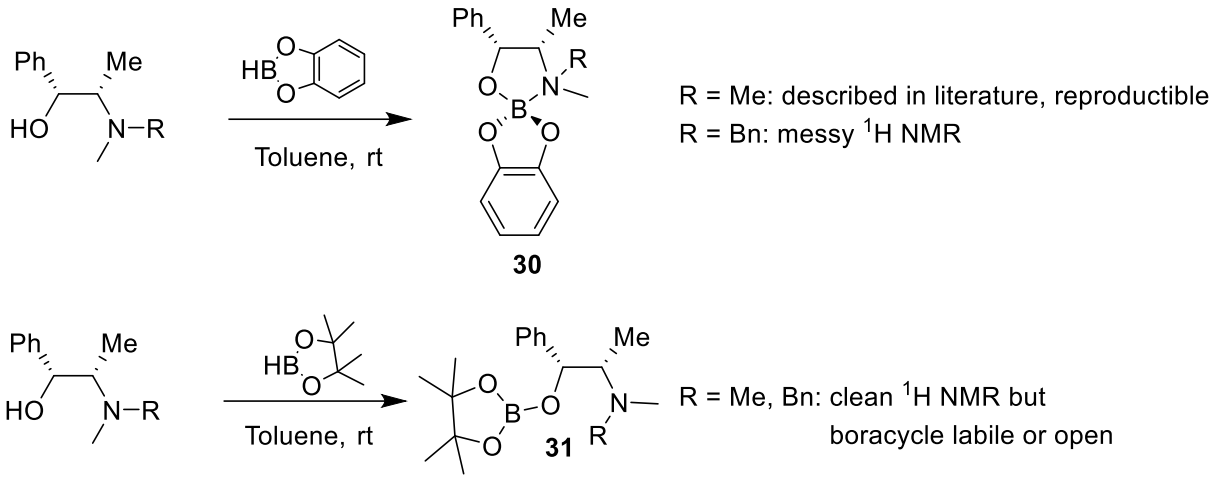

*Figure 135: Synthesis of boric esters **30-Me/Bn** and **31-Me/Bn** from NME and NBE, respectively. **30-Me** is described in the literature and could be reproduced. **30-Bn** didn't give conclusive results, while **31-Me** and **31-Bn** are partly or totally non-N-coordinated boric esters.*

V.2.1.2 Zinc complexes

Next, we wanted to verify that the presence of zinc, a high MW_D-metal, doesn't lead to underestimation of MW with Stalke's ECCs. To avoid complex aggregation as with NBE-ZnMe, the zinc atom needs to be coordinatively saturated; the whole molecule's MW_D must also be below $5.2 \cdot 10^{-29}$ $gmol^{-1}m^{-3}$. We decided to make simple ZnX_2-complexes with diamine ligand and carbon-based counter-ions (Figure 136); classical counter-ions like halides would increase the molecules' MW_D. The complexes are all within the upper MW_D-limit except **32-OAc**, which is just on the limit of $5.2 \cdot 10^{-29}$ $gmol^{-1}m^{-3}$.

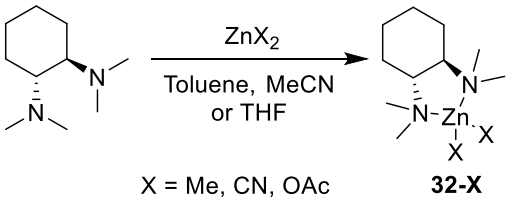

X	MW_D(**32**) [$\cdot 10^{-29}$ $gmol^{-1}m^{-3}$]
Me	4.68
CN	4.94
OAc	5.20

*Figure 136: Reaction scheme for the synthesis of **33-X** and calculated MW_D.*

Figure 137 shows the deviation of the DOSY-determined MW from the calculated MW of the diamine complexes. **33-Me** has a satisfying -3% deviation at -20°C but shows a stronger underestimation at higher temperatures. This can be interpreted as a systematic underestimation which is compensated by a solvation sphere or aggregation as in Figure 40, although this is not very likely as the molecule lacks aromatic rings capable of π-stacking. The other possibility is that heat promotes the

decoordination of the ligand and therefore a MW underestimation. This wouldn't be surprising as $ZnMe_2$ already is quite electron-rich, additional electron density from the ligand may be not very favourable. Indeed, the two NMe-signals in the ^1H NMR spectrum are separated at -20°C as expected for enantiotopic groups, but start to coalesce at 25°C to give a single NMe_2 peak. This is accompanied by significative deshielding (Δδ = -0.19) of the ligand signals and shielding (Δδ = -0.19) of the ZnMe-signal: both move towards the chemical displacement of the starting materials. However, the coalescence and the peak shift can also be due to topomerization as observed in enantiopure DAIB-ZnMe.[28]

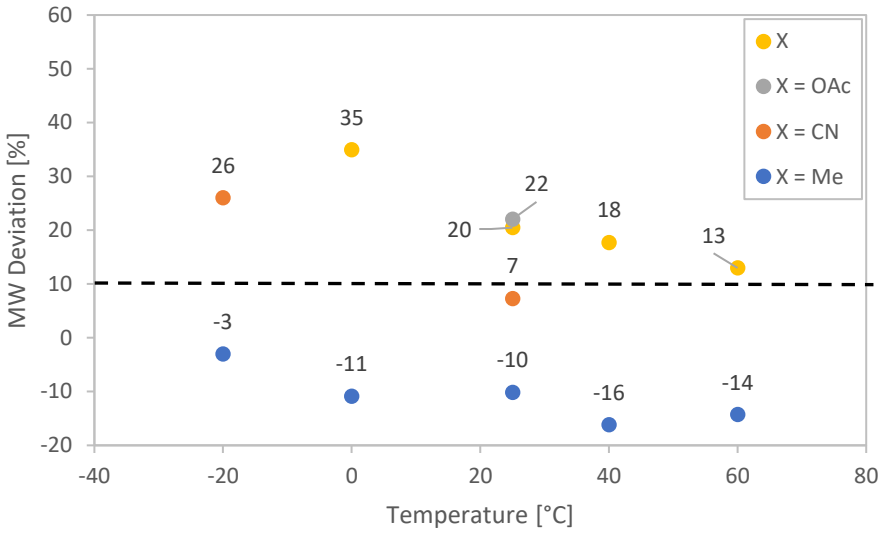

*Figure 137: Temperature-dependent MW deviation of complexes **32-Me**, **32-CN** and **32-OAc**.*

On the other hand, Zn in complexes **32-CN** and **32-OAc** is less electron-rich and should be more tightly bound to the ligand. **32-CN** is highly overestimated at -20°C but within the 9% limit at room temperature; **32-OAc** is overestimated by 22% even at room temperature. An *over*estimation is contrary to the possible pitfall we await for Zn-containing analytes: here, we have to consider the possibility of aggregation induced by CN- or OAc-bridging between two Zn centres.

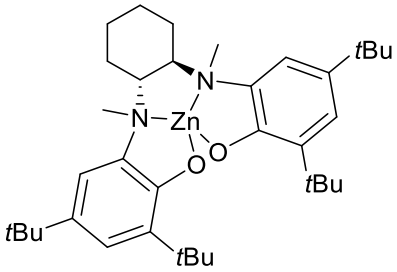

*Figure 138: Complex **33**-Zn*

In order to prevent anion-bridging, we designed L_2X_2-type ligand **33** and reacted it with $ZnEt_2$ to form complex **33-Zn** (Figure 138). Since the ligand acts as a counteranion it is tightly bound and the bulky tBu-groups should prevent the phenols from binding to other complexes. However, as shown in Figure 137, it is even more overestimated than the complexes from ligand **32**. Recent, unpublished results from the group of Charles Romain (Imperial College London) revealed that the phenol's oxygen actually does bridge two Zn centres to form a dimeric complex, in the XRD-structure of an Al(III)-OR-complex of **33**. Thus, it seems that none of the complexes of **32** and **33** are suitable, non-aggregating DOSY references.

V.2.2 K_S' calculation

ee_L [%]	K_S' (**R = Et**) [$\cdot 10^{-6}$]	With:
2	2.82	α = 0.973
1	5.39	$[Cat_{tot}]$ = 0.185 M
Mean K_S':	$4.11 \cdot 10^{-6}$	

➔ $s'(\boldsymbol{R = Et}) = \sqrt{K_S'} = 2.03 \cdot 10^{-3}\ \frac{mol}{L}$

ee_L [%]	K_S' (**R = Me**) [$\cdot 10^{-6}$]	With:
3	1.78	α = 0.966
2	5.25	$[Cat_{tot}]$ = 0.167 M
1	7.33	
Mean K_S':	$4.78 \cdot 10^{-6}$	

➔ $s'(\boldsymbol{R = Me}) = \sqrt{K_S'} = 2.19 \cdot 10^{-3}\ \frac{mol}{L}$

It should be noted that the K_S' values at different ee_Ps are quite different, ranging from $1.78 \cdot 10^{-6}$ (ee_L = 3%) to $7.33 \cdot 10^{-6}$ (ee_L = 1%) (Table 3, R = Me). This comes from Kagan's definition of α being a constant, although the part of non-reacting catalyst necessarily changes when varying ee_L. α is best defined as a *maximal fraction* of non-reacting catalyst which is attained only at ee_L = 0. The NLE curve thus should *converge* to the dashed lines in Figure 32 for ee_Ls close to 0 and K_S' being valid only at ee_L = 0. However, we didn't determine α by drawing a tangent line on the NLE curve but by fitting the plot for equation (7) to low-ee_L datasets, giving a slightly underestimated α. The resulting increase of the quadratic term in equation (27) can be compensated by taking ee_Ls slightly higher than 0. Therefore, it is best practice to *use the same ee_Ls than those used to determine α* to obtain representative values of K_S'. A proper α determination by drawing the tangent line at ee_L = 0 would probably give more accurate results but would require also a well-defined NLE curve for ee_L < 1%.

V.2.3 NBE-catalysed reaction of $ZnMe_2$ to *para*-substituted substrates: conversion

This section is an appendix to chapter I.2.3.4(a), where we did a screening of different *para*-substituted benzaldehydes in the NBE-catalysed addition of dialkylzincs. In addition to the reactions' ee_P, we have had also a look at the conversion of the reactions with $ZnMe_2$. $ZnEt_2$ gives conversions over 90% after overnight stirring at 0°C, regardless of the aldehyde and ee_L, $ZnMe_2$ proves to be more sensitive to the substrate.

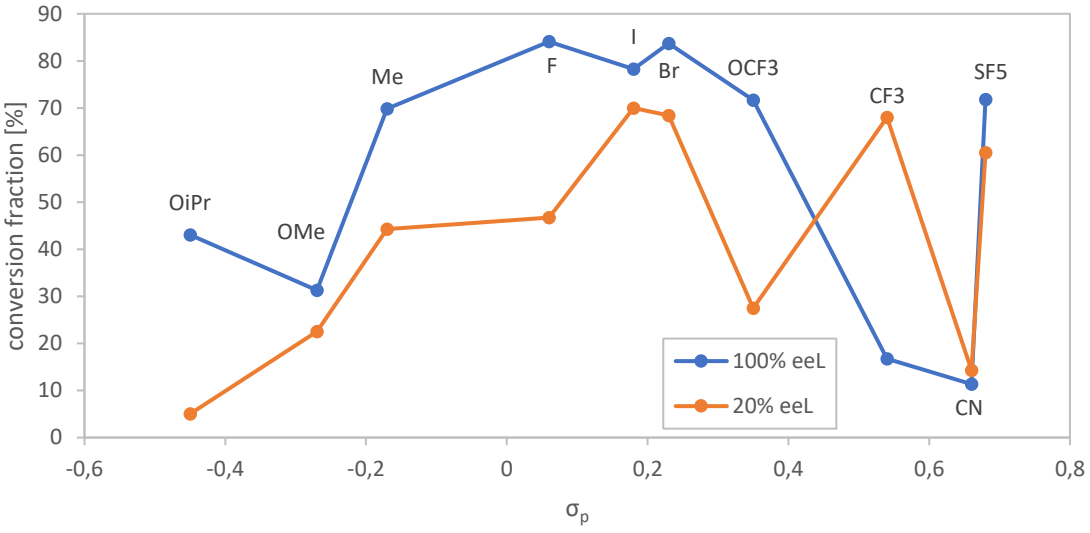

Figure 139: Conversions of the reactions from Figure 60 after 3.5 days.

Figure 139 shows the conversion of the reaction, with $ZnMe_2$ and different aldehydes, after 3.5 days reaction time, at 20% (orange line) or 100% ee_L (blue line). The conversion follows roughly the trend of ee_P in Figure 60: the higher σ_p/ee_P, the higher the conversion, the runs with scalemic ligand showing a throughout lower conversion than those with 100% ee_L.

Here again, the substrates at $\sigma_p > 0.1$ don't necessarily follow the trend of the substrates at lower σ_p. CF_3 is of particular interest since it shows a much higher conversion at 20% ee_L than at 100% - although there is 5 times less catalyst in solution in the first case than in the latter! This may be due to a low affinity or activity of the CF_3-substrate for/with the dimeric catalyst – which is more present at 100% than at 20% ee_L – or to a greater tendency of the chiral zinc alkoxide product to inhibit the catalyst at 100% ee_L. It should be also noted that *p*CN-benzaldehyde shows a very low conversion with both scalemic and enantiopure ligand, however the next substrate in increasing σ_p-order, SF_5, shows a normal behaviour: high conversions with both enantiopure and scalemic ligand, the latter being ca. 10% lower than the first.

V.2.4 16-catalysed addition of $ZnMe_2$ to benzaldehyde

We performed catalysis with **16** and $ZnMe_2$ as the dialkylzinc reagent. Figure 140 shows a temperature screening of the reaction with $ZnMe_2$ with either enantiopure (blue dots) or 20% ee ligand (orange dots). The switch to $ZnMe_2$ parallels our results with NBE: compared to $ZnEt_2$ ee_P dramatically decreases (12% at 0 °C) but it also increases at higher temperatures, much like in the temperature screenings of NBE and $ZnMe_2$ (chapter I.2.2.2, p. 36). To our great surprise the scalemic ligand (20% ee_L) gives a significantly higher ee than the enantiopure one: with $ZnMe_2$ the **16**-catalysed reaction is hyperpositive! The ee_P difference between scalemic and enantiopure ligand (Δee_P) oscillates between 5 and 10%, the maximum being at 23 °C, there is no clear trend as with $ZnEt_2$ in Figure 87.

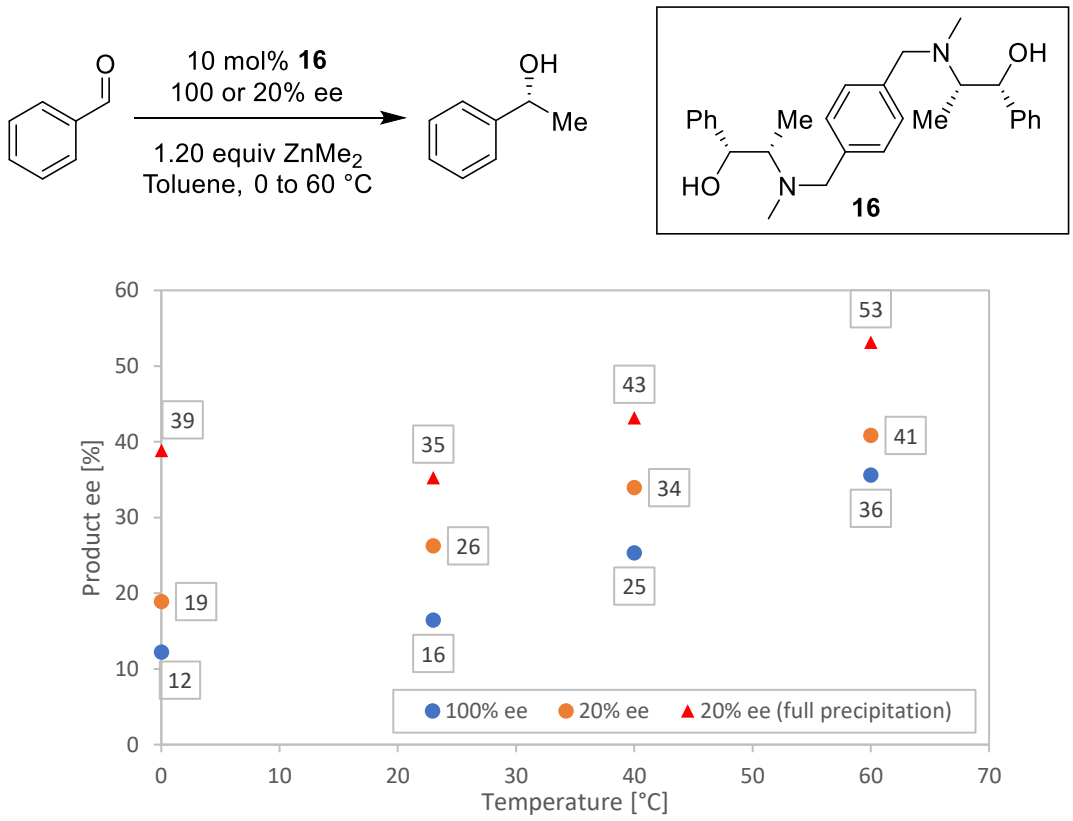

*Figure 140: Temperature profile of the **16**-catalysed addition of $ZnMe_2$ to benzaldehyde, with enantiopure (blue dots) and 20% ee ligand (orange dots). The orange triangles represent catalytic runs where the precipitate has been formed by overnight stirring at 60 °C, prior to the addition of benzaldehyde.*

Another astonishing observation is the emergence of a white precipitate in the 20% ee_L-runs over the course of the reaction, not right from the start like with scalemic NBE. The higher the reaction temperature, the faster the precipitation: it appears after a few hours in the 60 °C-samples, whereas in the 0 °C-samples it becomes visible only at the end of the reaction (3.5 days) as a fine haze. We couldn't observe any precipitate in the runs with enantiopure ligand.

This drove us to conduct a 2nd series of experiments with 20% ee_L using a modified procedure (Figure 141): the ligand/$ZnMe_2$-solution was let to stir at 60°C overnight to force the precipitate to appear in all samples, which were then let to cool down to the appropriate temperature; only then the benzaldehyde substrate was added and the catalysis started. Indeed, all samples contained a thick white precipitate after overnight stirring which persisted over the course of the catalytic reactions, regardless of the reaction's temperature. The ee_P (Figure 140, reed triangles) are significantly higher than in the standard 20% ee_L-runs, around +9-12% at 23 °C and higher; the 0°C-run stands out with +20%-difference.

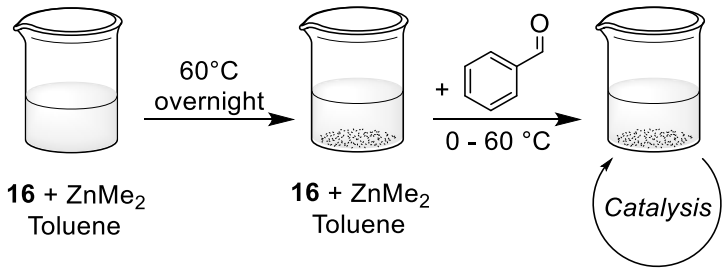

*Figure 141: Scheme for the **16**-catalysed addition of ZnMe2 to benzaldehyde after the precipitation of the presumably heterochiral aggregate.*

This precipitate is most probably a heterochiral aggregate whose production is increased or accelerated at high temperature. It is tempting to conclude that this illustrates an equilibrium shift towards a heterochiral aggregate, as discussed in chapter II.2.2.3(c). However, precipitation can also tip equilibria towards thermodynamically unfavoured species, therefore we cannot conclude on this result without having more data at hand.

V.3 Product characterisation: NMR- and FTIR-spectra

V.3.1 Ephedrine-derived ligands

(1*R*,2*S*)-*N*-(4-methylbenzyl)ephedrine **(-)-Me-NBE**

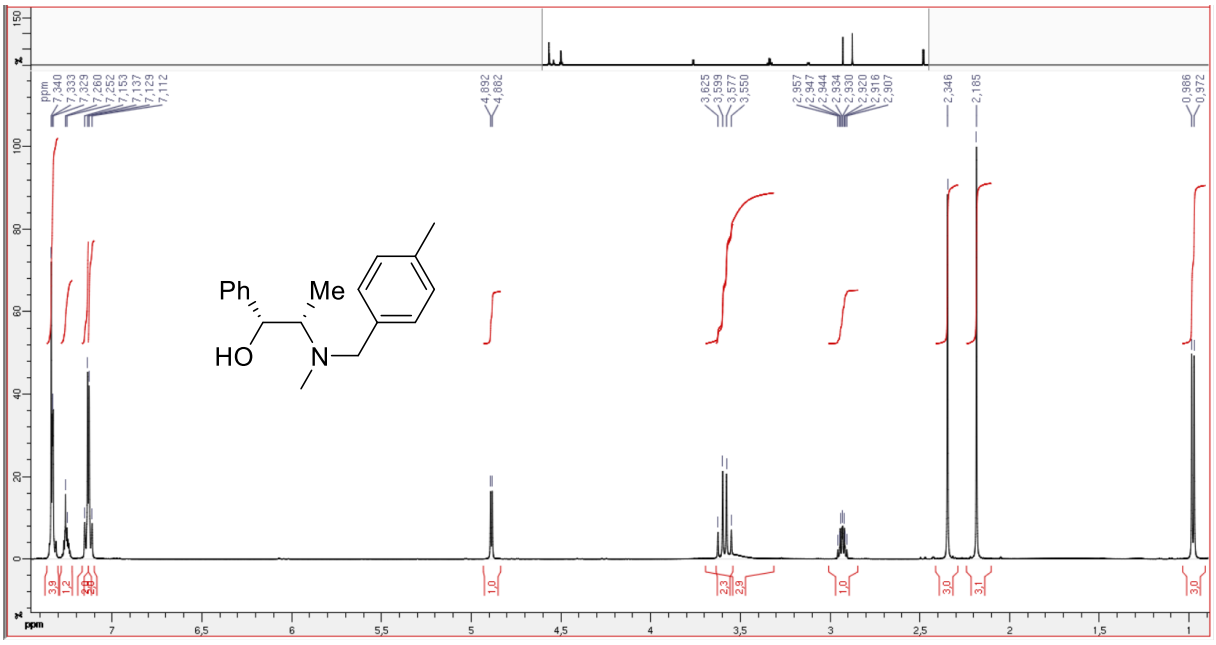
Ph
Me
HO
N


Ph
Me
HO
N

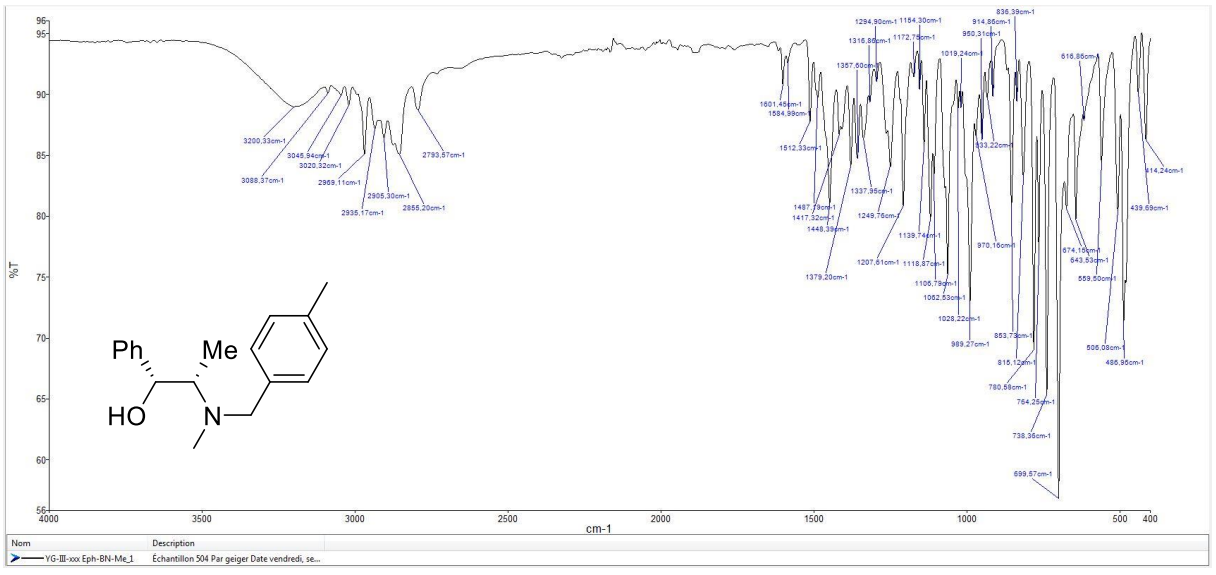
Ph
Me
HO
N
%T
cm-1

(1*R*,1'*R*,2*S*,2'*S*)-2,2'-(decane-1,10-diylbis(methylazanediyl))bis(1-phenylpropan-1-ol) **15**:

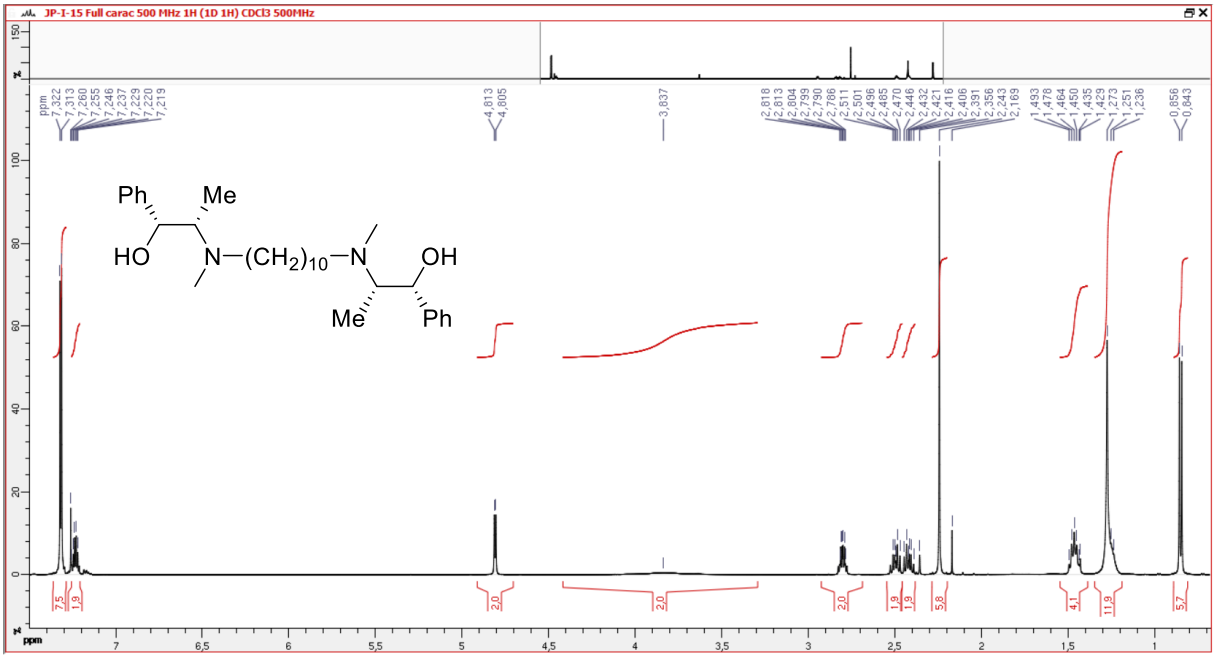

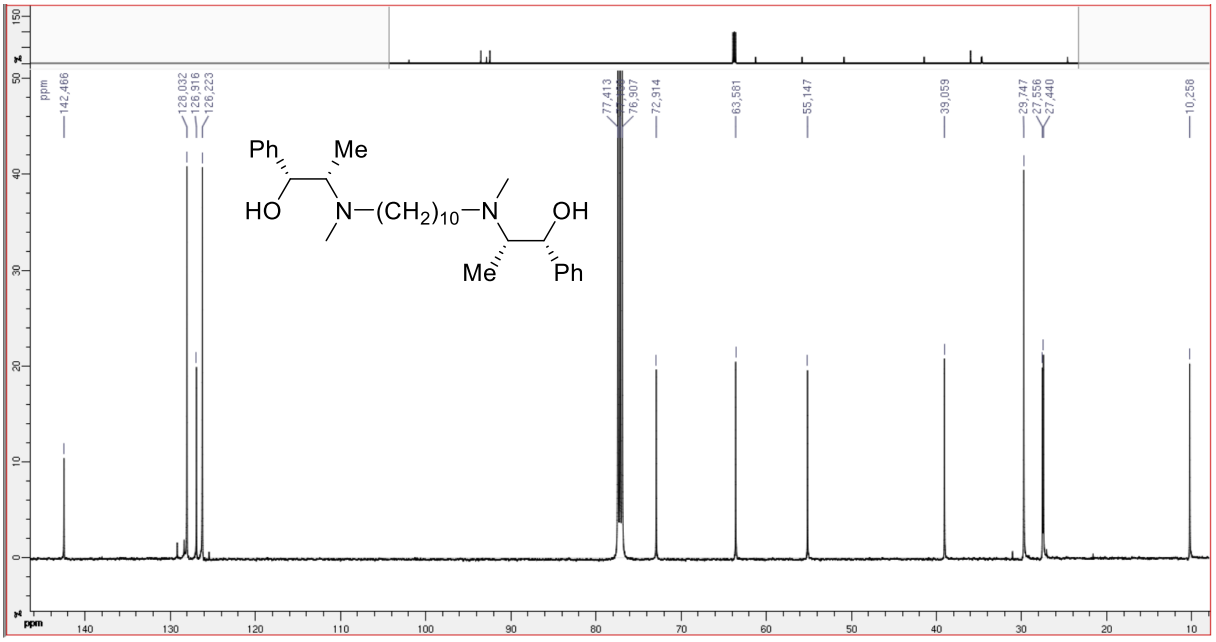

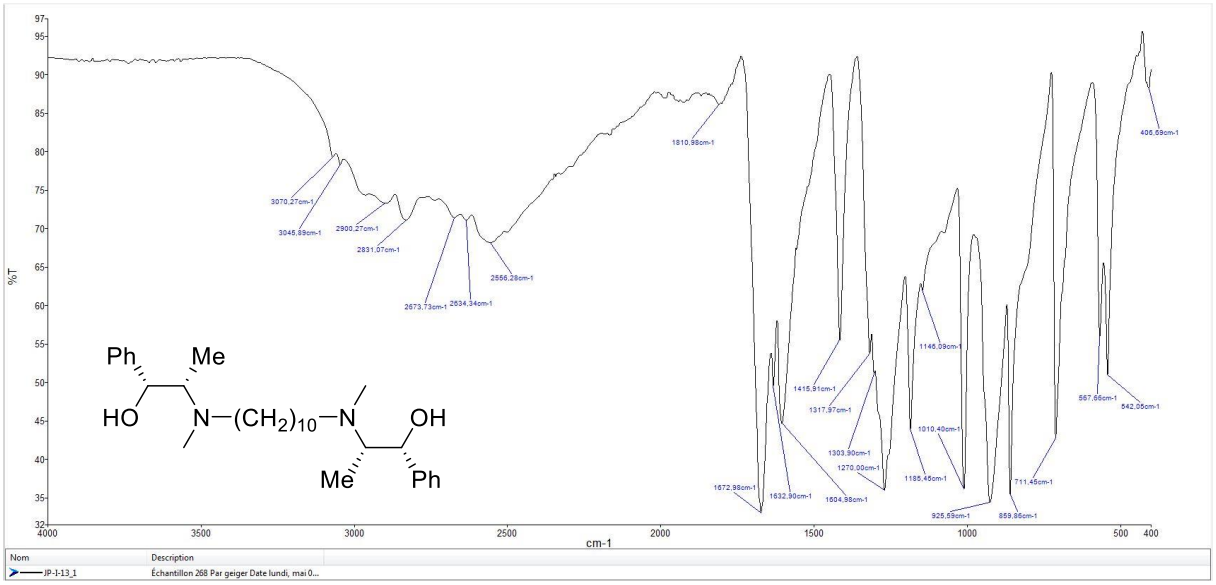

(1*R*,1'*R*,2*S*,2'*S*)-2,2'-((1,4-phenylenebis(methylene))bis(methylazanediyl))bis(1-phenylpropan-1-ol) **16:**

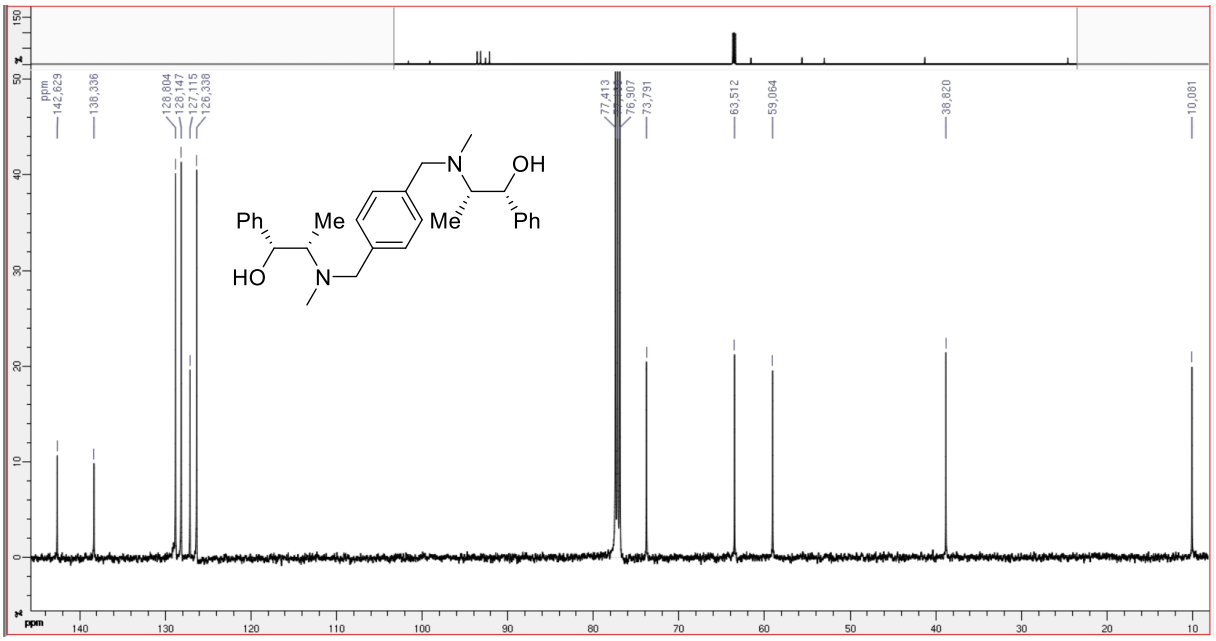

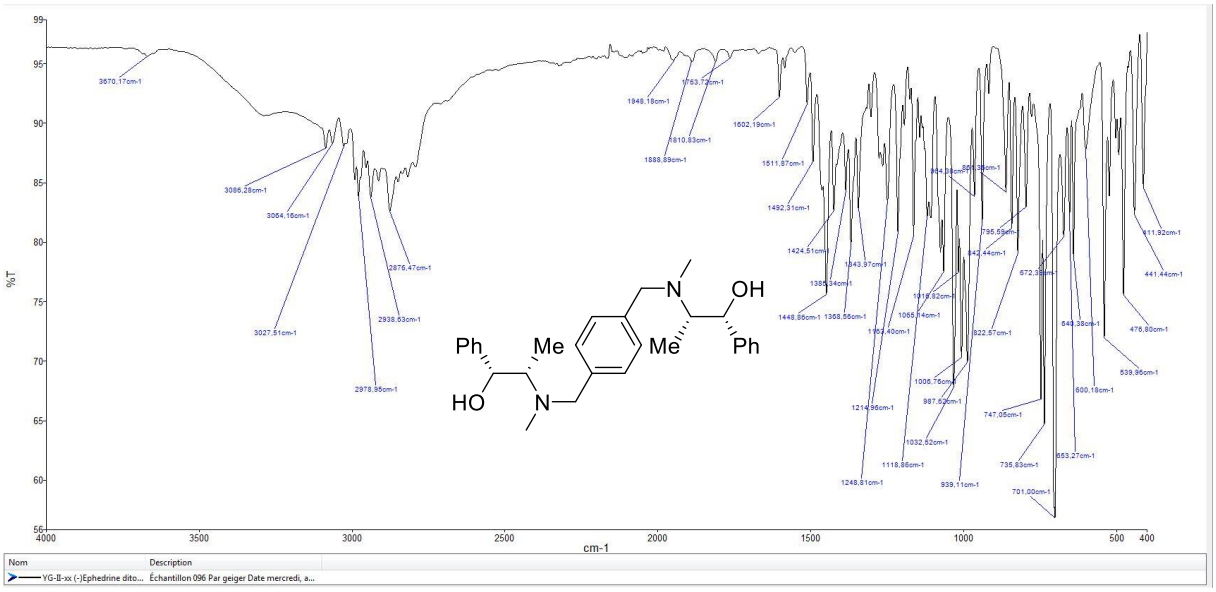

(4*S*,5*R*)-3-benzyl-2,2,4-trimethyl-5-phenyloxazolidine **2**:

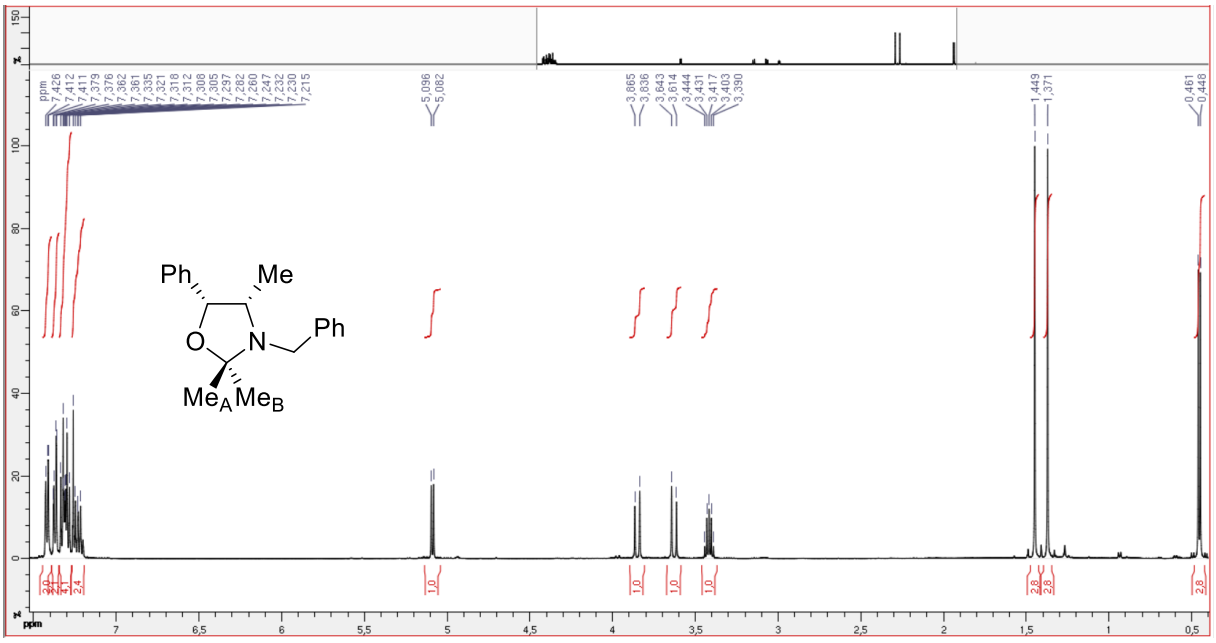
Ph
Me
Ph
O
N
MeA MeB

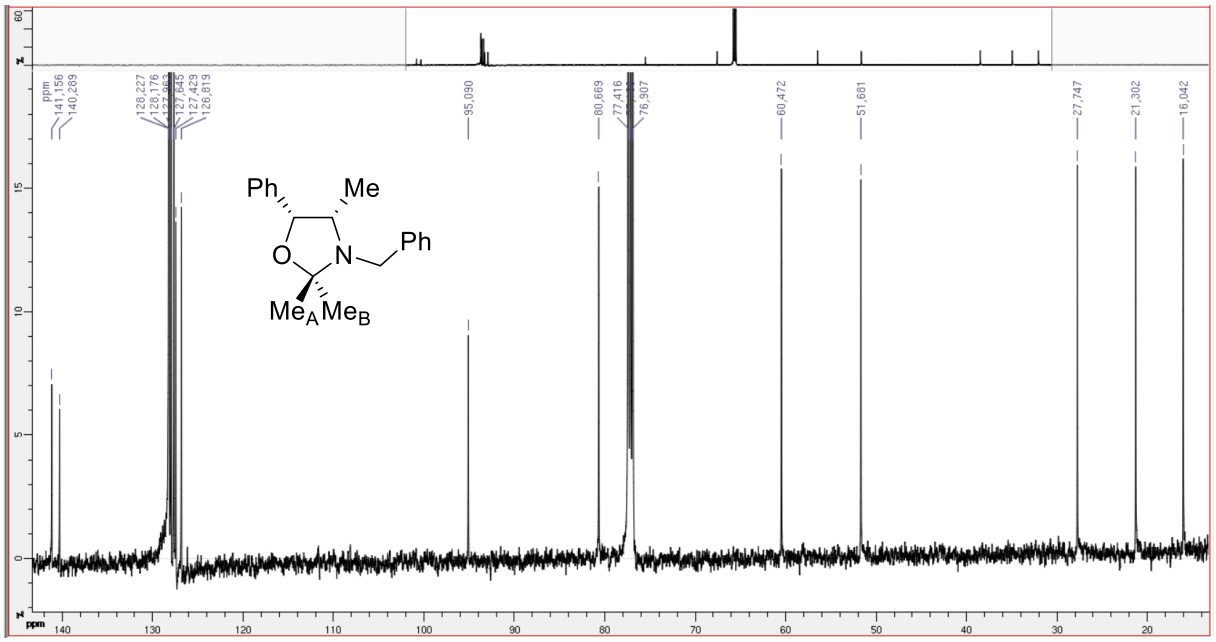
Ph
Me
Ph
O
N
MeA MeB

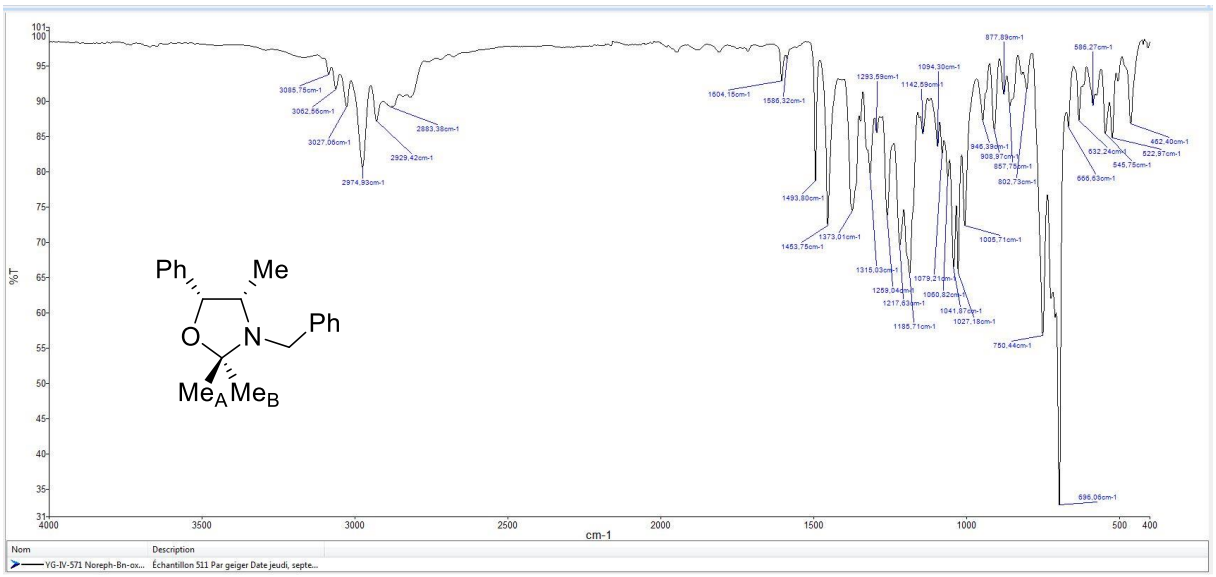

V.3.2 Camphor-derived compounds

(3a*R*,4*S*,7*S*,7a*S*)-7,8,8-trimethyl-3-(4-(((3a*R*,4*S*,7*R*,7a*S*)-7,8,8-trimethyl-2-oxohexahydro-4,7-methanobenzo[d]oxazol-3(2H)-yl)methyl)benzyl)hexahydro-4,7-methanobenzo[d]oxazol-2(3H)-one **8a**:

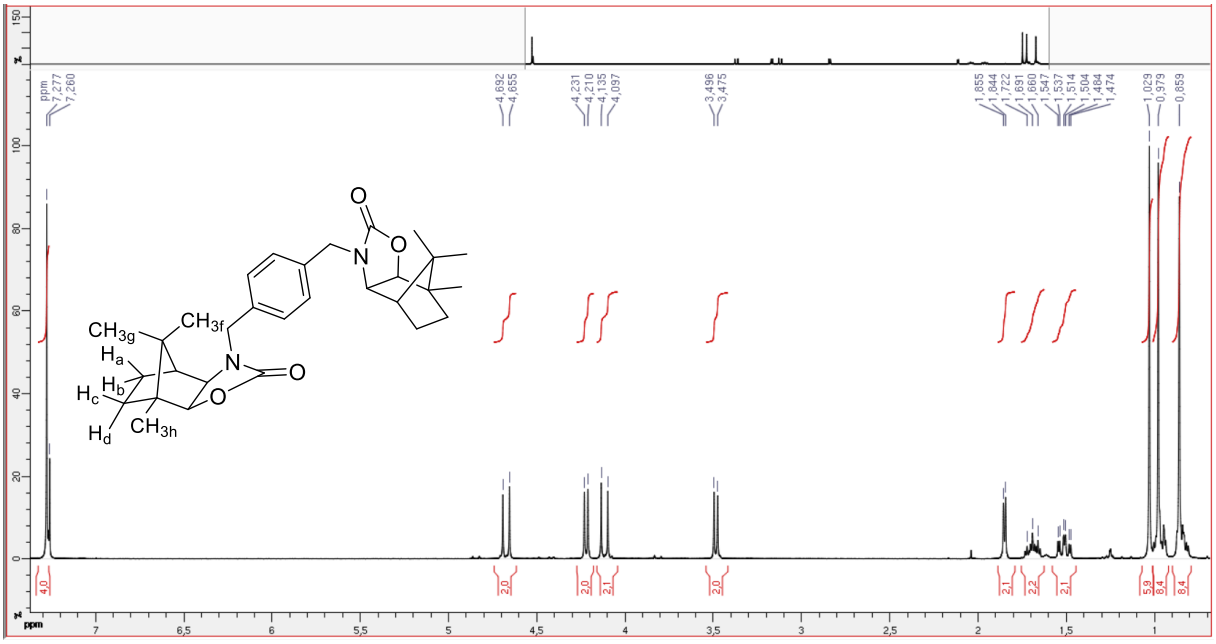

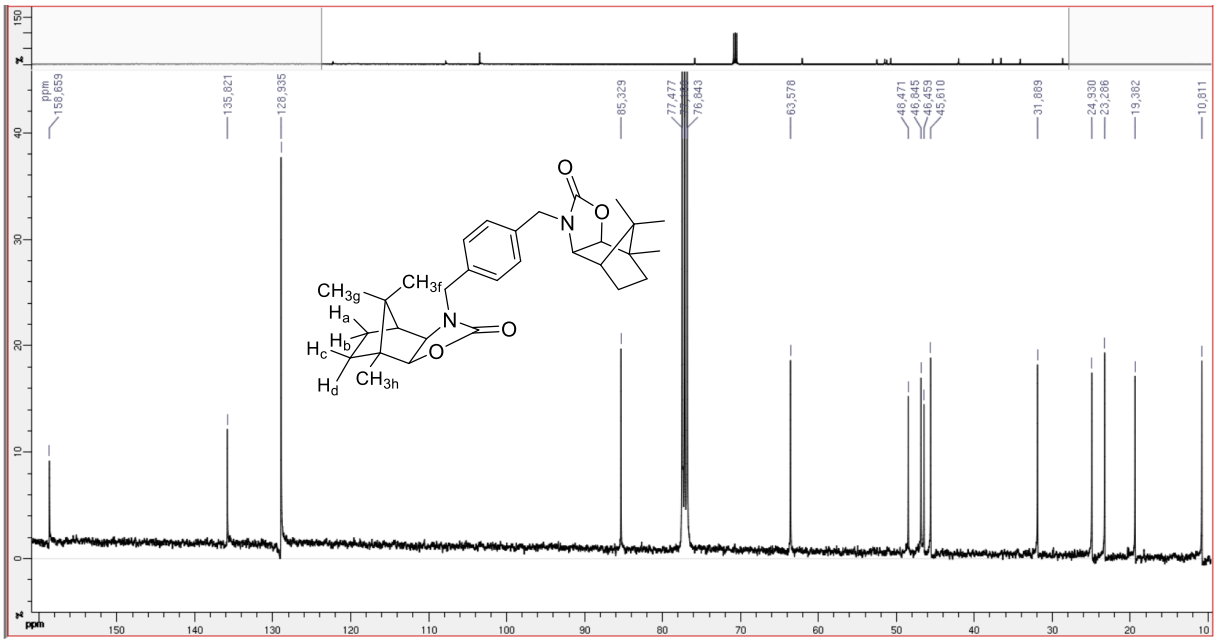

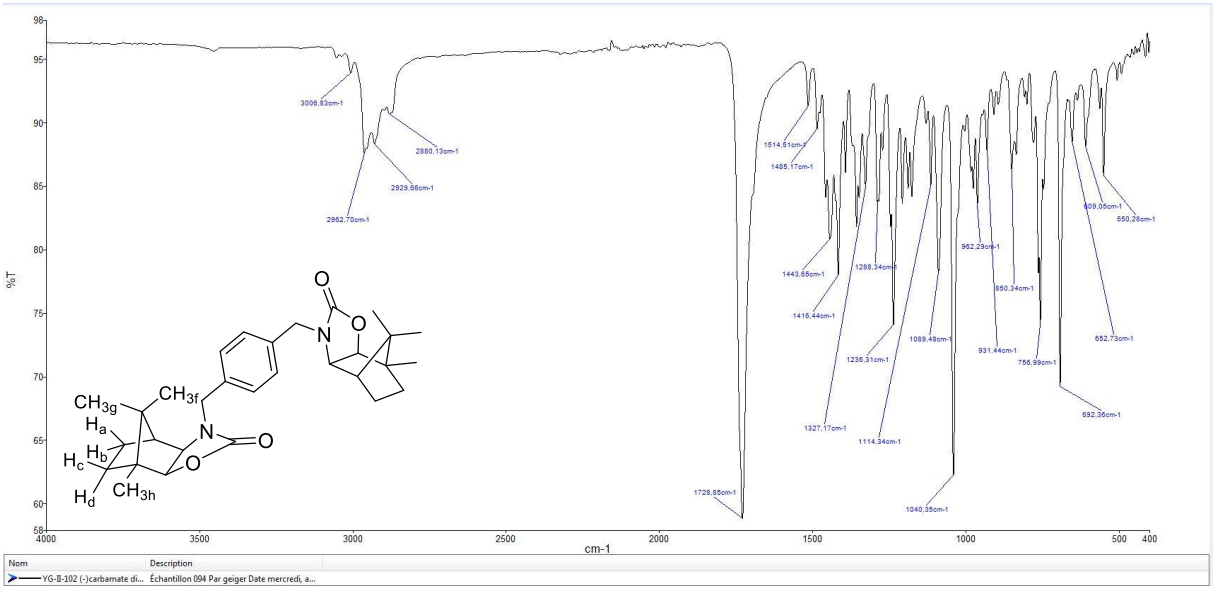

(1S,2S,3R,4S)-3-((4-((((1S,2R,3S,4R)-3-hydroxy-4,7,7-trimethylbicyclo[2.2.1]heptan-2-yl)(methyl)amino)methyl)benzyl)(methyl)amino)-1,7,7-trimethylbicyclo[2.2.1]heptan-2-ol **9**

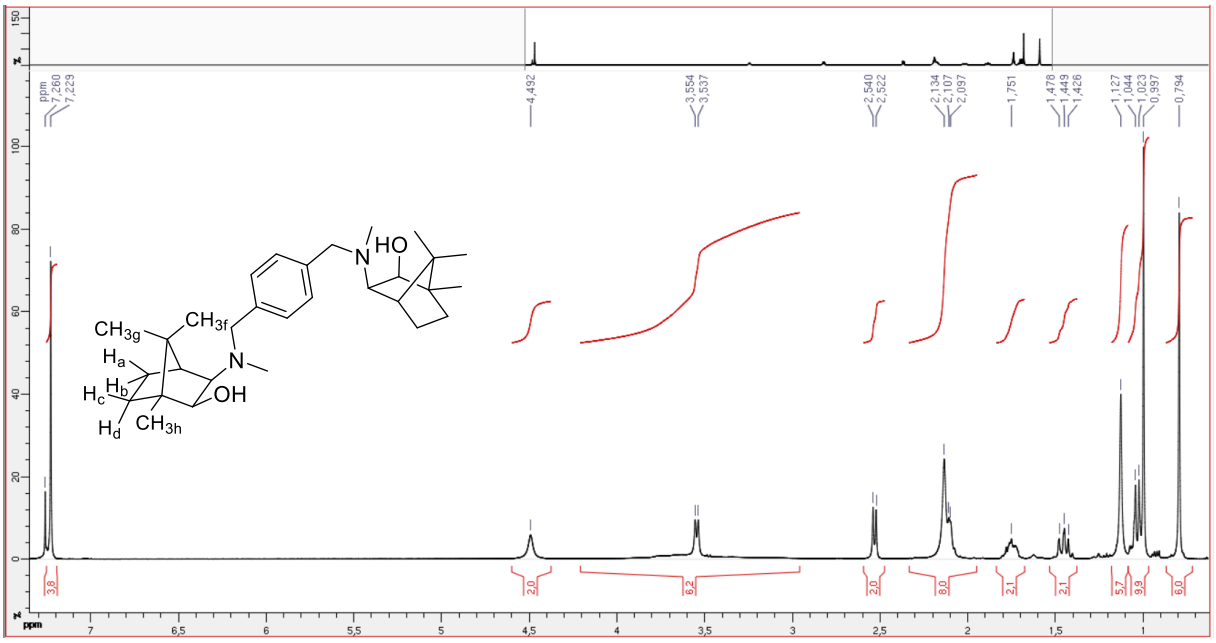
ppm
7,260
7,229
4,492
3,554
3,537
2,540
2,522
2,134
2,107
2,097
1,751
1,478
1,449
1,426
1,127
1,044
1,023
0,997
0,794
HO
N
CH3g
CH3f
Ha
Hb
Hc
Hd
CH3h
OH
3,8
2,0
6,2
2,0
8,0
2,1
2,1
5,7
9,9
6,0

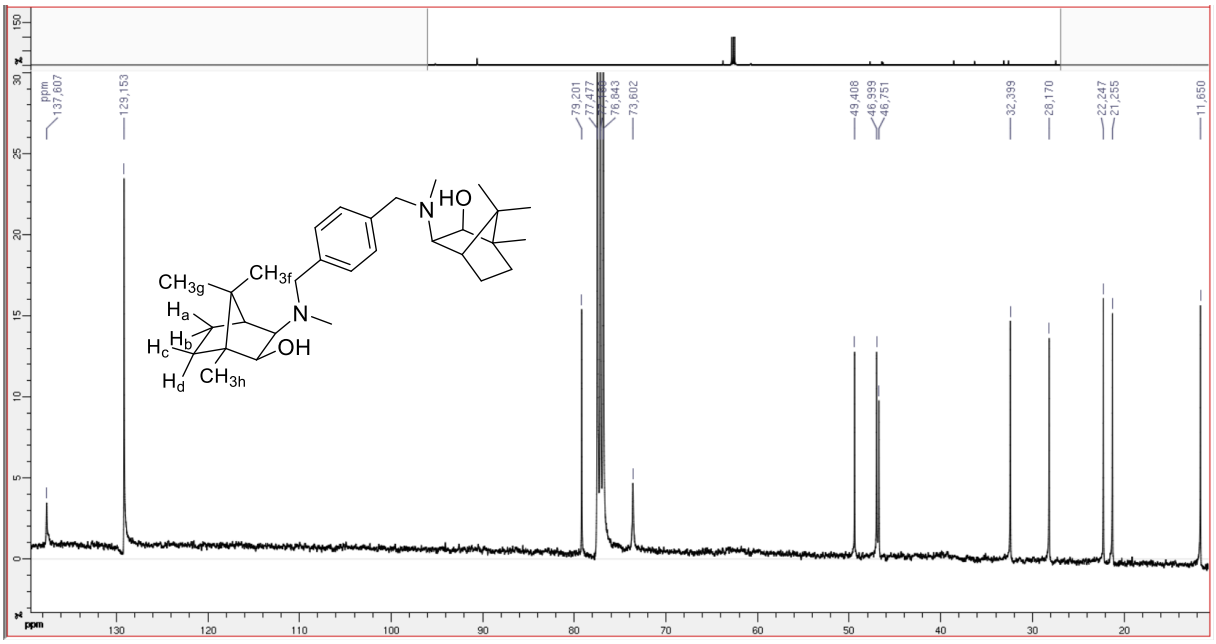
ppm
137,607
129,153
79,201
77,477
76,843
73,602
49,408
46,999
46,751
32,399
28,170
22,247
21,255
11,650
HO
N
CH3g
CH3f
Ha
Hb
Hc
Hd
CH3h
OH

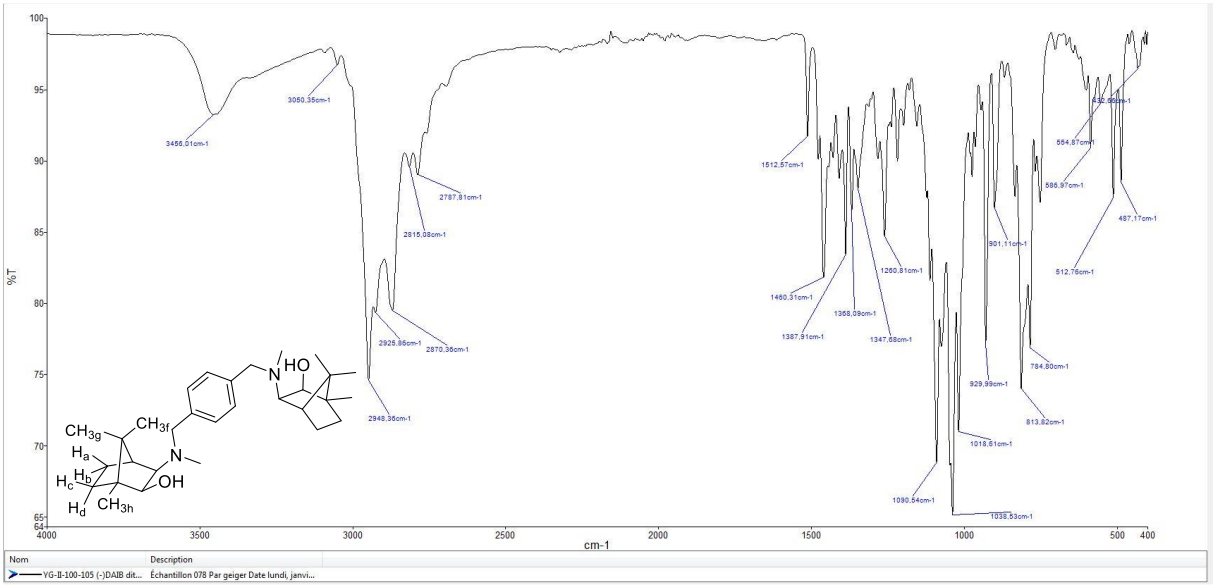

V.3.3 Ditopic iminoalcohol ligands

(2*S*,2'*S*)-2,2'-((1,4-phenylenebis(methaneylylidene))bis(azaneylylidene))bis(propan-1-ol) **19a**

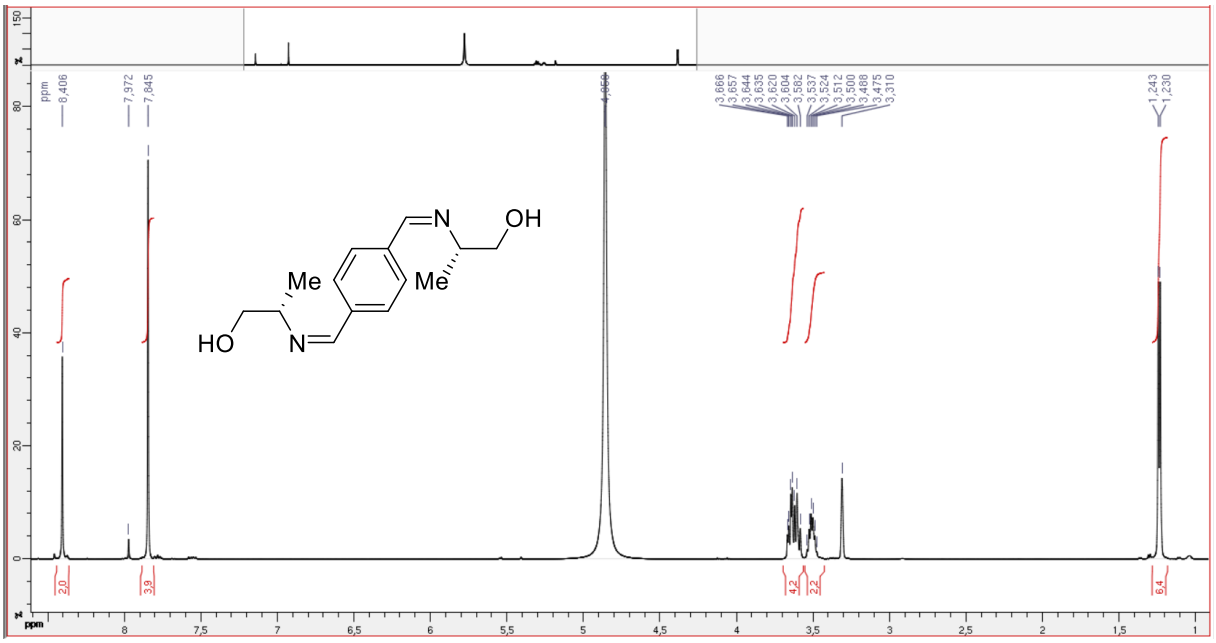

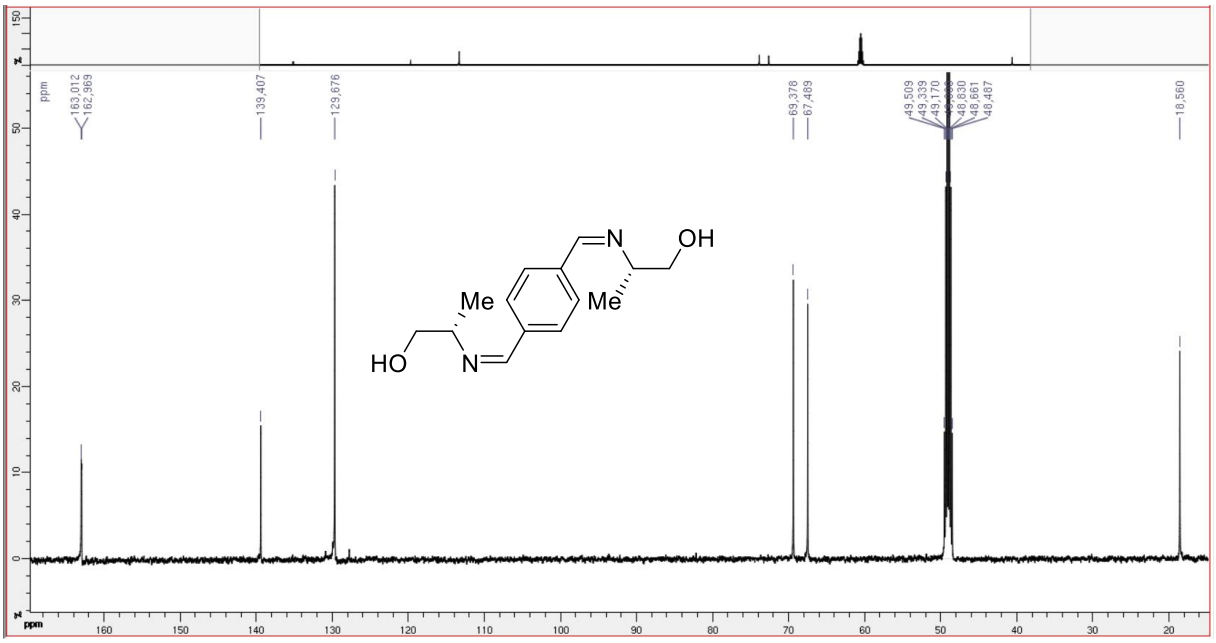

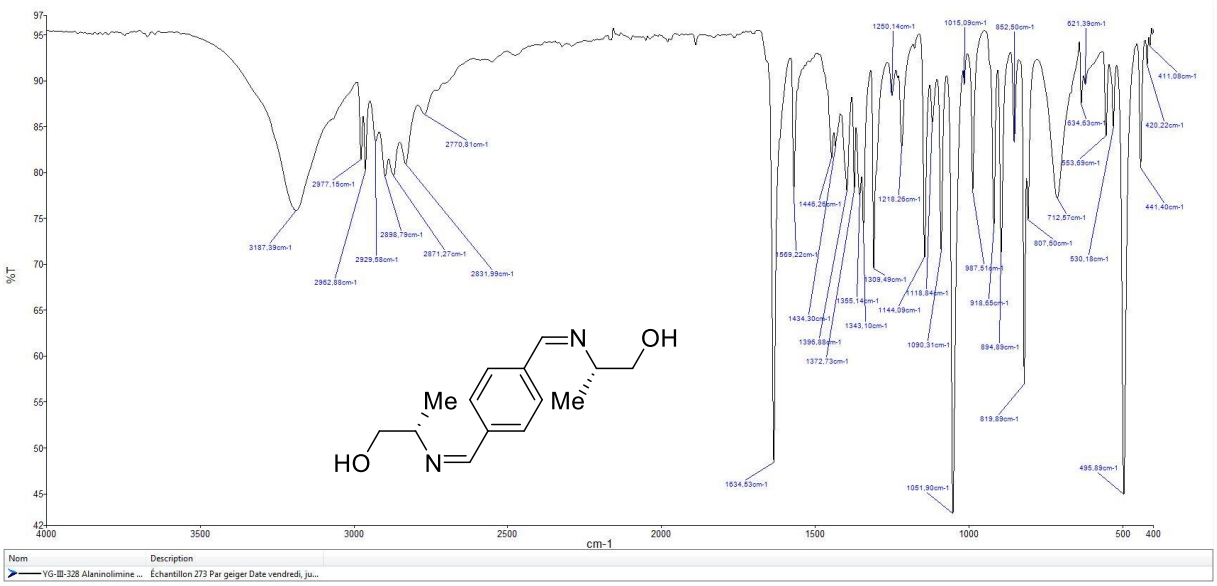

(2*R*,2'*R*)-2,2'-((1,4-phenylenebis(methaneylylidene))bis(azaneylylidene))bis(2-phenylethan-1-ol) **19b**

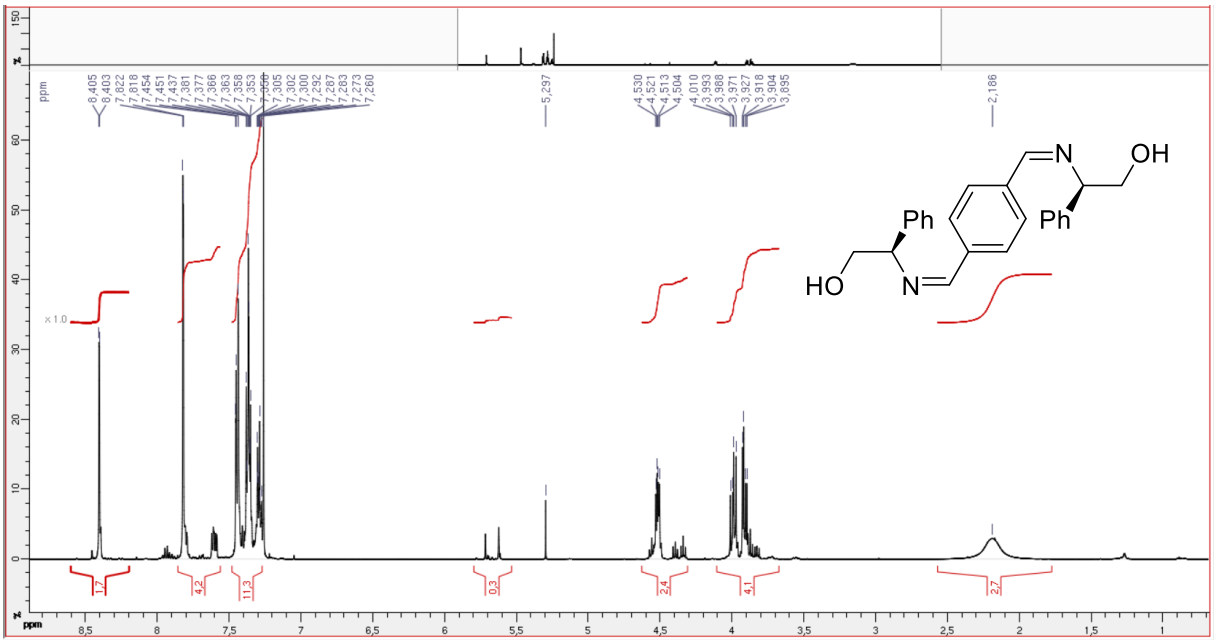
ppm
8,405
8,403
7,822
7,818
7,454
7,451
7,437
7,381
7,377
7,366
7,363
7,358
7,353
7,305
7,302
7,300
7,292
7,267
7,263
7,273
7,260
5,297
4,530
4,521
4,513
4,504
4,010
3,993
3,986
3,971
3,927
3,918
3,904
3,895
2,186
x 1.0
1,7
4,2
11,3
0,3
2,4
4,1
2,7
N
OH
Ph
Ph
HO
N

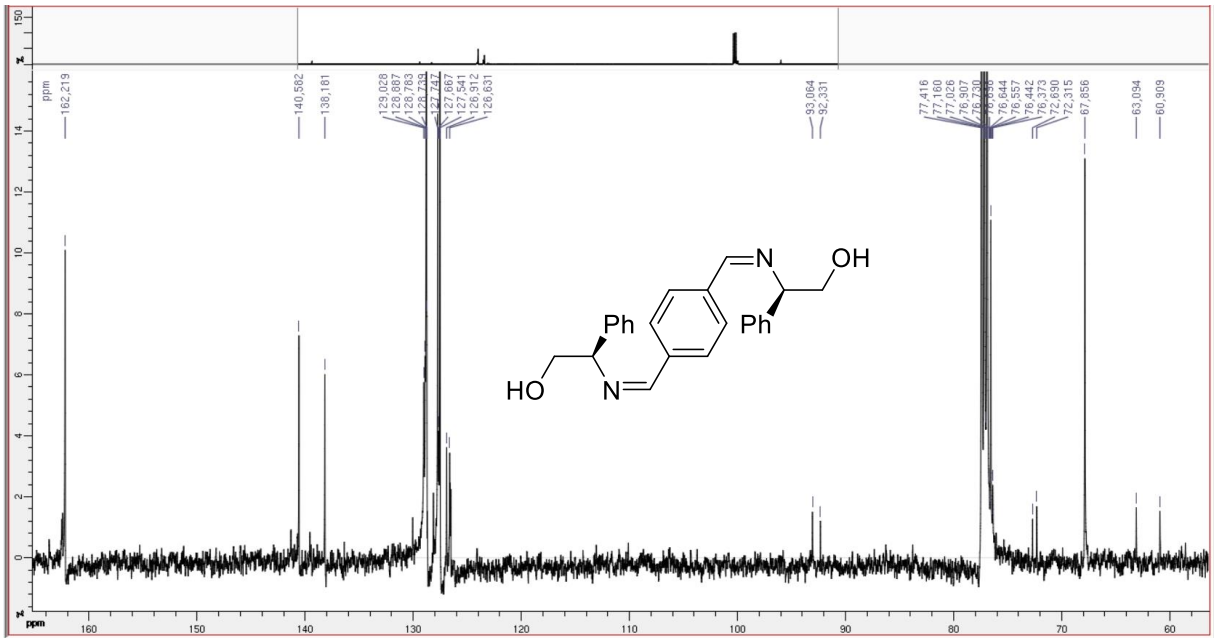
ppm
162,219
140,582
136,161
129,028
128,887
128,783
128,739
127,747
127,667
127,541
126,912
126,631
93,064
92,331
77,416
77,160
77,026
76,907
76,644
76,557
76,442
76,373
72,690
72,315
67,856
63,094
60,909
N
OH
Ph
Ph
HO
N

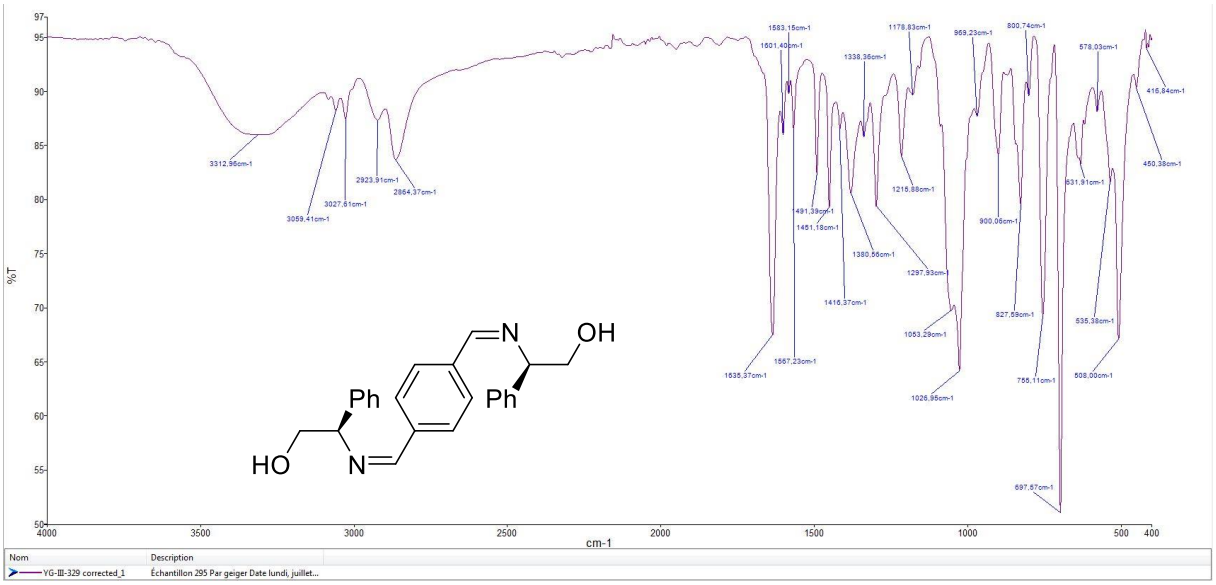

(2*R*,2'*R*)-2,2'-((1,4-phenylenebis(methaneylylidene))bis(azaneylylidene))bis(3-methylbutan-1-ol) **19c**

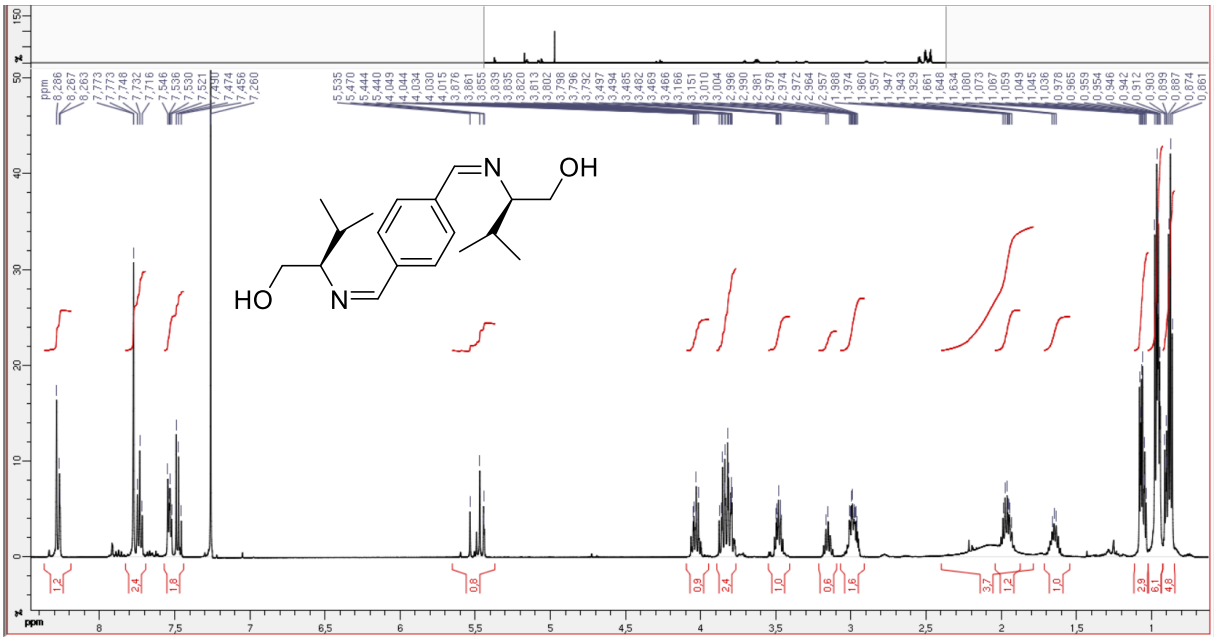

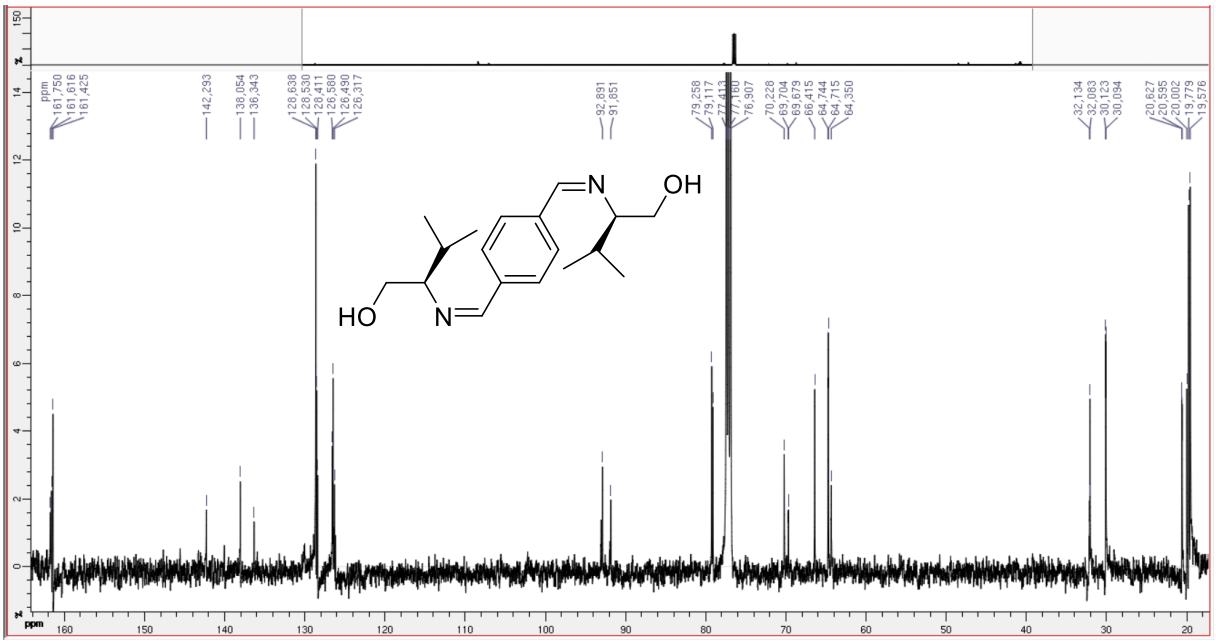

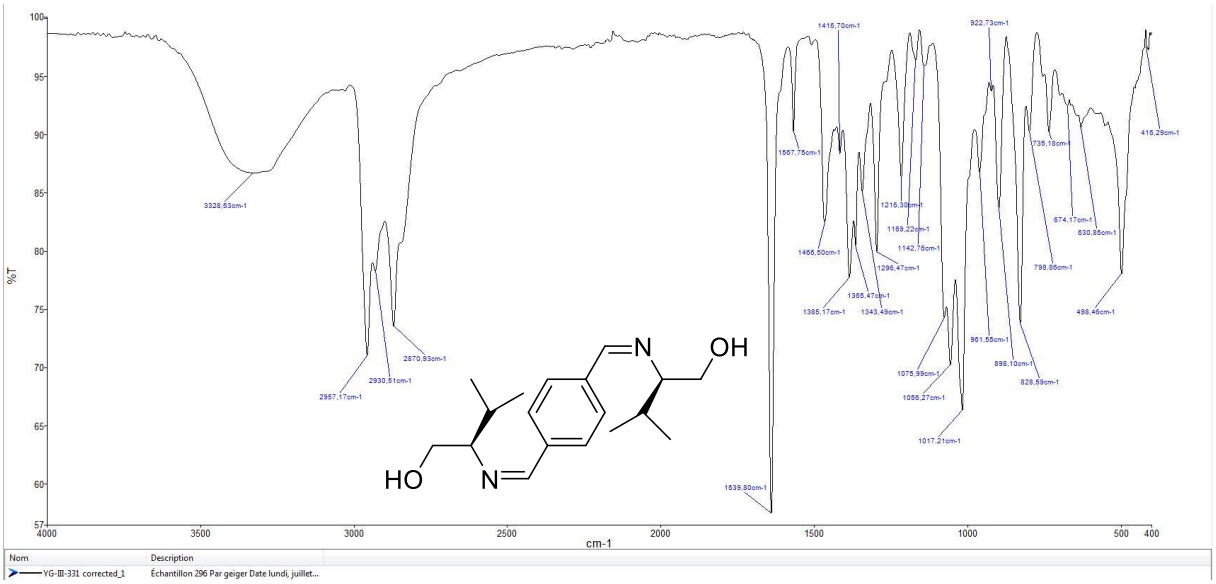

(1*R*,1'*R*,2*R*,2'*R*)-1,1'-((1,4-phenylenebis(methaneylylidene))bis(azaneylylidene))bis(2,3-dihydro-1H-inden-2-ol) **19d**

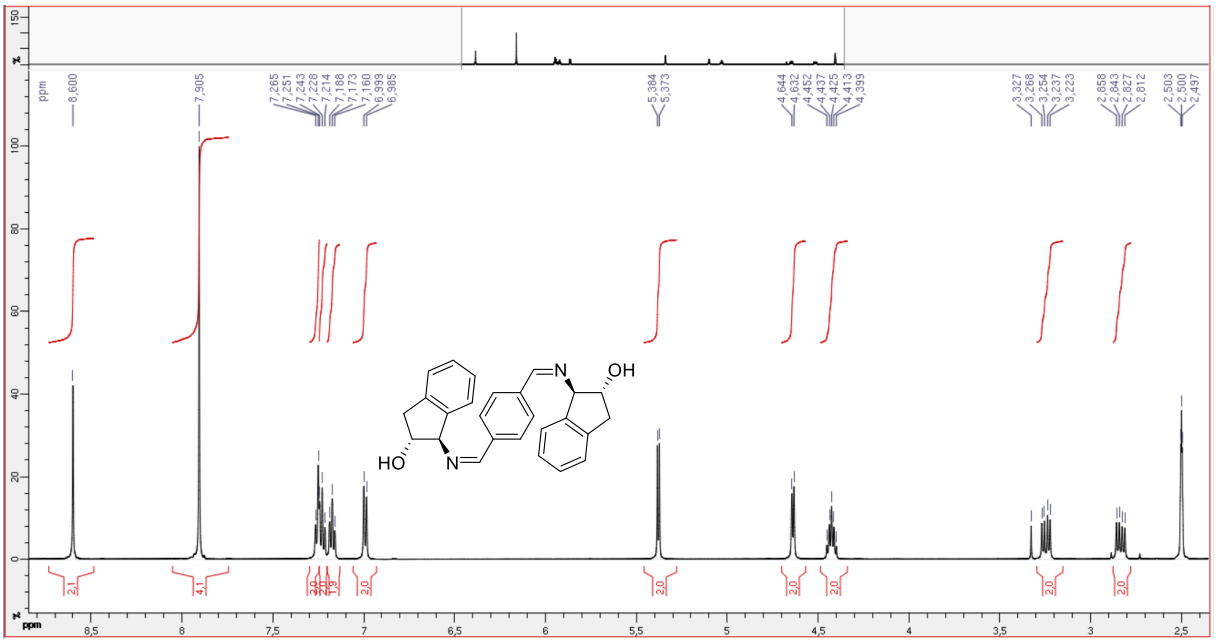
ppm
8,600
7,905
7,265
7,251
7,243
7,228
7,214
7,186
7,173
7,160
6,999
6,985
5,384
5,373
4,644
4,632
4,452
4,437
4,425
4,413
4,399
3,327
3,268
3,254
3,237
3,223
2,858
2,843
2,827
2,812
2,503
2,500
2,497
HO
N
N
OH

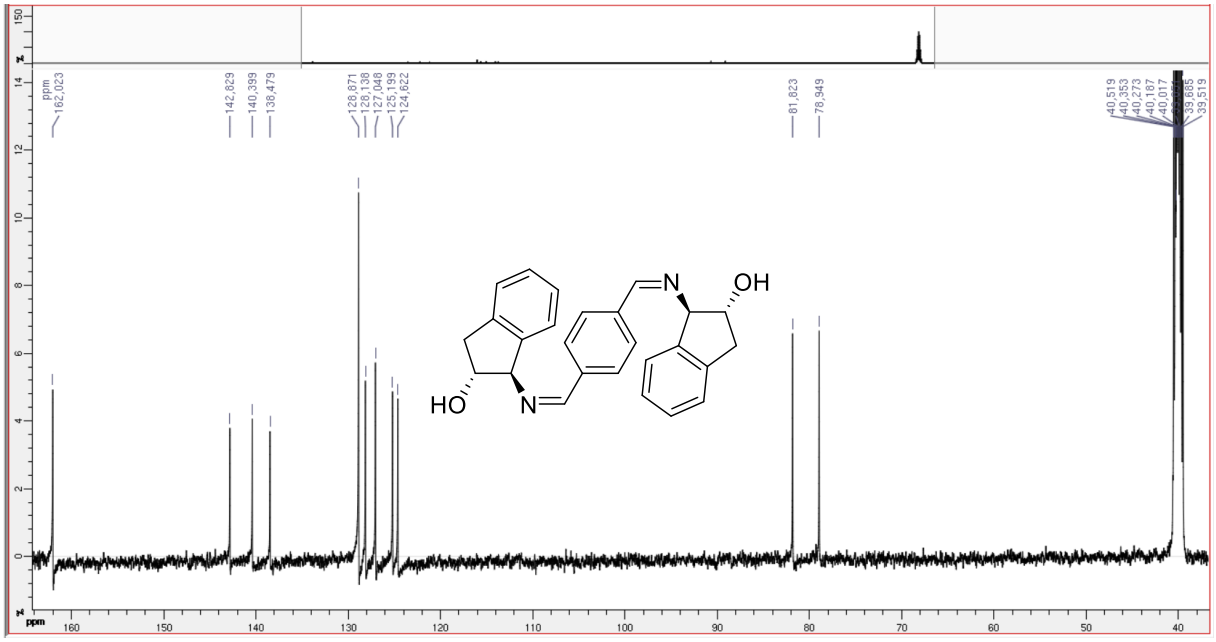
ppm
162,023
142,829
140,399
138,479
128,871
128,138
127,048
125,199
124,822
81,823
78,949
40,519
40,353
40,273
40,187
40,017
39,685
39,519
HO
N
N
OH

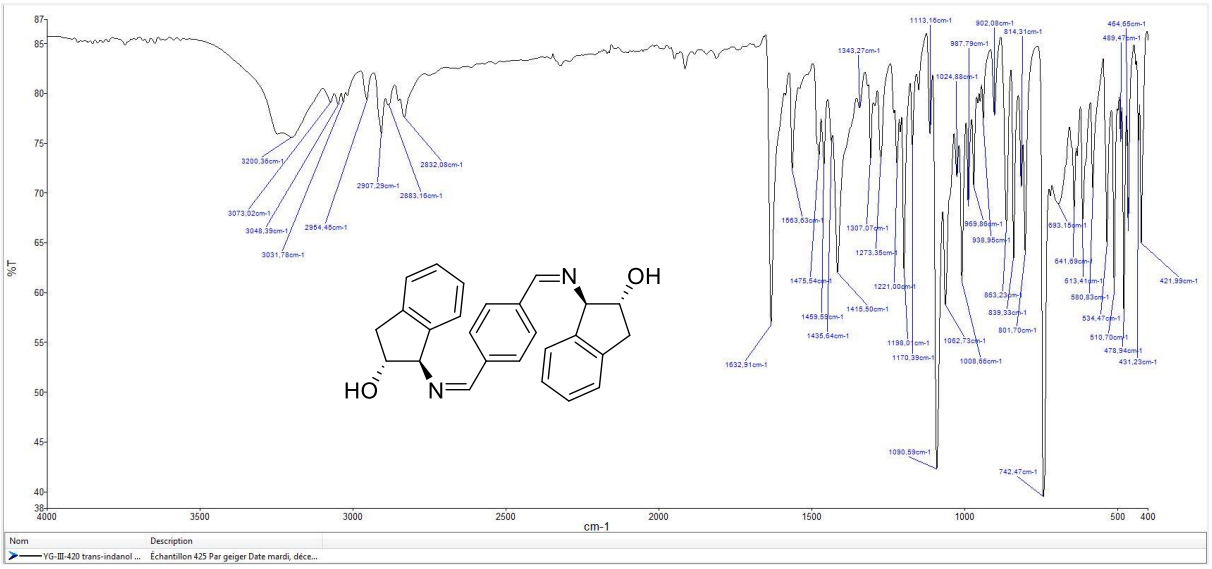

(1R,1'R,2S,2'S)-2,2'-(((1Z,1'Z)-1,4-phenylenebis(methaneylylidene))bis(azaneylylidene))bis(1-phenylpropan-1-ol) **19e**

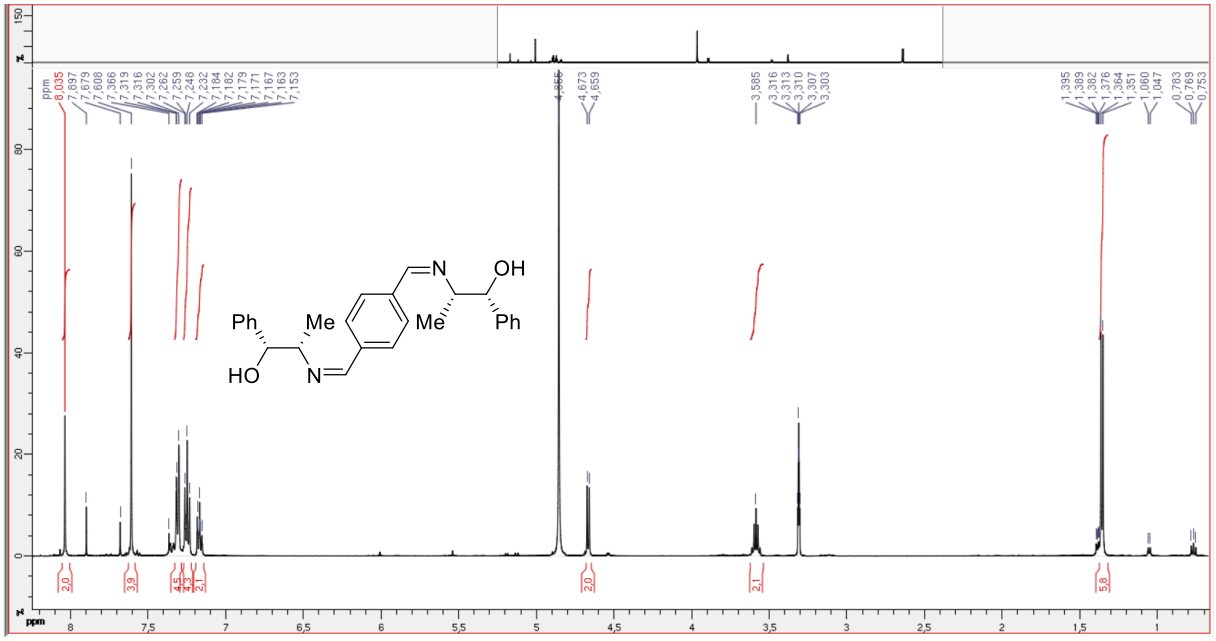

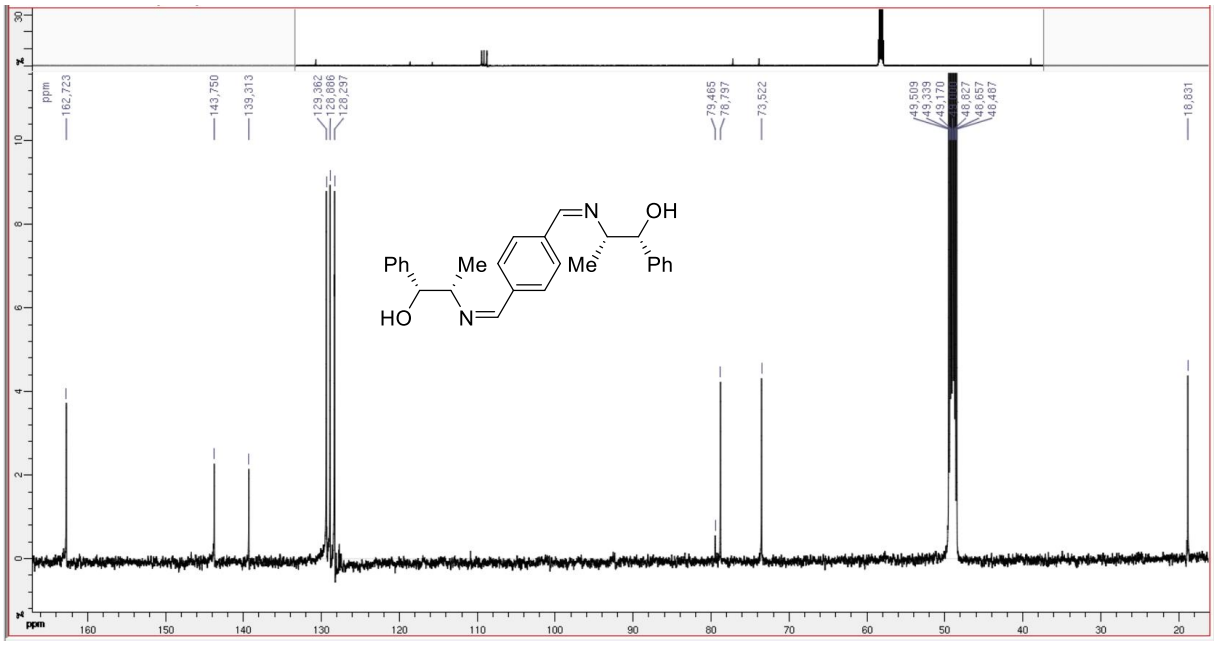

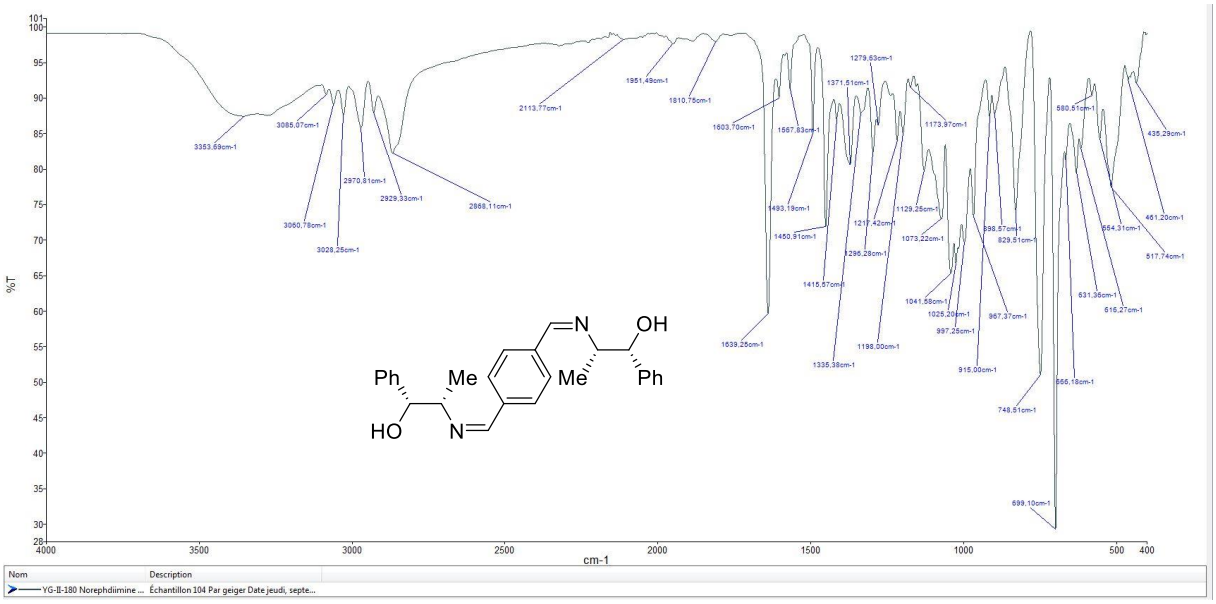

(1*S*,1'*S*,2*R*,2'*R*)-1,1'-((1,4-phenylenebis(methaneylylidene))bis(azaneylylidene))bis(2,3-dihydro-1H-inden-2-ol) **19f**

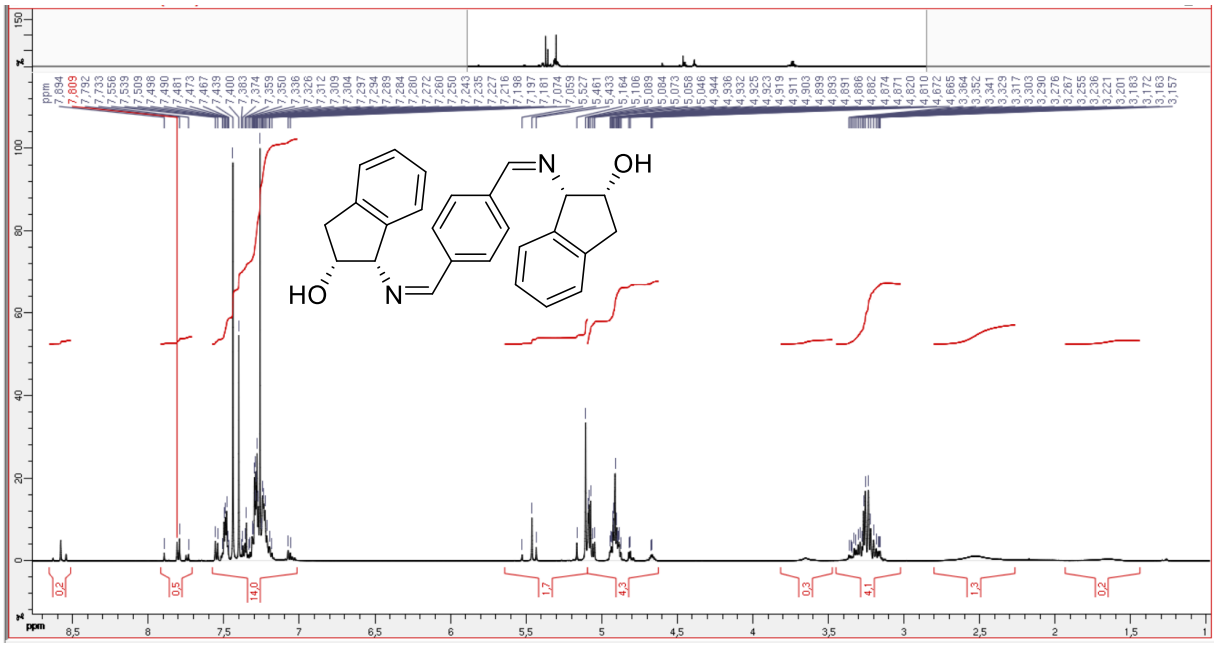
HO
N
N
OH

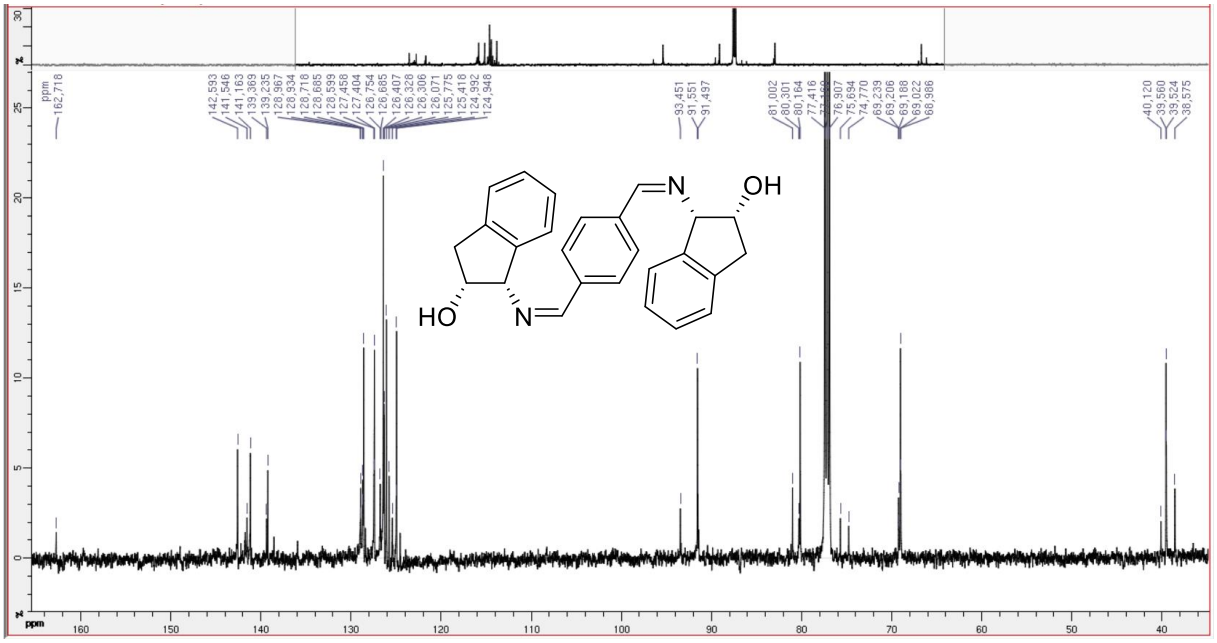
HO
N
N
OH

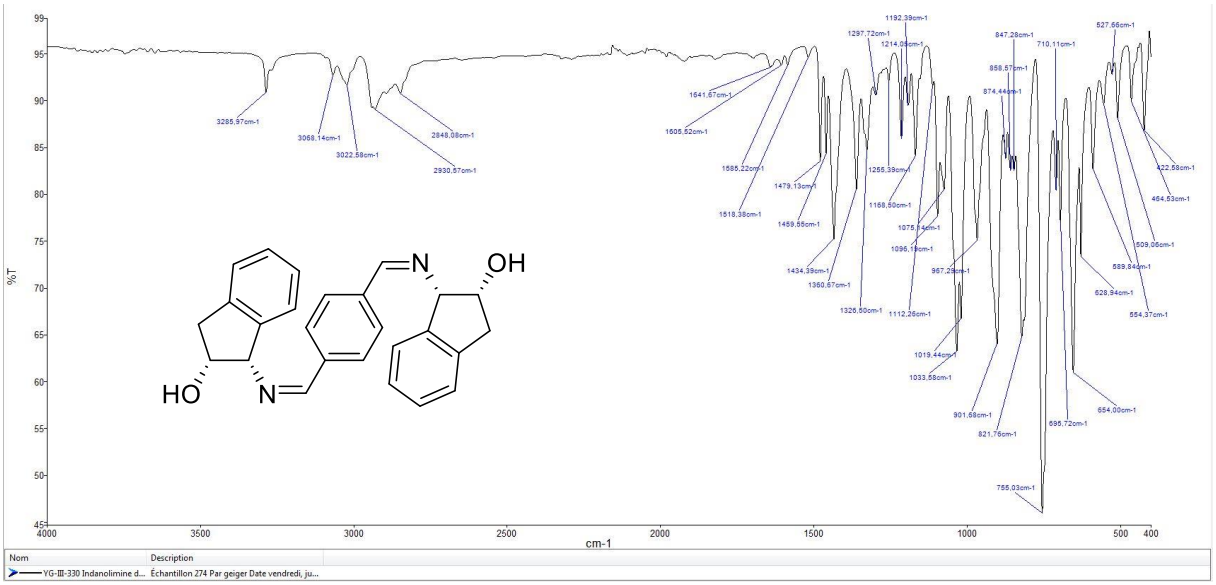

(1*R*,1'*R*,2*R*,2'*R*)-2,2'-((1,4-phenylenebis(methaneylylidene))bis(azaneylylidene))bis(cyclohexan-1-ol) **19d**:

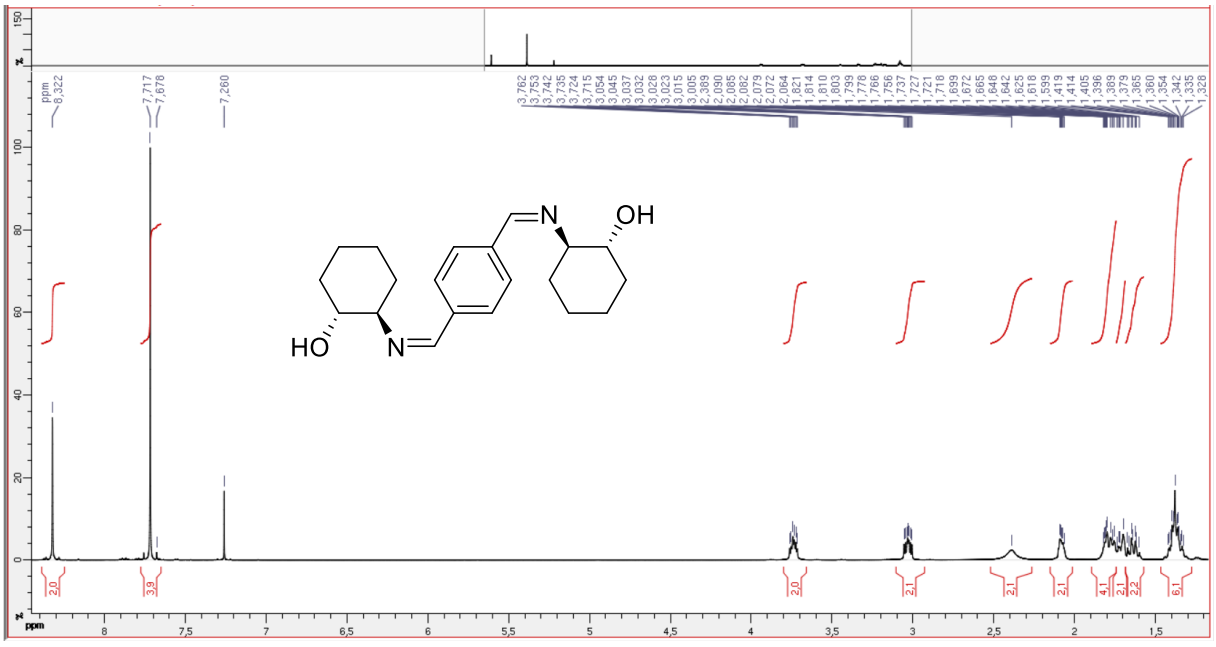

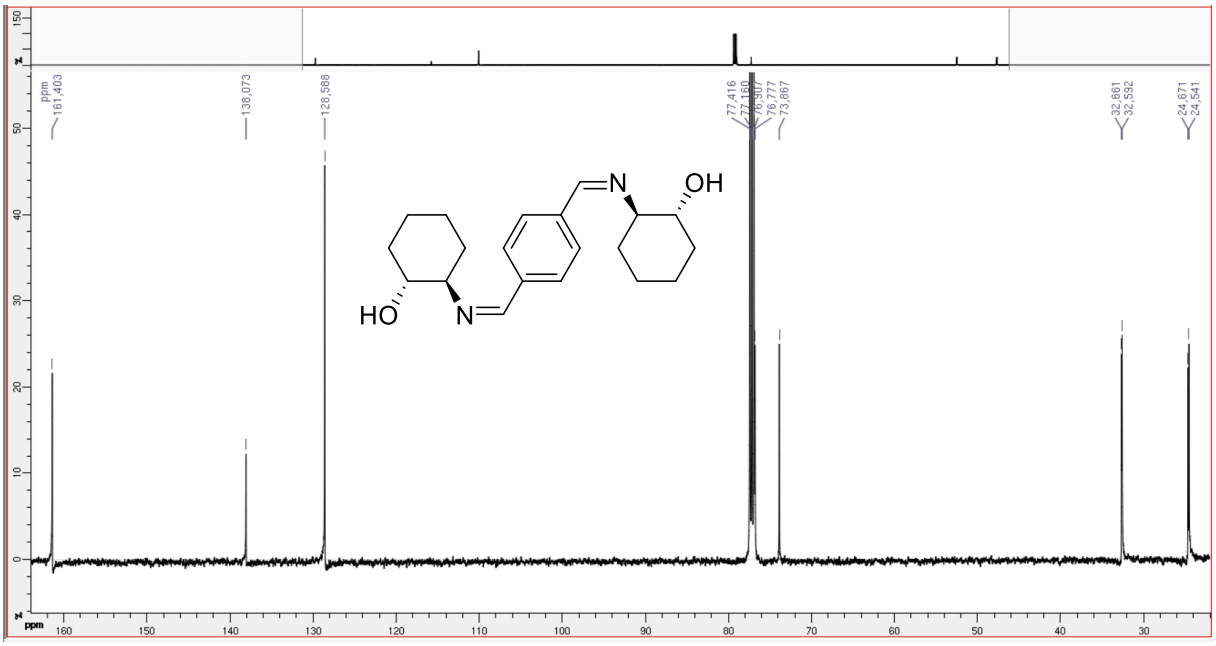

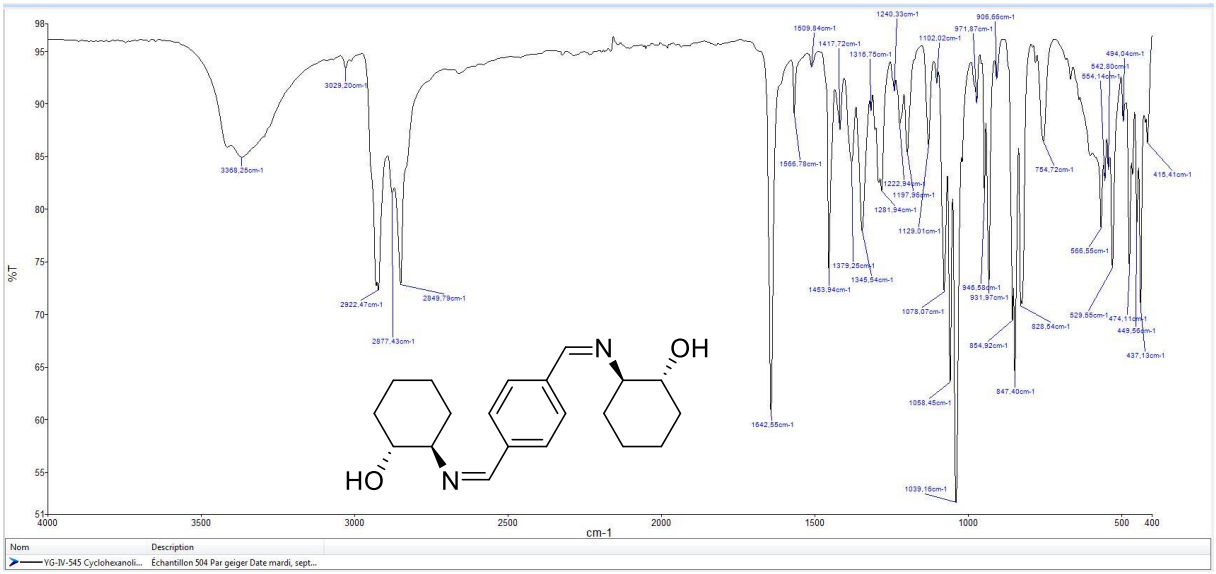

V.3.4 Ditopic iminoamine ligand

(1*R*,1'*R*,2*R*,2'*R*)-2,2'-((1,4-phenylenebis(methaneylylidene))bis(azaneylylidene))bis(N,N-dimethylcyclohexan-1-amine) **23**

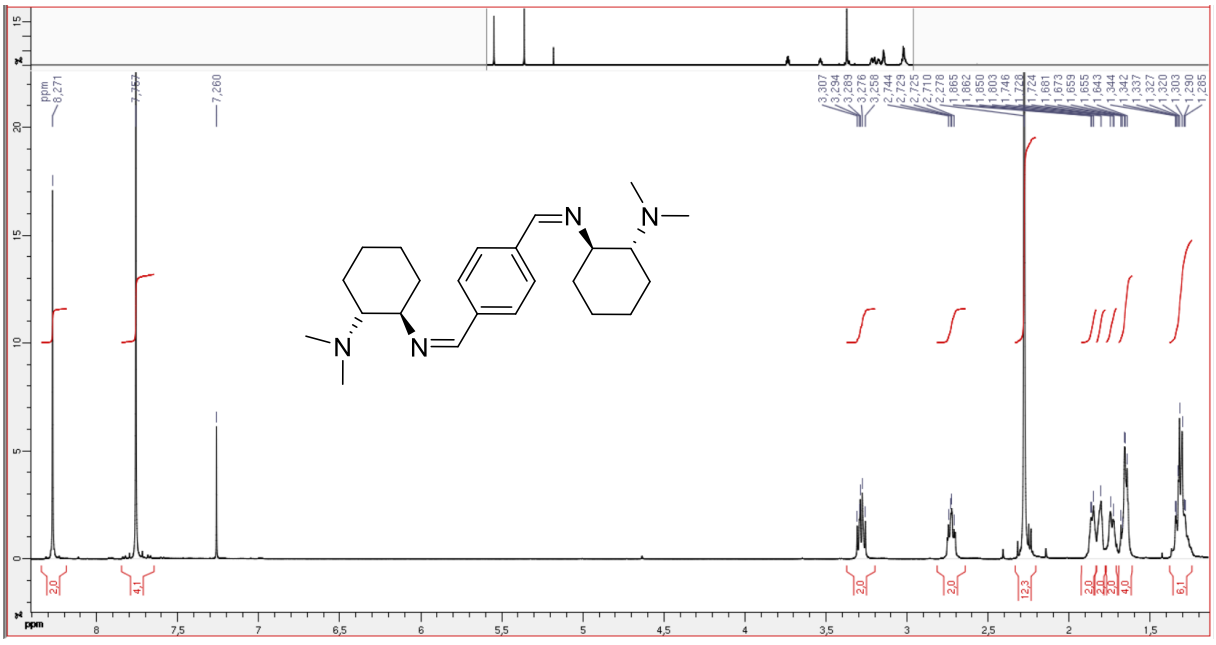
ppm
8,271
7,767
7,260
3,307
3,294
3,289
3,276
3,258
2,744
2,729
2,725
2,710
2,278
1,865
1,862
1,850
1,803
1,746
1,724
1,681
1,673
1,659
1,655
1,643
1,344
1,342
1,337
1,327
1,320
1,303
1,290
1,285
2,0
4,1
2,0
2,0
12,3
2,0
2,0
4,0
6,1

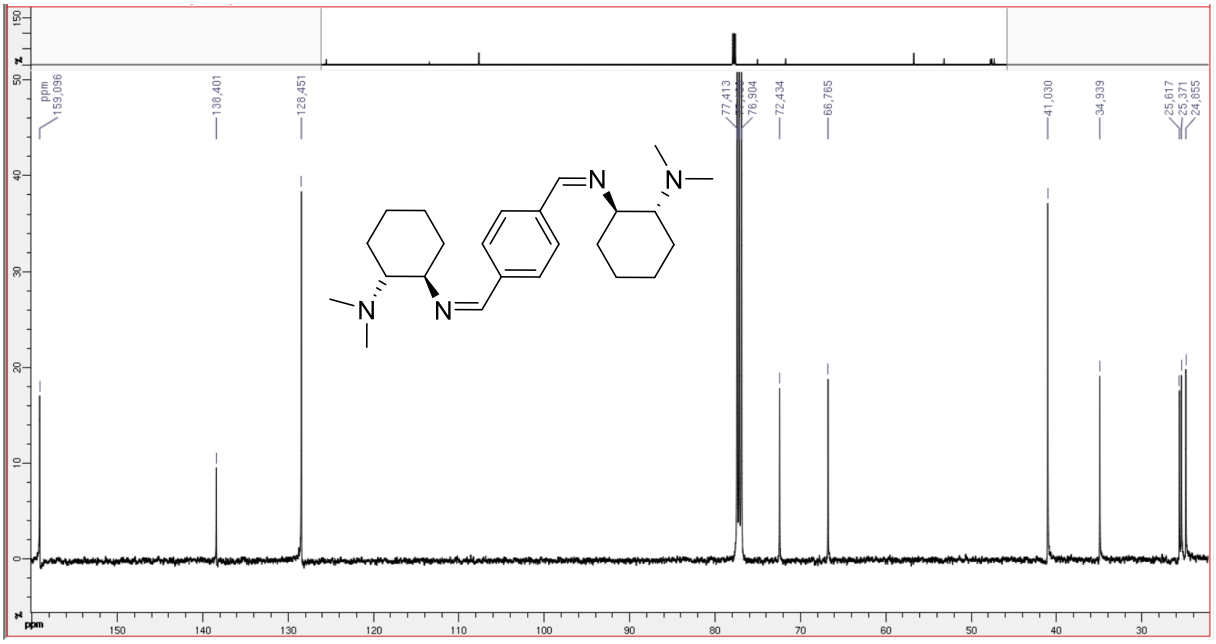
ppm
159,096
138,401
128,451
77,413
76,904
72,434
66,765
41,030
34,939
25,617
25,371
24,855

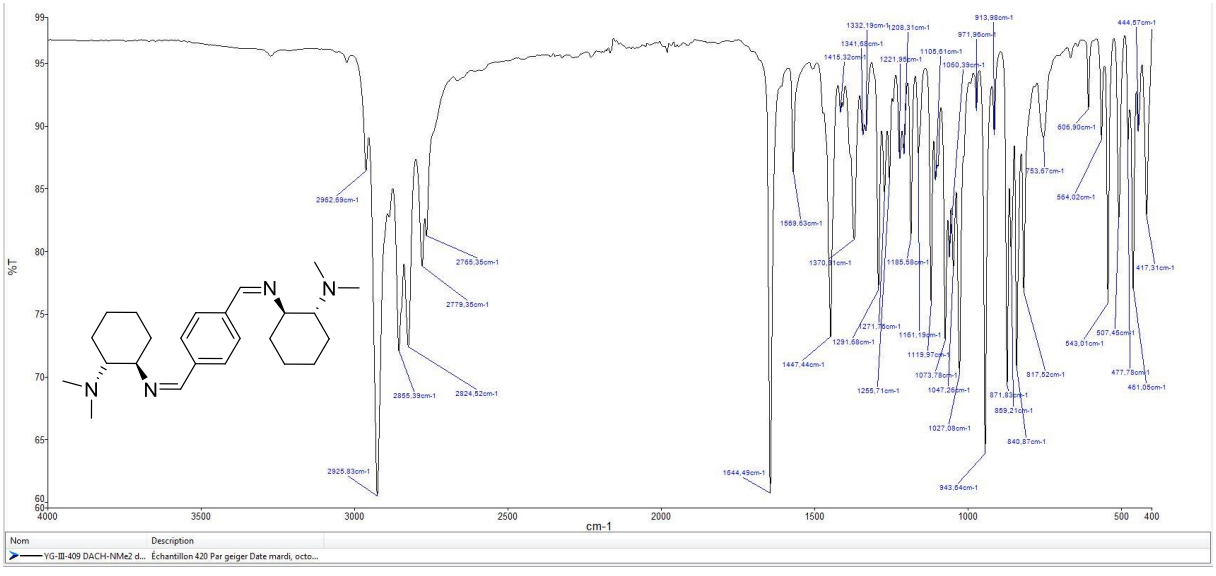
%T
cm-1
2962,89cm-1
2925,83cm-1
2855,39cm-1
2824,62cm-1
2785,35cm-1
2779,35cm-1
1644,49cm-1
1569,83cm-1
1447,44cm-1
1370,31cm-1
1332,19cm-1
1341,68cm-1
1291,58cm-1
1271,75cm-1
1255,71cm-1
1208,31cm-1
1185,58cm-1
1161,19cm-1
1119,37cm-1
1105,61cm-1
1073,78cm-1
1060,39cm-1
1047,25cm-1
1027,08cm-1
971,95cm-1
943,64cm-1
913,98cm-1
871,63cm-1
859,21cm-1
840,87cm-1
817,62cm-1
783,67cm-1
606,90cm-1
597,45cm-1
564,02cm-1
543,01cm-1
477,78cm-1
461,05cm-1
444,57cm-1
417,31cm-1
Nom
Description
YG-III-409 DACH-NMe2 di...
Échantillon 420 Par geiger Date mardi, octo...

V.3.5 Ditopic iminoaniline ligand

(*R*)-2-nitro-N-(1-phenylethyl)aniline **24**

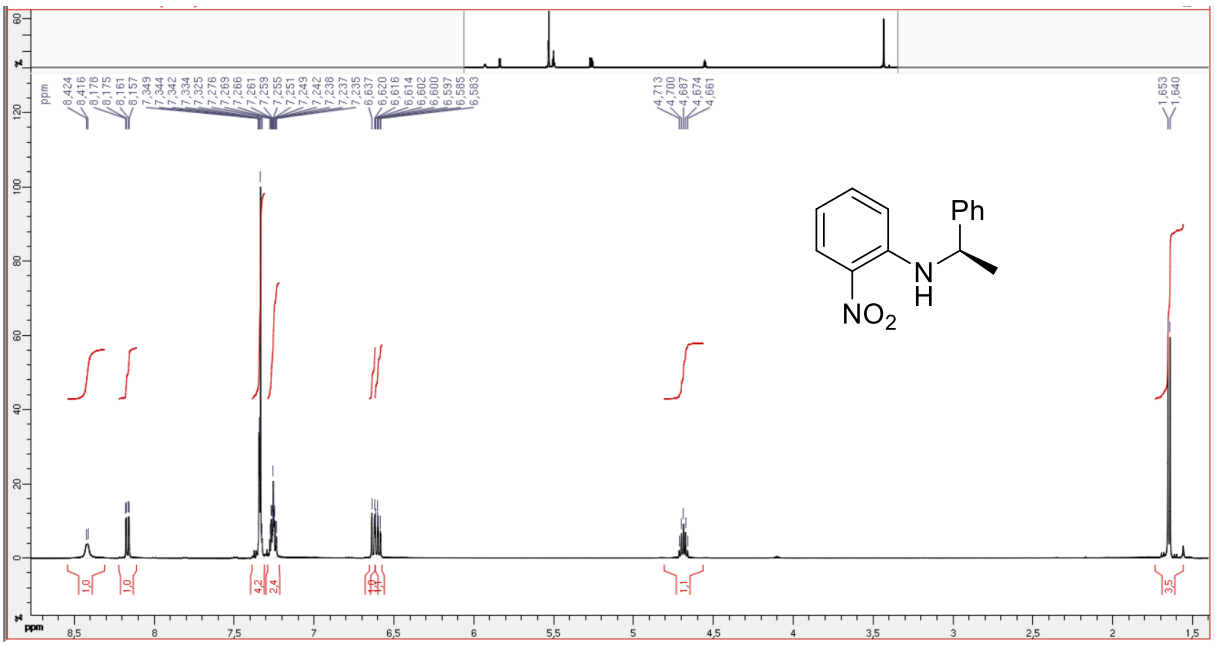

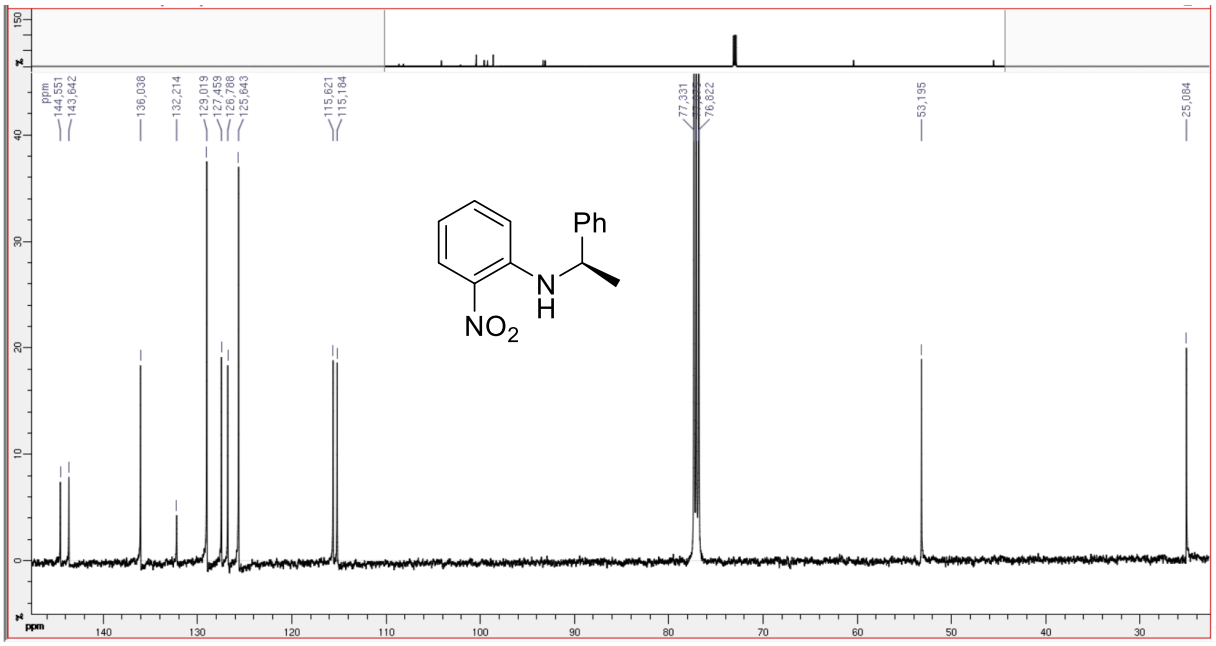

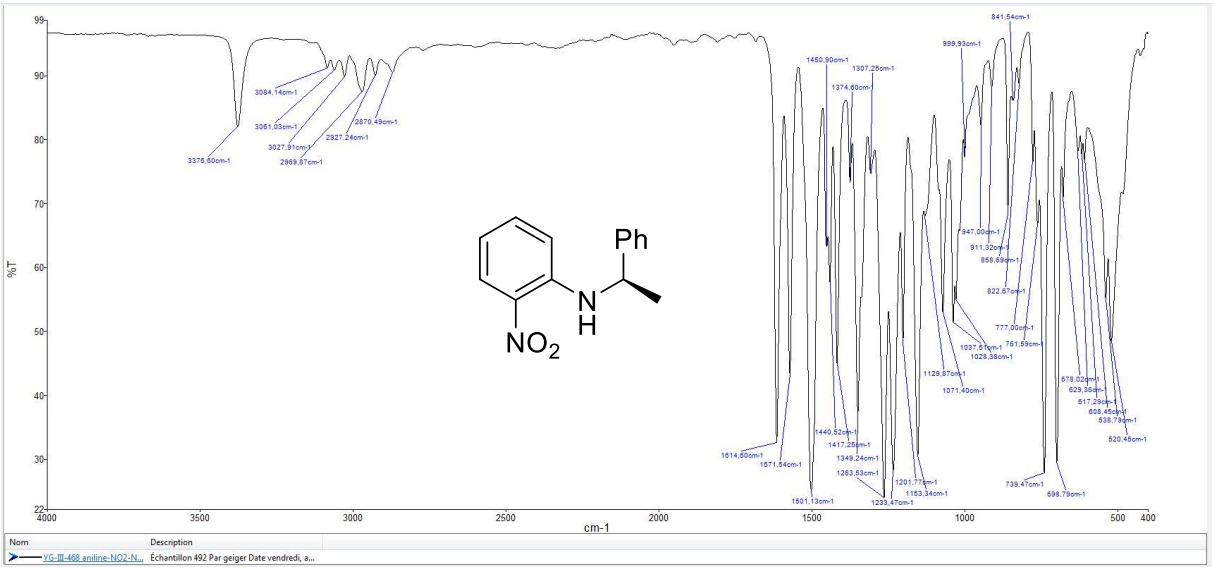

(*R*)-*N*^{1}-(1-phenylethyl)benzene-1,2-diamine **25**

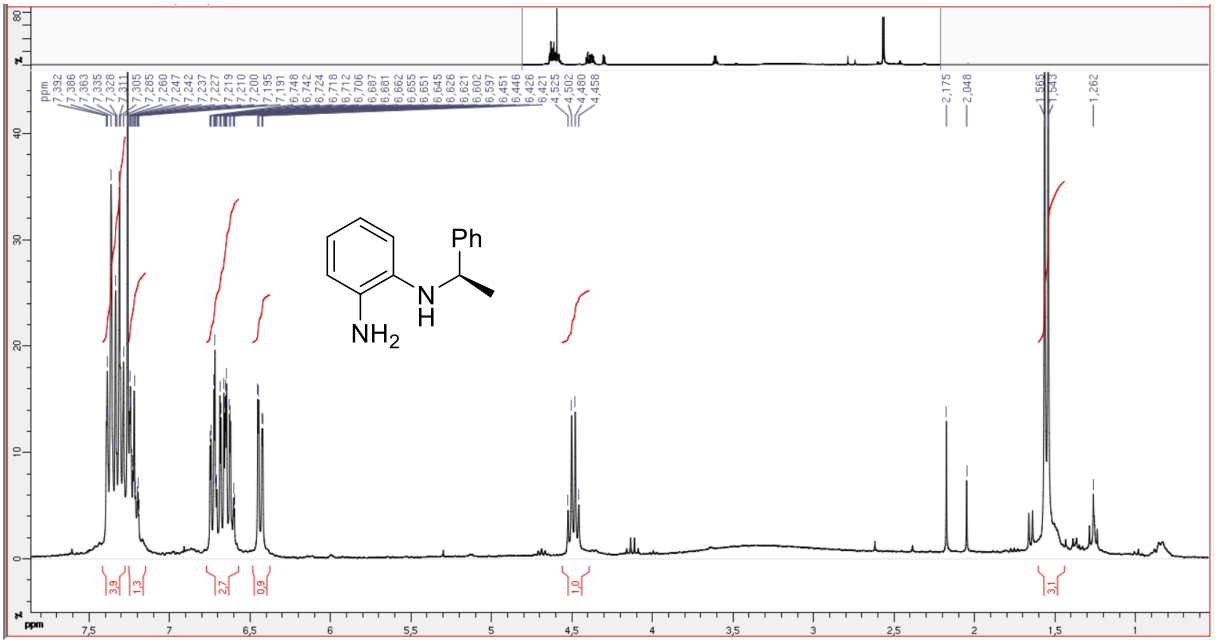

2,2'-(((*1Z,1'Z*)-1,4-phenylenebis(methaneylylidene))bis(azaneylylidene))bis(*N*-((*R*)-1-phenylethyl)aniline) **26**


ppm
8,662
8,071
7,432
7,430
7,415
7,401
7,354
7,351
7,339
7,327
7,324
7,315
7,313
7,260
7,255
7,253
7,240
7,228
7,226
7,223
7,121
7,118
7,105
7,102
7,027
7,024
7,010
7,009
6,996
6,993
6,673
6,671
6,658
6,656
6,643
6,641
6,457
6,455
6,441
6,439
5,516
4,611
4,598
4,584
4,571
1,633
1,619
2,0
3,9
4,2
4,4
3,8
1,9
1,9
2,1
1,9
1,9
2,0
5,9
N
H
N
Ph
N
N
H
Ph

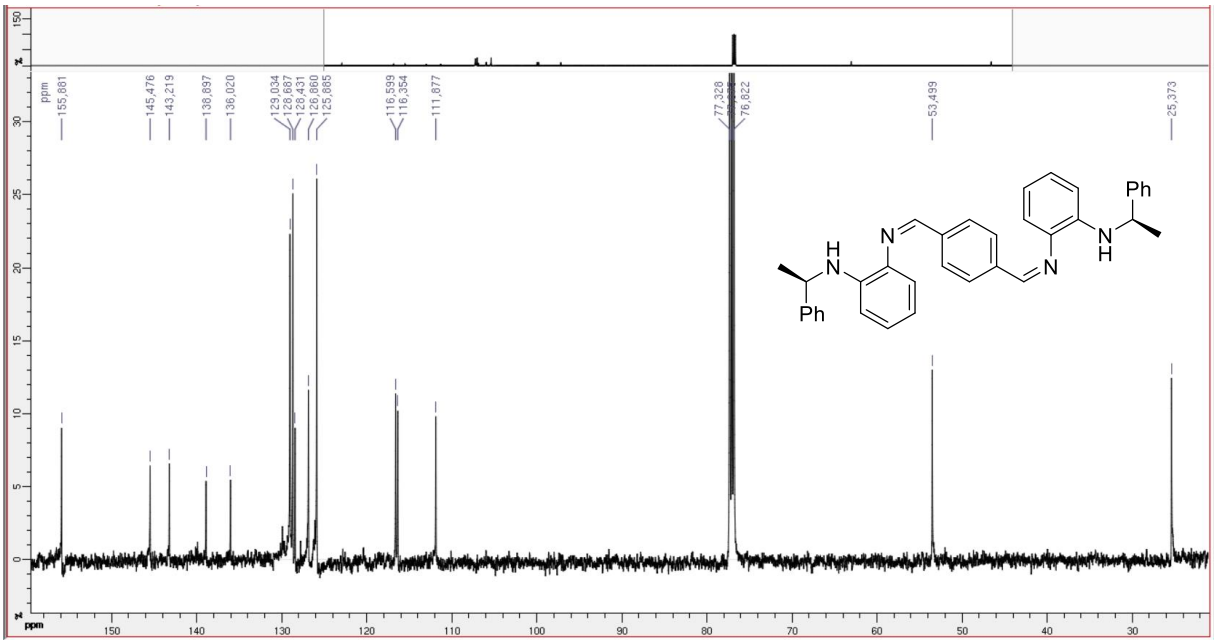
ppm
155,881
145,476
143,219
138,897
136,020
129,034
128,687
128,431
126,860
125,885
116,599
116,354
111,877
77,328
76,822
53,499
25,373
N
H
N
Ph
N
N
H
Ph

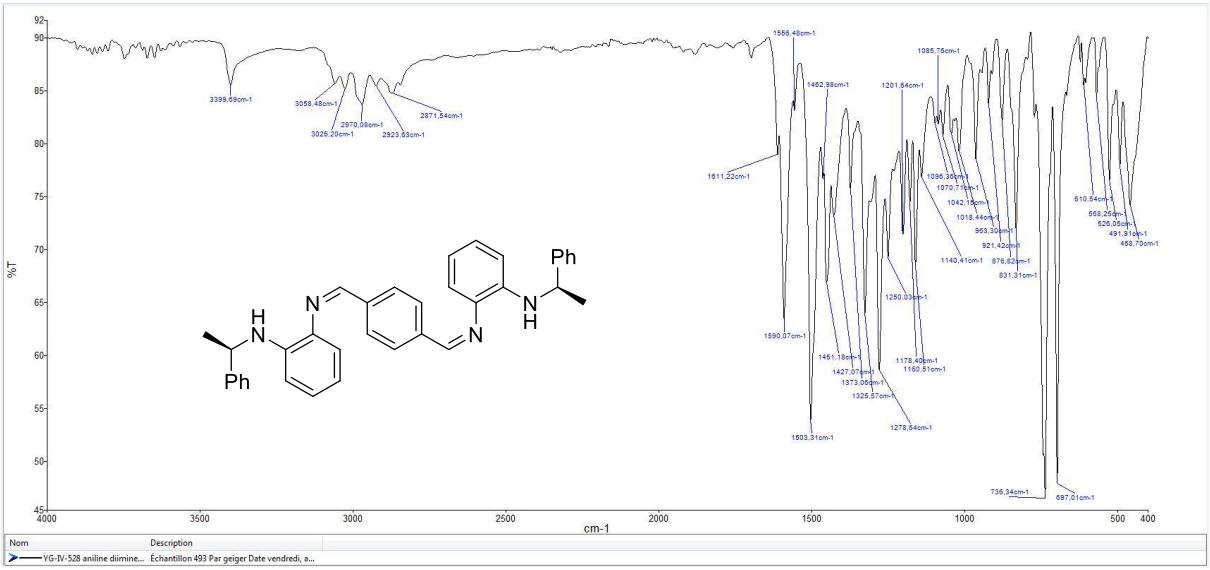

V.3.6 Ditopic iminoalcohol complexes

19e-CuPF$_6$

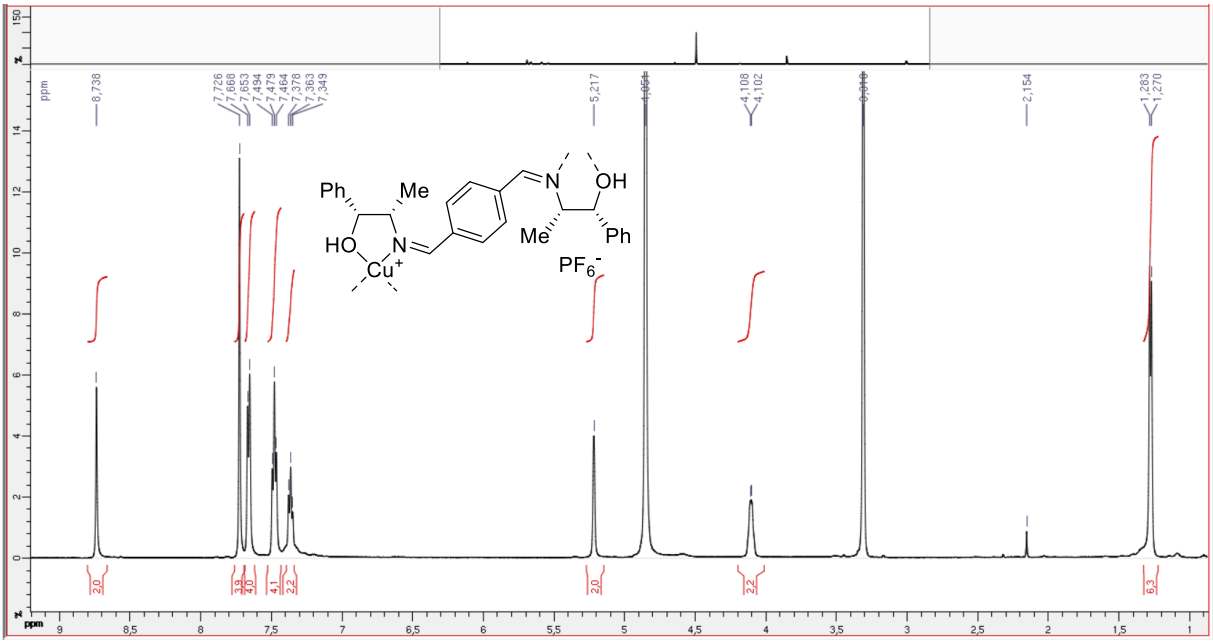

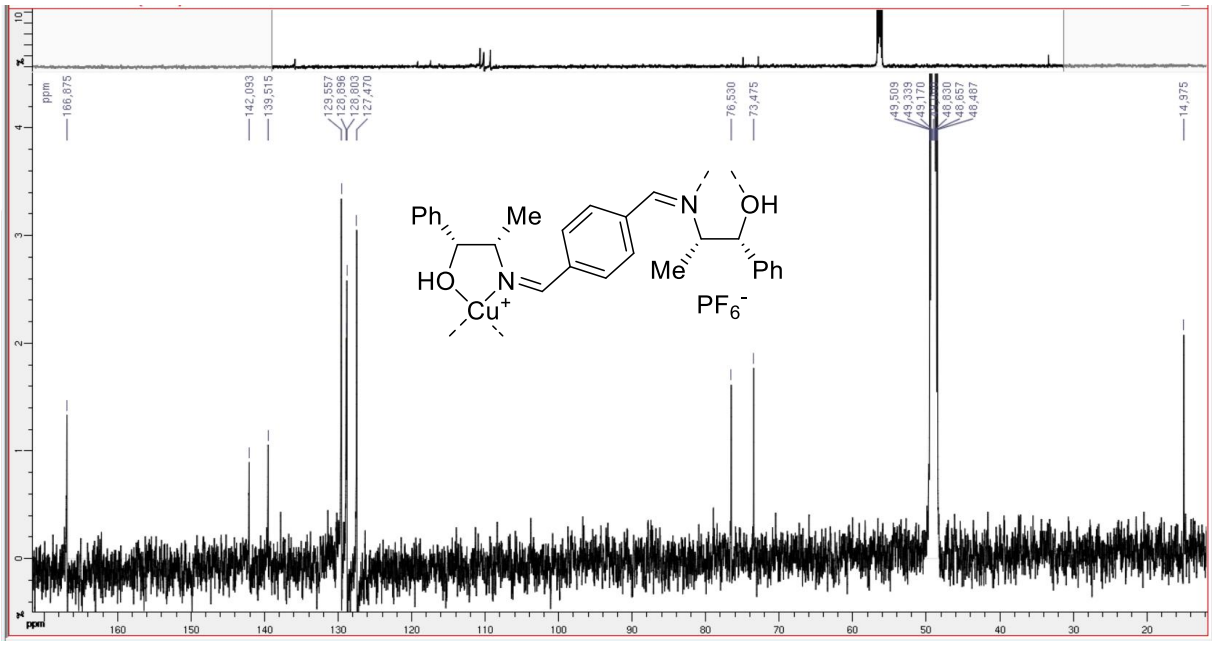
ppm
166,875
142,093
139,515
129,557
128,896
128,803
127,470
76,530
73,475
49,509
49,339
49,170
48,830
48,657
48,487
14,975
Ph
Me
HO
N
Cu+
N
OH
Me
Ph
PF6-

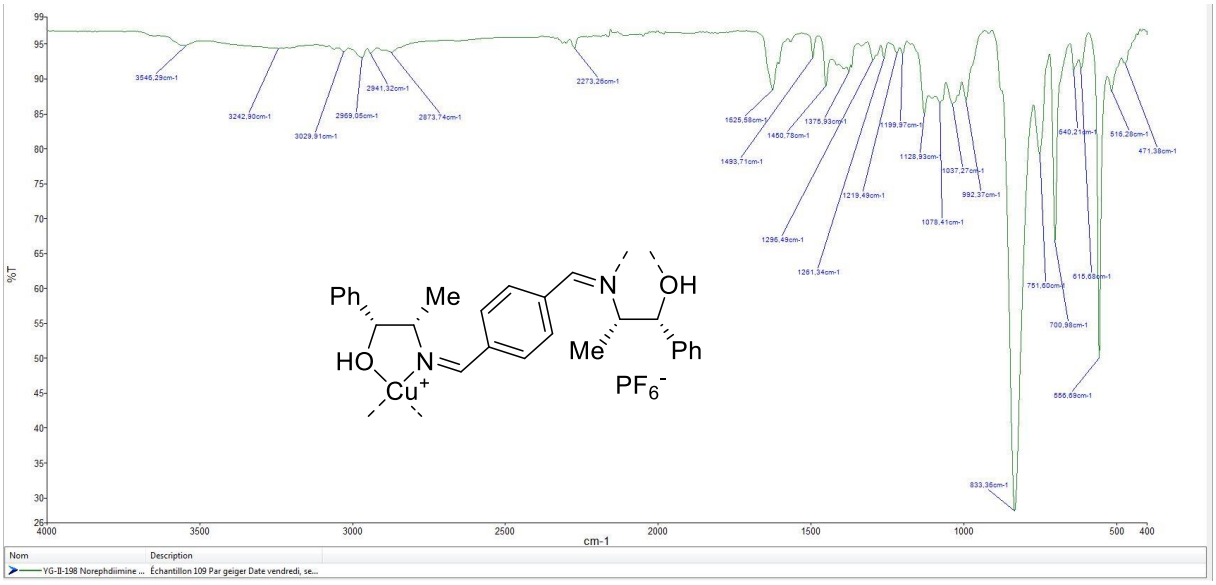
%T
cm-1
3546,29cm-1
3242,90cm-1
3029,91cm-1
2969,05cm-1
2941,32cm-1
2873,74cm-1
2273,26cm-1
1625,58cm-1
1493,71cm-1
1450,78cm-1
1375,93cm-1
1296,49cm-1
1261,34cm-1
1219,49cm-1
1199,97cm-1
1128,93cm-1
1078,41cm-1
1037,27cm-1
992,37cm-1
833,36cm-1
751,60cm-1
700,98cm-1
640,21cm-1
615,69cm-1
556,69cm-1
516,28cm-1
471,38cm-1
Ph
Me
HO
N
Cu+
N
OH
Me
Ph
PF6-
Nom
Description
YG-II-198 Norephdiimine ...
Échantillon 109 Par geiger Date vendredi, se...

19e-Cu(OTf)$_2$

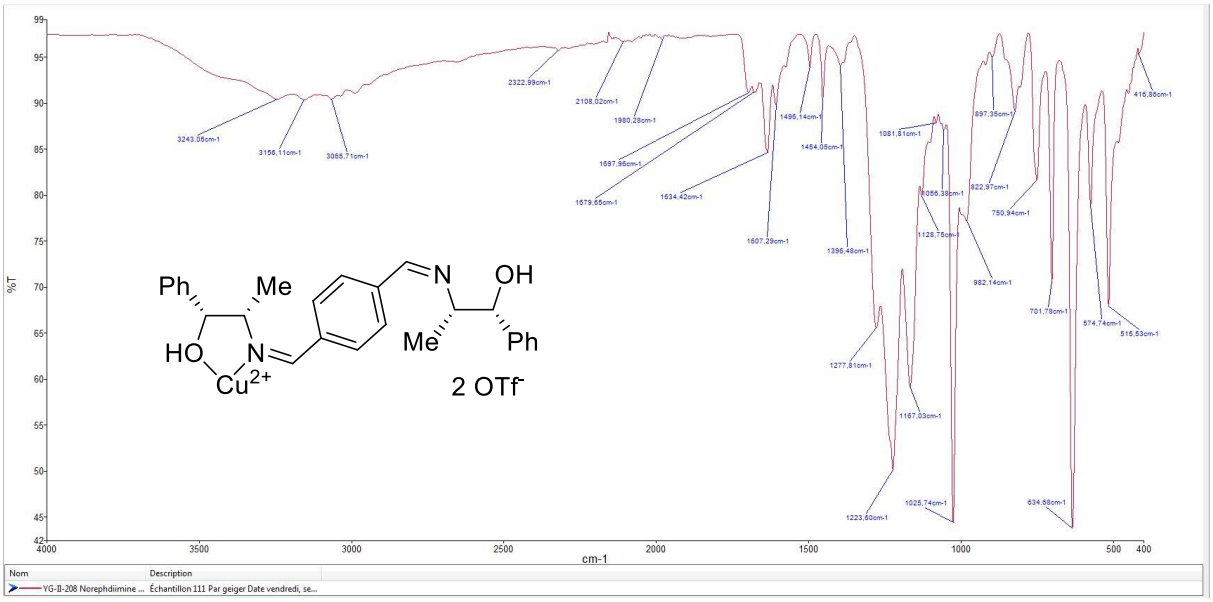
%T
cm-1
Ph
Me
HO
N
Cu2+
N
OH
Me
Ph
2 OTf-
Nom
Description

19f-CuPF$_6$

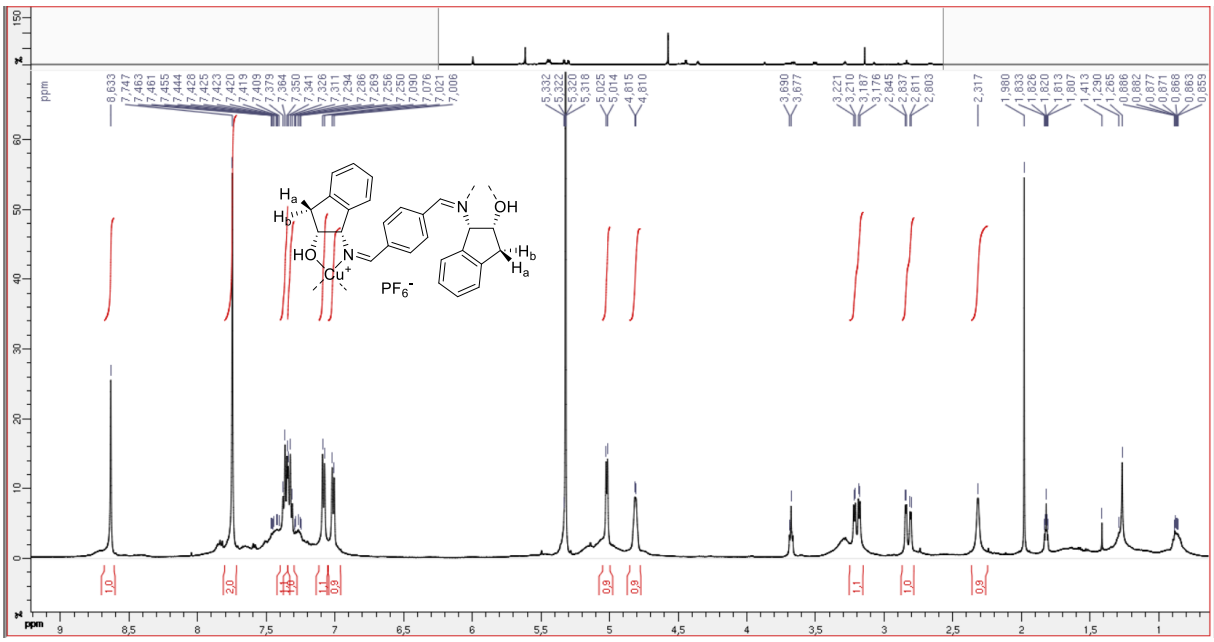
ppm
Ha
Hb
HO
N
Cu+
PF6-
N
OH
Hb
Ha

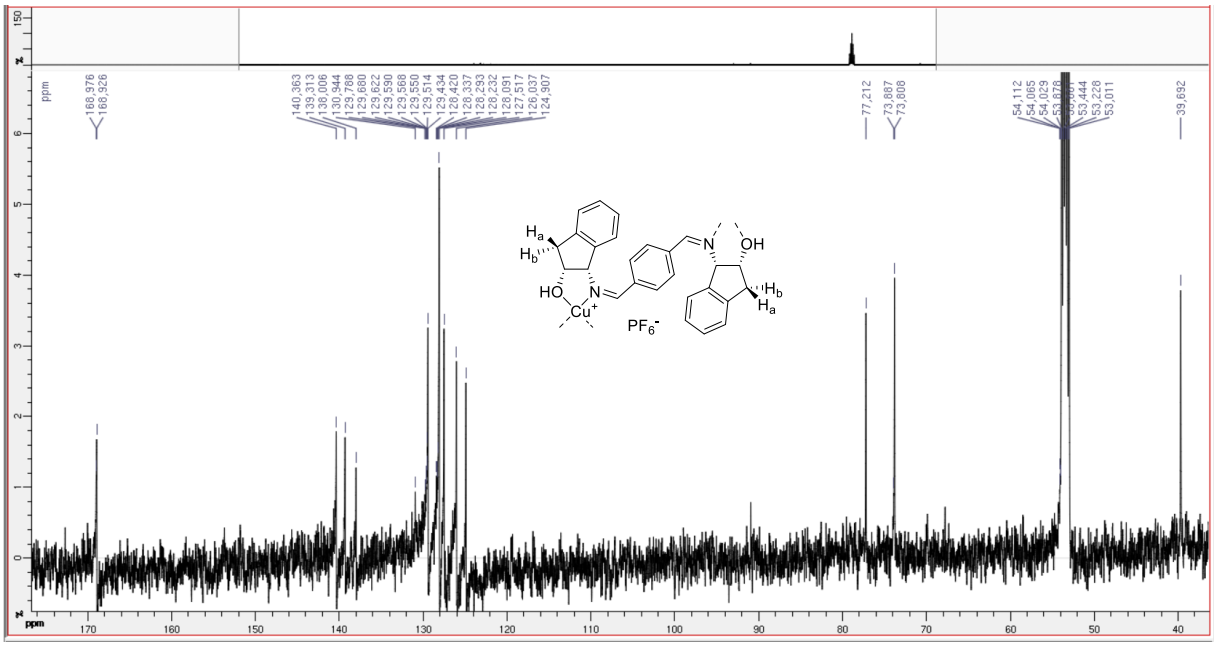
ppm
168,976
168,926
140,363
139,313
138,006
130,944
129,788
129,680
129,622
129,568
129,550
129,514
129,434
128,420
128,337
128,293
128,232
128,091
127,517
126,037
124,907
77,212
73,887
73,808
54,112
54,085
54,029
53,878
53,444
53,228
53,011
39,692
Ha
Hb
HO
N
Cu+
PF6-
OH

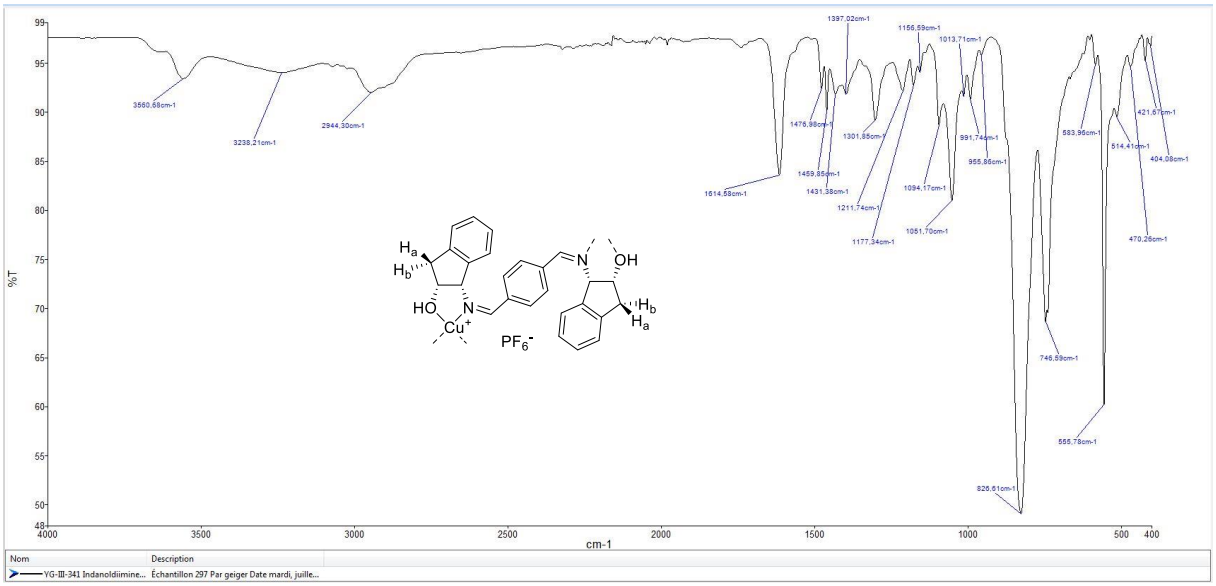
%T
cm-1
3560,68cm-1
3238,21cm-1
2944,30cm-1
1614,58cm-1
1476,98cm-1
1459,85cm-1
1431,38cm-1
1397,02cm-1
1301,85cm-1
1211,74cm-1
1177,34cm-1
1156,59cm-1
1094,17cm-1
1051,70cm-1
1013,71cm-1
991,74cm-1
955,86cm-1
826,61cm-1
746,59cm-1
555,78cm-1
583,96cm-1
514,41cm-1
470,26cm-1
421,87cm-1
404,08cm-1
Ha
Hb
HO
N
Cu+
PF6-
OH
Nom
Description
YG-III-341 Indanoldiimine...
Échantillon 297 Par geiger Date mardi, juille...

19f-Cu(OTf)$_2$

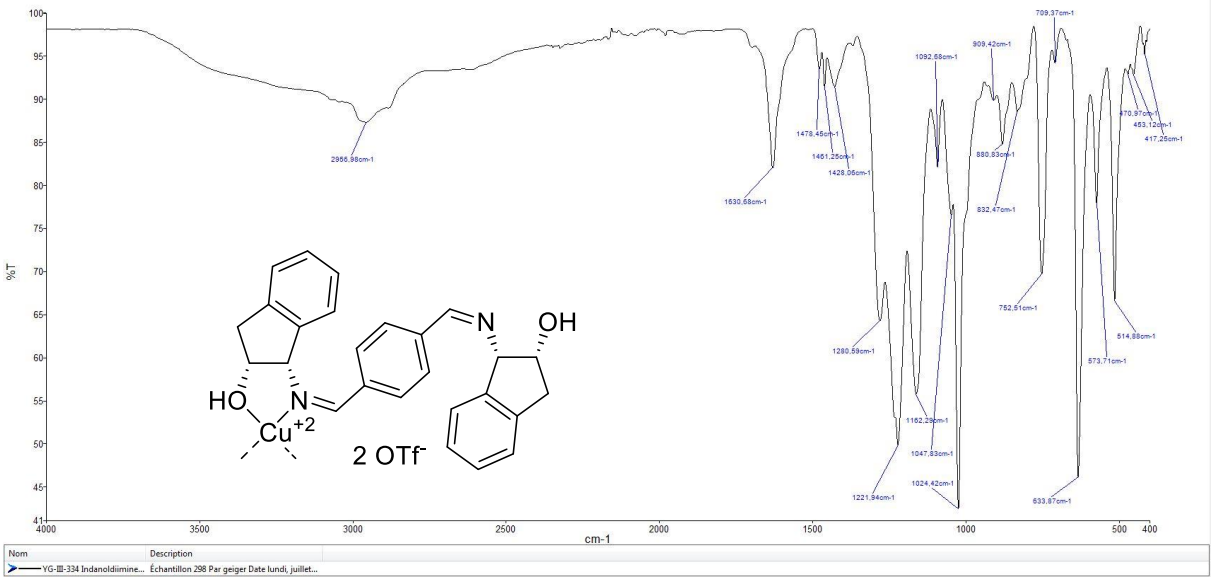

19g-CuPF$_6$

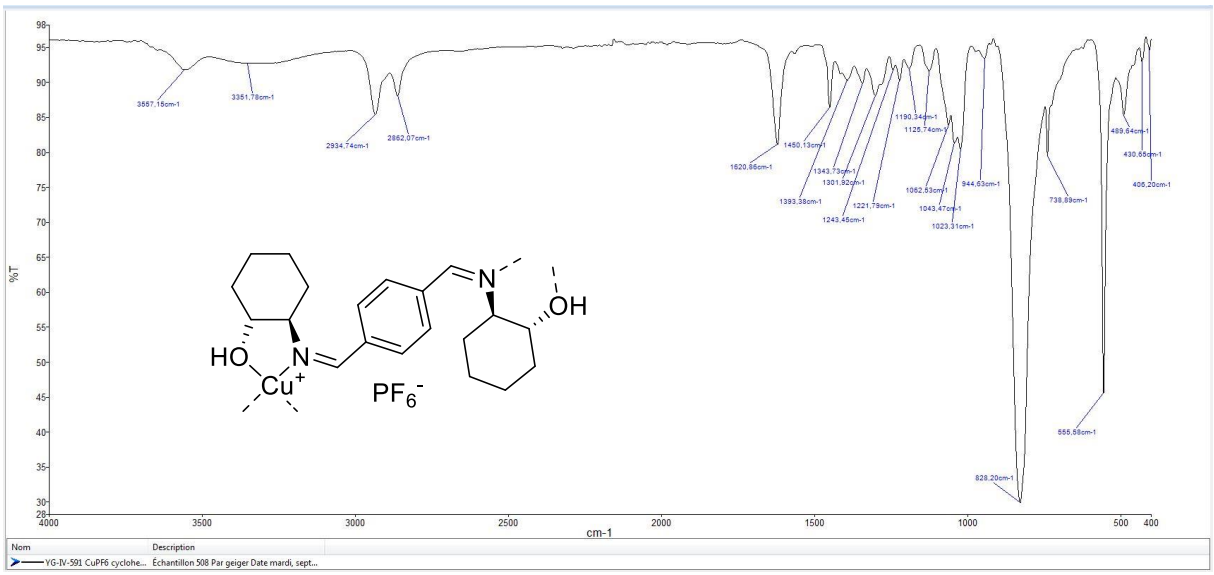

19g-Cu(OTf)$_2$

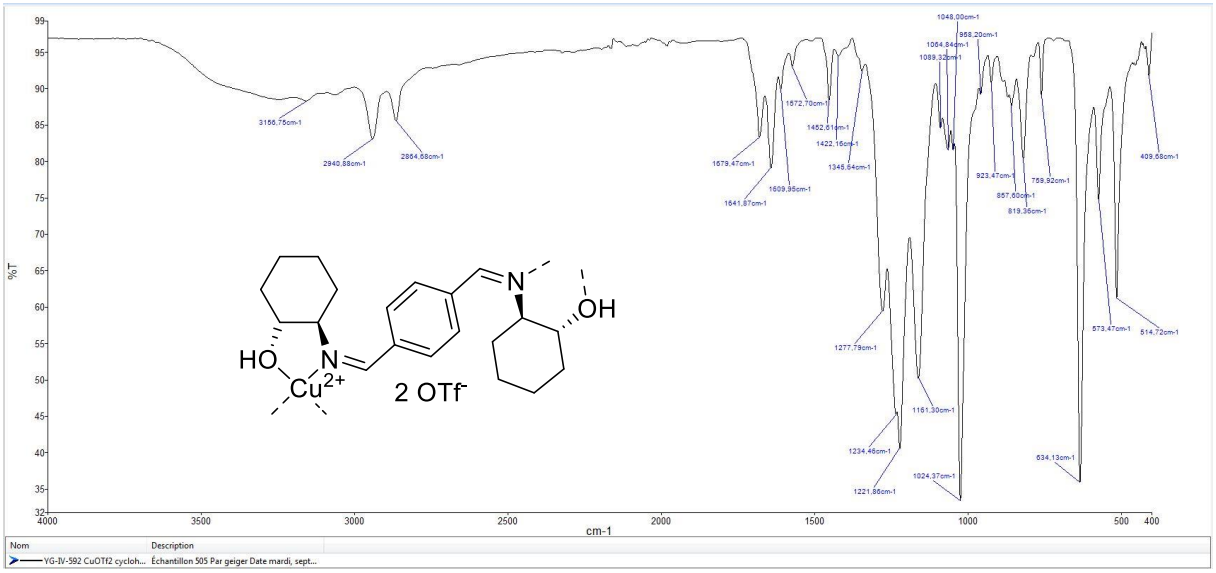

19g-Zn(OTf)$_2$

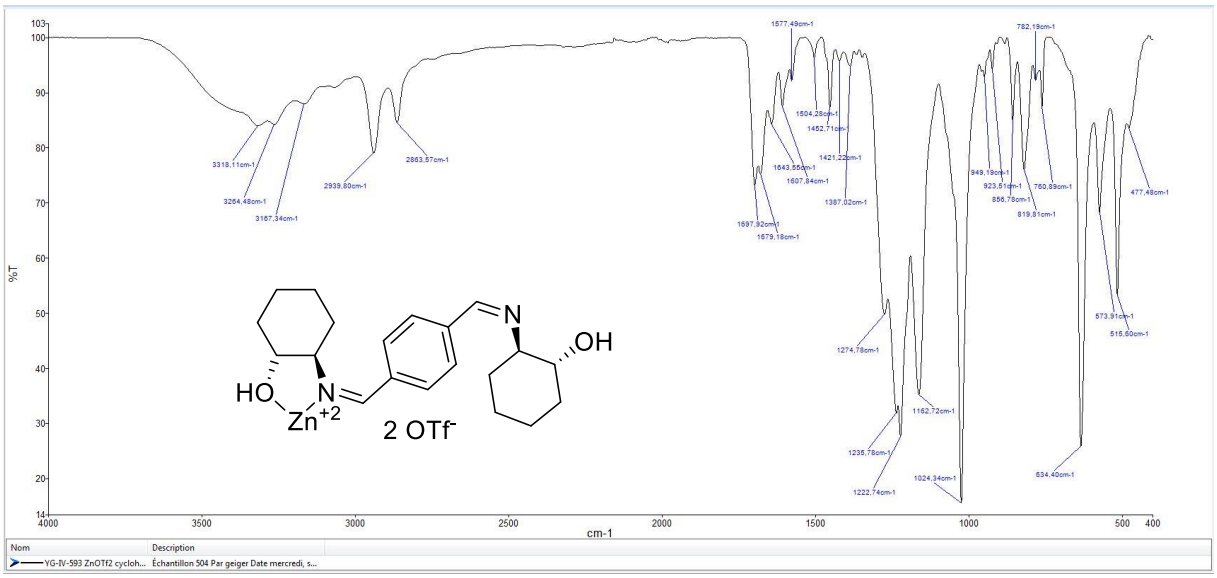

V.3.7 Ditopic iminoamine complexes

23-CuPF$_6$

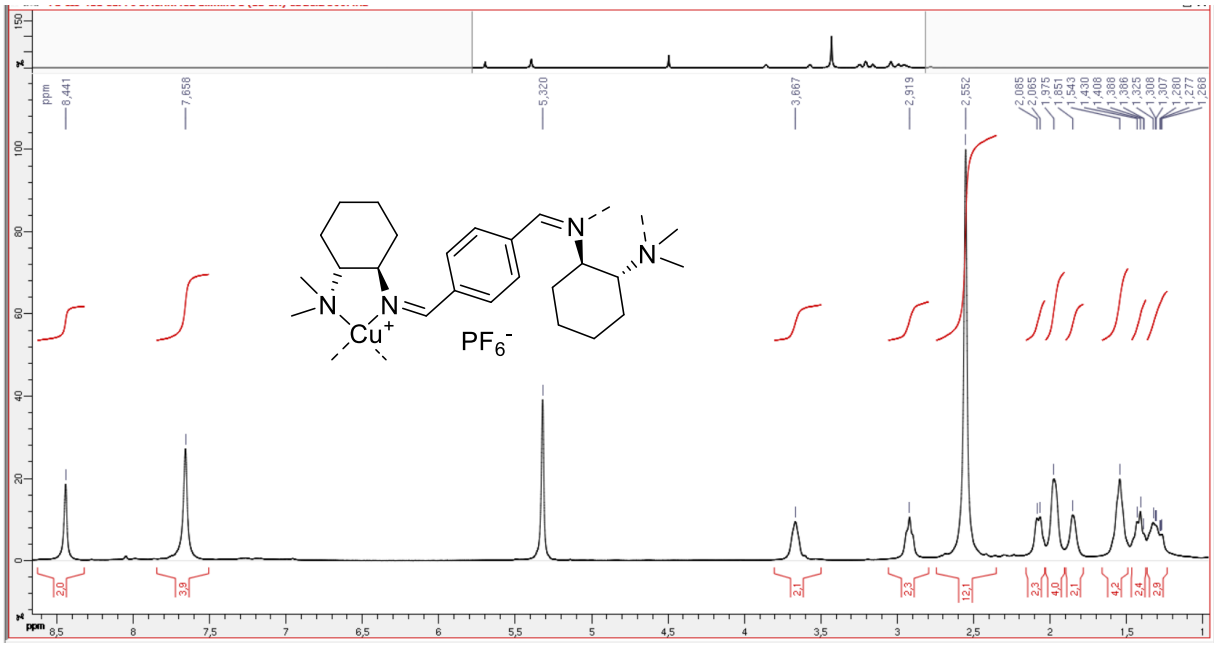
ppm
8,441
7,658
5,320
3,667
2,919
2,552
2,085
2,065
1,975
1,851
1,543
1,430
1,408
1,388
1,386
1,325
1,308
1,307
1,280
1,277
1,268
N
N
Cu+
PF6-
N
N
2,0
3,8
2,1
2,3
12,1
2,3
4,0
2,1
4,2
2,4
2,3

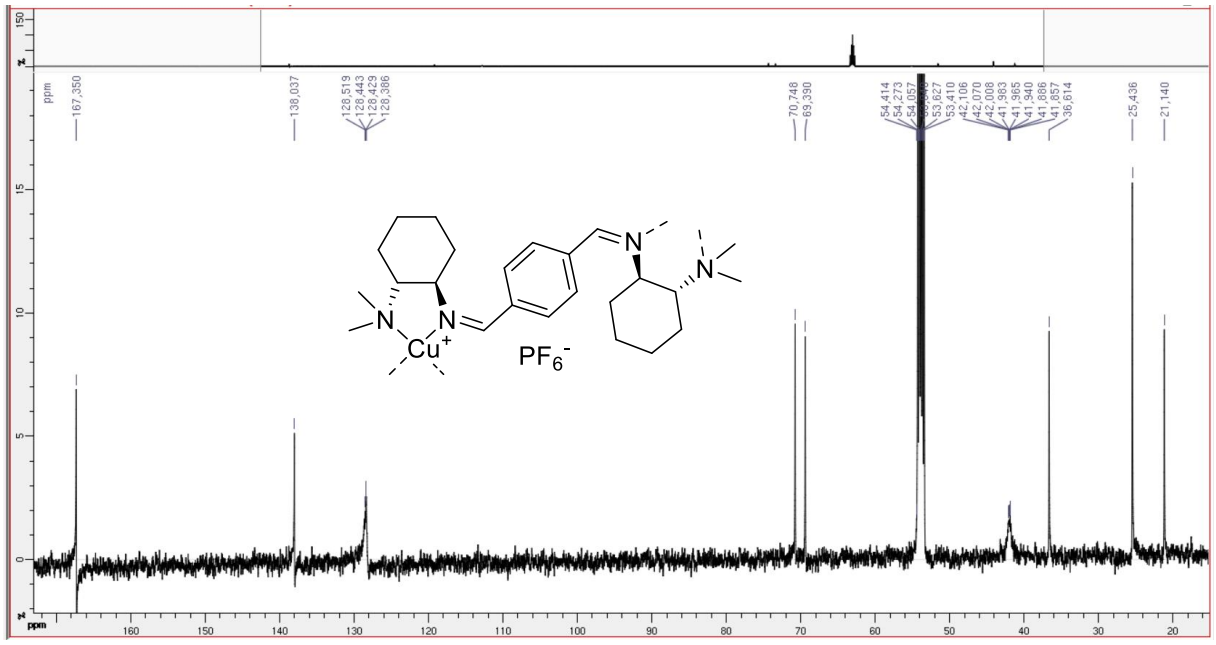
ppm
167,350
138,037
128,519
128,443
128,429
128,386
70,748
69,390
54,414
54,273
54,057
53,627
53,410
42,106
42,070
42,008
41,983
41,965
41,940
41,886
41,857
36,614
25,436
21,140
N
N
Cu+
PF6-
N
N

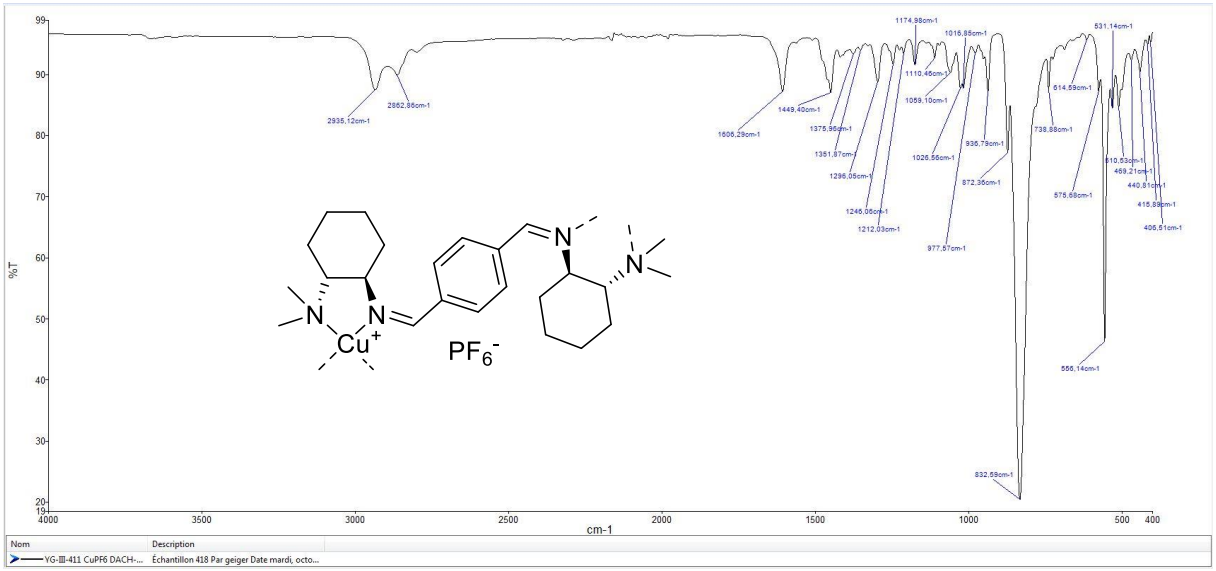

23-Cu(OTf)$_2$

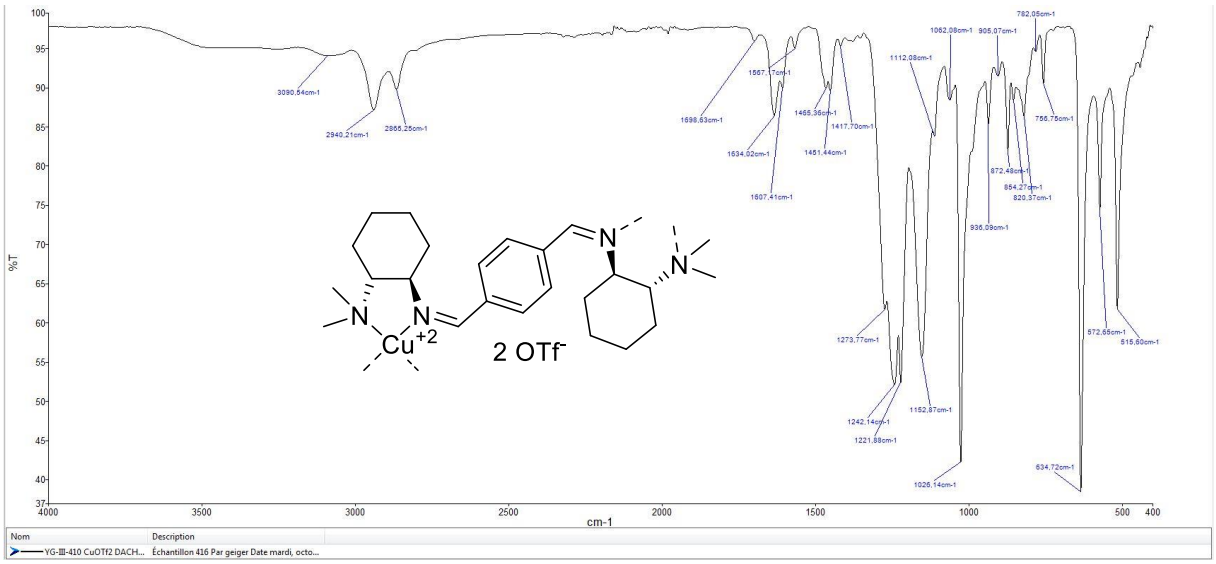

23-Zn(OTf)$_2$

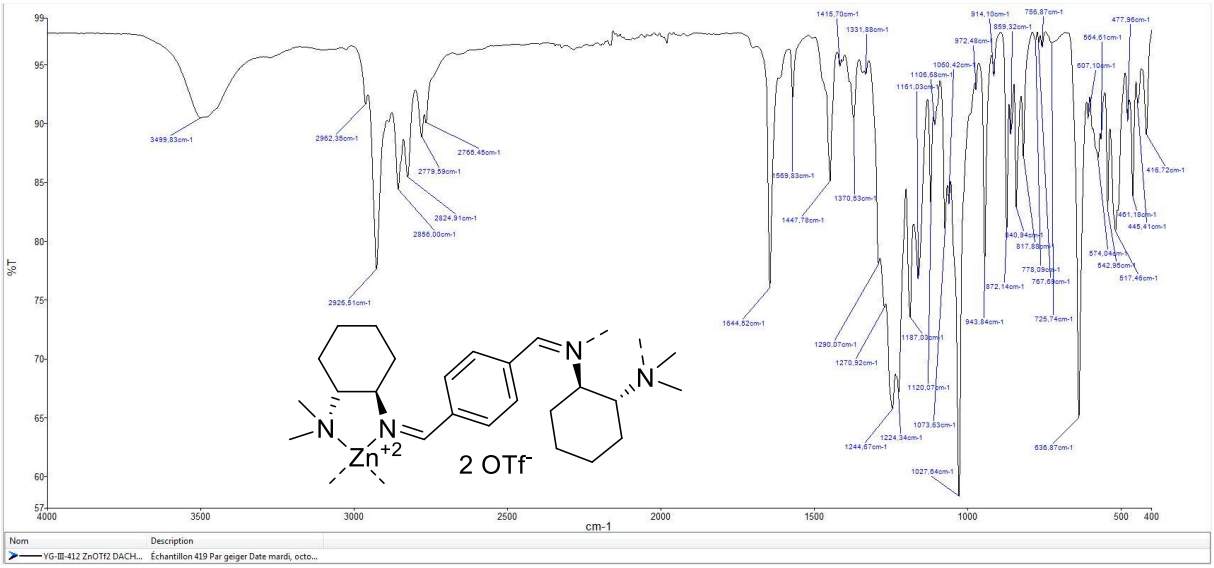

V.3.8 Ditopic iminoaniline complexes

26-CuPF$_6$

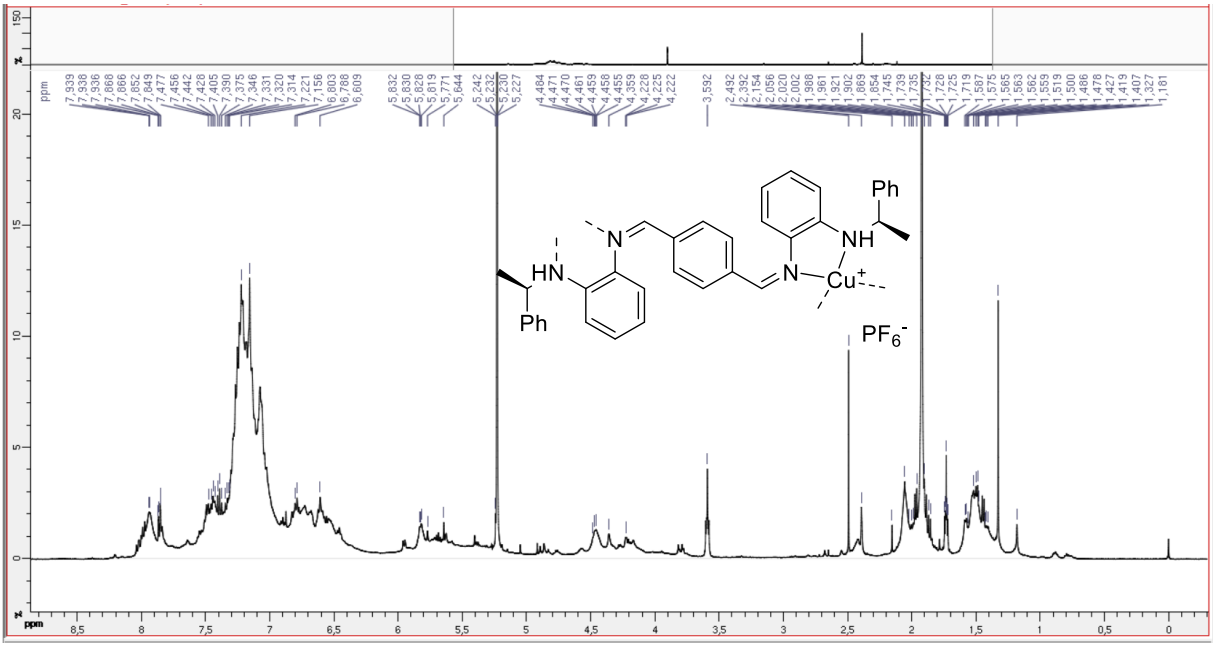

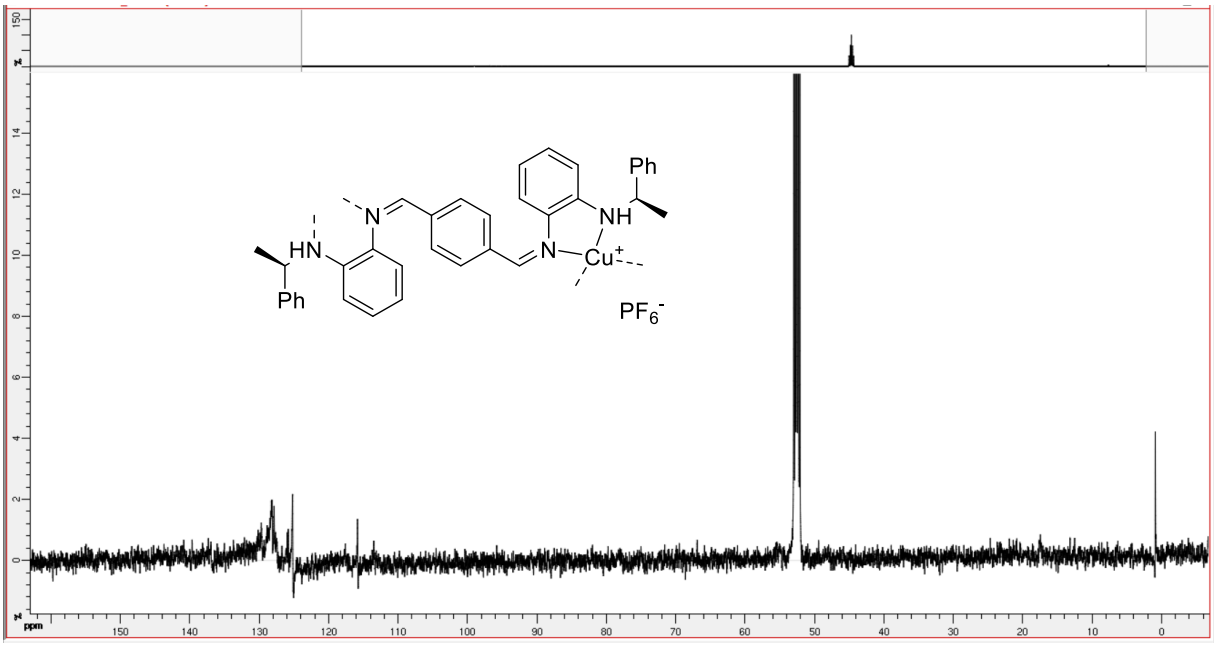
Ph
NH
HN
N
Cu+
Ph
PF6-
ppm

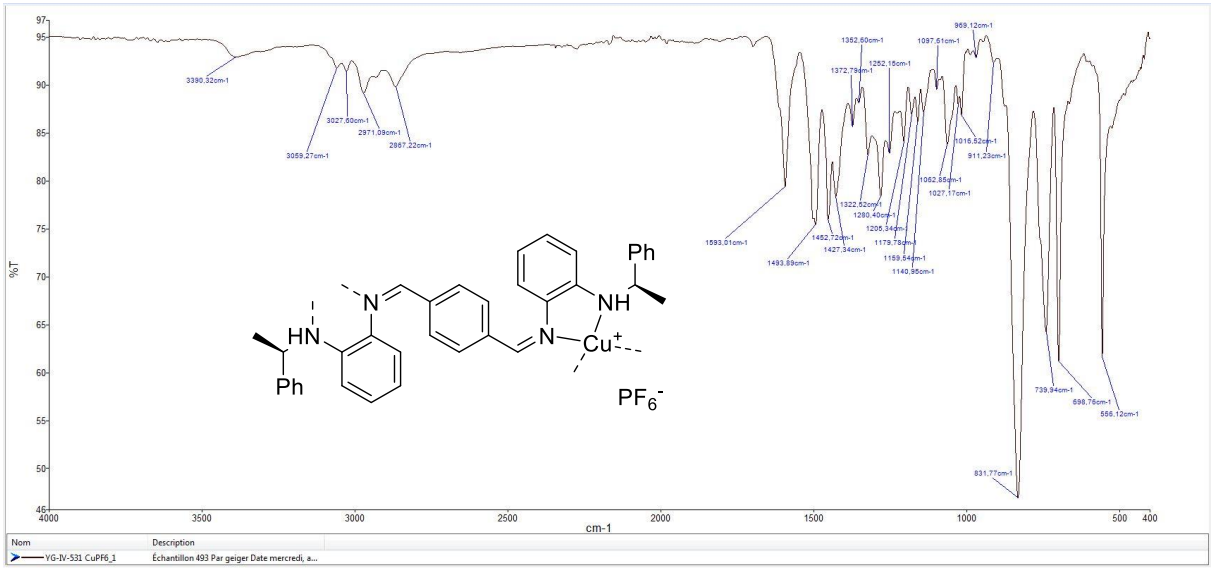
3390.32cm-1
3059.27cm-1
3027.60cm-1
2971.09cm-1
2867.22cm-1
1593.01cm-1
1493.89cm-1
1452.72cm-1
1427.34cm-1
1372.78cm-1
1352.60cm-1
1322.52cm-1
1280.40cm-1
1252.18cm-1
1205.34cm-1
1179.78cm-1
1159.54cm-1
1140.95cm-1
1097.61cm-1
1062.85cm-1
1027.17cm-1
969.12cm-1
1016.52cm-1
911.23cm-1
831.77cm-1
739.94cm-1
698.76cm-1
556.12cm-1
%T
cm-1
Ph
NH
HN
N
Cu+
Ph
PF6-
Nom
Description
YG-IV-531 CuPF6_1
Échantillon 493 Par geiger Date mercredi, a...

26-Cu(OTf)$_2$

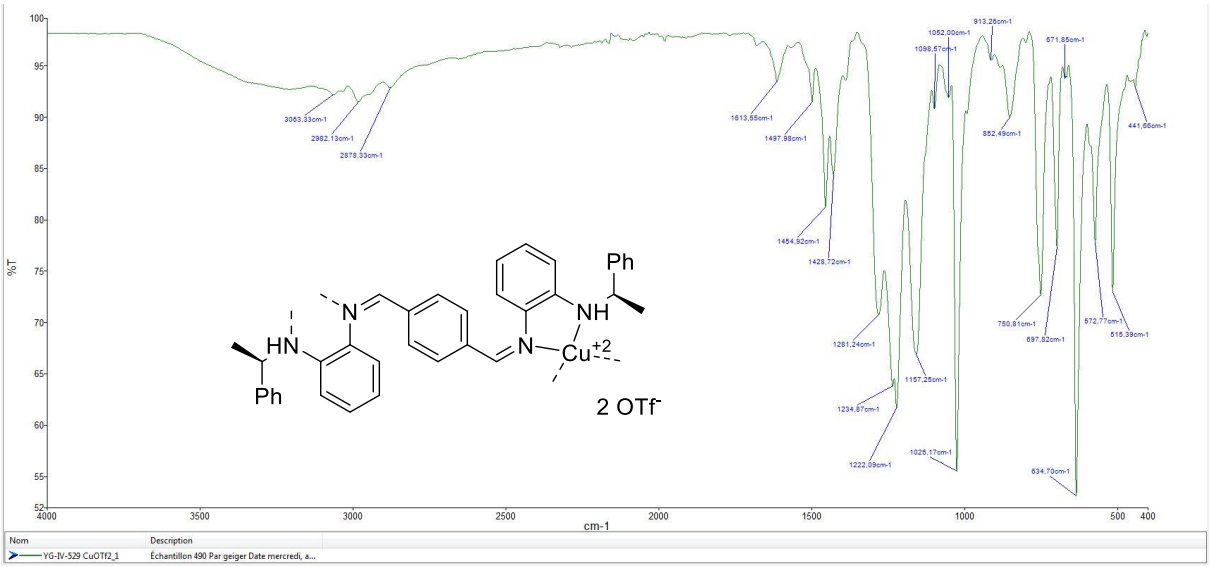
%T
cm-1
3063,33cm-1
2982,13cm-1
2878,33cm-1
1613,55cm-1
1497,98cm-1
1454,92cm-1
1428,72cm-1
1281,24cm-1
1234,87cm-1
1222,09cm-1
1157,25cm-1
1098,57cm-1
1052,00cm-1
1025,17cm-1
913,26cm-1
852,49cm-1
760,81cm-1
697,92cm-1
671,85cm-1
634,70cm-1
572,77cm-1
515,39cm-1
441,66cm-1
Ph
NH
HN
Ph
N
N
Cu+2
2 OTf-
Nom
Description
YG-IV-529 CuOTf2_1
Échantillon 490 Par geiger Date mercredi, a...

26-Zn(OTf)$_2$

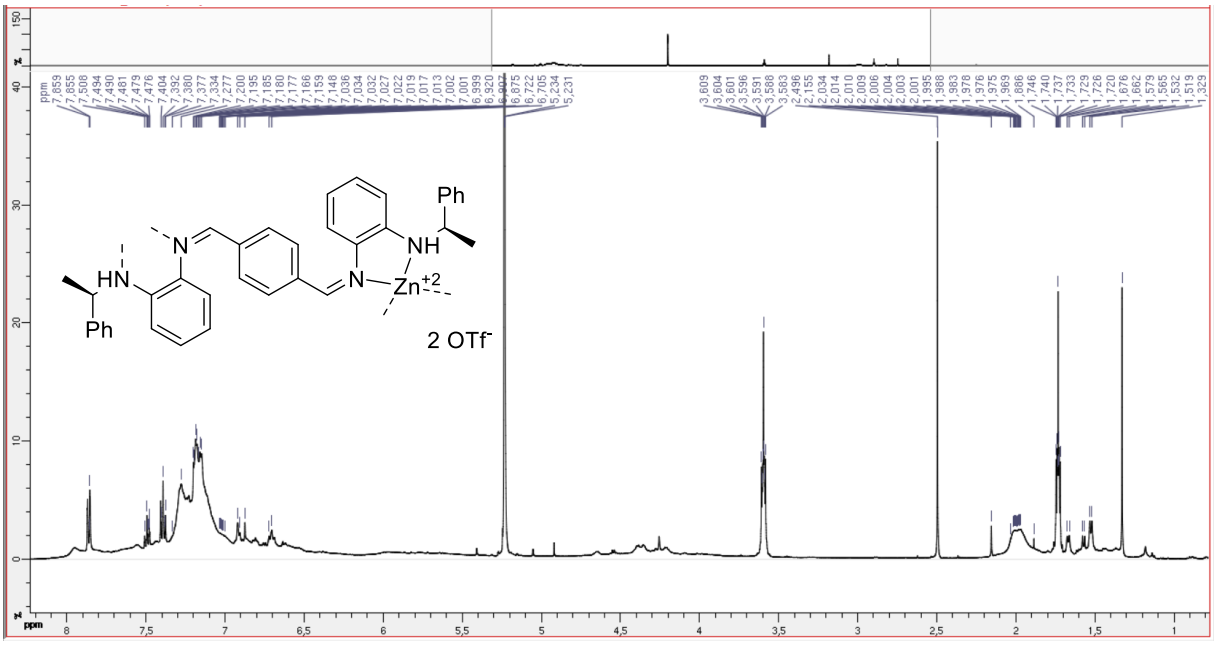
ppm
Ph
NH
HN
Ph
N
N
Zn+2
2 OTf-

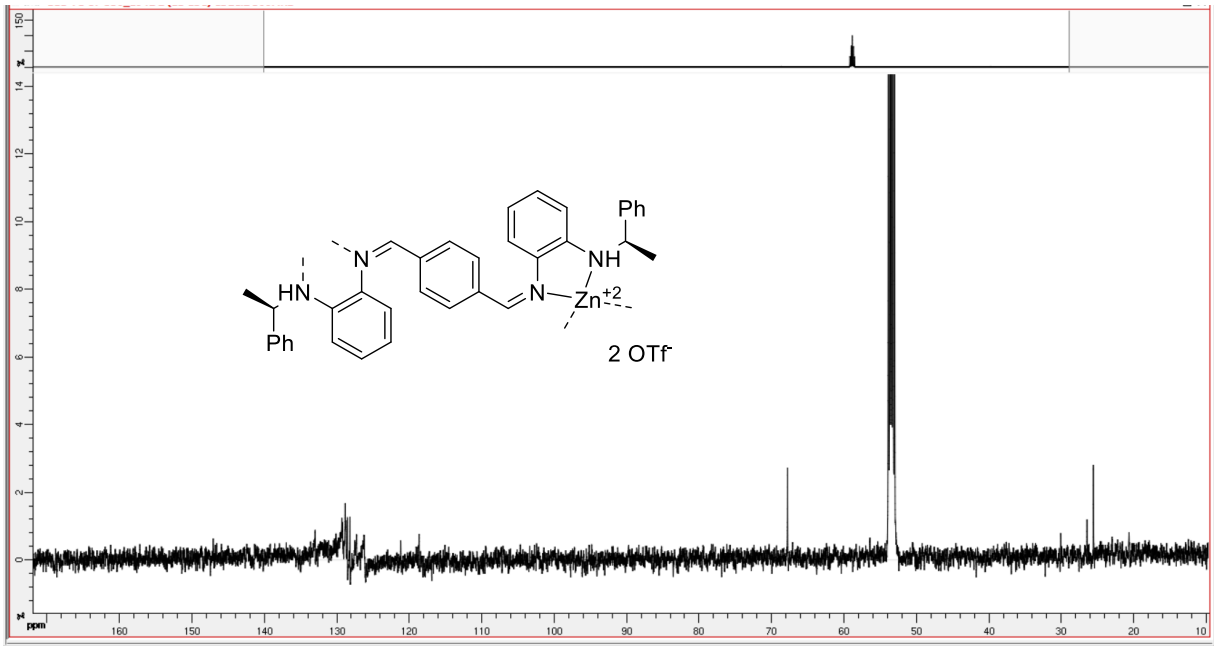
Ph
NH
N
HN
Ph
N
Zn+2
2 OTf-

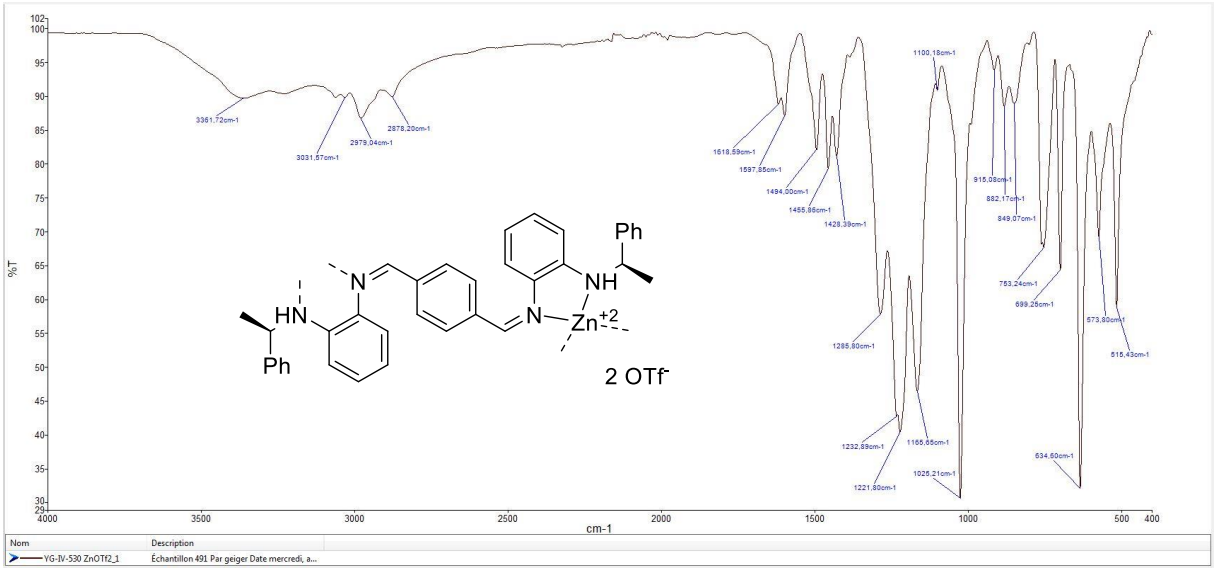
3361.72cm-1
3031.57cm-1
2979.04cm-1
2878.20cm-1
1618.89cm-1
1597.85cm-1
1494.00cm-1
1455.98cm-1
1428.39cm-1
1100.18cm-1
915.08cm-1
882.17cm-1
849.07cm-1
753.24cm-1
699.26cm-1
573.80cm-1
515.43cm-1
1285.80cm-1
1232.89cm-1
1221.89cm-1
1165.65cm-1
1025.21cm-1
634.50cm-1
%T
cm-1
Ph
NH
N
HN
Ph
N
Zn+2
2 OTf-
Nom
Description
YG-IV-530 ZnOTf2_1
Échantillon 491 Par geiger Date mercredi, a...

26-Ni(BF_4)$_2$

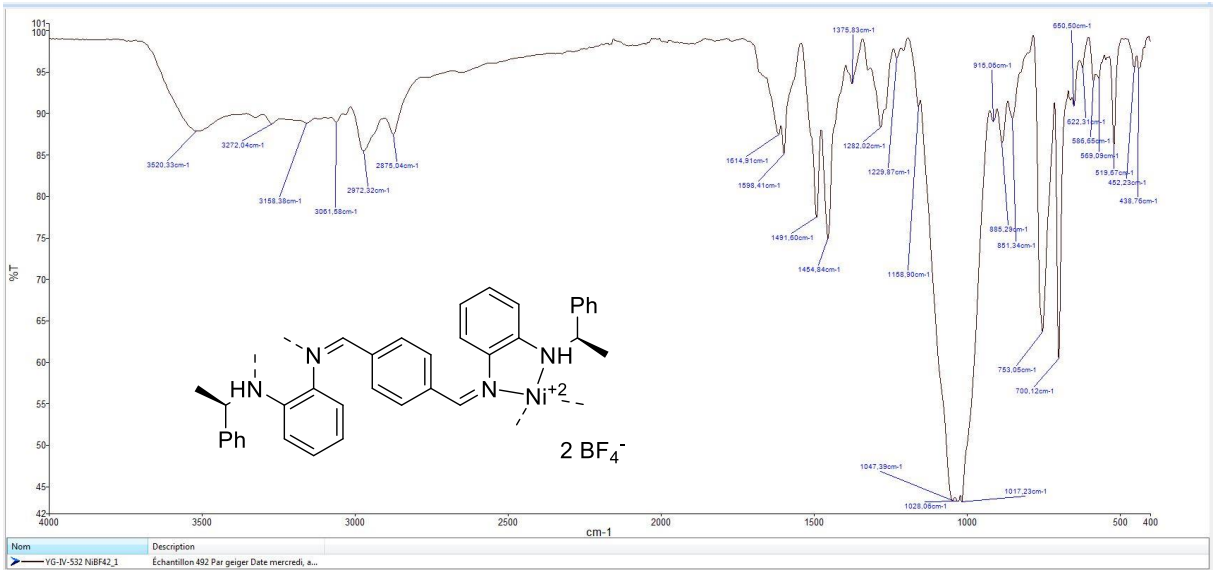
3520.33cm-1
3272.04cm-1
3159.38cm-1
3051.58cm-1
2972.32cm-1
2875.04cm-1
1614.91cm-1
1598.41cm-1
1491.60cm-1
1454.84cm-1
1375.83cm-1
1282.02cm-1
1229.87cm-1
1158.90cm-1
1047.39cm-1
1028.05cm-1
1017.23cm-1
915.05cm-1
885.29cm-1
851.34cm-1
753.05cm-1
700.12cm-1
650.50cm-1
622.31cm-1
586.65cm-1
569.09cm-1
519.67cm-1
452.23cm-1
439.76cm-1
%T
cm-1
Ph
NH
N
HN
Ph
N
Ni+2
2 BF4-
Nom
Description
YG-IV-532 NiBF42_1
Échantillon 492 Par geiger Date mercredi, a...

VI : Résumé de la thèse en français

VI.1 Chapitre I

Les effets non-linéaires (NLE) en catalyse asymétrique sont des phénomènes où l'excès énantiomérique (ee) du produit final d'une réaction catalytique ne corrèle pas de façon linéaire avec le ee du catalyseur utilisé. Ainsi, il est possible d'obtenir des produits avec un ee supérieur au catalyseur même, comme p. ex. dans le l'éthylation énantiosélective du benzaldéhyde par le $ZnEt_2$ catalysée par le ligand diaminoisobornéol (DAIB) de Noyori (Figure 142). Ici, un produit avec 95% de ee est obtenu d'un ligand qui n'a qu'un ee de 15%.

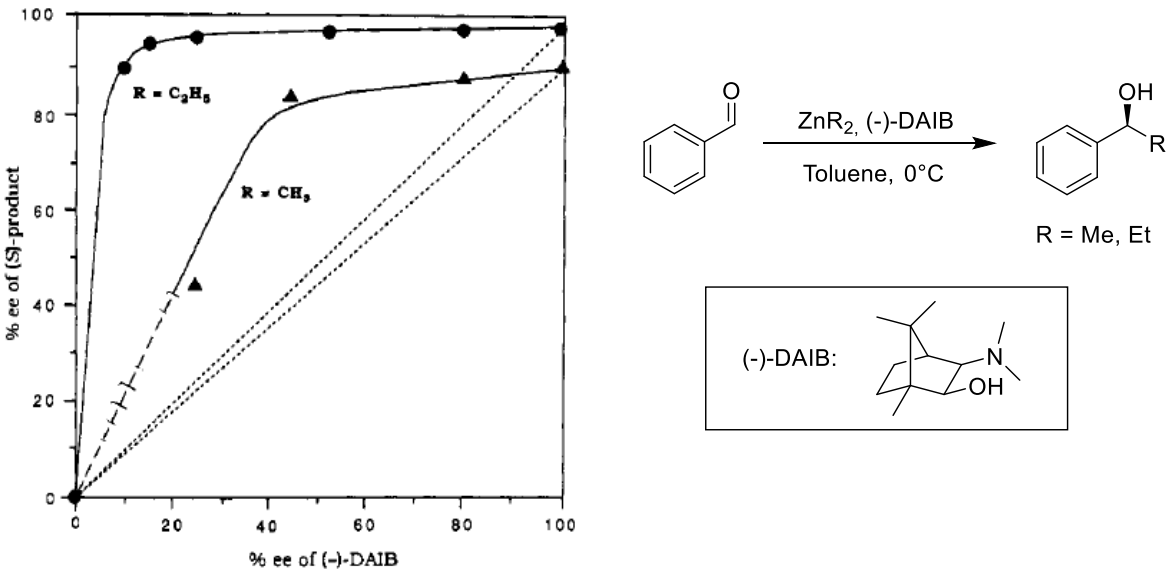

Figure 142: (+)-NLE observé pour l'addition énantiosélective de dialkylzincs au benzaldéhyde catalysée par le (-)-DAIB.

Les NLE ont été décrit et analysé pour la première fois par le groupe de Henri Kagan. En plus de montrer les premiers exemples de NLE, Kagan a aussi développé des modèles mathématiques qui non seulement expliquent mais aussi quantifient ces phénomènes. Le modèle « ML_2 » part du fait que le complexe, portant un ligand chiral, dimérise de façon irréversible en solution (Figure 143). Dans le cas où le ligand n'est pas énantiopur mais scalémique trois dimères différents sont possibles : les dimères homochiraux MRR et MSS ainsi que le dimère hétérochiral MRS. Si les premiers sont plus actifs en catalyse le ee du produit final (ee_P) augmente par rapport au ee du ligand, on a un NLE positif [(+)-NLE]; si l'hétérochiral est plus actif ee_P diminue et mène à un NLE négatif [(-)-NLE]. L'amplification ou diminution de ee_P est renforcée si l'équilibre entre les différents dimères est déplacé vers le dimère hétérochiral. Noyori a développé par la suite un modèle adapté au DAIB qui est plus complexe puisqu'il fait intervenir plus d'équilibres. Ici, les dimères sont inactifs, ce sont des complexes monomériques qui catalysent. Le ratio entre complexes R et S va déterminer ee_P et donc la présence ou non d'un NLE ; il dépend des constantes de dissociation des dimères respectifs, des constantes d'association avec le substrat et le réactif ainsi que de leurs concentrations respectives.

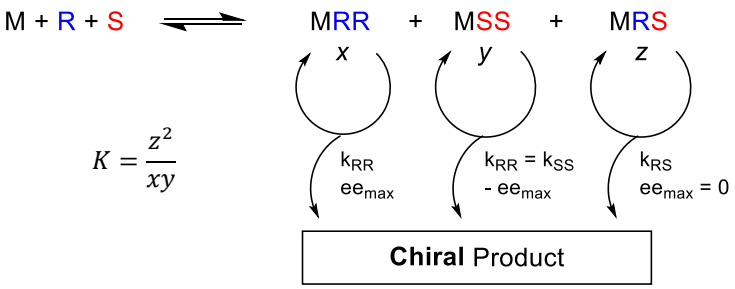

Figure 143: Schéma général pour la catalyse énantiosélective suivant le modèle ML_2. x, y et z représentent les concentrations respectives de MRR, MSS et MRS.

Ce sujet a reçu beaucoup d'attention puisque ce genre d' « amplification chirale » est présumée de jouer un rôle majeur dans l'émergence de l'homochiralité biologique et donc de la vie elle-même. Les NLE ont également été beaucoup utilisé comme outil mécanistique afin de vérifier l'agrégation de catalyseurs.

Pour ce travail, nous nous sommes penchés sur l'addition de dialkylzincs au benzaldéhyde catalysée par des ligands dérivés de l'éphédrine. Ce dernier est un aminoalcool bon marché qui est censé agir de la même façon que le DAIB, nous nous sommes donc posé la question s'il génère également des NLE en catalyse asymétrique. Des ligands éphédrine *N*-monoalkylées ont montré une relation strictement linéaire entre ee_P et le ee du ligand (ee_L), par contre la version benzylée, la *N*-benzyléphédrine (NBE) montre non seulement un NLE très marqué mais particulier : c'est un NLE hyperpositif (Figure 144). En partant d'un ligand énantiopur et diminuant son ee_L, ee_P ne diminue pas et ne reste pas constant, mais augmente – de 76 à 81% ee_P avec $ZnEt_2$, de 16 à 53% ee_P avec $ZnMe_2$. Le ligand scalémique est donc un meilleur catalyseur que le ligand énantiopur, dans le sens qu'il est plus énantiosélectif. Ce genre de comportement n'a, à ce jour, jamais été observé, mais étudié de façon théorique par Henri Kagan. En utilisant son système ML_3 (qui diffère du ML_2 par l'agrégation du complexe en trimères, non en dimères) il a pu prédire des courbes de NLE qui sont hyperpositives. Par contre, elles ne peuvent qu'être hyperpositives que de la moitié supérieure de l'axe ee_L, ce qui diffère de nos propres courbes ; l'effet hyperpositif du NBE doit donc suivre un autre mécanisme que le ML_3 de Kagan. Le but de ce travail va être de mettre en évidence ce mécanisme.

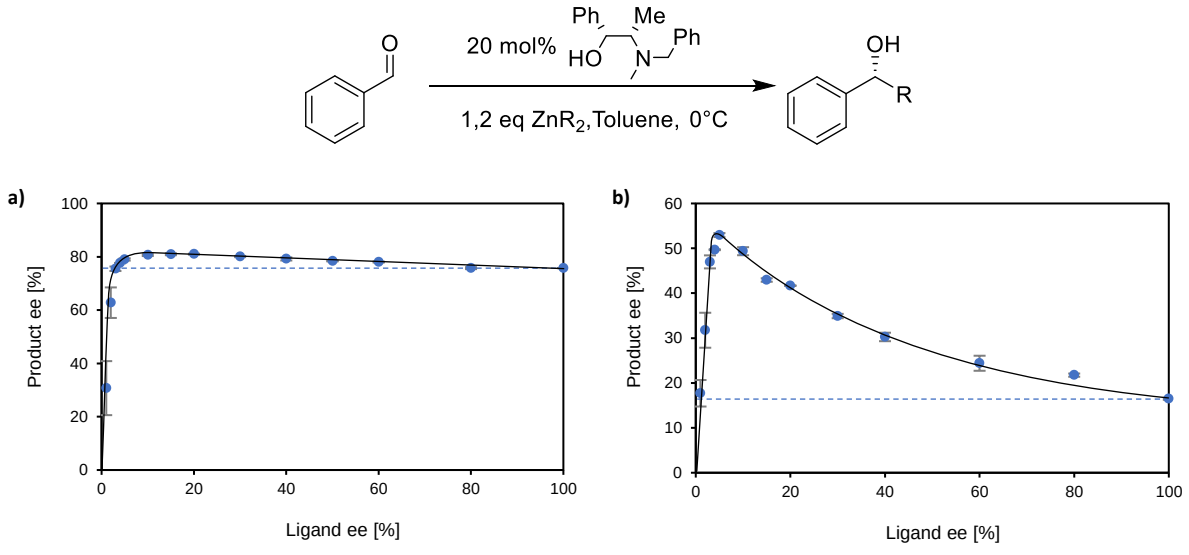

Figure 144: Effet non-linéaire hyperpositif observé dans l'addition énantiosélective de a) $ZnEt_2$, b) $ZnMe_2$ au benzaldéhyde catalysée par (-)-NBE.

Une observation que nous avons faite lors de la catalyse avec NBE est qu'un précipité blanc apparait dès qu'on ajoute le dialkylzinc au ligand, mais uniquement si le ligand est scalémique – avec du NBE énantiopur la solution reste limpide. Ceci indique la présence d'un agrégat hétérochiral insoluble qui précipite ; en effet, filtration et hydrolyse du précipité résulte en l'obtention de NBE sous forme racémique (vérifié par polarimétrie). Ceci implique qu'à bas ee_L, la concentration effective de catalyseur est faible puisque la majorité précipite sous forme racémique. Nous avons donc étudié l'évolution de ee_P en variant la charge catalytique du ligand, cette fois uniquement énantiopur (Figure 145a). En effet, ee_P augmente plus la charge en catalyseur est basse ; une conversion de l'axe « charge catalytique » en « ee_L simulé » (on considère qu'un résultat à 10 mol% de ligand énantiopur est équivalent à 20 mol%, mais à 50% ee_L où la moitié du catalyseur précipite) permet de superposer le screening de charge catalytique avec le NLE hyperpositif (Figure 145b). Les deux courbes concordent quasi parfaitement, l'hyperpositivité du NLE semble donc être lié à la concentration effective de catalyseur.

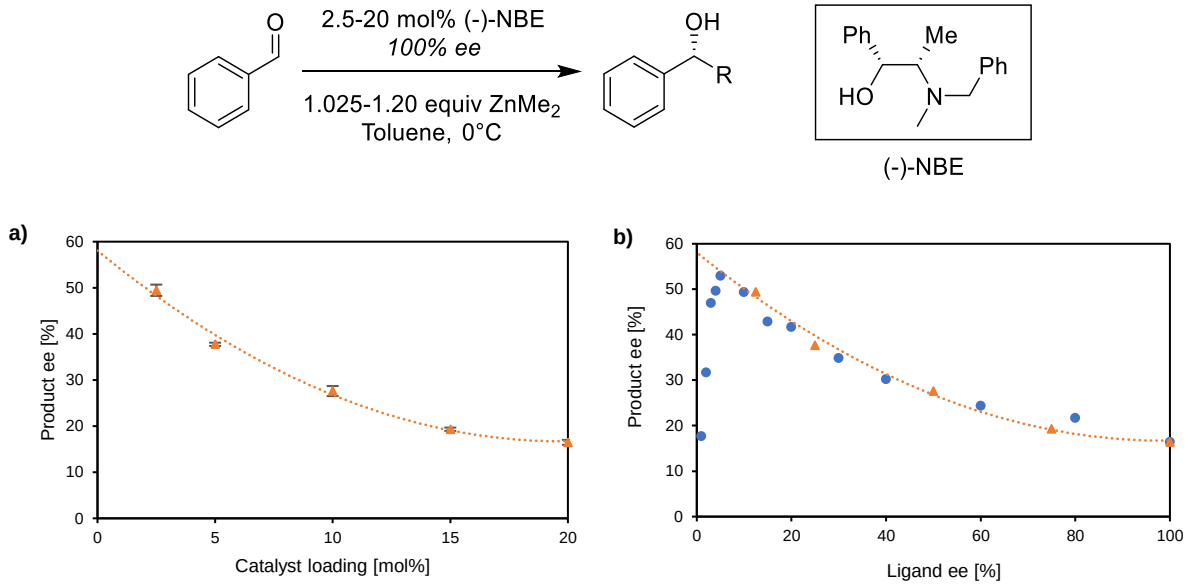

Figure 145: a) ee_P en fonction de la charge en catalyseur dans l'addition énantiosélective de $ZnMe_2$ au benzaldéhyde catalysée par (-)-NBE, b) superposition de a) avec l'effet non-linéaire hyperpositif.

Suite à ces observations, nous avons émis l'hypothèse d'un système catalytique où deux complexes de zinc issus du NBE catalysent : le complexe discret NBE-ZnMe et son dimère homochiral, tandis que le dimère hétérochiral précipite et ne participe pas à la réaction. Les monomère et le dimère homochiral donnent des ee_P différents, le dimère étant moins énantiosélectif que le monomère, ce qui expliquerait la dépendance envers la charge catalytique : plus la concentration en catalyseur est grande (ce qui est équivalent à un haut ee_L), plus l'équilibre monomère-dimère est déplacé vers le dimère, plus ee_P est bas ; à basse concentration les dimères se dissocient en monomères qui sont plus énantiosélectifs et ee_P augmente.

Cette hypothèse a été vérifiée par plusieurs études : l'augmentation de la température de réaction, en utilisant $ZnMe_2$ comme dialkylzinc, mène à une augmentation de ee_P (Figure 146). Ceci est contraire à toute attente puisque l'énantiosélectivité d'une réaction diminue à température croissante, mais concorde avec notre hypothèse puisque les aggrégats se dissocient à haute

température. Une plus grande proportion de monomères plus énantiosélectifs à haute température doit en effet mener à une augmentation de ee_P.

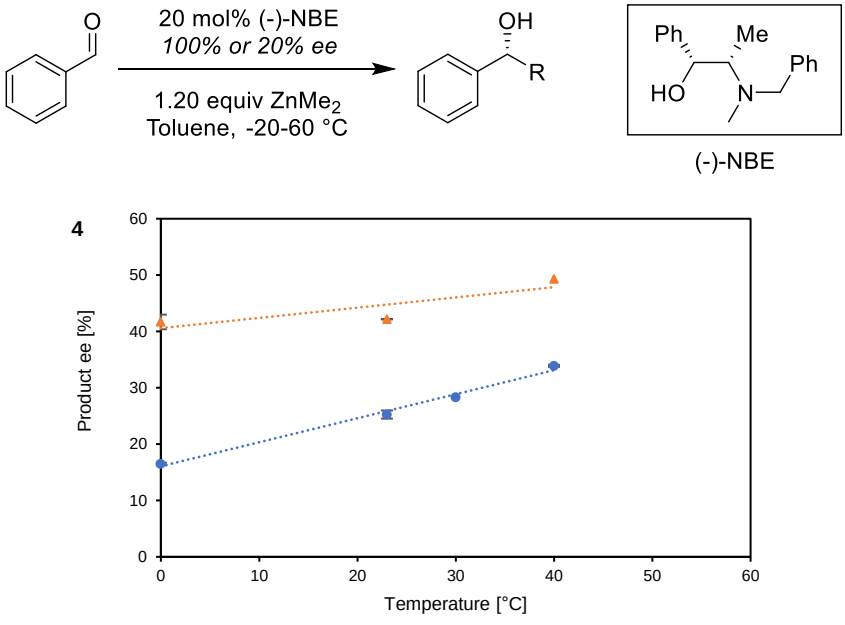

Figure 146: Étude de l'effet de la température sur ee_P dans l'addition énantiosélective de $ZnMe_2$ au benzaldéhyde catalysée par (-)-NBE.

Le monomère et le dimère homochiral ont été observé en spectrométrie de masse ; des études en RMN ^{1}H DOSY ont mis en évidence l'agrégation du complexe NBE-ZnMe en solution à des températures de -20 à 60 °C, dans les mêmes conditions que pour les réactions catalytiques, en présence de $ZnMe_2$ et en présence ou absence de benzaldéhyde (Figure 147a). La masse moléculaire moyenne (les échanges entre les différents complexes sont trop rapides pour pouvoir les distinguer à l'échelle de temps de la RMN) est plus haute que la masse du NBE-ZnMe seul à toute température, mais diminue plus la température est haute : ceci confirme la dissociation de dimères observé en catalyse plus tôt. En plus, des molécules ont été synthétisé qui miment la forme du NBE-ZnMe (notamment le squelette éphédrine et le cycle à 5 génération par la chélation du zinc) mais sans pouvoir s'agréger par coordination vu qu'elles sont purement organiques. Elles nous ont permis de valider la méthodologie que nous utilisons pour relier les résultats de la DOSY avec le poids moléculaire (Figure 147b).

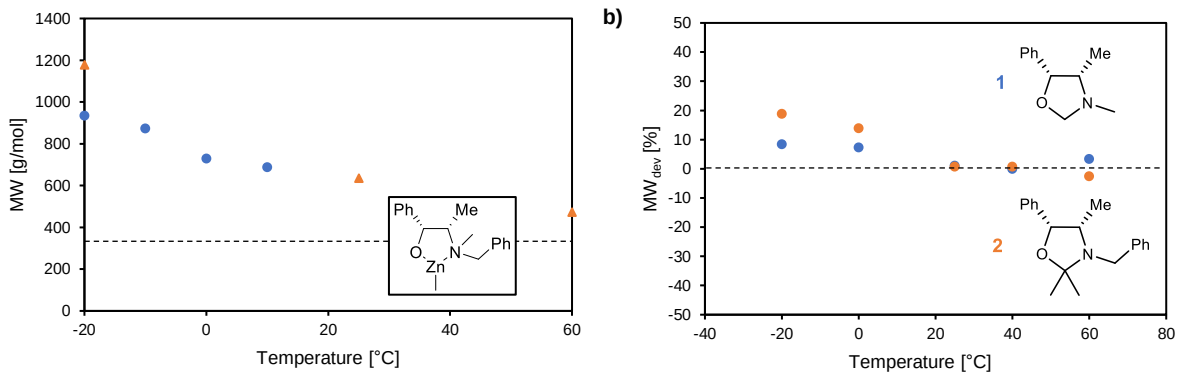

Figure 147: a) Masse moléculaire moyenne (MW) de (-)-NBE-ZnMe en fonction de la température obtenue de RMN ^{1}H DOSY, en présence uniquement de 5 équivalents de $ZnMe_2$ (triangles oranges) ou en plus avec 5 équivalents de benzaldéhyde

*(points bleus) ; la ligne en tirets indique le poids moléculaire de (-)-NBE-ZnMe monomérique, b) déviation du poids moléculaire attendu (MW_{dev}) des molécules **1** et **2** en RMN DOSY ^1H, qui est négligeable en dehors de température en dessous de ta.*

Finalement, nous avons fait des études cinétiques du système catalytique. L'ordre partiel en catalyseur est un bon indicateur pour l'agrégation de celui-ci : en général, cet ordre partiel est un paramètre constant mais qui peut varier avec la concentration en catalyseur si celui-ci s'agrège. Dans le cas d'un monomère actif et d'un dimère inactif, où une seule molécule du monomère participe à l'étape limitante de la catalyse, l'ordre est proche de 1 à basse concentration de catalyseur mais baisse et converge ver 0,5 à haute concentration ; ceci compense mathématiquement le fait que la concentration effective diminue à cause de la dimérisation. Nous avons donc fait des réactions catalytiques à diverses charges en catalyseur en suivant l'avancement de la réaction in situ par spectroscopie infrarouge. Les profils cinétiques obtenus ainsi ont été analysé par VTNA (Visual Time-Normalised Analysis) afin d'obtenir de manière l'ordre en catalyseur. La VTNA consiste à faire une transformation mathématique de l'axe du temps des profils cinétiques en une axe du temps normalisée au catalyseur. Ceci fait que, si le seul paramètre varié est la concentration en catalyseur, toutes les courbes se superposent à condition de choisir le bon ordre partiel. Ainsi, on peut obtenir l'ordre partiel de façon visuelle.

L'analyse par VTNA de tous les profils cinétiques n'a pas donné de résultats concluants : les courbes ne se superposent pas toutes à la fois, à aucun ordre en catalyseur. Ceci indique qu'en effet, l'ordre change avec la concentration en catalyseur. Nous avons donc procédé à une analyse segmentée ou uniquement deux profils adjacents ont été analysé à la fois. Le résultat (Figure 148) donne un graphe ordre partiel en catalyseur vs. charge en catalyseur atypique : l'ordre est de 1 à faible charge, diminue vers environ 0,4 à charge moyenne, puis augmente à nouveau à haute charge en catalyseur. Nous ne connaissons pas de précédent pour ce genre de comportement dans la littérature. Par contre, ce comportement atypique peut être expliqué par notre hypothèse : si nous considérons qu'à basse charge nous n'avons que du monomère et à haute charge que du dimère qui catalyse, et que les deux suivent un mécanisme réactionnel similaire (un seul complexe réagit avec un substrat et un réactif pour donner le produit final), alors nous nous attendons à un ordre partiel en catalyseur de 1 à haute et à basse charge, ce qui concorde avec nos observations. À charge catalytique intermédiaire, les deux catalyseurs sont présents : l'ajout de ligand n'augmente pas la vitesse de la réaction de façon proportionnelle puisqu'une partie du complexe résultant dimérise. Cette augmentation non linéaire de la vitesse résulte nécessairement en un ordre partiel en catalyseur différent de 1, ce qui correspond à ce que nous observons. Une étude théorique du système cinétique montre qu'en effet, la constante cinétique observée k_{obs} (qui est constituée des constantes cinétiques respectives du dimère et du monomère et d'un facteur décrivant leur ratio par rapport à la quantité de ligand total) varie à charge catalytique intermédiaire.

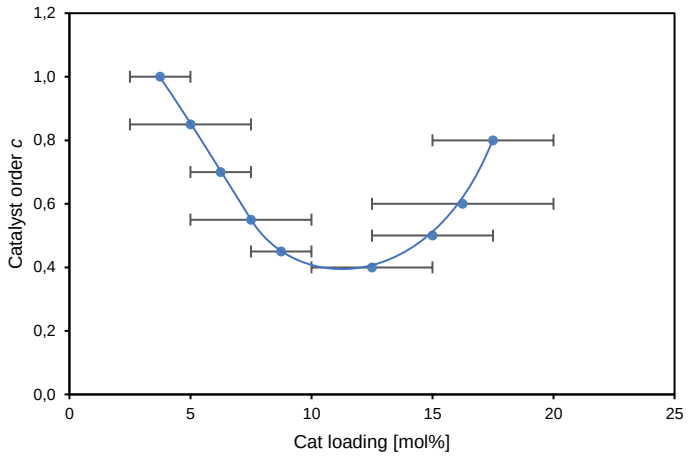

Figure 148: Ordre partiel en catalyseur c en fonction de la charge en catalyseur. Les barres horizontales indiquent la charge en catalyseur deux profils cinétiques qui ont été utilisé pour obtenir c.

Une autre étude cinétique, dans laquelle nous avons étudié ee_P en fonction du temps, montre en plus que le ratio monomère/dimère n'est pas constant durant la réaction (Figure 149). Plus la charge en catalyseur est basse, plus la réaction commence avec un ee_P haut, mais dans tout les cas ee_P augmente au fur et à mesure de l'avancement de la réaction. Ceci montre que le ratio monomère/dimère augmente au fur et à mesure du temps vu que le monomère est le catalyseur le plus énantiosélectif. La raison pour ce changement n'est pas totalement claire mais résulte probablement d'une interférence du produit de la réaction, qui influence l'équilibre monomère-dimère et la concentration en complexes libres.

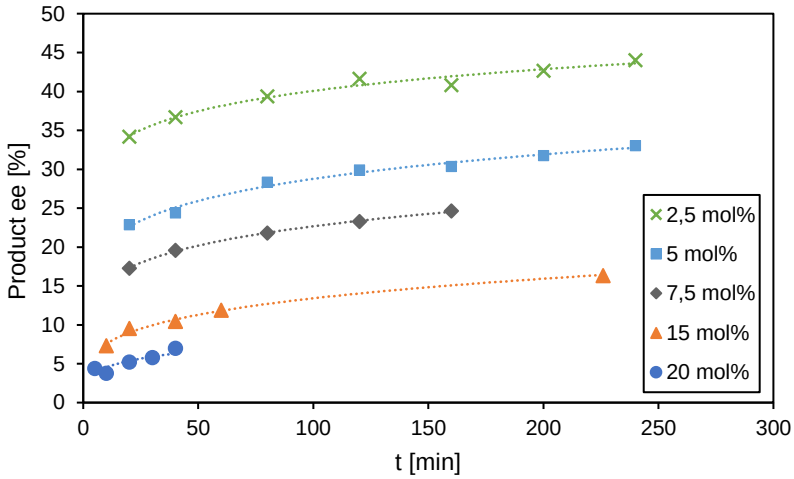

Figure 149: Évolution de ee_P en fonction du temps de réaction, à différentes charges en catalyseur.

Toutes ces études confirment l'hypothèse formulée initialement pour expliquer le NLE hyperpositif, nous pouvons donc conclure que nous avons bien un système catalytique où deux catalyseurs qui sont reliés par un équilibre monomère-dimère, catalysent l'addition de dialkylzincs au benzaldéhyde. Ces deux catalyseurs donnent le même produit mais avec un ee_P différent, ce qui cause avec la précipitation du dimère hétérochiral l'apparition d'un effet non-linéaire hyperpositif.

En plus, nous avons fait des études additionnelles pour obtenir plus d'information sur le système catalytique. Nous avons varié le substrat en utilisant des benzaldéhydes *para*-substitués. Globalement, le NLE hyperpositif diminue et devient même un (+)-NLE simple en présence de substituants très donneurs ou très attracteurs. Nous avons utilisé ces substrats pour construire des plots de Hammett, où il s'est avéré que, pour quantifier le pouvoir donneur/attracteur des substituants en *para*, l'échelle σ^+ donne la meilleure corrélation entre les différents résultats de catalyse. Ceci diffère du DAIB qui marche mieux avec l'échelle σ et ceci pourrait donc être symptomatique du système à deux catalyseurs monomère et dimère ; par contre le système du NBE corrèle mieux avec l'échelle σ si on omet les substrats encombrants (tBu, OPh, OiPr), il pourrait donc y avoir aussi un biais par de la gène stérique. Cette étude nécessite plus de travaux, notamment des plots de Hammett faits à basse charge en catalyseur afin de pouvoir mieux discerner l'impact du système à deux catalyseurs sur ce genre de corrélation.

En revanche, l'étude de substrats substitués en *ortho* a montré que le catalyseur dimérique est probablement sensible aux effets stériques autour du centre réactionnel : le *ortho,para,ortho'*-triméthylbenzaldéhyde donne un ee_P anormalement haut avec le ligand énantiopur, qui n'augmente que très peu puis même baisse avec un ee_L décroissant. Ceci indique que le catalyseur dimérique, qui est moins sélectif, ne joue qu'un rôle minoritaire dans la conversion du substrat et que le déplacement de l'équilibre du dimère vers le monomère n'a donc que peu d'influence sur le résultat de la réaction.

L'étude de variantes du NBE, où le groupement *N*-benzyle porte un méthyle ou bromure en *para*, ou bien est remplacé par un 2-naphtylméthylène, n'a pas donné de résultats significativement différents par rapport au NBE. Par contre, la N-méthyléphédrine (NME) montre une augmentation de ee_P avec une charge en catalyseur décroissante similaire au NBE. Bien que le NME ne montre pas de NLE du tout (ce qui est probablement dû à l'absence de précipité hétérochiral), il semble être constitué du même système à deux catalyseurs monomère-dimère ; le NBE n'est donc pas un cas unique.

Finalement, nous avons fait aussi des études théoriques où nous avons appliqué le « modèle réservoir » de Henry Kagan au NLE hyperpositif du NBE. Ceci nous a permis d'obtenir le paramètre α, qui prend en compte la proportion de catalyseur inactif, et d'en déduire la constante K_S' qui contient la constante de solubilité du dimère hétérochiral et sa constante d'association à partir de NBE-ZnMe monomérique. Nous avons également varié la charge catalytique et la température de réaction afin de trouver les conditions dans lesquelles uniquement le monomère est présent ; des plots de Eyring nous ont alors permis de trouver l'énantiosélectivité du monomère seul à 0 °C en utilisant $ZnEt_2$. La forme des plots de Eyring, qui laisse deviner une double courbure en forme de vague, est corrélée au système à deux catalyseurs monomère-dimère ; ceci a pu être démontré par une prédiction mathématique des courbes de Eyring.

VI.2 Chapitre II

La deuxième partie de cette thèse de doctorat traite toujours sur les NLE en catalyse asymétrique, mais en utilisant un autre type de ligand : des ligands ditopiques qui, après coordination à un métal, sont capables de former des métallopolymères. Les métallopolymères ont des applications diverses en tant que matériaux, surtout par les propriétés qu'apporte le métal à la chaîne polymérique (magnétisme, luminescence, conductivité électrique, changement d'état redox…). Notre groupe a

également utilisé des métallopolymères en catalyse asymétrique (avec un ligand ditopique chiral) en profitant des propriétés dynamiques du métallopolymère : la labilité de la liaison ligand-métal fait que le polymère peut être dissocié en espèces oligomériques ou discrètes, qui sont solubles et qui catalysent la réaction énantioselective, puis à nouveau réassocié par précipitation dans un contre-solvent pour pouvoir être filtré et réutilisé.

Certains de ces métallopolymères ce sont avérés avoir un NLE. Le cas d'un ligand ditopique à base de diaminocyclohexane chiral est particulièrement curieux car son homologue monotopique et donc non-polymérique ne présente pas de NLE, alors que la structure des sites chélatants est quasi identique dans les deux ligands. Ceci laisse penser que la structure polymérique en elle-même est responsable de l'émergence du NLE et nous a poussé à étudier ce phénomène plus en détail.

Dans un premier temps, nous avons voulu faire une version ditopique d'un ligand possédant déjà un NLE marqué, dans l'idée que la structure polymérique de la version ditopique amplifie d'avantage le NLE déjà présent. Nous avons choisi le DAIB qui possède un (+)-NLE puissant et synthétisé le ligand ditopique **9** en 5 étapes à partir de camphre. Ce ligand **9** a ensuite été appliqué dans l'addition énantiosélective du $ZnEt_2$ au benzaldéhyde (Figure 150). Le ligand s'est avéré avoir un (+)-NLE marqué, mais moins intense que celui du DAIB monotopique ; une variation des conditions (solvant, charge catalytique) n'a pas amené d'amélioration des résultats. Il semble que la fonctionnalisation sur l'azote pour relier les deux entités DAIB est trop proche du site chélatant et diminue la stabilité des associations hétérochirales, ce qui mène a une diminution du (+)-NLE. Des ligands ditopiques alternatifs avec une fonctionnalisation sur le squelette carboné du DAIB ont été conçu et des possibles voies de synthèse ont été discutées.

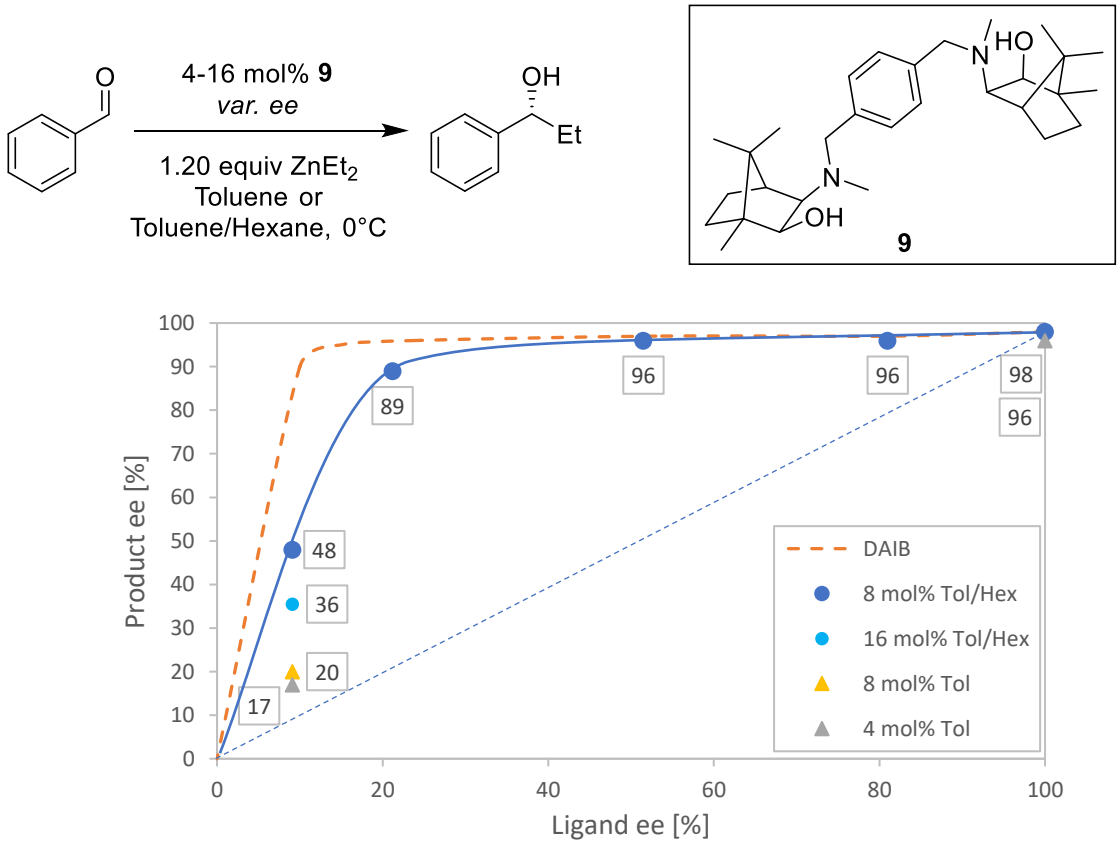

*Figure 150: Effet non-linéaire dans l'addition énantiosélective de $ZnEt_2$ au benzaldéhyde catalysée par le ligand ditopique **9** (points bleus), effet non-linéaire de la même réaction catalysée par le ligand monotopique DAIB (tirets oranges).*

Par la suite, nous nous sommes penchés sur des ligands ditopiques à base d'éphédrine, non plus dans l'idée d'amplifier des NLE déjà existants mais d'étudier l'effet de la structure polymérique sur l'émergence de NLE. Deux ligands ditopiques ont été obtenu par une simple addition de deux équivalents d'éphédrine sur un équivalent d'un double électrophile. Le ligand **15** avec une chaîne alkyle comme liaison entre les deux sites chélatant ne montre pas de NLE, tandis que le ligand **16** avec un lien aromatique possède un (+)-NLE (Figure 151). Étonnamment, ce (+)-NLE est amplifié si on augmente la température de réaction de -20 à 40 °C, ce qui est contre-intuitif puisque les agrégats causant le NLE devraient plutôt se dissocier à haute température et diminuer l'amplitude du NLE. Une explication possible serait une grande différence de sensibilité à la température des constantes d'association homo- et hétérochirales (grande différence de leur ΔG respectifs). Si la constante d'association homochirale diminue plus que l'hétérochirale à température croissante, l'agrégation hétérochirale prend une ampleur de plus en plus grande et intensifie le (+)-NLE. Ceci peut provenir des agrégats hétérochiraux qui forment une superstructure (conformation de la chaîne polymérique, interactions entre chaînes) plus stable que leurs équivalents homochiraux. Le lien aromatique joue probablement un rôle par sa rigidité accrue comparée à la chaîne alkyle dans le ligand **15** : un lien trop flexible empêche la formation de superstructures bien définies, ce qui pourrait expliquer l'absence de NLE avec le ligand **15** ; il est également possible qu'il ne forme pas d'agrégats mais plutôt des macrocycles en interagissant avec lui-même, ce qui empêche la génération de NLE.

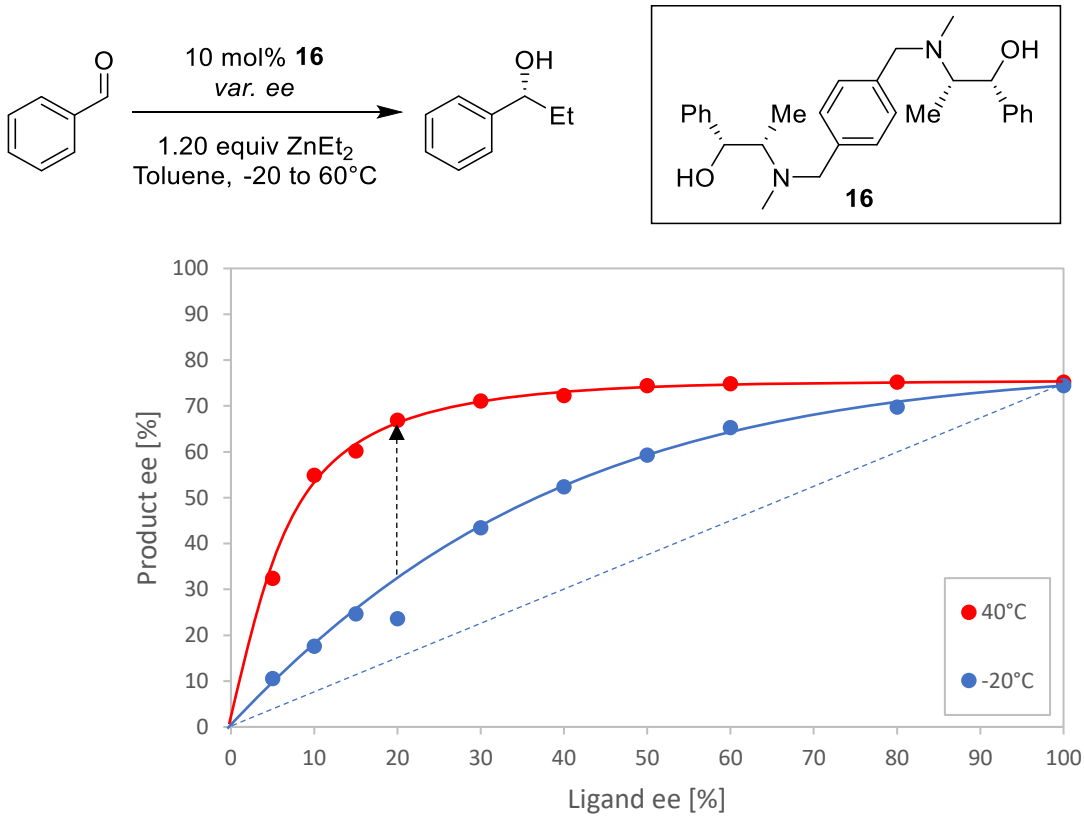

*Figure 151: Effet non-linéaire dans l'addition énantiosélective de $ZnEt_2$ au benzaldéhyde catalysée par le ligand ditopique **16**, à -20 (points bleus) et +40 °C (points rouges).*

Une variation de la charge catalytique montre qu'avec un ligand **16** énantiopur, ee_P augmente avec une charge catalytique décroissante de la même façon que NBE (Figure 152). Ceci indique qu'il y a apparemment le même phénomène de double catalyse qu'avec NBE, avec des bouts de chaînes qui catalysent avec un haut ee_P et des milieux de chaîne (équivalent au catalyseur dimérique homochiral

avec NBE) qui catalysent avec un ee_P plus bas. Plus la charge catalytique et basse, plus le polymère se dissocie et le nombre de bouts de chaîne augmente. Avec un ligand **16** scalémique, ee_P diminue avec une charge catalytique décroissante, ce qui est un phénomène usuel en NLE : plus la concentration en catalyseur est faible, moins on forme les agrégats responsables du NLE.

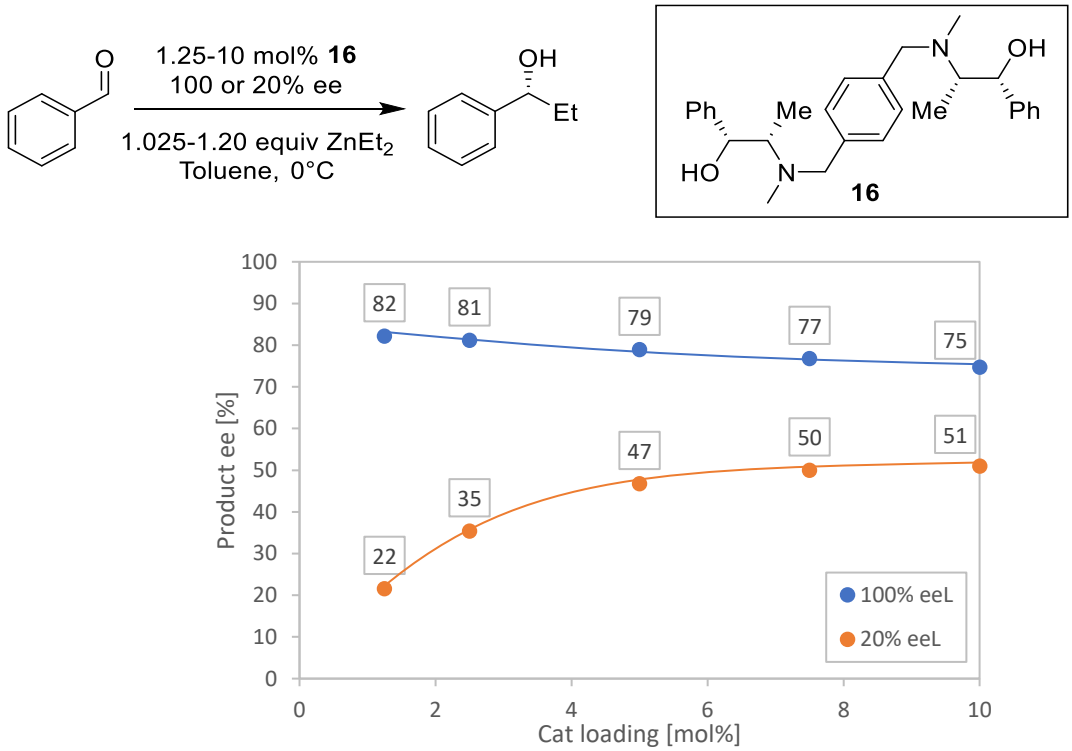

Figure 152: Variation de la charge en catalyseur dans l'addition énantiosélective de ZnEt2 au benzaldéhyde catalysée par 16 à 100% ee_L (points bleus) et 20% ee_L (points oranges).

VI.3 Chapitre III

Ce chapitre traite à nouveau de métallopolymères chiraux mais dans un contexte très différent. Ils sont utilisés non comme catalyseurs mais comme matériaux, en génération de somme de fréquences (SFG) chirale. La SFG chirale est un phénomène d'optique non-linéaire, dans lequel un matériau (dans notre cas un métallopolymère chiral) est irradié par deux lasers à deux longueurs d'onde différentes (900 et 450 nm, Figure 153). Les lasers interagissent avec le matériau et génèrent une nouvelle radiation (300 nm) qui a l'énergie additionné des deux lasers incidents. Ce phénomène n'est possible que si le matériau est chiral, s'il absorbe à la longueur d'onde sortante (300 nm dans notre cas) et s'il est isotrope. Cette dernière condition est la raison pour laquelle nous travaillons avec des métallopolymères : ils ne sont généralement pas cristallins mais amorphes et donc isotropes. Des molécules discrètes comme le BINOL doivent être encapsulées dans un sol-gel de silice pour empêcher leur cristallisation et pouvoir les appliquer en SFG.

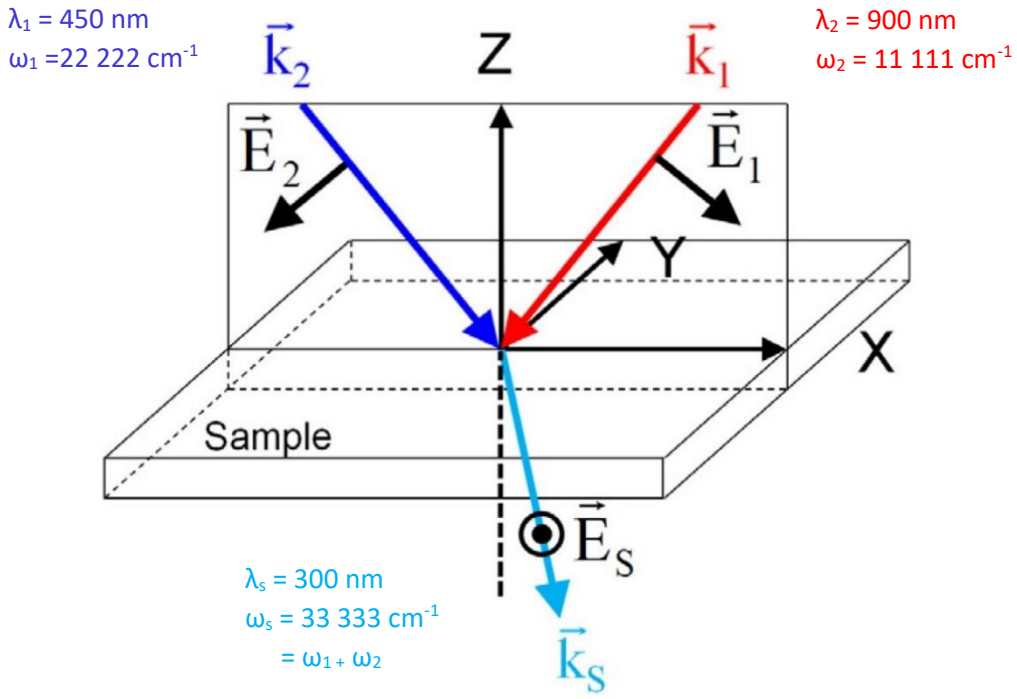

Figure 153: Schéma pour la génération de somme de fréquences (SFG) chirale dans un milieu isotrope.

Notre groupe a travaillé auparavant sur un métallopolymère chiral à base de d'une bisoxazoline ditopique, où les deux unités bisox sont reliées par un aromatique conjugué en *para* avec deux doubles liaisons carbone-carbone, qui joue le rôle de chromophore absorbant vers 300 nm. Le ligand forme des métallopolymères avec des ions Ni(II), Cu(II) et Zn(II) qui génèrent tous un signal SFG à 300 nm ; le ligand seul est inactif en SFG.

Le but de ces travaux est de synthétiser et d'appliquer en SFG de nouveau métallopolymères chiraux. Pour ceci, nous avons conçu des ligands ditopiques avec un lien aromatique doublement conjugué avec deux imines, de façon similaire que dans le ligand ditopique bisoxazoline. Une série de ligands a été obtenue par condensation de deux équivalents d'aminoalcools chiraux sur un équivalent de terephtaldéhyde ; une diamine dissymétrique à base de *trans*-diaminocyclohexane a également été utilisée (Figure 154). Les ligands ont été ensuite coordiné sur des sels de métaux à contre-ions peu coordinants ($Cu(OTf)_2$, $Zn(OTf)_2$, $CuPF_6$) pour former des complexes.

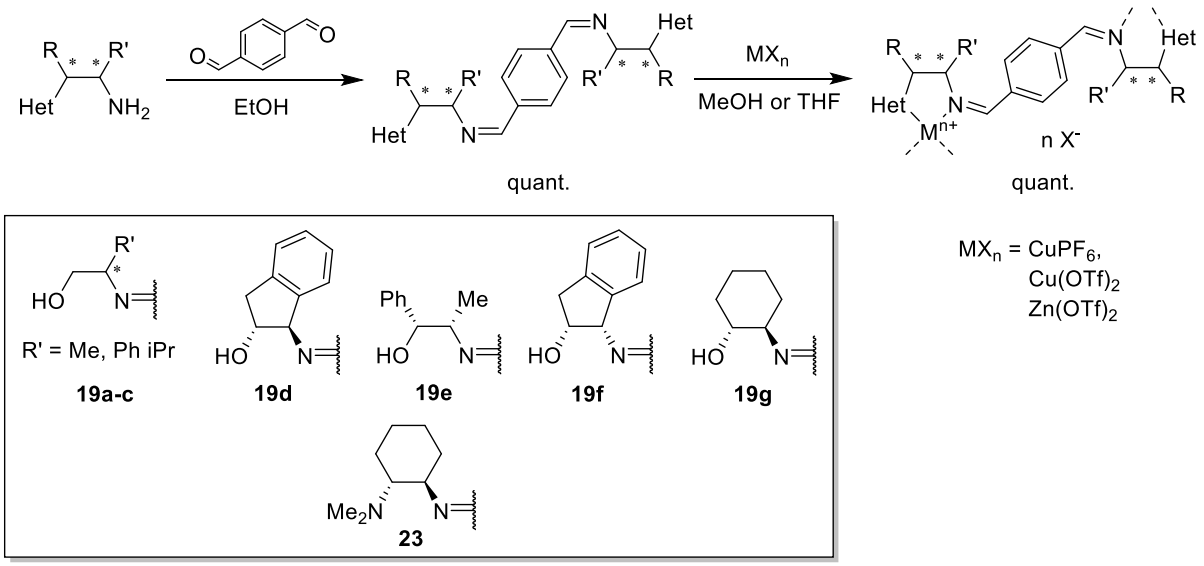

Figure 154: Schéma réactionnel pour la synthèse de ligands ditopiques bis-imine et de leurs complexes respectifs.

Les complexes à base de métaux +II se sont avéré être très sensible à l'hydrolyse ; les complexes au Cu(I) le sont moins mais sont en revanche sensible à l'oxydation. Les complexes n'existent pas tous non plus sous forme de métallopolymère : tandis que les complexes au Cu(I) forment tous des métallopolymères, uniquement le ligand **23** à base de diaminocyclohexane en forme aussi avec le Cu(II) et le Zn(II) ; une exception est le ligand **19f** à base de cis-2-aminoindanol qui forme un métallopolymère avec le Cu(II). Tous les autres complexes sont soit des complexes discrets mononucléaires, ce qui est visible en spectroscopie infrarouge par la présence de bande imine distinctes ; les métallopolymères ne possèdent qu'une seule bande en IR puisque les imines y sont toutes équivalentes. En revanche, tous les complexes absorbent proche de 300 nm en spectroscopie UV-visible. La bande π-π* du lien aromatique doublement conjugué est autour de 277 nm pour la plupart des ligands et est déplacée d'environ 10 nm vers le bleu dans les complexes.

Certains de ces complexes ont été ensuite appliqué en spectroscopie SFG. Les échantillons de métallopolymères sont préparés par dépôt et évaporation à l'air libre d'une goutte d'une solution du complexe étudié sur une plaque en verre, qui est ensuite inséré dans le dispositif de microscopie SFG. Faute de temps et de ressources nous n'avons pu étudier que deux complexes en détail : **23-Cu(OTf)$_2$** et **19f-CuPF$_6$** (Figure 155). **23-Cu(OTf)$_2$** génère bien un signal à 300 nm, et ce en un temps d'acquisition d'uniquement 10 secondes – les complexes à base de bisoxazoline ditopique prennent 10 fois plus temps à générer un signal d'intensité comparable. Par contre, il génère un signal en deux modes différent, SPP (rouge) et PPP (bleu). Ce dernier est un signal parasite non désiré qui indique que la SFG observée peut être d'origine achirale. Nous suspectons des produits d'hydrolyse d'être à l'origine de ceci : le complexe est sensible à l'humidité et l'échantillon a été préparé à l'air libre ; un changement de couleur du violet vers le brun lors du dépôt de l'échantillon pourrait être symptomatique de ceci. **19f-CuPF$_6$** connait le même problème, il génère même un signal PPP négatif qui n'a pas de sens scientifique, mais qui pourrait être originaire d'un signal PPP croissant durant l'acquisition, dû à une décomposition du complexe pendant ce même laps de temps.

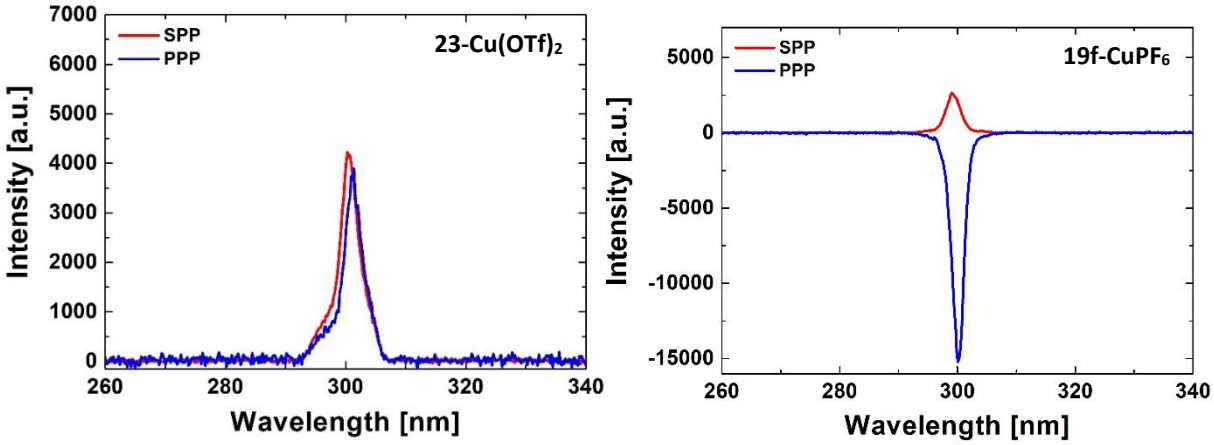

*Figure 155: Spectres SFG des complexes **23-Cu(OTf)$_2$** et **19f-CuPF$_6$**.*

Ces résultats nous ont mené à poursuivre ce projet en développant de nouveaux complexes plus stables envers l'hydrolyse, afin de contrer les problèmes rencontrés jusqu'à présent. Le ligand ditopique **26** possède la même structure aromatique bis-conjuguée en guise de lien entre les deux sites chélatant, par contre les imines sont stabilisées par un 2nd groupe aromatique qui sert support aux deux azotes chélatant. Les groupements chiraux sont maintenant attachés aux azotes périphériques (qui ne font pas partie du chromophore bis-imine). La synthèse a été effectuée en trois étapes simples, sans purifications et avec de bons rendements (Figure 156). L'intermédiaire **25** s'est avéré être très sensible au dioxygène et cause **26** à n'avoir qu'une pureté modérée, que nous n'avons pas pu améliorer à ce jour, mais qui suffit pour des études préliminaires. Les complexes métalliques de **26** se sont avérés être parfaitement stable à l'hydrolyse : la complexation a pu être faite dans du THF technique non séché et nous avons pu utiliser un précurseur de Ni(II) hydraté, ce qui était impossible avec les ligands précédents.

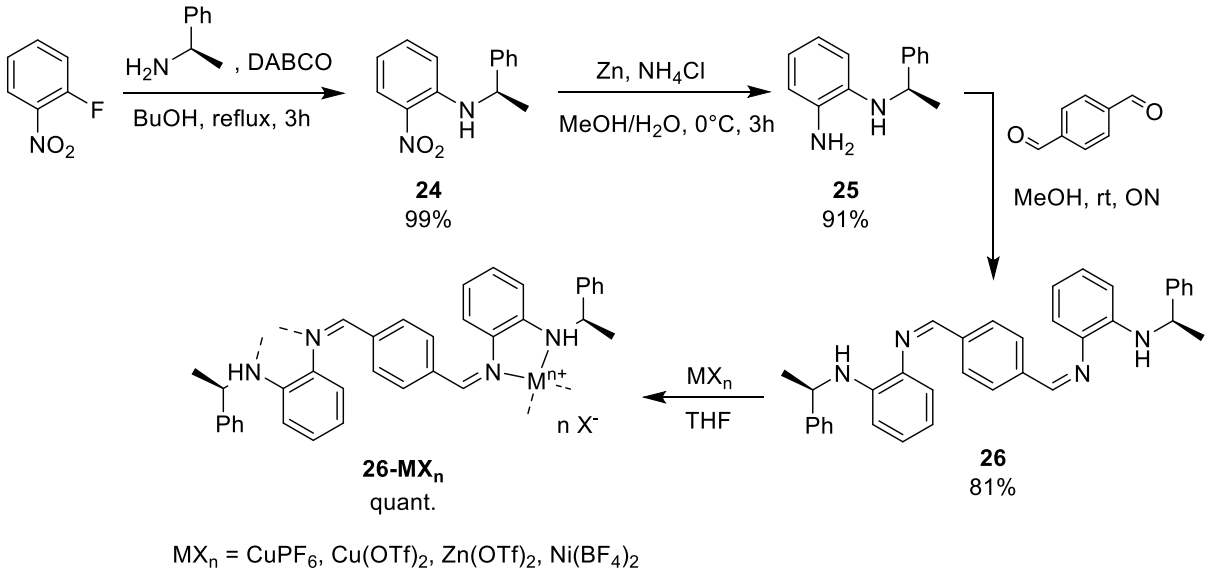

*Figure 156: Schéma réactionnel pour la synthèse du ligand ditopique **26** et de ses complexes respectifs.*

Les complexes du ligand **26** forment tous des métallopolymère à l'état solide et absorbent vers 300 nm. Malheureusement nous n'avons pas pu les appliquer en SFG, en revanche nous avons pu faire des études spectroscopiques qui nous ont donné des informations structurales sur le ligand et les complexes. Le ligand 26 possède, en plus de sa bande UV, une bande centrée autour de 446 nm en spectroscopie UV-visible. Cette bande est inexistante dans les autres ligands et dans les complexes du ligand **26**. Elle provient probablement d'une conjugaison englobant le lien bis-imine et en plus les aromatiques qui y sont attachés, le ligand libre doit donc être plan (Figure 157). Ceci a été confirmé par comparaison avec une molécule similaire comportant une bis-imine attaché à deux aromatiques et par des calculs DFT. La bande en question est sujette à un solvatochromisme négatif, que nous avons pu quantifier par une analyse de Kamlet-Taft, qui provient selon ces calculs DFT d'une réduction du moment quadrupolaire de la molécule. On peut lui associer deux pôles positifs sur le lien, correspondant aux imines pauvres en électrons, et un pôle négatif sur chaque aromatique périphérique, riches en électrons. Lors de l'excitation par absorption de lumière de la densité électronique est transférée des pôles – vers les pôles +, causant le solvatochromisme négatif et nécessitant la molécule d'être plane et conjuguée. Lors de la coordination avec le métal la conjugaison entre la bis-imine et les aromatiques périphériques est brisée, probablement parce que le ligand n'est plus plan.

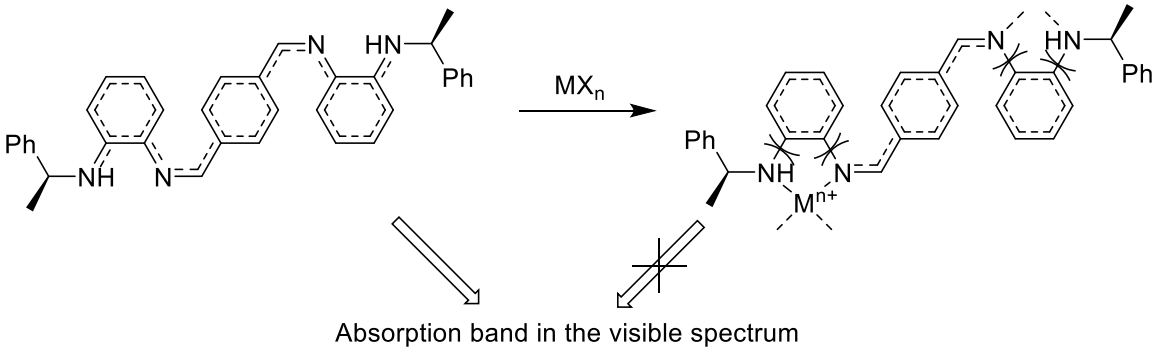

*Figure 157: Schéma montrant la délocalisation du système π sur le ligand **26** libre et le ligand complexé.*

La stabilité des complexes et les particularités UV-vis discutées nous en plus permis de faire un dosage UV-visible du ligand avec le métal. L'addition continuelle d'une solution de $Cu(OTf)_2$ à une solution de **26** suivie par spectroscopie UV-vis montre que le spectre évolue jusqu'à l'addition d'environ 1 équivalent de métal. D'avantage de métal de métal ne change pas le spectre UV-vis de façon significative, ce qui indique que le ratio ligand/métal 1:1 est particulièrement stable et qu'un complexe 1:2 n'est pas formé. Ceci indique que le complexe 1:1 forme un métallopolymère non seulement en phase solide mais aussi en solution.

References

[1] L. D. Barron, *Chem. Soc. Rev.* **1986**, *15*, 189–223.

[2] R. Naaman, Y. Paltiel, D. H. Waldeck, *Nat. Rev. Chem.* **2019**, *3*, 250–260.

[3] C. Train, M. Gruselle, M. Verdaguer, *Chem. Soc. Rev.* **2011**, *40*, 3297–3312.

[4] C. Puchot, O. Samuel, E. Dunach, S. Zhao, C. Agami, H. B. Kagan, *J. Am. Chem. Soc.* **1986**, *108*, 2353–2357.

[5] A. Horeau, J. P. Guetté, *Tetrahedron* **1974**, *30*, 1923–1931.

[6] H. Wynberg, B. Feringa, *Tetrahedron* **1976**, *32*, 2831–2834.

[7] C. Girard, H. B. Kagan, *Angew. Chem. Int. Ed.* **1998**, *37*, 2922–2959.

[8] T. Satyanarayana, S. Abraham, H. B. Kagan, *Angew. Chem. Int. Ed.* **2009**, *48*, 456–494.

[9] R. F. Ismagilov, *J. Org. Chem.* **1998**, *63*, 3772–3774.

[10] D. W. Johnson, D. A. Singleton, *J. Am. Chem. Soc.* **1999**, *121*, 9307–9312.

[11] T. O. Luukas, C. Girard, D. R. Fenwick, H. B. Kagan, *J. Am. Chem. Soc.* **1999**, *121*, 9299–9306.

[12] D. G. Blackmond, *J. Am. Chem. Soc.* **2001**, *123*, 545–553.

[13] M. Zhao, A. O. King, R. D. Larsen, T. R. Verhoeven, P. J. Reider, *Tetrahedron Lett.* **1997**, *38*, 2641–2644.

[14] C. Girard, H. B. Kagan, *Tetrahedron: Asymmetry* **1995**, *6*, 1881–1884.

[15] C. Girard, H. B. Kagan, *Tetrahedron: Asymmetry* **1997**, *8*, 3851–3854.

[16] D. G. Blackmond, *J. Am. Chem. Soc.* **1998**, *120*, 13349–13353.

[17] D. G. Blackmond, *Tetrahedron: Asymmetry* **2010**, *21*, 1630–1634.

[18] W. Langenbeck, G. Triem, *Z. Phys. Chem.* **1936**, *177A*, 401–408.

[19] D. Heller, H.-J. Drexler, C. Fischer, H. Buschmann, W. Baumann, B. Heller, *Angew. Chem. Int. Ed.* **2000**, *39*, 495–499.

[20] D. Guillaneux, S.-H. Zhao, O. Samuel, D. Rainford, H. B. Kagan, *J. Am. Chem. Soc.* **1994**, *116*, 9430–9439.

[21] M. Kitamura, S. Suga, K. Kawai, R. Noyori, *J. Am. Chem. Soc.* **1986**, *108*, 6071–6072.

[22] M. Kitamura, S. Okada, S. Suga, R. Noyori, *J. Am. Chem. Soc.* **1989**, *111*, 4028–4036.

[23] R. Noyori, S. Suga, K. Kawai, S. Okada, M. Kitamura, N. Oguni, M. Hayashi, T. Kaneko, Y. Matsuda, *J. Organomet. Chem.* **1990**, *382*, 19–37.

[24] R. Noyori, M. Kitamura, *Angew. Chem. Int. Ed. Engl.* **1991**, *30*, 49–69.

[25] M. Kitamura, S. Suga, M. Niwa, R. Noyori, Z.-X. Zhai, H. Suga, *J. Phys. Chem.* **1994**, *98*, 12776–12781.

[26] M. Kitamura, S. Suga, M. Niwa, R. Noyori, *J. Am. Chem. Soc.* **1995**, *117*, 4832–4842.

[27] M. Yamakawa, R. Noyori, *J. Am. Chem. Soc.* **1995**, *117*, 6327–6335.

[28] M. Kitamura, M. Yamakawa, H. Oka, S. Suga, R. Noyori, *Chem. Eur. J.* **1996**, *2*, 1173–1181.

[29] M. Kitamura, S. Suga, H. Oka, R. Noyori, *J. Am. Chem. Soc.* **1998**, *120*, 9800–9809.

[30] M. Kitamura, H. Oka, R. Noyori, *Tetrahedron* **1999**, *55*, 3605–3614.

[31] M. Yamakawa, R. Noyori, *Organometallics* **1999**, *18*, 128–133.

[32] R. Noyori, S. Suga, H. Oka, M. Kitamura, *Chem. Record.* **2001**, *1*, 85–100.

[33] Y. K. Chen, A. E. Lurain, P. J. Walsh, *J. Am. Chem. Soc.* **2002**, *124*, 12225–12231.

[34] J. Kang, J. B. Kim, J. W. Kim, D. Lee, *J. Chem. Soc., Perkin Trans. 2* **1997**, 189–194.

[35] Y. K. Chen, A. M. Costa, P. J. Walsh, *J. Am. Chem. Soc.* **2001**, *123*, 5378–5379.

[36] F. Buono, P. J. Walsh, D. G. Blackmond, *J. Am. Chem. Soc.* **2002**, *124*, 13652–13653.

[37] K. Soai, T. Shibata, H. Morioka, K. Choji, *Nature* **1995**, *378*, 767–768.

[38] Y. Saito, H. Hyuga, *Rev. Mod. Phys.* **2013**, *85*, 603–621.

[39] T. Shibata, S. Yonekubo, K. Soai, *Angew. Chem. Int. Ed.* **1999**, *38*, 659–661.

[40] I. Sato, H. Urabe, S. Ishiguro, T. Shibata, K. Soai, *Angew. Chem. Int. Ed.* **2003**, *42*, 315–317.

[41] K. Soai, T. Kawasaki, A. Matsumoto, *Tetrahedron* **2018**, *74*, 1973–1990.

[42] I. Sato, R. Sugie, Y. Matsueda, Y. Furumura, K. Soai, *Angew. Chem. Int. Ed.* **2004**, *43*, 4490–4492.

[43] T. Kawasaki, M. Sato, S. Ishiguro, T. Saito, Y. Morishita, I. Sato, H. Nishino, Y. Inoue, K. Soai, *J. Am. Chem. Soc.* **2005**, *127*, 3274–3275.

[44] K. Soai, S. Osanai, K. Kadowaki, S. Yonekubo, T. Shibata, I. Sato, *J. Am. Chem. Soc.* **1999**, *121*, 11235–11236.

[45] T. Kawasaki, H. Tanaka, T. Tsutsumi, T. Kasahara, I. Sato, K. Soai, *J. Am. Chem. Soc.* **2006**, *128*, 6032–6033.

[46] I. Sato, D. Omiya, T. Saito, K. Soai, *J. Am. Chem. Soc.* **2000**, *122*, 11739–11740.

[47] K. Soai, I. Sato, T. Shibata, S. Komiya, M. Hayashi, Y. Matsueda, H. Imamura, T. Hayase, H. Morioka, H. Tabira, et al., *Tetrahedron: Asymmetry* **2003**, *14*, 185–188.

[48] F. C. Frank, *Biochim. Biophys. Acta* **1953**, *11*, 459–463.

[49] D. G. Blackmond, *J. Am. Chem. Soc.* **1997**, *119*, 12934–12939.

[50] D. G. Blackmond, *Acc. Chem. Res.* **2000**, *33*, 402–411.

[51] F. G. Buono, D. G. Blackmond, *J. Am. Chem. Soc.* **2003**, *125*, 8978–8979.

[52] M. Quaranta, T. Gehring, B. Odell, J. M. Brown, D. G. Blackmond, *J. Am. Chem. Soc.* **2010**, *132*, 15104–15107.

[53] I. D. Gridnev, J. M. Serafimov, J. M. Brown, *Angew. Chem. Int. Ed.* **2004**, *43*, 4884–4887.

[54] J. Klankermayer, I. D. Gridnev, J. M. Brown, *Chem. Commun.* **2007**, 3151–3153.

[55] I. D. Gridnev, A. Kh. Vorobiev, *ACS Catal.* **2012**, *2*, 2137–2149.

[56] A. Matsumoto, T. Abe, A. Hara, T. Tobita, T. Sasagawa, T. Kawasaki, K. Soai, *Angew. Chem. Int. Ed.* **2015**, *54*, 15218–15221.

[57] T. Gehring, M. Quaranta, B. Odell, D. G. Blackmond, J. M. Brown, *Angew. Chem. Int. Ed.* **2012**, *51*, 9539–9542.

[58] D. A. Evans, D. Seidel, *J. Am. Chem. Soc.* **2005**, *127*, 9958–9959.

[59] D. A. Evans, S. Mito, D. Seidel, *J. Am. Chem. Soc.* **2007**, *129*, 11583–11592.

[60] M. Magrez, J. Wencel-Delord, A. Alexakis, C. Crévisy, M. Mauduit, *Org. Lett.* **2012**, *14*, 3576–3579.

[61] R. Pollice, M. Schnürch, *Chem. Eur. J.* **2016**, *22*, 5637–5642.

[62] M. E. Noble-Terán, T. Buhse, J.-M. Cruz, C. Coudret, J.-C. Micheau, *ChemCatChem* **2016**, *8*, 1836–1845.

[63] M. Kalek, G. C. Fu, *J. Am. Chem. Soc.* **2017**, *139*, 4225–4229.

[64] R. R. Julian, S. Myung, D. E. Clemmer, *J. Phys. Chem. B* **2005**, *109*, 440–444.

[65] G. F. Joyce, G. M. Visser, C. A. A. van Boeckel, J. H. van Boom, L. E. Orgel, J. van Westrenen, *Nature* **1984**, *310*, 602–604.

[66] S. Toxvaerd, *J. Theor. Biol.* **2018**, *451*, 117–121.

[67] J. D. Carroll, *Chirality* **2009**, *21*, 354–358.

[68] Blackmond Donna G., *Phil. Trans. R. Soc. B* **2011**, *366*, 2878–2884.

[69] L.-C. Sögütoglu, R. R. E. Steendam, H. Meekes, E. Vlieg, F. P. J. T. Rutjes, *Chem. Soc. Rev.* **2015**, *44*, 6723–6732.

[70] H. Kuhn, *Curr. Opin. Colloid Interface Sci.* **2008**, *13*, 3–11.

[71] A. J. Wagner, D. G. Blackmond, *ACS Cent. Sci.* **2016**, *2*, 775–777.

[72] S. F. Mason, G. E. Tranter, *Proc. R. Soc. A* **1985**, *397*, 45–65.

[73] D. K. Kondepudi, G. W. Nelson, **1985**, 4.

[74] G. E. Tranter, *Nature* **1985**, *318*, 172–173.

[75] U. J. Meierhenrich, L. Nahon, C. Alcaraz, J. H. Bredehöft, S. V. Hoffmann, B. Barbier, A. Brack, *Angew. Chem. Int. Ed.* **2005**, *44*, 5630–5634.

[76] A. J. MacDermott, *Nature* **1986**, *323*, 16.

[77] R. M. Hazen, D. S. Sholl, *Nature Mater.* **2003**, *2*, 367–374.

[78] K. L. Kovacs, L. Keszthelyi, V. J. Goldanskii, *Orig. Life Evol. Biosph.* **1981**, *11*, 93–103.

[79] F. Hamba, K. Niimura, Y. Kitagawa, K. Ishii, *Physics of Fluids* **2014**, *26*, 017101.

[80] K. Soai, S. R. Hitchcock, in *Encyclopedia of Reagents for Organic Synthesis*, American Cancer Society, **2005**.

[81] R. Contreras, A. Flores-Parra, H. C. López-Sandoval, N. Barba-Behrens, *Coord. Chem. Rev.* **2007**, *251*, 1852–1867.

[82] A. Cruz, I. I. Padilla-Martínez, M. E. Bautista-Ramirez, *Curr. Org. Synth.* **2018**, *15*, 38–83.

[83] A. Cruz, I. Irene Padilla-Martínez, M. Esther Bautista-Ramirez, *Current Organic Synthesis* **2016**, *13*, 2–40.

[84] K. Soai, S. Yokoyama, K. Ebihara, T. Hayasaka, *J. Chem. Soc., Chem. Commun.* **1987**, *0*, 1690–1691.

[85] K. Soai, S. Yokohama, T. Hayasaka, *J. Org. Chem.* **1991**, 4264–4268.

[86] K. Soai, T. Konishi, T. Shibata, *Heterocycles* **1999**, *51*, 1421.

[87] J. Kang, D. S. Kim, J. I. Kim, *Synlett* **1994**, *1994*, 842–844.

[88] J. Kang, J. W. Lee, J. I. Kim, *J. Chem. Soc., Chem. Commun.* **1994**, 2009–2010.

[89] M.-J. Jin, S.-J. Ahn, K.-S. Lee, *Tetrahedron Lett.* **1996**, *37*, 8767–8770.

[90] K. Fitzpatrick, R. Hulst, R. M. Kellogg, *Tetrahedron: Asymmetry* **1995**, *6*, 1861–1864.

[91] J. Kang, J. B. Kim, J. Kim, D. Kim, *Bull. Korean Chem. Soc.* **1998**, *19*, 475–481.

[92] G. D. Potter, M. C. Baird, S. P. C. Cole, *Inorg. Chim. Acta* **2010**, *364*, 16–22.

[93] P. Goodrich, H. Q. N. Gunaratne, L. Hall, Y. Wang, L. Jin, M. J. Muldoon, A. P. C. Ribeiro, A. J. L. Pombeiro, V. I. Pârvulescu, P. Davey, et al., *Dalton Trans.* **2017**, *46*, 1704–1713.

[94] S. J. Coote, S. G. Davies, A. M. Fletcher, P. M. Roberts, J. E. Thomson, *Chem. Asian J.* **2010**, *5*, 589–604.

[95] P. A. Chaloner, E. Langadianou, *Tetrahedron Lett.* **1990**, *31*, 5185–5188.

[96] D. W. L. Sung, P. Hodge, P. W. Stratford, *J. Chem. Soc., Perkin Trans. 1* **1999**, 1463–1472.

[97] P. A. Chaloner, E. Langadianou, S. A. R. Perera, *J. Chem. Soc., Perkin Trans. 1* **1991**, *0*, 2731–2735.

[98] M. A. Dean, S. R. Hitchcock, *Tetrahedron: Asymmetry* **2009**, *20*, 2351–2356.

[99] C. Bolm, G. Schlingloff, K. Harms, *Chem. Ber.* **1992**, *125*, 1191–1203.

[100] S. Crosignani, G. Desimoni, G. Faita, S. Filippone, A. Mortoni, P. Righetti, M. Zema, *Tetrahedron Lett.* **1999**, *40*, 7007–7010.

[101] C. Girard, J.-P. Genêt, M. Bulliard, *Eur. J. Org. Chem.* **1999**, *1999*, 2937–2942.

[102] H. Furuno, T. Hayano, T. Kambara, Y. Sugimoto, T. Hanamoto, Y. Tanaka, Y. Z. Jin, T. Kagawa, J. Inanaga, *Tetrahedron* **2003**, *59*, 10509–10523.

[103] A. Bayer, M. M. Endeshaw, O. R. Gautun, *J. Org. Chem.* **2004**, *69*, 7198–7205.

[104] A. Watanabe, K. Matsumoto, Y. Shimada, T. Katsuki, *Tetrahedron Lett.* **2004**, *45*, 6229–6233.

[105] F. Estevan, J. Lloret, M. Sanaú, M. A. Úbeda, *Organometallics* **2006**, *25*, 4977–4984.

[106] S. Liu, C. Wolf, *Org. Lett.* **2007**, *9*, 2965–2968.

[107] T. Satyanarayana, B. Ferber, H. B. Kagan, *Org. Lett.* **2007**, *9*, 251–253.

[108] H. Du, X. Zhang, Z. Wang, K. Ding, *Tetrahedron* **2005**, *61*, 9465–9477.

[109] G. E. Coates, D. Ridley, *J. Chem. Soc. A* **1966**, *0*, 1064–1069.

[110] J. Boersma, J. G. Noltes, *J. Organomet. Chem.* **1968**, *13*, 291–299.

[111] P. A. van der Schaaf, E. Wissing, J. Boersma, W. J. J. Smeets, A. L. Spek, G. van Koten, *Organometallics* **1993**, *12*, 3624–3629.

[112] R. Neufeld, D. Stalke, *Chem. - Eur. J.* **2015**, *6*, 3354–3364.

[113] S. Bachmann, B. Gernert, D. Stalke, *Chem. Commun.* **2016**, *52*, 12861–12864.

[114] S. Bachmann, R. Neufeld, M. Dzemski, D. Stalke, *Chem. - Eur. J.* **2016**, *22*, 8462–8465.

[115] A.-K. Kreyenschmidt, S. Bachmann, T. Niklas, D. Stalke, *ChemistrySelect* **2017**, *2*, 6957–6960.

[116] J. Burés, *Top. Catal.* **2017**, *60*, 631–633.

[117] J. Burés, *Angew. Chem. Int. Ed.* **2016**, *55*, 2028–2031.

[118] T. Rosner, P. J. Sears, W. A. Nugent, D. G. Blackmond, *Org. Lett.* **2000**, *2*, 2511–2513.

[119] M. P. Mower, D. G. Blackmond, *ACS Catal.* **2018**, *8*, 5977–5982.

[120] J. Boersma, Wilkinson, G.; Ed.; Pergamon Press, New York, **1982**.

[121] E. V. Anslyn, D. A. Dougherty, *Modern Physical Organic Chemistry*, University Science, Sausalito, CA, **2006**.

[122] H. Zhang, K. Shing Chan, *J. Chem. Soc., Perkin Trans. 1* **1999**, 381–382.

[123] A. Winter, U. S. Schubert, *Chem. Soc. Rev.* **2016**, *45*, 5311–5357.

[124] C.-L. Ho, W.-Y. Wong, *Coord. Chem. Rev.* **2011**, *255*, 2469–2502.

[125] M. Mauro, S. Bellemin-Laponnaz, C. Cebrián, *Chem. Eur. J.* **2017**, *23*, 17626–17636.

[126] M. T. Nguyen, R. A. Jones, B. J. Holliday, *Coord. Chem. Rev.* **2018**, *377*, 237–258.

[127] J. Xiang, C.-L. Ho, W.-Y. Wong, *Polym. Chem.* **2015**, *6*, 6905–6930.

[128] J.-Y. Shao, B.-B. Cui, J.-H. Tang, Y.-W. Zhong, *Coord. Chem. Rev.* **2019**, *393*, 21–36.

[129] M. Enke, D. Döhler, S. Bode, W. H. Binder, M. D. Hager, U. S. Schubert, in *Self-Healing Materials* (Eds.: M.D. Hager, S. van der Zwaag, U.S. Schubert), Springer International Publishing, Cham, **2016**, pp. 59–112.

[130] S. Bellemin-Laponnaz, T. Achard, D. Bissessar, Y. Geiger, A. Maisse-François, *Coord. Chem. Rev.* **2017**, *332*, 38–47.

[131] M. Torres, A. Maisse-François, S. Bellemin-Laponnaz, *ChemCatChem* **2013**, *5*, 3078–3085.

[132] T. Arai, K. Sakagami, *Eur. J. Org. Chem.* **2012**, *2012*, 1097–1100.

[133] M. Torres-Werlé, A. Nano, A. Maisse-François, S. Bellemin-Laponnaz, *New J. Chem.* **2014**, *38*, 4748–4753.

[134] L. Aldea, I. Delso, M. Hager, M. Glos, J. I. García, J. A. Mayoral, O. Reiser, *Tetrahedron* **2012**, *68*, 3417–3422.

[135] B. Angulo, J. I. García, C. I. Herrerías, J. A. Mayoral, A. C. Miñana, *J. Org. Chem.* **2012**, *77*, 5525–5532.

[136] B. Angulo, J. I. García, C. I. Herrerías, J. A. Mayoral, A. C. Miñana, *Org. Biomol. Chem.* **2015**, *13*, 9314–9322.

[137] J. I. García, B. López-Sánchez, J. A. Mayoral, *Org. Lett.* **2008**, *10*, 4995–4998.

[138] J. I. García, C. I. Herrerías, B. López-Sánchez, J. A. Mayoral, O. Reiser, *Adv. Synth. Catal.* **2011**, *353*, 2691–2700.

[139] J. I. García, J. García, C. I. Herrerías, J. A. Mayoral, A. C. Miñana, C. Sáenz, *Eur. J. Inorg. Chem.* **2014**, *2014*, 1531–1540.

[140] S.-W. Chen, J. H. Kim, C. E. Song, S. Lee, *Org. Lett.* **2007**, *9*, 3845–3848.

[141] S.-W. Chen, J. H. Kim, H. Shin, S. Lee, *Org. Biomol. Chem.* **2008**, *6*, 2676–2678.

[142] D. Bissessar, T. Achard, S. Bellemin-Laponnaz, *Adv. Synth. Catal.* **2016**, *358*, 1982–1988.

[143] M. Hager, S. Wittmann, A. Schätz, F. Pein, P. Kreitmeier, O. Reiser, *Tetrahedron: Asymmetry* **2010**, *21*, 1194–1198.

[144] M. Torres, B. Heinrich, K. Miqueu, S. Bellemin-Laponnaz, *Eur. J. Inorg. Chem.* **2012**, *2012*, 3384–3387.

[145] M. Torres-Werlé, B. Heinrich, A. Maisse-François, S. Bellemin-Laponnaz, *Chirality* **2019**, *31*, 903–909.

[146] M. Marinova, M. Torres-Werlé, G. Taupier, A. Maisse-François, T. Achard, A. Boeglin, K. D. "Honorat" Dorkenoo, S. Bellemin-Laponnaz, *ACS Omega* **2019**, *4*, 2676–2683.

[147] T. Portada, M. Roje, Z. Hameršak, M. Žinić, *Tetrahedron Lett.* **2005**, *46*, 5957–5959.

[148] B. M. Armstrong, R. I. Sayler, B. H. Shupe, T. A. Stich, R. D. Britt, A. K. Franz, *ACS Catal.* **2019**, *9*, 1224–1230.

[149] Y. K. Chen, S.-J. Jeon, P. J. Walsh, W. A. Nugent, *Org. Synth.* **2005**, *82*, 87.

[150] J. D. White, D. J. Wardrop, K. F. Sundermann, *Org. Synth.* **2002**, *79*, 130.

[151] J. D. White, D. J. Wardrop, K. F. Sundermann, *Org. Synth.* **2002**, *79*, 125.

[152] K. Tanaka, H. Ushio, Y. Kawabata, H. Suzuki, *J. Chem. Soc., Perkin Trans. 1* **1991**, 1445–1452.

[153] V. Santhi, J. M. Rao, *Synth. Commun.* **2000**, *30*, 4329–4341.

[154] Y. Nagata, T. Yamada, T. Adachi, Y. Akai, T. Yamamoto, M. Suginome, *J. Am. Chem. Soc.* **2013**, *135*, 10104–10113.

[155] Y. Nagata, R. Takeda, M. Suginome, *ACS Cent. Sci.* **2019**, *5*, 1235–1240.

[156] J. H. Hutchinson, D. L. Kuo, T. Money, B. Yokoyama, *J. Chem. Soc., Chem. Commun.* **1988**, 1281–1282.

[157] T. Money, *Nat. Prod. Rep.* **1985**, *2*, 253–289.

[158] J. E. H. Buston, I. Coldham, K. R. Mulholland, *J. Chem. Soc., Perkin Trans. 1* **1999**, 2327–2334.

[159] M. J. Spallek, G. Storch, O. Trapp, *Eur. J. Org. Chem.* **2012**, *2012*, 3929–3945.

[160] K. Soai, M. Nishi, Y. Ito, *Chem. Lett.* **1987**, *16*, 2405–2406.

[161] J. Gawroński, H. Kołbon, M. Kwit, A. Katrusiak, *J. Org. Chem.* **2000**, *65*, 5768–5773.

[162] H. F. Nour, A. M. Lopez-Periago, N. Kuhnert, *Rapid Commun. Mass Spectrom.* **2012**, *26*, 1070–1080.

[163] M. Chadim, M. Buděšínský, J. Hodačová, J. Závada, P. C. Junk, *Tetrahedron: Asymmetry* **2001**, *12*, 127–133.

[164] G. Taupier, A. Boeglin, O. Crégut, L. Mager, A. Barsella, K. Gąsior, J.-L. Rehspringer, K. D. (Honorat) Dorkenoo, *Opt. Mater.* **2015**, *45*, 22–27.

[165] J. A. Giordmaine, *Phys. Rev.* **1965**, *138*, A1599–A1606.

[166] M. A. Belkin, T. A. Kulakov, K.-H. Ernst, L. Yan, Y. R. Shen, *Phys. Rev. Lett.* **2000**, *85*, 4474–4477.

[167] M. A. Belkin, *Phys. Rev. Lett.* **2001**, *87*, DOI 10.1103/PhysRevLett.87.113001.

[168] M. A. Belkin, T. A. Kulakov, K.-H. Ernst, S. H. Han, Y. R. Shen, *Optical Materials* **2003**, *21*, 1–5.

[169] N. Ji, K. Zhang, H. Yang, Y.-R. Shen, *J. Am. Chem. Soc.* **2006**, *128*, 3482–3483.

[170] G. Taupier, M. Saad, M. Romeo, O. Crégut, A. Boeglin, L. Mager, A. Barsella, H. Arhach, J.-L. Rehspringer, K. D. (Honorat) Dorkenoo, *Appl. Phys. Lett.* **2012**, *101*, 241911.

[171] G. Taupier, Microscopie Par Génération de Somme de Fréquences Optiques : Application Aux Polymères de Coordination Chiraux, PhD Thesis, Université de Strasbourg, **2016**.

[172] G. Taupier, M. Torres-Werlé, A. Boeglin, A. Maisse-François, T. Achard, S. Bellemin-Laponnaz, K. D. (Honorat) Dorkenoo, *Appl. Phys. Lett.* **2017**, *110*, 021904.

[173] K. C. Nicolaou, C. J. N. Mathison, T. Montagnon, *Angew. Chem. Int. Ed.* **2003**, *42*, 4077–4082.

[174] K. C. Nicolaou, C. J. N. Mathison, T. Montagnon, *J. Am. Chem. Soc.* **2004**, *126*, 5192–5201.

[175] P. C. B. Page, M. M. Farah, B. R. Buckley, Y. Chan, A. J. Blacker, *Synlett* **2016**, *27*, 126–130.

[176] J. Žurek, E. Svobodová, J. Šturala, H. Dvořáková, J. Svoboda, R. Cibulka, *Tetrahedron: Asymmetry* **2017**, *28*, 1780–1791.

[177] S. K. Sythana, S. R. Naramreddy, S. Kavitake, V. K. CH., P. R. Bhagat, *Org. Process Res. Dev.* **2014**, *18*, 912–918.

[178] A. Korich, T. Hughes, *Synlett* **2007**, *2007*, 2602–2604.

[179] B. Valeur, M. N. Berberan-Santos, *Molecular Fluorescence*, Wiley-VCH Verlag GmbH & Co. KGaA, Weinheim, Germany, **2009**.

[180] S. Nigam, S. Rutan, *Appl. Spectrosc.* **2001**, *55*, 362A-370A.

[181] M. J. Kamlet, J. L. M. Abboud, M. H. Abraham, R. W. Taft, *J. Org. Chem.* **1983**, *48*, 2877–2887.

[182] M. J. Kamlet, J. L. Abboud, R. W. Taft, *J. Am. Chem. Soc.* **1977**, *99*, 6027–6038.

[183] P. Thordarson, *Chem. Soc. Rev.* **2011**, *40*, 1305–1323.

[184] I. Welterlich, B. Tieke, *Macromolecules* **2011**, *44*, 4194–4203.

[185] N. Berova, L. D. Bari, G. Pescitelli, *Chem. Soc. Rev.* **2007**, *36*, 914–931.

[186] G. R. Fulmer, A. J. M. Miller, N. H. Sherden, H. E. Gottlieb, A. Nudelman, B. M. Stoltz, J. E. Bercaw, K. I. Goldberg, *Organometallics* **2010**, *29*, 2176–2179.

[187] S. Banerjee, A. J. Camodeca, G. G. Griffin, C. G. Hamaker, S. R. Hitchcock, *Tetrahedron: Asymmetry* **2010**, *21*, 549–557.

[188] T. Suzuki, Y. Hirokawa, K. Ohtake, T. Shibata, K. Soai, *Tetrahedron: Asymmetry* **1997**, *8*, 4033–4040.

[189] G. P. Moloney, M. N. Iskander, D. J. Craik, *J. Pharm. Sci.* **2010**, *99*, 3362–3371.

[190] R. W. Parrott II, S. R. Hitchcock, *Tetrahedron: Asymmetry* **2008**, *19*, 19–26.

[191] C. D.-T. Nielsen, J. Burés, *Chem. Sci.* **2019**, *10*, 348–353.

[192] H. Li, Y.-F. Han, G.-X. Jin, *Dalton Trans.* **2011**, *40*, 4982–4993.

[193] A. Mouret, L. Leclercq, A. Mühlbauer, V. Nardello-Rataj, *Green Chem.* **2013**, *16*, 269–278.

[194] T. D. W. Claridge, in *High-Resolution NMR Techniques in Organic Chemistry*, Elsevier, **2009**, pp. 303–334.

[195] A. I. Ojeda-Amador, A. J. Martínez-Martínez, A. R. Kennedy, C. T. O'Hara, *Inorg. Chem.* **2016**, *55*, 5719–5728.

[196] J. Burés, *Angew. Chem. Int. Ed.* **2016**, *55*, 16084–16087.

[197] L. P. Hammett, *J. Am. Chem. Soc.* **1937**, *59*, 96–103.

[198] Corwin. Hansch, A. Leo, R. W. Taft, *Chem. Rev.* **1991**, *91*, 165–195.

[199] V. K. Aggarwal, E. Anderson, R. Giles, A. Zaparucha, *Tetrahedron: Asymmetry* **1995**, *6*, 1301–1306.

[200] F. Santiesteban, M. A. Campos, H. Morales, R. Contreras, B. Wrackmeyer, *Polyhedron* **1984**, *3*, 589–594.

Université de Strasbourg

Yannick GEIGER

IPCMS

COMPLEXES CHIRAUX EN CATALYSE ET OPTIQUE NON-LINÉAIRE

Un effet non-linéaire (NLE) hyperpositif a été observé dans l'addition énantiosélective de dialkylzincs sur du benzaldéhyde catalysée par un ligand chiral éphédrine N-benzylé. Ceci est la première preuve expérimentale d'un NLE hyperpositif, où le ee de produit maximal n'est pas obtenu avec un catalyseur énantiopur mais scalémique. L'origine de ce NLE hyperpositif a été identifiée comme venant d'un double système catalytique où des catalyseurs monomériques mais aussi dimériques homochiraux catalysent la réaction, avec des énantiosélectivités différentes. Avec un ligand scalémique, la précipitation d'un aggrégat hétérochiral diminue la quantité de catalyseur homochiral actif et en solution, déplaçant ainsi l'équilibre du catalyseur agrégé vers son homologue monomérique et plus énantiosélectif. Le système catalytique a été étudié en variant la concentration de catalyseur et la température, en déterminant l'état d'agrégation du catalyseur par RMN ^{1}H DOSY, par des études cinétiques et des courbes de Hammett. Une version ditopique du ligand a également été étudiée pour ces effets non-linéaires en catalyse, qui se sont avérés être en partie hyperpositifs.

De nouveaux métallopolymères constitués d'un ligand ditopique chiral et d'un métal ont été développé pour l'application en génération de somme de fréquence (SFG). Les ligands sont préparés par la double addition d'un aminoalcool ou d'une diamine chirale sur du terephtaldehyde pour obtenir des bis-imine-1,4-phenylènes absorbant vers 300 nm. Certains de ces complexes montrent une très forte activité en SFG mais s'avèrent être sensible à l'humidité et donc être difficile à manipuler. Une variante plus stable à base d'une 2-aminoaniline chirale a été développée par la suite et ces propriétés en spectroscopie UV-visible ont été étudiées.

Catalyse énantiosélective, Chimie die coordination, éphédrine, effet non-linéaire hyperpositif, optique non-linéaire, génération de somme de fréquence.

A hyperpositive non-linear effect (NLE) was observed in the enantioselective addition of dialkylzincs to benzaldehyde catalyzed by chiral N-benzyl ephedrine. This is the first experimental evidence of such phenomenon were the maximum product ee is not achieved with an enantiopure, but a scalemic catalyst. The origin for this hyperpositive NLE was traced back to a joint catalysis by monomeric as well as homochiral aggregated catalysts which bear different enantioselectivities. With scalemic ligands, the precipitation of heterochiral aggregates decreases the amount of active homochiral catalyst in solution, thus shifting the equilibrium from the aggregated to the more enantioselective monomeric catalysts. The catalytic system was studied by varying catalyst concentration and reaction temperature, by analysis of the catalyst aggregation state via ^{1}H DOSY NMR, by kinetic studies and Hammett plots. A ditopic version of the ligand was also studied for NLEs, which in part turned out to be also hyperpositive.

New metallopolymers consisting of a ditopic, chiral ligand and a metal were developed for the application in sum-frequency generation (SFG). The ligands are prepared by the double addition of a chiral aminoalcohol or diamine on terephtaldehyde to obtain bis-imine-1,4-phenylenes absorbing at 300 nm. Some complexes exhibited a very strong activity in SFG but proved to be sensitive to moisture and thus were difficult to handle. A more stable variant based on a 2-aminoaniline was developed and its UV-vis-characteristics were studied.

Enantioselective catalysis, coordination chemistry, ephedrine, hyperpositive non-linear effect, non-linear optics, sum-frequency generation.